«Saint Petersburg OPEN 2020»

BOOK of ABSTRACTS

7th International School and Conference on Optoelectronics, Photonics, Engineering and Nanostructures

April 26-30, 2020 • Saint Petersburg, Russia

“Saint Petersburg OPEN 2020”

7th International School and Conference on Optoelectronics, Photonics, Engineering and Nanostructures

St. Petersburg, Russia, April 26 – 30, 2020

BOOK of ABSTRACTS

Academic University Publishing
St. Petersburg, 2020

7th International School and Conference "Saint Petersburg OPEN 2020" on Optoelectronics, Photonics, Engineering and Nanostructures carries on the tradition of annual conferences and schools organized at St Petersburg Academic University for students, PhD students and young scientists.

More detailed information on the School and Conference is presented on *http://spbopen.spbau.com/*

The Book of Abstracts includes abstracts of contributed works accepted for presentation at the Conference.

The volume was composed by St. Petersburg Academic University from electronic files submitted by the authors. Only minor technical corrections were made by the composers.

Chief Editor: A. E. Zhukov

Published by
St. Petersburg Academic University, Khlopina 8(3),
194021 St Petersburg, Russia
Printed in Russian Federation

Organizer

St Petersburg Academic University

Acknowledgements

RSF

SPIE. STUDENT CHAPTER
SAINT-PETERSBURG ACADEMIC UNIVERSITY RUSSIAN ACADEMY OF SCIENCES

IOP Institute of Physics

Head of Program Committee

Alexey E. Zhukov

corr. member of the RAS, *HSE University, Russia*

Program Committee

Andrey A. Lipovskii (Peter the Great St.Petersburg Polytechnic University, Russia)

George E. Cirlin (Alferov University, Russia)

Valentina V. Zhurikhina (Peter the Great St.Petersburg Polytechnic University, Russia)

Head of Organizing Committee

Alexey E. Zhukov (Alferov University, Russia)

Organizing Committee

Mikhail V. Maximov (Ioffe Institute, Alferov University, Russia)

Andrey A. Lipovskii (Peter the Great St.Petersburg Polytechnic University, Russia)

Valentina V. Zhurikhina (Peter the Great St.Petersburg Polytechnic University, Russia)

Vladimir V. Korenev (Alferov University, Russia)

Eduard I. Moiseev (Alferov University, Russia)

Anna S. Dragunova (Alferov University, Russia)

Svetlana A. Kadinskaya (Alferov University, Russia)

Crystal growth and structural properties of nanostructures

Nanobiotechnology, Biophysics and Biophotonics

Lasers, solar cells and other optoelectronic devices

Nanophotonics, Spectroscopy, Microcavities, Optics, Plasmonics

Spintronics, Electro- and Magnetooptics

Electric, Magnetic and Microwave Devices

Other Aspects of Nanotechnology

Optical and photoelectric characteristics of the ZnS / por-Si / Si structure performed by different technological routes

D A Lizunkova[1], **I A Shishkin**[1], **N V Latukhina**[1]
[1]Samara National Research University, Samara 443086, Russia

Abstract. The research object is multilayer photosensitive structures with a porous silicon working layer and a semiconductor zinc sulphide. The purpose of this work is to study the effect of the zinc sulphide coating thickness on the structure optical properties. The reflection and photosensitivity spectral characteristics of structures with various thicknesses zinc sulphide coating were studied. It was shown that the optimal coating thickness is 0.056 micrometers

A promising direction to improve the efficiency of silicon solar cells is the transition to multilayer structures with anti-reflective coatings. The main losses in structures based on single crystal silicon(c-Si) are associated with the inability to absorb photons whose energy is less than the width of the silicon band gap and thermalize photons with energy greater than the band gap width. To eliminate these losses in the construction of silicon solar cells, the strategy of using multilayer structures of materials with different density is applied. Nanocrystalline silicon is a material with a band gap greater than that of monocrystalline silicon.

A simple and effective way to obtain nanocrystalline silicon is to create a layer of porous silicon on a monocrystalline silicon substrate [1]. The advantages of the resulting porous layer are a high degree of absorption of incident light on the surface, reducing the rate of surface charge recombination. A significant light reflection coefficient (35-40%) from the silicon surface in the spectral sensitivity range of photovoltaic devices (400-1100 nm) necessitates the clarification of the working surface of the silicon solar cell. At the heart of the action of most antireflective coatings is the phenomenon of interference of light waves. For silicon solar cell, a semiconductor coating of zinc sulfide is often used, which is also a sub-alloying layer that reduces contact resistance. Experiments with porous silicon conducted by a number of researchers have shown that it exhibits good anti-reflective properties [2]. However, the combined effect of the porous layer and the interference coating on the properties of solar cells has not been investigated.

In this paper, the optical and photoelectric properties of multilayer photosensitive structures containing layers of porous silicon and zinc sulfide are investigated. The porous layer was prepared by electrochemical etching in an alcoholic solution of hydrofluoric acid. Zinc sulfide films were deposited by thermal evaporation in vacuum at different deposition times. The thickness of the porous layer was about 8 microns, the thickness of zinc sulfide films ranged from 0.027 to 0.063 microns.

Studies of the spectral characteristics of reflection have shown that the thickness of the ZnS film has little effect on the course of the curve in the visible range, indicating a high transparency of zinc sulfide in this region of the spectrum (Fig.1).At the same time, the reflection in the infrared part of the spectrum decreases with increasing thickness.

Photosensitivity studies also show a dependence on coating thickness. A thin layer of ZnS (0.027 μm) and a thick layer (0.063 μm) reduce the sensitivity of the samples. Better sensitivity was shown by structures with a film thickness of about 0.056 microns (Fig.2).

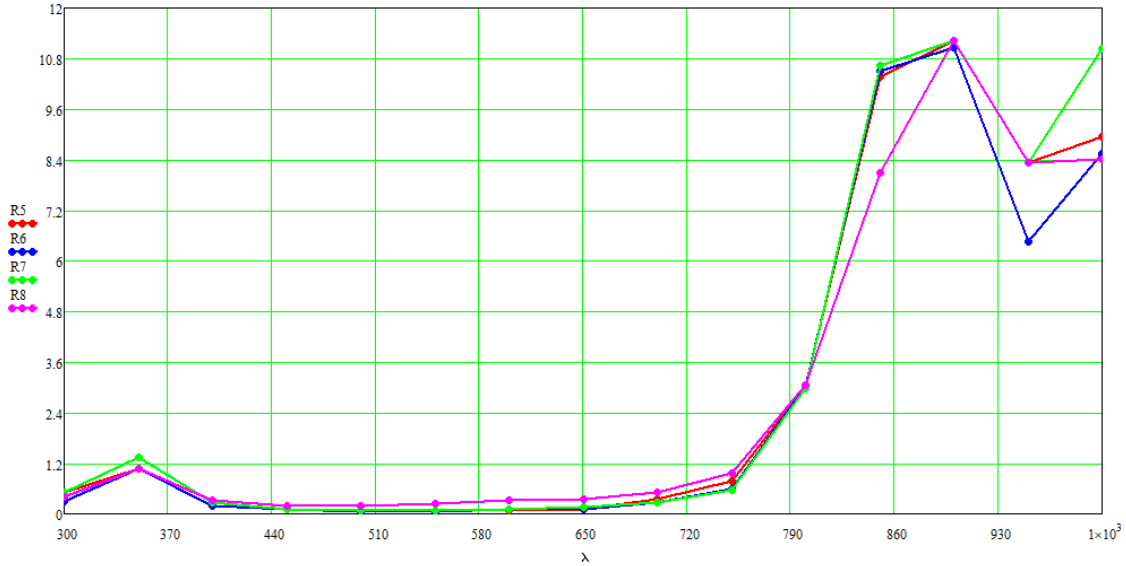

Figure 1. Spectral reflection characteristic of structures with different ZnS thickness

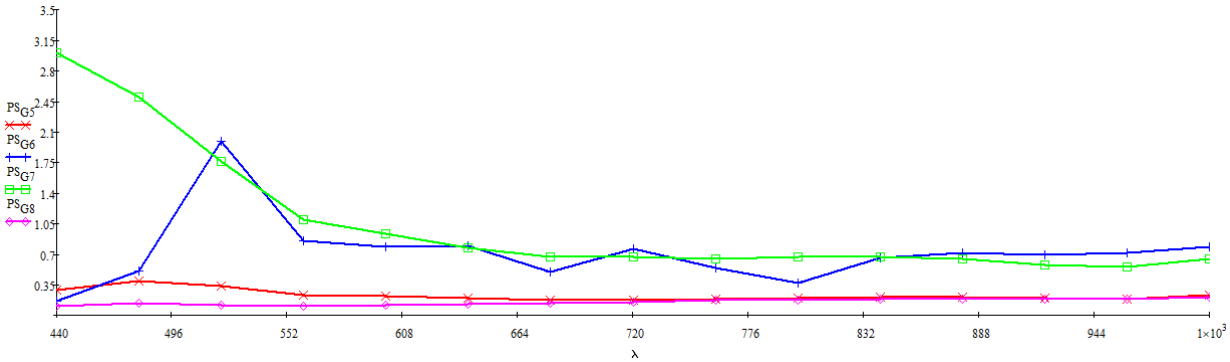

Figure 2. Spectral characteristic of photosensitivity of structures with different ZnS thickness

Acknowledgments

This work was supported by the Foundation for Assistance to Small Innovative Enterprises, grant № 12980GU/2018.

References

[1] N. Latukhina, A. Rogozin, G. Puzyrnaya, D. Lizunkova, A. Gurtov, S. Ivkov *Procedia Engineering* **V.104, 31** (2015). P. 157-161

[2] V.M. Aroutiounian, K.R. Maroutyan, A.L. Zatikyan, K.J. Touryan. *Thin Solid Films* 403 –404 (2002) 517–521

.

Au nanoparticle buried between magnetron oxide thin layers

A Kondrateva[1,2], Ya Enns[1,2], I Komarevtsev[1], D Kudryashov[2], M Mishin[2]

[1]Peter the Great St.Petersburg Polytechnic University, St. Petersburg 194021, Russia
[2]St. Petersburg Academic University, St. Petersburg 194021, Russia

Abstract. In this work, a versatile method to increase the optical response of the oxide nanostructures is proposed. It combines a magnetron deposition of oxide matrix with the thermal deposition and aggregation of metallic nanoparticles, allowing the preparation of wide band gap oxide heterostructures with buried plasmonic Au nanoparticles. Thin layers of Si/TiO_2 and Si/NiO were deposited by reactive magnetron sputtering in a 2D nanostructure, followed by 2.5 nm gold layer thermal deposition and thermal annealing at 550 °C to induce the growth of the Au nanoparticles. Then Si/TiO_2/AuNP and Si/NiO/AuNP were covered by TiO_2 and NiO respectively. The reflectance maximum of the LSPR band appeared at around 720-750 nm for both heterostructures. It is demonstrated that Si/TiO_2/AuNP/TiO_2 and Si/NiO/AuNP/NiO nanostructures can enhance optical response in comparison with Si/TiO_2 and Si/NiO. The results obtained indicate a broad prospect of using the formed structures in the field of integrated optoelectronic devices.

1. Introduction

The ability to control the propagation of electromagnetic waves underlies integrated nanophotonics [1]. One of the control methods is the organization of surface plasmon resonance. Localized plasmon resonance (LPR) is a development of the model of surface plasmons for the case of geometrically isolated nano-objects whose geometrical dimensions are comparable to the wavelengths of the excitation plasmon radiation [2]. Specifying the shape and size of the nanoobject allows to control the optical absorption of the nanoparticle due to the displacement of the resonance peak. For example, an increase in the diameter of gold nanoparticles from 25 to 84 nm leads to a shift in the peak of the photoluminescence peak from 300 to 500 nm under ultra violet irradiation [3].

Plasmonic vibrations are sensitive to the properties of the medium in which they propagate. So, for example, a change in the refractive index of the medium leads to a shift in the resonance frequency. This effect is used in Surface Enhanced Raman Spectroscopy (SERS). The LPR effect is also used in magnetic data recording [4], cancer phototherapy [5] and in thermovoltaic devices [6].

The introduction of plasmon nano-objects, for example, gold nanoparticles (AuNP), into the matrix of wide-gap material allows to translate the edge of the fundamental absorption of the material into the visible region [7] and control the type and magnitude of the conductivity of the material [8].

In this paper, we propose the implementation of LPR on gold hemispherical particles buried in a semiconductor oxide matrix (fig.1). An analysis of the literature shows that such heterostructures turn out to be effective highly sensitive elements of optical sensors for various purposes. The aim of this work was to obtain Si/TiO_2/AuNP/TiO_2 and Si/NiO/AuNP/NiO nanocomposite coatings active in the visible wavelength range and study their properties.

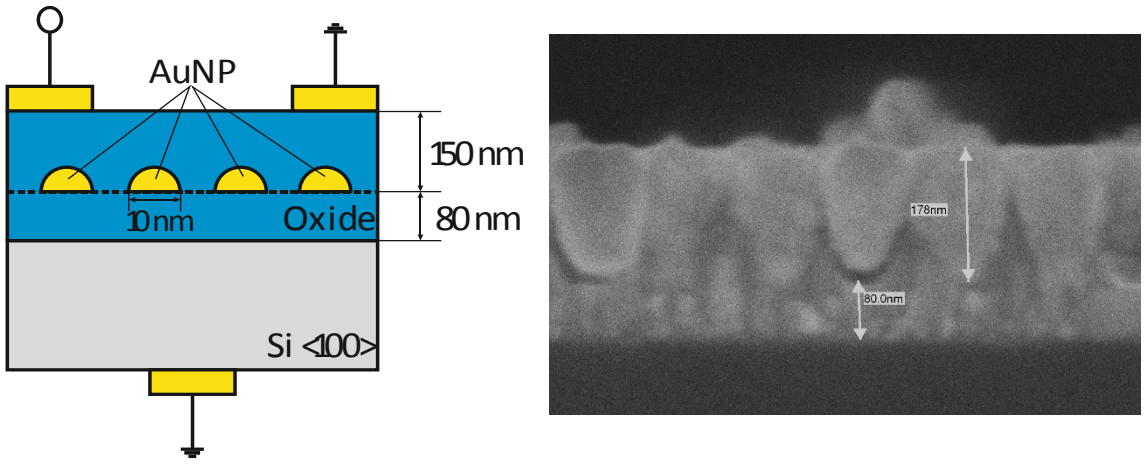

Figure 1(a, b). (a) Schematic plasmonic heterostructures Si/TiO_2/AuNP and Si/NiO/AuNP; **(b)** Top-view Si/TiO_2/AuNP.

2. Results

In this work, a technique for optically active nanocomposite structures consisting of an oxide matrix containing plasmonic NPs formation were demonstrated. The aim of the work was to validate the proposed methodology and study the optical and electrical characteristics of the plasmonic heterostructures Si/TiO_2/AuNP/TiO_2 and Si/NiO/AuNP/NiO. The structures coatings fabricated showed a maximum reflection in the visible (red region) of the spectrum, which corresponds to the LPR region of gold nanoparticles. The resulting structures were characterized by satisfactory surface and through conductivity, the ratio of light and dark currents reached 5/1 in the case of Si/TiO_2/AuNP/TiO_2.

3. Acknowledgments

Authors wishing to acknowledge the Ministry of Education foundation for financial support assistance (№ FSRM-2020-009).

References

[1] Aderhold J, Davydov V Yu, Fedler F, Klausing H, Mistele D, Rotter T, Semchinova O, Stemmer J, Graul J 2001 *J. Cryst. Growth* **151** 701
[2] Strite S, Morkoc H 1992 J. Vac. Sci. Technol. B **10** 1237
[3] Nakamura S, Senoh M, Nagahama S, Iwase N, Yamada T, Matsushita T, Kiyoku H and Sugimoto Y 1996 *Japan. J. Appl. Phys.* **35** L74
[1] Kirchain R, Kimerling L 2007 *Nature Photonics* **6** 303
[2] Guo J, Li E, He J 2020 *Bulletin of the American Physical Society*
[3] Petryayeva E, Krull U 2011 *Analytica chimica acta* **706** 8
[4] Ashizawa Y, Ota T, Tamura K 2013 *J. Magnetics Soc. Jap.* **37** 111
[5] Chen C, Chan Y-C, Hsiao M, Liu R-S 2016 *ACS Appl. Mat. Int.* **8** 32108
[6] Silva-Oelker G, Jerez-Hanckes C, Fay P 2019 *J. Quant. Spec. Radiative Transfer* **231** 61
[7] Mishin M, Vorobyev A, Kondrateva A, Koroleva E, Karaseov P., Bespalova P, Shakhmin A, Glukhovskoy A,Wurz M, Filimonov A 2018 *Sem. Sci. Tech.* **33** 075014
[8] Bespalova P, Vorobyev A, Kondrateva A, Maxim M 2019 *IEEE EExPolytech* 244.

Self-organization of nano-islands of pure components during growth of a multicomponent crystal via step-flow mode

A V Redkov, S A Kukushkin

Institute for Problems in Mechanical Engineering RAS, St. Petersburg 199178, Russia
E-mail: avredkov@gmail.com

Abstract. The work is devoted to an analysis of the processes taking place at the surface of the multicomponent crystal during its growth in step-flow mode. It is shown, that at certain conditions nucleation and even self-organization of pure components in a form of nanoislands can take place. The mechanism of formation of such islands is discussed. The criterion for the conditions at which nucleation takes place is derived.

1. Introduction

Nowadays, multicomponent crystals and thin films are increasingly being used in modern electronics, optics, and many other directions of technology, instead of single-components ones (like classical semicondutors: silicon and germanium). Such materials as widebandgap semiconductors (GaN,AlN,SiC) found applications in optoelectronic devices and high electron mobility transistors. In order to make a device of high efficiency, it is necessary to produce its basement – crystalline thin films of high quality. In this regard, a detailed understanding of the crystal growth mechanisms and their theoretical description is one of the high priority tasks. The theory of the single-component crystal growth is well-developed, however, there are still some white spaces in the multicomponent crystal growth. In papers [1-2] authors have extended the existing theory of crystal growth via step-flow mode (Burton-Cabrera-Frank mode [3]) for multicomponent case. The main equations, describing growth rate and distribution of adatoms of different components near the step were derived. Some phenomena inherent to multicomponent systems were also demonstrated. One of the effects mentioned in [1] was the formation of islands of pure components at the terraces. Indeed, during the growth of some materials (like gallium nitride in excess of gallium [4]) one can observe in certain cases nucleation of pure single-component islands at the terraces. Since nucleation of nanoislands greatly affects distribution of adatoms at the terrace, it also greatly influences the advancement of steps and thus the overall crystal growth process. Even single-component crystals [5] demonstrate such behaviour sometimes. Thus, the main goal of this work is to analyze the process and to find criterion, at which conditions the formation of nanoislands at the terraces between the steps take place.

2. Nucleation mechanism

Let us consider multicomponent crystal, growing from its vapors according to the reaction:

$$\boldsymbol{A_1 + A_2 + .. + A_n \leftrightarrow C_{(s)}}$$

where A_i are the initial components, $\mathbf{C}_{(s)}$ is the crystalline phase. This chemical reaction is in equilibrium when $\prod_{i=1}^{n} \boldsymbol{P_i} = \boldsymbol{K_{eq}}$, that is the product of pressures $\boldsymbol{P_i}$ of all components equals to equilibrium constant $\boldsymbol{K_{eq}}$ and thus evaporation of adatoms of all components is stabilized with fluxes from vapor to surface. If $\prod_{i=1}^{n} \boldsymbol{P_i} < \boldsymbol{K_{eq}}$ the crystal starts to evaporate, whereas if $\prod_{i=1}^{n} \boldsymbol{P_i} > \boldsymbol{K_{eq}}$ it grows. If

supersaturation is very low $\frac{\prod_{i=1}^{n} P_i}{K_{eq}} - 1 \ll 1$, the preferable mechanism of growth is step-flow growth [1,3]. At this mechanism, as it was shown in [1,3], the surface concentrations of each component are maximal at the terrace between the steps. Thus, if the concentration of some component exceeds critical value for single-component nucleation, the formation of nanoislands will begin. Schematic representation of the described process and growth modes for two-component AB crystal is shown at Fig. 1. If the fluxes J_A and J_B from vapors are too low, then evaporation (or dissolution) of the crystal takes place. If the fluxes J_A and J_B not exceed equilibrium value too much, then the crystal grows in step-flow mode. If the flux of one of the components is too high and exceeds critical value (J_{Acr} or J_{Bcr}), then surface concentrations of adatoms (n_A or n_B) exceed their critical values (n_{Acrit} or n_{Bcrit}) and nucleation of the corresponding component at the terrace begins. Figure 1b demonstrates relation between (n_A, n_B, n_{Acrit} or n_{Bcri}) and shows the resulting nanoislands at the terraces at three cases, marked at Fig. 1a.

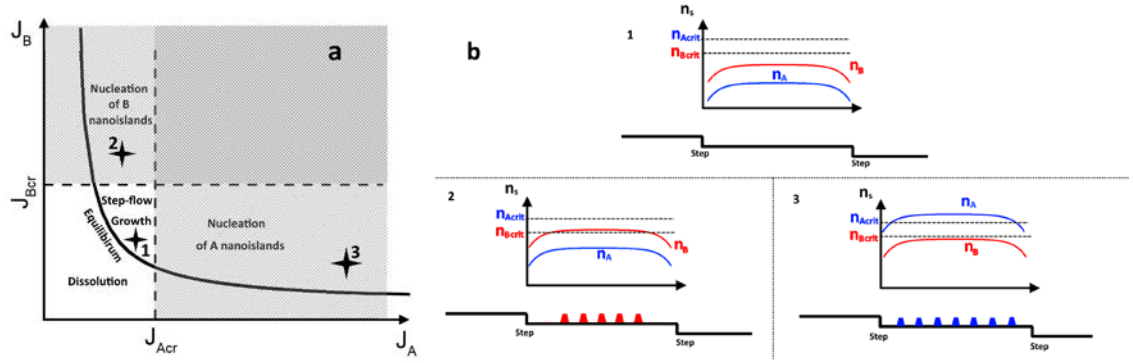

Figure 1. Schematic representation of the growth modes of two-component AB crystal depending on the fluxes of the individual components J_a, J_b (a). Distribution of adatom concentrations n_A and n_B (b) at the terrace at the modes, marked with 1, 2 and 3 on figure (a) and resulting nanoislands.

In this work we found relations between the multicomponent crystal growth rate derived in [1] and fluxes of the components, at which nucleation and self-organization of pure components into nanoislands may begin. The calculations were made based on the classical theory of nucleation. Comparing time of nucleation of single pure-nanoisland τ_n with the time τ_s, which is needed for the moving step to overcome interstep distance allows one to make the following estimates. If $\tau_n < \tau_s$, then at least one island will have time to nucleate. It will change the surface distribution of adatoms and thus the theory proposed in [1,3] for step-flow mode will become inapplicable. If vice versa $\tau_n > \tau_s$ then the crystal growth will proceed via the classical BCF [1,3] mechanism.

3. Conclusions

The formation and self-organisation of pure components at multicomponent crystal growth via step-flow mode is considered. A criterion is found for the regimes at which nucleation of pure components takes place. The results can be used to choose crystal growth conditions at which growth proceeds via classical step-flow mode.

A.V. Redkov thanks the Russian Science Foundation (grant #19-72-00082) for the support of this work.

[1] Redkov A V, Kukushkin S A 2020 *Crystal Growth and Design* doi: 10.1021/acs.cgd.9b01721
[2] Redkov, A. V.; Kukushkin, S. A.; Osipov, A. V. Spiral growth of a multicomponent crystal from vapor of its components. Unpublished work, Proceedings of ECCG6 Conference in *J. Cryst. Growth*, 2018
[3] Burton W K, Cabrera N, Frank F C 1951 *Philos. Trans. R. Soc. A* **243** 299– 358
[4] Karpov S Y, Bord O V, Talalaev R A, Makarov Y N 2001 *Mater. Sci. Eng. B* **82** 22–24 doi: 10.1016/S0921-5107(00)00784-4
[5] Latyshev A V, Aseev A L 1998 *Phys.-Usp.* **41** 1015 doi: 10.1070/PU1998v041n10ABEH000462

Oriented nanonetworks and submicron fibres of nickel as a conducting coating

I Nizameev[1,2], **M Morozov**[2], **G Nizameeva**[3], **S Spiridonov**[2], **M Kadirov**[1]
[1]Arbuzov Institute of Organic and Physical Chemistry, FRC Kazan Scientific Center, Russian Academy of Sciences, Kazan 420088, Russia
[2]Kazan National Research Technical University named after A.N. Tupolev - KAI, Kazan 420111, Russia
[3]Kazan National Research Technological University, Kazan 420015, Russia

Abstract. Within the framework of the work, a methodology was developed for applying oriented nickel nanonetworks to glass, combined into a single system with an oriented network of submicron nickel fibres. The applying technique is original and has not been previously reported in the literature. The basis of the technique is precipitation from the liquid phase by chemical reduction of the nickel salt. The created coating could be interesting for the application in the transparent electrodes field.

1. Introduction

The use of conductive optically transparent coatings has expanded significantly thanks to the development of optoelectronic devices operating on transparent electrodes, such as touch displays and sensors, smart windows and solar panels. In this work, we develop an alternative to indium tin oxide (ITO). ITO is an electrically conductive coating on a glass surface. The developed coating will have good transparency. The basis of the coating is oriented networks [1-7] of nano- and submicron nickel wires. Nickel is a good conductor of electric current. The basis of the technique is precipitation from the liquid phase by chemical reduction of the nickel salt. The main aspects and concepts of the idea were discussed in our previous works [7-8]. The use of an external magnetic field allows obtaining a long-range orientation.

2. Results and discussion

The shaping and orientation of the resulting system are carried out using a micellar template of a surfactant and a magnetic field. Submicron nickel fibres are used to impart unity to the plurality of individual-oriented nickel nanonetworks. The result is a single conductive coating on the surface of the glass.

The nickel nanowires synthesized in this work have a height of less than 10 nm and a width of about 30 nm. Elemental analysis of nanowires was carried out on a transmission electron microscope (TEM) with an energy dispersion attachment. Nickel submicron fibres, also synthesized in a magnetic field by chemical reduction of nickel chloride, are used to create the second level of the network. The submicron network plays two roles: the role of the supporting frame for oriented nanonetworks and the role of the electrically connecting element between the oriented domains of the nanonetworks (Figure 1). Studies by spot X-ray fluorescence analysis confirmed that the fibres are composed of nickel.

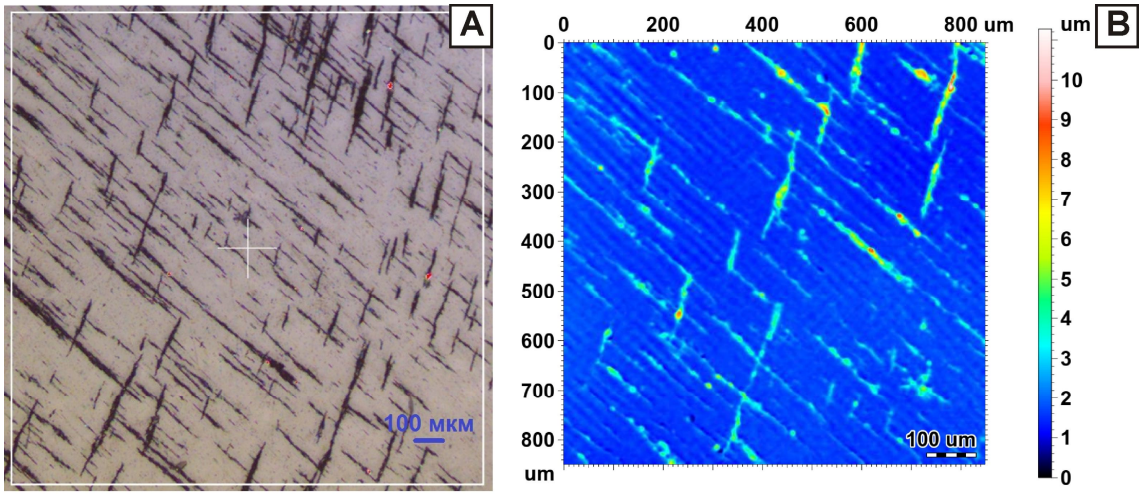

Figure 1. Microscopy images of surface areas of a glass substrate coated with an oriented nickel network: optical microscopy (A), confocal microscopy (B)

In addition to nickel lines, the spectrum contains lines corresponding to the substrate: carbon line ($K_{\alpha 1}$ = 0.28 keV) and copper lines ($L_{\alpha 1}$ = 0.93 keV, $K_{\alpha 1}$ = 8.05 keV, $K_{\beta 1}$ = 8.90 keV).
The surface resistance of the obtained coating on the glass surface was studied by the standard Van der Pauw technique of four-probe measurements. The surface resistance value of the oriented nickel network plus PEDOT: PSS polymer system was 220 Ohm / sq. For comparison, a pure polymer deposited by the same procedure has a surface resistance of 5730 Ohm / sq.

Acknowledgments
The reported study was funded by RFBR according to the research project № 19-03-00345.

References
[1] Deng B. et al. 2015 *Nano letters* **15** 4206.
[2] An, Byeong Wan, et al. 2015 *Nano letters* **16.1** 471.
[3] Zhang, Shupeng, et al. 2016 *Organic Electronics* **32** 149.
[4] Kim, Jiye, et al. 2016 *The Journal of Physical Chemistry C* **120.2** 956.
[5] Chou, Tsu-Ruey, et al. *Organic Electronics* 2017 **48** 223.
[6] Xiong, Zhaoting and Changqing Liu. 2012 *Organic Electronics* **13.9** 1532.
[7] Nizameev I R, Nizameeva G R, Kadirov M K 2019 *ChemistrySelect* **4** 13564.
[8] Nizameev I R, Nizameeva G R, Kadirov M K 2019 *Journal of Physics: Conference Series* **1409** 012038.

Creation of profiled nanostructured surfaces of SiC on Si by the method of substitution of atoms

A.S. Grashchenko[1], **S.A. Kukushkin**[2] **and A.V. Osipov**[3]
[1] Institute for Problems in Mechanical Engineering RAS, Saint Petersburg, 199178, Russia
[2] Peter the Great St. Petersburg Polytechnic University, Saint Petersburg, 195251, Russia
[3] ITMO University, Saint Petersburg, 197101, Russia

Abstract. In the presented work, the method of substitution of atoms was used to form an epitaxial nanostructured profiled SiC layer with a given geometry on a Si crystal. The effect of the process of substitution of atoms on the morphology of a nanostructured Si surface depending on the synthesis time is studied. The conditions are found under which a SiC layer is synthesized on a nanostructured Si surface without modernization of the initial structure.

Introduction

In the works [1, 2], the method of atomic substitution was presented and theoretically described, which is a fundamentally new technology of coating a Si crystal with a thin layer of silicon carbide (SiC) using the chemical reaction (1).

$$2Si(crystal) + CO(gas) = SiC(crystal) + SiO(gas) \uparrow \quad (1)$$

The new principle of this method is that the growth of SiC occurs inside the matrix of the Si crystal by replacing part of the Si atoms with carbon atoms (C). Previously, the method of atomic substitution was used to grow epitaxial SiC layers on porous Si substrates [3, 4]. In this work, the method of atomic substitution is used for the first time to coat a nanostructured ridgy surface of a Si crystal with a thin layer of SiC.

Experimental methods

For the research, we used Si substrates of KDB-12 grade with a crystallographic orientation of (001), which were nanostructured by the Wostec technology. Using this technology, a nanoscale ridgy structure of a triangular shape, oriented along the [011] direction with an average period $\lambda \approx 86$ nm and a height $h \approx 63$ nm, is obtained. Top and bottom images of the initial nanostructure are shown in Figure 1. For all samples, the SiC coating was synthesized in an atmosphere of carbon monoxide (CO) and silicon tetrahydride (SiH_4) with a pressure of 2-3 torr within 10 minutes. For each sample, the synthesis temperature was different. The process of substitution of the surface layer of Si with SiC was carried out at synthesis temperatures from 700 °C to 1300 °C. The increase in the chemical stability of

SiC/Si nanostructures was checked by etching in 5% hydrofluoric acid (HF) for 30, 45, and 120 seconds. Changes in the geometry of the nanostructure after synthesis and chemical etching were monitored using a Supra 40 scanning electron microscope (SEM).

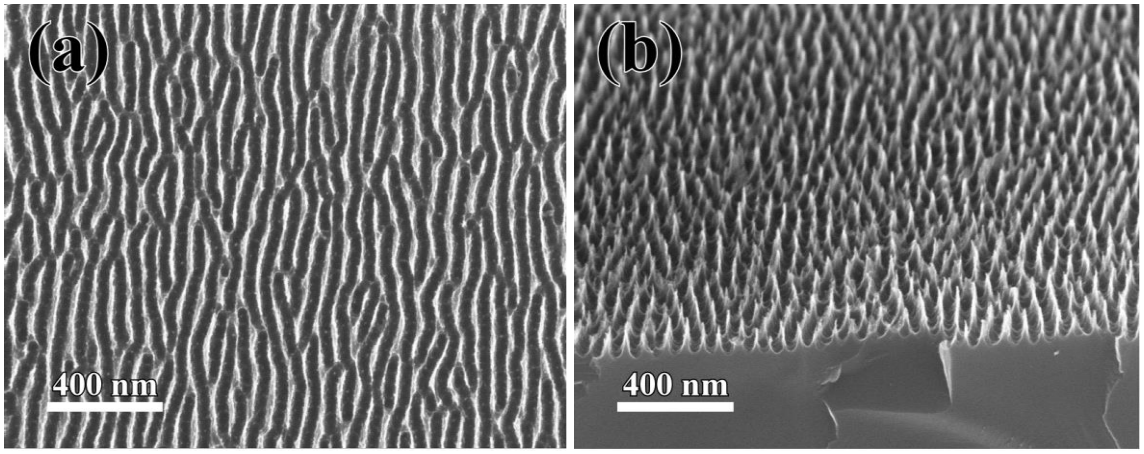

Figure 1(a, b). SEM images of the initial Si nanostructure. **(a)** View from above; **(b)** Side view.

Results

Etching of the initial nanostructured Si surface in 5% HF during 30 seconds led to the complete disappearance of the characteristic ridgy nanostructure. Analysis of SEM images of synthesized structures showed that the samples according to structural features can be divided into two types. The first type includes samples that were synthesized at a temperature of 1100 °C and above. As can be seen from Fig. 2a, the structure of samples of this type radically changed, the sharpness of the ridgy nanostructure became dull, and pores formed under the surface. The structure of these samples did not change after etching during 120 seconds, which indicates the presence of a protective layer of SiC on the surface. Note that as the synthesis temperature increases, the surface roughness decreases, i.e. the height of the characteristic ridgy nanostructure decreases. The remaining samples retained their characteristic ridgy nanostructure without visible changes. Figure 2b shows an image of a sample that was synthesized at a temperature of 1000 °C.

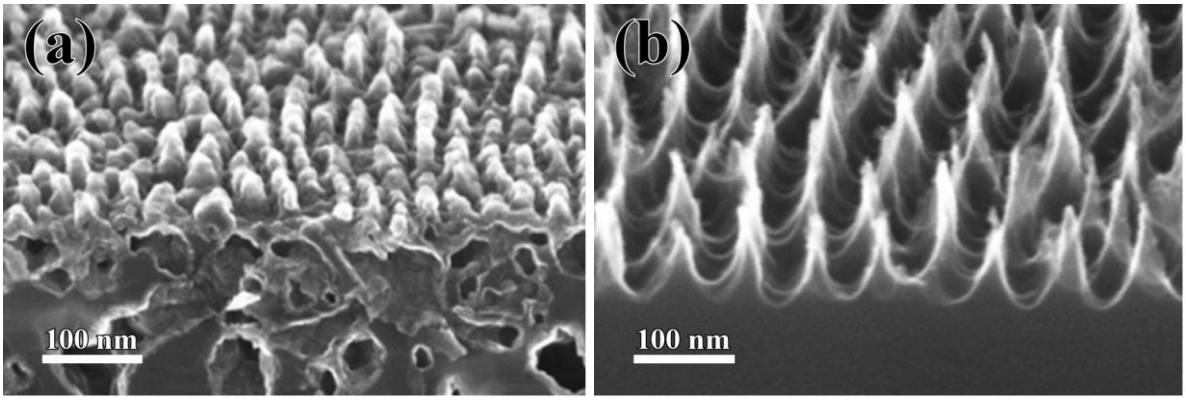

Figure 2(a, b). SEM images of the SiC / Si nanostructure. **(a)** Sample after synthesis at a temperature of 1100 °C; **(b)** Sample after synthesis at a temperature of 1000 °C.

According to the SEM data, it is clear that the structure is identical to the initial one. Etching for 30 seconds did not affect the nanostructure of the samples of the second type except for the sample that

was synthesized at a temperature of 700 °C. In this case, the ridgy structure completely disappeared, indicating the absence of a SiC protective layer. An increase in the etching time to 45 seconds leads to an appearance of structural changes on the surface of the samples synthesized at temperatures of 800, 900, and 1000 °C. These changes are the complete or partial etching of the nanostructure. The sample with a synthesis time of 1000 °C turned out to be the most resistant to etching. The image of the surface of this sample after 45-second etching is shown in Figure 3a, the residual ridgy structure is clearly visible, which is significantly decreased in height. Note that with increasing synthesis temperature, the effect of etching decreases. Etching for 120 seconds completely dissolves the ridgy structure of the samples synthesized at temperatures of 800 – 1000 °C. The analysis of synthesized nanostructures showed that in order to form an effective profiled SiC layer on a nanostructured Si surface, it is necessary to carry out its synthesis by the method of substitution of atoms at temperatures between 1000 °C and 1100 °C. In order to select the optimal conditions, a Si substrate with a ridgy nanostructure was synthesized at a temperature of 1050 °C. According to SEM, the synthesized structure retained its original geometry. Etching of this sample in 5% HF for 30 and 45 seconds did not affect the nanostructured surface. Figure 3b shows the surface of the sample, which was synthesized at a temperature of 1050 °C after 120-second etching in 5% HF. It is seen that the initial ridgy structure was preserved in its original form.

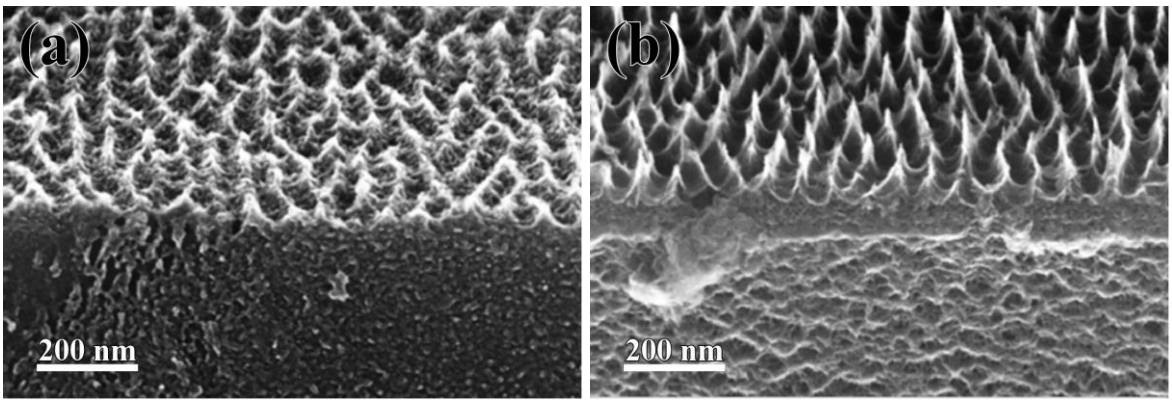

Figure 3(a, b). SEM images of the SiC/Si nanostructures after etching. **(a)** SiC/Si nanostructure synthesized at 1000 °C after 45-second etching; **(b)** SiC/Si nanostructure synthesized at 1050 °C after 120-second etching.

Thus, it has been shown that the method of substitution of atoms can be successfully used to create profiled and chemically stable nanostructured surfaces on Si. Optimal conditions have been selected, under which, on the one hand, the nanostructure retains its characteristic geometric features, and on the other hand, it is coated with an effective protective, profiled SiC layer.

Acknowledgments

The authors thank Quantum Silicon LLC (Moscow, Russia) for providing Si (001) substrates nanostructured using Wostec technology, for SEM images of the carbide coating on the surface of the silicon nano-ridges, and thank V.K. Smirnov for useful discussions of the results.

References

[1] Kukushkin S. A., Osipov A. V. Physics of the Solid State 2008, 50, 1238.
[2] Kukushkin S. A., Osipov A. V. J. Appl. Phys. 2013, **113,** 4909.
[3] Kidalov V. V. et al. ECS Journal of Solid State Science and Technology 2018, 7 №4, 158.
[4] Kidalov V. V. et al. Materials Physics and Mechanics 2018, 36 №1, 39.

Preparation of Si substrates for monolithic integration of III−V quantum dots by selective MBE growth

N A Fominykh[1], M S Sobolev[1], I V Ilkiv[1], T N Berezovskaya[1], D V Mokhov[1], A D Bouravleuv[1]
[1]Alferov University, St. Petersburg 194021, Russia

Abstract. A new method of nanoholes formation by molecular-beam epitaxy (MBE) on different silicon substrates has been investigated. The dependence of substrate orientation and doping type on the shape of the nanoholes has been studied. The samples with an array of nanoholes with 25 nm depth and $6 \cdot 10^8$ cm^{-2} density for subsequent monolithic selective growth of quantum dots (QD) have been received.

Currently silicon plays a key role in the semiconductor electronic industry. However, indirect nature of its band structure extremely complicates the optoelectronic devices implementation on silicon [1]. On the other hand, direct-band compounds of III-V materials are widely used in different photonic devices, such as lasers and photo detectors. Thus, the integration of direct bandgap A_3B_5 compounds with Si is crucial for the realization of photonic integrated circuits [2].

There are several methods of integration direct-band A_3B_5 compounds and silicon. One of them is based on incorporation of QDs as active regions directly in silicon substrate [3]. It has been shown yet that the utilization of pre-patterned substrate surface can be used to control position and form of QDs on the substrate [2]. Different methods of pre-growth substrate treatment are usually used for patterned surface preparation, such as electron beam lithography and dry chemical etching [4]. These methods provide an opportunity to form an ordered array of nanoholes on the substrate surface with certain precision. In the paper [5] it has been shown that subsequent epitaxial growth can be used to synthesize QDs of given composition in the formed array of nanoholes. However, existing methods of pre-growth substrate treatment can lead to increase of the structure cost and degradation of the growth surface and therefore the active region.

Here we report on a new method of nanoholes formation on silicon surface for subsequent monolithic selective growth of QDs. The method of chemical preparation of the Si substrate and certain conditions for the growth of the buffer layer by MBE to create an array of nanoholes with 25 nm depth and $6 \cdot 10^8$ cm^{-2} density has been developed. The dependence of the nanoholes depths on the buffer layer thickness has been investigated. Furthermore, the dependence of the orientation and doping type of substrate on the shape of the nanoholes has been studied.

Acknowledgments
The work was supported by the grant of Minobrnauki № FSRM-2020-0008.

References
[1] Guo X, He A, Su Y 2019 *Journal of Semiconductors* **40** 101304
[2] Reithmaier J P, Benyoucef M 2018 *Semiconductors and Semimetals* **99** 27-42

[3] Norman J C, Jung D, Zhang Z, Wan Y, Liu S, Shang C, Herrick R W, Chow W W, Gossard A G, Bowers J E 2019 *IEEE Journal of Quantum Electronics* **55** 1-11
[4] Benyoucef M, Usman M, Alzoubi T, Reithmaier J P 2012 *physica status solidi (a)* **209** 2402-2410
[5] Zhao Z, Hao Z, Yadavalli K, Wang K L, Jacob A P 2008 *Applied Physics Letters* **92** 083111.

Optical transparency and conductivity of oriented platinum nanonetworks on a glass surface

G Nizameeva[1], **I Nizameev**[1,2], **E. Nefedev**[1], **M Kadirov**[1,2]
[1] Kazan National Research Technological University, Kazan 420015, Russia
[2]Arbuzov Institute of Organic and Physical Chemistry, FRC Kazan Scientific Center, Russian Academy of Sciences, Kazan 420088, Russia

Abstract. In work, the dependence of the sheet resistance of oriented platinum nanowires network on the amount of metal used is investigated. Oriented platinum nanowires are obtained by chemical deposition from an aqueous solution of hexachloroplatinic acid on a glass surface. The topography of the deposited metal layer on the glass is visualized by atomic force microscopy. It has been established that the platinum layer has good optical transparency. The synthesized coating would be of interest in terms of applicability as an optically transparent electrode.

1. Introduction

Recently, much attention has been paid around the world to the creation of optoelectronic devices that operate on transparent electrodes. These include organic transistors, touch displays and sensors, smart windows and solar panels, flexible screens with a large diagonal. Coatings of this kind should combine such properties as transparency in the visible range of radiation and high conductivity. In work, we develop an alternative to indium tin oxide (ITO). ITO is an excellent transparent electrode, but it has some disadvantages.

2. Results and discussion

An original technique was developed for creating a transparent electrically conductive coating based on oriented networks of platinum nanowires [1]. Platinum nanowires are obtained by chemical deposition from the liquid phase using the micellar template cetyltrimethylammonium bromide (CTAB) as the form-setting and orienting component. The application of nanonetworks is made on glass, using a small amount of platinum. Platinum nanowires at the height of 3-6 nm have a width of 50-60 nm, which corresponds to the shape of tape or strip. The ratio of strip length to width is approximately 500 : 1. The strip orientation is high, and the density on the glass surface is low [1]. This phenomenon contributes to obtaining high optical transparency of the layer with a small value of the surface resistance of the coating (Fig. 1).

In addition to developing the concept of creating new types of transparent electrodes, the dependence of the electrical conductivity of the coating on the amount of platinum used is investigated. Different values of platinum concentrations on the surface of the glass substrate were used to synthesize coatings. The coatings were investigated by the van der Pauw method of four-probe measurements of surface resistance. The concentrations of the metal used in the initial solution are as follows: 0.01 mM, 0.02 mM, 0.05 mM, 0.1 mM, 0.2 mM, 0.5 mM and 1 mM. Percolation conductivity arises only at concentrations of platinum equal to 0.1 mM. Sheet conductivity at this concentration is 521 S / cm. For other concentrations, the average conductivity is 0 S / cm.

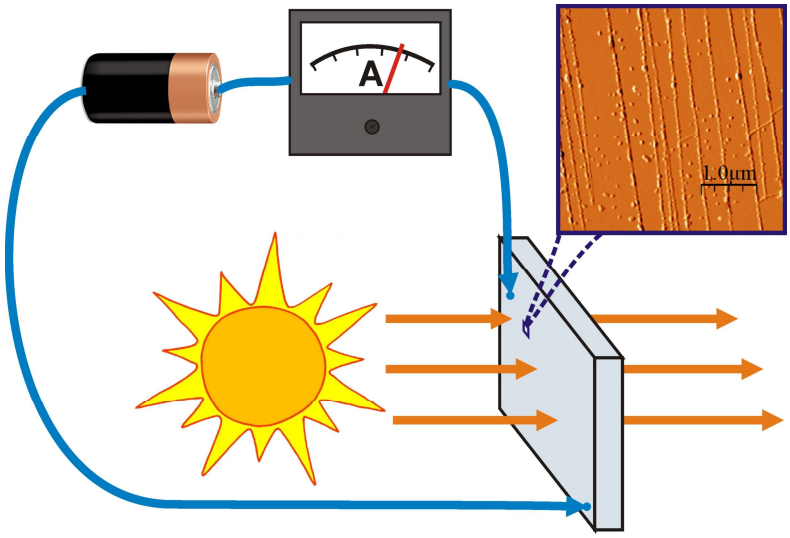

Figure 1. Schematic representation of the results of work

Elemental composition of the samples was investigated by means of X-ray fluorescence analysis using EDX attachment of transmission electron microscopy (TEM-EDX). Figure 2 shows spectrum corresponding to the pure sample (platinum lines are $M_{\alpha 1}$ = 2.050 keV, $L_{\alpha 1}$ = 9.442 keV). The spectrum contains lines of copper and carbon, which corresponds to a substrate on which nanowires of platinum are deposited.

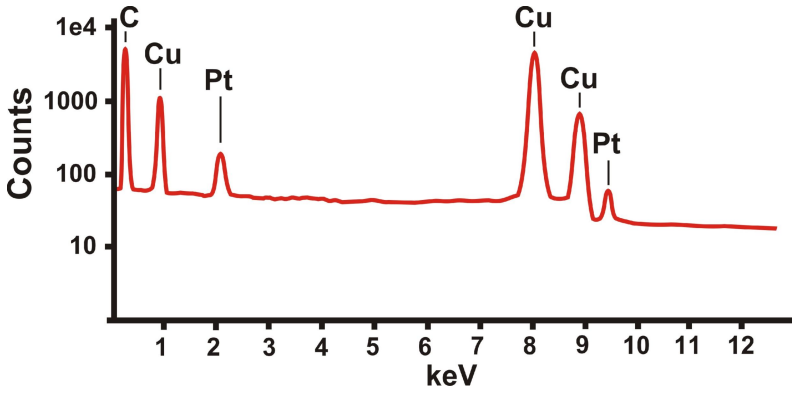

Figure 2. TEM-EDX spectrum of platinum nanowires

Acknowledgments
This work was supported by the President of Russian Federation grant for the governmental support of young Russian scientists [MK-2264.2019.3]

References
[1] Nizameev I R, Nizameeva G R, Kadirov M K 2019 *ChemistrySelect* **4** 13564.

On the synthesis of the carboxylated graphene via graphene oxide liquid-phase modification with alkaline solutions

S A RYZHKOV [1,2], M K RABCHINSKII [1], V V SHNITOV [1], M V BAIDAKOVA [2], S I PAVLOV[1], D A KIRILENKO [1], P N BRUNKOV [1]
[1] Ioffe Institute, 26 Politekhnicheskaya, Saint-Petersburg 194021, Russia
[2] ITMO University, 49 Kronverksky Pr., 197101 Saint Petersburg, Russia

Abstract. In this work we present a facile method for the synthesis of the carboxylated graphene derivate. The resulting material contains up to 7 at.% of carboxyl groups and with negligible content of other oxygen-containing groups. Moreover, formation of large round-shaped nanoscale holes is observed due to the applied synthesis process. The synthesized graphene derivative is of high interest for the sensing applications due to combination of its conductive nature and chemical reactivity provided by the attached carboxyl groups.

1. Introduction

Chemical reduction is considered as a cost-effective and simple approach for graphene manufacturing, which does not require complex and expensive equipment and allows the production of graphene materials in a large scale [1,2]. However, the quality of the material obtained by this method is still far from pure graphene: about 3–10 at.% of oxygen-containing groups remain [1] as well as defects such as tears and holes appear. However, the GO chemical reduction can be considered from a different perspective – not the formation of graphene, but the production of chemically modified graphene materials. The preparation of graphene derivatives nowadays is becoming an important topic in the field of graphene research, since functionalization allows to tune physical and chemical properties, significantly improving the characteristics of graphene materials in various applications.

In this study, we present our results on the synthesis, analysis of physical properties and application of one of these derivatives - carboxylated (C-xy) graphene. We have already reported on the possible synthesis of carboxylated graphene using soft UV radiation [3,4]. This time carboxylated (C-xy) graphene was obtained by one-stage treatment of graphene oxide with sodium hydroxide with the addition of hydrogen peroxide under moderate heating.

2. Materials and methods

Graphene oxide was synthesized via a modified Hummers method with excluding sodium nitrate [5]. Sonication was excluded to obtain suspensions with the utmost size of GO flakes.

Carboxylated graphene was prepared via chemical reduction of GO aqueous suspension applying sodium hydroxide as a reducing agent with the addition of hydrogen peroxide. Briefly, graphene oxide suspension was poured into fluoroplastic cups, sodium hydroxide was added with stirring to reach pH = 11 in the resulting mixture after that hydrogen peroxide was added to reach pH = 10.5. The obtained mixture was heated at 80 °C for 72 hours. The resulting suspension was washed via centrifugation with dilution by deionised water to finally obtain the carboxylated graphene suspension.

3. Results and discussion

As a result of the applied process, partial reduction of the graphene oxide proceeds with part of the functional groups being removed from the surface of graphene oxide, as is seen from the obtained C 1s X-ray photoelectron spectrum. Particularly, the peak at 286.7 eV substantially diminishes after the treatment. At the same time, part of the functional groups of the basal plane of graphene oxide has converted into carboxyl ones, as is seen from the presence of a distinguishable spectral feature at ~289.2 eV. This transformation is accompanied by the formation of a large number of holes in the graphene network, the edges of which are decorated with formed carboxyl groups. The formed holes are large in size, of about 50-70 nm, with sparse distribution, and have a round shape. The latter fact indicates the isotropic nature of etching on chemically active centers of the flake, which proceeds, probably, due to the aforementioned transformation of the basal-plane groups into carboxyl ones.
Owing to the partial reduction, this material is conductive, while chemically active carboxyl groups are retained and increase in concentration in comparison to the case of GO. Collectively, all this makes it possible to consider carboxylated graphene as a promising material for sensory applications.

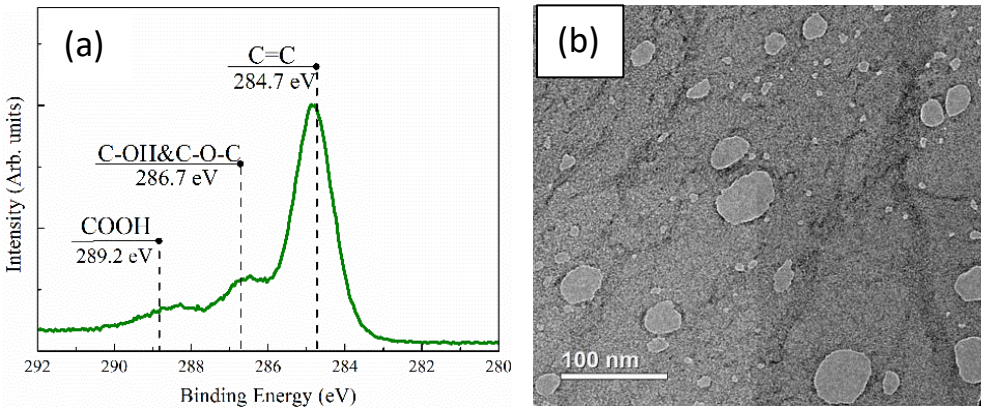

Figure 1 (a) C 1s XPS spectrum and (b) TEM image of the carboxylated graphene

4. Conclusion

In this work, we presented a simple synthesis method for carboxylated graphene suitable for large-scale production. The carboxylated graphene obtained by this method contains structural defects, namely large holes with a low population density decorated with up to 7 at.% of carboxyls. This makes it possible to use this material for further modification. As one of the possible approaches, the modification of carboxylated graphene with aptamers and the formation of reusable, sensitive and selective sensors for the detection of viral diseases, in particular hepatitis B and C is considered.

5. Acknowledgments

This work was financially supported by the Russian Foundation for Basic Research (grant no. 18-29-19172).

References

[1] M.S.A. Bhuyan, M.N. Uddin, M.M. Islam, et al. Int. Nano. Lett., 2016, **6**, 65–83
[2] C.K. Chua and M. Pumera, Chem. Soc. Rev., 2014, **43**, 291–312
[3]M.K. Rabchinskii, V.V. Shnitov, A.T. Dideykin et al. J. of Phys. Chem. C, 2016, **120(49)**, 28261-28269.
[4] M. K. Rabchinskii, V.V. Shnitov, D.Yu. Stolyarova et al. Fullerenes, Nanotubes and Carbon Nanostructures, 2019, **28:3**, 221-225
[5] Hummers, W. S. & Offeman, R. E. Preparation of Graphitic Oxide. J. Am. Chem. Soc., 1958, 80, 1339–1339

Change in the forming voltage of the resistive switching in Pt/HfO_2(10нм)/TaN(5нм)/TiN structure after Ne^+, Ar^+ or Kr^+ ion implantation

O O Permyakova[1, 2], **A V Miakonkikh**[1], **K V Rudenko**[1], **A E Rogozhin**[1]
[1]Laboratory of Microstructuring and Submicron Devices, Valiev Institute of Physics and Technology RAS, Moscow 117218, Russia
[2]Department of Physical and Quantum Electronics, Moscow Institute of Physics and Technology (State University), Moscow 141701, Russia

Abstract. Plasma immersion ion implantation for the HfO_2(10нм)/TaN(5нм)/TiN memristive structures allows to decrease forming voltage of resistive switching process or increase percentage of forming-free structure. In this research we found that ion implantation with Ne^+ ions allows to decrease average forming voltage from -2.3 V to -1.7 V, with heaver Ar^+ ions allows to increase percentage of forming-free structures from 0.1 to 0.6 and ion implantation with Kr^+ ions demolish initial structure and resistive switching is not observe for most structures. Also ion implantation with Ne^+ or Ar^+ doubles resistance ration compared to initial structure.

1. Introduction

The next-generation non-volatile memory should be compatible with modern CMOS technologies one of such is resistive switching memory (ReRAM). Usually, ReRAM cell has metal-insulator-metal (MIM) structure and has following advantages: comparatively simple structure, low power consumption, amazing scalability and high-speed operation [1]. Main disadvantage of ReRAM in the case of compatibility it is forming process due to sharp increase in current.

Several ways to make the ReRAM structure forming-free or reduce forming voltage were proposed such as: oxygen ion implantation [2], grain boundary engineering [3], selection of fabrication parameters [4] and other ways. In this paper we present the investigation of the effect of Ne^+, Ar^+ or Kr^+ ion implantation on the forming voltage for the HfO_2(10нм)/TaN(5нм)/TiN structure.

2. Experiment

The HfO_2(10нм)/TaN(5нм)/TiN structures were formed by PEALD using TEMAH and oxygen plasma for HfO_2 layer, TBTDET and hydrogen plasma for TaN layer. For some samples plasma immersion ion implantation of Ne^+, or Ar^+, or Kr^+ was used to incorporate defects in the dielectric stack. The energy of implanted ions was 5 keV and the dose was 10^{12} cm^{-2}. After that via magnetron sputtering structures were coated with Pt and Ni. Current-voltage characteristics were measured using semiconductor characterization system Keithley 4200-SCS.

3. Result and Discussion

Typical I-V characteristic of measured structure presented on Figure 1a. Effect of ion implantation on the forming voltage could be seen from Table 1. We found that 10% cells of initial structures did not

require forming process. Also after Ne^+ implantation the average forming voltage decreased from 2.3 V to 1.7 V and the number of forming-free structures remained the same. However for heavier Ar^+ ions forming voltage increased on 0.2 V, but in this case we found 60% forming-free structures. When we used even heavier Kr^+ ions resistive switching was observed for only a few cycles, this might be connected with the fact that Kr^+ ions breakdown structure too hard.
Another effect of immersion ion implantation is that ion implantation doubled median resistance ration compared to initial structure (Figure 1b, 1c) and dispersion of resistance values also increased.

Table 1. Forming voltages.

Structure	Forming voltage, V	SET voltage, V	RESET voltage, V	Yield
Initial	-2.3 ± 1.0	0.71 ± 0.07	-0.90 ± 0.09	0.1
Ne^+ ion implantation	-1.7 ± 1.0	0.80 ± 0.10	-0.84 ± 0.05	0.1
Ar^+ ion implantation	-2.5 ± 0.9	0.81 ± 0.14	-0.89 ± 0.07	0.6

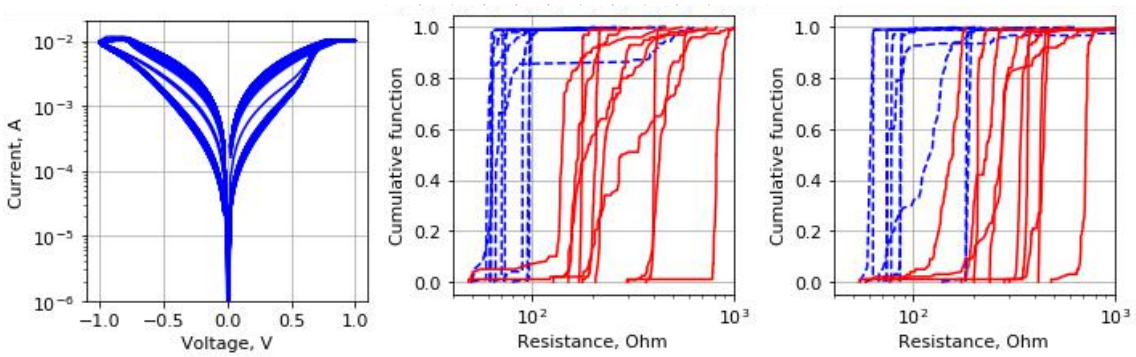

Figure 1. a) I-V characteristic of initial structure for 100 first cycles; Cumulative diagram for resistance values of initial structure - (b), after implantation with with Ar+ - (c), values of every structures shown for 10 different devices, R_{ON} - blue dashed line and R_{OFF} - red solid line.

4. Acknowledgments
The investigation was supported by Program №0066-2019-0004 of the Ministry of Science and Higher Education of Russia for Valiev Institute of Physics and Technology of RAS and partially supported by RFBR, grant №18-37-20076.

References

[1] F. Pan et al. 2014 *Materials Science and Engineering R: Reports* **83** 1-59
[2] W. Kim et al. 2016 IEEE International Electron Devices Meeting (San Francisco) pp. 4.4.1-4.4.4.
[3] Stefan Petzold et al. 2019 *Advanced Electronic Materials* **5** 1900484
[4] N. Ghenzi et al. 2015 Applied Physics Letters **106** 123509

Modified silicone rubbers for fabrication and contacting of flexible suspended membranes of n-/p-GaP nanowires with single-walled carbon nanotube transparent contact

F.M. Kochetkov,[1] V.V. Neplokh,[1] V.V. Fedorov,[1] A.D. Bolshakov,[1] G.E. Cirlin,[1] R.M. Islamova,[2] I.S. Mukhin[1]

[1]*Alferov University, St. Petersburg, 194021, Russia*

[2]*Saint Petersburg State University, 199034 Saint Petersburg, Russia*

e-mail: azemerat@rambler.ru

The appealing properties of organic light emitting diodes (OLEDs), i.e. relatively easy and inexpensive fabrication, and efficient electroluminescence (EL) allowed the OLED-based industry to conquer a significant market share. For instance, modern smartphones are mostly produced with the OLED displays [1]. However, organic materials are far behind the inorganic materials in terms of stability and external quantum efficiency (EQE) of EL in optical range, especially in blue and red region [2], which for inorganic devices becomes close to 100%. Inorganic LEDs based on compounds of arsenides, nitrides, phosphides etc. are envisioned to be the materials for the LEDs with the efficiency close to the theoretical limit. The recent commercial application of OLEDs instead of inorganic materials is explained mainly by difficulties of combination of different radiative materials necessary for an RGB full color screen. Indeed, the mainstream thin film technology is hard to adapt for small high resolution screen, because it requires either advanced post-growth processing, or combination of very different crystalline materials [3]. The flexible devices fabrication based on thin films imposes even greater complications, i.e. ultra thin wafer epitaxy or release of the synthesized material from the wafer. Nanowire (NW) or microwire (MW) design of inorganic devices has several significant advantages, especially for substrate-free device fabrication. Wires have a small footprint, therefore they can be mechanically removed from the initial growth substrate [4]. High surface to volume ratio leads to an effective relaxation of the elastic strain due to the lattice mismatch of III-V heterostructures, therefore low structural defect concentration can be achieved even for a high lattice mismatch. Core-shell wire heterostructures also have effective light extraction and current injection, which is very important for optoelectronic applications, e. g. LEDs. One of the main attractive features of NW devices is the possibility to combine very different materials, e. g. nitrides and arsenides or phosphides. The NWs can be encapsulated into a polymer matrix (i.e. elastomer) [5] and then released from the wafer. The elastomer/NW membrane can then be electrically connected with conductive transparent electrodes, and the membranes of different materials may be stacked onto each other to form composite device with multiple line EL. The pixel contacts to membranes with different color channels could be provided independently, thus the elastomer/NW devices can be considered as inorganic analogue to OLED devices.

The main goal of this work was a synthesis of the advanced silicon rubber specially for the membrane device fabrication. In order to complete this task, a demonstration of electrical current transport through the NWs encapsulated in the polymer matrix was required. However, the electrical current can go through shuntings or other defects of the polymer/NW membrane system (e. g. NW surface or interface states in polymer/NW border). Therefore, for a direct demonstration, that the fabricated membranes feature desirable electrical performance, i.e. the current spreads through the front contact layers, then goes inside the NWs and finally is collected by the rear contact, we made a high Schottky barriers for both/one side of the membranes. In this case we have a distinguishable signature in the I-V curves, and EBIC mapping is possible. Alternatively, a low Schottky or an absence of it (which is, actually,

desirable in the final optoelectronic devices) is very difficult to distinguish from the shunting and the samples are not suitable for the EBIC microscopy, therefore we discuss the fabricated samples with ohmic contacts after demonstrating reliable Schottky contacting.

References

[1] W. Telieps and E. Bauer, Surf. Sci., 1985, 162, 163–168

[2] A. Ishizaka and Y. Shiraki, J. Electrochem. Soc., 1986, 133, 666–671.

[3] K. Imamura, M. Takahashi, Asuha, Y. Hirayama, S. Imai and H. Kobayashi, J. Appl. Phys., 2010, 107, 054503.

[4] V. V. Fedorov, A. D. Bolshakov, L. N. Dvoretckaia, G. A. Sapunov, D. A. Kirilenko, A. M. Mozharov, K. Y. Shugurov, V. A. Shkoldin, G. E. Cirlin and I. S. Mukhin, Semiconductors, 2018, 52, 2092–2095.

[5] A. Kaskela, A. G. Nasibulin, M. Y. Timmermans, B. Aitchison, A. Papadimitratos, Y. Tian, Z. Zhu, H. Jiang, D. P. Brown, A. Zakhidov and E. I. Kauppinen, Nano Lett., 2010, 10, 4349–4355.

The influence of the Fe^{2+} doping concentration on structure and spectroscopic properties of transparent glass-ceramics based on Fe^{2+}:$ZnAl_2O_4$ nanocrystals

K Eremeev[1], O Dymshits[2], I Alekseeva[2], A Khubetsov[2], M Tsenter[2], A. Zhilin[2], L Basyrova[3], P Loiko[4], V Popkov[1]

[1]Saint-Petersburg State Institute of Technology, 26 Moscovsky Pr., 190013 St. Petersburg, Russia

[2]S.I. Vavilov State Optical Institute, 36 Babushkina St., 192171 St. Petersburg Russia

[3]ITMO University, 49 Kronverkskiy Pr., 197101 St. Petersburg, Russia

[4] CIMAP, CNRS, Université de Caen Normandie, 6 Boulevard du Maréchal Juin, 14050 Caen Cedex 4, France

Abstract. Transparent glass-ceramics based on Fe^{2+}-doped gahnite nanocrystals were prepared by melt-quenching technique. The glass-ceramics were characterized by X-ray diffraction, Raman and optical spectroscopy. Increasing the iron content speeds up liquid phase separation, gahnite and crystobalite crystallization due to iron ions entering the crystals. Glass-ceramics exhibit a broadband (1.6-2.3 μm) absorption due to the $^5E \rightarrow {}^5T_2$ (^5D) transition of Fe^{2+} ions in T_d sites in gahnite crystals. The glass-ceramics are promising as saturable absorbers for the mid-infrared spectral range.

1. Introduction

Materials doped with tetrahedrally (T_d) coordinated Cr^{2+} and Fe^{2+} ions and demonstrating intense broadband absorption in the mid-IR spectral range of 2–3 μm are promising for applications in saturable absorbers for lasers of this spectral region. One of such materials is spinel, $MgAl_2O_4$, doped by Fe^{2+} ions [1]. Gahnite, $ZnAl_2O_4$ also belongs to spinel family. Recently, transparent gahnite ceramics were fabricated [2]. Compared with single crystals and optical ceramics, glass ceramics (GCs) containing nanoscale gahnite crystals have advantages due to flexibility and convenience of glass technology production, a variety of phase assemblages, structures and crystal sizes. In this work, we aimed to study novel transparent GCs based on Fe^{2+}:$ZnAl_2O_4$ nanosized crystals and elucidate the role of iron ions in formation of these materials.

2. Experimental

The glass of the ZnO-Al_2O_3-SiO_2 system nucleated by TiO_2 was doped with 0.6 and 1.0 mol% FeO and melted at 1560 °C with stirring. To promote the growth of spinel nanocrystals, the glass was subjected to secondary two-stage heat-treatments at 720 to 1200 °C with a holding time of 6 h. The structure of the glass and transparent GCs was studied by differential scanning calorimentry (DSC), density measurements, X-ray powder diffraction (XRD), Raman and absorption spectroscopy.

3. Results and discussion

In transparent GCs prepared at 720 – 950°C, Fe:$ZnAl_2O_4$ is the only crystalline phase; TiO_2 (rutile) additionally crystallizes in the range of 1000 - 1200 °C. The size of gahnite crystals increases from 50 to 400 Å with increasing the heat-treatment temperature, the volume fraction of gahnite increases as well. Addition of iron oxide facilitates gahnite (Fig. 1(a)) and crystobalite (Fig. 1(b)) crystallization. With increasing the iron content, the gahnite unit-cell parameter *a* increases for all heat-treatment temperatures. Raman spectroscopy data indicate the formation of iron-doped liquid phase-separated titanium-containing regions and their preservation until rutile starts to crystallize at 1000 °C.

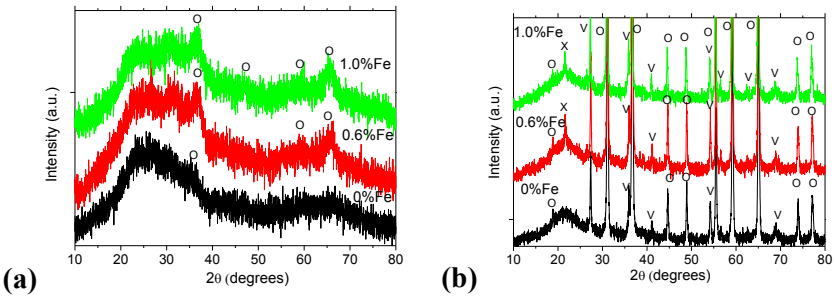

Figure 1(a, b). XRD patterns of Fe:$ZnAl_2O_4$ GCs **(a)** prepared at 720 °C for 6 h; **(b)** at 720 °C/6 h + 1200 °C/6 h. Symbol "o" stands for $ZnAl_2O_4$,, "v" for rutile and "x" for cristobalite.

In absorption spectra of GCs, a broad band from 1.6 to 2.3 μm is observed due to the $^5E \rightarrow {}^5T_2$ (^5D) transition of Fe^{2+} ions in T_d sites in gahnite nanocrystals (Fig. 2). Its intensity increases with temperature. The Beer's law is obeyed for this absorption band implying that the iron ions distribution between phases in GCs doped with 0.6 and 1.0 mol% FeO is independent of the iron content in GCs.

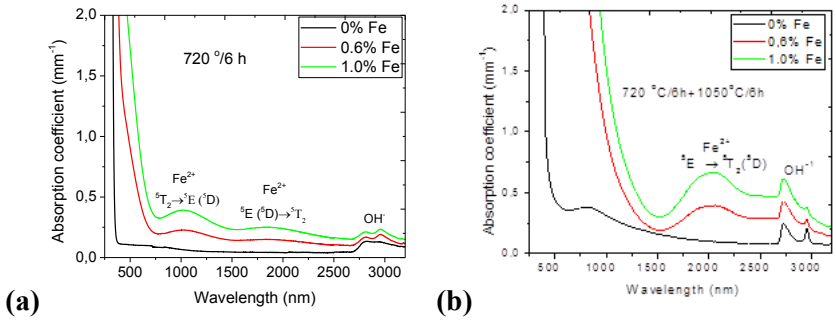

Figure 2. Absorption spectra of Fe^{2+}:$ZnAl_2O_4$ GCs **(a)** prepared at 720 °C/6 h**; (b)** 720 °C/6 h + 1050 °C/6 h.

4. Conclusions

We report on synthesis, structure and optical properties of novel transparent Fe^{2+}-doped gahnite glass-ceramics in dependence of iron content. These nanosized materials are promising for saturable absorbers of mid-infrared lasers (1.6-2.5 μm). Further studies will focus on the measurements of absorption saturation and laser damage threshold of these glass-ceramics.

Acknowledgments

This work was partly supported by the RFBR (Grant 19-03-00855).

References

[1] Basyrova L, Balabanov S, Belyaev A, Drobotenko V, Volokitina A, Vitkin V, Dymshits O, Loiko P 2019 *J. Phys.: Conf. Ser.* **1410** 012123.

[2] Belyaev A, Basyrova L, Sysoev V, Lelet M, Balabanov S, Kalganov V, Mikhailovski V, Baranov M, Vitkin V, Dymshits O, Loiko P 2020 *J. Alloy Compd*, **829** 154514.

Effect of the Al content in the substrate on the In nanodroplets growth by droplet epitaxy

M S Solodovnik[1,2], **S V Balakirev**[2], **M M Eremenko**[1], **N E Chernenko**[1,3], **O A Ageev**[1]

[1]Research and Education Center "Nanotechnologies", Southern Federal University, Taganrog 347922, Russia

[2]Department of Nanotechnologies and Microsystems, Southern Federal University, Taganrog 347922, Russia

[3]Department of Radio Engineering Electronics, Southern Federal University, Taganrog 347922, Russia

Abstract. The paper presents the results of an experimental study of the effect of Al content in the epitaxial surface layer on the growth of In nanostructures formed by droplet epitaxy. We have shown that an increase in the Al content leads to a decrease in the droplet density and an increase in their size. We also showed that the influence of the Al content on the droplet characteristics is much less significant than that in case of the Stranski-Krastanov growth. The increase in the critical thickness of droplet formation on Al-containing surfaces when the temperature decreases is not significant. It allows us to control quantum dot emission wavelength almost independently of their geometric characteristics.

The growth of InAs quantum dots on $Al_xGa_{1-x}As$ surfaces with different Al content allows for control of the radiation wavelength over a wider range, in contrast to InAs/GaAs systems. However, in the Stransky-Krastanov growth mode InAs QDs significantly increase their density and decrease their average size with increasing Al content. In addition, the Stransky-Krastanov mode involves the formation of a wetting layer, which can reduce the efficiency of devices based on such QDs due to the casting of charge carriers on states in the wetting layer. In contrast to the Stransky-Krastanov mechanism, the droplet epitaxy method allows suppressing the formation of a wetting layer, thereby providing better quality of nanostructures based on them.

The purpose of this work is experimentally study the growth of In metal nanodroplets on $Al_xGa_{1-x}As$ surfaces with different Al content formed by the droplet epitaxy method. To do this, we used Semiteq STE 35 to grow three series of samples that differ in the Al content on the surface – 0, 50 and 100%. The growth temperature and deposition thickness in each series varied in the range from 150 to 450°C and from 0.75 to 3 ML, respectively. Then all samples were investigated by the method of SEM.

Analysis of the results showed that with increasing Al content, the average diameter of in drops also increases, while their density on the surface decreases (**Figure 1 (a, b)**). This contradicts the growth of QDs in the Stransky-Krastanov mode on AlGaAs and Ga/AlGaAs surfaces in a droplet epitaxy. This effect is most significant at temperatures above 250°C. **Figure 2** shows that the critical thickness of in droplet formation on the $Al_{0.5}Ga_{0.5}As$ and AlAs surfaces is 1.25 and 1.5 ML at T = 150°C, whereas for the GaAs surface it is 3 ML. That is, the critical thickness on Al-containing surfaces remains virtually unchanged with increasing temperature, while on the GaAs surface it decreases from 3 to 1 ML.

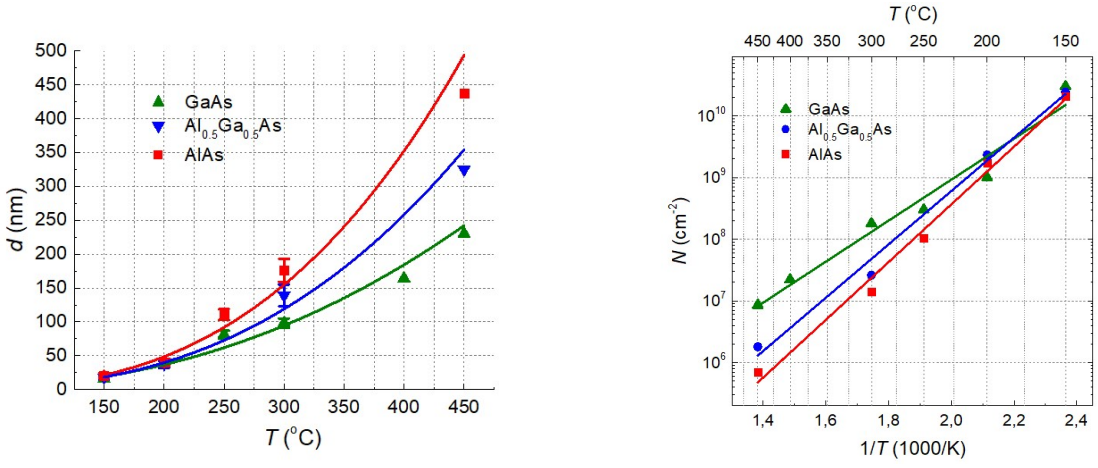

a) **b)**

Figure 1 (a, b). Temperature dependences of the (a) average diameter and (b) surface density of nanostructures after deposition of 3 ML In on the GaAs, $Al_{0.5}Ga_{0.5}As$ and AlAs surfaces.

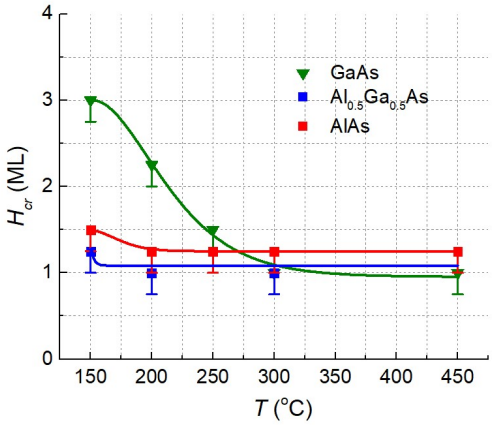

Figure 2. Temperature dependences of the critical thickness of droplet formation on various surfaces.

Thus, we have shown that the mobility of adatoms in the process of droplet epitaxy demonstrates abnormal behavior with an increase in the Al content in the surface layer compared to the Stransky-Krastanov method. It means, a significant change in the bandgap of a QD matrix induced by the addition of Al atoms into the epitaxial layer does not lead to a significant change in QD geometrical characteristics.

Thus, we can conclude that droplet epitaxy allows controlling the device characteristics by altering the bandgap width almost without an influence on the size and density of QDs.

Acknowledgments

This work was supported by the Russian Science Foundation Grant No. 19-79-10099. The results were obtained using the equipment of the Research and Education Center and Center for Collective Use "Nanotechnologies" of Southern Federal University.

References

[1] Balakirev S V , Solodovnik M S and Ageev O A 2018 *Phys. Status Solidi B* **255** 1700360.

[2] Balakirev S V, Solodovnik M S, Eremenko M M, Konoplev B G and Ageev O A 2019 *Nanotechnology* **30** 505601

GaAs epitaxial growth on modified on-axis Si(001) substrates

M M Eremenko[1], M S Solodovnik[1,2], S V Balakirev[1,2], N E Chernenko[1], I N Kots[1], O A Ageev[1]

[1]Research and Education Center "Nanotechnologies", Southern Federal University, Taganrog 347922, Russia

[2]Department of Nanotechnologies and Microsystems, Southern Federal University, Taganrog 347922, Russia

Abstract. In this work, the effect of the dose of implantation of Ga atoms into the silicon surface on the epitaxial growth of GaAs was investigated. We demonstrate that the deposition of GaAs occurs mainly on modified areas. Separate crystallites of GaAs with an irregular shape are formed on modified areas at the lowest dose of Ga implantation equal to 1 pC/μm^2, whereas an increase in the dose of Ga implantation leads to the coalescence of GaAs areas. At a maximum dose of 21 pC/μm^2, degradation of the morphology and a decrease in the degree of filling of the area are observed, which is also confirmed by an increase in the roughness of the structure.

The integration of highly efficient light emitting sources based on III/V structures with silicon technology remains a difficult task today [1]. The preparation of III/V on silicon devices is complicated due to the presence of a large number of threading dislocations, antiphase domains, and thermal cracks formed during the growth of a polar semiconductor on a non-polar substrate with different lattice constants and thermal expansion coefficients [1]. To date, a large number of techniques are used to reduce more defects during the monolithic integration of III/V on Si [1, 2], but they do not allow achieving the desired results – the monolithic integration of III/V structures on the on-axis silicon substrates. This is expected to combine the advantages of GaAs technology (high-performance laser sources) and Si technology (high-speed information processing). Therefore, the development of completely new approaches to solve this problem is required.

In this paper, we study the effect of the dose of implanted Ga in the Si substrate on the subsequent growth of GaAs on these modified Si areas. Ga implantation was carried out by the method of focused ion beams at a constant current and at a different implantation dose. The epitaxial materials were fabricated using a SemiTEq STE 35 molecular beam epitaxy system with solid-state sources. The removal of native oxide was carried out by annealing the samples in a chamber at 900°C, after which the substrate was cooled and a 200 nm GaAs buffer layer was grown.

Figure 1 shows scanning electron microscopy images of the morphology of GaAs deposited on Si. Based on the results obtained, the degree of filling of the structures and their roughness at various doses of implantation of Ga atoms were calculated. It was shown that the deposition of GaAs occurs mainly on modified areas. At the lowest dose of Ga implantation equal to 1 pC/μm^2, the deposition of GaAs on modified areas occurs as separate crystallites with an irregular shape. An increase in the implantation dose leads to GaAs coalescence and further filling of the areas. At doses of 1, 3, 7, 21 pC/μm^2, the degree of filling of the modified areas was 67%, 91%, 99%, and 95%, the roughness was 55, 27, 23, 37 nm for each dose, respectively. As can be seen, at a maximum dose of 21 pC/μm^2, a

morphology deterioration and a decrease in the degree of filling of the area are observed, which is also confirmed by an increase in the roughness of the structure.

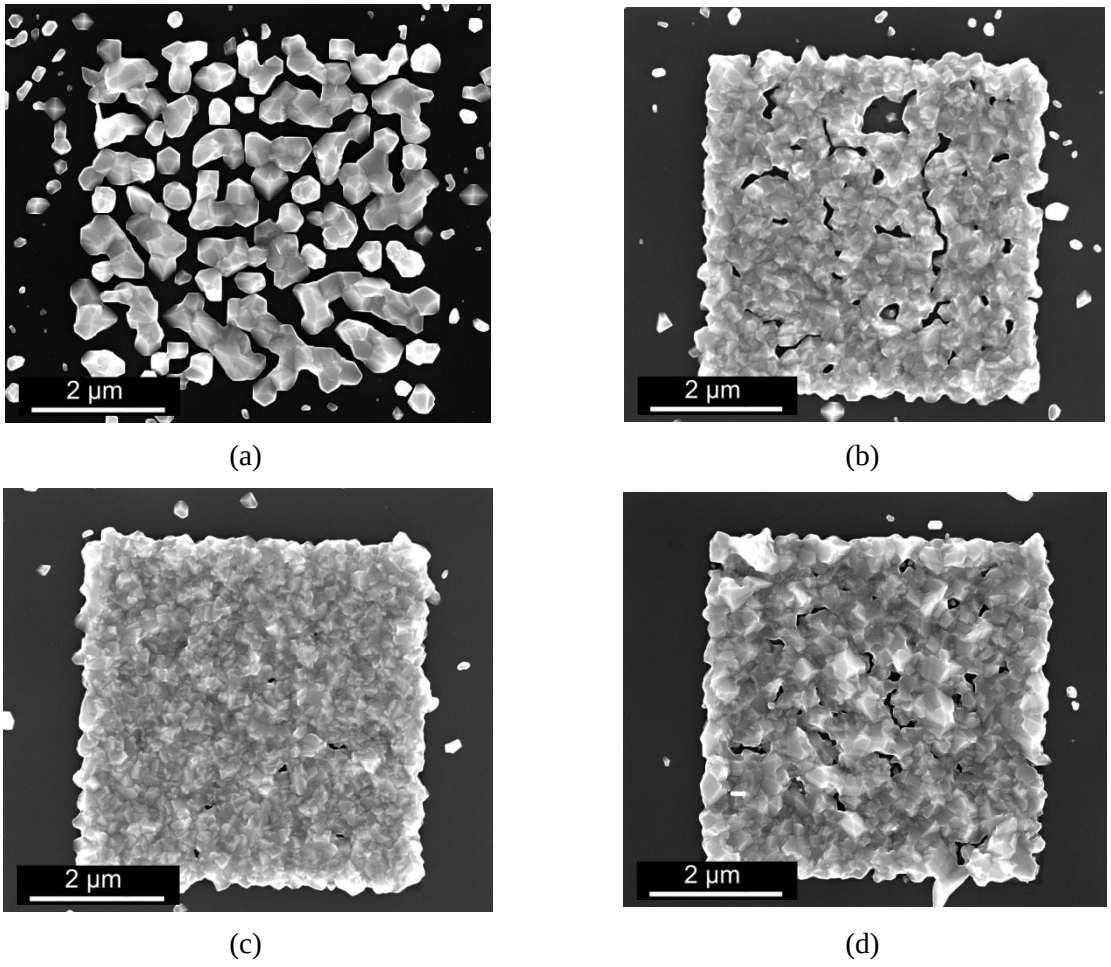

(a) (b)

(c) (d)

Figure 1. SEM images of the amorphous areas of Si after deposition of 200 nm GaAs with different dose of Ga implanted: a) 1 pC/μm^2, b) 3 pC/μm^2, c) 7 pC/μm^2, (d) 21 pC/μm^2

Therefore, we can conclude that there is an optimal dose of Ga implantation into the silicon surface at which the best parameters of the grown structures are observed. Despite the fact that the GaAs buffer is defective, the use of nucleation layers and the technique of multi-stage growth of buffer layers will provide a smooth two-dimensional interface.

Acknowledgments
This work was supported by the Grant of the President of the Russian Federation No. MK-477.2019.8. The results were obtained using the equipment of the Research and Education Center and Center for Collective Use "Nanotechnologies" of Southern Federal University.

References
[1] Tang M, Park J-S, Wang Z, Chen S, Jurczak P, Seeds A, Liu H 2019 *Prog. Quant. Electron* **66** 1-18
[2] Wan Y, Li Q, Geng Y, Shi B, Lau K M 2015 *Appl. Phys. Lett.* B **107** 081106

The misfit stresses of dilatation lines in semiconductor nanoheterostructures with angular boundaries

Zh V Gudkina[1, 2], **M Yu Gutkin**[2, 3, 4], **S A Krasnitckii**[1, 3, 4], **T S Argunova**[1]
[1]Ioffe Institute RAS, St. Petersburg 194021, Russia
[2]Peter the Great St. Petersburg Polytechnic University, St. Petersburg 195251, Russia
[3]Institute of Problems of Mechanical Engineering RAS, St. Petersburg 199178, Russia
[4]ITMO University, St. Petersburg 197101, Russia

E-mail: gudkinazhanna@mail.ru

Abstract. Misfit strains and stresses of a dilatation line in an elastic body with an angular free surface are studied with potential application to semiconductor nanoheterotechnology. The misfit stresses are obtained by the method of virtual surface dislocations. Analysis of this solution is carried out numerically by using the misfit stress maps built in a cross section of the system.

1. Introduction

Studying the fields of misfit strains and stresses in semiconductor nanoheterostructures of complex architecture is an important problem for development of these nanoheterotechnologies. Differences in crystal lattices and thermal expansion coefficients of materials that compose nanostructure devices, significantly influence their work properties. Misfit stresses and residual thermoelastic stresses cause changes in the physical and service characteristics of the corresponding nanostructure devices. The relaxation of these stresses is accompanied by the formation of various defects, in particular, misfit dislocations, which also lead to degradation of device properties and shorten their service life. Therefore, the development of theoretical models of such defective structures is one of the key areas of fundamental research necessary for the development of modern semiconductor nanoheterotechnologies.

The solution of the boundary-value problems in the theory of elasticity allows us to study the features of the misfit stress fields at the stage preceding their relaxation, therefore, the formulation of such problems is an important initial stage in the development of theoretical models. In particular, one of such tasks is the search for elastic fields caused by dilatation inclusions with various shapes in an elastic body with an angular boundary. Such a boundary can be considered as a wedge-shaped protrusion or cut with an arbitrary opening angle. In this case, an infinitely thin dilatation line with its three-dimensional (3D) dilatational eigenstrain can serve as an elementary misfitting inclusion. Having a solution for such a line, it is possible to obtain by simple integration similar solutions for long inclusions with cross sections of arbitrary shape.

2. Methods and approaches

Consider an infinitely thin dilatation line embedded in an elastic body having the shape of a long straight wedge (Fig. 1). We assume that this line is subjected by a 3D dilatational eigenstrain, while its elastic moduli are the same as in the surrounding matrix. To solve this boundary-value problem, we

use the method of virtual surface dislocations (VSDs). In the past, this method was successfully applied to various boundary-value problems of the theory of defects. In particular, similar problems were solved for edge dislocations in homogeneous [1] and composite [2] wedge-shaped bodies and screw dislocations placed near a triple junction of different wedge-shaped phases [3]. Within this method, the desired stress field is written as $\boldsymbol{\sigma} = \boldsymbol{\sigma}^{\infty} + \boldsymbol{\sigma}^{\boldsymbol{v}}$, where $\boldsymbol{\sigma}^{\infty}$ is the well-known stress field of the dilatation line in an infinite elastic medium [4], and $\boldsymbol{\sigma}^{\boldsymbol{v}}$ is an extra stress field of the VSDs, continuously distributed over the free surfaces of the body in such a way that to ensure the fulfilment of traction boundary conditions on its angular boundary (Fig. 1). In such a formulation, the problem is reduced to finding four unknown functions of distribution of the VSDs from the boundary conditions of the problem that gives a system of four integral equations. With the Mellin integral transform, this system reduces to a system of algebraic equations for determining the Mellin images of the distribution functions of the VSDs. As a result, the additional field $\boldsymbol{\sigma}^{\boldsymbol{v}}$ is found in an integral form, as the inverse Laplace-Mellin transform of the products of the well-known Mellin images of the stresses of individual VSDs and the found Mellin images of distribution functions of the VSDs. The analysis of the obtained solution was carried out numerically using the stress maps built in the cross section of the system. These maps showed, in particular, that the boundary conditions of the problem are satisfied with good accuracy.

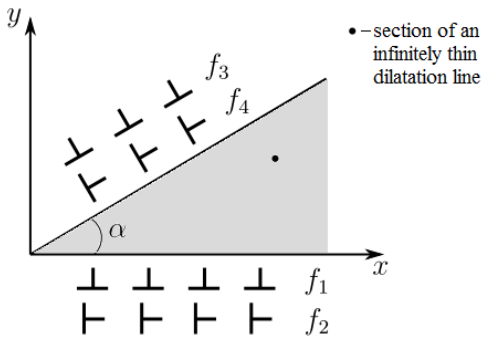

Figure 1. Dilatation line in a wedge-shaped elastic body with free boundaries. The distribution functions f_1, f_2, f_3, and f_4 of virtual surface dislocations are sketched at the boundaries.

3. Summary

In the present work, the method of virtual surface dislocations (VSDs) is used to find a solution of the boundary-value problem in the theory of elasticity for a dilatation line embedded in an elastic body with an angular boundary. The solution is found as a superposition of the well-known stress field of the dilatation line in an infinite elastic medium [4] and an extra stress field of the VSDs. The latter is given by the inverse Laplace-Mellin transform of the products of the Mellin images of the stresses of individual VSDs and their distribution functions. With this solution on hand, one can obtain by simple integration similar solutions for long inclusions of arbitrary-shape cross sections in various semiconductor nanoheterostructures.

Acknowledgments

The authors are thankful to the Russian Foundation of Basic Research (grant No 19-29-12041) for financial support.

References

[1] Hecker M, Romanov A E 1992 *Phys. Stat. Sol.* A **130** 91
[2] Hecker M, Romanov A E 1993 *Mater. Sci. Eng.* A **164** 411
[3] Gutkin M Yu, Romanov A E, Aifantis E C 1996 *Phys. Stat. Sol.* A **153** 65
[4] Kolesnikova A L, Soroka R M, Romanov A E 2013 *Mater. Phys. Mech.* **17** 71

Infrared absorption and photoconductivity in Be-doped GaAs/AlGaAs quantum wells

N Yu Kharin[1], M Ya Vinnichenko[1], I S Makhov[1], V Yu Panevin[1], L E Vorobjev[1], S V Sorokin[2], I V Sedova[2] and D A Firsov[1]

[1] Peter the Great St. Petersburg Polytechnic University, 29 Polytechnicheskaya, St. Petersburg, 195251, Russia
[2] Ioffe Institute, 26 Polytechnicheskaya, St. Petersburg, 194021, Russia

E-mail: mvin@spbstu.ru

Abstract. The energy spectrum of acceptor and subband states in Be-doped GaAs/AlGaAs quantum wells was calculated. Acceptor-related light absorption and photoconductivity spectra were experimentally studied at low lattice temperatures in the infrared spectral range. The features in the spectra can be attributed to the hole transitions from the ground acceptor states to the excited acceptor states and size-quantized subbands. Spectral positions of experimentally observed absorption peaks are in satisfactory agreement with theoretical calculations.

1. Introduction

Quantum cascade lasers [1] are promising sources of far-infrared radiation but their high cost and complicated technology require the development of new methods for generating the far-infrared light emission. The use of optical carrier transitions through the acceptor states in quantum wells (QWs) makes it possible to create a new mid- and far-infrared radiation sources. The studies of optical transitions associated with acceptors are also interesting since in narrow GaAs-based QWs the binding energy of acceptors can exceed the energy of optical phonons [2]. Therefore, in narrow QWs the nonradiative capture of excited by light or ionizing electric field nonequilibrium holes on the ground acceptor states will be significantly suppressed due to the impossibility of optical photon emission. In order to investigate the energy spectrum of acceptors in QWs it is useful to analyze the equilibrium infrared absorption and photoconductivity (PC). Note, that complicated structure of the acceptor wavefunctions [3, 4] leads to non-trivial spectral and polarization dependencies of acceptor-related optical absorption and PC.

In this work, we used and modified the method based on determining the energy of the impurity levels by solving the Schrödinger equation with the Hamiltonian in the form of a sum of kinetic energy (the Luttinger Hamiltonian), the potential energy of holes, and the energy of the Coulomb interaction with the charged acceptor. Also, this paper focuses on the experimental verification of calculated band diagram and absorption spectra by study of infrared absorption and PC in Be-doped GaAs/AlGaAs QWs.

2. Sample and experimental technique

The Be-doped GaAs/$Al_{0.4}Ga_{0.6}As$ multiple QW nanostructure (200 QWs) was MBE grown. The 3 nm QWs were separated with 7 nm barriers. Samples were prepared in multipass geometry which allows the independent studies of the absorption of light of two polarizations. Infrared absorption and photoconductivity spectra were obtained using a vacuum Fourier transform spectrometer with a spectral resolution less than 2 meV. The samples were placed into a closed cycle optical cryostat with an operation temperature range of 4–320 K.

3. Results and discussion

We used the finite-difference method to quantize the Luttinger-Kohn Hamiltonian and the decomposition of the impurity potential over the eigenstates of the Luttinger-Kohn Hamiltonian with the quantum wells profile to obtain the acceptor states energies and wavefunction in momentum space [3, 4]. Acceptor-

related absorption spectra for two light polarization were calculated.

In experiments, we first characterized grown structures measuring the interband photoluminescence and interband photoconductivity at different lattice temperatures. As a result, the high quality of the grown structures was established.

The spectra of intensity of two light polarizations were obtained at T = 4 K in multipass geometry for samples with and without QWs. The absorption spectra obtained from the Beer-Lambert-Bouger law are shown in figure 1. Spectra at other temperatures look similar, absorption smoothly disappears at temperatures above 160 K. We associate the short-wavelength peak observed near the photon energy ($h\nu$) of about 205 meV to the optical transitions of holes from the ground acceptor state to continuum states above the QW. The peak near $h\nu$ = 150 meV can be connected to the hole transitions from the ground state to the second hole subband. Positions of both of these peaks are in good agreement with our calculations. The peak at $h\nu$ = 75 meV can be associated with hole transitions from the ground acceptor state to the first hole subband. Two-phonon absorption in GaAs [5] makes it difficult to get spectrum at longer wavelengths. This leads to a slight discrepancy between the position of the acceptor absorption peak and the theoretically calculated value $h\nu$ = 60 meV.

The measured spectrum of acceptor-related photoconductivity of the QWs sample is presented in figure 1 with red curve at T = 10 K. It should be noted that photoconductivity spectrum is not corrected with the spectrum of radiation source (globar) and transmission spectrum of the experimental setup (of cryostat and spectrometer windows, beam splitter, etc). Spectra at other temperatures look similar, peaks smoothly disappears at temperatures above 30 K. One can see three photocurrent peaks at $h\nu \approx$ 205, 150, 95 meV. The first two peaks match well with absorption peaks discussed above. The peak at $h\nu \approx$ 95 meV can be a part of the peak associated with hole transitions from ground acceptor state to the first hole subband. The calculated position of spectral maximum of this peak is about $h\nu$ = 60 meV and this peak should be very wide. It was not detected in photoconductivity studies due to the low intensity of globar in this spectral range. No acceptor-related peak was presented in the photoconductivity spectra of the reference sample without QWs.

Good agreement between the experimentally received absorption and photoconductivity spectra and theory confirms the applicability of the finite-difference method to obtain the acceptor state energies and wavefunctions in momentum space. Also, we can conclude that absorption coefficient determined by acceptor-related optical transitions is rather high (~10^3 cm^{-1}). This could be used as physical basis of sources of infrared light operating under electrical and optical pumping.

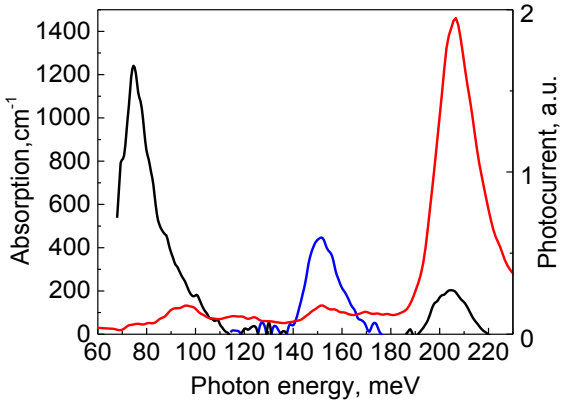

Figure 1. Absorption spectra of light of *s*-polarization (black curve) and *p*-polarization (blue curve) measured at T = 4 K. Red curve shows the photoconductivity spectrum of QWs, measured at T = 10 K.

Acknowlengements

This work was supported by the Russian Science Foundation (grant 18-72-00034).

References

[1] Bosco L, Frankie M, Scalari G, Beck M, Wacker A and Faist J 2019 *Applied Physics Letters* **115** 010601

[2] Cheng W M *et al* 2002 *Journal of Applied physics* **92**(10) 6039

[3] Aleshkin V Y *et al* 2000 *Semiconductors* **34**(5) 563

[4] Chen H H, Wang Yeong-Her and Houng Mau-Phon 1996 *IEEE Journal of Quantum Electronics* **32**(3) 471

[5] Cochran W, Fray S J, Johnson F A, Quarrington J E and Williams N (1961) *Journal of Applied Physics* **32** 2102

3D+2D: Incorporation of 3D printing and graphene nanomaterials for the fabrication of encapsulated flexible electronic devices

V. Bogoslovskiy[1], **R. D. Rodriguez**[1], **A. Lipovka**[1], **E. Sheremet**[2]
[1]Research School of Chemistry & Applied Biomedical Sciences, Tomsk Polytechnic University, Tomsk, 634050 Russia
[2]Research School of High-Energy Physics, Tomsk Polytechnic University, Tomsk, 634050 Russia

Abstract. This research demonstrates how two modern technological trends can complement each other for the fabrication of flexible and robust sensors. The major advantage of this combination is the ability to adjust the fabrication process to customize the device for specific applications. 3D printing allows using a wide range of polymers as well as high flexibility in terms of design. The nanomaterial is two-dimensional graphene oxide (GO) that is well-known for the tunability of its electrical properties *via* reduction process. In this contribution, we show an application of this synergistic combination with the fabrication of a polymer-encapsulated sandwich-like temperature sensor based on laser-reduced graphene oxide. The final device has temperature sensitivity comparable to previous reports, but additionally shows water and scratch resistance thanks to the integration with 3D printing.

1. Introduction

3D printing is setting a new technological paradigm for the fabrication and prototyping of devices and materials varying from simple designs from school education to organ transplants. At the same time, nanotechnology is revolutionizing many technological fields in the XXI century. The combination of these two approaches results in new materials and devices such as graphene and carbon nanotubes in 3D printing filaments, as demonstrated recently [1,2].
Moreover, the use of graphene oxide (GO) in 3D printing can provide additional benefits, such as the selective modification of complex three-dimensional projections with the creation of conductive structures on all surfaces of the created device[3]. In this way, the integration of 3D printing and graphene oxide accompanied by laser reduction opens the opportunity to develop inexpensive but complex structures for a wide range of applications (for instance, wearable sensors).

2. Results and discussion

The main objective of the present work is to combine 3D printing and the use of graphene materials by developing sandwich-like graphene-based structures for prototyping in flexible electronics. The integration of these two technologies allows creating a conductive surface and the introduction of this surface into a personalized enclosure. For this, as shown in Figure 1, we used laser modification of graphene oxide surface and 3D printing to encapsulate the device. After creating and preparing the 3D-printed device case, copper contacts were made, and a layer of GO was deposited on the working surface of the device. The next step was the laser irradiation of the deposited GO film and its subsequent surface processing with the removal of oxygen groups that creates an electrically conductive layer. After investigating and optimizing the operability of the device, it was encapsulated using 3D printing. During this technological step, molten plastic fills all the voids and sinters the upper conductive layer of reduced GO, improving the properties of the final device and ensuring the tightness of the structure.
This configuration shows a negative temperature coefficient of resistance suggesting that the sensitive material has semiconducting properties. Thus, it can be used as a temperature sensor.

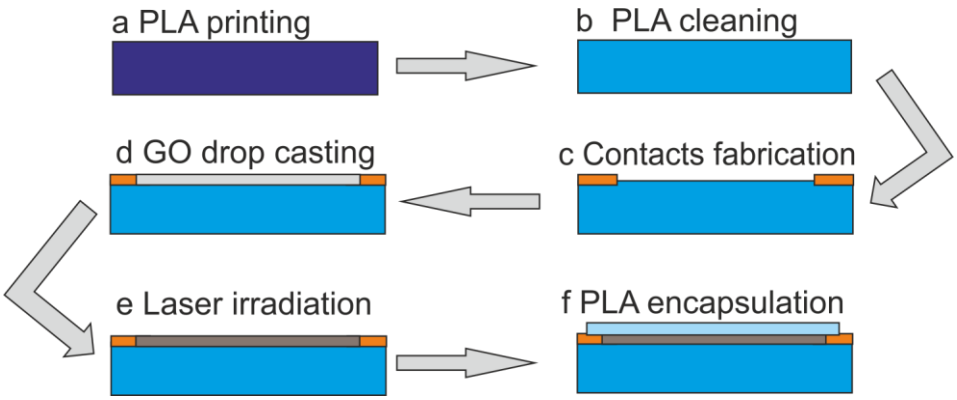

Figure 1. The manufacturing process of temperature sensor

When the temperature sensor was fully assembled, a three-dimensional, closed, conductive structure with a maximum contact surface and high thermal stability of the material acting as the device housing was fabricated. The resistance change of these structures was measured, and their water and bending stabilities were evaluated as well as temperature sensing. The devices were characterized using Raman spectroscopy, scanning electron microscopy (SEM), electrical characteristics (IV curves), and current-sensing atomic-force microscopy (CSAFM).
Figures 2a and 2b demonstrate the sensitivity of the sensor. The sensor was heated with a step of 1°C, and the temperature was kept for 1 min. Then the temperature was increased or decreased.

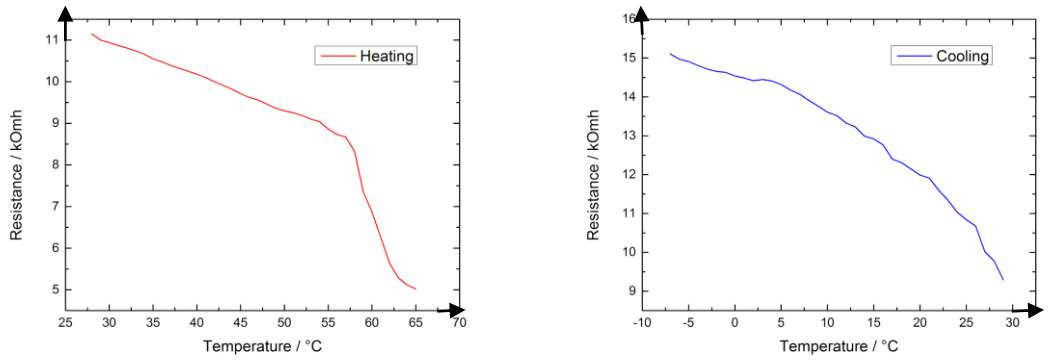

Figure 2. Resistance changes during heating and cooling of the sensor.

3. Conclusion

A laser-reduced GO device was encapsulated using a 3D-printed polymer to enable operation in liquid conditions and under mechanical bending. It was revealed that the sensor has a negative temperature coefficient of resistance, thereby suggesting that the sensitive material of the sensor is a semiconductor. The presented facile technology gives the flexible sensors a new degree of customization by benefiting from the power of additive technology with 3D printing.

References

[1] G. Liu, Q. Tan, H. Kou, L. Zhang, J. Wang, W. Lv, H. Dong, J. Xiong, Sensors. **18** (2018) 1400.
[2] K. Kanao, S. Harada, Y. Yamamoto, W. Honda, T. Arie, S. Akita, K. Takei, RSC Advances. **5** (2015) 30170–30174.
[3] S. Poonam, Abid SSI and M Prabhash, Sens. Actuators B Chem. **258** (2018) 424–435.

Investigation of optical and structural properties of three-dimensional InGaPAs islands formed by substitution of elements of the fifth group

V V Andryushkin[1], A G Gladyshev[1,2], A V Babichev[1,2], E S Kolodeznyi[1], I I Novikov[1,2], L Ya Karachinsky[1,2], V N Nevedomskii[3] and A Yu Egorov[1]

[1]ITMO University, St. Petersburg 197101, Russia
[2]Connector Optics LLC, St. Petersburg 194292, Russia
[3]Ioffe Institute, St. Petersburg 194021, Russia

Abstract. We propose a new method to obtain the three-dimensional quantum-sized objects arrays with reduced surface density formed by elastic transformation of the InGaPAs layer grown on the GaAs surface. The influence of the InGaP layer thickness, substrate temperature, and exposure time in the arsenic flow on the optical and structural properties of the formed three-dimensional islands was studied.

1. Introduction

At present, the creation of single photons sources and micro-emitter arrays are of great interest. The best candidates for the role of light emitting active region for such emitters are quantum dots (QDs). However, in contrast to typical laser applications where QD arrays must have a high surface density, the opposite requirement is imposed on QD arrays in the above applications — low QD density (less than $1 * 10^{10}$ cm^{-2}) [1]. The use of special technological regimes of epitaxial growth allows decreasing the density of InAs QDs from a typical value of $5 * 10^{10}$ cm^{-2} to ~ $1 * 10^{9}$ cm^{-2}, however, further progress is difficult. In this work, we propose a new method to obtain the three-dimensional quantum-sized objects (QD) arrays with reduced surface density formed by elastic transformation of the InGaPAs layer grown on the GaAs surface.

2. Experiment

QDs are formed by replacement of phosphorus in the InGaP epitaxial layer by arsenic, upon exposure of InGaP layer in the As flow at temperatures of 520-535°C. Using this procedure, a several heterostructures were grown on GaAs (100) substrates by molecular beam epitaxy (MBE). Fabricated heterostructures was composed of a GaAs buffer layer, a 200-nm-thick GaAs-based carrier collection region sandwiched by AlGaAs barrier layers of thickness 100 nm, and a 5 nm thick GaAs cap layer. An InGaP layer lattice-matched with GaAs, which was placed at the center of the charge carrier collection region, was transforming into an array of three-dimensional InGaPAs islands during the exposition under arsenic flow while the epitaxy process was stopped. The influence of the InGaP layer thickness, substrate temperature, and exposure time in the arsenic flow on the optical and structural properties of the formed three-dimensional islands was studied.

3. Results

It was found that in addition to the GaAs peaks, the photoluminescence (PL) spectra of fabricated heterostructures contain peaks in the region of 953–979 nm, corresponding to radiation from three-dimensional InGaPAs islands. The wavelength of the maximum of the PL spectrum for a heterostructure where an InGaP layer 2 nm thick was transformed at 520 °C for 5 minutes was 973 nm. The peak width in the PL spectrum corresponding to radiation from three-dimensional InGaPAs islands measured at half maximum (FWHM) was 95 meV, which indicates a significant scatter of three-dimensional islands in size and / or composition. An increase in the holding temperature by 15 °C leads to a red-shift of peak PL wavelength of three-dimensional islands by 6 nm. At the same time, the uniformity of three-dimensional InGaPAs islands improves, as evidenced by a decrease in the FWHM value to 90 meV. An increase in the exposure time to 10 minutes and InGaP layer thickness of up to 3 nm leads to a short-wavelength shift of the PL maximum to 953 nm and an increase in the PL intensity and the expansion of the PL peak (FWHM = 97 meV). In transmission electron microscopy (TEM) images, three-dimensional islands are clearly visible having an oval shape, elongated along the direction [1-10]. Moreover, they often line up “one after another” along the same direction. It is also worth to mention that no such effects along the orthogonal direction [110] were observed, i.e. directions [110] and [1-10] are not equivalent. It could be assumed that this fact is associated with the anisotropy of the surface diffusion rate during the exposure of the InGaP layer, which is due to the directivity of the dangling bonds. Based on the TEM analysis, the density of three-dimensional islands was estimated at about $1.3 * 10^{10}$ cm^{-2}. It was shown earlier [3] that the use of three-dimensional islands makes it possible to increase the oscillator strength, which, along with a low density, indicates the possibility of using this type of three-dimensional islands to create active regions of single photon sources and micro-emitter arrays.

4. Acknowledgments

The work was supported by the Ministry of Science and Higher Education of the Russian Federation (research project No. 2019-1442).

References

[1] Michler P 2009 *Single semiconductor quantum dots* vol 231 (Berlin: Springer)
[2] Trevisi G, Seravalli L, Frigeri P and Franchi S 2009 *Nanotechnology* **20** 415607
[3] Reithmaier J P, Sek G, Löffler A, Hofmann C, Kuhn S, Reitzenstein S, Keldysh L V, Kulakovskii V D, Reinecke T L and Forchel A 2004 *Nature* **432** 197–200

Kinetic Monte Carlo simulation of the growth of In nanostructures by droplet epitaxy on AlGaAs nanopatterned surfaces

S V Balakirev[1], M S Solodovnik[1,2], M M Eremenko[2], N E Chernenko[2], O A Ageev[2]

[1]Department of Nanotechnologies and Microsystems, Southern Federal University, Taganrog 347922, Russia

[2]Research and Education Center "Nanotechnologies", Southern Federal University, Taganrog 347922, Russia

Abstract. In this paper, the results of the simulation of the In/AlGaAs growth on nanopatterned surfaces using modified analytical–Monte Carlo model are presented. The surface density of nanostructures on the flat surface is shown to slightly decrease with increasing Al content. A decrease of an interhole distance leads to the occupation of a small part of a hole which can be prevented by a decrease of a hole volume. The best localization of In nanostructures on AlGaAs surfaces nanopatterned with holes at a distance of more than 125 nm can be achieved at a temperature of 300°C or higher. A decrease in temperature requires a sufficient decrease of an interhole distance to avoid nucleation beyond predefined positions.

To fabricate quantum dot arrays with required characteristics in given positions, appropriate techniques and technological parameters should be chosen. A new method of droplet epitaxy enables formation of nanostructures with independent control of their size, surface density and chemical composition [1,2]. In this paper, kinetic Monte Carlo simulation of the growth of In nanostructures on AlGaAs nanopatterned surfaces by droplet epitaxy is presented.

Previously developed hybrid analytical–Monte Carlo model [3] was upgraded to take into account the growth on patterned surfaces with different Al content. We demonstrate that the surface density of nanostructures on the flat surface slightly decreases with increasing Al content x in the epitaxial layer from $2.2 \cdot 10^{10}$ cm^{-2} to $1.9 \cdot 10^{10}$ cm^{-2} at $x = 0$ and $x = 1$, respectively (Figure 1, 2a).

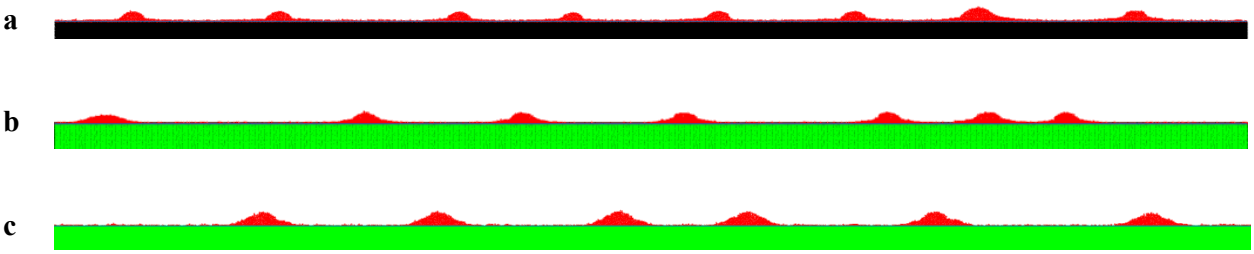

Figure 1. Morphology of nanostructure arrays after deposition of 3 ML of In at a temperature $T = 150$°C and a growth rate $v = 0{,}25$ ML/s on different epitaxial surfaces: a) GaAs, b) $Al_{0.5}Ga_{0.5}As$, c) AlAs. The width of the simulation area is 500 nm.

In a low-temperature range ($T = 150$°C) at an insufficiently small distance between holes ($r \geq 125$ nm) nucleation on a flat part of the surface is possible whereas the best localization of nanostructures is achieved at a high temperature ($T = 300$°C) or with decreasing interhole distances. Perfect localization of In droplets was also experimentally observed after deposition on nanopatterned GaAs surface at the same temperature of 300°C [2].

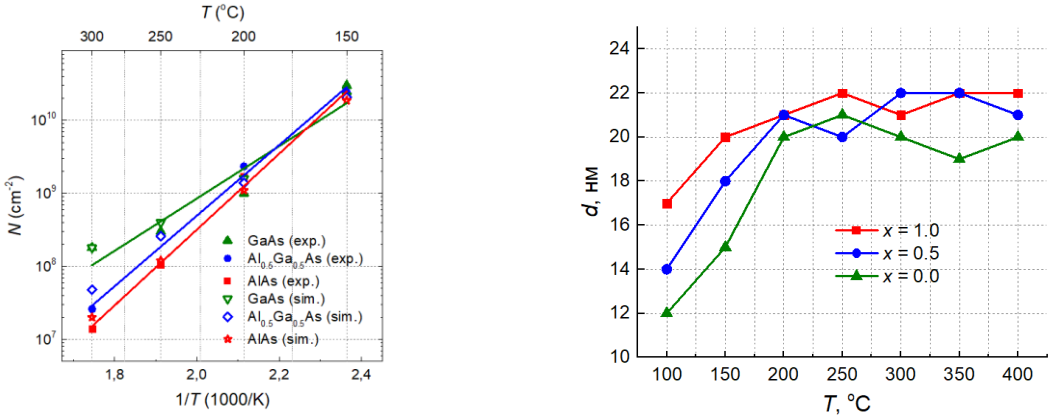

a **b**

Figure 2(a, b). Temperature dependences of **(a)** surface density and **(b)** average diameter of In nanostructures on triangle-patterned $Al_xGa_{1-x}As$ surfaces after deposition of 3 ML of In.

A decrease of r leads to a uniform distribution of In material between holes, but in this case droplets occupy a small part of a hole. In order to achieve the best hole filling, a hole volume should be decreased or deposition amount increased. An average diameter of In nanostructures formed on triangle-nanopatterned surfaces increases with rising temperature and then reaches saturation (Figure 2b). This is attributed to the fact that a temperature increase leads to the enhancement of the compliance of nanostructure and hole parameters which is technologically valuable for precise site-controlled growth.

Thus, the best localization of In nanostructures on AlGaAs surfaces nanopatterned with holes at a distance of more than 125 nm can be achieved at a temperature of 300°C or higher. A decrease in temperature requires a sufficient decrease of an interhole distance to avoid nucleation beyond predefined positions.

This work was supported by the Russian Science Foundation Grant No. 19-79-10099 and the Grant of the President of the Russian Federation No. MK-477.2019.8. The results were obtained using the equipment of the Research and Education Center and Center for Collective Use "Nanotechnologies" of Southern Federal University.

References

[1] Koguchi N, Takahashi S, Chikyow T 1991 *J. Cryst. Growth* **111** 688-692
[2] Kim J S, Kawabe M, Koguchi N 2006 *Appl. Phys. Lett.* **88** 072107
[3] Balakirev S V, Solodovnik M S, Eremenko M M, Konoplev B G, Ageev O A 2019 *Nanotechnology* **30** 505601

Synthesis of mixed germanium tin nanoparticles by spark discharge

A A Lizunova[1], **V I Borisov**[1], **B I Masnaviev**[1], **V R Solovey**[1], **V V Ivanov**[1]
[1]Research Center for Functional Materials, Moscow Institute of Physics and Technology, Dolgoprudny, 141701, Russia

Abstract. The paper represents the investigation of dimensional and structural properties of nanoparticles produced by pulsed-periodic spark discharge by simultaneous electrical erosion of germanium and tin electrodes in inert atmosphere. Two alloys of GeSn nanoparticles with different mass fractions of tin were obtained by altering the polarity of the electrodes. The nanoparticles sizes from 4 to 45 nm were observed. It was shown that the samples consist of core-shell nanoparticles agglomerates, where both β-tin crystals and cubic germanium ones presence as a core; the shell is a mixed germanium tin oxide. Furthermore, a shift of Raman peak by 2 cm^{-1} to lower wave numbers with an increase in relative mass fraction of tin was detected.

1. Introduction

The increased interest in GeSn compounds in recent years is associated with the possibility of regulating the width band gap in the range 0 - 0.55 eV to obtain direct-gap materials which can be base for creating solar cells, quantum-cascade lasers and photodetectors operating in the IR region (from 1 to 8 mkm) at room temperature [1]. The transition from the indirect-gap structure of the $Ge_{1-x}Sn_x$ semiconductor to the direct-gap can occur according to calculations in the range of tin fraction x from 2 to 20 %. Experimentally, pseudomorphic heterostructures were formed with a direct forbidden zone with a concentration tin more than 9 %. The basic method for growing semiconductor GeSn alloys is low-temperature molecular beam epitaxy. An alternative technology for producing nanoparticles compounds from immiscible materials, such as Ag-Cu, Cu-W, is known to be pulse-periodic spark discharge synthesis [2]. Thus, the task of synthesizing mixed germanium tin nanoparticles by spark discharge and investigation its dimensional and structural properties is a future-oriented goal for material science.

2. Materials and Methods

Two samples of aerosol nanoparticles were produced in the pulsed-periodic spark discharge generator [3] under the following synthesis conditions: frequency of the discharges was 370 Hz, the battery voltage was 1.5 kV, pressure in the chamber - 1.5 atm, to synthesis the first alloy a cylindrical tin electrode was used as a cathode (Ge - anode), to get the second sample inversely the cathode was germanium (Sn - anode).The particles are generated under an inert atmosphere (Ar, 99.999%), and collected on a cellulose filter fixed and TEM carbon coated Cu grid. Micro-Raman spectroscopy studies was carried out with a LabRAM HR Evolution (Horiba Scientific) using the 532 nm excitation wavelength of the He-Ne laser (0.1mW). Transmission electron microscopy (TEM), energy dispersive X-ray spectroscopy (EDS) were

performed on the collected particles to study their size, morphology, composition and structure using the Jeol JEM 2100 (200 kV) microscope with energy dispersive X-ray spectrometer X-MAX^N Oxford Instruments. Fourier transform infrared (FTIR) spectra were recorded on a Nicolet™ iS50 FTIR Spectrometer (Thermo Scientific) directly from the alloy nanoparticles on a cellulose filter.

3. Results and Discussion

A typical TEM image of primary nanoparticles in large agglomerate, and the corresponding electron diffraction pattern are presented on Figure 1. The primary nanoparticles in the two samples are characterized by a spherical shape, with close values of mean sizes 23.4 ± 10.1 and 21.6 ± 9.3 nm. Most of the particles sizes are detected to be from 4 to 45 nm, a few single particles with sizes of 50 - 75 nm were observed. Pursuant to high-resolution TEM images, we had concluded that all particles had a core-shell structure with a crystalline core and an amorphous shell. Herewith, small crystals with sizes of 2-7 nm were found to be diamond-like germanium (Figure 1d), while large particles were detected to be β-Sn crystals (Figure 1c). According to the EDX spectra obtained from different areas of sample 1 (Sn - cathode), the average percentage of mass fractions of germanium to tin was 1:2.2, for sample 2 (Ge - cathode) - 1:3.7, a significant amount of oxygen was also existed in the samples. That is, if the material is a cathode, its relative mass fraction in nanoparticles alloy is higher with respect to the material of anode.

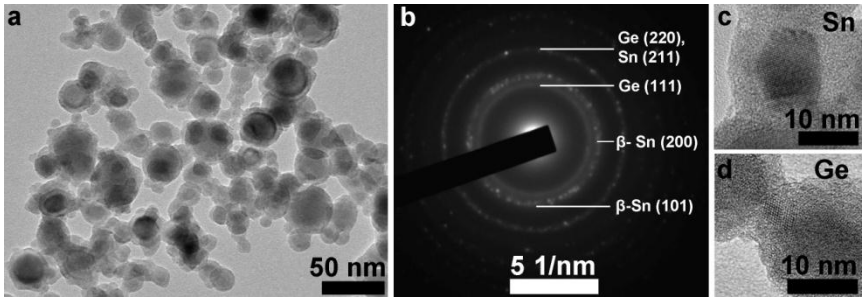

Figure 1(a-d). (a) Typical TEM image; **(b)** SAED pattern; **(c)** HRTEM of Sn crystal; **(d)** Ge crystal.

According to FTIR absorption spectra the main absorption bands at 525 and 780 cm^{-1} were detected for two alloys. It is known that peaks at 570 and 850 cm^{-1} are attributed to germanium oxide and 460 and 620 cm^{-1} - for tin oxide bands. Reference core-shell nanoparticles of Ge- Ge oxide and tin-tin oxide, produced by spark discharge at the study were described by similar FTIR peaks positions as mentioned above for Ge and Sn. Consequently, it was assumed that nanoparticles' shell consist of the amorphous mixed Ge - Sn oxide. The Raman spectroscopy spectra showed the presence of one intense peak at the 282 and 284 cm^{-1} positions for the first (Sn-cathode) and second (Ge - cathode) samples, respectively.

4. Acknowledgments

This work was financially supported by Russian Science Foundation (project No. 19-79-00337).

References

[1] D Marris-Morini, V Vakarin, J M Ramirez, Q Liu, A Ballabio, J Frigerio, M Montesinos, C Alonso-Ramos, X Le Roux, S Serna, D Benedikovic, D Chrastina, L Vivien, G Isella 2018 *Nanophotonics* **7** 1781
[2] N S Tabrizi, Q Xu, N M Van Der Pers, A Schmidt-Ott. 2010 *J. Nanopart. Res*. **12** 247
[3] V V Ivanov, A A Efimov, D A Mylnikov, A A Lizunova, A V Bagazeev, I V Beketov, S V Shcherbinin 2016 *Tech. Phys. Lett.* **42** 876

Raman and AFM studies of epitaxial graphene intended for manufacturing of transistors

I A Eliseyev[1], A V Babichev[2], P A Dementev[3], V Yu Davydov[1]
[1]Laboratory of Optics of Solid State, Ioffe Institute, Saint Petersburg 194021, Russia
[2]Laboratory of Nanoelectronics, Alferov University, Saint Petersburg 194021, Russia
[3]Laboratory of Surface Optics, Ioffe Institute, Saint Petersburg 194021, Russia

Abstract. Graphene is considered as a promising material for electronic applications. In this work, two types of commercially available epitaxial graphene samples are studied by means of micro-Raman spectroscopy, atomic force microscopy and Kelvin-probe force microscopy. Analysis of the measurements data demonstrates significant differences in homogeneity of strain and doping level, concentration of bilayer inclusions, surface topography and surface potential. The results of these studies will help to understand the characteristics of transistors that are to be made on the basis of the studied samples.

1. Introduction

One of the main proposed fields of graphene commercial use is the field of electronics and namely the transistors. Thermal decomposition of the Si (0001) face of semi-insulating SiC substrates is currently one of the most promising technologies of commercial graphene growth. The most important advantage of this method for electronic applications is the lack of the need to transfer the grown film onto a dielectric substrate. In this work, we investigate two commercially available epitaxial graphene samples intended for use as a basis of transistors.

2. Experimental

The samples studied in this work were marked as Sample 1 and Sample 2 and are distinguished by the manufacturer.

Micro-Raman spectra of graphene were measured at room temperature in the backscattering geometry using a Horiba Jobin-Yvon T64000 spectrometer. For the excitation of the Raman spectra, a Nd:YAG 532 nm laser was used. The laser power was limited to 4 mW in a spot with 1 μm diameter. Apart from local measurements, Raman mapping of the sample areas of ~ 10 × 10 μm^2 was carried out.

Atomic force microscopy (AFM) and Kelvin-probe force microscopy (KPFM) within the two-pass technique were employed in order to obtain information on surface topography, roughness and surface potential distribution in the same areas that were studied by Raman spectroscopy.

3. Results and discussion

The Raman spectra obtained after scanning the 10 × 10 and 12 × 12 μm^2 areas of both samples demonstrated characteristic Raman features of this material: *G* (~1600 cm^{-1}) and 2*D* (~2700 cm^{-1}) lines originating from vibrations in the graphene lattice and the broad spectral profile with two maxima in the 1200-1600 cm^{-1} range corresponding to the buffer layer [1]. The high quality of samples was indicated by the absence of the defect-related *D* line (~1350 cm^{-1}) in the Raman spectra.

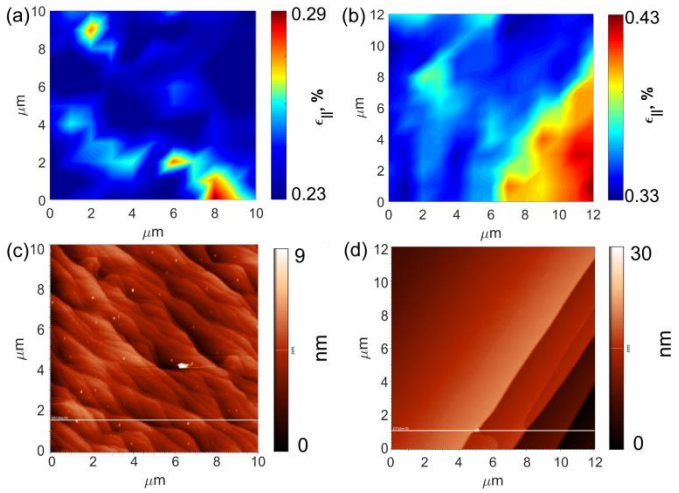

Figure 1 (a, b). Raman maps of biaxial strain ($\varepsilon_{||}$) values for samples 1 **(a)** and 2 **(b)**. AFM surface topography maps for samples 1 **(c)** and 2 **(d).**

Using the analysis first introduced by Lee et al [2] and taking into account the influence of the SiC substrate [3], we determined the values of biaxial strain ($\varepsilon_{||}$) and electron concentration (n_e) for each sample. For sample 1, we obtained $\varepsilon_{||} = (0.26\pm0.03)$ % and $n_e = (6.0\pm0.8)*10^{12}$ cm^{-2}. In case of sample 2, the values of strain and electron concentration, as well as their variation across the studied area ($\varepsilon_{||} = (0.38\pm0.05)$ %, $n_e = (7.5\pm1.5)*10^{12}$ cm^{-2}) were significantly higher compared to the values obtained for the sample 1. Another important difference between the two samples is the presence of the areas with 2*D* line shape characteristic of bilayer graphene in the Raman map of the sample 1, whereas for the sample 2 no fingerprints of bilayer graphene were revealed in its Raman spectra.
The AFM studies revealed essential differences between the topography of the samples. The surface of the sample 1 was formed by relatively small and irregular steps with average width of ~600-700 nm and height of ~2-3 μm (Fig. 1, c). Topography of the sample 2 was completely different, showing wide (~10 μm) and high (~5-7 μm) steps. In addition, steps of smaller (~1-2 μm) width but similar height (Fig. 1, d) were observed between them. According to the data of Raman mapping (Fig. 1, b), it is the areas of narrow and high steps on sample 2 that contributed to the local inhomogeneity of strain. KPFM measurements revealed areas in the surface potential map of sample 1 characteristic of bilayer graphene, while in case of the sample 2 such features in its surface potential were not found. These findings are in a good agreement with the conclusions obtained from the analysis of Raman data.

4. Conclusion

Two epitaxial graphene samples were studied by a combination of AFM, KPFM and Raman mapping. Combined analysis of the data of these three techniques allowed us to conclude that presence of high and wide regular steps on the surface of the sample results in absence of bilayer inclusions, however, leads to large strain and doping level inhomogeneity. In case of smaller steps of irregular shape, the average values of strain and doping level as well as inhomogeneity of these parameters decrease, but concentration of bilayer graphene increases. The influence of strain inhomogeneity, doping level and surface topography of the graphene/SiC samples on their electronic properties will be investigated by studying the transport characteristics of the transistors manufactured on the basis of studied samples.

References

[1] Fromm F, Oliveira M H, Molina-Sánchez A, Hundhausen M, Lopes J M J, Riechert H, Wirtz L, Seyller T 2013 *New J. Phys.* **15** 1
[2] Lee J E, Ahn G, Shim J, Lee Y S, Ryu S 2012 *Nat. Commun.* **3** 1024
[3] Eliseyev I A, Davydov V Y, Smirnov A N, Nestoklon M O, Dementev P A, Lebedev S P, Lebedev A A, Zubov A V, Mathew S, Pezoldt J, Bokai K A, Usachov D Yu 2019 *Semiconductors* **53** 1904

MICROSTRUCTURE OF THIN FILMS OF THE Sb-Te SYSTEM STUDIED BY TRANSMISSION ELECTRON MICROSCOPY

V.Yu. Kolosov, A.A. Yushkov
Electron Microscopy Laboratory, Institute of Natural Sciences and Mathematics, Ural Federal University, Ekaterinburg 620000, Russia

Abstract. Thin films of the Sb-Te system were obtained by thermal evaporation in vacuum and studied by transmission electron microscopy. Strong bending of the crystal lattice reaching 190 deg/μm was revealed.

Sb_2Te_3 is considered today as a promising material for non-volatile memory and thermoelectric elements [1]. Thin films of Sb-Te composition in a ratio of 2 to 3 were obtained by sequential thermal depositing in vacuum (Te was deposited first) with specially designed thickness gradient. The TEM examination was performed along the gradient in the bright (b.f.) and dark field (d.f.) modes with the help of bend contour method [2], supported by the selected area electron diffraction (SAED). Film thickness varies from 7 to 30 nm. In the thinnest part, the film has the structure of merging partially crystallized islands, Fig. 1 a. With an increase in the film thickness, individual grains, fig. 1 b, c, pairs (h k l and $\bar{h}\bar{k}\bar{l}$) of bend extinction contours, fig. 1 c, d, e [2], zone-axis patterns, fig. 1 c, become discernible in TEM. Close pairs of bend contours are often formed during crystallization of thin amorphous films of various substances and indicate strong internal bending of the crystal lattice [2]. The value of the lattice bending determined from the distance between the contours in a pair, fig. 1 d, e, reaches 190 deg/μm in the thickest part of the film. According to the SAED interpretation, the Sb_2Te_3 phase (ASTM card № 15-0874) with the orientation of the zone axis [001], fig. 1 a, and Te phase (ASTM card № 04-0554) with the orientations [110], fig. 1 b, and [120], fig. 1 c, are observed in the film.

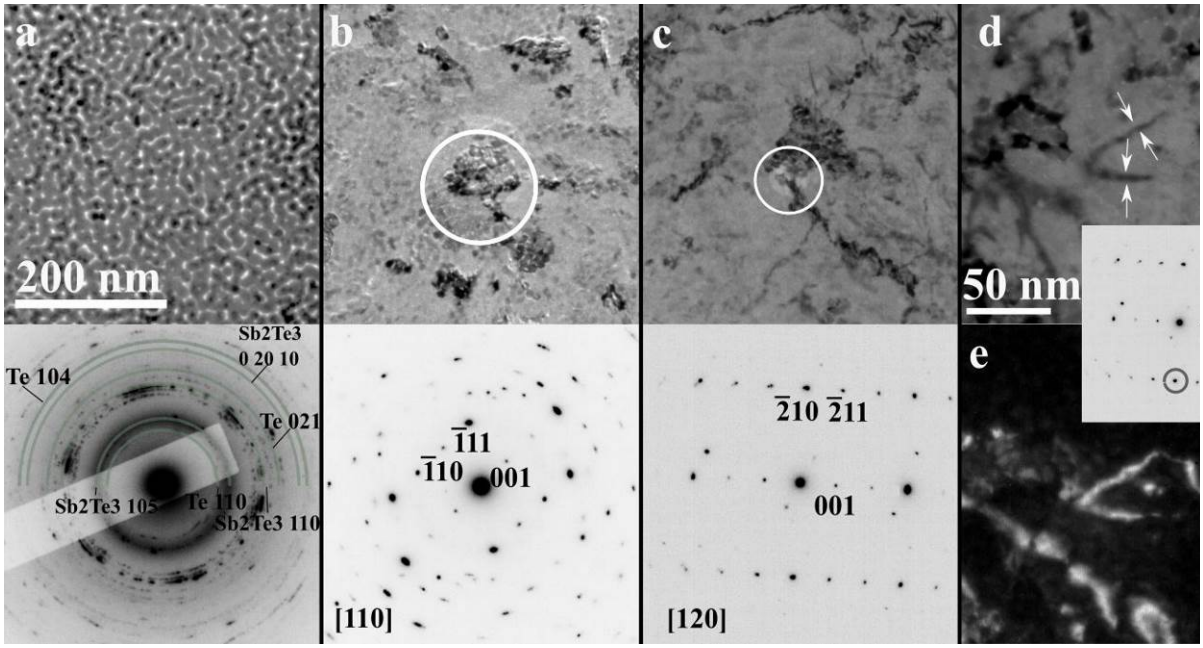

Figure 1. : TEM: a – film area in the thinner part of the gradient (above) and the corresponding SAED with bright rings indicated (below); b - film area in the middle part of the gradient (above) and SAED from the contrasting grain (highlighted in a circle) with indicated spots (below); c - film area in the thick part of the gradient (above) and SAED from the zone-axial pattern (highlighted by a circle) (below). d – TEM image of a film region with an identified extinction bend contour (highlighted by arrows) in the b.f. mode (corresponding SAED in insertion, with the d.f. spot pointed out); e – TEM image of the region in Fig 1 d in the d.f. mode, individual contour from pair is visible.

Acknowledgments
The partial support of Agreement No. 02.A03.21.0006 (Act 211 Government of the Russian Federation) and RFBR grant 20-02-00906A are acknowledged.

References
[1] Xiao Z., Kisslinger K. et al. 2018, *Microelectronic Engineering* **197** 8
[2] Kolosov V. Yu. and Thölen A. R. 2000 *Acta Mater.* **48** 1829

Investigation of the mechanical properties of epitaxial gallium nitride for applications in MEMS

Y Enns, A Kazakin, A Mizerov, K Shubina, I Morozov, A Bouravleuv

Saint Petersburg National Research Academic University RAS, St. Petersburg, Russia

Annotation. This work is presented results experimental determination of the mechanical parameters of a GaN films grown by molecular beam epitaxy on silicon substrates. The study determined the values of Young's modulus and internal stresses for films with different growth parameters. The study was carried out by contact and optical methods on the formed cantilever and beam microstructures. The measured values can be used to develop the design and evaluate the characteristics of MEMS based on gallium nitride films.

1. Introduction

In the last decades, there has been a continuous development of the technology of epitaxial growth of gallium nitride inexpensive silicon substrates. The development of these technologies allows to obtain high-quality films at a significantly lower cost. First of all, this fact contributes to the wide distribution of these films in the microelectronic industry as a material for optoelectronics and high-power radio-frequency electronics. However, its piezoelectric properties, high chemical, temperature and radiation resistance make it a promising material for the development of sensitive and actuator MEMS devices [1]. The development of such sensor devices requires the development of both technologies for the growth of high-quality GaN layers and post-processing [2]. In this case, the electric and elastic properties, as well as the internal stresses of the resulting films, will depend on their growth parameters [3]. Thus for designing MEMS devices with structural layers of GaN requires preliminary measurements of mechanical properties and evaluation of the influence of process parameters on their properties. In this work, we studied the Young's modulus and internal stresses for gallium nitride films grown by molecular beam epitaxy on silicon substrates.

2. Research results

In the course of the work, a technology was developed for the post-processing of gallium nitride films grown by molecular beam epitaxy on silicon substrates to form mechanical structures. This technology is based on plasma-chemical etching of GaN structural layers with the subsequent release of mechanical structures. According to this technology, micromechanical structures were produced in the form of cantilever and bridge arrays of elements.

The obtained experimental samples made it possible to determine the mechanical parameters of GaN films using approved methods [4,5]. The elastic parameters of the films were determined using contact methods. The obtained values of Young's modulus are in the range of 200 ± 25 GPa and hardness of 15 ± 4 GPa, which corresponds to published data [1]. The obtained values are comparable with the values typical for bulk GaN single crystals and differ by about 1.5 times [6,7]. Based on the measurement results obtained and deformation strained film structures were obtained values of the internal stresses.

These values are in the range 1.39 ± 12 GPa and do not go beyond the literature data for structures grown by molecular beam epitaxy [8].

3. Conclusion

In the course of work, a technology was developed for the post-processing of GaN films for the development of micromechanical structures. Experimental evaluation of mechanical properties of the gallium nitride epitaxial film in order to use them as functional layers MEMS sensors. The results showed the high promise of this material as a structural layer of MEMS devices.

4. Acknowledgments

The work was done as a part of the state assignment (№FSRM-2020-0008) of the Ministry of Education.

References

[1] Rais-Zadeh M, Gokhale V J, Ansari A, Faucher M, Théron D, Cordier Y, Buchaillot L 2014 *J. Microelectromechanical Syst.* **23(**6) 1252-1271
[2] Shubina K Yu, Berezovskaya T N, Mokhov D V, Morozov I A, Kotlyar K P, Mizerov A M, Nikitina E V, Bouravleuv A D 2018 *J. Semiconductors* **52**(16) 2117–2119
[3] Kazakin A, Enns Y, Mizerov A, Kleimanov R, Bouravleuv A 2019 *J. IOP: Conf. S.* **1410** 012214
[4] Enns Y, Kleimanov R 2019 *J. IOP: Conf. S.* **1410** 012213
[5] Nikishkov G. P., 2003, *J. Appl. Phys.*, **94**(8) 5333
[6] Nowak R, Pessa M, Suganuma M, Leszczynski M, Grzegory I, Porowski S, Yoshida F 1999 *Appl. Phys. Lett.* **75**(14) 2070–2072
[7] Drory M D, Ager J W, Suski T, Grzegory I, Porowski S 1996 *J. Appl. Phys. Lett*., **69**(26) 4044
[8] Baron N, Cordier1 Y, Chenot S, Vennéguès1 P, Tottereau O, Leroux M, Semond F, Massies J., 2009 *J. Appl. Phys.* **105**(3) 033701-1.

Investigation of the effect of substrate temperature upon PLD on the morphology and electrophysical properties of ZnO:In nanocrystalline films

A A Geldash[1], Z E Vakulov[2], V N Dzhuplin[1], O A Ageev[1]
[1]Department of Nanotechnology and Microsystems, Southern Federal University, Taganrog 347922, Russia
[2]Southern Scientific Center of the Russian Academy of Sciences, Rostov-on-Don 344006, Russia

Abstract. The effect of the temperature of the Si substrate and the glass is studied on the morphology and electrophysical parameters of ZnO:In nanocrystalline films obtained by pulsed laser deposition (PLD). A study was carried out of ZnO:In films obtained at substrate temperatures of 150, 300, and 400 °C. Studies have shown that with an increase in the substrate temperature from 150 ° C to 400 ° C, the film thickness decreases from 190 nm to 50-60 nm, and the grain size increases from 5 nm to 10 nm, while the concentration of current carriers increases from $2.12 \cdot 10^{18}$ cm^{-3} to $3.5 \cdot 10^{19}$ cm^{-3}, their mobility increased from 2.51 $cm^3/(V \cdot s)$ to 6.17 $cm^3/(V \cdot s)$, and the resistivity decreased from 0.93 Ω·cm to 0.029 Ω·cm.

1. Introduction

Pulsed laser deposition (PLD) is by far one of the most promising methods for producing nanocrystalline oxide films by condensation of the products of the interaction of laser radiation with the target material on the substrate surface. The main advantage of PLA is a high degree of compliance of the stoichiometry of the formed films with the target material. In addition, a high degree of supersaturation during condensation of ablation products leads to intense nucleation on all surfaces of the substrate and high morphological homogeneity of the formed film, which is important in the formation of transparent thin layers [1-3]. The main goal of this work was to study the influence of the temperature of the substrate during the formation of ZnO:In nanocrystalline films by the PLD method on their morphology and electrophysical parameters.

2. Materials and Methods

ZnO:In nanocrystalline films were obtained using the Pioneer 180 PLD (Neocera Inc., USA), which is part of the NANOFAB NTK-9 nanotechnological complex (NT-MDT, Russia). Si (111) and glass were used as substrates for the deposition of nanocrystalline films. Before applying the films, the substrates were chemically cleaned. The mode of ZnO:In film formation is characterized by laser wavelength λ=248 nm, energy density on the target surface 1.5 J/cm^2, number of pulses 50000, laser pulse energy 10 Hz, pressure Ar $1 \cdot 10^{-4}$ Torr, target distance - substrate 75 mm, cooling rate of samples 2 °C per min. The variable parameter was the temperature of the Si substrate and glass: 150, 300, and 400 °C.

3. Results

The morphology of the obtained ZnO:In nanocrystalline films and their thickness was studied using a Nova Nanolab 600 scanning electron microscope. In Fig. 1a, an image of the surface of a ZnO:In film,

190 nm thick, formed at a temperature of 150 °C is presented. The film has a continuous structure without visible defects, but its surface has a roughness, which is due to the presence of grains. Also, on the surface of the film were found structures similar to whiskers, with a length of about 200-250 nm and a width of 10-20 nm. In fig. 1b, an image of the surface of a ZnO:In film, 85 nm thick, formed at a temperature of 300 °C is presented. This film also has a continuous structure and consists of grains with a diameter of 5 nm. In fig. 1c shows a surface image of a ZnO:In film, 60 nm thick, formed at a temperature of 400 °C. The film also has a continuous structure, and consists of grains with a diameter of 8-10 nm.

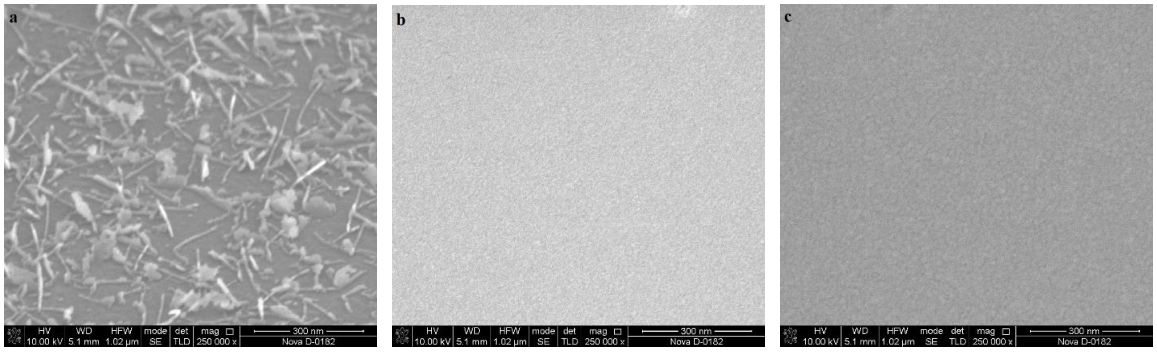

Figure 1 - SEM images of the surface of ZnO: In nanocrystalline films formed at various substrate temperatures: a) 150 ° C; b) 300 ° C; c) 400 ° C.

Then, the electrophysical parameters of the obtained ZnO:In films were investigated by the EMF method, the results of which are presented in discussions and conclusions.

4. Discussion and Conclusions.

As a result of the study, it was revealed that ZnO:In nanocrystalline films formed using the pulsed laser deposition method have different surface morphologies. The grain size in the films was the smallest at a substrate temperature of 300 °C. As the temperature of the substrate increases from 150 °C to 400 °C, the ZnO:In film thickness decreases from 190 nm to 60 nm and the film resistivity decreases from 0.93 Ω·cm to 0.029 Ω·cm. In this case, the mobility of current carriers increased from 2.51 $cm^3/(V \cdot s)$ to 6.17 $cm^3/(V \cdot s)$ and the concentration of current carriers increased from $2.12 \cdot 10^{18}$ cm^{-3} to $3.5 \cdot 10^{19}$ cm^{-3}. It was also revealed that at a temperature of 300 °C and 400 °C the film consists of grains with a diameter of 5-10 nm. The difference in the data obtained for the studied ZnO:In nanocrystalline films is due to the mode of their formation. This is due to a decrease in the density of defects with increasing grain diameters due to an increase in the temperature of the substrate. The obtained ZnO:In nanocrystalline films can be used as transparent conducting contact layers to various nanostructures.

5. Acknowledgments

The reported study was funded by RFBR, projects numbers 19-37-90139, 19-38-60052, 18-28-11019 mk. The work was done on the equipment of the Research and Education Centre «Nanotechnology» Southern Federal University.

References

[1] Vakulov Z E and Zamburg E G et al. 2017 *Mater. Sci. Semicond. Process*. **66** 21

[2] Chirakkara S and Nanda K K et al. 2011 *Thin Solid Films* **519** 3647

[3] Ageev O A and Konoplev B G et al. 2019 *Nanotechnology in microelectronics* (Moscov: Nauka) p 511

Aluminum nanoparticles synthesis in spark discharge for ultraviolet plasmonics

V I Borisov[1], A A Lizunova[1], A K Mazharenko[1], D Malo[1], A A Ramanenka[2], V V Ivanov[1]

[1]Phystech School of Electronics, Photonics and Molecular Physics, Moscow Institute of Physics and Technology, Dolgoprudny 141701, Russia

[2]National Academy of Sciences of Belarus, B.I. Stepanov Institute of Physics, Minsk 220072, Belarus

Abstract. In this paper, we demonstrate an ability to produce aerosol metal Al nanoparticles with plasmon resonance in the ultraviolet region in a spark discharge generator in pure argon atmosphere. The sizes of the obtained primary particles with metal Al core and natural oxide shell in the range from 4 to 50 nm, which were collected in agglomerates with mean size from 190 to 260 nm, were observed. It was found that obtained nanoparticles ensembles demonstrate the broad extinction peaks with maximum in the range from 205 to 300 nm depending on the synthesis conditions. It is shown that the experimental Al extinction spectra are in good agreement with simulation spectra calculated according to Mi theory for resulting Al nanoparticles ensembles.

1. Introduction

The effect of plasmon enhancement of luminescence in organic dyes and semiconductor structures near metal particles is used in chemical and biological sensors, solar energy and analytical spectroscopy. A plenty of studies were discussed the properties of plasmon structures of noble metals - Au and Ag nanoparticles characterized by plasmon resonance in the visible range. However, recently, interest in metal Al nanoparticles synthesis has been increased as promising alternative plasmon material with the following advantages: demonstration of surface plasmon resonance in the ultraviolet (UV) region, low cost, abundant in nature and high stability due to the presence of the shell natural oxide. Thus, the research of new methods for synthesis of Al nanoparticles and the study of its dimensional and optical properties is an actual task for science and technology.

2. Methods and materials

The spark discharge process [1] was performed with the following conditions: pulse repetition rate of 500 Hz at a voltage of 1.5 kV in an argon flow 2 L/min. Argon working gas of purity 6.0 at a pressure of 1,3 atm and two D16 grade aluminum alloy electrodes were used. Nanoparticles aerosol passed through a custom-build tube furnace with the temperature from 25 to 700 ºC [2] and were collected on a nanofiber filter AFA-RMB-20 and TEM copper grid with carbon film. For the formation of a thin oxide film on the nanoparticles surface, which prevents their oxidation in air, an argon atmosphere of 4.8 was created in the gas path, in which the nanoparticles remained for 1 hour.

The microscopy studies were carried out on transmission electron microscopy (TEM) Jeol JEM 2100 (200 kV) with energy dispersive X-ray spectrometer X-MAX^N OXFORD Instruments. The UV-vis-NIR spectra of nanoparticles dispersions in a quartz cuvette were obtained using JASCO V–770

spectrophotometer. The agglomerates size distribution in the flow was measured using a TSI SMPS 3936 Aerosol spectrometer.

3. Results and Discussions

A change in the median diameter of the agglomerates with a sintering temperature shows only a small decrease in size below 400 °C from ~ 250 to ~ 190 nm (Figure 1).

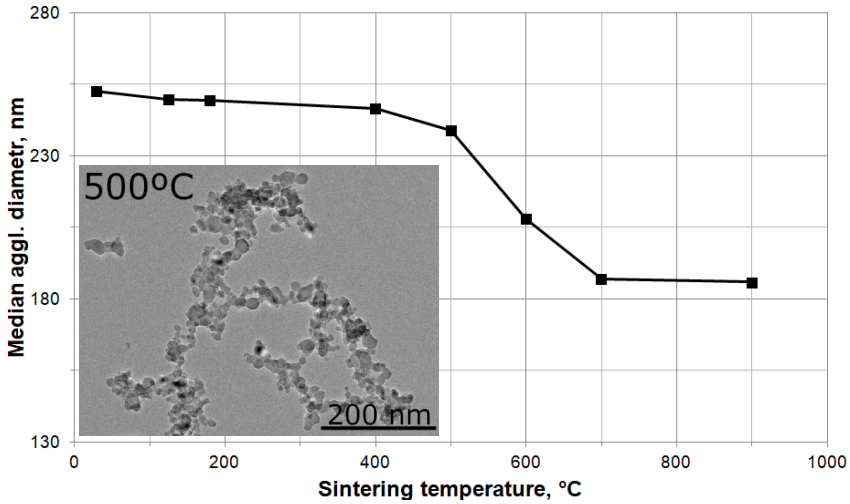

Figure 1. Dependence of median particle diameter of the agglomerates on the sintering temperature; Insets: TEM image of typical particles at 500 °C.

According to TEM images, the particles has core-shell structure, the average particle size in five samples, synthesized at 25, 260, 500, 600 and 700 ºC, varies from 13 to 18 nm, most particles in all samples are characterized by sizes in the range from 5 to 40 nm, for samples synthesized at high temperatures from 500 to 700 °C, there are some single particles with sizes from 50 to 120 nm. It was found that with an increase in sintering temperature the width of the particle size distribution also grows. The measurements of the Al nanoparticles extinction spectra in isopropan ol alcohol showed the presence of wide absorption peaks in the ultraviolet region with peak positions from 205 (for nanoparticles synthesized at 500 °C) to 300 nm (700 °C). The extinction spectra calculated for nanoparticles ensembles with a log-normal size distribution obtained by TEM for aerosol Al-nanoparticles shows that the multimode structure characteristic of large nanoparticles is “masked” and, due to the wide size distribution, the extinction spectra of the nanoparticles ensembles have one maximum at 210 - 270 nm and an extended long-wavelength wing of the spectrum.
Thus, we demonstrated that using the gas discharge method metal Al nanoparticles with plasmon resonance in the ultraviolet region can be produced.

Acknowlegments

The reported investigations of Al nanoparticles’ sizes, its optical properties and Mi simulations were funded by RFBR (project № 19-53-040011) and BRFFR (grant № F19RM-020). Authors acknowledge the Ministry of Science and Higher Education of the Russian Federation for support of spark discharge synthesis by the project “Development of functional materials with controlled electrical, chemoresistive and catalytic properties for manufacturing sensor microsystems by using methods of printed electronics”.

References

[1] Mylnikov D, Efimov A and Ivanov V 2019 Aerosol Sci. Technol. **53** 1393-1403
[2] Lizunova A, Efimov A, Arsenov P, Ivanov V 2018 IOP Conf. Ser.: Mater. Sci. Eng. **307** 012081

Investigation of multilayer $Ge_2Sb_2Te_5$/ITO/Al structures for application in optical reflective displays.

V Glukhenkaya[1], P Lazarenko[1], A Yakubov[1], N Tolkach[2], A Sherchenkov[1]
[1]National Research University of Electronic Technology, Zelenograd 124498, Russia
[2] Ryazan State Radio Engineering University, RSREU, Ryazan, 390005, Russia

Abstract. Influences of the $Ge_2Sb_2Te_5$ (GST225) phase state and thickness of the functional films on the optical parameters of multilayer GST225/ITO/Al structure were investigated. It was shown, that the ITO thickness determine the primary color, while the GST phase state – the tint of the investigated structure Simulation reflective spectra and calculation of CIE color coordinates allowed to optimize multilayer GST225/ITO/Al structure and identify thickness of each layer necessary for obtaining certain RGB-colors. In this work we also demonstrated how the sRGB colour gamut can be expanded by application of GST225 thin films.

1. Introduction

The optical displays are necessary elements of the visual information representation. Contemporary transmissive displays (LED/OLED) have high resolution video-matrix, but are volatile and need power consumption to show information. Alternative displays made are produced by refractive E-ink technology and can work in autonomous mode. However, low color variety and pixel switching rate (~100 ms) limits their application area and does not allow multicolor dynamic video playback. Non-volatile full color dynamic refractive displays can be constructed by multilayer structures based on $Ge_2Sb_2Te_5$ (GST225) layers [1, 2]. The aim of this work is investigation of the influence of layer's thicknesses in the GST225/ITO/Al (GIA) multilayer structure and GST225 phase state on the optical parameters of the structure and possibility of creation a full color non-volatile pixel RGB-matrix.

2. Methods and materials

The thin films of multilayer GIA structures were deposited by the magnetron sputtering. The layer thicknesses were chosen according to the literature data and simulation results (GST225 – 7 nm; ITO – t nm, where t was equal 180, 205 or 250 nm; Al – 100 nm) and were controlled by stylus profilometer (KLA Tencor P-7). The simulation in Mathcad with using formulas of Fresnel, and refractive index $n(\lambda)$ and extinction coefficient $k(\lambda)$ obtained by ellipsometer for each layer was performed. The phase transition of amorphous GST225 (a-GST) into crystalline state (c-GST) occurs under thermal exposure (T = 220 °C, annealing time – 15 minutes). Structure analysis before and after thermal annealing was performed by X-ray diffraction method (Rigaku Smart Lab).

3. Results and discussion

A schematic image of the formed multilayer structures is shown in Fig. 1 (a). The primary color can be varied in a wide range, and is determined by the ITO thickness. A significant change in the optical properties of GST225 during the phase transition is responsible for controlling of reflected light and change of the GIA tint (Fig. 1, b). Fig. 1 (c) demonstrates the changes in optical properties of multilayer structure after phase transition: the spectral maximum of the diffuse reflection coefficient has a shift.

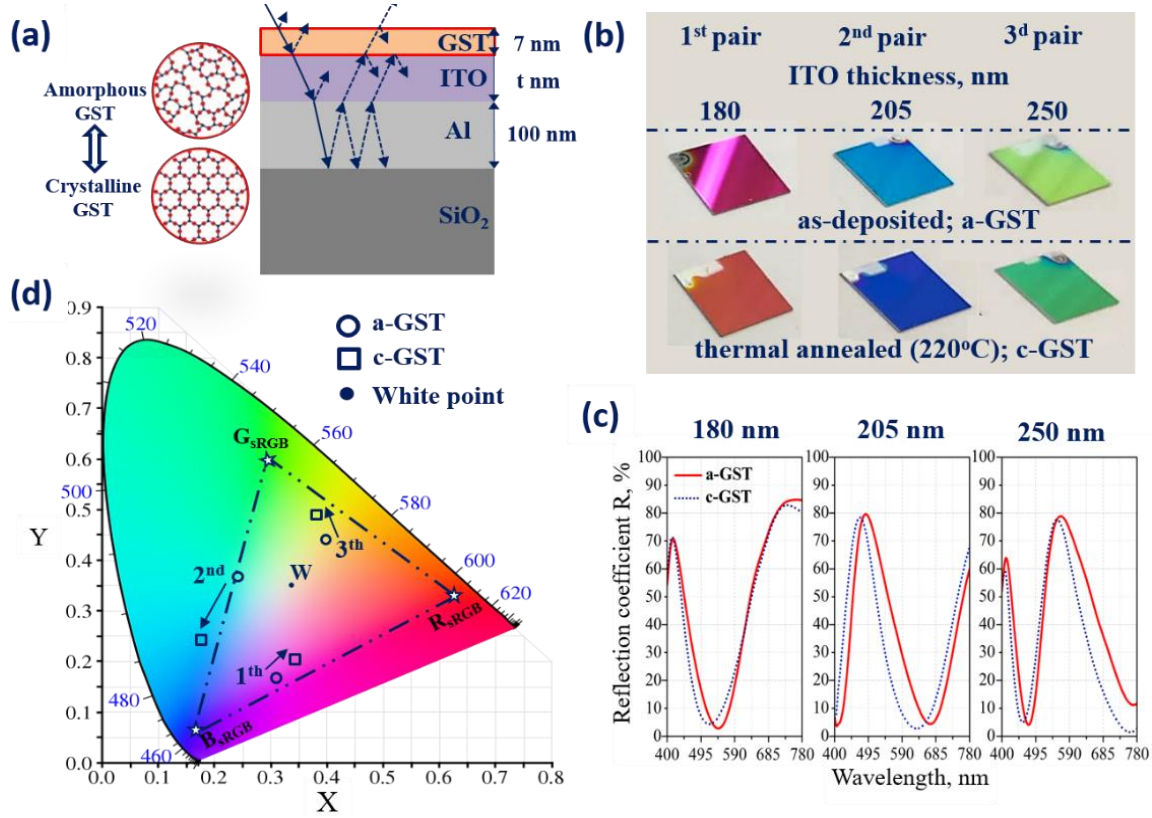

Figure 1 (a, b, c, d). (a) Multilayer structure (schematic image); **(b)** Fabricated samples; **(c)** Experimental diffusion reflection spectra; **(d)** sRGB color gamut expansion with GST225 thin films.

The obtained experimental results are somewhat different from the standard RGB-colors (see Fig. 1, b). However, the simulation reflective spectra and calculation of CIE color coordinates allowed to optimize multilayer GST225/ITO/Al structure and identify thickness of each layer necessary for obtaining standard RGB-colors. According to the CIE-diagram (Fig. 1, d), we can say that the application of GST225 thin films insure the expansion of the sRGB color gamut and allows to get more saturated and brighter image with improved white balance.

4. Conclusion

The fabrication technology of GST225/ITO/Al multilayer structure was developed in the work. It was found that the ITO thickness determine the primary colour, while the GST225 phase state – the tint of the investigated structure. The ability to control optical parameters, in particular, diffusion reflection in a wide wavelengths range is shown. A calculation algorithm has been developed and implemented for the evaluation of the influence of the structure parameters (GST225 and ITO thicknesses; GST225 phase state) on the samples optical properties, which is promising for the creation of a full-colour non-volatile pixel RGB matrix and controlling of the light flux.

5. Acknowledgements

The study was supported by RFBR (project 20-07-01092).

References

[1] Hosseini P, 2014 J. Nature. **511** 13487
[2] Zhigang N, 2018, J. App. Opt. **57** 3385

Morphological parameters and density of states of 3d-element doped hydroxyapatite nanoparticles

A V Sadetskaya, N P Bobrysheva, M G Osmolowsky, O M Osmolowskaya, M A Voznesenskiy
Institute of Chemistry, St. Petersburg State University, St. Petersburg 199034, Russia

Abstract. Present work is devoted to the synthesis of nanoparticles of hydroxyapatite - demanded material for bone tissue engineering and cosmetology. The synthesis was carried out by the hydrothermal method. Double charged ions of 3d elements (Ni, Co, Cu) were used as dopants. XRD, Raman spectroscopy, TEM and BET methods as well as IR spectroscopy were used to characterise obtained nanoparticles. Quantum-chemical calculations were performed and the values of the optical band gap were calculated from the absorption spectra and were verified with the calculations data.

1. Introduction

Hydroxyapatite ($Ca_{10}(PO_4)_6(OH)_2$, HAp) is the main inorganic component of human bone tissue. It possesses an important biological features like osteoinduction and osteoconduction, as well as capablity of producing collagen formation, which makes it a demanded material for bone tissue engineering and cosmetology. Recently, great attention was paid to giving HAp additional functionality - for example, the ability to conduct electric current (to stimulate cell growth) or to be colored (to produce multifunctional pigments), which can be achieved by changing the electronic structure of a solid by doping. However, at the present moment in the literature there is no unequivocal opinion on how to correctly characterize these changes, and no understanding of how to conduct doping process to obtain objects with desired properties.

2. Results and discussion

In the present work, double charged ions of 3d elements (Ni, Co, Cu) were used as dopants. The synthesis of nanoparticles was carried out by the hydrothermal method, the phase composition, size and shape of the nanoparticles were determined using XRD, Raman spectroscopy, TEM and BET methods. The surface composition of nanoparticles and the presence of dopant-oxygen bonds were studied by IR spectroscopy. The values of the optical band gap were calculated from the absorption spectra and were used to verify the data of quantum chemical calculations. Quantum-chemical calculations were performed using the Abinit software package in the framework of the density functional theory (DFT) in local density approximation (LDA) and generalized gradient approximation (GGA) using standard and original approaches.

It was shown that the synthesized nanoparticles have a size of about 26 nm in thickness and 54 nm in length. The resulting nanoparticles form the following size range (by size reduction) - HAp, Co-HAp, Ni-HAp, Cu-HAp, which is associated with the peculiarities of the chemical behavior of dopants in the initial reaction medium. For all doped nanoparticles, a change in the unit cell parameters was registered, as well as a decrease in crystallite sizes relative to the undoped HAp, which indicates the

success of the doping. It was found that the introduction of the dopant allows to decrease the band gap from 4.6 to 2.5 eV.

It was shown that out of the two nonequivalent positions of the calcium atom in the lattice, the position indicated in the literature Ca2 is the most favorable for substitution by dopant atoms. An original approach used together with the GGA functional allows us to achieve the correspondence between the calculated and experimental values of the band gap. According to the data of partial densities of states (contributions to the density of states for individual atoms), it is shown that the introduction of a dopant leads to the appearance of additional levels in the band gap. It was established that the Fermi level of the synthesized samples linearly depends on the electronegativity of the dopant, and the calculation of the densities of states in highly symmetric crystallographic directions (band structure) allowed us to conclude that the obtained materials are direct-gap semiconductors.

Thus, for the first time, a complete quantum-chemical description of doped hydroxyapatite nanoparticles was carried out and the possibility of controlling the position of the Fermi level and the width of the band gap by selecting the dopant according to its electronegativity was shown.

3. Acknowledgments

Scientific research were performed at the research park of St. Petersburg State University educational resource centre of chemistry: Centre for X-ray Diffraction Studies, Centre for Innovative Technologies of Composite Nanomaterials, Chemical Analysis and Materials Research Centre and Centre for Optical and Laser Materials Research.

Raman analysis of epitaxial GaN layers grown on Si (111) by PA MBE

E.A. Lubyankina[1], **B.H. Bairamov**[1,2], **A.D. Bouravleuv**[1]
[1]Alferov University, St. Petersburg, 194021, Russia
[2]Ioffe Institute, St. Petersburg, 194021, Russia

Abstract. This paper demonstrates the results of precise frequency measurements of Raman spectra of the epitaxial GaN layers grown on Si (111) by PA MBE. It was demonstrated that the optical Si phonon exhibits negative shift and so does the E_2^h GaN phonon. Thus, it proves that the GaN layer less than a micrometer leads to the appearance of tensile stress in the structure. The stress was calculated and compared for the structure with nitridation and without it.

1. Introduction.

Gallium nitride is considered to be an excellent material for the development of power electronics. GaN gadgets cover the broad spectral range from the IR to UV regions. This semiconductor with the wide bandgap can possibly lessen consumption of energy and size of electronic devices compared to existing ones. Due to their mechanical properties, chemical stability, good thermal conductivity, structures based on GaN more and more penetrate the market.

Over the past decades many studies have been concerned with improvement of the quality of epitaxial GaN grown on silicon substrate. The lattice mismatch is huge as well as the difference in thermal expansion coefficients of these two materials, leading to the appearance of large number of defects and even cracking. In addition, diffusion of impurities from the silicon substrate into the gallium nitride epitaxial layer can occur [1].

One of the ways to overcome some of these issues is a surface nitridation before the growth process. The nitridation at substrate temperature $T_s = 850^oC$ was proven to lead to high quality optical properties [2].

2. Experimental details.

The studied GaN layers were grown on Si (111) substrates by PA-MBE on a Veeco Gen 200. We used a high - frequency (13.56 MHz) plasma source Riber RFN 50/63 for nitrogen activation.

The thickness of the epitaxial layers were 860 nm and 770 nm for the samples with substrate surface nitridation (Si_xN_y) and without it respectively.

The morphology of both epitaxial GaN layers were studied by scanning electron microscopy. The structural properties of GaN films were studied by Raman spectroscopy using Horiba Jobin Yvon LABRAM HR 800 spectrometer with an excitation wavelength of 532 nm.

3. Results

We measured the Raman spectra for both samples and Si (111) substrate and presented the example in figure 1.

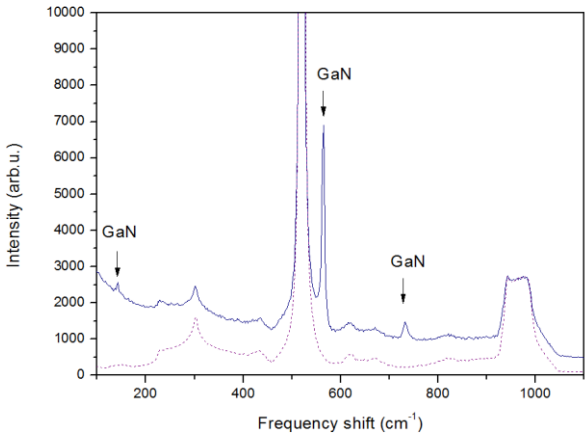

Fig. 1. Raman spectra of and GaN/Si and Si (111) substrate. The solid curve corresponds to the GaN/Si. The dotted curve corresponds to the normalized Si (111) spectrum.

The experimental data showed that the spectra of both GaN/Si (111) layers contain the same phonon modes. In both samples the optical Si phonon experienced the negative shift $0.4\ \mathrm{cm}^{-1}$ with respect to the value obtained in Si (111) substrate ($520.6\ \mathrm{cm}^{-1}$).

The position of E_2^h GaN phonon is extremely sensitive to biaxial deformation in this structure. It should be noted that many studies still apply incorrect value for the calculation of stress, although the position in stress-free GaN was carefully studied recently in [3]. Thus, we obtained the biaxial stress in both samples. The frequency of LO GaN phonon was compared for both structures as well.

We showed that the PA MBE growth of gallium nitride layers leads to the changes on both sides of this structure interface: both GaN layer and Si surface at the interface are under compressive strain.

Acknowledgments

The author at the Ioffe Institute acknowledges the support from Presidium RAS Program No. 5: Photonic technologies in probing inhomogeneous media and biological objects.

References

[1] Sobanska M, Klosek K, Zytkiewicz Z R, Borysiuk J, Witkowski B S, Lusakowska E, Reszka A, Jakiela R 2012 *Cryst. Res. Technol*. **47** 307

[2] Shubina K Y, Berezovskaya, T N, Mokhov D V, Mizerov A M, Nikitina E V 2017 *Technical Physics Letters* **43** 11

[3] Holmi J T 2018 Journal of Crystal Growth **499** 47

Nanocrystalline ZnO thin films prepared by new pyrolysis method

V Yu Storozhenko[1], **M G Volkova**[1], **V V Petrov**[2], **E M Bayan**[1]
[1]Department of Chemistry, Southern Federal University, Rostov-on-Don, 344090, Russia,
[2]Research and Education and Centre "Microsystem technics and multisensor monitoring systems", Southern Federal University, Taganrog, 347922, Russia

Abstract. New pyrolysis method of synthesis was employed to prepare high-quality nanocrystalline transparent ZnO films. The fabricated material was investigated by X-ray diffraction, scanning electron microscopy to determine the structure, phase composition, thickness and surface morphology of the ZnO film. The structural analysis of the films indicates that they are polycrystalline and have a wurtzite structure. The film structure consists of nanocrystallites about 10–20 nm in size uniformly distributed over the surface of the substrate and over the film thickness.

1. Introduction

During the last decade special attention has been paid to obtaining highly dispersed forms of zinc oxide (ZnO) in the form of nanoparticles, rods, and films. ZnO is one of the most used materials due to its good electrical, optical properties, non-toxicity and low cost [1-2]. ZnO-based films can be used as deposition of conductive transparent contacts, which are necessary in the manufacture of optoelectronic devices [3], as well as gas sensors [4]. Many techniques have been used to fabricate ZnO films, including the vapor–liquid–solid epitaxial, CVD, pulsed laser deposition, hydrothermal [5] and sol-gel methods [6], etc. But they have disadvantages, such as the high cost of equipment (pulsed laser deposition, hydrothermal method), the duration of the process (sol-gel method), so one of the main tasks of materials science is to find ways to obtain thin films of ZnO from available reagents using inexpensive methods to control thickness, composition and other characteristics of finished materials. This paper presents the results of a new method for the zinc oxide synthesis in the form of transparent films using an organic zinc compound as a precursor.

2. Experiment

To obtain these films, the following main reagents were used: zinc acetate hydrate ($Zn(CH_3COO)_2 \cdot 2H_2O$ (chemically pure), acetone, dioxane, distilled water and organic acid. The organic compound of zinc was obtained by reacting organic acid with zinc hydrate. The amount of organic acid was calculated using the reaction equation with a 10% excess. As a synthesis result, an amorphous powder was obtained, which was used as a precursor for the film coatings production. To achieve this, the organic zinc compound was dissolved in dioxane in a ratio of 1:5, the solution was applied to a pre-prepared purified substrate (glass, polycor and silicon were used as substrates), dried first at room temperature, and then at 373 K. In this way 3 layers of the precursor solution were applied. Heat treatment of the films was carried out under heating at a speed of 10 deg/min, with exposure at 723K for 1 h. After firing, the films were cooled to room temperature.

The phase composition of the obtained films was studied X-ray diffraction (XRD) using a diffractometer ARLX'TRA, Thermo ARL (Switzerland) with CuKα X-rays. The morphology and thickness of the films studied by scanning electron microscope (SEM) on an EMXplus 10/12 Bruker (Germany).

3. Results and discussion

Fig. 1(a) shows the XRD pattern of an as-prepared ZnO thin film deposited on a glass substrate. The main phase of the obtained films is the crystal structure of wurtzite as expected for zinc oxide. The average crystallites size was 9 nm as calculated by Sherrer's equation. SEM analysis revealed a crack-free surface morphology. The film structure consists of nanocrystallites about 10–20 nm in size uniformly distributed over the surface of the substrate and over the film thickness. The film structure is similar to a "finely porous sponge". The average thickness of three-layer films is 180 nm. Separate layers on cleaved or scratched films do not differ, which indicates a high-quality technology for its formation.

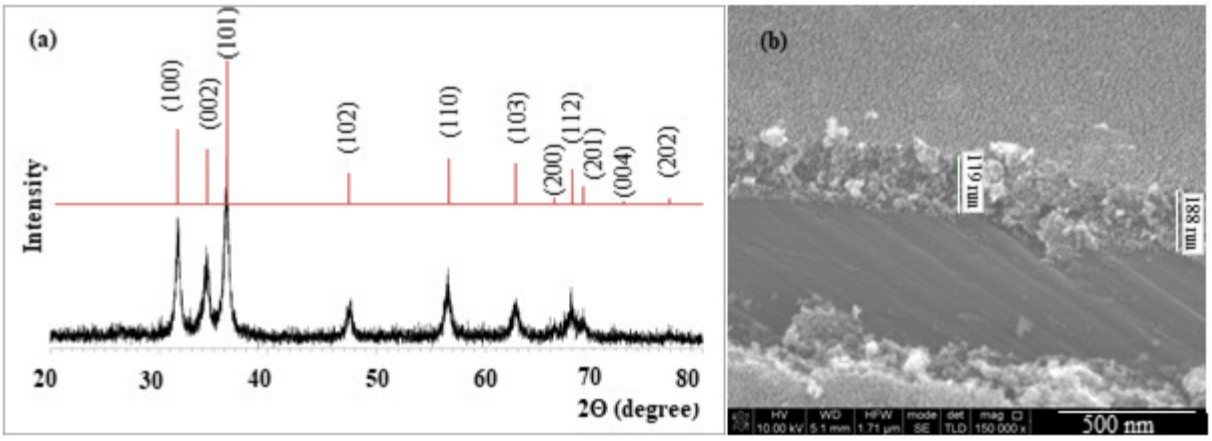

Figure 1(a, b). (a) X-ray diffraction patterns of synthesized ZnO film; **(b)** SEM images of ZnO film.

4. Conclusion

The proposed new method for producing thin films of zinc oxide is an economical and simple technique, requiring non-expensive equipment and non-toxic reagents. This method allows to obtain high-quality transparent films of controlled thickness, which include crystallites 10-20 nm in size.

5. Acknowledgments

The present study was performed with financial support of RFBR, project number 20-07-00653 A.

References

[1] Petti L, Münzenrieder N, Vogt C, Faber H, Büthe L, Cantarella G, et al. 2016 *Applied Physics Reviews* **3(2)** 021303

[2] Petrov V V, Varzarev Y N, Bayan E M, Storozhenko V Yu, Rozhko A A 2019 *Proceedings of the 2019 IEEE International Conference on Electrical Engineering and Photonics* **8906834** 242

[3] Abdullin Kh A, Gabdullin M T, Gritsenko L V, Ismailov D V, Kalkozova Zh K, Kumekov S E, Mukash Zh O 2016 *Semiconductors* **50** 8

[4] Petrov V V, Abdullin Kh A, Starnikova A P, Varzarev Yu N 2019 *J. of Physics: Conf. Series* **1410** 012006

[5] Liang J, Liu J, Xie Q, Bai S, Yu W, Qian Y 2005 *J. Phys. Chem. B.* **109** 9463

[6] Znaidi L 2010 *Mater. Sci. Eng. B* **174** 18

Technological features of growth and optical properties of gallium oxide

D.I.Panov[1], V.A.Spiridonov[1], D.A. Zakgeim[1], Kremleva A.V. [1], D.A. Bauman[1], A.E. Romanov[1], V.E. Bougrov[1].
[1]ITMO University, St. Petersburg, 197101, Russia

Abstract. The influence of growth zones and growth medium on the production of a bulk gallium oxide crystal by the Czochralski method is considered. The optical properties of the obtained gallium oxide crystal were studied. Structural properties were studied by X-ray diffraction.

Semiconductors and semiconductor structures are widely used today. Nowadays, people create diodes, transistors, solar cells and other devices with their help. The demand for the capabilities of electronics and the constant growth of capacities for use in microelectronics leads to the need to search for new materials for power electronics and optoelectronics. [1,2] One such material is gallium oxide. Gallium oxide is a wide-gap semiconductor with a band gap of 4.8-4.9 eV.[3-6] Gallium oxide is one of the few crystals that can be obtained as a bulk crystal by the Czochralski or Stepanov method.[7-10]
To obtain a crystal, a NIKA-3 growth unit with induction heating was used, which allows to grow crystals by the methods of Czochralski and Stepanov. Gallium oxide powder was used as the starting material. An iridium crucible was used to produce the melt. All samples were synthesized in a closed system with a constant atmosphere. As the atmosphere, carbon dioxide and argon gas were used in different ratios.
As a result of experiments on the production of a gallium oxide crystal by the Czochralski method, 3 configurations of the growth zone were studied. By switching from a re-emitting ring to induction heating of the crucible itself, oxygen-containing atmospheres were achieved. Due to the transformation of growth zones, the transition to the zone of the type of "ceramic pipes" and the use of oxygen-containing atmospheres, it was possible to achieve a symmetrical crystal growth.

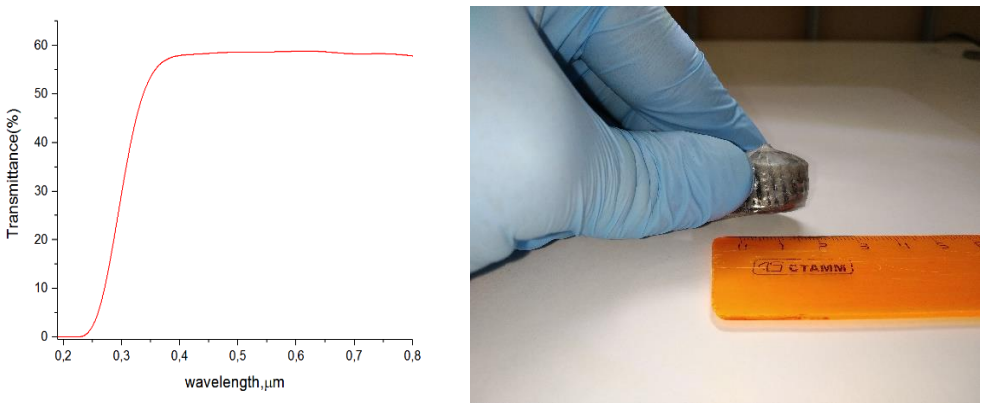

Figure 1. Figure of transparent spectrum on the left and obtained sample on the right.

A plane-parallel sample 1 mm thick was obtained by cleaving a crystal and its optical properties were studied. Spectroscopic studies of the obtained sample showed that it is transparent in the near UV and visible range, the absorption band starts from 250 nm. (figure 1). The band gap was estimated from the experimental absorption spectrum, which was about 4.7 eV. According to the results obtained, it can be assumed that today the technology is not fully developed and defects are present in the crystal.
Structural properties were studied by X-ray diffraction. X-ray diffraction scan showed that crystal faces were formed by (200),(400),(600) family of crystallographic planes (figure 2).

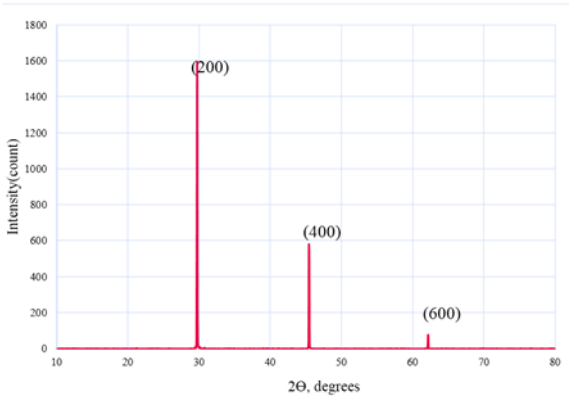

Figure 2. Figure of X-ray diffraction obtained bulk crystal Ga2O3.

The paper considers the possibilities of practical application of the material. The influence of growth zones and media on the possibility and quality of obtaining a gallium oxide crystal is investigated and shown. It is concluded that the best growth condition is the use of growth zones such as "ceramic pipes" and the use of oxygen-containing atmospheres. The optical properties of the sample were studied and the band gap of the crystal was estimated at 4.7 eV. Based on the estimated band gap, it was concluded that at the moment the crystal has defects and structural damage.

Acknowledgements. This work was supported by the Russian Science Foundation, Project No. 19-19-00686.

References

[1] Hu, Z., Nomoto, K., Li, W., Tanen, N., Sasaki, K., Kuramata, A., Nakamura, T., Jena, D., Xing, H.G. 2018. *IEEE Electron Device Letters* **39**, 869–872.
[2] Víllora, E.G., Arjoca, S., Shimamura, K., Inomata, D., Aoki, K. 2014. *Presented at the SPIE OPTO, San Francisco, California, United States*, p. 89871U.
[3] Pearton, S.J., Yang, J., Cary, P.H., Ren, F., Kim, J., Tadjer, M.J., Mastro, M.A., 2018. *Applied Physics Reviews* **5**, 011301.
[4] Stepanov, S.I., Nikolaev, V.I., Bougrov, V.E., Romanov, A.E., 2016. *Rev.Adv.Mater.Sci*. **44**, 63–86.
[5] Galazka, Z., 2018. *Semicond. Sci. Technol*. **33**, 113001.
[6] Galazka, Z., Irmscher, K., Uecker, R., Bertram, R., Pietsch, M., Kwasniewski, A., Naumann, M., Schulz, T., Schewski, R., Klimm, D., Bickermann, M., 2014. *Journal of Crystal Growth* **404**, 184–191.
[7] Mohamed, H.F., Xia, C., Sai, Q., Cui, H., Pan, M., Qi, H., 2019. *J. Semicond*. **40**, 011801.
[8] Butenko, P.N., Panov, D.I., Kremleva, A.V., Zakgeim, D.A., Nashchekin, A.V., Smirnova, I.G., Bauman, D.A., Romanov, A.E., Bougrov, V.E., 2019. *Materials Physics and Mechanics* **42**, 802–807.
[9] Kuramata, A., Koshi, K., Watanabe, S., Yamaoka, Y., Masui, T., Yamakoshi, S., 2016. *Jpn. J. Appl. Phys.* **55**, 1202A2.
[10] Masuya, S., Sasaki, K., Kuramata, A., Yamakoshi, S., Ueda, O., Kasu, M., 2019. *Jpn. J. Appl. Phys*. **58**, 055501.

Controlled Ultra-Thin Suboxide Films Generation in Metal-Oxide Systems by Ar^+ Ion Irradiation

A.V. Lubenchenko[1], D.S. Lukyantsev[1], A.B. Pavolotsky[2], D.A. Ivanov[1], O.I. Lubenchenko[1], I.V. Ivanova[1], V.A. Iachuk[1], O.N. Pavlov[1]
[1]National Research University "Moscow Power Engineering Institute", Moscow, 111250, Russia
[2]Chalmers University of Technology, Göteborg, 41296, Sweden

Abstract. A method of controlled generation of metal suboxide films is proposed, basing on low-current ion sputtering of native oxides of ultra-thin metallic films and XPS chemical and phase depth profiling. Niobium suboxide ultra-thin films are generated and controlled using this approach.

Metal-suboxide ultra-thin films are used for manufacture of memristors [1]. Memristors are the base for memory cells and/or bidirectional selectors for resistive random access memory (RRAM) [2]. To generate an oxide layer, various methods are used, i.e. electrostatic spray deposition (ESD) and atomic layer deposition (ALD) [3]. However, controlled production of suboxide layers of a certain thickness is a matter of significant difficulties. In [4], Ar^+ sputtering of a natural metallic oxide layer for generation of a suboxide layer was used and the results of sputtering were observed with the help of X-ray photoelectron spectroscopy (XPS). For interpretation of results, standard methods were used that didn't enable to determine the film thicknesses and oxide phases.

In our research, we used low-current ion sputtering of native oxides on ultra-thin metal films. After each stage of sputtering, depth chemical and phase profile of multi-layer films was controlled by our new method [5]. This approach enabled us to choose sputtering parameters for generation of ultra-thin suboxide films of desired profiles.

In this work, oxidized Nb films 5, 10, 15 and 100 nm were studied. The niobium films were deposited on a silicon substrate using magnetron sputtering technique performed with the experimental setting Pfeiffer Vacuum SLS630G. During the deposition process, the film thicknesses were controlled through a known deposition rate. The deposition rate was confirmed by transmission electron microscopy.

Depth profiling was performed by means of XPS using the method [5]. The photoelectron spectra were recorded with the help of an electron and ion spectroscopy module based on the platform Nanofab 25 (NT-MDT) by a semi-spherical energy analyzer SPECS Phoibos 225.

The probing depth was about 10 nm. The films were sputtered delicately with the help of an ion gun: Ar^+, energy 0.5 keV, incidence angle of the beam 70 degrees, ion current about 50 nA, sputtering cycle time 20 min.

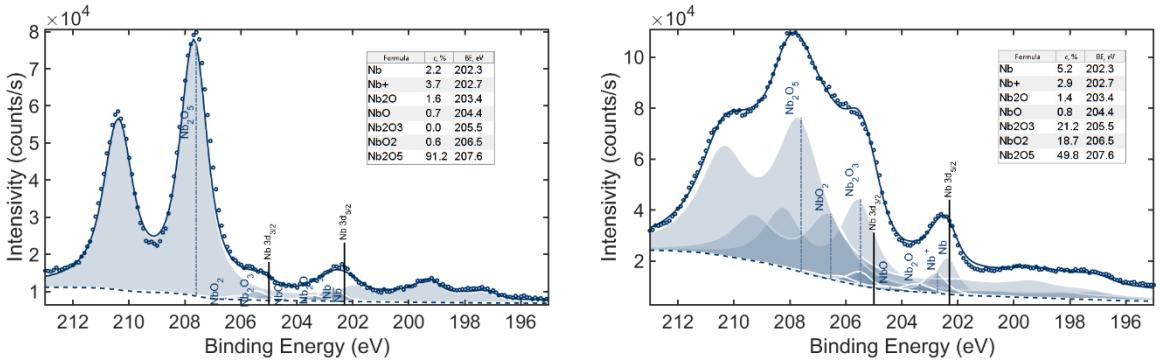

(a) **(b)**

Figure 1(a, b). XPS spectra. Line Nb3d, Target: NbO_x/Nb/Si: **(a)** before sputtering; **(b)** after sputtering, sputtering time 20 min. Circles: experimental data. Solid lines: calculation. Filled areas: partial peaks.

Figure 1 presents the results of XPS spectra deconvolution for oxidized Nb films 5 nm thick before and after sputtering. Table 1 displays computing results for thicknesses following the formula from work [5] which accounts for partial intensities obtained by decomposition of the line Nb3d.

Table 1. Chemical and Phase Depth Profiling of a NO_x/Nb/Si Target

	Before sputtering		After sputtering	
	d (nm)	Formula	*d* (nm)	Formula
5	7.2	Nb_2O_5	2.1	Nb_2O_5
4	1.3	0.21 NbO_2 + 0.24 NbO + 0.55 Nb_2O	0.5	NbO_2
3			3.8	Nb_2O_3
2			0.8	0.35 NbO + 0.65 Nb_2O
1	–	Nb	–	Nb
Substrate		SiO_2/Si		SiO_2/Si

Our investigation shows that the structure of generated suboxide Nb films is always complex, depending on initial film thickness, sputtering conditions. Information about chemical and phase depth profiles of films by certain sputtering parameters will enable to generate films of desired structures for memristors.

References

[1] Strukov D B, Snider G S, Stewart D R and Williams R S 2008 *Nature* **453** 80–3

[2] Yang J J, Pickett M D, Li X, Ohlberg D A A, Stewart D R and Williams R S 2008 *Nature Nanotechnology* **3** 429–33

[3] Salaün A L, Mantoux A, Blanquet E and Djurado E 2009 *Journal of The Electrochemical Society* **156** H311

[4] Song W D, Ying J F, He W, Zhuo V Y-Q, Ji R, Xie H Q, Ng S K, Ng S L G and Jiang Y 2015 *Applied Physics Letters* **106** 031602

[5] Lubenchenko A V, Batrakov A A, Pavolotsky A B, Lubenchenko O I and Ivanov D A 2018 *Applied Surface Science* **427** 711–21

Formation of metal catalytic centers from atomic flows of matter for the growth of carbon nanostructures using PECVD method

V S Klimin[1,2], **A A Rezvan**[1], **J V Morozova**[1]
[1]Department of Nanotechnology and Microsystems, Southern Federal University, Taganrog 347922, Russia
[2]Research and Education Center "Nanotechnologies", Southern Federal University, Taganrog 347922, Russia

Abstract. The formation of nickel catalytic centers from atomic flows obtained by the method of vacuum resistive evaporation is described. A model of kinetics of nickel catalytic centers formation from atomic flows has been constructed. According to the results of theoretical studies, it was learned that flux of nickel atoms to the substrate $F=1.296*10^{18}$, residence time of the nickel atom on the substrate in the adsorbed state $t_g=5.135*10^{-7}$, and concentration of adsorbed atoms as a function of time $N=6.657*10^{11}$.

1. Introduction

Currently, carbon nanostructures are the structural basis for many micro and nanoelectronic devices. Each modification of which has its own individual properties and possible prospects. So carbon nanotubes have been used for transistors, diodes, memory elements, nanocathodes, batteries and others [1-4]. However, although many publications indicate experimental confirmation of these applications and confirmations of formation of carbon nanostructures that satisfy given process parameters, the theoretical basis of process of growth and formation of carbon nanotubes is still a weak point of nanotechnology [5, 6]. This work is aimed at carrying out theoretical studies of kinetics of catalytic centers formation from atomic flows of matter for oriented growth of carbon nanotubes.

2. Discerption of investigation

Formation of catalytic centers from transition metals on surface of substrate is the initial and one of the most important stages in technology of producing carbon nanotubes by plasma chemical vapor deposition (PECVD). The consideration was based on formation of nickel catalytic centers.

In further considerations, it is assumed that nickel catalytic center is a single crystal with an axis [100] parallel to axis of nanotube and a base face (001) on which acetylene does not decompose and carbon is not deposited. According to the growth mechanisms considered earlier in another papers, there is a difference in activity of dissociation at different faces of nickel single crystal. With the single crystal structure of catalytic center, complete dissociation of acetylene occurs on Ni (100) faces, while molecular desorption is observed on Ni (110) and Ni (111) faces.

It's considered that formation of nickel catalytic centers from atomic flows obtained by method of vacuum resistive evaporation. The initial data used in the calculations: the binding energy of two

nickel atoms adsorbed on the surface of the substrate W_G = 1.6 eV, residence time of atom on substrate $t_0 = 10^{-13}$ sec, evaporation temperature T_E = 1200 K and substrate temperature T_S = 750 K.

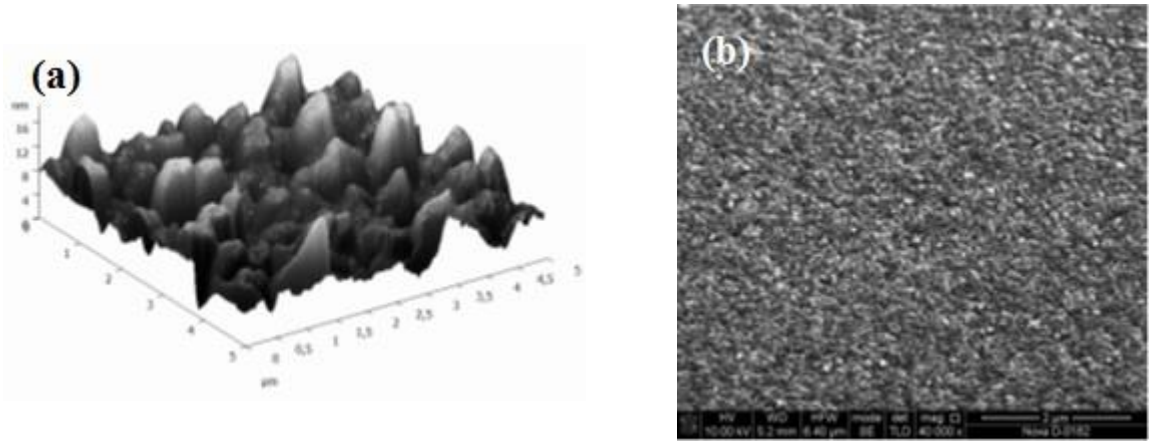

Figure 1 (a, b). AFM (a) и REM (b) images of catalytic centers fabricated on Ni/V/Si structures under 600°C.

So, for example, in theoretical model, the particle evaporation flow rate, taking into account assumption that there is no reevaporation of adsorbed single atoms, can be estimated based on kinetic theory of sublimation according to the Knudsen equation:

$$\boldsymbol{F = \frac{P}{\sqrt{2\pi mkT}}} \quad (1)$$

m – mass of molecule, P – equilibrium vapor pressure at the evaporation temperature T.

3. Results and Discussion

The model obtained in the course of theoretical studies allows us to evaluate dynamics of catalytic centers formation, taking into account their sizes. Based on the results of which we obtained the following values of flux of nickel atoms to substrate $F=1.296*10^{18}$, residence time of the nickel atom on the substrate in the adsorbed state $t_g=5.135*10^{-7}$, concentration of adsorbed atoms as a function of time и $N=6.657*10^{11}$.

Acknowledgments

This work was supported by the Grant of the President of the Russian Federation No. МК-3512.2019.8 The results were obtained using the equipment of the Research and Education Center "Nanotechnologies" of Southern Federal University.

References

[1] Aderhold J, Davydov V Yu, Fedler F, Klausing H, Mistele D, Rotter T, Semchinova O, Stemmer J, Graul J 2001 *J. Cryst. Growth* **151** 701
[2] Strite S, Morkoc H 1992 J. Vac. Sci. Technol. B **10** 1237
[3] Nakamura S, Senoh M, Nagahama S, Iwase N, Yamada T, Matsushita T, Kiyoku H and Sugimoto Y 1996 *Japan. J. Appl. Phys.* **35** L74
[4] Orloff J, Swanson L W, Utlaut M 2003 Springer New York
[5] Nagase M, Nakamatsu K, Matsui S, Namatsu H 2005 Japanese J. of Appl. Phys. 44(7) 5409
[6] Han J, Lee H, Min B, Lee S 2010 Microelectron. Eng. 87 1

Temperature effect on the luminescent properties of chromium-doped ceramics: in situ measurements

E V Kulpina, A N Babkina, K S Zyryanova

Research Institute of Nano-Photonics and Optical Information Technology, ITMO University, Saint Petersburg 199034, Russia

Abstract. This work is devoted to studying the influence of the temperature on the spectral and luminescent properties of nanoglassceramics obtained by high-temperature heat treatment of the initial glass containing chromium oxide. The luminescence spectra are obtained for samples with different concentrations of antimony oxide, which plays the role of a reducing agent, during heating and subsequent cooling. The dependence of the luminescence intensity on temperature is established. The possibility of using the materials under study as luminescent temperature sensors is also considered.

1. Introduction

One of the promising areas of optical material science is the development of glass-ceramics, wherein one or more crystalline phases are distributed in the amorphous glass matrix. Glass-ceramics are produced by controlled crystallization of certain glasses, which is generally induced by nucleating additives. This is in contrast with spontaneous surface crystallization, which is normally not wanted in glass manufacturing [1]. Such materials at the same time possess the advantages of both crystals (high quantum yield of luminescence, the absence of inhomogeneous broadening of spectral lines), and glasses (production simplicity and speed, lower costs for equipment and materials).

Currently, crystalline materials activated by transition metals ions are being actively studied. Glass-ceramics doped with chromium ions are of interest as materials for luminescent temperature sensors. The operation principle of these optical devices is based on the effect of temperature redistribution of energy over excited levels [2]. This technique provides a non-contact temperature measurement by probing the temperature dependence of fluorescence intensities. Compared with conventional temperature monitoring devices, fluorescence based thermometry system does not affect the temperature field and is particularly advantageous operating in electromagnetically and / or thermally harsh environments, such as at electrical power stations, near high power electric transmission lines, and remote temperature detection in buildings on fire [3].

In the present work, the temperature effect on the luminescent properties of chromium-doped borate glass-ceramics was studied. The results indicated that material under study has great potential to be used as optical temperature sensor with various advantages over the existing fluorescence-based sensors.

2. Methods and measurements

In the present work, glasses of the composition $12.5K_2O$-$12.5Li_2O$-$25Al_2O_3$-$50B_2O_3$ containing 0.1 mol. % Cr_2O_3 were synthesized. Antimony oxide was used as a reducing agent, the concentration of which varied from 0.5 to 0.005 mol. %. The obtained samples were heat treated at a temperature of 600°C thus forming stable volumes of the crystalline phase throughout the interior of the glass.

The temperature influence on the luminescent properties of ceramics under study were measured for several compositions containing different amount of antimony oxide. The measurements were carried out using an experimental setup consisting of a diode laser (wavelength 532 nm), a furnace wherein a sample was placed for heating, a focusing lens, and a spectrometer recording the luminescence spectra of the sample in real time. The sample was heated to a temperature of 600℃, followed by cooling to room temperature.

3. Results

Figure 1(a) shows the luminescence spectra of the sample containing 0.5 mol. %. Of antimony oxide with a change in temperature from 30 to 600. As we can see from the graph, the intensity of Cr^{3+} luminescence bands located in the 700 nm region rapidly decreases with increasing temperature and becomes insignificant when reaching 300℃. In addition, at high temperatures, a wide luminescence band in the region of 850-1150 nm is observed. Its appearance can be explained by the oxidation of trivalent chromium to a tetravalent state under the influence of the temperature. Figure 1(b) shows the temperature dependence of the luminescence intensity upon heating and cooling of the sample. It can be noticed that in the temperature range of 30-150℃ the intensity decreases linearly, which is a good reason for using the studied material as a temperature sensor.

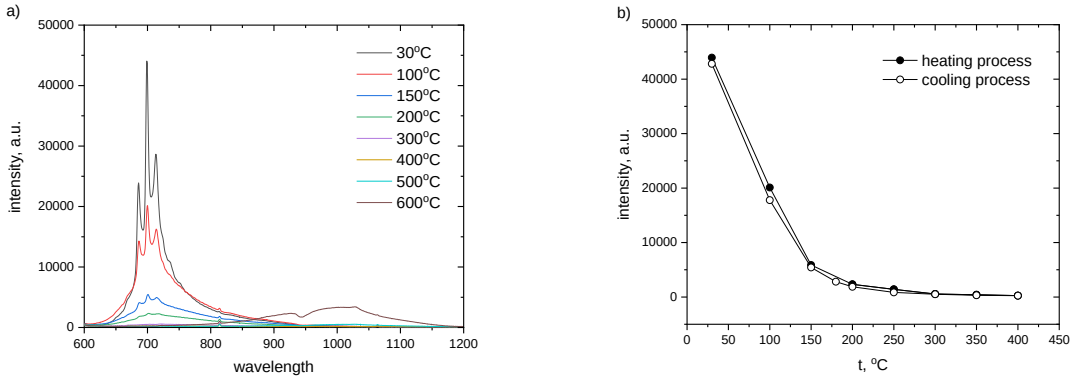

Figure 1. a) Luminescence spectra of chromium-doped ceramic with a change in temperature; b) Temperature dependence of the luminescence intensity upon heating and cooling of the sample.

4. Conclusions

During this study, the temperature dependence of Cr^{3+} luminescence intensity was obtained for samples with different concentrations of antimony oxide. It was found that rapidly decreases with increasing temperature, but high temperature causes the appearance of luminescence band in another spectral region.

Experiment showed that in the temperature range of 30-150℃ the luminescence intensity decreases linearly. Based on this, it was considered that chromium-doped ceramics can be used in construction of luminescent temperature sensors.

5. Acknowledgments

This work was funded by Russian Science Foundation (No. 19-72-10036).

References

[1] Zanotto E 2010 *Am. Ceram. Soc. Bulletin* **89** 19
[2] Collins S, Baxter G, Wade S, Sun T, Grattan K, Zhang Z and Palmer A 1998 *J. Appl. Phys.* **84** 4649
[3] Xua W, Gaob X, Zhengb L, Zhanga Z and Caoa W 2012 *Sensors and Actuators B: Chem.* **173** 250

Application of carbon nanoscale materials in instrument structures sensitive to the gas atmosphere

J V Morozova[1], A A Rezvan[1] and V S Klimin[1]
[1]Department of Nanotechnology and Microsystems, Southern Federal University, Taganrog 347922, Russia

Abstract: This paper presents a study of a vacuum meter with a sensitive element based on an array of carbon nanotubes. The study used a method of plasma chemical deposition from the gas phase, which allows to obtain oriented CNT arrays on various substrates. A special feature of this method is the use of catalytic centers. The results obtained during the study show that the vacuum meter has a sensitivity of about 2.4×10^{-8} A/PA, a speed of 4 seconds, at U=20 V, and a power consumption of 1.5×10^{-7} W.

1.Introduction

Increased interest in the study of carbon nanotubes (CNT) is due, on the one hand, to their unique physical and chemical properties, which make them an attractive object of fundamental research, and, on the other hand, to their broad prospects for applied use. The development of technologies for obtaining arrays of oriented carbon nanotubes with controlled parameters opens up wide opportunities for their application in microelectronic sensors for creating sensitive elements of gas sensors. Such sensitive elements can reduce the operating voltage and improve the weight and size characteristics of devices [1-3].

2.Materials and methods

When creating the vacuum meter, the substrate was made of Si silicon plates, which were coated with a film of Ti (300 nm) sublayer, which provides electrical contact to the CNT array, and a layer of Ni (10 nm) catalytic center material. Metal films were applied by magnetron sputtering. An array of vertically oriented CNT with a height of 5 microns and a diameter of 30-50 nm nanotubes was grown on the formed structure. the size of the array was 5x5 mm. As an insulator between the anode and cathode, self-conducting silicon plates were used, thinned by chemical etching to 55 microns, as a result, the gap between the tops of the CNT and the upper flat electrode was 50 microns. Next, the upper electrode was attached to the structure, which was a silicon plate Si with a layer of titanium 300 nm deposited on it, electrical contacts and load resistance were supplied.

3.Results

Figure 1 shows the Volt-ampere characteristics (VAC) of the vacuum meter at different air pressure in the chamber.

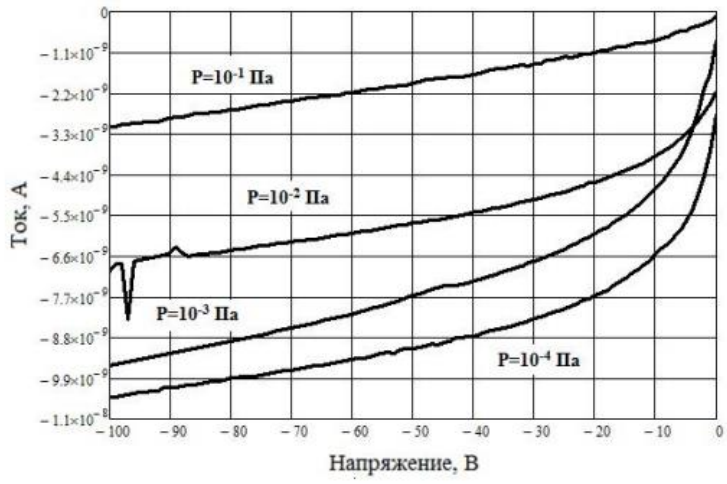

Figure 1-Volt-ampere characteristics of the layout at different pressures

The analysis of dependencies shows a decrease in current when the pressure decreases, which corresponds to Paschen's law. The dependence of current on pressure allows us to determine the sensitivity of the layout of the ionization gas sensor, when used as a vacuum meter, which is 2.4×10^{-8} A/PA at U = 20 V. in this case, the power consumption is 1.5×10^{-7} W. To determine the reaction time and recovery, experimental studies were conducted in which the vacuum chamber was pumped out from 770 Torr to 330 Torr in 120 seconds. The measurements were performed at a temperature of 300 K, with a potential of -20 V. under these conditions, the current changes from 8×10^{-7} A to 3×10^{-10} A in 124 seconds, with a pumping time of 120 seconds, which corresponds to a reaction time of about 4 seconds. The vacuum meter at U=20 V has a sensitivity to air pressure of the order of 2.4×10^{-8} A/PA with a speed of ~ 2 seconds, power consumption of 1.5×10^{-7} W.

4.Acknowledgments
This work was supported by the Grant of the President of the Russian Federation No. МК-3512.2019.8 The results were obtained using the equipment of the Research and Education Center "Nanotechnologies" of Southern Federal University.

5.References
[1] Aderhold J, Davydov V Yu, Fedler F, Klausing H, Mistele D, Rotter T, Semchinova O, Stemmer J, Graul J 2001 J. Cryst. Growth 151 701
[2] Strite S, Morkoc H 1992 J. Vac. Sci. Technol. B 10 1237
[3] Nakamura S, Senoh M, Nagahama S, Iwase N, Yamada T, Matsushita T, Kiyoku H and Sugimoto Y 1996 Japan. J. Appl. Phys. 35 L74

Formation of carbon nanoscale elements of vacuum microelectronics by plasma treatment of SiC

A A Rezvan[1], I N Kots[1,2], R V Tominov[1,2], V S Klimin[1,2], O A Ageev[1,2]
[1]Department of Nanotechnology and Microsystems, Southern Federal University, Taganrog 347922, Russia
[2]Research and Education Center "Nanotechnologies", Southern Federal University, Taganrog 347922, Russia

Abstract. The use of focused ion beams and atomic plasma chemical etching for forming an array of field emission structures on surface of SiC substrates is considered. SF_6 was used as the fluorine-containing gas. Topology of formed elements was monitored using scanning electron microscopy method at Nova NanoLab 600. Dependences of geometric parameters of formed structures (topology of tip and its depth) on emission current were determined. Dependence of change in applied voltage and generated electric field of used to study probe on emission current density is also considered.

1. Introduction

SiC is a promising material for micro- and nanoelectronics, and finds application in various manifestations, ranging from bulk MEMS structures to transistor elements. The instrumental output of SiC-based products largely depends on the Si or C side, which used with their distinctive physical and electrical parameters [1-3]. For each side, there are various technological methods for formation of structures, however, many of them either introduce significant damage to structural layers or require presence of additional dielectric layers to protect influence of substrate on the growth of working elements on SiC [4-6]. In this connection, development of formation technology of nanoscale emission structures based on SiC by focused ion beam and atomic plasma etching methods, a characteristic feature of which would be low influence of presence of bulk and structural defects in surface region of the substrate, is relevant.

2. Method

The studies are based on SiC substrates, surface of which was subjected to standard chemical cleaning processes. Initially, a frame of future nanoscale structure of a SiC-based field emitter was formed on surface of substrates using nanoscale profiling based on focused ion beams. For this, samples were placed in vacuum chamber of Nova NanoLab 600 module of focus ion beams and oriented in such a way that stream of accelerated ions fell on the substrate in the normal direction. During exposure to beams, working vacuum was maintained at a level of $1 \div 2 \times 10^{-4}$ Pa.
The next step was formation of a carbon nanoscale layer on the surface of array to reduce electron work function and start of electron emission. This process was carried out on basis of atomic layer etching in a fluoride plasma. SF_6 was used as a fluorine-containing gas, due to which it was possible to etch the surface layer of SiC. In this case, only Si was removed from their crystal lattice and a thin carbon layer was formed on the surface of the samples.

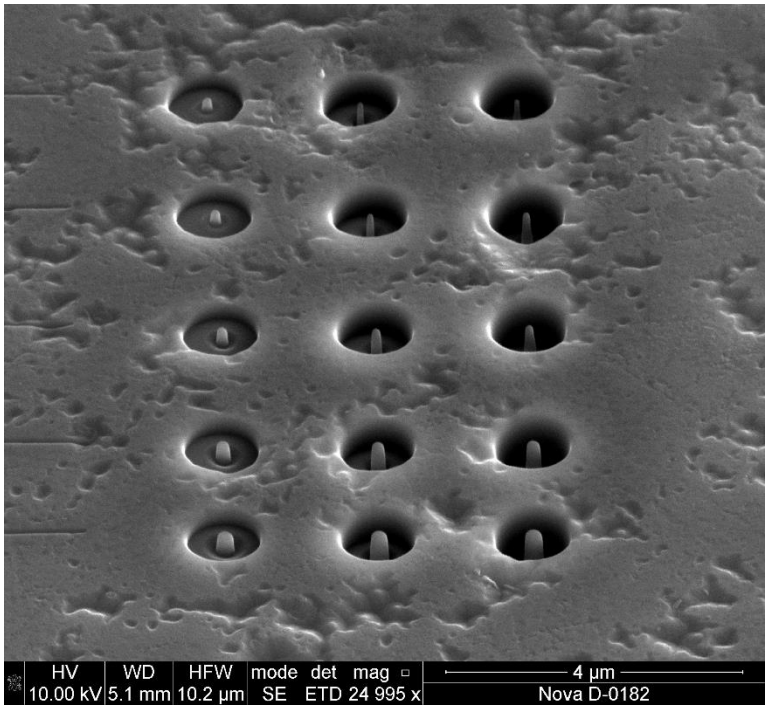

Figure 1. REM-images of SiC surface with auto emission structures massive based on graphene layer

Topology of formed elements was monitored using the Nova NanoLab 600 scanning electron microscopy method.

3. Results and Discussion

At the end of experimental series of studies, an array of field emission structures was formed on surface of SiC substrate, as shown in fig. 1. Dependences of geometric parameters of formed structures (topology of tip and its depth) on emission current were determined. Dependence of change in applied voltage and generated electric field of used to study probe on emission current density is also considered.

Acknowledgments

This work was supported by the Grant of the President of the Russian Federation No. MK-3512.2019.8 The results were obtained using the equipment of the Research and Education Center "Nanotechnologies" of Southern Federal University.

References

[1] Tok E S, Neave J H, Zhang J, Joyce B A and Jones T S 1997 Surf. Sci. 374 397
[2] Kley A, Ruggerone P and Scheffler M 1997 Phys. Rev. Lett. 79 5278
[3] Shiraishi K and Ito T 1998 Phys. Rev. B 57 6301
[4] Hou, Z., Xu, D., Cai, B. (2006) *Appl. Phys. Lett.*, 89, pp. 21-24.
[5] Modi, A., Koratkar, N., Lass, E., Wei, B., Ajayan, P.M. (2003) *Nature*, 424 (6945), pp. 171-174.
[6] Jitschin, W., Ludwig, S. (2004) *Vacuum*, 75 (2), pp. 169-176.

Luminescent Vertically oriented nanosheets MoS_2

Y.Khattab[1]* , S. E. Alexandrov[2] and I. Mukhin[3]

[1,2] Peter the Great Saint Petersburg State Polytechnic University, higher school of physics and materials technology, Polytechnicheskaya str. 29, 195251 St. Petersburg, Russia

[3] St. Petersburg Academic University

Abstract: In this work large-area vertically oriented MoS_2 (V-MoS_2) nanosheets were synthesized by single growth step using low temperature MOCVD on silicon, SiO2 and quartz substrates and there's optical properties were investigated.

Introduction:

MoS_2 has an attractive properties such as possibility to transform band structure of MoS_2 from an indirect band gap to a direct one when decreasing its thickness from bulk to a single, high mobility and absorption over broad spectral range layer [1], making it as a promising candidate in Nano-electronics and optoelectronics for manufacturing of enhanced transistors, sensors and electronic displays because of those unique properties. In addition, MoS_2 yielded the progressive results in the fields of solar cells, energy storages, energy conversions and catalytical applications [2]. However recently formation of vertically aligned MoS_2 nanosheets has been achieved and remarkable interest due to their features including high aspect ratio, maximum surface area, extensively exposed edges [3].

Experiments:

The deposition process was carried out in the hot-wall low pressure tubular CVD reactor . $Mo(CO)_6$ powder and H_2S were used for MOCVD growth of MoS_2 films. The Mo precursor $Mo(CO)_6$ was introduced into the deposition chamber by using argon as a carrier gas from the evaporator, which was maintained at temperature 30 °C, and H_2S were used as the reacting gas . Total pressure in the reaction chamber was fixed at 2 torr and deposition temperatures 250 °C, S/Mo ratio in reactor were 375, finally Time of deposition was 30 min.

Results:

The SEM images in figure 1 show as-deposited MoS2 film surface and cross-section, film compose of vertical aligned sheets with hight of 185 nm, while EDX (not shown) confirm the stoichiometry of the MoS2 film 2.05.

Raman spectrum of vertical nanosheets in figure 2 ,spectrum has two strong characteristic Raman modes E^1_{2g} and A_{1g} were observed at 382 cm^{-1} (FWHM ~18 cm^{-1}) and 407 cm^{-1} (FWHM ~ 8 cm^{-1}) corresponding to in-plane vibration of molybdenum and sulfur atoms, and out-of-plane vibration of sulfur atoms, respectively .The frequency difference (Δf) between the E^1_{2g} and A_{1g} modes can be reliably used to count the number of MoS2 layers. The Δf value observed is ~25 cm^{-1}, This indicates the presence of five or more layers of MoS2 in the Nanosheets. Integrated intensity ratio of the Raman modes (A_{1g}/E^1_{2g}) ~ 2.5,3. confirm vertical sheets[4].

MoS_2 has Two optical transitions denoted as mode A and mode B appearing at 1.85 and 1.95 eV (in the visible region). The PL spectra of vertical nanosheets is in figure 3, spectrum recorded at room temperature using laser argon (488 nm) , Vertical nanosheets has mode A at 1.87 eV while mode B disappear, and peak around 1.75 eV appear maybe due to trion and bound exciton. Interestingly, the PL feature observed here occurs at a similar energy position to that of the direct band-gap monolayer MoS2 indicating the growth of nanosheets with comparable optical quality to that of the monolayer MoS2.

References

[1] B. Radisavljevic, A. Radenovic, J. Brivio, V. Giacometti, A. Kis, Single-layer MoS2 transistors. Nat. Nanotechnol. 6, 147–150 (2011).

[2] H. Li, J. Wu, Z. Yin, H. Zhang, Preparation and applications of mechanically exfoliated single-layer and multilayer MoS2 and WSe2 nanosheets, Acc. Chem. Res. (2014)

[3] S. Li et al., Edge-enriched 2D MoS2 thin films grown by chemical vapor deposition for enhanced catalytic performance. ACS Catal. 7, 877–886 (2017).

[4] Saikumar Inguva, Jian-Hui Cai, Cong Hu, Jing Wu, Youming Lu and Xinke Liu, MATER. RES. EXPRESS, 2018 , V.5, N.7 , 075026.

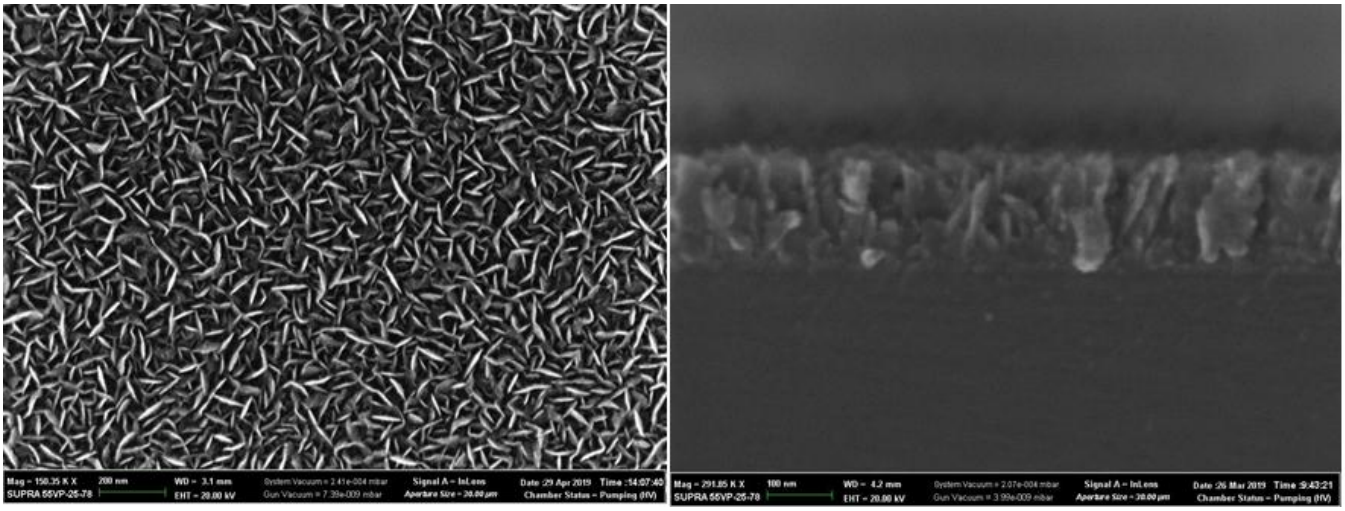

Figure 1, SEM images of vertical nanosheets from surface and cross section

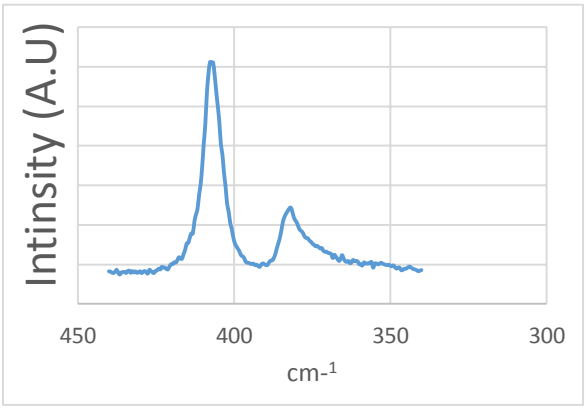

Figure 2, Raman spectra of vertical nanosheets

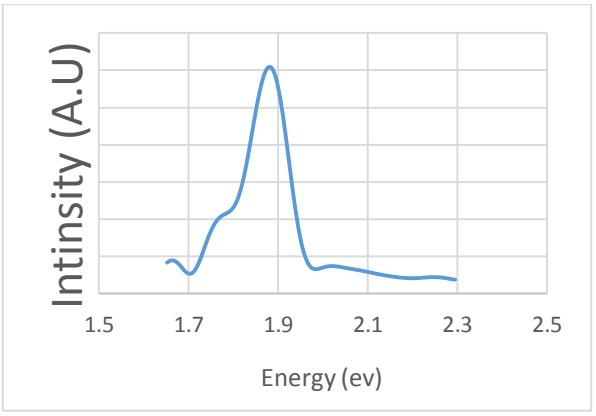

Figure 3, PL spectra of MoS2 vertical nanosheets

MBE growth and properties of InGaN nanostructures on Si substrates

V O Gridchin[1], R R Reznik [1-3], K P Kotlyar[1], D A Kirilenko[4], S V Morozov[5 6], N V Kryzhanovskaya[1], G E Cirlin[1-4]
[1]Alferov University, St. Petersburg 194021, Russia
[2]IAI RAS, St. Petersburg 198095, Russia
[3]ITMO University, St. Petersburg 197101, Russia
[4]Ioffe Institute, St. Petersburg 194021, Russia
[5]IPM RAS, Nizhny Novgorod 603950, Russia
[6]Lobachevsky University, Nizhny Novgorod 603950, Russia

Abstract. The work is concerned with a detailed study of the growth and physical properties of InGaN nanostructures with branched morphology. The InGaN nanostructures are grown by molecular beam epitaxy on unprepared Si (111) substrates. The study of a morphological properties shows that InGaN nanostructures such as nanoflowers and nanowires are formed. It is determined that the chemical composition of the obtained InGaN nanostructures corresponds to the miscibility gap.

1. Introduction

InGaN is a paramount material for applications in solid-state lighting [1] and renewable energy sources [2] because it has a direct band gap in the range from 0.7 to 3.43 eV achieved by tuning the alloy composition. However, the synthesis of high-quality InGaN epitaxial layers is difficult due to the lack of lattice-matched substrates, the miscibility gap and the different thermal expansion coefficients between InGaN and other materials. These problems can be tackled via the synthesis of InGaN nanostructures of branched morphology such as nanowires and nanoflowers. Due to a branched morphology of nanostructures, mechanical strains caused by the difference in lattice constants and thermal expansion coefficients between InGaN and substrates, effectively relax, leading to a significant decrease in the number of defects and a circumvent of the miscibility gap [3, 4].
This work presents the results on the growth by molecular beam epitaxy and investigation of morphological and optical properties of InGaN nanostructures of a branched morphology on unprepared Si (111) substrates.

2. Experiments

The InGaN nanostructures were grown using Riber Compact 12 MBE system equipped with In and Ga effusion cells and a nitrogen source.
Morphological properties of the samples were examined using a SUPRA 25 C. Zeiss scanning electron microscope (SEM). The optical properties of the samples were studied using the photoluminescence (PL) method at room temperature.

3. Results

A study of morphological properties of the samples synthesized shows that InGaN nanostructures have a complex shape. At the initial stage of growth, an array of high-density nanocolumns is formed. At the next growth stage, three-dimensional InGaN nanostructures, such as ‘nanoflowers’, are shaped. While

the growth of InGaN nanostructures at an elevated substrates temperature leads to the formation of uniform nanowires on the surface.
The studies of optical properties show that InGaN nanostructures of a complex shape exhibit PL spectra in a wide wavelength range of visible emission at room temperature. The photoluminescence spectra of the samples grown at an elevated substrates temperature are shifted to the short-wavelength area. The chemical composition of InGaN nanostructures estimated from the PL spectra correspond to the range inside of the miscibility gap.

4. Conclusion

In the work, InGaN nanostructures with a branched morphology like the nanoflowers and nanowires have been grown by MBE method on unprepared Si (111) substrates. The morphological and optical properties of the obtained samples have been studied. Our estimates of the In content in the InGaN nanostructures have shown that the chemical composition corresponding to the miscibility gap.

References

[1] Shubert E 2006 *Light-Emitting Diodes* (New York: Cambridge University Press)
[2] Li J, Ling J Y, Jiang H X 2011 *Appl. Phys. Lett.* **93** 162107
[3] Dubrovskii V G, Cirlin G E, Ustinov V M 2009 *Semiconductors* **43** 1539
[4] Roche E, André Y, Avit G, Bougerol C, Castelluci D, Réveret F, Gil E, Médard F, Leimarie J, Jean T, Dubrovski V G, Trassoudaine A 2018 *Nanotechnology* **29** 465602

Misfit stress relaxation in core-shell nanoparticles with pentagonal structure due to generation of prismatic dislocation loop

S A Krasnitckii[1,2,3], M Yu Gutkin[1,2,3], A L Kolesnikova[2,3], A E Romanov[2]
[1]Peter the Great St. Petersburg Polytechnic University, Polytekhnicheskaya 29, St. Petersburg 195251, Russia
[2]ITMO University, Kronverkskiy pr. 49, St. Petersburg 197101, Russia
[3]Institute of Problems of Mechanical Engineering, Russian Academy of Sciences, Bolshoj 61, Vasil. Ostrov, St. Petersburg 199178, Russia

Abstract. Theoretical models of stress relaxation in icosahedral and decahedral core-shell nanoparticles through the formation of circular prismatic misfit dislocation loops at the core-shell interface are proposed. It is shown that decahedral core-shell nanoparticles are more stable to dislocation formation than icosahedral ones. The theoretical results are compared with experimental observations available in the literature and are shown to be in a good agreement with the latter.

Crystalline composite core-shell nanoparticles (CSNPs) arouse a great interest due to their excellent functional properties. In particular, pentagonal CSNPs find various applications in catalysis [1–5,7], fuel cells [3], magnetics [5], nanoelectronics [3], optics [3,5,7], plasmonics [5], photocatalysis [5,7], sensors [3], biomedicine [5–7], etc. The stability of functional properties of pentagonal CSNPs is largely determined by their structural features such as the presence of multiple twins and either coherent or semicoherent interface state. These features induce the lattice distortion and misfit strains which are responsible for high residual stresses that could relax through various mechanisms. The experimental observations clearly indicate that, at the initial stages of the relaxation process in pentagonal CSNPs, the dislocation mechanisms are activated [8,9].

In the present work, we theoretically analyse the strain relaxation in icosahedral and decahedral CSNPs (Ic-CSNPs and Dh-CSNPs, respectively) through the generation of circular prismatic misfit dislocation loops (PMDLs). The strained state caused of the pentagonal symmetry is modelled by the Marks-Yoffe disclinations of strength 0.0613 sr in the case of Ic-CSNPs [10] and by partial positive wedge disclinations of strength 7º20' in the case of Dh-CSNPs [11]. This approach is a combination of previously solved problems for generation of similar dislocation loops in single-crystalline CSNPs [12] and in homogeneous Ic-NPs [13] and Dh-NPs [14]. In doing so, we analysed the change in the total energy of Ic-CSNPs and Dh-CSNPs caused by the generation of PMDLs at the core-shell interfaces in the approximation of equal and isotropic elastic moduli of the core and shell

materials. It is shown that there is such a critical value of the misfit parameter, which is determined by the nanoparticle sizes, that when it is overcome, the PMDL nucleation becomes energetically favorable. For a given value of the misfit parameter exceeding this critical value, there are two critical values of the normalized core radius, within which the formation of a PMDL is energetically favorable. Our theoretical results are in a good agreement with available experimental observations of perfect misfit dislocations in bimetallic Dh-CSNPs [8,9].

The reported study was funded by RFBR according to the research project № 18-33-00725.

References

[1] Toshima N, Yonezawa T 1998 *New J. Chem*. **22** 1179
[2] Ferrando R, Jellinek J, Johnston R L 2008 *Chem. Rev.* **108** 845.
[3] Shah A, Latif-ur-Rahman, Qureshi R, Zia-ur-Rehman 2012 *Rev. Adv. Mater. Sci.* **30** 133.
[4] Kharisov B I, Rasika Dias H V, Kharissova O V, Vázquez A 2014 *J. Nanopart. Res.* **16** 2665.
[5] Gilroy K D, Ruditskiy A, Peng H C, Qin D, Xia Y 2016 *Chem. Rev.* **116** 10414.
[6] Nasrabadi H T, Abbasi E, Davaran S, Kouhi M, Akbarzadeh A 2016 *Artificial Cells, Nanomedicine, and Biotechnology* **44** 376.
[7] Zaleska-Medynska A, Marchelek M, Diak M, Grabowska E 2016 *Adv. Coll. Interf. Sci.* **229** 80.
[8] Ding Y, Sun X, Wang Z L, Sun S 2012 *Appl. Phys. Lett*. **100** 111603.
[9] Khanal S, Casillas G, Bhattarai N, Velázquez-Salazar J J, Santiago U, Ponce A, Mejía-Rosales S, José-Yacamán M 2013 *Langmuir* **29** 9231.
[10] Howie A, Marks L D 1984 *Phil. Mag. A* **49** 95.
[11] Kolesnikova A L, Gutkin M Yu, Proskura A V, Morozov N F, Romanov A E 2016 *Int. J. Solids Struct.* **99** 82
[12] Gutkin M Yu, Kolesnikova A L, Krasnitckii S A, Romanov A E, Shalkovskii A G 2014 *Scripta Mater.* **83** 1.
[13] Gutkin M Yu, Kolesnikova A L, Krasnitckii S A, Dorogin L M, Serebryakova V S, Vikarchuk A A, Romanov A E 2015 *Scripta Mater.* **105** 10
[14] Krauchanka M Yu, Krasnitckii S A, Gutkin M Yu, Kolesnikova A L, Romanov A E, Aifantis E C 2018 *Scripta Mater.* **146** 77.

Light-emitting hexagonal 9R-Si phase obtained by Kr^+ ion implantation into Si and SiO_2/Si

A A Nikolskaya, D S Korolev, A A Konakov, A N Mikhaylov, A I Belov, R I Murtazin, D A Pavlov and D I Tetelbaum
Lobachevsky University, 23/3 Gagarin prospect, Nizhny Novgorod, 603950, Russia

Abstract. To study the mechanism of a 9R-Si hexagonal phase formation upon ion irradiation of the SiO_2/Si system, three types of experimental samples have been investigated by photoluminescence (PL) spectroscopy and transmission electron microscopy (TEM): SiO_2/Si irradiated by Kr^+, Si irradiated by Kr^+ and Si irradiated by (Kr^+ + O^+) ions. All the samples were annealed after irradiation. The first type sample shows the presence of the 9R-Si phase and PL band at ~ 1240 nm; the third type sample shows the same PL band and twinning defects; for the second type sample, the PL at 1240 nm is not detected. Based on the results, the role of mechanical stresses, radiation defects and oxygen in the formation of the hexagonal phase is discussed.

1. Introduction

The idea of using optical signal instead of electrical one was offered in order to increase the rate of signal transmission inside supercomputing devices. But silicon, being a traditional material of microelectronics, cannot be used as light emitter in its conventional cubic form due to the peculiarities of its band structure. Therefore, there is a demand in the silicon processing methods which would allow improving its optical properties. Previously [1], it was found by us that inclusions of hexagonal silicon of the 9R-Si phase were formed in silicon substrate at the interface with the film upon irradiation of the SiO_2(160 nm)/Si system by Kr^+ ions followed by annealing. The average projected range (R_P) of Kr^+ ions was less than the film thickness. For such samples, a photoluminescence (PL) band was detected at ~ 1235 nm, which was assigned to the emission of the 9R-Si phase. It was supposed that the formation of this phase occurred under the action of mechanical stresses arising in a dielectric film during implantation and/or annealing. To check this interpretation, in the present work, we have carried out additional experiments on the irradiation of silicon without a dielectric film with Kr^+ and (Kr^+ + O_2^+) ions, followed by annealing.

2. Experimental

Three types of samples were investigated. The first type was the SiO_2(140 nm)/Si system irradiated by Kr^+ ions (80 keV, $5 \cdot 10^{16}$ cm^{-2}) with R_P ~ 50 nm in SiO_2. The second type was silicon (without SiO_2 film) irradiated by Kr^+ ions with such values of energy (9 keV) and dose ($2.5 \cdot 10^{16}$ cm^{-2}), at which the displacements profile was close in shape and height to that in silicon substrate for the first type sample according to the SRIM code [2]. The third type was the same as the second one but additionally irradiated by O_2^+ ions (6 keV) at such a dose ($1 \cdot 10^{15}$ cm^{-2}), at which the number of oxygen atoms implanted per unit area was approximately equal to the number of oxygen recoil atoms when the SiO_2/Si system was irradiated by Kr^+ ions (for the first type sample). After irradiation, all the samples

were annealed at 800 °C (30 min). The PL spectra were measured at liquid nitrogen temperature upon laser excitation at 405 nm with a power of 10 mW. The cross-sections of the samples were studied by high-resolution transmission electron microscopy (TEM) using the JEOL JEM-2100F microscope.

3. Results and discussion

A PL band at ~ 1240 nm (Figure 1(a)) is revealed for the first and third type samples, which was previously observed by us for the samples with ion-irradiation-induced 9R-Si phase [1, 3]. The PL intensity is higher for the first type sample compared to the third one. No PL bands are observed for the second type sample. The TEM investigation of the first type sample shows the presence of inclusions of the 9R-Si phase in silicon substrate at the interface with SiO_2 film [3]. For the third type sample, only twin defects are observed in TEM images (Figure 1 (b)), which can be considered as the nucleation centers of the 9R-Si phase.

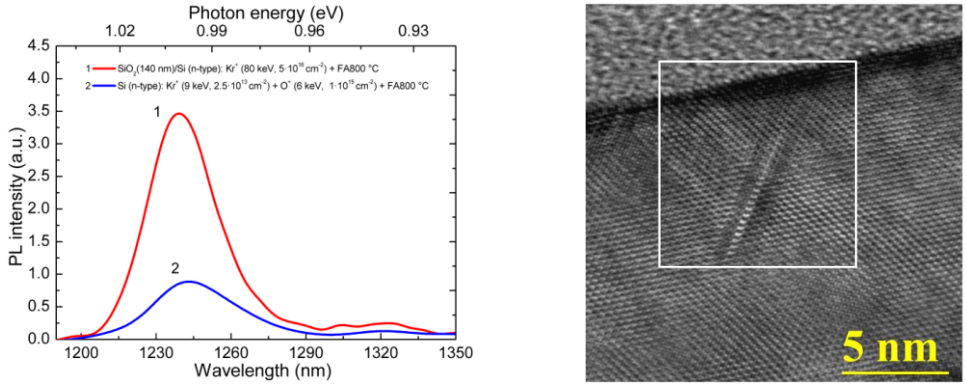

a) b)

Figure 1(a, b). (a) PL spectra of the first and third type samples; **(b)** high-resolution TEM image of the third type sample.

The results can be explained as follows. Kr atoms implanted into the SiO_2/Si system introduce additional mechanical stresses, the relaxation of which upon annealing causes the phase transformation in the silicon substrate. In addition, part of the implanted ions penetrates to the substrate from the film creating defects and mechanical stresses in it, which can also form inclusions of a new phase upon annealing. These factors together can synergistically contribute to the formation of the 9R-Si phase. This is confirmed by the experiments with the third type sample. Since only the second factor takes place in this case, the process of hexagonal phase formation is not so strongly expressed, so the TEM method, which probe only small parts of samples, cannot reveal local inclusions of the 9R-Si phase. This assumption about the presence of only local regions of the 9R-Si phase is confirmed by PL data: the PL intensity for the third type sample is much lower. Since no PL is found for the second type sample, we can make a conclusion about the role of oxygen in the 9R-Si phase formation. Probably, oxygen stabilizes defects during annealing, which induce stresses contributing to a new phase formation.

4. Acknowledgements

The work was supported by Russian Foundation for Basic Research (Grant No. 18-32-20168).

References

[1] Nikolskaya A A, Korolev D S, Mikhaylov A N, Belov A I, Sushkov A A, Krivulin N O, Muhamatchin K R, Elizarova A A, Marychev M O, Konakov A A, Tetelbaum D I and Pavlov D A 2018 *Appl. Phys. Lett.* **113** 182103
[2] Ziegler J F, Ziegler M D and Biersack J P 2010 *Nucl. Instrum. Methods Phys. Res. B* **268** 1818
[3] Nikolskaya A A, Korolev D S, Mikhaylov A N, Konakov A A, Belov A I, Marychev M O, Murtazin R I, Pavlov D A, Tetelbaum D I 2020 *Surf. Coat. Technol.* **386** 125496.

Diffusion-induced growth of ordered vertical nanowire arrays

K R Bikmeeva, A D Bolshakov

Alferov University (former St.Petersburg Academic University), 194021,
St. Petersburg, Russia

Abstract. Novel scalable techniques for the sub-micron substrate patterning provide intriguing possibilities for the development of devices based on ordered arrays of semiconductor nanowires. This work is devoted to theoretical investigation of semiconductor nanowires growth kinetics depending on the mask geometry (i.e. pitch and diameter of the mask openings). Diffusion of the growth species on substrate and sidewall with the respect to spacing arrangement and deposition rate has been studied. Dependencies of the nanowire growth rate on several parameters including pitch and its temporal dependence are investigated.

1. Introduction

Semiconductor nanowires (NWs) are very promising structures for the development of nanophotonic, opto- and nanoelectronic devices, such as light-emitting diodes, semiconductor lasers, solar cells, etc [1]. For the development of highly efficient devices based on NWs, it is important to obtain ordered NWs array with controlled diameter and spatial Solution of this problem requires theoretical studies of the growth processes. One of the promising methods to obtain nanostructures with controlled morphology is fabrication of the patterned growth mask [2] with the use of microsphere photolithography.

The aim of present work is the development and study of the kinetic model of the vertical NWs growth via vapor-liquid-solid mechanism on patterned substrate. By changing various model parameters, mask geometry and molecular flux rate we studied kinetics of the ordered NWs growth.

2. Model

The NWs growth generally involves several stages. On the first step the substrate is activated by liquid droplets of catalyst and is heated to a temperature above the eutectic melting temperature of the semiconductor and catalyst solution. The semiconductor material is then deposited at a fixed temperature. Adatoms diffuse through the droplet, creating a supersaturated solution and crystallize. As a result, NW monocrystal is formed perpendicularly to the substrate surface. Collection of the growth species into the droplet can be attained in the following ways: (a) direct impingement from the vapor phase; (b) diffusion of adatoms deposited on the NW lateral surface (sidewalls); (c) diffusion of adatoms from the substrate surface through side walls [3].

The model is based on the following approximations: NWs are cylinders with constant diameter, distribution of adatoms on the substrate has cylindrical symmetry, the NW footprint and the droplet are ideal absorbers. To address the problem of the adatom concentration distribution on the substrate and sidewalls two diffusion equations are solved, taking into account surface adsorption with flux intensity, depending on the lifetime and diffusion flux from substrate and sidewalls.

The boundary conditions for the substrate diffusion processes are 1) zero concentration along the perimeter of the NW footprint and 2) maximum adatoms concentration in-between two NWs. The dependence of the diffusion flux from the substrate to NW on the distance between NWs is shown in Figure 1 (a), where D – diffusion coefficient, Ω – volume per atomic pair in the solid phase, V – deposition rate. The flux increases by changing substrate diffusion length from 25 nm to 100 nm.
Figure 1 (b) represents NWs height-dependent growth rate. In calculations we assumed: 1) droplet acts as the perfect species collector; 2) continuity of the diffusion flux along the footprint perimeter. Results demonstrate that the highest growth rate corresponds to the larger value of sidewall diffusion length.

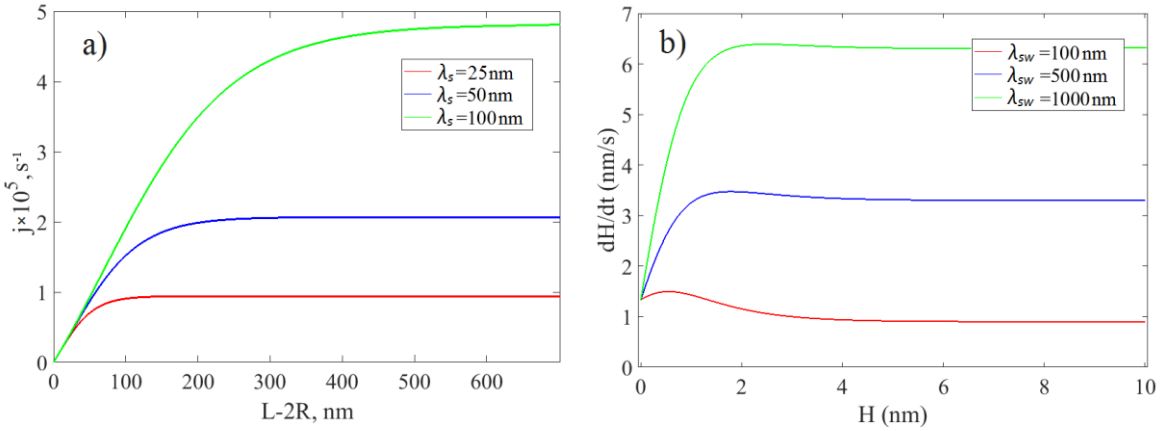

Figure 2 (a, b). (a) Dependence of the substrate diffusion flux on the distance between the NWs with the following parameters: R = 100 nm, D_s = 250 nm^2/s, Ω = 0.056 nm^3, V = 1 MS/s; **(b)** Dependence of the growth rate on NW length H with the following parameters: R = 100 nm, D_{sw} = 250 nm^2/s, Ω = 0.056 nm^3, V = 1 MS/s, $n_s'(r=R)$ = 3.7 nm^{-3}, λ_s = 100 nm, L = 1000 nm.

References

[1] Liu A Y, Peters J, Huang X, Jung D, Norman J, Lee M L, et al 2017 *Optics letters* **338-341** 42(2)
[2] Bolshakov A D, Dvoretckaia L N, Fedorov V V, et al 2018 *Semiconductors* **52** 2088–2091
[3] Dubrovskii V G, Cirlin G E, Ustinov V M 2009 *Semiconductors* **43** 1539

The influence of the morphology of oxidized copper nanoparticles on the electrical properties of microstructures obtained by dry aerosol printing

D.V. Kornyushin[1], A.A Efimov[1], K.M. Khabarov[1], V.V. Ivanov[1]
[1]Moscow Institute of Physics and Technology (National Research University), Dolgoprudny 141701, Russia

Abstract. The influence of the morphology of oxidized copper nanoparticles on the deposition efficiency, packing density, and resistivity of microstructures obtained by dry aerosol printing was studied. It has been established that the thermal treatment of aerosol nanoparticles allows to vary their morphology from branched submicron agglomerates to compact spherical nanoparticles with a size of 20-50 nm. It is shown that the use of spherical nanoparticles in comparison with agglomerates allows one to obtain densely packed nanoparticles on substrate. Moreover, obtaining of semiconductor microstructures from oxidized copper nanoparticles on a plastic substrate with a resistivity of 0.01 Ohm • m was demonstrated.

Today, printing technologies for the production of electronic devices (RFID tags, flexible displays, solar cells and others) on flexible plastic substrates are actively developing [1]. It is expected that these devices will have low cost, low weight and flexibility. The formation of electronic devices on plastic substrates is a difficult task, since plastic substrates have a high sensitivity to thermal treatment. In this regard, the formation of functional elements on plastic substrates is carried out using nanoparticles having a lower sintering temperature than bulk material. At the same time, the use of nanoparticles leads to additional difficulties associated with their low deposition efficiency on the substrate and high oxidative ability, which changes the electrical properties of the microstructure. For this reason, the establishment of the formation of microstructures from nanoparticles on plastic substrates requires multifactorial research. So in this paper, we study the influence of the size and shape of oxidized copper nanoparticles on the electrical properties of microstructures obtained using the dry aerosol printing method on substrates of polyimide and silicon.

The experimental setup for the formation of microstructures from nanoparticles in the form of lines includes the following key elements: a gas-discharge nanoparticles generator [2], a thermal optimizer for controlling the size and shape of nanoparticles, a coaxial micro-nozzle for focused deposition of nanoparticles on a substrate and a coordinate table with the possibility of moving the substrate from a given speed relative to the micro nozzle, see **Figure 1a**. The formation of microstructures from nanoparticles is carried out in dry form without the use of solvents or surfactants. The generation and deposition of nanoparticles obtained by electrical erosion of copper electrodes is carried out in an atmosphere of a gas mixture Ar+H2(5%).

The size, shape and elemental composition of the nanoparticles is studied using a transmission electron microscope and aerosol spectrometer. The geometry of the microstructures of the nanoparticles is measured using a scanning electron microscope and an optical profilometer. Microstructures of nanoparticles are formed in the form of lines having a width and thickness of 200-300 μm and 0.1-8 μm, respectively. By varying the operating modes of the thermal optimizer, the size and shape of the nanoparticles are controlled. At the same time, the efficiency of the deposition of nanoparticles on the

substrate, their packing density is qualitatively investigated, and the resistivity of microstructures on substrates of polyimide and silicon is measured.

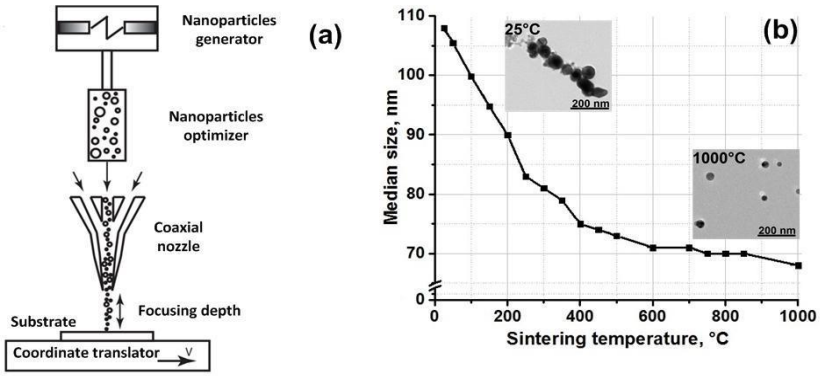

Figure 1(a, b). (a) Experimental setup for the formation of microstructures from nanoparticles on substrates of polyimide and silicon; **(b)** Median particle size of the agglomerates vs the sintering temperature. Insets: TEM micrographs of typical particles at 25 °C and 1000 °C.

Figure 1b shows that with an increase in the sintering temperature of nanoparticles from 25°C to 1000 °C, the median size of nanoparticles decreases from 108 to 65 nm, respectively. Moreover, from the analysis of TEM images of unsintered (25 °C) and sintered (1000 °C) nanoparticles shown in the inset in **Figure 1b**, it is shown that branched fractal agglomerates > 200 nm in size are transformed into compact spherical particles of the order of 20-50 nm.

From analysis of the efficiency of deposition of nanoparticles on polyimide and silicon substrates, it was found that both agglomerates and spherical nanoparticles are more efficiently deposited on a polyimide substrate. In this case, spherical nanoparticles have a lower deposition efficiency on a silicon substrate in comparison with agglomerates. This result is probably associated with a higher coefficient of rebound of spherical nanoparticles from a solid silicon substrate.

The packing density of microstructures of nanoparticles deposited on a silicon substrate depending on the morphology of the nanoparticles was studied using scanning electron microscopy. It was found that microstructures formed from deposited spherical nanoparticles have lower porosity than microstructures consisting of agglomerates. For this reason, it is likely that the resistivity of microstructures formed from spherical nanoparticles is less than microstructures consisting of agglomerates. Thus, the resistivity of microstructures formed from agglomerates and spherical nanoparticles were 0.04 and 0.01 Ohm•m, respectively.

It was found that the deposition efficiency and the packing density of nanoparticles on the substrate significantly depends on the size and shape of the nanoparticles and the type of substrate. From analysis of the efficiencies of the deposition of nanoparticles on polyimide and silicon substrates, it was found that both agglomerates and spherical nanoparticles are more efficiently deposited on a polyimide substrate. At the same time, microstructures formed from compact spherical nanoparticles have higher values of the packing density of nanoparticles and, as a result, the minimum resistivity.

Acknowledgments

This work was supported by the Russian Science Foundation (project # 19-79-00375).

References

[1] Yang C, Zhou E, Miyanishi S, Hashimoto K, Tajima K 2011 *ACS Appl. Mater. Interfaces* **3**, 4053–4058.

[2] Ivanov V V, Efimov A A, Myl'nikov D A, Lizunova A A 2018 *Russ. J. Phys. Chem.* **92**, 607–612

Influence of thermal treatment on the morphology and composition of Ge Nanowires

F S Lipilin[1], **I M Gavrilin**[2]
[1]Institute of advanced materials and technologies, National Research University of Electronic Technology, Moscow, Zelenograd 124498, Russia; [2]Frumkin Institute of Physical Chemistry and Electrochemistry, RAS, Bld. 4, 31, Leninsky prospect, Moscow, Russia

Abstract. In this work we studied influence of thermal treatment on Ge nanowires (GeNW). The obtained results showed that thermal treatment can be used for control the composition of GeNW, what is important for technologies,-where the presence of In may negatively affect the operation of the device.

1.Introduction

Nowadays much attention is paid to the formation of GeNW, which find application in lithium-ion batteries, field-effect transistors and optoelectronic devices. Work [1] describes synthesis of it using various methods. However, the most convenient is electrochemical deposition from an aqueous Ge solution with a mechanism electrochemical liquid−liquid-solid (ec-LLS), which group led by Maldonado [2] has presented. The advantages of this method are low-temperature procedure, low-cost and non-toxic sources of Ge. The growth of structures is carried out by the following mechanism: Ge (IV) ions are reduced on the surface of low-melting metal nanoparticles (in this case, In) to Ge^0, followed by dissolution in In; the solubility of Ge in In is 10^{-2} at.% , so the volume of particles is rapidly saturated and Ge crystallizes at the metal-substrate interface. But it has as specificity of dissolving In in Ge during the growth of the nanowires (about 5-6 at. %), what could be critical for some applications. Accordingly, it is important to control the In concentration into GeNW. Our previous results showed [3] that nanowires obtained by the ec-LLS method are sensitive to thermal effects. So, in this work we investigated influence of thermal treatment on the morphology and composition of GeNW.

2. Methods

Electrochemical deposition of GeNW was performed in chronopotentiometry mode at current densities of 0.2 mA/cm^2 and 2 mA/cm^2 at 20°C.The thermal treatment of samples was done in a vacuum at 300°C and 600°C.The structures as-prepared and after treatment were examined using Scanning Electron Microscope (SEM).The study of elemental analysis of samples before and after thermal treatment (table 1) was made by using high-angle annular dark-field scanning transmission electron microscopy (HAADF-STEM) with energy-dispersive microanalysis.

3. Results

The results of elemental analysis showed certain effect of thermal treatment on GeNW. The morphology of GeNW does not change after treatment (figure 1), but concentration of In has decreased (table 1). After heating in a vacuum at 600°C, the concentration of In in GeNW was less than 1 at.%. It can be explained by evaporation of In, because it has low melting point (156°C). In case of 300°C such result

was not achieved. This confirms the possibility to control the composition of GeNW by following thermal treatment, what is important for technologies, where the presence of In may negatively affect the operation of the device

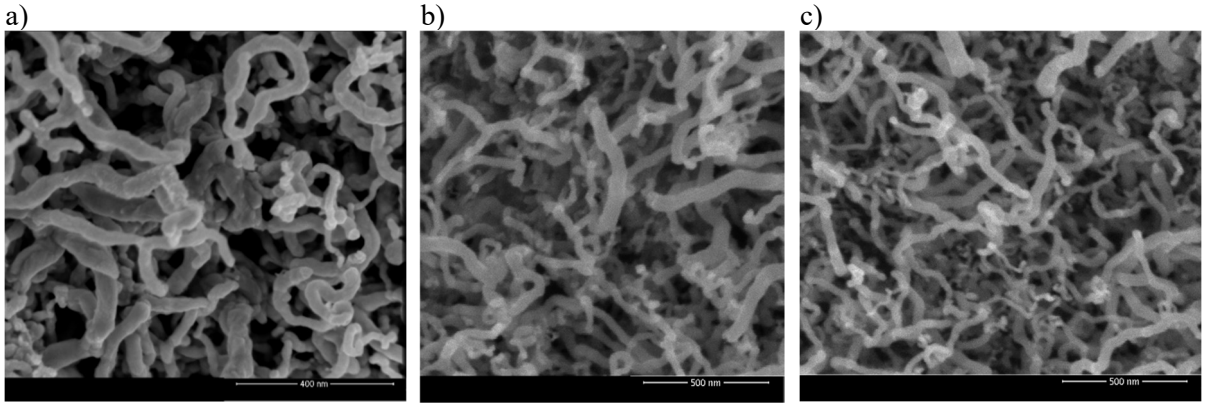

Figure 1. SEM-image of GeNW after different thermal treatment procedure: a) as-prepared; b) after 300°C, 30 minutes; c) after 600°C, 30 minutes.

Table 1. Elemental composition of GeNW

thermal treatment	Ge, at. %	In, at. %	O, at. %
as-prepared	97	3	0
300°C, 30 minutes	95	4	1
600°C, 30 minutes	96	0	4

References

[1] Li Z. Pei. A Review on Germanium Nanowires / Li Z. Pei and Zheng Y. Cai // Re-cent Patents on Nanotechnology. – 2012. - № 6. - P 44-59.

[2] Stephen Maldonado. Template-Free Preparation of Crystalline Ge Nanowire Film Electrodes via an Electrochemical Liquid−Liquid−Solid Process in Water at Ambient Pressure and Temperature for Energy Storage / Junsi Gu, Sean M. Collins, Azhar I. Carim, Xiaoguang Hao, Bart M. Bartlett and Stephen Maldonado // Nano Lett. – 2012. - P 4617-4623

[3] Alexander V. Pavlikov. Investigation of the Stokes to anti-Stokes ratio for germanium nanowires obtained by electrochemical deposition / Alexander V. Pavlikov, Pavel A. Forsh, Pavel K. Kashkarov, Sergey A. Gavrilov, Alexey A. Dronov, Ilya M. Gavrilin, Roman L. Volkov, Nikolay I. Borgardt, Sofia N. Bokova-Sirosh, Elena D. Obraztsova // Journal Raman Spectroscopy. – 2020. – 1–6.

Ordering mechanism of silver nanoparticles synthesized in a ZnO:Al polycrystalline film by sol gel method

L A Sokura[1,2], Zh G Snezhnaia[1], V N Nevedomskiy[2], A E Romanov[1]
[1]Saint Petersburg National Research University of Information Technologies, Mechanics and Optics (ITMO University), Saint Petersburg 197101, Russia
[2]Ioffe Institute RAS, Saint Petersburg 194021, Russia

Abstract. The optical absorption spectra and structural properties of ZnO:Al films with an intermediate layer of silver nanoparticles with a different number of inserted layers of silver nitrate solution are studied. The study of optical properties showed that with an increase in the number of layers, the intensity of the plasmon absorption peak of nanoparticles increases. Consequently, with an increase in the number of layers, their concentration increases, this was confirmed by studies of the obtained samples structural properties by transmission electron microscopy.

Silver nanoparticles introduced into the zinc oxide matrix, due to their plasmonic properties, significantly change its optical characteristics. Such composite materials are very promising for applications in thin-film devices [1-2]. And the use of simplicity and cheap technology for their manufacture, for example, sol gel technology, would ensure their industrial applicability [3].

The correlation of the optical and structural properties of composite coatings consisting of ZnO:Al oxide films (AZO) with an intermediate layer of silver nanoparticles obtained by the sol-gel technology were investigated. Previously, the authors found that when layers of a silver nitrate solution are inserted between the layers of a zinc oxide matrix, an ordered structure of silver nanoparticles is formed in the film [4-5]. An important fact for controlling the obtained composite structure was that the time and temperature of annealing of the film affect the sizes of nanoparticles. Optical measurements showed that the position of the peak of plasmon nanoparticles in AZO also depends on them.

The present work of the authors is devoted to elucidating the influence of technological factors for producing silver nanoparticles in a zinc oxide matrix by the described method on the concentration of nanoparticles. It was found that the increase of inserted layers number of silver nitrate solution leads to the intensity of nanoparticles plasmon absorption peak also increases (Figure 1). To find out the reasons for this optical behavior property, a series of samples consisting of AZO oxide films with an intermediate layer of silver nanoparticles with a different number of layers will be studied by transmission electron microscopy (TEM).

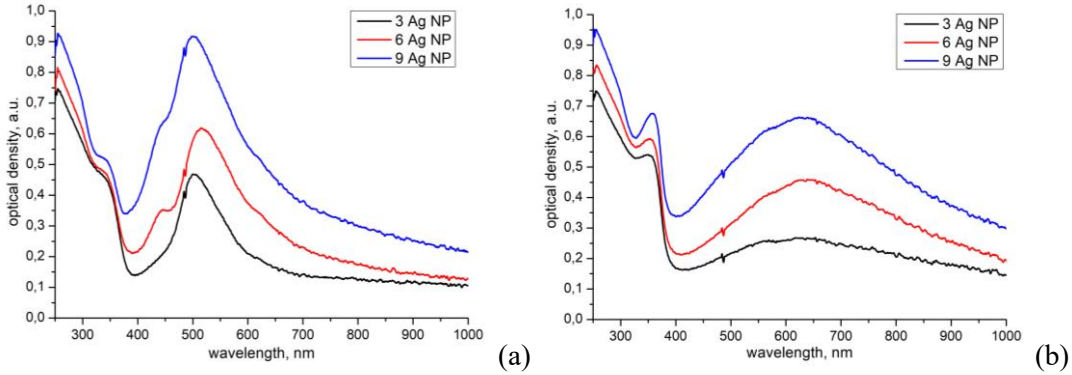

Figure 1. Optical density spectra of polycrystalline ZnO:Al (0.5%) films with 3, 6 and 9 layers of silver nanoparticles, before (a) and after (b) annealing at 570 ºC.

The TEM studies were performed using equipment owned by the Joint Research Center “Material science and characterization in advanced technology” (Ioffe Institute).

References

[1] Szabó O, Flickyngerová S, Ignat T, Novotný I, Tvarožek V 2016 *Facta Universitatis, Series: Electronics and Energetics* **29** (1) 77-88
[2] Inamura R, Toyoda T, Tanaka T, Uzumaki T 2009 *Journal of Applied Physics* **105** (3) 034314
[3] Bochkareva S S 2016 *Proceedings of Universities. Applied Chemistry and Biotechnology* **6** 81-93
[4] Shirshneva-Vaschenko E V, Sokura L A, Baidakova M V, Yagovkina M A, Snezhnaia Zh G, Shirshnev P S, Romanov A E 2019 *Journal of Physics: Conference Series* **1400** (1) 055026
[5] Sokura L A, Shirshneva-Vaschenko E V, Kirilenko D A, Snezhnaia Zh G, Shirshnev P S, Romanov A E 2019 *Journal of Physics: Conference Series* **1410** (1) 012170

Photoluminescence of n-InP (100) surface, passivated with aqueous Na_2S solution

Y M Serov, M V Lebedev, O V Rakhimova, T V Lvova, I V Sedova
Ioffe Institute, Saint Petersburg 194021, Russia

Abstract. Passivation of the n-InP(100) surface with an aqueous solution of sodium sulphide has been investigated by spectroscopic photoluminescence (PL). After sulphide treatment the PL signal of InP increased and this increase is dependent on time of sulphide treatment and conditions of PL measurements. In addition, the enhancement of the PL intensity after sulphide treatment correlates with the variation of the solution pH in contact with InP(100) surface, which makes possible the optimization of the passivation process by monitoring of the solution pH value in the course of sulphide treatment of the semiconductor.

1. Introduction

Indium phosphide (InP) is a III–V direct gap semiconductor used in high frequency electronics and optoelectronics. However, its applications, especially the ones based on InP nanostructures, are suffering from the surface instability inducing detrimental effects on the surface electronic and optical properties. Sulphur-based surface passivation intended to mitigate these effects has been investigated since late 1980s and is proved to improve device properties, such as Schottky barrier temperature stability [1] and field-effect transistor parameters [2]. Nevertheless, early works show no impact of sulphur passivation on the InP photoluminescence (PL) intensity [3]. More recent results [4] demonstrate that InP PL signal might be enhanced essentially by sulphide treatment, though the dependence of PL on the time of sulphide treatment is non-monotonic, and thus the optimization of the sulphide passivation process should be performed. On the other hand, it was shown that in the process of GaSb surface passivation with an aqueous sodium sulphide (Na_2S) solution the PL results correlate with the variation of the solution pH during the process [5]. Here we adopt this approach and study the effect of the surface passivation with aqueous Na_2S solution on the PL of InP(100).

2. Experimental procedure

The samples under investigation have been prepared from the n-doped InP (100) wafer with the doping density of about 10^{18} cm^{-3}. The sulphide treatment was performed with 1M aqueous solution of Na_2S at the temperature of about 40 ^{o}C for various periods of time from 1 to 15 min. The smallest time of treatment of 1 minute was chosen because after approximately 1 minute of InP contact with the solution, the sharp increase in the solution pH was observed. After one minute of contact the pH value slightly decreased and then remained almost constant up to 3 minutes of contact, while afterwards it monotonically went up. So it was of high interest to examine the surface state and PL intensity of InP treated for different periods of time corresponding to the features in the pH(t) dependence.

The samples were fixed in the cryostat and studied either at room temperature (300 K) or at liquid nitrogen temperature (77 K). The photoluminescence was excited with a diode laser with the wavelength of 377 nm in continuous mode or 405 nm in pulsed mode. The laser beam was focused on the sample surface into the spot with the diameter of about 50 μm by the lens with the focal length of

79 mm. The photoluminescence signal was collected with the apochromatic triplet and focused on the spectrometer entrance slit. PL spectra were obtained with a Princeton Instruments SP-2500 spectrometer ($L = 0.5$ m, grating – 300 lines/mm) and detected with a CCD-camera.

3. Results and discussion

The shapes of PL spectra measured both at 300K and 77K were unaffected by the sulphide treatment, while the integral PL intensity was significantly enhanced after passivation. The obtained dependence of the integral PL intensity on the time of sulphide treatment is presented in fig. 1. The curve (a) shows that even after sulphide treatment for 1 min the PL intensity was more than 6 times higher than that of the reference sample, while longer treatment caused slightly lower enhancement. Another set of samples was studied at 300K and at 77K, and the results obtained are shown by curves (b) and (c), respectively. One can observe, that even though the achieved enhancement is less for this set probably due to lower excitation power density, the effect of surface passivation on InP PL intensity is more significant at room temperature than at 77K. We associate this to the fact that at low temperature the surface recombination is suppressed and thus the surface exerts less influence upon the PL intensity.

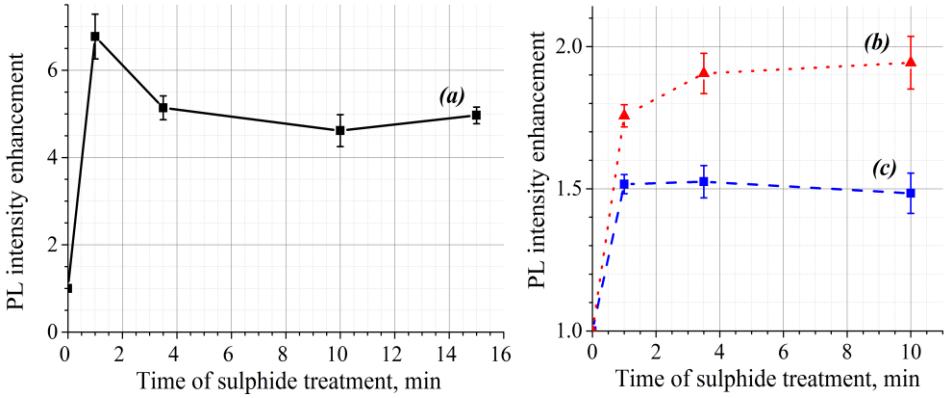

Figure 1. PL intensity enhancement as a function of time of sulphide treatment for the first set of samples measured at 300 K (a) in continuous mode with the excitation density of 250 $W \cdot cm^{-2}$ and the second set of samples measured at 300 K (b) and 77 K (c) in pulsed mode with the excitation density of 50 $W \cdot cm^{-2}$.

4. Conclusion

Passivation of n-InP(100) surface with an aqueous Na_2S solution can improve essentially the PL properties of the semiconductor without any significant changes in spectral shape. Our approaches to the determination of the specific mechanism of passivation have not yield unambiguous results yet, so this issue needs further investigation. In addition, it was proved, that the optimization of the InP sulphide passivation process can be based on the control of the solution pH value.

5. Acknowledgments

The reported study was funded in part by RFBR, project number 20-03-00523.

References

[1] Ahaitouf A, Bath A, Losson E, Abarkan E 1997 *Mater. Sci. Eng. B* **52** 208
[2] Iyer R, Chang R, Lile D 1988 *Appl. Phys. Lett.* **53** 134
[3] Suniiararaman C, Poulin S, Currie J, Leonelli R 1991 *Can. J. Phys.* **69** 329
[4] Tian S, Wei Z, Li Y, Zhao H, Fang X, Tang J, Fang D, Sun L, Liu G, Yao B, Ma X 2014 *Mater. Sci. Semicond. Process.* **17** 33
[5] Lebedev M, Lvova T, Sedova I 2018 *J. Mater. Chem.* **6** 5760

The study of Si/Ge interdiffusion using molecular dynamics simulation

M V Bastrakova, K R Mukhamatchin, Yu M Kuznetsov, M V Dorokhin
Lobachevsky State University of Nizhny Novgorod, Nizhny Novgorod, 603950, Russian Federation

Abstract. The coefficients of mutual diffusion of silicon into germanium (and vice-versa) at sintering temperatures of 900-1300K were found based on molecular dynamics simulation. For the characteristic temperature T_c=1100 K, implemented in experiments on spark plasma sintering technique, we determined the thickness of the diffusing layer for each type of atom. It is shown that the depth of diffusing significantly depends on the sintering time, and silicon atoms penetrate 1.5 times deeper into bulk germanium than germanium into silicon.

1. Introduction

Various materials with pronounced thermoelectric properties are being actively studied. At the same time, one of the promising materials is Si/Ge solid solutions, which have high mechanical strength, low volatility, radiation and high temperature stability, which allows us to consider them as nanostructured thermoelectric material of the future [1]. Such compounds are usually obtained by spark plasma sintering technique due to the action of compression and heating forces on the Si/Ge powder. In this case, it is important to identify and study the diffusion processes that occur during sintering.

This work is aimed at studying the processes of interdiffusion of Ge and Si, occurring at different temperatures of heating and isothermal holding, simulating the processes of spark plasma sintering technique. In this paper, the simulation of diffusion processes in the Si/Ge system was performed using the method of molecular dynamics (MD). The advantage of the MD method is that it has a high spatial and temporal resolution, and allows us to study both thermodynamic properties and time-dependent phenomena.

2. Simulation model and numerical results

In this paper, the MD simulation of the Si/Ge system was performed using the LAMMPS package. The Tersoff potential was used to describe the interaction between Si and Ge atoms [2]. It was assumed that the initial thermal velocities of atoms are subject to the Gaussian distribution at room temperature, and it is also taken into account that the contacting surfaces are subjected to compression in the direction perpendicular to the weld of the contacting materials. For MD calculations, the system relaxes during 100 ps with a microscopic (nve) ensemble from the loading temperature T = 300K to the set sintering temperature T_c. Then the system evolves 1000 ps at a given pressure p =70 MPa and temperature T_c (net). In this work, we numerically studied the mean square displacements (MSD) of Si and Ge atoms from their equilibrium positions at T_c = 900 K – 1300 K to study the diffusion processes

$$\mathrm{MSD}_{Si,Ge} = \frac{1}{N_{Si,Ge}} \sum_{i}^{N_{Si,Ge}} [r_i(t) - r_i(t_0)]^2 , \quad (1)$$

where $r_i(t)$ represents the position *i* of the Si/Ge atom at time t, and $r_i(t_0)$ indicates the initial position of the corresponding atom; $N_{Si,Ge}$ are the number of atoms.

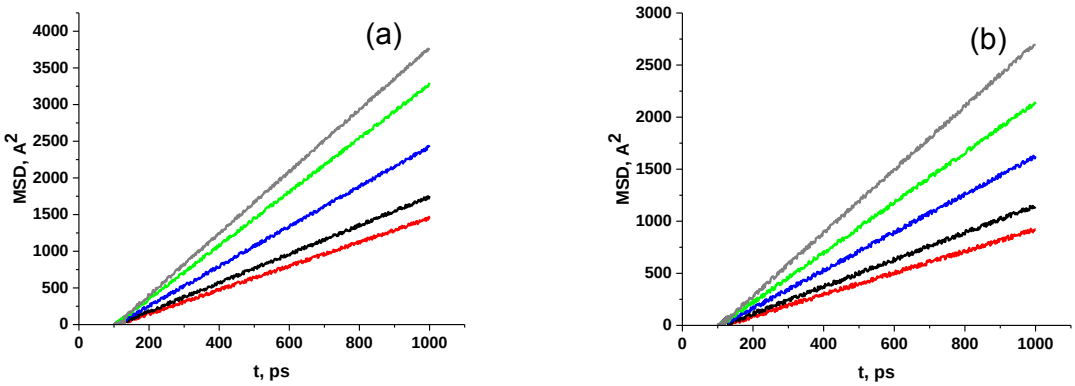

Figure 1 (a, b). The mean-square displacement plots (MSD) of Si/Ge interlayer: **(a)** Si, **(b)** Ge at different sintering temperatures T_c = 900 K (red curves), 1000 K (black curves), 1100 K (blue curves), 1200 K (green curves), 1300 K (gray curves).

Figure 1 shows that the slopes of the MSD curves become steeper with increasing temperature for both Si and Ge. It is known that the MSD profile is linear to the delay time in the long-time limit, and thus the diffusion coefficients of Si and Ge atoms at the interface can be derived from the slopes of MSD profiles after a longer delay time by the Einstein equation:

$$D_{Si,Ge} = \frac{1}{2d}\lim_{t\to\infty}\frac{d}{dt}\mathrm{MSD}_{Si,Ge}, \qquad (2)$$

where d = 3 is the dimension of space. Based on the numerical calculation data presented in Fig. 1, we found the diffusion coefficients $D_{Si,Ge}$ for various temperatures by the least squares method and calculated the thickness of the diffusion layer [3]: $L_{Si,Ge} \sim 3\sqrt{2D_{Si,Ge}t}$. Moreover, for a characteristic sintering temperature T_c = 1100 K and a holding time of 15 min, the width of the diffusion layer is L_{Si} ~ 6 μm and L_{Ge} ~ 4 μm.

The simulation results were extrapolated to a minute scale for a qualitative comparison with the sintering experiment, and it was shown that the diffusion depth significantly depends on the sintering time, while silicon atoms penetrate 1.5 times deeper into bulk germanium than germanium into silicon, which consistent with experiments.

3. Acknowledgments

This work was supported by a grant from the Russian Science Foundation № 17-79-20173.

References

[1] GaynerC, Kar K 2016 Prog. Mat. Science. **83** 330
[2] Tersoff J 1990 Phys. Rev. B **41** 3248
[3] Chen S Y, Wu Z W 2013 Journal of Applied physics **113** 044901

Research of the effect of solvents on the rheological characteristics of drop-on-demand inkjet liquid toner.

K. Klimontov[1], V. Vaganov[1], A. Kruglov[1]
[1]Peter the Great St. Petersburg Polytechnic University, 195251

Abstract. In this work the relationship of the rheological characteristics of liquid toner with external factors (shear strain rate, temperature) depending on the solvent used is investigated, experiments with a number of solvents (sulfolane, 3-methoxypropionitrile or acetonitrile) are carried out.

1. Introduction

Inkjet printing offers oil-free toner application with micrometer accuracy and material saving [1]. Liquid toner is a substance consisting of a complex mixture of particles, which are separated due to mutual immiscibility and the repulsive force of the material in a stationary state, so that the system remains unmixed [2]. After the application of deformation and shear, the toner may first exhibit induced elasticity, since the mixing resistance reaches a maximum, which causes dilatation. Dilatancy caused by high shear rates leads to rapid evaporation during ejection, and hence to undesirable clogging of nozzles [3].

2. Research and results

Dynamic measurements of toner viscosity (Figure 1 (a)) indicate thinning behavior at low and medium shear strain rates and thickening behavior at higher shear strain rates. Complex viscosity (Figure 1 (b)) is the structural deformation characteristic of toner.

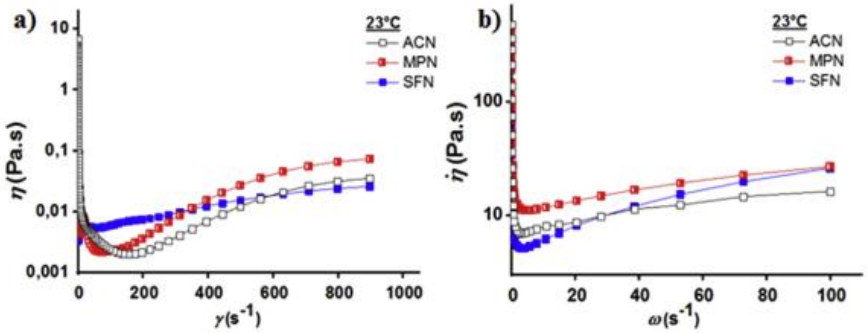

Figure 1. a) Rheological properties of toner: a) dynamic shear viscosity (η), **b)** complex (η *) viscosity

The atomic-force microscope (AFM) images of the bare and room temperature inkjet printed substrates (Figure 2) were used to further investigate the printouts. As revealed form Figure 2 (d) printout morphology of SFN inks has the best uniformity and homogeneity.

The behavior curves of dynamic viscosity at different temperatures, 23 ° C, 40 ° C and 60 ° C (Figure 3) show that an increase in temperature leads to a decrease in the signs of dilatants at high shear strain rates.

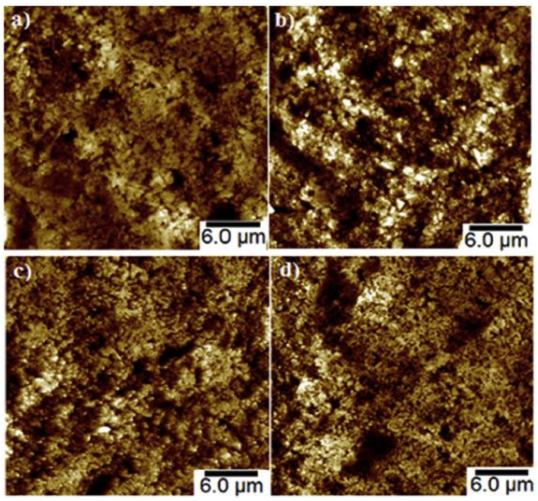

Figure 2. AFM images of printouts produced at room temperature for all three inks:
a) unprinted surface used as a reference, **b-d)** room temperature inkjet printed substrates (ACN, MPN and SFN respectively)

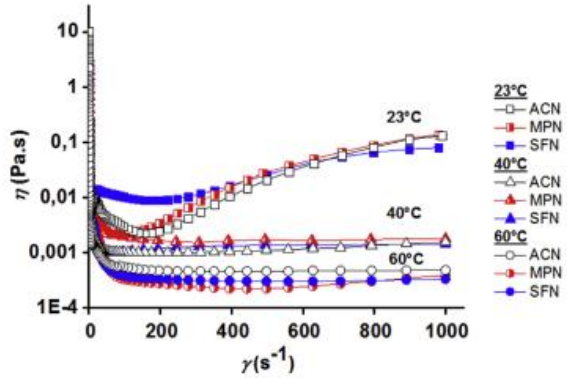

Figure 3. Dynamic viscosity (h) and shear strain rate (γ) at various temperatures

Figure 4 shows the contact angle of droplets on a printed substrate (paper) and the surface tension of suspended drops, respectively.

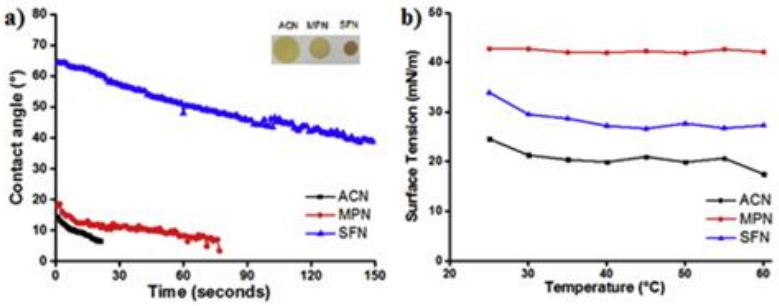

Figure 4. The behavior of toners: **a)** the contact angle of the toners as a function of time, **b)** the surface tension of the toners with a change in temperature.

3. Conclusion

Research has shown that the use of sulfolane as a solvent for liquid toner for drop-on-demand inkjet printing allows you to get the best print quality due to optimal rheological characteristics depending on shear strain rate and temperature.

References

[1] H. Kang, D. Soltman, V. Subramanian, Hydrostatic optimization of inkjet-printed films, Langmuir 26 (2010) 11568-11573.
[2] B. Derby, Inkjet printing of functional and structural materials: fluid property requirements, feature stability, and resolution, Annu. Rev. Mater. Res. 40 (2010) 395-414.
[3] Vinogradov, E.L., Vaganov, V.V. Physical foundations of contact and contactless printing. St. Petersburg: Publishing House of the Polytechnic University, 2017. 122-123.

The influence of the temperature and Ti and TiN sublayer material on carbon nanotubes growth

N N Rudyk[1], **O I Il'in**[1], **M V Il'ina**[1], **O I Osotova**[1], **A A Fedotov**[1]
[1]Southern Federal University, Institute of Nanotechnologies, Electronics and Equipment Engineering, Taganrog, 347922, Russia

Abstract. The influence of the temperature and Ti and TiN sublayer material on the height, diameter, density, and uniformity of carbon nanotubes (CNTs) growth is studied. It was found that on the TiN sublayer, CNTs form an array with a more uniform diameter distribution of CNTs than on the Ti sublayer (minimum dispersion 5.6 nm versus 8.1 nm). It is shown that for the Ti sublayer, with an increase in the growth temperature, an almost linear increase in the CNT height occurs. It was found that an increase in the CNT height is accompanied by a decrease in their diameter for both sublayers.

1. Introduction

The unique properties of carbon nanotubes (CNTs) have long attracted the interest of scientists for their device application [1]. However, at present CNTs have not found mass application in modern micro- and nanoelectronics devices. This problem is mainly associated with a high dispersion of the geometric dimensions of CNTs, which do not allow ensuring the stability of the developed devices. For device applications, CNTs must be grown on an electrically conductive contact sublayer. In this case, the parameters of the technological process, as well as the material of the sublayer [2], have a significant effect on the geometric dimensions of CNTs and their uniformity. The aim of this work was to research the influence of the growth temperature and the material of the Ti and TiN sublayer on the height, diameter, density and uniformity of CNTs in the array.

2. Experiments and methods

Experimental studies were carried out on the Ni/Ti/Si and Ni/TiN/Si structures. The formation of catalyst films (Ni, 10 nm) and a sublayer (Ti and TiN, 100 nm) was provide by magnetron sputtering on Auto500 (BOC Edwards, UK). In these structures, the sublayer acts as a conductive material, and the Ni film acts as a catalytic material for the CNTs growth.

The formation of CNTs was carried out in the temperature range of 615–690 °C with a step of 15 °C. Heating to a set temperature was conducted in Ar (40 sccm) and NH_3 (15 sccm) flows for 20 minutes. CNTs were grown by the PECVD method for 15 min in the ammonia (210 sccm) and acetylene (70 sccm) flows with plasma initiation (40 W). Throughout the process, a pressure of 4.5 Torr was maintained. The study of the geometric dimensions, density, and uniformity of the grown CNTs was carried out by SEM on a Nova Nanolab 600 (FEI, Netherlands).

3. Results and discussion

The analysis of SEM images showed that the formation of CNTs occurred according to the «tip-growth» mechanism, and the nature of the change in the geometric parameters of CNTs (Fig. 1) did not vary with temperature for different materials of the Ti and TiN sublayer.

For the Ti sublayer, with an increase in the growth temperature, an almost linear increase in the CNT height occurs (Fig. 1, a). This may be due to the fact that during the growth of CNTs by the «tip-growth» mechanism, the catalyst become estranged from the substrate. With an increase in the length of the CNTs, the estrangement of the catalytic particle leads to its gradual cooling and loss of catalytic ability. An increase in temperature can lead to the maintenance of catalytic activity at large distances with an increase in the total length of CNTs. The minimum height dispersion for the Ti sublayer was provided at 630 °C and was 10.05 ± 0.63 μm.

The height of CNTs grown on the TiN sublayer was significantly higher than on the Ti sublayer. In this case, a section with an almost linear decrease in height in the temperature range 630–675 °C was accompanied by an almost linear increase in the diameter of the CNTs. Also interesting is the fact that an increase in the height of CNTs is accompanied by a decrease in their diameter (Fig. 2, b). This may be due to the loss of the volume of the catalytic particle inside the CNT cavity during growth.

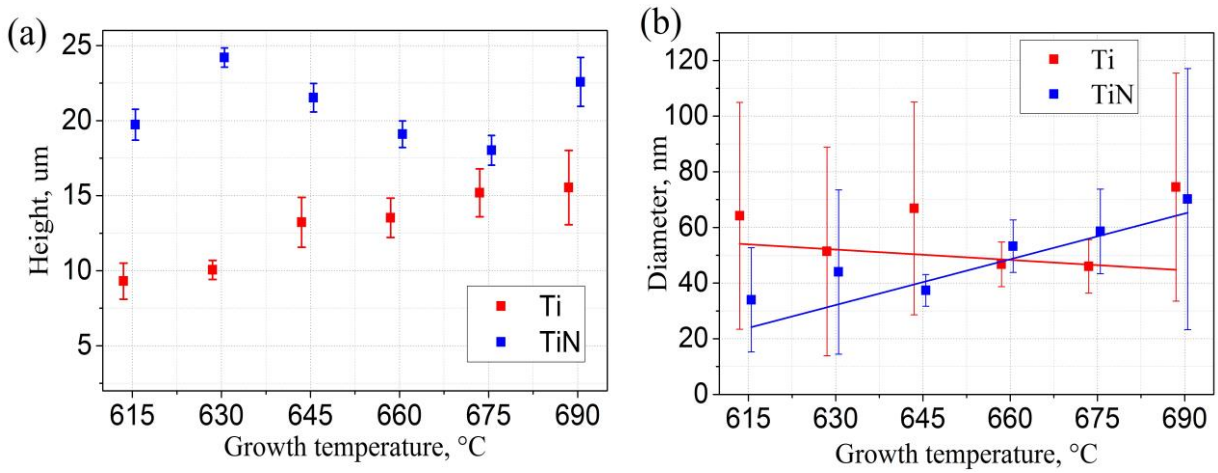

Figure 1(a,b). Dependence of the height **(a)** and diameter **(b)** of the CNTs on the growth temperature.

Also, it was found significantly more uniform distribution of the diameter of CNT grown on the TiN sublayer as compared to a sublayer Ti (minimal dispersion 5.6 nm compared to 8.1 nm).

The obtained dependences of the distribution density of CNTs in the array showed that their character is similar for both sublayers. With an increase in the synthesis temperature from 630 °C, a decrease in the density of CNTs is observed. The uniformity of the distribution of CNTs in the array is estimated. It was found that for both sublayers in the temperature range 645 - 660 °C, the minimum coalescence and formation of CNT bundles with a uniform distribution of 79 and 85% for Ti and TiN, respectively.

The obtained results can be used for creating elements and devices of micro- and nanoelectronics, nanopiezotronics, sensitive elements of gas sensors, as well as materials with increased adhesive ability.

4. Acknowledgments

This work was funded by the Russian Foundation for Basic Research according to the research project No. 20-37-70034.

References

[1] Il'ina M V., Il'in O I, Guryanov A V., Osotova O I and Ageev O A 2020 *Fullerenes, Nanotub. Carbon Nanostructures* **28** 78–82

[2] Shawat A E, Westover A S, Itzhak A, Shani L, Mor V, Girshevitz O, Pint C L and Nessim G D 2018 *Carbon* **130** 273–80

Supercapacitors based on nanostructured electrodes

I O Yavtushenko[1], **M Yu Makhmud-Akhunov**[1]
[1]Ulyanovsk State University, Ulyanovsk 432017, Russia

Abstract. The paper presents the results of studies on the creation of supercapacitors based on carbon nanotubes (CNTs) coated with a layer of polyaniline (PANI). Based on the voltammetry data, the capacitance of the studied system was determined, which amounted to 67.3 mF.

1. Introduction

With the development of modern science and technology, more and more there is a need for autonomous energy sources with high capacity and durability. Since the effectiveness of alternative energy sources, such as solar panels, thermoelectric cells, etc., remains low, technologies continue to develop to improve traditional batteries, in particular lithium-ion batteries (LIB) and supercapacitors [1,2]. The advantage of the latter over LIA is the greater value of capacitance and power, as well as the ability to pass discharge charge cycles almost unlimitedly without loss of efficiency.

2. Experimental

In this paper, we studied two types of electrodes for a titanium foil-based supercapacitor with a layer of carbon nanotubes coated with a thin layer of polyaniline (emeraldine form) and 1) deposited from a solution by dropping and 2) organic compounds grown by pyrolysis. A solution of polyvinyl alcohol and phosphoric acid was used as a layer between the electrodes. The parameters of the system under study were evaluated by cyclic voltammetry on a P-40X pulsed potentiostat-galvanostat in the range from –0.3 V to 0.3 V at a potential sweep speed of 20 mV/s.

3. Results and discussion

A typical type of voltammograms for the studied structures is shown in Fig. 1. Capacitive properties showed a sample based on electrodes with an array of CNTs grown on titanium foil. The processing results showed a significant increase in the capacitance of the capacitor from 6.15.10–5 to 6.73.10–2 F. Obviously, this fact is associated not only with an increase in the specific surface area of the electrode due to the ordered arrangement of CNTs on the substrate normal to the surface, but also with the presence of an ohmic contact between the titanium substrate and CNTs. The application of CNTs coated with a PANI layer from solution leads to difficulties in charge distribution due to the contact barrier of a thin PANI layer and a titanium substrate. It is typical that holding the system for a month leads to a slight decrease in capacitance (2.02.10–2 F), which is probably due to processes of changing the structure of the polyvinyl interlayer during exposure to air.

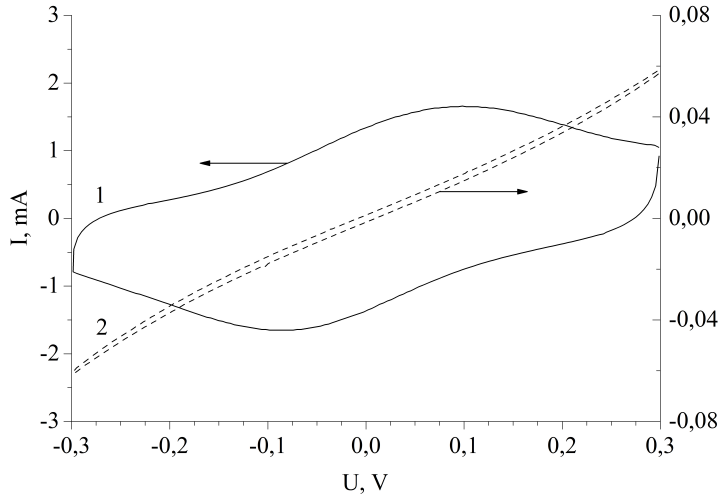

Figure 1. Cyclic voltammograms of supercapacitors based on CNTs and PANI: 1 - applied from a solution; 2 - pyrolysis-grown organic compounds.

4. Conclusions

Thus, the features of creating supercapacitors based on an array of CNTs in a medium of a conductive polymer material (PANI) were considered. The properties of a supercapacitor appear only in a sample with an array of CNTs grown on the surface of a metal electrode, where, along with a good current collector, a developed electrode structure and charge states of the barrier layer with PANI are manifested. This result opens the prospect of using such CNT-based capacitors with polymer interlayers, which surpass traditional ones in a number of characteristics.

5. Acknowledgments

This work is supported by the Russian Scientific Fund (project no. 19-71-10063).

References

[1] Pankratov D V, Shumakovich G P, Gorshkov K V, Seifman Yu S, Gorbacheva M A, Vasilieva I S, Morozova O V, Lipkin A V 2012 *Sovremennyye problemy nauki i obrazovaniya* **4** 336.
[2] Yoo J J, Balakrishnan K, Huang J S, Meunier V, Sumpter B G, Srivastava A, Conway M, Reddy A L M, Yu J, Vajtai R, Ajayan P M 2011 *Nano Letters* **4** 1423.

Investigation of the influence of control parameters on the forming-free resistive switching in nanocrystalline zinc oxide films for neuromorphic systems

A A Avakyan[1], **R V Tominov**[1], **V I Avilov**[1], **V A Smirnov**[1]
[1]Southern Federal University, Institute of Nanotechnologies, Electronics and Equipment Engineering, Taganrog, 347922, Russia

Abstract. The influence of control parameters on the resistive switching effect in forming-free nanocrystalline zinc oxide films was studied. It was shown, resistive switching from HRS to LRS was observed at +3.3±0.4 V, and from LRS to HRS at -2.8±0.6 V. Endurance test for experiment with signal №1 showed, that R_{HRS} was equaled 52.7±5.2 kΩ, R_{LRS} was equaled 3.3±2.2. HRS/LRS was about 17. Endurance test for experiment with signal №2 showed, that R_{HRS} was equaled 38.3±20.2 kΩ, R_{LRS} was equaled 4.5±3.1 kΩ. HRS/LRS was about 9. The results can be useful for based on forming-free nanocrystalline zinc oxide films neuromorphic systems manufacturing.

1. Introduction

Recently, tasks related to unstructured data classification and inaccurate initial conditions become more and more relevant. Traditional computers were ineffective in solving such problems, and solving this problem is to transfer computing systems to an architecture close to the human brain (neuromorphic systems). One of the methods for the technical implementation of the biological brain is neuromorphic systems based on ReRAM structures, the principle of operation of which is based on a change in the electric resistance in a certain range under external electric field (resistive switching effect) between the states of high resistance (HRS) and low resistance (LRS) [1]. Many metal oxide films exhibit a resistive switching effect, among which forming-free nanocrystalline zinc oxide is especially prominent, due to its high speed and compatibility with silicon technology [2]. But neuromorphic systems creating based on nanocrystalline films of zinc oxide faced with a lack of systematic modes of studying the influence of control parameters on the effect of resistive switching in them.

2. Experiment details

Forming-free nanocrystalline zinc oxide films were grown using pulsed laser deposition technique (Pioneer 180, Neocera, USA). Si/TiN structure as a wafer was used. Deposition was carried out under wafer temperature: 500°C, target–wafer distance: 40 mm, O_2 pressure: 1 mTorr, pulse energy: 400 mJ. Electric measurements were carried out using semiconductor characterization system Keithley 4200-SCS (Keithley, USA) with W probes. During experiments, the TiN film was used as the bottom contact. Current-voltage curves were obtained at with different forms of control signal (signal №1 at inset of figure 1b and signal №2 at inset of figure 1c) at –4 to +4 amplitude voltage. Using the results obtained, resistance of forming-free nanocrystalline zinc oxide films dependences on number of cycle number

(endurance test) for different forms of control signal were built. Curves analyzing was implemented using Origin 8.1 software.

3. Results

Figure 1 a shows average current-voltage characteristic (CVC) of forming-free nanocrystalline zinc oxide films, performed from the fifteen current-voltage curves in the same point. It was shown, resistive switching from HRS to LRS was observed at +3.3±0.4 V, and from LRS to HRS at -2.8±0.6 V. Endurance test for experiment with signal №1 showed, that R_{HRS} was equaled 52.7±5.2 kΩ, R_{LRS} was equaled 3.3±2.2 kΩ (figure 1 b). R_{HRS}/R_{LRS} ratio was about 17. Endurance test for experiment with signal №2 showed, that R_{HRS} was equaled 38.3±20.2 kΩ, R_{LRS} was equaled 4.5±3.1 kΩ (figure 1 c). R_{HRS}/R_{LRS} ratio was about 9.

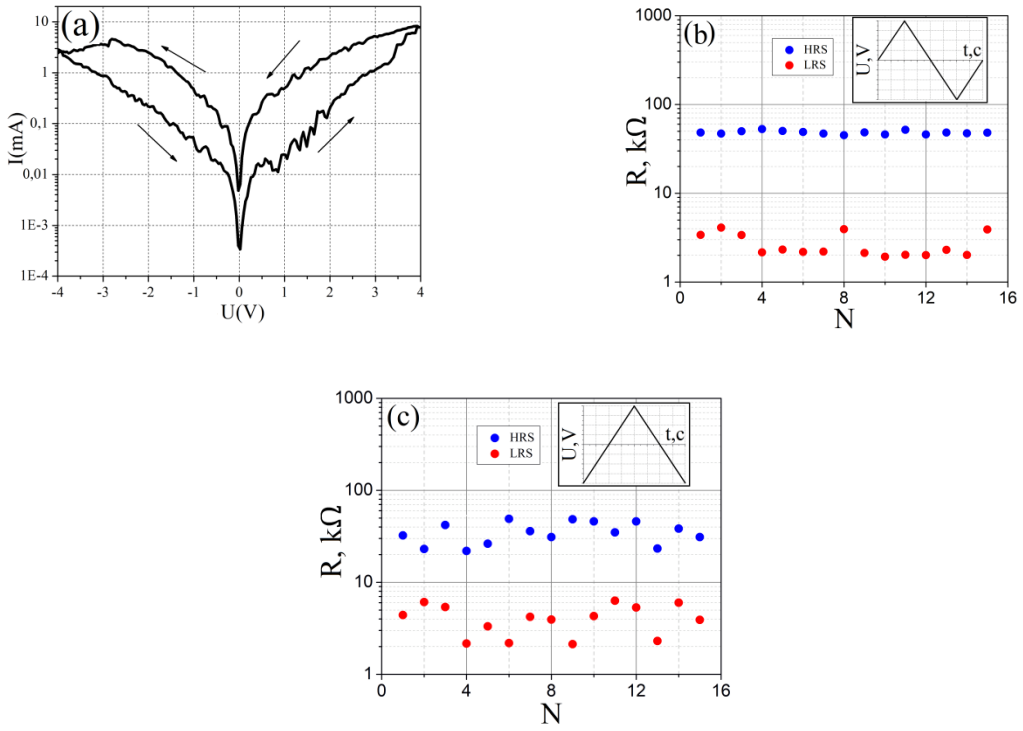

Figure 1(a, b, c). Investigation of the influence of control parameters on the resistive switching effect in forming-free nanocrystalline zinc oxide films: **(a)** current-voltage characteristic; **(b)** endurance test for signal №1; **(c)** endurance test for signal №2

The results can be useful for based on forming-free nanocrystalline zinc oxide films neuromorphic systems manufacturing.

4. Acknowledgments

This work was supported RFBR (№ 19-29-03041 mk project).

References

[1] Smirnov V A, Tominov R V, Avilov V I, Alyabieva N I, Vakulov Z E, Zamburg E G, Ageev O A 2019 *Semiconductors* **53(1)** 72

[2] Shandyba N A, Panchenko I V, Tominov R V, Smirnov V A, Pelipenko M I, Zamburg E G, Chu Y H 2018 In *Journal of Physics: Conference Series* **1124** 081036

Structure and spectral-luminescent properties of Er^{3+}:ZnO optical ceramics

E Gorohova[1], E Oreschenko[1], L Basyrova[2], I Venevtsev[3], S Eron'ko[1], I Alekseeva[1], A Khubetsov[1], O Dymshits[1], P Loiko[4], A Zhilin[1], P. Rodnyi[3]

[1]S.I. Vavilov State Optical Institute, 36 Babushkina St., 192171 St. Petersburg, Russia

[2]ITMO University, 49 Kronverkskiy Pr., 197101 St. Petersburg, Russia

[3] Peter the Great St. Petersburg Polytechnic University, 29 Polytechnic str., 195251, St. Petersburg, Russia

[4]CIMAP, CNRS, Université de Caen Normandie, 6 Boulevard du Maréchal Juin, 14050 Caen Cedex 4, France

Abstract. Transparent ZnO ceramics doped with erbium ions were fabricated by uniaxial hot pressing of commercial oxide powders. They were characterized by X-ray diffraction, SEM, EDX, Raman, X-ray and optical spectroscopy. The ZnO grain size decreases with addition of Er_2O_3. Er^{3+} ions are distributed between the ZnO grains and the Er_2O_3 crystals. As the erbium concentration is increased, the defect luminescence band becomes less intense, and the X-ray luminescence decay time decreases.

1. Introduction

ZnO is widely studied and applied in industry due to its unique properties of wide band gap of 3.37 eV, large exciton binding energy of 60 meV, excellent mechanical–electrical coupling characteristics, high radiation tolerance and low cost. ZnO performance can be adjusted by means of doping with rare-earth ions. Er3+ addition can induce the variation of the luminescence properties of ZnO while the 1.54 μm photoemission caused by Er^{3+} intra-4f shell transition can be enhanced due to the ZnO → Er^{3+} energy transfer. In this work, undoped and Er-doped ZnO optical ceramics were prepared. The effect of Er doping content on the microstructure and spectral-luminescent properties of ZnO were studied.

2. Fabrication of ceramics

Optical ceramics Er:ZnO with Er content of 0.1-2.0 wt% were fabricated from commercial reagent grade ZnO and Er_2O_3 by hot pressing in vacuum at 1150 and 1180 °C. The resulting polished samples (diameter: 25 mm, thickness: ~0.5 mm) had a slight rose-grey coloration.

3. Results and discussion

The XRD pattern is typical for hexagonal phase of ZnO, see Fig. 1(a). The unit cell parameters of ZnO within the experimental error do not change with the Er^{3+} doping concentration (a=3.250 Å, c=5.202 Å). It implies that Er^{3+} ions do not enter into the ZnO crystals. The pattern also contains traces of Er_2O_3 crystals, their content increases with Er^{3+} doping concentration (see Fig. 1(b)). The morphology of the fracture surface was characterized by Scanning Electron Microscopy in combination with EDX. Er^{3+} ions are located on the ZnO grain boundaries and within the Er_2O_3 crystals. The average ZnO grain size decreases with Er^{3+} addition and equals to 5-15 μm.

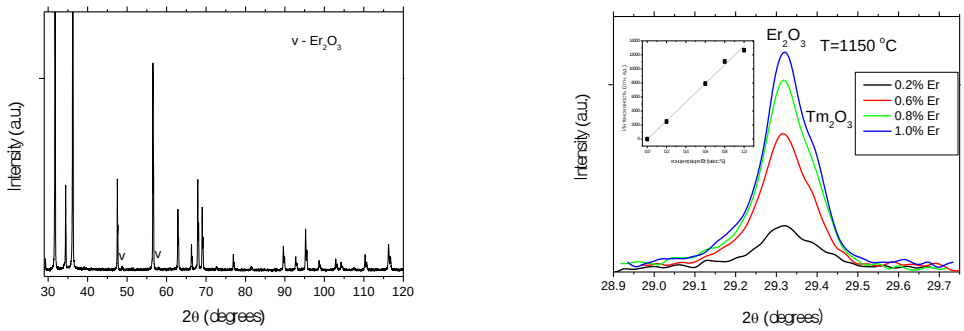

Figure 1(a, b). (a) X-ray powder diffraction (XRD) pattern of Er:ZnO ceramic; **(b)** XRD pattern of of Er:ZnO ceramic in the 2θ range of 28.9 – 29.7°.

The characteristic ZnO vibrations were observed in Raman spectra at 97, 202, 331, 378, 406, 438, 536, 663, 1096 and 1153cm^{-1}. A rise in the Raman spectrum in the region of 200–600 cm^{-1}, which corresponds to wavelengths of ~ 520–530 nm, can be caused by luminescence of Tm^{3+} ions impurity in Er_2O_3 crystals. Transmission spectra of the polished ceramic samples are shown in Fig. 2(a). In the spectral range of 600 to 750-800 nm, transmission changes from 60 to 45% with an increase in the erbium concentration from 0.2 to 2 wt%. Absorption and luminescent properties of Er^{3+} ions are mainly determined by Er_2O_3 crystals. The Beer's law is observed for all absorption bands of Er^{3+} ions. The short-wavelength transparency boundary for erbium-doped samples s about 390 nm, and the long-wavelength boundary is in the range of 2.4–2.5 μm. It corresponds to free-carrier concentration between $3.13 \cdot 10^{18}$ and $11.9 \cdot 10^{18}$ cm^{-3}.

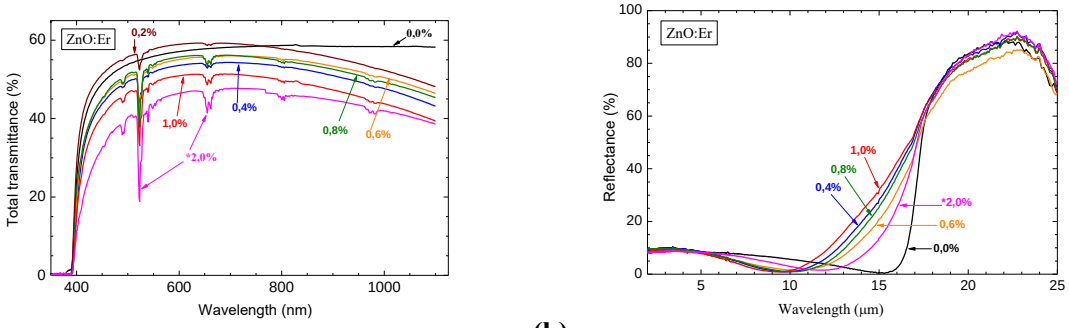

Figure 2(a, b). Total transmittance **(a)** and reflectance **(b)** spectra of Er^{+3}:ZnO ceramics.

4. Conclusions

We report on synthesis, structure and spectral-luminescent properties of novel Er^{3+}-doped ZnO optical ceramics promising for optoelectronic applications. It possesses a high radiation stability and a mean X-ray luminescence decay time of about 6-8 ns in the range of 0 – 50 ns.

Acknowledgments

This work was partly supported by the RFBR (Grant 19-03-00855).

On the properties of AlN/Si(111) epitaxial structures grown by PA MBE via coalescence overgrowth of AlN nanocolumns

K Yu Shubina, D V Mokhov, T N Berezovskaya, A M Mizerov, A D Bouravleuv
Nanoelectronics Lab, Alferov University, St. Petersburg 194021, Russia

Abstract. The AlN/Si(111) epitaxial structures were synthesized by coalescence overgrowth of AlN nanocolumns using PA MBE technique. Structural, electrical and chemical properties of AlN epitaxial layers were studied. It was shown that etching of such AlN/Si(111) structures in KOH solution can be prospective method for separation of AlN layers from Si(111) substrates.

1. Introduction

Wide bandgap semiconductors, especially III-N compounds, are one of the most prospective materials for the development of modern electronics. III-nitrides have a set of unique electrical, optical and mechanical properties, which are of importance for optoelecronics, high-power and high frequency electronics and MEMS industry [1]. Among III-N materials, AlN attracted huge attention due to its giant piezoelectric properties, which are important for surface and bulk acoustic wave devices [2]. However, there is well-known problem for further development of nitride electronics connected with the lack of natural substrates. Since AlN and GaN substrates are very expensive, low-cost A^3N-on-Si epitaxial structures become more and more relevant.

Here we report on the results of the studies of AlN/Si(111) structures synthesized by coalescence overgrowth of AlN nanocolumns using plasma-assisted molecular beam epitaxy (PA MBE) technique.

2. Samples and experimental details

The AlN/Si(111) samples were obtained by PA-MBE using Veeco Gen 200 MBE system equipped with RF plasma source. AlN was grown on the semi-insulating (R > 10 kOhm) silicon substrates with (111) crystallographic orientation. Preliminarily Si(111) substrates were prepared according to modified Shiraki method [3]. Synthesis of AlN nanocolumns and lateral overgrowth was carried out using procedure described in [4]. Crystallographic polarity of the AlN was identified by wet chemical etching in KOH solution. The samples grown were studied using scanning electron microscopy (SEM) (see figure 1), X-ray difractometry (XRD) and Hall measurements.

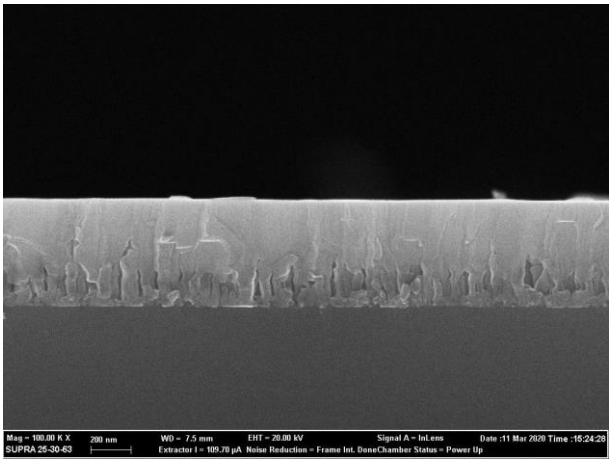

Figure 1. Cross-section SEM image of the AlN/Si(111) sample.

3. Acknowledgments
This work was supported by the the Ministry of Education and Science of the Russian Federation (grant № FSRM-2020-0008).

References
[1] Amano H et al 2018 *J. Phys. D: Appl. Phys.* **51** 163001
[2] Tamariz S, Martin D, Grandjean N 2017 *J. Cryst. Growth* **476** 58
[3] Ishizaka A and Shiraki Y 1986 *J. Eltrochem. Soc.* **133** 666
[4] Mizerov A M, Kladko P N, Nikitina E V, Egorov A Yu 2015 *Semiconductors* **49** 274

Non-affine deformations in amorphous medium with nanoinclusions

D A Conyuh[1, 2], **Y M Beltukov**[1]
[1] The Ioffe Institute RAS, St. Petersburg 194021, Russia
[2] Peter the Great St. Petersburg Polytechnic University, St. Petersburg 195251, Russia
E-mail: conyuh.dmitrij@yandex.ru

Abstract. The influence of non-affinity (heterogeneity) on the macroscopic stiffness of amorphous systems with solid nanoinclusions was studied in the context of the random matrix model. The numerical analysis shows, that the macroscopic theory of elasticity is applicable only for large radius R of spherical nanoinclusions, and it defines the addition to the Young's modulus as $\Delta E \sim R^3$. Nevertheless, a decrease of nanoinclusion radius makes this dependence quadratic, i.e. $\Delta E \sim R^2$. It determines the scale of heterogeneity of the amorphous solids as a certain nanoinclusion radius, which defines the lowest characteristic nanoparticle size and the applicability of the macroscopic theory of elasticity. Furthermore, around the inclusions, there is a certain transition region with special elastic properties, which depends on the rigidity of the whole medium and on the size of the particles themselves.

1. Introduction

The physics of nanocomposites based on polymer matrices has recently become an increasingly promising field of research. One of the pressing issues is how nanoparticles embedded in a polymer matrix effect its elastic properties. As was shown in many works, the addition of nanoinclusions to amorphous structures significantly increases the rigidity of the entire nanocomposite [1, 2]. However, the macroscopic theory of elasticity is not applicable to describe deformations around nanoparticles due to the non-affinity (heterogeneity) of amorphous matrix. The lengthscale of microscopic non-affinity is estimated as dozens of interatomic distances and can be comparable with the size of the nanoparticles [3]. Therefore, it is expected that non-affine displacements play a crucial role in the process of deformation of the entire system. In this paper, we study the influence of non-affinity on the elastic properties of an amorphous medium with nanoparticles using random matrix methods.

2. Random matrix approach

The random matrix method has been successfully applied to describe various amorphous systems [4]. In this model, the dynamic matrix has the form $\widehat{M} = \hat{A}\hat{A}^T + \mu\widehat{M}_0$, where $\hat{A}$ is a random square matrix responsible for the disorder in the system, built on a simple cubic lattice with a Gaussian distribution of non-diagonal matrix elements between the nearest neighbors. Matrix $\widehat{M}_0$ is a regular crystalline matrix built on the same lattice, with unit springs between the nearest neighbors. The dimensionless parameter μ characterizes the relative degree of order in the system, varies in the interval $0 \leq \mu < \infty$, and determines the Young's modulus $E_0 \propto \mu^{1/2}$.

3. Result

According to the macroscopic theory of elasticity, the addition of solid spherical inclusions with a low concentration n and a radius R leads to a change in Young's modulus in the form

$$\Delta E \sim E_0 n R^3,$$

where E_0 is the Young's modulus of the initial medium without inclusions. However, with a decrease in the radius of such inclusions, non-affine deformations begin to play an increasingly important role. Numerical calculations showed that at some scales of the radius of nanoparticles $R < R_c$ the macroscopic theory of elasticity is not applicable. In this case, the change in Young's modulus has the form

$$\Delta E \sim \mu^{1/4} n R^2.$$

The scale $R_c \sim \mu^{-1/4}$ characterizes the scale of heterogeneity of the amorphous body and determines the smallest characteristic size of nanoinclusions, at which the macroscopic theory of elasticity is applicable. Also around the inclusions there is a certain transition region with special elastic properties, which depend on the rigidity of the whole medium and on the particle sizes (see Fig. 1). Such a feature was observed earlier in other works [5, 6].

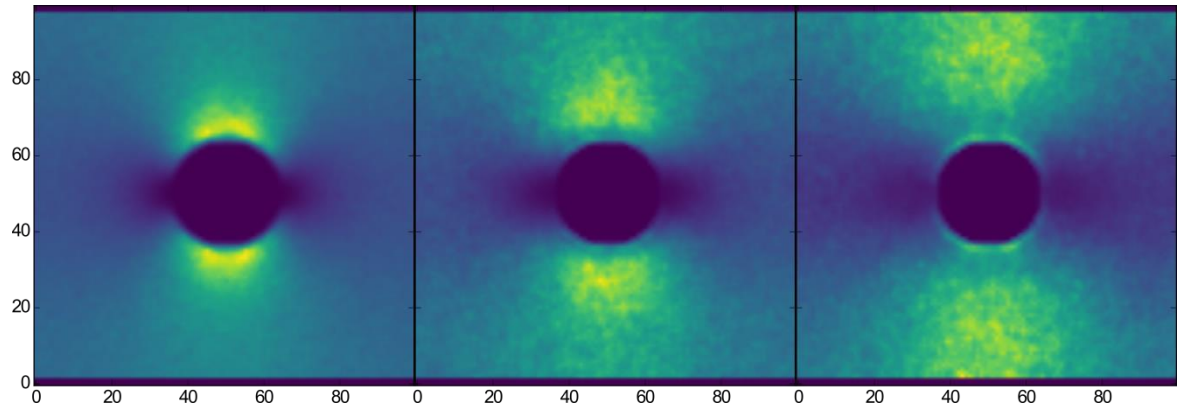

Figure 1. Energy distribution around spherical nanoinclusion with radius $R = 15$ a.e. Left panel: $\mu = 10^{-1}$; central panel: $\mu = 10^{-3}$; right panel: $\mu = 10^{-5}$.

Acknowledgments

The authors thank the Russian Science Foundation (grant No 17-72-20201) for financial support.

References

[1] Stojanovic D, Orlovic A, Markovic S, Radmilovic V, Uskokovic P S, and Aleksic R 2009 *J. Mater. Sci.* **44** 6223

[2] Moskalyuk O A, Samsonov A M, Semenova I V, Smirnova V E, and Yudin V E 2017 *J. Techn. Phys.* **87** 266

[3] Leonforte F, Boissière R, Tanguy A, Wittmer J P, and Barrat J-L 2005 *Phys. Rev. B* **72** 224206

[4] Beltukov Y M, Kozub V I, Parshin D A 2013 *Phys. Rev. B* **87** 134203

[5] Moczo J, Pukansky B 2008 *J. Indust. Eng. Chem.* **14** 535

[6] Fu S Y, Feng X Q, Lauke B, Mai Y W 2008 *Composites: Part B* **39** 933

Semiconductor core - shell nanoparticles SnO_2@SnO_2 (TiO_2, ZnO): synthesis, structural characteristics and the effect of structure on photocatalytic activity

A Podurets[1], D Kolokolov[1], M K S Barr[2], M Osmolowsky[1], N Bobrysheva[1], J Bachmann[1,2], O Osmolovskaya[1]

[1]Institute of Chemistry, Saint Petersburg University, Saint Petersburg 199034, Russia
[2]Department of Chemistry and Pharmacy, Friedrich-Alexander University of Erlangen-Nürnberg, Erlangen 91058, Germany

Abstract. In this work, SnO_2@MO_x (MO_x = SnO_2, TiO_2, ZnO) core-shell nanoparticles were synthesized by ALD method and characterized in terms of their structural, optical and photocatalytic properties. The band gap values are found to be in the region of 2.8 to 4.5 eV, whereby distinct values were demonstrated for the core and shell materials in the case of SnO_2@SnO_2 and SnO_2@TiO_2. Under UV and visible light irradiation, the as-prepared nanoparticles exhibited clearly distinct activities towards the photocatalytic degradation of methylene blue, depending on the structure and band gap values. Without using any complex sample preparation, a full degradation of the pollutant model was achieved in 10 minutes with the novel particles, conditions in which simpler particles do not achieve a comparable performance. These results make the core-shell nanoparticles under study a promising UV or visible-light photocatalyst for efficient environmental remediation photocatalysis.

Introduction

Tin dioxide (SnO_2) is a widely investigated simple way synthesized semiconductor with a band gap of 3.6 eV, and seems to be a promising nanomaterial for different photocatalytic reactions. A number of practical-oriented papers were dedicated to the water treatment based on the full removal of different pollutants using photodegradation process driven by UV and Visible light irradiation. We propose a novel strategy for regulating of photocatalytic activity of nanoparticles based on SnO_2 by producing a core-shell, which makes it possible to control the functional properties of materials by producing thin layers. In order to obtain optimal photocatalytic characteristics, the forming layer should be thin and ordered, and this could be achieved by atomic layer deposition (ALD). This method is widely used to obtain thin films, however, the range of nanopowder substrates is quite limited [1]-[4].

This research is focused on the first principle study of the effect of structural characteristics on the photocatalytic activity of SnO_2@SnO_2 (TiO_2, ZnO) core-shell nanoparticles under ultraviolet and visible irradiation.

To obtain a core (SnO_2 nanoparticles of 4 nm) precipitation method was used, and after the semiconductor shells of different compositions (SnO_2, TiO_2, ZnO) were synthesized by the ALD method under 150-200 °C using H_2O and organic precursors (TDMA, TTIP, DEZ). The shell formation is confirmed by XPS techniques and the presence of the ions Sn^{4+}, Ti^{4+}, Zn^{2+} demonstrated that the valence state of Sn, Ti and Zn were kept constant during the synthetic procedure.

The constant phase composition of the samples was confirmed by the XRD method; an increase in crystallite sizes and a change in lattice parameters were found, which indirectly confirms the success of ALD synthesis. According to HR-TEM and specific surface area data, the shell thickness varies from 0.9 to 1.4 nm, depending on the nature of its material. No additional indices were found for the shell, which indicated its oriented growth and agreed well with the absence of peaks from the shell on XRD patterns. The analysis of HR-TEM images allows us to suggest that in the case of SnO_2 and TiO_2 shell during the ALD process the atoms built up the core crystal structure because those materials could crystallize in the same crystal system as the core. The ZnO shell with a distinct crystal system was not well crystallized.

The presence of the ALD shell is evident in the lattice parameters change, which may be affected by surface tension and epitaxial strain effects. The different values of zeta potential for core-only and core-shell samples as well as the decrease of hydrodynamic sizes (HS) also confirm the shell formation.

It has been demonstrated that the presence of a shell significantly reduces the band gap of the material (from 3.7 eV for a core to 2.8 eV for a SnO_2 shell), while the fundamental absorption edge of the "core" shifts to higher photon energies, the band gap derived from the adsorption spectrum is 4.6 and 4.5 eV A significant increase of this value as compared to bare nanoparticles may be caused by the relaxed lattice parameters and higher sample crystallinity after ALD treatment, or by the removal of near-edge surface defects via the presence of the shell's oxide. It can be noticed that the shell materials SnO_2 and TiO_2 crystallize in the same crystal system as the core, as opposed to ZnO. In this regard, the difference observed between ZnO, on the one hand, and SnO_2 and TiO_2, on the other hand, may be due to the distinct epitaxial constraints on shell growth. The decrease of "shell" band gap for SnO_2@SnO_2 sample in comparison with bulk tin oxide (3.7 eV) is probably due to the surface defects and the oxygen vacancies which are a very common factor affecting the functional properties of nanoparticle tin dioxide.

The photocatalytic activity of the samples (kinetic dependences of degradation and the composition of the products determined by mass spectroscopy) was tested using MB ($2 \cdot 10^{-3}$ g / l) and three light sources with predefined different emission spectra: ordinary room light (e.g. the sunlight that goes from the window), Vis lamp (441 nm, 2.8 eV), and UV lamp (205-315 nm, 3.9 eV). The "dark" adsorption of MB on the surface of all samples was studied and shown that it does not exceed 5%, which excludes its effect on the photocatalytic process. In the present work, the photocatalytic experiments were conducted without the widely used stage of dark adsorption to avoid the important limitation of photocatalytic systems – the time needed to surface loading of pollutant on the NPs. It has been established that photocatalytic properties depend on the structure of nanoparticles; in this case, for an optimal SnO_2@SnO_2 sample, 90% degradation is achieved after 5 minutes using visible radiation. Photocatalysis results indicate that the band gap value was the key factor affecting the photocatalytic activity, as expected, and the production of core-shell structures is one powerful method to adjust the band gap.

Acknowledgments

Scientific research was performed using the equipment of the Research Park of St. Petersburg State University (Centre for X-ray Diffraction Studies, Chemical Analysis and Materials Research Centre, Centre for Innovative Technologies of Composite Nanomaterials, Centre for Optical and Laser Materials Research, Interdisciplinary Resource Centre for Nanotechnology).

References

[1] S. Seong, I.-S. Park, Y.C. Jung, T. Lee, S.Y. Kim, J.S. Park, J.-H. Ko, J. Ahn, 2019 *J. Mater. Des.* **107** 831

[2] M.J. Weber, M.A. Verheijen, A.A. Bol, W.M.M. Kessels, 2015 *J. Nanotechnology*. **26** 094002

[3] Y. Zhou, D.M. King, J. Li, K.S. Barrett, R.B. Goldfarb, A.W. Weimer, 2010 *J. Ind. Eng. Chem. Res.* **49** 6964

[4] O. Kéri, L. Kócs, Z. Hórvölgyi, Z. Baji, K. László, V. Takáts, Z. Erdélyi, I.M. Szilágyi, 2019 *J. Period. Polytech. Chem. Eng.* **63** 378

Morphology and doping concentration effect on functional properties of Eu-SnO_2 nanoparticles

D.S.Kolokolov, I.E. Kolesnikov, M.G.Osmolowsky, N.P. Bobrysheva, O.M.Osmolovskaya, M.A. Voznesenskiy
St. Petersburg State University, St. Petersburg, 199034, Russia

Abstract. Morphology and effect of Eu-doping concentration on structural and functional properties of tin dioxide nanoparticles obtained by co-precipitation and hydrothermal methods are analysed and reported for the first time. The samples were characterized by means of transmission electron microscopy (TEM), powder X-ray diffraction (XRD), specific surface area (SSA) estimation. TEM, XRD and SSA analyses showed that in the case of co-precipitation method the nanoparticles were spherical. Hydrothermal treatment leads to formation of cubic nanoparticles. An average particle size increased from 3 to 5 nm and from 6 to 11 nm along with increase of Eu concentration for spherical and cubic nanoparticles, respectively. Photoluminescence, electrical and photocatalytical properties of nanoparticles with different morphology were studied and compared. It was shown, that the dopant positions in SnO2 host differ depending on particle morphology and functional properties.

1. Introduction

Tin oxide (SnO_2), an n-type semiconductor with a wide band gap (Eg = 3.6 eV at 300 K), have a wide range of applications including the transparent conducting media, gas sensors and photocatalysts. The luminescence properties of rare earth doped SnO_2 have been the subject of numerous investigations. A significant number of works have been dedicated to the synthesis and photoluminescence of Eu-SnO_2 NPs that exhibit orange-red emission. The photocatalytical performance of doped SnO_2 are also under discussion. It is well known that luminescence just like the other optical properties are highly dependent on doping ions positions in a host crystal lattice. So, the recent work is dedicated to the synthesis Eu-SnO_2 nanoparticles with different size, shape and dopant position and to study of its functional characteristics.

2. Experimental

Two concentration series of Eu-SnO_2 NPs with different shape were prepared by using two common wet chemistry methods. The samples of the 1st series were synthesized with wide Eu doping concentration range (1, 2, 5, 7, 10, 15, 25, 50 at.%) at room temperature by co-precipitation method to provide an uniform distribution of dopant in crystal lattice and obtain the spherical NPs. To get the NPs with the other morphology (2nd series) freshly prepared suspensions of 5, 15 and 25 at.% Eu-SnO_2 were held at the sealed autoclave (e.g. hydrothermal treatment) to initiate the particle growth and shape change.

3. Results and discussion

Based on TEM and BET data it was shown that under mild conditions (co-precipitation method), spherical particles with sizes less than 5 nm are formed. The hydrothermal treatment (harsh conditions) leads to the production of cubic particles are formed with the size less than 10 nm depending on the dopant concentration. For all doped nanoparticles, a change in the unit cell parameters was registed in comparison with the reference SnO_2 samples, which confirms the success of the doping.

Positions of dopants in the SnO_2 crystal lattice were determined by the quantum-chemical calculations in the frameworks of density functional theory (DFT), using an original approach. It has been established that doping promotes the formation of polycrystalline particles, the crystallite size vs dopant concentration dependences are multidirectional for the samples obtained under mild and harsh conditions. The presence of oxygen vacancies in all the samples under study were shown by Raman spectroscopy and XPS methods, the amount of which can be controlled by changing the dopant concentration and the synthesis conditions.

The band gap values calculated from optical absorbance spectra using Tauc equation were close for all the samples and equal to 3.5 eV.

According to the impedance spectroscopy data for all the samples in the range of 77–400 K the volume conductivity and also conductivity of grain boundary were determined, which is consistent with polycrystallinity of nanoparticles.

The photocatalytic activity of the obtained samples was studied under the UV and visible light irradition using the model organic dye methylene blue (MB) with a adsorption maximum at 664 nm, which simplify its determination procedure. Preliminary the absence of dye adsorption on nanoparticles surface was confirmed. The kinetic dependences of MB degradation were studied under different pH values (6 and 9), the structure of by-product were studied by mass spectra. It was shown that the effectiveness of photocatalysis is due to the dopant position and the number of oxygen vacancies in the material; the process occurs at wavelengths significantly greater than the corresponding optical band gap.

The samples showed the presence of luminescence quenching at 25 mol% dopant in nanoparticles obtained by the hydrothermal method associated with the close arrangement of atoms relative to each other.

Thus, it was shown that by varying the synthesis procedure, the position of the dopant in the SnO_2 structure can be regulated, which leads to the controlled appearance of defects that determine the functional activity of the material.

4. Acknowledgments

The reported study was funded by RFBR, project number 20-03-00762A.

Experimental studies were performed using the equipment of the Research Park of St. Petersburg State University (Centre for X-ray Diffraction Studies, Chemical Analysis and Materials Research Centre, Centre for Innovative Technologies of Composite Nanomaterials, Centre for Optical and Laser Materials Research).

Observation of the influence of complex SiC porous buffer layer on properties of GaN/Si(111) heterostructures

D.S. Zolotukhin*[1], P.V.Seredin[1], D.L. Goloshchapov[1], A.S. Lenshin[1], A.M. Mizerov[2], I.N. Arsentyev[3]

[1]Voronezh State University, Universitetskaya pl. 1, Voronezh, 394018,
[2]St. Petersburg Academic University, Khlopina 8/3, 194021 St. Petersburg, Russia
[3]Ioffe Institute, St. Petersburg, 194021, Russia

E-mail: seredin@phys.vsu.ru

Abstract. 1-μm-thick GaN layers were obtained in one growth procedure on complex SiC/Si(111) substrates using plasma-assisted molecular beam epitaxy (PA MBE). Si(111) substrates were modified by the atoms substitution technique. Prior to the atoms substitution procedure, on the one substrate the transition porous Si layer (por-Si) was preformed. The GaN layer grown on this substrate revealed better surface morphology and structural quality, less threading dislocation density and as a result showed lower free carrier concentration and higher carrier mobility. Moreover XRD study revealed less strain level in GaN layer grown on por-Si layer.

1. Introduction

Si(111) substrates are commercially available and fairly cheap in comparison with all others traditional substrates, which used for III-N devices fabrication since the silicon technology is the most common and well-established. However, large lattice and thermal expansion coefficient (TEC) mismatch between Si and GaN (~17% and ~54%, respectively) [1] led to high density of threading dislocations and other defects which affects on end-device efficiency. At the present time, there is an acute problem of the integration of GaN technology with silicon technology, in order to create new classes of semiconductor devices using the advantages of both technologies on a single chip. In this paper we describe the novel approach for GaN layers fabrication on Si(111) substrates, using por-Si layer which prior to growth was modified by the atoms substitution technique [2,3] to achieve 3H-SiC porous transition layer. Due to less lattice and TEC mismatch between 3H-SiC and GaN (~3.4% and <1%, respectively) [1], formation of porous transition layer led to incensement in structural, optical and physical properties of GaN/SiC/por-Si(111) heterostructure grown by PA MBE in comparison with GaN/SiC/Si(111).

2. Experiment

Porous layer of silicon, por-Si in the process of “compliant” virtual substrate was formed on a single-crystalline c-Si (111) plate by its electrochemical etching in the alcohol solution of the fluoric acid according to the standard procedure [3]. The thickness of the obtained porous layer was 30 nm. The specified technological mean diameter of the pores was ~1-5 nm. Growth was performed on Veeco Gen 200 PA MBE setup. Both samples were grown in one growth procedure. The nucleation layer with 3- dimensional surface morphology was grown at the equal nitrogen and gallium fluxes $F_{Ga}=F_N$~0.05 μm/hour at the growth temperature T_s=650°C. Upper laying high-temperature 350-nm-thick GaN layer was formed at T_s=700°C and metal-rich conditions F_{Ga}~0.4 μm/hour and F_N~0.05 μm/hour. The top GaN layer was grown at the T_s=650°C and less metal-rich conditions - F_{Ga}~0.2 μm/hour and F_N~0.05 μm/hour up to GaN thickness of ~1 μm. The surface morphology was studied by means of atomic force microscope (AFM), scanning electron microscopy (SEM). Crystalline quality was evaluated by means of and X-ray diffraction (XRD) analysis. Optical properties were studied by means of PL, Raman, UV spectra analysis. Carrier concentration and type of conductivity were determined by Hall Effect technique applying Van der Pau method.

3. Results

The cross-section SEM image confirms revealed reasonable quality of the obtained layer and layer–substrate interface. Both interfaces have porous structure independent of either using of por-Si sublayer or not. It follows from the fact that under the formation of the SiC layer when employing substitution of the atoms technique porous transition layer of silicon carbide is formed. However, as can be seen from Fig. 1,a and 1,b the depth of the porous region in the substrate is considerably greater for the sample grown on SiC/por-Si/Si substrate

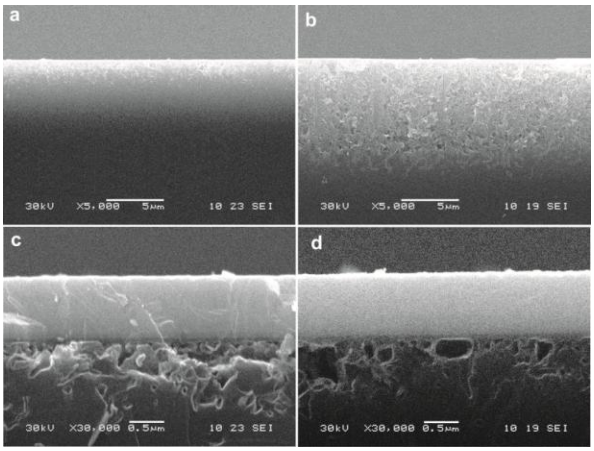

Fig. 1 Cross-section SEM image of samples grown on SiC/por-Si/Si (**a**, **c)** and SiC/c-Si (**b**, **d**) substrates at the different magnification

The PL spectra of the samples demonstrates two emission areas localized near 3.4 eV and broad emission band within the yellow-green range of the spectrum (500 – 600 nm) more intensive for GaN/por-Si/Si(111) heterostructure. The peak localized near 3.4 eV corresponds to hexagonal symmetry but not the cubic one (in the latter case exciton emission would be of about 3.2 eV).

Hall measurement revealed n-type conductivity for both samples. Carrier concentration was measured as $9.2 \cdot 10^{17}$ and $1.8 \cdot 10^{19}$ cm^{-3} for the sample grown on SiC/c-Si and SiC/por-Si/Si respectively, with Hall carrier mobility of 52 $\frac{cm^2}{V * s}$ and 990 $\frac{cm^2}{V * s}$.

UV spectra analysis revealed that up to the range of extremes (500 – 900 nm) the value of refractive index in GaN layer grown on the template with porous silicon is slightly higher (+7%), than for the film obtained on the substrate of SiC/c-Si.

XRD analysis showed that GaN grown on substrate with preformed por-Si layer is less strained and have less density of vertical dislocations.

Acknowledgments

The work was performed under financial support of the grant of Russian scientific foundation 19-72-10007. Access to KNMF equipment was obtained under the grant of the President of the Russian Federation MD-42.2019.2.

REFRENCES

[1] Kukushkin *et al.* Rev Adv Mater Sci n.d. **17**, 1 (2008)
[2] S.A. Kukushkin, A.V. Osipov, J. Phys. D **47**, 313001 (2014)
[3] A.S. Lenshin, *et al.*, Mat. Sci. Semicond. Proc. **30**, 25 (2015)

Perovskite nanoparticles and films: optical properties and lighting stability

A G Son[1], **E V Krivogina**[2], **S A Kozyukhin**[2], **S S Shapovalov**[2]
[1] The Moscow Institute of Physics and Technology, Moscow 141701, Russia
[2] Kurnakov Institute of General and Inorganic Chemistry of the Russian Academy of Sciences, Moscow 119991, Russia

Abstract. In this paper, we obtained nanoparticles based on ABX_3 type of metal halide perovskites at room temperature. The development of technological processes allowed us to synthesize the studied nanoparticles with room temperatures. Perovskite materials problem is degradations in moist environment, by light and unsteadiness to differential temperature. We studied perovskite degradation phenomena from light exposure. And were select the optimal layers for perovskite solar cell stability.

1. Introduction

Perovskite structure materials of the type AMX_3 (A = Cs, CH_3NH_3, $CH_3CH_2NH_3$, $(NH_2)_2CH$; M = Sn, Pb; X = Cl, Br, I,) are promising for solar energy. They have optimal parameters using in photovoltaics, such as band gap energy, high mobility of charge carriers and their long lifetime. Currently, the organo-inorganic perovskites solar cell (PSC) efficiency has reached a certified value of 25.2%, it exceeds the obtained values cadmium telluride (CdTe) and indium gallium selenide (CIGS) solar cells (SC) [1]. However, such materials are unstable under the influence of a humid environment, in the presence of oxygen, high temperatures and light radiation [2-3]. One of the solutions of this problem and improvement the properties of solar cells are using of mixed perovskite layers and stabilization of the layers by other materials, including perovskite nanoparticles (NPs). At present, perovskite NPs are especially popular in photovoltaics. They have a high photoluminescence quantum yield and their optical properties depending on NPs size and composition [4].

In this work, we developed a modified method for the NPs synthesis at room temperature and NPs films with mixed perovskite layers. We studied their optical properties and degradation under illumination. Particle sizes vary between 20-200 nm, depending on the synthesis conditions. The optical properties of NPs and films were studied by optical spectroscopy. Perovskite NPs structure was determined by electron diffraction. The films morphology was obtained by scanning electron microscope. It was experimentally found that during the synthesis of NPs, the dimensions of which are 200 nm, have a layered structural structure, and cubic shapes have NPs with a size of 20 nm [5]. Perovskite and NP layers was applied on substrates by various methods. After exposure to sunlight simulator, the photoluminescence (PL) intensity decreased significant. We repeatedly irradiated substrates with different NP perovskite layers. Based on the PL intensity dependences were selected the most optimal substrates and layers. We associate film degradation phenomenon from lighting with various mechanisms of ion mass transfer.

2. Figures

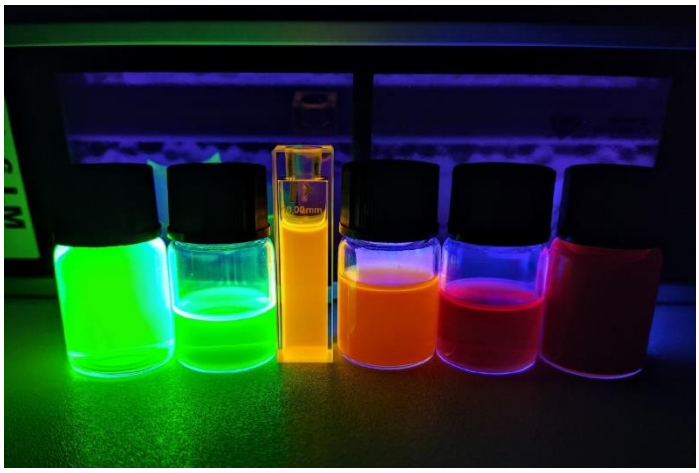

Figure 1. Perovskite NPs different composition.

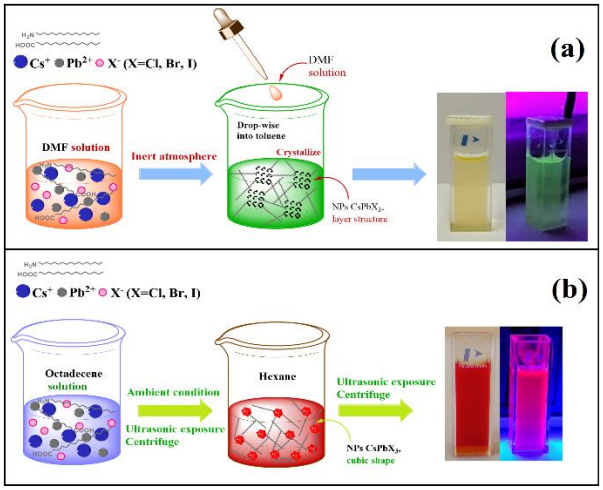

Figure 2. Perovskite NP synthesis at room temperature: (a) layer structure NPs, (b) cubic shape NPs.

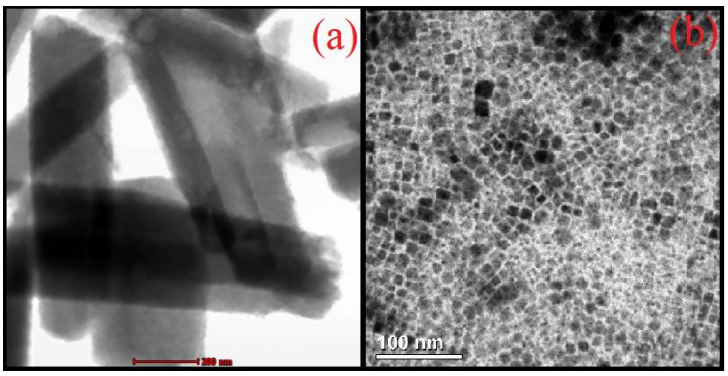

Figure 3. Perovskite NPs $CsPbI_3$ TEM-images: (a) 200 nm, (b) 20 nm.

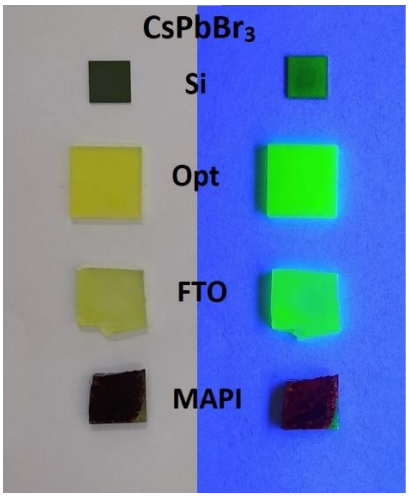

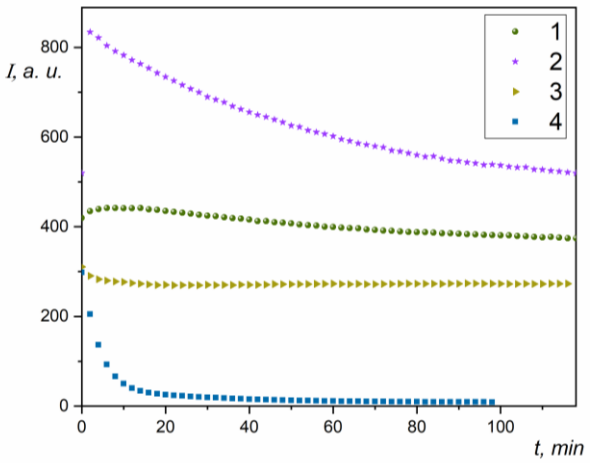

Figure 4 (a, b). (a) $CsPbBr_3$ NPs films with various layers; **(b)** PL peak (λpeak = 515 nm) dependence on the time of irradiation CsPbBr3 NPs films: 1 - Si, 2 - optical glass (Opt), 3 - FTO, 4 - MAPI

3. Acknowledgments

This work was supported by the Russian Science Foundation №18-13-00409

References

3.1. For papers:

[1] National Renewable Energy Laboratory, Best research-cell efficiencies chart (2020), https://www.nrel.gov/pv/assets/pdfs/best-research-cell-efficiencies.20200128.pdf

[2] Yang S. et al. Stabilizing halide perovskite surfaces for solar cell operation with wide-bandgap lead oxysalts // Science, **365**, 473-478, 2019

[3] Wei Z. et al. Solution-processed highly bright and durable cesium lead halide perovskite light-emitting diodes // Nanoscale, **8**, 18021-18026, 2016

[4] Tong Y. et al. Highly luminescent cesium lead halide perovskite nanocrystals with tunable composition and thickness by ultrasonication // Angew. Chem. Int. Ed., **55**, 1-7, 2016

[5] Son A. et al. CsPbI3 perovskite nanoparticles: room-temperature synthesis and optical study // Russian Journal of Inorganic Chemistry, **64 (12)**, 1587-1591, 2019

Atomic layer deposition of Ruthenium on different interfaces for an advanced metallization system of ICs

E A Smirnova[1], **A V Miakonkikh**[1], **A E Rogozhin**[1], **K V Rudenko**[1]
[1]Valiev Institute of Physics and Technology of Russian Academy of Sciences, Moscow 117218, Russia

Abstract. Nucleation effects were experimentally studied for ruthenium thin films grown by plasma-enhanced atomic layer deposition (PEALD) using O_2 plasma. Bis(ethylcyclopentadienyl)ruthenium (II) ($Ru(EtCp)_2$) was used as Ru precursor. The growth was performed on different underlying thin layers (interfaces), including Ta_2O_5, TiN, and TaN to investigate the effects of interfaces for nucleation of the Ru in the ALD process. Some of the samples were previously processed in ammonia and oxygen plasma to enhance nucleation. The processes of forming barrier layers based on titanium and tantalum nitrides by plasma-enhanced atomic layer deposition were also studied. Films properties were evaluated by spectral ellipsometry, scanning electron microscopy and atomic force microscopy.

1. Introduction

Highly conformal Ruthenium thin films have many applications in microelectronics; for example, as a gate electrode for p-FET [1], capacitor electrodes in new generation dynamic random access memories (DRAMs) [2], and capacitor electrode for ferroelectric random access memories (FRAMs) [3]. Thermal and plasma-enhanced atomic layer deposition Ruthenium were reported by several groups [4]. The novel application of Ruthenium is metallization systems of integrated circuits [5]. Cobalt and Ruthenium are the two leading materials to replace copper at small dimensions. The advantage of Ruthenium is the possibility to use it without diffusion barriers or apply Ru as a barrier for other metals [6]. One of the main disadvantages of the thin Ruthenium film growth process is the effect of delayed nucleation. It manifests itself in the presence of idle cycles at the beginning of the ALD process. In the case of incomplete nucleation, this results in island growth on the surface, which leads to the high roughness of the films. The present paper performs research on the initial stages of Ruthenium growth on surfaces coated with different interfaces and subjected to various pretreatments. The processes of forming barrier layers based on titanium and tantalum nitrides by plasma-stimulated atomic layer deposition were also developed.

2. Experiment

Ru films were deposited on different substrates by PEALD at a growth temperature of 400 °C using an alternating supply of $Ru(EtCp)_2$ and O_2 plasma. The deposition pressure was kept at 65 mTorr during plasma steps and 80 mTorr in others. $Ru(EtCp)_2$ was contained in a bubbler, which was heated to 70°C and delivered to the reactor by argon carrier gas at a flow rate of 150 sccm. The feeding line and chamber were heated to 120 °C to prevent the condensation of the $Ru(EtCp)_2$ precursor.
There were 300 deposition cycles for each sample. One deposition cycle of PEALD-Ru consisted of six steps: (i) dose of $Ru(EtCp)_2$; (ii) pump during 1 s; (iii) purge pulse with 150 sccm of Ar; (iv)plasma gas stabilization; (v) O_2 plasma exposure and (vi) another purge with 150 sccm of Ar.

During the plasma pulse, the radio-frequency plasma was operated at 75 W with 60 sccm of gas flow. The conductivity of ruthenium stacks was measured by the four-probe method.

3. Results and discussion

It was found that the nucleation rate for Ruthenium in a plasma-stimulated deposition process substantially depends on the surface of the substrate. Measurements by atomic layer microscopy showed that the formed films have a characteristic roughness, which occurs due to the gradual formation of nuclei on the surface. Thus, the stimulation of nucleation leads to a decrease in the roughness of the films. It has been established that films of metals deposited by plasma-stimulated deposition - (TiN and TaN) of a second precursor compositionally optimized to produce films with minimal electrical resistance - are favorable for deposition.

4. Conclusion

It was shown that the nucleation delay could be achieved during the deposition of Ruthenium of several hundred cycles and its effects significantly depend on the interface material. It also determines the roughness of the resulting films. It has been shown that RMS roughness during the deposition of ruthenium films with a thickness of 10-15 nm on the surface of TiN and TaN during the plasma conditioning of the surfaces is in the range of 1.7-4.2 nm and depends on the interface material. The results can be used to develop ruthenium deposition processes in trench coats in ICs metalization systems, as well as to develop promising area selective deposition processes.

5. Acknowledgments

The investigation was partially supported by Program no. 0066-2019-0004 of the Ministry of Science and Higher Education of Russia for Valiev Institute of Physics and Technology of RAS and partially funded by RFBR, according to the research project № 18-29-27029.

References

[1] H.-C. Wen, P. Lysaght, H.N. Alshareef, C. Huffman, H.R. Harris, K. Choi, Y. Senzaki, H. Luan, P. Majhi, B.H. Lee, M.J. Campin, B. Foran, G.D. Lian, D.-L. Kwong, J. Appl. Phys. **98** (2005) 043520.
[2] C. Manke, S. Miedl, O. Boissiere, P.K. Baumann, J. Lindner, M.Schumacher, A. Brodyanski, M. Scheib, Microelectron. Eng. **82** (3–4 Special issue) (2005) 242.
[3] N. Inoue, N. Furutake, A. Toda, M. Tada, Y. Hayashi, IEEE Trans. Electron Dev. **52/10** (2005) 2227.
[4] S.-J. Park, W.-H. Kim, W. Maeng, H. Kim Microelectron Eng, **85** (2008), pp. 39-44
[5] L. G. Wen, P. Roussel, O. V. Pedreira, B. Briggs, B. Groven, Shi. Dutta, M. I. Popovici, N. Heylen, I. Ciofi, K. Vanstreels, F. W. Østerberg, O. Hansen, D. H. Petersen, K. Opsomer, Ch. Detavernie, Ch. J. Wilson, S. Van Elshocht, K. Croes, J. Bömmels, Z. Tőkei, and Ch. Adelmann
ACS Applied Materials & Interfaces 2016 **8** (39), 26119-26125
[6] R. Bernasconi and L. Magagnin 2019 J. Electrochem. Soc. **166** D3219

Optical properties of InGaN/GaN QDs nanorods by top-down fabrication after KOH treatment

K P Kotlyar[1,6], **E M Kiseleva**[2], **A K Menzelincev**[2], **V B Shcherbakova**[2], **V A Shilov**[2], **E O Smolina**[2], **T N Berezovskaya**[1], **E V Nikitina**[1], **I P Soshnikov**[1,4,5], **G E Cirlin**[3]

[1]Alferov University, Khlopina 8/3, St. Petersburg 194021, Russia

[2]Alferov Winter School of Alferov University, 27 January – 1 February, Khlopina 8/3, St. Petersburg 194021, Russia

[3]ITMO University, Kronverkskiy pr. 49, St. Petersburg 197101, Russia

[4]Ioffe Physical-Technical Institute of the RAS, Politekhnicheskaya 26, St. Petersburg 194021, Russia

[5]Institute for Analytical Instrumentation of the RAS, Rizhsky pr. 26, St. Petersburg 190103, Russia

[6]St Petersburg University, Universitetskaya Emb. 13B, St.Petersburg 199034, Russia

Abstract. In this work were studied properties of InGaN/GaN nanorods before and after wet chemical etching with the aim of sidewall defects removal and morphology configuration, which, consequently, allowed to manipulate with the optical properties of the light emission of the nanorods.

1. Introduction

InGaN/GaN nanorods have a promising potential for the fabrication of highly efficient LEDs, nanoscale sources of light for photon probe production, and similar applications [1]. One the most commonly used techniques for nanorods creation is plasma etching of planar light emitting heterostructures with a mask assembled on the surface. The key problem of this method is the sidewall defects formation. In this work, the wet etching method of InGaN/GaN nanorods was studied with the aim of sidewall defects removal and morphology configuration, which, consequently, allowed to manipulate with the optical properties of the light emission of the nanorods.

2. Experiment and results

The initial sample represents an array of nanorods of size d = 100 nm and density $3.4 \cdot 10^9$ $см^{-2}$. The average height of the nanorods was 300 nm: GaN (p-type) 100 nm (top), InGaN QD/GaN, AlGaN/GaN superlattice (100 nm), and GaN (n-type) 100 nm, which altogether form a heterostructure. The etching process occurred in 2 stages: first etching in liquid solution KOH:H_2O (1:5) at 70°C temperature for 10 seconds, second etching in liquid solution KOH:H_2O:$C_3H_8O_3$ (7.8:11:48.7) at 70°C temperature for 2-27 minutes. Using the well-known method for determining the semiconductor polarity [2], we came to the conclusion about the Ga- polar crystallographic structure of our sample and the possibility of etching. Morphology of the structure was measured using Zeiss Supra 25 scanning electron microscope and spectrum of the photoluminescence intensity were received on Accent RPM Sigma facility. As a result of etching, the nanorods became thinner, the

photoluminescence intensity increased. Due to the different etching rates of the heterostructure materials, as a result of further etching, the quantum dots disappeared and the photoluminescence intensity decreased. To explain the experimental results, we performed a numerical simulation of structures in the Optiwave and Lumerical software, which showed that the geometry of the nanorod affects the extraction of light from the sample. During etching, the shape of the nanorods changed from a trapezoidal to a vertical resonator. Along with this, defects were removed from the sidewall surface of nanorods. These factors served to increase the intensity of photoluminescence at the first stage of etching in a KOH solution.

Acknowledgments
These studies were financially supported by the Russian Foundation for Basic Research (project 19-32-90156).

References
[1] Yu-Lin Tsai, Kun-Yu Lai, Ming-Jui Lee, Yu-Kuang Liao, Boon S. Ooi, Hao-Chung Kuo, Jr-Hau He. 2016 *Progress in Quantum Electronics* **49** 1–25
[2] Shubina K Yu, Berezovskaya T N, Mokhov D V, Mizerov A M, Nikitina E V 2017 *Technical Physics Letters* **43**(21) 47

Wet chemical etching of III-N nanowires on Si substrate for micro and nano-devises fabrication

V V Lendyashova[1], K P Kotlyar[1], R R Reznik[2], T N Berezovskaya[1], E V Nikitina[1], I P Soshnikov[1,3,4], G E Cirlin[1,2,4]
[1]Alferov University, Khlopina 8/3, St. Petersburg 194021, Russia
[2]ITMO University, Kronverkskiy pr. 49, St. Petersburg 197101, Russia
[3]Ioffe Physical-Technical Institute of the RAS, Politekhnicheskaya 26, St. Petersburg 194021, Russia
[4]Institute for Analytical Instrumentation of the RAS, Rizhsky pr. 26, St. Petersburg 190103, Russia

Abstract. In this work, it is experimentally shown that the etching of GaN or InGaN NWs in the KOH solution allows to manage the morphology and optical properties of the NWs array. The diameter of the NWs decrease from 200-100 to 30-40 nm. When etching the sample increases the intensity of photoluminescence structure.

1. Introduction

In the last few years, nanowires (NWs) based on III-N (in particular, InGaN) materials are widely used in nanophotonics and optoelectronics to create high-efficient light-emitting diodes, solar cells and etc. Firstly, InGaN has a direct band gap in the range from 0.7 to 3.43 eV available by tuning the chemical composition. Secondly, nanowires can be grown practically defect-free on substrates whose lattice constants differ significantly from the NW lattice constants [1]. However, the synthesis NWs with lateral sizes of nanometers requires special preparation of the substrates, including electron lithography method. At the same time, wet chemical etching is a promising and simply method due to which it is possible to control the morphology [2] and, as a consequence, the electrical and optical properties of NWs. The work presents results of the wet chemical etching in the KOH solution of InGaN and GaN nanowires.

2. Experiment and results

The NWs were grown by molecular-beam epitaxy (Riber Compact 12 MBE system) on Si (111) substrates. The surface morphology of the samples was studied using Supra 25 (Carl Zeiss, Germany) scanning electron microscope (SEM). Optical properties was exanimate by photoluminescence spectroscopy (Accent RPM Sigma machine).

Morphology studies of InGaN NWs initiall samples show (figure 1a) a pencil-like shape with an 80-100 nm truncated top. Wet chemical etching of III-N materials is carried out in the solution KOH:H_2O (1:5) at a temperature of 75℃ with a variation of time [3]. SEM studies show that at the initial stage of etching (10-60 sec.) there is a decrease in the diameter of the NWs perpendicular to the direction of growth (figure 1b), as well as etching of existing defects of the structure array. The diameter of the NWs decrease from 100 to 30-40 nm. Changing the viscosity of the etching solution allows to control the rate of etching with high accuracy. This mechanism of etching occurs to formation an uniform surface morphology of the layer. It achieves a greater homogeneity of the photoluminescence map.

Note that when etching the structure increases the intensity of photoluminescence structure, presumably due to the removal of the oxidative layer and surface defects.

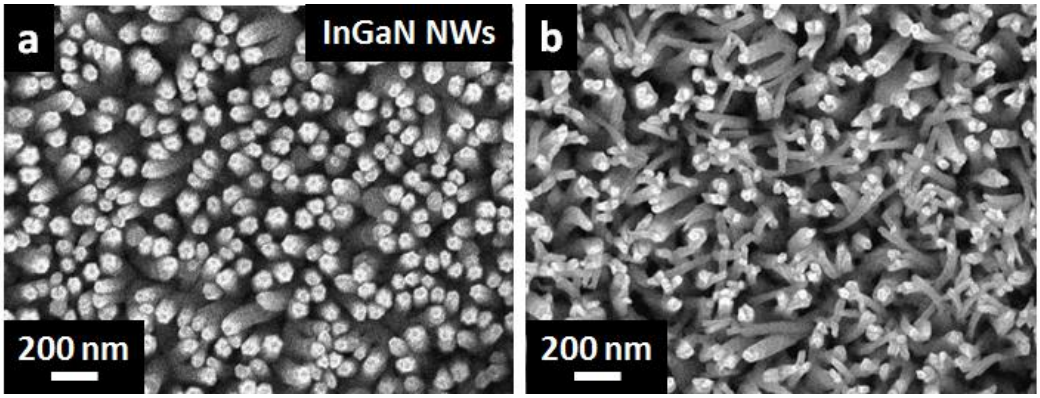

Figure 1(a, b). (a) initial sample; **(b)** sample after 10-60 sec. etching..

The etching occurs along the semi-polar and then along the no-polar crystallographic directions [4] perpendicular to the growth direction of the NWs, which led to a homogeneous reduction in diameter to the diameter of the NWs top. Since the height of the NWs has not changed during the etching process, it is possible that the synthesized InGaN NWs have a Ga-polar crystallographic structure [3].

With further etching (60-180 sec), the NWs are etched at the tops and roots (fig. 1(3)), which provides to a decrease in the overall height of the structure and separation of the NWs from the substrate. As a result, it is experimentally shown that the etching of InGaN NWs in the KOH solution allows to control the morphology and optical properties of the NWs array.

Acknowledgments
These studies were financially supported by the Russian Foundation for Basic Research (project 19-32-90156, 18-07-01364 A).

References
[1] Dubrovskii V G, Cirlin G E, Ustinov V M 2009 *Semiconductors* **43**(12) 1539
[2] Duk-Jo Kong, Si-Young Bae, Chang-Mo Kang and Dong-Seon Lee 2013 *Optics Express* **21**(19) 22320
[3] Shubina K Yu, Berezovskaya T N, Mokhov D V, Mizerov A M, Nikitina E V 2017 *Technical Physics Letters* **43**(21) 47
[4] Hak Dong Cho, Im Taek Yoon, Sh. U. Yuldashev, Tae Won Kang, Deuk Young Kim, Jong-Kwon Lee 2017 *RSC Advances* **7**(80) 50853-50857

The use of optical chopper increases the efficiency of femtosecond laser-induced cell fusion

Osychenko A.A.[1], Zalessky A.D.[1], Tochilo U.A.[1], Martirosyan D.U.[1], Nadtochenko V.A.[1]
[1]N.N. Semenov Federal Research Center of Chemical Physics, Russian Academy of Sciences

Abstract. Artificial cell fusion is a widely used approach in cell biology and biomedicine. Femtosecond laser-induced cell fusion is considered to be a precise and low-invasive tool for the cell fusion. However, the percentage of somatic cell fusion remains not very high, and the use of polyethylene glycol is often required. In our research we propose the use of rotating optical chopper to create ultra-short trains of femtosecond pulses (up to 1 ms) to decrease the laser impact. It helps to control the appearance and size of gas-vapor bubbles, avoiding cell destruction. We achieved the cell fusion efficiency of 50% without the use of polyethylene glycol.

1. Introduction.

Artificial cell fusion is a widely used approach in cell biology and biomedicine, e.g., for hybridoma production [1] or for tetraploid embryo obtainment [2]. Femtosecond (fs) laser-induced cell fusion is known as a precise and low-invasive tool for the embryo cell fusion. It allows fusing 2-cell embryos with 50% efficiency, but percentage of somatic cell fusion does not exceed 15-20% [3] or 37% according another data [4]. One research reports on 80% level of fusion [5], but in this work fusion medium is supplemented with polyethylene glycol, which is known as a fusogen. Relatively low percentage of somatic cell fusion can be explained by the appearance of the gas-vapor bubble, which occurs in the contact area of the cells due to the laser exposure. On the one hand, gas-vapor bubble is required to initiate cell fusion by destabilizing plasma membranes of the cells. On the other hand, gas-vapor bubble can impair plasma membranes of the cells and can be resulted in cell destruction [6]. So, the success of fusion depends on the cell size (consequently, on the cell-adhesion area) and on the gas-vapor bubble size. Therefore it is easier to fuse 2-cell embryos, which have size 30-50 μm (each blastomere) and natural cell-adhesion area, than to fuse somatic cells, which are significantly smaller (10-20 μm).

In this research we propose the use of optical chopper to improve the fusion technique. We used optical chopper to reduce the length of femtosecond pulse trains up to 1 ms. It allowed to rise up the pulse energy but to diminish heat accumulation, therefore to lower vapor-gas bubble size.

2. Materials, methods and results.

Cell culture and sample preparation.

Frozen THP1 cells (human monocytic cells) were thawed in a 37°C water bath and then diluted with pre-warmed medium (DMEM supplemented with 10% FBS). Cell suspension was centrifuged at approximately 200G for 5 minutes. Supernatant were decanted and cell pellet were resuspensed with M2 (Sigma, M7167) medium. During the experiments cells were kept in M2 medium on the ice to avoid cell adhesion.

Experimental setup for the cell fusion.

In the experiments we used the Olympus IX71 microscope (objective 60×, NA = 0.7). Cell fusion was performed using a fs laser Mai-Tai (Spectra Physics). Laser parameters: λ = 800 nm, pulse duration = 100 fs, pulse energy = 1,5 nJ, 80 MHz repetition rate. The diameter of the beam waist was 1,39 μm, peak power density for the pulse in the beam waist was $1{,}1 \cdot 10^{12}$ W·cm^{-2}. Optical chopper was set up

with frequency 26 Hz to incise laser pulse trains with 1 ms duration. After optical chopper mechanical shutter was used to control number of femtosecond pulse trains for one exposure.

Fusion protocol and results.

For the fusion experiments suspended THP1 cells were placed onto a cover glass in 50 µl M2 supplemented with 40 µg/ml lectin (Sigma, L8902) to provide cell-cell adhesion. Single cells were joined by an optical tweezer and adhered by the action of lectin (Fig. 1, a, b). Laser radiation was focused at the cell-adhesion area and resulted in a gas-vapor bubble (Fig. 1, c). Estimated bubble size is 2 µm, its lifetime is 40 ms. Gas-vapor bubble broke plasma membranes of the cells and caused fusion immediately (Fig. 1, d, e). 27 of 60 pairs (45%) successfully fused forming a single cell with 2 nuclei (Fig. 1, f). Complete cell fusion took nearly 10 seconds from the moment of gas-vapor bubble appearance.

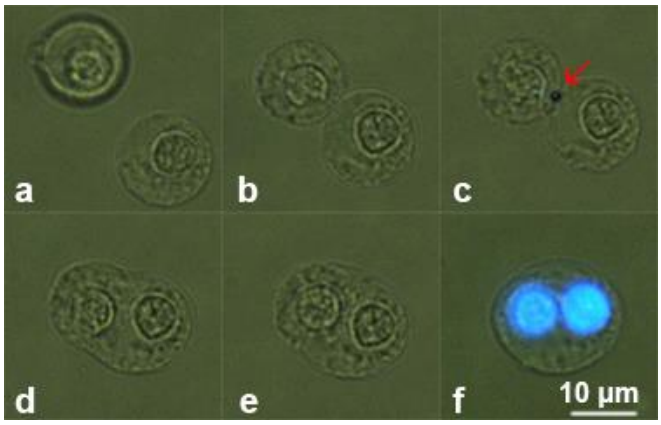

Figure 1. Laser-induced fusion of THP1 cells. **(a)** Optical tweezer moves a cell towards to another one and joins them **(b)**. Gas-vapor bubble occurs as a result of the laser impact (shown by an arrow, **c**) and induces cell fusion immediately **(d, e)**. Presence of 2 nuclei within a one cell is confirmed by Hoechst 33342 staining **(f)**.

3. Acknowledgments

The work has financial support from the Russian Foundation for Basic Research grant 19-53-52007. Experimental facilities were supported by the State task of FRCCP RAS AAAA-A19-119012990175-9. The work was performed on facilities of Semenov FRCCP RAS CCE (no.506694).

References

[1] Wilson T 1983 *BioTechnology* **1** 390-391
[2] Spindle A 1981 *Exp Cell Res* **131** (2) 465-470
[3] Kuetemeyer K, Lucas-Hahn A, Petersen B, Niemann H, Heisterkamp A 2011 *J Biomed Opt* **16** (8)
[4] He H, Kong S K, Chan K T 2011 *J Innov Opt Heal Sci* **4** (2) 113-125
[5] Gong J, Zhao X, Xing Q, Li F, Li H, Li Y, Chai L, Wang Q, Zheltikov A 2008 *Appl Phys Lett* **92** 093901.
[6] Osychenko A A, Zalessky A D, Kostrov A N, Ryabova A V, Krivokharchenko A S, Nadtochenko V A 2017 *J Biomed Opt* **22** (12) 1-9

Overexpression of the recombinant IbpA protein from *Acholeplasma laidlawii* in *Escherichia coli* cells increases thermotolerance

L S Chernova[1,2], **M S Fedorova**[1], **I E Vishnyakov**[2], **A R Kayumov**[1,2]
[1] Kazan Federal University, 18 Kremlevskaya str., 420008, Kazan, Russia
[2] Institute of Cytology, Russian Academy of Sciences, 4 Tikhoretsky av., 194064, St. Petersburg, Russia

Abstract. The presence of a gene encoding small heat shock protein IbpA in *Acholeplasma laidlawii* (*Al*IbpA) appears to be one of the key factors determining the high adaptive capabilities of this mycoplasma. Previously, we showed a participation of the N-and C-terminal regions of *Al*IbpA in functions of chaperone *in vitro*. The aim of this work was to establish the involvement of the N - and C-terminal motifs of the recombinant *Al*IbpA in the survival of *Escherichia coli* cells under temperature stress *in vivo*. To determine this, we used genetically engineered versions of the *Al*IbpA with truncations and mutations in the N - and C-terminal domains. Viability was determined by counting CFU and differential fluorescent staining. Studies have shown that hyperproduction of the N-termini-modified IbpA from *Al*IbpA is able to exhibit thermotolerance *E. coli* cells.
This research was funded by the Russian Science Foundation (project No. 17-74-20065).

Introduction

Small heat shock proteins of α-crystalline type (sHSPs) play a key role in the cell survival under stress conditions. The primary function of sHSPs is preventing the irreversible denaturation and aggregation of partially denatured proteins [1, 2]. Some sHSPs are known to interact with cytoskeletal proteins and to protect them from denaturation under stress conditions [3; 4]. They are also necessary for the cell membrane fluidity regulation, since they stabilize the liquid-crystal state of the bilayer and maintain the membrane integrity during thermal fluctuations [5; 6]. Their importance for the cell survival under extremely unfavorable conditions may also be confirmed by their presence in most well studied microorganisms that can exist in dormant state forms. Remarkably, sHSPs were not found in many bacteria which belong to Mollicutes (mycoplasmas). Among them sHSP homologs were identified only in some members of the Spiroplasmataceae and Anaeroplasmataceae families, and to a greater extent in bacteria of Acholeplasmataceae family, including *Acholeplasma laidlawii* [7]. In contrast to most mycoplasmas which are parasites of human and animals, *A. laidlawii* is the only mollicute that is able to exist free of any host [8] and survives under a variety of stresses. We suggest that IbpA protein (the sHSP orthologue) can be one of the key factors governing the extensive stress adaptive abilities of *A. laidlawii*. Our early investigations suggest that IbpA participates both in the stabilization of individual polypeptides and probably in the maintenance of various cellular structures upon temperature stress [9]. Recently we have shown that IbpA protein with truncated or mutated N-terminal domain forms fibrils and exhibits higher chaperon activity *in vitro* [1].

In this paper we report that overexpression of the recombinant IbpA with truncated or mutated N-terminal domain increases the viability of *E.coli* cells under heat shock.

2. Materials and Methods

2.1 *Bacterial strains and growth conditions*

Escherichia coli BL21 was used in this assay. Plasmids providing the overexpression of recombinant mutated and truncated IbpA proteins from *A. laidlawii* used in this study were obtained earlier by cloning of the truncated *ibpA* genes into pET15b vector [1,7]. Bacteria were grown in LB broth with rigorous shaking at 37°C for 24 hours and subjected to heating for 1 h at various temperatures as indicated.

2.2 *Evaluation of survival of* IbpA *overproducing E. coli cells under heat shock*

E. coli BL21 pIbpA and *E. coli* BL21 pET15b cells were grown in LB medium until OD600~0.6 and IPTG was added until the final concentration of 1 mM followed by cultivation during 1 h. Next the cells were exposed to the heat shock (56ºC) for 1 h. Cells from the same aliquots before and after the heat treatment were seeded on a solid LB medium and CFUs were calculated after 24h cultivation at 37ºC. Alternatively, cells subjected to the heat shock for 1 h were stained by acridine orange and propidium iodide and analyzed by differential fluorescent microscopy. The fraction of non-viable cells was estimated as the relative fraction of the red cells among all cells in the combined images obtained by overlaying of the green and the red fluorescent microphotographs (10 images per each sample).

2.3 *Statistical analysis*

Experiments were carried out in three biological repeats. The fraction of non-viable cells in microscopic images was estimated as the relative fraction of the red cells among all cells in the combined images obtained by overlaying of the green and the red fluorescence microphotographs (10 images per each sample) by using BioFilmAnalyzer software [10].

Results

One of the known functions of sHSPs is the enhancement of cellular resistance to heat shock by prevention of partially denatured proteins aggregation. As shown previously, sHSP from the rice increased the tolerance of *E. coli* cells to the 30 min exposure to 47.5 °C [11]. In our recently research *Al*IbpA with damaged N-terminal domain was characterized by increased chaperone activity of sHSP *in vitro* [1], so we asked whether an overexpression of modified *Al*IbpA would affect the survival of the recombinant *E. coli* cells under heat shock conditions. *E.coli* BL21 cells carrying either pIbpA plasmids providing the expression of IbpA proteins with various mutations/truncations of N- and C-terminal domains or pET15b vector (the latter used as control) were induced by the addition of IPTG followed by 1 h incubation at 30 °C for protein overproduction. Next the cells were incubated at 56 °C for 1 h, and CFUs were calculated before and after the exposure to heat shock. Count of viable cells with empty pET15b vector decreased approximately 10-fold after heat treatment. In contrast, the cells producing recombinant IbpA with truncated (N12, ΔN25) or mutated (ΔN11N12) N-terminus survived after heating suggesting that IbpA increases the cell survival under the heat shock. Additionally to the CFUs counting, the viability of the cells after heat shock was evaluated by differential fluorescent microscopy. Cells were stained by both acridine orange and propidium iodide and the fraction of non-viable cells was estimated as the relative fraction of the red cells. Similarly to CFUs count data, an increased viability of cells producing IbpA with truncated (N12, ΔN25) or mutated (ΔN11N12) N-terminus has been observed.

Taken together our results indicate that the overexpression of N-termini-modified IbpA from *Al*IbpA more effectively protects *E.coli* cells from heat shock than other variants including full-sized *Al*IbpA itself.

References

[1] Chernova L S, Bogachev M I, Chasov V V, Vishnyakov I E, & Kayumov A R 2020 *RSC Advances*, 10(14), 8364-8376

[2] Haslbeck M, & Vierling E 2015 *J. of molecular biology*, 427(7), 1537-1548

[3] Mounier N, Arrigo A P 2002 *Cell Stress Chaperones* 7(2):167–176

[4] Treweek T M, Meehan S, Ecroyd H, Carver J A 2015 *Cell Mol Life Sci* 72(3):429-451

[5] Horváth I, Glatz A, Varvasovszki V, Török Z, Páli T, Balogh G, Kovács E, Nádasdi L, Benkö S, Joó F, Vigh L 1998 *Proc Natl Acad Sci USA* 95(7):3513–3518

[6] Tsvetkova N M, Horváth I, Török Z, Wolkers W F, Balogi Z, Shigapova N, Crowe L M, Tablin F, Vierling E, Crowe J H, Vígh L 2002 *Proc Natl Acad Sci USA* 99(21):13504–13509

[7] Vishnyakov I E, Borchsenius S N 2013 *Microbiology Moscow* 82(6):653-667

[8] Lazarev V N, Levitskii S A, Basovskii Y I, et al 2011 *J Bacteriol* 193(18):4943-53

[9] Vishnyakov I E, Levitskii S A, Manuvera V A, Lazarev V N, Ayala J A, Ivanov V A, Snigirevskaya E S, Komissarchik Y Y, Borchsenius S N 2012 *Cell Stress Chaperones* 17(2):171-180

[10] Bogachev M I,Volkov V Y, Markelov O A, Trizna E Y, Baydamshina D R, Melnikov V, Murtazina R R, Zelenikhin P V, Sharafutdinov I S, Kayumov A R 2018 *Plos One* 13 (5)

[11] Yeh C H, Chang P F L, Yeh K W, Lin W C, Chen Y M, Lin C Y 1997 *Proc Natl Acad Sci USA* 94:10967–10972

Catalytic properties of nanostructured nickel-containing pectin biopolymers on a glassy carbon surface

K V Kholin[1,2], V P Shirobokov[1], I R Nizameev[1,2], S T Minzanova[1,2], M K Kadirov[1,2]

[1]Kazan National Research Technological University, Kazan 420015, Russia

[2]Arbuzov Institute of Organic and Physical Chemistry, FRC Kazan Scientific Center, Russian Academy of Sciences, Kazan 420088, Russia

Abstract. We obtained coordination pectin biopolymers with different nickel ions contents (PG-NaNi). Morphology of PG-NaNi on a glassy carbon surface provides very high surface to volume ratio. Cyclic voltammetry on the modified glassy carbon working electrode in water solution saturated with carbon dioxide shows catalytic properties of PG-NaNi for CO_2 reduction reaction.

1. Introduction

Efficient conversion of carbon dioxide into useful products is an important task of science. Electrochemical reduction of carbon dioxide to various products is considered as one of the main approaches to solve this problem. Selectivity and yield of the electrochemical CO_2 reduction reaction at room temperature strongly depend on the working electrode material and solvent. Main problems consist in the relatively high potential of this reaction (-1.90 V vs SHE in water) and low current density. However, these problems can be solved using efficient, cheap and stable catalysts. Unfortunately, no catalysts were found that met all the requirements and could be used on an industrial scale.

Coordination polymers with metal ions can be considered as polymerized forms of molecular catalysts. They have several advantages as electrocatalysts - significant design flexibility, high surface to volume ratio and they allow functionalization with multivalent ligands and metal centres. In this work, we propose coordination pectin biopolymers with nickel ions as heterogeneous electrocatalysts for the electrochemical CO_2 reduction reaction.

2. Results and Discussion

Coordination polymers PG-NaNi were obtained as a result of total pectins deesterification with 100% degree of salt formation and its subsequent involvement in complexation [1]. The following reagents were used as starting reagents: citrus pectin Classic C-401 manufactured by Herbstreith & Fox (Germany) with 65% esterification degree, nickel chloride $NiCl_2$ and sodium hydroxide NaOH with 99,9% degree of purity. Since results for different PG-NaNi polymers are similar, further we will focus on the results for PG-NaNi with 20% substitution degree of Na with Ni ions.

Direct single-electron reduction of linear CO_2 to the nonlinear anion radical $CO_2^{\cdot-}$ occurs at high negative potential -2.21 V vs. SCE. But multi-electron reduction reactions are possible in the presence of water molecules. These reactions have much less standard electrode potential, for example:

$CO_2 + 6H_2O + 8e = CH_4 + 8OH$ (-0.25 V vs. SHE)

$CO_2 + 9H_2O + 12e = C_2H_5OH + 12OH$ (-0.33 V vs. SHE)

In addition, more useful products are formed as a result, as can be seen.
Our idea was to deposit PG-NaNi on the surface of a glassy carbon (GC) electrode, then to lower the electrode into water saturated with carbon dioxide and try to catalytically reduce CO_2. When water is saturated with carbon dioxide, pH level of the solution greatly decreases (in our conditions, up to pH = 4). This is an undesirable process, therefore pH=7.0 of solutions throughout the entire electrochemical experiments was supported by the addition of small amounts of HCl (≥99.9%) and KOH (≥99.9%). In addition, 0.1 M NaCl (≥99.9%) was added to the water as the supporting electrolyte.
Deposition of PG-NaNi on the GC electrode surface technique was as follows: 7.5 mg PG-NaNi was dissolved in 400 µl mixture of deionized water and isopropyl alcohol (1:1). The resulting solution was placed in an ultrasonic bath for 10 minutes, then was dripped onto the surface of a glassy carbon electrode. After drying in the open air, the modified GC electrode was considered ready for use. An atomic force microscope (MultiMode V) was used to reveal the morphology of PG-NaNi on the GC surface. As you can see in Figure 1a, there are fibers of biopolymer PG-NaNi with 40 nm diameter on the GC surface. Fiber agglomeration can be observed in some places (top right in the figure), while single fibers are observed in other places. Such morphology provides a very high surface to volume ratio, and it is very good for a heterogeneous catalyst.

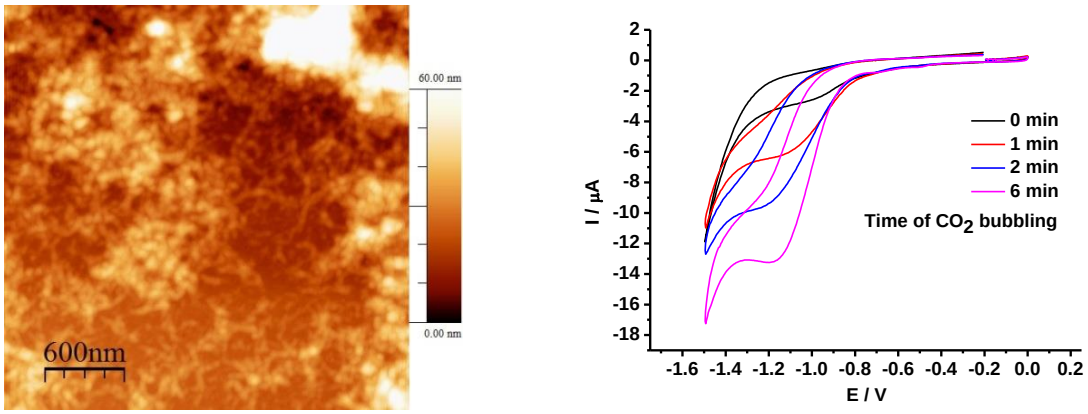

Figure 1(a, b). (a) Atomic force microscope image of the PG-NaNi modified GC surface; **(b)** CV on the modified GC electrode in water saturated with Ar or CO_2 with different bubbling times.

Figure 1b shows the results of cyclic voltammetry on the modified working electrode in water solutions saturated with argon (0 min CO_2 bubbling) or carbon dioxide with different bubbling times. The curves show an irreversible reduction peak with potential E = 1.2 V vs. Ag/AgCl. It can be noted that an increase in CO_2 bubbling time leads to an increase in the peak current. CV curves with bubbling time over 6 min. do not show an increase in reduction peak current. Worth noting cyclic voltammetry on the unmodified working electrode in water does not show any peaks in this potential range. All this confirms catalytic properties of nanostructured nickel-containing pectin biopolymers PG-NaNi on a glassy carbon surface for CO_2 reduction reaction.

3. Acknowledgments
This work was supported by the President of Russian Federation grant for the governmental support of young Russian scientists MK-1555.2019.3.

References
[1] Minzanova S T, Mironov V F, Vyshtakalyuk A B, Tsepaeva O V, Mironova L G, Mindubaev A Z, ... & Milyukov V A 2015 *Carbohydrate polymers* **134** 524

Analysis of methodological errors in measuring a digital automated bio-impedance meter

V V Antipenko, E A Pecherskaya, T O Zinchenko, O A Melnikov, G V Kozlov and A V Fimin
Department of Information and measuring equipment and metrology, Penza State University, Penza 440026, Russia

Abstract. The development of medical technology is an integral component of preserving the future generations health, which consists of the prevention and early diseases diagnosis using modern diagnostic measuring instruments. One such instrument is a bio-impedance analyzer (BIA). This article presents the results of modeling and metrological analysis of the BIA electrical circuit, which allowed to minimize the main relative error to 0.1%.

1. Introduction

Bio-impedance analyzers offer portability, mobility and enhanced comfort for long-term monitoring. The frequency measurement spectrum from 100 to 2500 kHz allows to distinguish the introduction of errors by extracellular and intracellular fluid [1]. To increase the measurement accuracy, the following problems were solved: a review of electrical models of biological objects was carried out, a circuitry solution for measuring nodes was developed and the errors of bio-impedance measurements were analyzed.

2. Analysis of methodological errors of bio-impedance measurement

Methodological errors in bio-impedance measurement can occur when registering the current flowing through a system of parallel-series resistances and capacitors - the equivalent of a person's electrical circuit [2]. They manifest themselves as a result of spurious current leaks to the common wire, because the measuring electrodes are connected to the extreme points [3, 4]. The developed current source circuit that minimizes the errors is shown in Figure 1. According to the accepted notation, R1 is the resistance of the intercellular fluid, C1 is the capacitor formed by the dielectric membrane of the cells, and R3 is the resistance of the intracellular fluid. The human body is a stray capacitor at high frequencies, in which the clothes act as a dielectric, one of the plates is the human body, and the second is the earth. C3 = 200 pF acts as such a stray capacitor (see Figure 1), its reactance is 398 Ohms, at a voltage of 10 V and a frequency of 2 MHz. According to the first Kirchhoff rule, it is determined that the stray current is 12.2%. Figure 2 shows the phase - frequency characteristics (PFC) of the considered circuit. The PFC analysis showed that when the frequency increases above 150 kHz, the effect of current leakage to earth through the capacitor C3 is manifested, which affects the error of bio-impedance measurement.

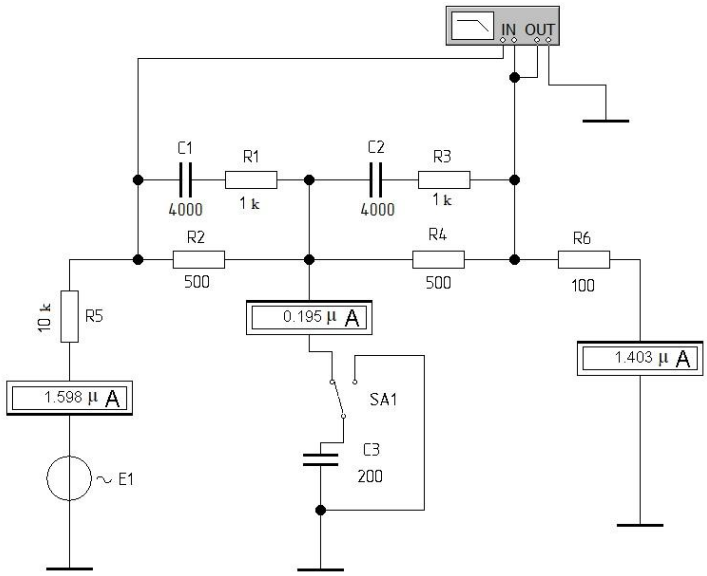

Figure 1. Circuit simulating earth leakage.

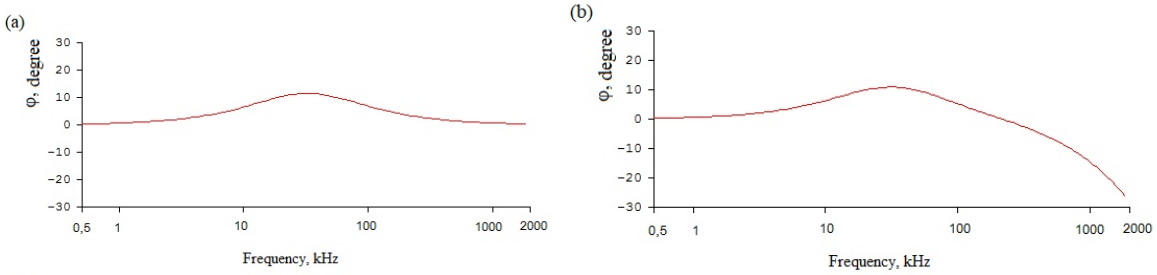

Figure 2(a, b). (a) PFC when the capacitor C3 is off; **(b)** PFC when the capacitor C3 is on.

3. Conclusion

In this work, a circuit is modeled that takes into account the leakage current to earth. The measurement object is presented in the form of an electric model and the process is simulated in a CAD system, which made it possible to improve the circuitry part of the current source in order to increase the measurement accuracy and minimize the influence of the object stray capacitance. Therefore, changing the currents proportions of the electric circuit model on the RC elements can reduce the influence of spurious interference.

References

[1] Abtahi F, Gyllensten I C, Lindecrantz K and Seoane F 2012 *Journal:Journal of Physics* **12** 407
[2] Tronstad C and Strand-Amundsen R 2019 *Journal of Electrical Bioimpedance* **10** 24 - 33
[3] Golubkov P E, Pecherskaya E A, Karpanin O V, Kraynova K Y, Artamonov D V and Shepeleva Y V 2018 Proc. 19th International Conference of Young Specialists on Micro / Nanotechnologies and Electron Devices (EDM) p 641
[4] Artamonov D, Baranov V, Pecherskaya E, Pushkareva A, Tsypin B, Fimin A 2019 Proc. 20th International Conference of Young Specialists on Micro / Nanotechnologies and Electron Devices (EDM) p 760

Revealing nucleoplasm mechanics by optical trapping and Brownian motion of nucleolus within mouse GV-oocytes *in vivo*.

M S Syrchina, A M Shakhov, A V Aybush, A D Zalessky, V A Nadtochenko

Laboratory of nanophotonics, N.N. Semenov Federal Research Center of Chemical Physics RAS, Moscow 119991, Russia
e-mail: wrongclue@gmail.com

Abstract. Tracking the movement of the nucleoli by custom-made software and optical trapping in living oocytes with different types of chromatin distribution made it possible to identify specific patterns of nucleoplasm organization, depending on the chromatin packing profile of the nucleus.

1. Introduction

Chromatin and nuclear bodies experience dramatic biophysical changes during oogenesis. Nuclear mechanics affect the regulation of gene expression, availability of DNA for transcription factors, histones or other molecular complexes [1] and, as a result, the successful maturation and fertilization of the gamete.

Optical trapping of nucleoli within nucleoplasm of living oocytes provides unique model system and non-invasive technique for investigation of nuclear environment.

To characterize rheological properties of the nucleoplasm of GV-oocytes (germinal vesicle stage) with three main types of chromatin distribution in the nucleus (NSN, pNSN, pSN, SN) [2], we employed methods of active and passive rheology. By using of a single beam optical trap, formed by a tightly focused laser radiation at 780 nm wavelength, we performed subsequent stress-relaxation series of nucleoli in various directions and with different amplitudes. The oocytes' nucleolus, due to its large size and spherical shape, acted as a microprobe. The characteristic nucleolus relaxation times were also obtained for each type of chromatin configuration, which can subsequently be used to evaluate the viscoelastic properties of the nuclear material. Brownian motion of nucleoli was also extracted to estimate local forces acting within nucleolar environment.

2. Materials and methods

Oocytes were collected from 6-9 weeks old female mice (C57BL/CBA) 48 hours after injection of PMSG (pregnant mare′s serum gonadotropin) and stained with fluorescent dye Hoechst 33342 for visualization of chromatin. Optical trapping of the nucleolus was carried out by continuous radiation from a titanium-sapphire laser at a wavelength of 790 nm. The laser radiation was coupled to the microscope and then was focused into the oocyte with a 60x 0.7 NA objective lens. Laser power at the focus was 280 mW, corresponding to a maximum force of 10 pN. Videos of optical trapping and Brownian motion were captured by high-speed camera at 100 fps. Tracking of nucleoli were performed by custom-made software.

3. Results and conclusions

Relaxation of nucleoli in our model was best fitted by biexponential decay function (Fig.1). By triggering of displacement modes, we extracted variety of relaxation curves of nucleolar movement for the oocytes with NSN-type of chromatin configuration. For the small displacements and prolonged relaxation, fluctuations were detected. Distinctive states of nucleolar mechanics and appearance were observed: oocytes of NSN-type had a freely moving nucleolus through the whole volume of germinal vesicle, but SN-oocytes had nucleoli attached to the nuclear envelope. Four patterns of nucleolar motion were described for oocytes of NSN-type. In general, nucleoplasm of GV-oocytes showed anisotropic properties. Understanding of nuclear mechanics within oocytes can facilitate the introduction of new criteria for non-invasive estimation of developmental competence based on the mechanical properties of intranuclear space.

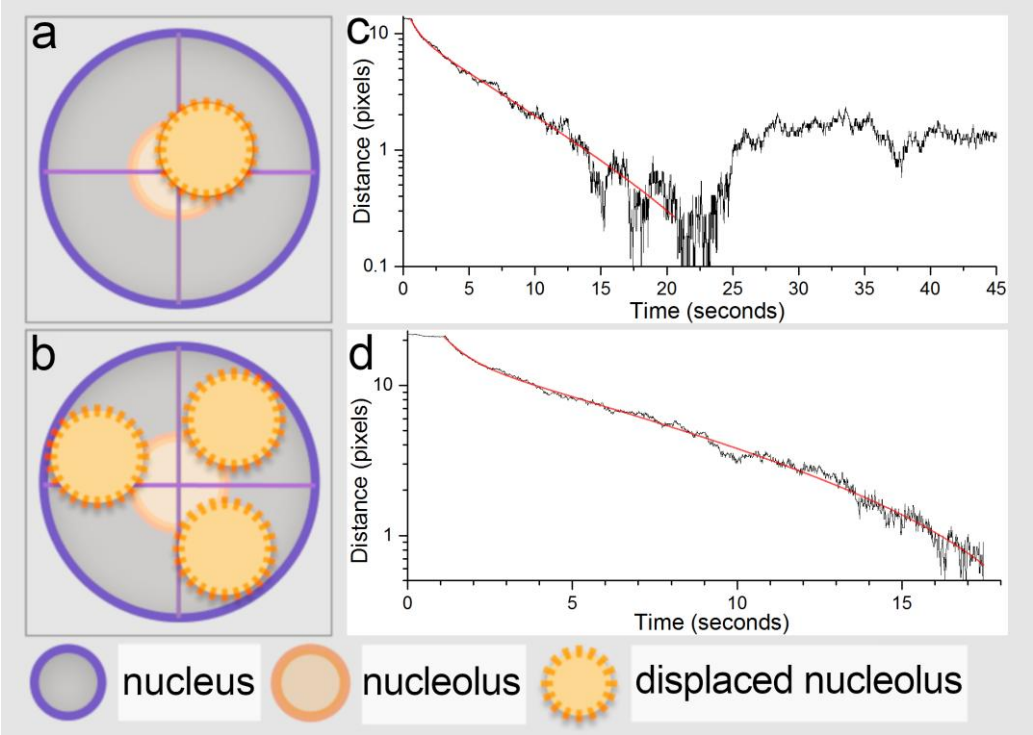

Figure 1(a,b,c,d). **(a,b)** Amplitudes of nucleolar displacement; **(c,d)** Two types of relaxation curves depending on the mode of displacement

Acknowlegements

This study was supported by RFBR (project №18-33-01080).

References

[1] Shin Y, Chang Y-C, Lee D S W, Berry J, Sanders D W, Ronceray P, Wingreen N S, Haataja M, Brangwynne C P 2018 *Cell* **175** 6 1481-1491

[2] Tan J H, Wang H L, Sun X S, Liu Y, Sui H S, Zhang J 2009 *Mol. Hum. Reprod.***15** 1 1-9

Study of droplet formation regimes in a pressure control mode in microfluidic chip for screening cell libraries

N A Filatov[1], A A Tyushkevich[2], A S Bukatin[1]
[1]Nanobiotech Lab, St. Petersburg Alferov University, St. Petersburg 194021, Russia
[2]Peter the Great St. Petersburg Polytechnic University, St. Petersburg 194021, Russia

Abstract. To create a system for screening cells in a microfluidic chip, a key role is played by the method of controlling fluid flows in the chip to form droplets. This is due to the fact that it is required to obtain monodisperse drops, place cells in them and be able to manipulate such microcapsules. For these purposes, the method of using a pressure controller is poorly understood and promising. In this work we investigated the conditions for reproducible generation of water-in-oil emulsions in the microfluidic chip by the pressure control mode of fluid flows. Also we study the possibility of packaging cells in these emulsions and their sorting.

In the middle of the 20th century [1] it was first proposed to study individual cells located in aqueous drops in oil. However, only the development of droplet microfluidics allowed to achieve a stable and reproducible formation of monodisperse drops with a volume of 1-100 pl., suitable for quantitative research. Microfluidics enables to generate stable emulsions with controlled sizes and with high forming rate (0.1 to 10 kHz (drops per second) or higher) to perform a large number of experiments. Also it is possible to create conditions for the isolation of single cells in drops by generating emulsions of small volumes [2]. In contrast to the classical methods, this provides a huge potential for efficient cell screening [3].

To create a system for screening cells in a microfluidic chip, a key role is played by the method of controlling fluid flows in the chip to form droplets. This is due to the fact that it is required to obtain monodisperse drops, place cells in them and be able to manipulate such microcapsules. As a simple solution and commercially available tools, syringe pumps is usually used to solve this aims. However, syringe pumps are typically operated open loop, specifying a particular rate at which the syringe is actuated, directly controlling the flow rate through the chip. While the mean flow rate for a period of time can be very accurate while using syringe pumps, the transient flow through the system is pulsed, with the pressure fluctuating over time within the chip. Additionally, syringe pumps have long response times, which limit their use in microfluidic studies requiring dynamic flow profiles [4,5]. They are also incompatible with a valve-based closing system and closed microchannels. At the same time, there are suitable alternative methods for controlling pressure of liquids, which have been little studied in application with systems for screening cells in microchips.

The aim of this work is to study the conditions for reproducible generation of water-in-oil emulsions in the microfluidic chip by the pressure control mode of fluid flows. And also we study the possibility of packaging cells in these emulsions and their sorting.

In experimental studies we have used microfluidic chips (polydimethylsiloxane, glass), manufactured by the "soft lithography" method [6]. The formation of the emulsion was carried out as follows: dispersed phase (aqueous medium) was supplied through the central channel, and continuous phase

(mineral oil) - through two side channels, thereby compressing and focusing the flow of the dispersed phase. In specific hydrodynamic conditions due to instabilities this leads to the formation of the emulsion [7]. By controlling the ratio of pressures of the dispersed and continuous phases, it is possible to obtain an emulsion with desired characteristics (for example, drop diameter). To predict coalesce of the emulsion, the presence of a surfactant in oil is necessary.

The experiment data of the dependence of the diameter of water emulsions in mineral oil on the ratio of water to oil pressures at the different concentrations of Abil EM180 surfactant in oil (3%, 4.3%, 5%) showed that the diameter of the emulsions is independent of absolute water and oil pressures, but depends only on their ratio. Controlled generation is observed at the ratio range from 0.55 to 0.95. It was found that the droplet size of the emulsions lies in the range from 5 μm to 160 μm. The amount of the surfactant significantly affects the size of emulsions. If the surfactant concentration increase to 5% then the droplets diameter doubles. There are generation modes where the droplet formation occurs in several rows.

The measurements of the droplet generation frequency as a function of water to oil pressure ratio for different amounts of the surfactant showed that the frequency depends on the absolute values of the water and oil pressures.

To create a method for packing single cells into drops, a model cell line of human chronic myeloid leukemia K562 was used. The experiments have shown that the probability of packing cells in droplets is described by Poisson statistics. In addition, it was experimentally shown that the emulsion droplets can be directed from one channel to another by dielectrophoresis at 25 V / μm electric field intensity, which can be used to sort them by fluorescence signal.

References

[1] Lederberg J, 1954 Journal of bacteriology **68** (2), 258
[2] Theberge A B et al., 2010 Angewandte Chemie International Edit **49** (34), 5846-5868
[3] Sackmannet E K et al., 2014 Nature **507**, 181-189
[4] Kim Y et al., 2011 PloS one **6** (1), 14624
[5] Kim Y, Kuczenski B, LeDuc P R, Messner W C, 2009 Lab on a Chip **9** (17), 2603–9
[6] Bukatin A S, Mukhin I S, Malyshev E I, Kukhtevich I V, Evstrapov A A, Dubina M V 2016 Tech. Phys. **61** 1566-1571
[7] Hsiung S K, Chen C T, Lee G B, 2006 J Micromech and Microeng **16** (11), 2403-2410

Lifetimes and Anisotropy of Polarized Fluorescence of FAD in Water-Methanol Solutions

M K Krasnopevtceva[1], **V P Belik**[1], **I V Semenova**[1], **A G Smolin**[1], **O S Vasyutinskii**[1]
[1]Ioffe Institute, Saint Petersburg 194021, Russia

Abstract. Time-resolved fluorescence kinetics of FAD under excitation by picosecond laser pulses at 452 nm has been studied. Fluorescence lifetimes, weighting coefficients, polarization anisotropy, and rotational diffusion times were determined in water-methanol solutions with various methanol concentrations. In aqueous solution FAD demonstrated two excited state lifetimes of 4.19±0.14 ns and 2.13±0.18 ns with a weighting coefficient ratio of about 0.6. The parameters in 20% methanol solution were close to those in aqueous solution, while at 40%, 60% and 80% methanol concentrations the excited state lifetimes shortened and became closer to each other.

1. Introduction

FAD (flavin adenine dinucleotide) is an important fluorescent probe that is contained naturally in cells of living organisms and is responsible for regulation of redox reactions. Therefore, investigation of FAD fluorescence in living cells allows for determination of essential information on cell behavior in norm and pathology and for development of the methods of early diagnostics of socially important diseases. The fluorescence parameters of FAD were investigated by means of picosecond laser excited polarized fluorescence spectroscopy in aqueous and water-methanol solutions containing 20%, 40%, 60%, and 80% of methanol.

2. Experimental Approach

The experimental setup was similar to that described in detail in our recent paper [1]. A quartz cuvette containing FAD solution was illuminated by pulsed radiation of a semiconductor laser at 452 nm with pulse duration of 30 ps and repetition rate of 2 MHz. The laser beam was vertically polarized. Emitted luminescence was collected at the right angle to the laser beam and then spectrally resolved by a monochromator MDR-12 (LOMO) at several wavelength bands centered at 510, 520, 530, 550, and 570 nm. A thin-film dichroic polarizer was placed in front of the monochromator input slit. The polarizer axis was fixed either along vertical, or horizontal direction, thus providing the analysis of the luminescence polarization. The luminescence from the monochromator output slit was detected by a photomultiplier (H10682-01, Hamamatsu). Time-resolved fluorescence decay curves were recorded successively at the vertical and horizontal positions of the polarizer axis by a time-correlated single photon counting (TCSPC) module (PicoHarp 300, PicoQuant). FAD was dissolved in water and in water-methanol mixtures (20%, 40%, 60%, 80% methanol solutions) at a concentration of 60 μM. The time-dependent experimental signals related to the vertically (I_y) and horizontally (I_x) polarized fluorescence components were fitted using known convolution expressions:

$$I_y(t) = K\, I(0) \int_{-\infty}^{t} IRF\left(t'\right) \sum_n \sum_k a_n e^{-\frac{t-t'}{\tau_n}} \left[1 + 2r_k e^{-\frac{t-t'}{(\tau_{rot})_k}}\right] dt' \quad (1)$$

$$I_x(t) = I(0) \int_{-\infty}^{t} IRF\left(t'\right) \sum_n \sum_k a_n e^{-\frac{t-t'}{\tau_n}} \left[1 - r_k e^{-\frac{t-t'}{(\tau_{rot})_k}}\right] dt' \quad (2)$$

where K is a channel sensibility coefficient, *IRF(t')* is an instrument function, τ_n are excited state lifetimes, $(\tau_{rot})_k$ are rotation diffusion times.

3. Results and Conclusions

The fluorescence parameters obtained from fit are summarized in Table 1. As shown in the table FAD in the aqueous solution demonstrated at various fluorescence wavelengths a double-exponential isotropic and a single-exponential anisotropic decay behaviors with almost the same characteristic times: the excited state lifetimes of about 4.19 ns and 2.13 ns, weighting coefficient ratio of 0.6 and rotation diffusion time of 0.26 ns. These values are in a good agreement with those reported recently elsewhere [2]. The experiments with water-methanol mixtures were carried out at a single fluorescence wavelength of 530 nm. The characteristic times of FAD in 20% methanol solution were close to those obtained in aqueous solution, while in 40%, 60% and 80% methanol solutions the excited state lifetimes had shorter values but close to each other.

TABLE 1. Fluorescence parameters

Wavelength, nm	τ_1, **ns, ± 0.14**	τ_2, **ns, ± 0.18**	a_1/a_2, **± 0.06**	**r, ± 0.03**	τ_{rot}, **ns, ± 0.03**
510	**4.25**	**2.15**	**0.58**	**0.34**	**0.27**
520	**4.15**	**2.07**	**0.61**	**0.35**	**0.24**
530	**4.15**	**2.14**	**0.62**	**0.35**	**0.24**
550	**4.16**	**2.15**	**0.63**	**0.35**	**0.26**
570	**4.24**	**2.14**	**0.60**	**0.33**	1.27

4. Acknowledgments

The financial support from Russian Foundation for Basic Research under the grant #18-53-34001 is gratefully acknowledged.

References

[1] Belik V P, Gadzhiev I M, Semenova I V, Vasyutinskii O S 2017 *Spectrochim. Acta A Mol. Biomol. Spectrosc.* **178** 181–184

[2] Sengupta A, Khade R V, Hazra P 2011 *J. Photoch. Photobio. A* **221** 105–112

Pump-probe polarization spectroscopy to study anisotropic relaxation in biological molecules.

I A Gorbunova[1], **M E Sasin**[1], **Y M Beltukov**[1], **A A Semenov**[1], **O S Vasutinskii**[1]
[1] Ioffe Institute, Saint Petersburg 194021, Russia

Abstract. A novel pump-probe method has been developed to study anisotropic relaxation and energy transfer in excited states of polyatomic molecules excited by femtosecond laser pulses. The method was used to study the rotational diffusion and anisotropic vibrational relaxation of NADH with a temporal resolution of about 0.6 ps at several pump and probe wavelength. The rotational diffusion times and anisotropic vibrational relaxation times were determined. The method developed allows for practically noninvasive monitoring of anisotropic relaxation in excited states of biological molecules at laser pulse energies less than 1 nJ.

1. Introduction

Nowadays the anisotropic relaxation in polyatomic biological molecules is successfully studied by either polarized fluorescence spectroscopy [1], or transient monitoring pump-probe methods [2]. The transient monitoring methods realized in the femtosecond time domain allowed to achieve the highest temporal resolution for investigation of energy transfer processes and photoisomerization of biomolecules [3], however till now all these methods required a relatively high laser pulse energies of about a few mkJ that could result in damaging the cells in the conditions of in vivo experiments. Also, all the methods suffered from a significantly large level of high frequency noise that was mainly due to instability of laser pulse. In this paper we report the development of a new anisotropy pump – probe method to study fast nonradiative anisotropic relaxation and energy transfer in the excited states of polyatomic biological molecules upon their excitation by femtosecond laser pulses. The method was used to study rotational diffusion and anisotropic vibrational relaxation of the reduced form of NADH (nicotinamide-adenine-dinucleotide) in solutions at various pump and probe wavelength. The method allows to reach the subpicosecond temporal resolution at laser pulse energies less than 1 nJ and to enhance significantly the accuracy of transient polarization-sensitive measurements.

2. Experimental method

We used a two-color pump-probe scheme where pump and probe pulses were generated by a Ti:Sapphire oscillator with pulse duration of about 100 fs and repetition rate of 80 MHz. The second harmonic of the laser output was used for pumping of NADH and the fundamental harmonic was used for probing. The wavelength of the probe beam was tuned form 720 nm to 800 nm with a step of 20 nm, and the pump beam wavelength was adjusted from 360 to 400 nm. The pump pulses promoted the transitions to the first electronic excited state of NADH that refers to the nicotinamide chromophore group and the probe pulses delayed with respect to the pump pulses by a time Δt were used for monitoring of the excited state dichroism as a function of time after excitation. The pump and probe beams co-directionally propagated along X axis. The pump beam polarization plane was modulated with a frequency of 100

kHz, between vertical (Y) and horizontal (X) directions using a photoelastic modulator and the probe beam polarization was adjusted at 45° with respect to the direction Y. Absorption of the pump beam polarized photons resulted in predominant excitation of the molecules with their axes aligned along the pump beam polarization direction. Therefore, the produced excited molecules axes alignment periodically changed its direction in space at 100 KHz with respect to the pump beam polarization rotation. Propagating through the sample the probe beam promoted absorption transitions to high laying molecular excited states, besides the transitions intensity depended on the angle between the probe beam polarization and the molecular axes alignment. Consequently, out-phase oscillations of the X and Y probe beam polarization components transmitted through the sample at 100 KHz were observed. These two orthogonal probe beam polarization components were simultaneously and independently detected by two photodiodes. The detected signals I_x and I_y were transmitted to two inputs of a differential integrator and the obtained differential signal I_x-I_y modulated at 100 kHz was analyzed by a lock-in amplifier. The differential signal I_x-I_y was recorded as a function of the delay time Δt between the pump and probe pulses. In fact, the recorded signals were due to the linear dichroism of the NADH solution induced by linearly polarized pump light. The balanced detection scheme used combined with the highly sensitive modulation scheme allowed for significant reducing of the excessive noises caused by the instability of laser pulses amplitude and density fluctuations in solution.

3. Results and discussion

The obtained experimental signals contained the contributions of a number of relaxation processes at different delay times. These are: nonlinear multiphoton excitation at delay times less than 3 ps, anisotropic vibrational relaxation at delay times of about 10 ps, and rotational diffusion with characteristic times of about 100 ps. As shown the rotation diffusion time determined from experimental data was independent on the excitation wavelength in the range 360 to 400 nm and found to be τ_{rot}= 218±15 ps that is a good agreement with the result obtained in our previous polarized fluorescence experiments [1]. The analysis of experimental signal at shoter delay time was carried out, as a result the anisotropic vibrational relaxation times were determined for the first time. A theoretical model has been developed that describes the processes of vibrational anisotropic relaxation of NADH in solution.

4. Acknowledgments

The study was supported by the Russian Foundation for Basic Researches under the grant No 18-03-00038 a.

References

[1] Sasin M E, Gorbunova I A, Bezverkhnii N O, Beltukov Y M, Vasyutinskii O S, and Rubayo-Soneira, J. 2019 *Tech. Phys. Lett.* **45** 672
[2] Lambert C, Scherpf T, Ceymann H, Schmiedel A, Holzapfel M, 2015 *J. Am. Chem. Soc.* **137** 3547
[3] Jonas D M, Lang M J, Nagasawa Y, Joo T, Fleming G R 1996, *J. Phys. Chem.* **100** 12660

The study of the properties of chitosan-based composite films filled with single-walled carbon nanotubes and treated with cold atmospheric plasma

***K. A. Kolbe*[1], *A. M. Kamalov*[1,2], *E. G. Feklistov*[1], *N. V. Smirnova*[1,2], *V. V. Kodolova-Chukhontseva*[1], *E. N. Dresvyanina*[3], *I. P. Dobrovolskaya*[1,2], *G. V. Vaganov*[1], *V. E. Yudin*[1,2]**

1. Peter the Great St. Petersburg Polytechnic University, St-Petersburg 195251, Russia
2. Institute of Macromolecular Compounds, Russian Academy of Sciences, St-Petersburg 199004, Russia
3. Saint-Petersburg State University of Industrial Technologies and Design, St-Petersburg 191186, Russia

Abstract

In the work composite films based on chitosan and single-walled carbon nanotubes (0.01%, 0.1%, 0.5% and 1%) were obtained. The electrical and mechanical properties of the composite films were measured. It was shown that a film with 1% SWCNT has sufficient electrical conductivity and optimal mechanical properties for the bioactivity of a culture of human dermal fibroblasts. It has been established that treating a film in a corona discharge changes the structure of the film and increases the adhesion and proliferation of human dermal fibroblast cells.

1. Introduction

The study of cell behaviors on biomaterials surface is of paramount importance because it can reveal many physiological and pathological events and eventually guide the design of biomaterials with better performance in tissue regeneration. Chitosan (CS), a promising biomaterial that by itself presents outstanding properties, revealed to improve the nanotechnology field when reinforced with various other nano-sized fillers. In the presence of fillers like single-walled carbon nanotubes (SWCNTs), enhanced mechanical, thermal and conductive properties are achieved.

In addition, it is known that non-thermal effects of gas discharges have proven to be very useful in the treatment of different biomaterials and in tissue engineering. Cold atmospheric plasma (CAP) is very far from thermodynamic equilibrium. Particularly, the electron temperature is about 10 000 K and significantly exceeds the gas temperature, which is close to room temperature. Besides that, cold plasma is a source of energetic and chemically active species (e.g., electrons, ions, excited atoms, and radicals). Owing to these features, CAP is used in the treatment of polymers and other temperature-sensitive materials.

2. Materials and Methods

Composite films were prepared from 4% chitosan (Biolog Heppe GmbH, Germany, M_m=1.64 x10^5, DD=92%) solutions containing SWCNTs (Carbon Chg, Russia) in 2% acetic acid solution. The content of SWCNTs with respect to chitosan was 0,01; 0,1; 0,5; 1 wt. %. Before the addition of chitosan, a suspension containing SWCNTs was dispersed to uniformly distribute particles throughout the volume. This was done using (1) an ultrasonic bath Sapphire for 30 min at a frequency of 35 kHz and power of 190 V; (2) an ultrasonic generator IL10-0.63 for 7 min at a frequency of 25 kHz and power of 630 V. The composite films were prepared according to [1].

A custom-designed portable CAP generator was used for polymer composite samples' processing. In contrast to a number of known types of plasma sources, this generator produces a stable air plasma using a self-sustained corona discharge of positive polarity (input voltage is 5.3 V while the output is about 15-16 kV, discharge current amplitudes are ranging from 10 up to 80 mA with a repetition rate of several tens of kilohertz, the average discharge current is about 100 – 150 μA). In the experiment, the samples were processed by the CAP at a distance of 1 cm for 10 min.

3. Results

The electrical conductivity of films was studied in isothermal conditions at 25°C. The currents were measured using a picoammeter A2-1 with a two-electrode system. The sensitivity of the picoammeter A2-1 is 10^{-15}A. The measurement error of current is 1%. The films were coated with platinum. The diameter of the electrodes was 16 mm. The charging currents were measured on constant voltage 10V, electrical field strength was ~2.5*10^5V/m. The time of current measurement was 1 minutes. The film with 1% SWCNT content was measured using four electrode systems (Fig. 1).

The wetting angles chitosan films filled with SWCNTs at a concentration of 1 wt% with respect to chitosan were measured without treatment and after treatment CAP. Processing with CAP leads to a

decrease in the hydrophobicity of the films: the wetting angle of the composite films decreases from 68 ° (before processing) to 61 ° (after processing). The values of the mechanical properties of chitosan-based composite films are obtained depending on the concentration of SWCNTs in the composition (table 1).

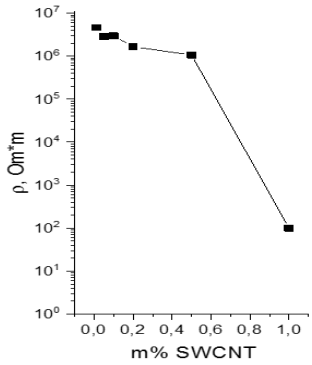

Figure 1. Volume resistivity of chitosan-based composite films filled with SWCNTs

	Tensile strength, MPa	Elastic modulus, GPa	Tensile strain, %
CS	128,5±12	4,7±0,12	20,4±6,9
CS+0,1%SWCNT	109,1±12	3,9±0,37	20,9±7,3
CS+0,5%SWCNT	141,1±0,3	4,8±1,1	30,5±5,8
CS+1% SWCNT	112,3±15	4,4±0,16	19,4±6,5

Table 1. Mechanical properties of chitosan-based composite films

After cell attachment, human dermal fibroblasts seeded on film matrices and cultural polystyrene surface (control) were incubated in culture medium at 37°C in a humidified 5% CO_2 incubator for 4 days. Studies of the viability and proliferation of the cells in the samples were performed using the MTT test.

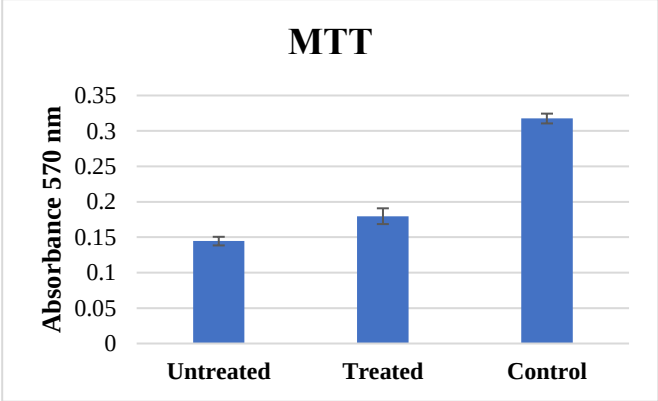

Figure 2. Human dermal fibroblast viability and proliferation on surfaces of film matrices and cultural polystyrene surface (control) as determined by MTT assay

The proliferation rate of cells (for 4 days) on treated film matrices was found to be greater than on untreated film matrices (Fig. 2). It has been shown that the filler addition and CAP treatment increase the conductivity of the composite material. By changing the conductivity, it is possible to obtain matrices with different bioactive properties.

4. Acknowledgments

This work was supported by the Russian Science Foundation, project no. 19-73-30003.

References

1. Natalia V. Smirnova, Konstantin A. Kolbe, Elena N. Dresvyanina, Sergey F. Grebennikov, Irina P. Dobrovolskaya, Vladimir E. Yudin, Thomas Luxbacher and Pierfrancesco Morganti Effect of Chitin Nanofibrils on Biocompatibility and Bioactivity of the Chitosan-Based Composite Film Matrix Intended for Tissue Engineering // Materials. 2019, 12, 1874; doi:10.3390/ma12111874.

Characterization of an RNase III mutant of *Rhodobacter sphaeroides*

J Boerner
Institute of Microbiology and Molecular Biology, Justus-Liebig-University Giessen, Giessen 35392, Germany

Abstract. In this work an RNase III deletion mutant of the facultative phototrophic α-proteobacterium *Rhodobacter sphaeroides* was characterized. The aim of this study was to identify differences in phenotype and RNA physiology between wild type and mutant, which can be explained by a loss of RNAse III activity. We analyzed the growth behaviour of the mutant and the wild type under different growth conditions, including microaerobic and phototrophic mode of growth. As *Rhodobacter sphaeroides* is known for its metabolic versatility, we were also interested in regulation of the transcriptome. To investigate the influence of RNase III on gene expression we performed RNA seq, Northern blot and qRT-PCR experiments. The results suggest that deletion of the RNase III coding gene (*rnc*) strongly impacts phenotype and transcriptome in *Rhodobacter sphaeroides*.

1. Introduction

As bacteria are exposed to an ever-changing environment, they have evolutionarily developed complex regulatory networks to adapt their proteom to different environmental conditions. At the same time, protein biosynthesis is one of the most ressource- and energy intensive biological processes in all living organisms [1]. Therefore, bacteria use different exo- and endoribonucleases to regulate gene expression quickly by degrading transcripts that are no longer needed. RNase III is a highly conserved dsRNA processing endoribonuclease. Previous studies have shown that RNase III plays a crucial role in RNA metabolism, by regulating the abundance of rRNAs, structured mRNAs and regulatory ncRNAs [2; 3].

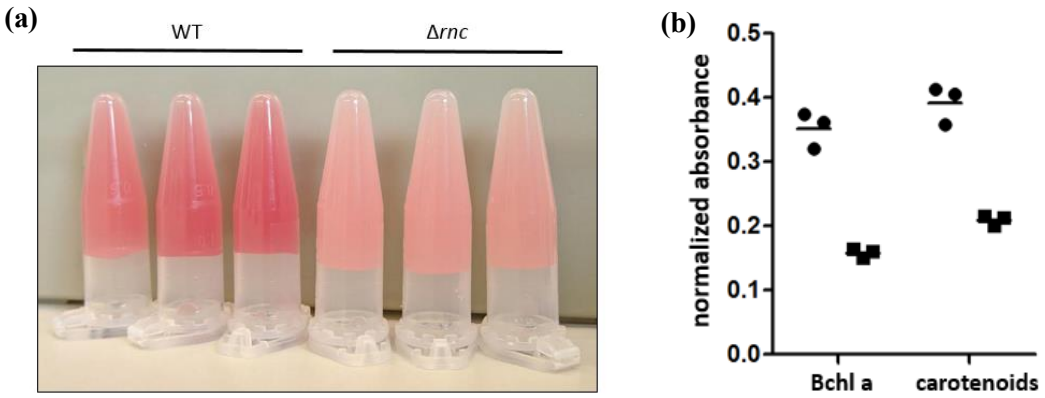

Figure 1(a, b). (a) Photo of microaerobically grown culture samples during mid exponential growth phase; **(b)** Extracted pigment amounts of wild type (dots) and Δ*rnc* mutant (squares).

The deletion mutant and the wild type of *R. sphaeroides* were cultivated under microaerobic and phototrophic conditions. Interestingly, a weaker pigmentation of the mutant was observed during microaerobic cultivation. To investigate the differences in pigmentation level, the pigments of both strains were extracted via formaldehyde/methanol extraction and photometrically quantified. In addition, full cell absorbance spectra were measured. The results indicate that pigment synthesis in general and especially synthesis of the photosynthetically active pigment-protein complexes is impaired in the Δ*rnc* mutant strain of *R. sphaeroides*.

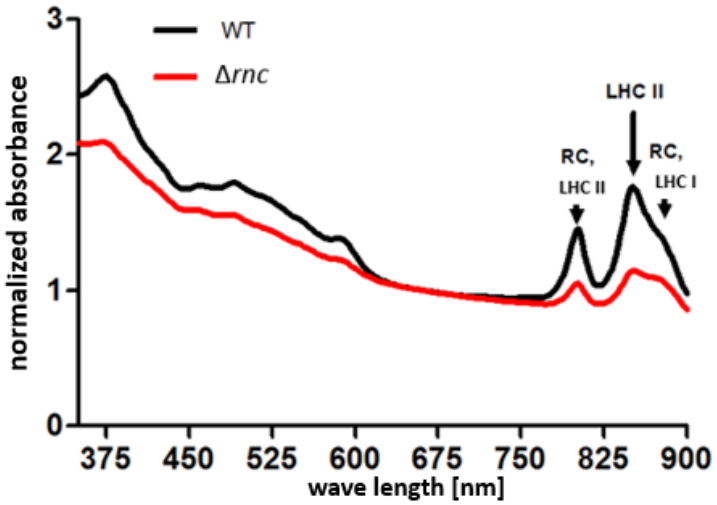

Figure 2. Full cell absorbance spectra. The absorbance spectra were measured under microaerobic conditions of biological triplicates from wild type and the Δ*rnc* mutant strain. The data was normalized to the absorbance$_{660\ nm}$ after calculating mean values of the triplicates. Characteristic absorbance peaks of the light-harvesting complexes (LHC) I & II, as well as for the reaction center, are marked with arrows.

To conclude the results, the Δ*rnc* mutant strain of *R. sphaeroides* 2.4.1 showed clear differences in phenotype of pigment production in comparison to the wild type. Moreover, an alteration in the steady state level of several transcripts coding for photosynthesis genes was observed in this mutant. Especially the expression of the *puf* genes (encoding the proteins of LHC I and the reaction center) were shown to be down regulated on RNA level in the mutant strain, which could be responsible for the impaired synthesis of photosynthetically active pigment-protein complexes.

2. Acknowledgment

I acknowledge Prof. Dr. Gabriele Klug (JLU Giessen) for funding and supervision of this project and Carina M. Reuscher (JLU Giessen) for outstanding technical support.

References

[1] Chang C, Stewart R C 1998 J. Plant Physiol. **117** 723
[2] Rische T, Klug G 2012 RNA biol. **9** 343
[3] Nicholson A W 2014 Wiley Interdiscep. Rev. RNA **5** 31

Multi-electrode silicon microprobes fabrication process for brain-computer interface

E Yu Gusev[1], J Y Jityaeva[2], S V Malohatko[1], O A Ageev[1,2]
[1]Southern Federal University, Institute of Nanotechnology, Electronics and Equipment Engineering, Taganrog 347922, Russia
[2]Southern Federal University, Research and Education Center "Nanotechnologies" Taganrog 347922, Russia
eyugusev@sfedu.ru

Abstract. Multi-electrode microprobes fabrication process based on silicon substrate was developed using surface micromachining and anisotropic wet etching. The process flow consists of 19 main operations, including 5 lithography steps using 5 photomasks. The minimum size of the elements is 2 μm. Experimental studies were carried out for some operations. As a result, the neural probe structures including two microprobes and electrical interface of 10 electrodes were fabricated.

1. Introduction

Neural probe is a highly informative instrument of brain activity study [1-3]. It is currently can be used for the formation of brain-computer interface and diagnosis of brain diseases in clinical settings [3]. The typical design includes a neural probe body, microprobes and electrical interface. One of the main problems in the use of neural probes is a damage of brain tissue during implantation of microprobes. Negative consequences are possible to decrease by reducing the overall dimensions of the probe to the microlevel. This can be done using bulk and surface micromachining [4,5]. However, microprobe materials should have enough margin of safety to withstand the mechanical stresses that arise when the probe is inserted and removed. Silicon is the main structural material of microprobes despite the inherent brittleness [1-3]. Devices based on it can be inserted to a greater depth, in comparison with polymer structures. The desire for a minimally invasive action and more precise positioning determines the need to improve neural probe concerning both its design and technological process.

The purpose of the work is to develop the fabrication process of a minimally invasive multi-electrode microprobes using surface micromachining and anisotropic wet etching of silicon.

2. Experimental details

The development of the fabrication process was carried out to implement the typical structure of a neural probe based on monocrystalline silicon. The structure includes a neural probe body with microprobes and a multichannel electrical interface isolated by a dielectric layer.

Monocrystalline silicon substrate (100) n-type with a thickness of 420 μm was used. The topology of layers on the front and back sides of the substrate was formed by photolithography using masks of silicon oxide and positive photoresists. The electrical interface was formed by lift-off lithography using *LOR/Ultra i* photoresists. The masking and isolation layers of silicon oxide were formed by plasma enhanced chemical vapor deposition and rapid thermal annealing [5]. Silicon oxide was etched

in buffer solution (HF (49%) : NH_4F (40%) = 1:6) [6]. Anisotropic etching of silicon was carried out in a solution of potassium hydroxide at a temperature of 80 °C.

A set of photomasks with cells from pairs of counter-directed probes suspended on a frame was designed and used to implement a special case of neural probe structures.

3. Results

The fabrication process based on 5 photolithography steps and includes 19 main operations like substrate cleaning, thermal oxidation, plasma-chemical deposition of silicon oxide and silicon nitride, rapid thermal annealing, plasma-chemical etching of silicon oxide and silicon nitride, wet isotropic and anisotropic etching of silicon oxide and monocrystalline silicon, electron-beam metal deposition and profiling structure by focused ion beam. The technological operation modes were determined.

A series of neural probe structures with two microprobes was produced. The thickness probe and midline width were 30 - 50 μm, 60 - 70 μm, respectively. The length was not more than 5 mm. The anisotropic nature of the silicon etching process determined the trapezoidal cross-sectional shape of the beams. The electrical interface of the neural probe was represented by 10 electrodes.

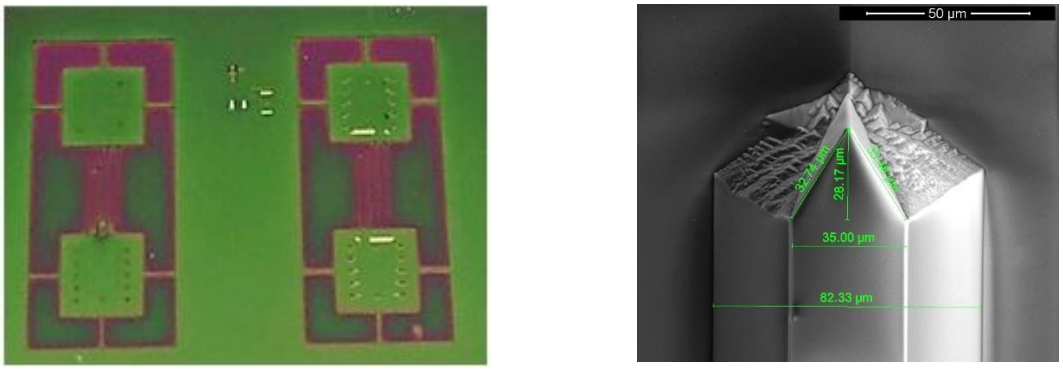

(a) **(b)**

Figure 1(a,b). Images of the microprobe from the front side **(a)** optical **(b)** SEM

4. Conclusion

The fabrication process of microprobes for the study of brain activity was developed. The series of samples of neural probe structures with 10 electrodes was fabricated. The thickness and midline width of each probe were 30 - 50 μm and 60 - 70 μm respectively. The results of the work can be used for development and fabricating of multielectrode neural probe with a different number of microprobes.

Acknowledgment

This work was financially supported by Southern Federal University. The equipment of the Research and Education Center "Nanotechnologies" of Southern Federal University was used for the study.

References

[1] Seymour J P, Wu F, Wise K D, Yoon E 2017 *Microsystems & Nanoengineering* **3** 16066
[2] HajjHassan M, Chodavarapu V, Musallam S 2008 *Sensors* **8 10** 6704-6762
[3] Govindarajan A V, Je M, Park W-T, Achyuta A K H 2012 *MEMS as implantable neuroprobes / in MEMS for Biomedical Applications* (Woodhead Publishing Limited) 361-395
[4] Gusev E Yu, Jityaeva J Y, Bykov A V 2017 *Journal of Physics: Conference Series* **929 1** 012055
[5] Ageev O A, Konoplev B G 2019 *Nanotechnology in microelectronics* (Moscow: Nauka) 511
[6] Gusev E Yu, Jityaeva J Y, Avdeev S P, Ageev O A 2018 *Journal of Physics: Conference Series* **1124 2** 022034
[7] Kirt R W, Muller R S 1996 *Journal of microelectromechanical systems* **5 4** 256-269

Living cell membrane structure study by high-resolution patch-clamp impedance spectroscopy

Mikhalina Lebedeva,[1] Daniil Stupin,[1] and Maxim Nikolaev[2]

[1]Alferov University, St.Petersburg, 194021, Russia

[2]Sechenov Institute of Evolutionary Physiology and Biochemistry, St.Petersburg, 194223, Russia

E-mail: mflebedeva@gmail.com

Abstract. In this paper, we improved the impedance-spectroscopy based patch-clamp technique by using high frequency-resolution impedance measurements. It was shown, that the proposed method gives the possibility to identify a cell membrane structure and monitor its properties. The obtained results could find the application in modern cytology and biophysics.

1. Introduction

In the last few decades, the patch-clamp technique has become the definitive technology for investigating the electric properties of cells [1]. Particularly, the data it provides is useful for studying ion channels and membrane conductivity. The standard application of this method consists of measuring the current passing across a membrane caused by applying DC voltage to a clamp pipette (usually, the "whole-cell" configuration is used). The changes in the current are then could be used, for example, to evaluate the time during which ion channels were open and close.

Applying to patch-pipette the AC voltage instead of DC voltage and studying the current frequency dispersion [2] – the so-called patch-clamp impedance spectroscopy (PCIS) – can provide more detailed data about the properties of the membrane such as conductivity and permeability. An example of such implementation is a recent study regarding how neuronal impedance changes upon membrane deformation [3]. However, usually in PCIS low-frequency resolution is used, and applying modern high-resolution impedance measuring techniques can significantly enhance the results of PCIS. For this reason, in this study, we have shown the benefits of high-resolution PCIS for determining cell membrane structure.

2. Materials and Methods

For providing the PCIS measurements the patch-clamp amplifier EPC-8 (HEKA, Germany) connected with L-Card ADC (L-Card, Russia) was used. The impedance measurements were provided using sweep-shape excitation AC voltage (from 2 Hz to 10 kHz with 2 Hz step, 5-mV peak-to-peak amplitude). Impedance spectra were calculated with the Fourier transformation technique based on fft routine in MATLAB package. The spectra analysis was performed also in MATLAB with a complex non-linear least-squares approach [2].

As a biological object, the CHO cell-line expressing proton-activated homomeric ion channels ASIC2a was used. As receptor activators, two solutions with different pH (4.5 and 7.4) were added to the cells with the Perfusion system ALA-VM8 (ALA Scientific Instruments, USA).

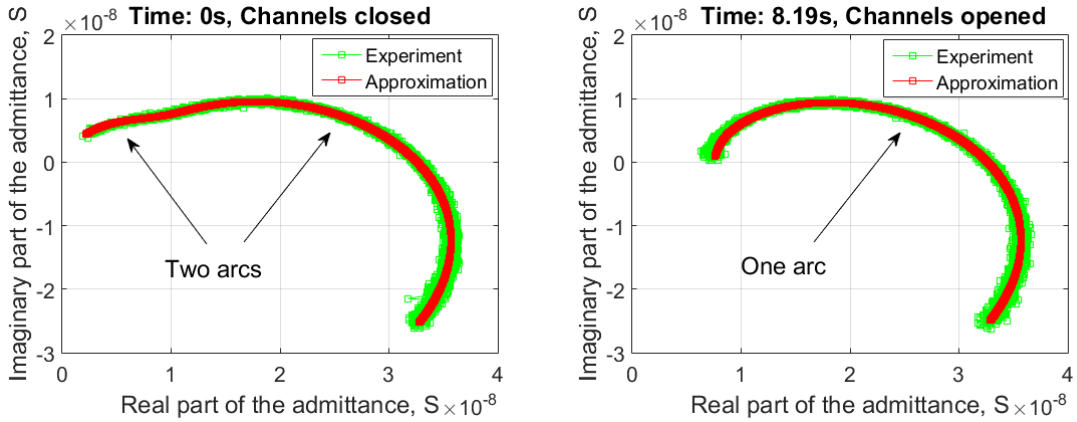

(a) (b)

Figure 1. The Nyquist plots of the CHO cells with closed channels (a) and opened channels (b). The green squares are denoted experimental data, and red line corresponds to double RC-circuit admittance for panel (a), and to single RC-circuit admittance for panel (b).

3. Results and Conclusion

The obtained results are presented in Fig. 1. One can see that in the case of the closed channels [Fig. 1(a), pH 7.4] the two arcs on the Nyquist plot are observed. Such a picture is typical for a system with two parallel RC-circuits. Contrary, on the plot Fig. 1(b) (pH 4.5), which correspond to open channels case, only one arc can be found, thus only one RC-circuit is needed to describe the spectrum. These effects allow us to consider a cell membrane as a two-phase structure – the pH-independent one, associated with the lipid bilayer, and pH-dependent one, related to ion channels. Furthermore, contrary to the standard patch-clamp technique, PCIS can discern both these phases. This result opens a direct path for the simultaneous measurement of the different cell membrane electrical characteristics. Therefore, it can provide a solution for actual cytology and biophysics problems.

Acknowledgements

Authors acknowledge V.E. Akulov, M.N. Ryazantsev, N.A. Verlov, D.B. Tikhonov, and M.V. Dubina for interesting discussions and support.

References

[1] Nicholls J G, Martin A R, Wallace B G and Fuchs P A 2001 *From neuron to brain* vol 271 (Sinauer Associates Sunderland, MA)

[2] Macdonald J R and Barsoukov E 2005 *History* **1** 1–13

[3] Matsumura R, Yamamoto H, Hayakawa T, Katsurabayashi S, Niwano M and Hirano-Iwata A 2018 *Scientific reports* **8** 1–10

Technology of gas thermal synthesis of thin-film ultrafine oxide structures with modifying components based on TiO_2, ZrO_2

I. Rodionov[1], V. Proskuryakov[1], I. Perinskaya [1], L. Kuts [1]
[1]Yuri Gagarin State Technical University of Saratov, Saratov 410054, Russia

Abstract.
A new highly efficient method for gas-thermal oxidation of VT6 bioinert titanium alloy with a dosed feed of TiO_2 / ZrO_2 ultrafine particles into the treatment zone has been developed. A physical model for the formation of thin-film oxide heterostructures modified with TiO_2 / ZrO_2 powders has been developed. A set of physicomechanical properties and surface characteristics of oxidized titanium samples was experimentally studied. Electron microscopic studies and microhardness measurements of the synthesized film coatings were performed. A high-tech electric furnace device has been developed for implementing the process of gas thermal oxidation with the simultaneous dosed supply of small-sized powder materials into the working chamber of the furnace.

1. Introduction

Thin-film oxide coatings of intraosseous implants, created by electrochemical and gas-thermal oxidation, protect the metal base from the corrosive effects of body fluids (blood, lymph, tissue fluid). Oxidized implants do not cause prolonged allergic reactions of the body and do not have a toxicological effect on the surrounding biostructures [1, 2]. This refers to the main indicators of biocompatibility of implantable structures.

High strength of fixation of oxidized implants in the bone is ensured by the creation of oxide coatings with the ability to effectively physico-mechanical adhesion to the surrounding biological tissue. This ability is due to the presence of pronounced roughness and morphological heterogeneity in the coatings. The structurally heterogeneous, microporous surface of the coatings provides better contact bone growth with more intense tissue reactions compared to a surface having a smooth, uniform microrelief. Therefore, the developed oxidized surface contributes, firstly, to the active growth of bone cell structures in the pores and depressions of the oxide layer with the course of the implant bio-integration, and secondly, to directed bone regeneration and accelerated osteogenesis.

2. Methodology

Samples for the preparation of thin-film oxide coatings were rectangular plates with a working surface area of 2 cm^2 and a thickness of 2 mm. Samples were made from bioinert titanium alloy VT6. The surface of the plates was sandblasted with Al_2O_3 corundum abrasive particles with a dispersion of 250 μm at a pressure of an air-abrasive jet of 0.67 MPa for 30 seconds to create the initial microroughness. After preliminary sandblasting, the samples were ultrasonically cleaned in an alcoholic washing solution at a frequency of ultrasonic vibrations of 22 kHz for 3 minutes to remove any greasy contaminants. Then, on the surface of titanium samples, a thin-film oxide coating was synthesized by gas thermal oxidation in an electric furnace with an air atmosphere. The oxidation mode provided for thermal modification of the surface at furnace temperatures of 400 and 450 °C with a holding time of 1.0 and 1.5 hours at each temperature. In the process of oxidation, nanosized and ultrafine powders of biocompatible and corrosion-resistant oxides were metered into the furnace. In the first experiment, TiO_2 oxide particles with a dispersion of the order of 25 nm were supplied. In the second experiment, ZrO_2 oxide powder with a dispersion of 20–30 μm was dosed. After gas thermal synthesis of thin-film ultrafine films with distributed TiO_2 or ZrO_2 particles, the surface of the modified titanium plates was

studied by scanning electron microscopy, profilometry, X-ray phase analysis, and microhardness and thickness measurements.

3. Results

A physical model has been developed for the structure formation of thin-film oxide coatings under the conditions of the reaction interaction of titanium samples with an oxygen-containing medium and during the spraying of oxide fine powders.

Powder material (TiO_2 or ZrO_2) is fed into the oxidation chamber through a metering device. Heated particles of the powder material are deposited and fixed on the thermally activated surface of the samples due to thermal diffusion processes. As a result, the oxidizable surface is modified and acquires enhanced physical and mechanical characteristics and protective properties. The thickness of such composite structures is 4-30 μm.

Modification of oxide coatings by nano- and ultrafine particles of TiO_2 / ZrO_2 during coating formation leads to the formation of oxide heterostructures (composites) with a matrix microstructure and a filler of nanoparticles of a powder material. Using the developed method, it is possible to simultaneously supply an oxidizing gas medium and powder materials. This makes it possible to obtain multifunctional metal oxide coatings in various reaction media (air atmosphere, superheated water vapor, argon-oxygen mixtures). The coatings created are characterized by a certain heterogeneity of the structure, the dimension of the elements of which is in the ultrafine and nanoscale ranges. It has been experimentally established that coatings with distributed particles of TiO_2 / ZrO_2 modifying powder can significantly increase the biological compatibility of the surface of titanium intraosseous implants.

4. Conclusions

A new method for the synthesis of thin-film heterostructured oxide systems based on VT6 medical titanium alloy has been developed, which provides for thermal oxidation in air with a dosed supply of ultrafine TiO_2 / ZrO_2 powders. Specialized electric furnace equipment has been created for gas thermal oxidation of titanium medical implants with the possibility of dosed supply of modifying powder materials into the furnace.

5. Acknowledgments

The studies were carried out in the framework of the RFBR grant (competition for the best fundamental research projects carried out by young scientists studying in graduate school - “Postgraduates”), project No. 19-33-90101.

6. References

1. Rodionov I.V. 2012 Biomedical Engineering **46 (2)** 58-61.
2. Rodionov I.V., Kuts L.E., Perinskaya I.V. 2017 AER **133** 665-670.

Development of a complex hyaluronan-nanoemulsion carrier for transdermal SPION delivery.

V S Fedorov[1], **N A Agadzhanian**[1]
[1]Saint-Petersburg State Institute of Technology (Technological University), Saint-Petersburg, Moscow Ave 26

Abstract. Stable biocompatible nanosuspensions of superparamagnetic iron oxide particles (SPIONs) for theranostics were prepared according to two laboratory technologies. SPIONs were synthesized by coprepicitation of Fe+2, Fe+3 solutions in alkaline nanoemulsion media. Hyaluronic acid coating was used for enveloping SPIONs for delivery through epidermis. Ternary system of oil, water and surfactant with addition of some amounts of hyaluronic acid was used as base for the transdermal delivery. The hyaluronic administration into magnetic nanosuspensions stimulates the formation of stable emulgel structure. The SPIONs can be focused via magnetic field through tissue and monitored by MRI and MPI methods.

1. Introduction

Biocompatible superparamagnetic iron oxide nanoparticles (which are referred to as SPIONs) with proper surface architecture and conjugated targeting ligands/proteins have attracted a great deal of attention for MRI and drug delivery applications. However, in order to effectively use SPIONs, one has to develop a biocompatible capsule that can take the particles through the patient's body to wherever the target is. Magnetic nanoparticles need to be stabilized to prevent sedimentation, aggregation and possible negative response from the body. It would be ideal to synthesize a stable suspension with micelles, which contain SPIONs. Different approaches of stabilizing metal nanoparticles in emulsions were proved to be efficient. For example, when using an inverted microemulsion there would be no aggregation due to sufficient particle repulsion. The mobility of the molecular layer around the particles can be manipulated by choosing the correct surfactant. By picking the emulsion as media there will be a great variety of reagents to achieve needed biocompatibility and other characteristics. In general, SPIONs are recognized by the innate immune system and can be cleared by mononuclear phagocyte systems. Some nanocarriers undergo rapid clearance due to activation of the complement immune system. The formation of hydrophilic polymer coat around nanoparticle reduces the destruction of SPIONs in tissue and bloodstream. Hyaluronic acid and its salts don't trigger such intense immune response and can be used as a defense shell of SPIONs. In this case the acid is used to achieve better biocompatibility

and SPION delivery. It is known to affect the permeability of the skin, and also is biodegradable. The goal of this work was to synthesize stable and biocompatible systems including superparamagnetic iron oxide particles (SPIONs) for theranostic uses.

2. Experimental methods.

Two methods of SPION synthesis were chosen. The first one is based on Massart methodic: magnetite is formed in water media by combining a mixed solution of Iron (II) sulfate and Iron (III) chloride (1:2 molar ratio) with ammonium hydroxide in a closed reactor under 80°C and inert N_2 atmosphere. The resulting particles were then rinsed, pulse-sonicated with 22 KHz ultrasound and dialyzed. Those treatments ensure particle low particle size dispersion and purity of their suspension. Then, the suspension of nanoparticles in water was combined with the solution of nonionic Tween-80 surfactant in non-polar media and 2% water solution of modified hyaluronic acid and pulse-sonicated again. For this work, several oil media were chosen based on their toxicity and micelle formation: mineral oil, peach oil and tridecane. Modified hyaluronic acid was prepared by mixing sodium hyaluronate (NaHA, 200-400 kDa) with NHS and EDC regents in water under magnetic stirring, and then adding this mixture to the GMS (glyceride monostearate) gel (dry GMS heated with low amounts of water). Second method was based on using nanoemulsion micelles as a reactor for magnetite forming. For synthesis purposes, several solutions were prepared: a 25% solution of surfactant in the iron salts mixture, in ammonium hydroxide solution and in 2% modified HA. Then, the solution containing iron was mixed in oil media (1:4 ratio) to form inverted micelles under stirring. Ammonium solution was added dropwise to the emulsion, which started to form micelles with magnetite. At last, the HA solution was added to coat micelles with modified HA.

3. Results and discussion.

The prepared nanoparticles were in superparamagnetic state as follows from the absence of appreciable magnetic hysteresis. Nanoemulsion samples were stable during two weeks. The presence of large magnetic moment was confirmed by measurement of magnetic relaxation of protons at resonance frequency 300 MHz. The nanoemulsion loaded by iron oxide nanoparticles can be considered a magnetic ferrofluid. Iron oxide nanoparticles shorten the spin-spin relaxation time from seconds to 1 ms and provides contrast of MRI images in a phantom study. Introduction of HA leads to a slight rise of viscosity and higher amounts of solubilized water. The mobility of the molecular layer was proved by magnetophoresis of the Fe_3O_4 nanoparticles under the influence of constant Nd magnet. In result, we have a stable biocompatible nanoemulsion loaded with superparamagnetic iron nanoparticles, which can be introduced transdermally and targeted via magnetic field.

References

[1] Seyed Mohammadali Dadfar, Karolin Roemhild, NataschaI.Drude et al/Advanced drug delivery reviews, 2019, 138, p 302-325
[2] G.S., Barcena C., Poudyal et al., / J. Am. Chem. Soc., 2007, 129, c. 7214-721
[3] Ming Kong, Xi Guang Chen et al / Carbohydrate Polymers, 2011

Revealing a possible sensor mechanism of DNA - based silver nanoclusters.

M.A Kapitonova[1], **Z.V. Reveguk**[1], **A.I. Kononov**[1].
[1]Department of Molecular Biophysics and Polymer Physics, Saint-Petersburg State University, 199034 St. Petersburg, Russia

Abstract. The mechanisms underlying the sensory activity of silver clusters synthesized on oligonucleotide matrices were not understood yet. It is known that close proximity of cytosine and guanine rich sequences causes color changes in the luminescence of clusters. We conducted spectroscopic and mass-spectrometry experiments and consider that this effect occurs due the cluster environment changes which causes structure rearrangement of the nanoclusters. Our results could be useful for further cluster based sensors development.

Introduction

Different molecules detection *in vitro* and *in vivo* is one of the challenges of modern science. As luminescent sensors, chemically synthesized dyes and quantum dots are often used. However, there remains a need for new types of sensors, especially those compatible with biological objects. More attention in the last decade has been paid to fluorescent silver nanoclusters. They have small sizes, high quantum yield and photo stability [1]. DNA serves as a good matrix for silver nanoclusters synthesis, in addition, it can bind to other molecules with high specificity [2]. One example of the development of sensors based on silver nanoclusters is the so-called g-enhancement. It is known that when a guanine-rich sequence is added to a cluster synthesized on a cytosine-rich DNA matrix, cluster luminescence is enhanced [3], but the mechanism of this phenomenon has not been fully studied. The aim of this work is to shed light at the enhancement mechanism for changing the photophysical properties of clusters.

Experiment

DNA strands were mixed with Ag^+ in Na-P buffer pH 6.6 then freshly prepared $NaBH_4$ were added to DNA/Ag^+ mixture. Final concentrations were 15uM G-rich/C-rich DNA, 90uM $AgNO_3$, 90uM $NaBH_4$, 20mM sodium phosphate buffer for g-enhancement experiment and 2.5uM DNA, 15uM $AgNO_3$, 7.5uM $NaBH_4$, 50mM sodium phosphate buffer for DNAx.1/DNAx.2 experiments. Absorbance spectra, luminescence spectra and mass spectra were recorded.

Sequences:
DNAx.1 5’-CCCCACCCC*TACCCACCATCACA-3’;
DNAx.2 5’-AGGAGTCCTTCTGA ** TCCCGTTTT-3’;
*: AAA - DNA4.1; AAAA - DNA2.1; AAACA – DNA0.1; ATGGCA – DNAstem.1;
**: AAA – DNA4.2; CAAA – DNA2.2; CCAAA – DNA0.2; CCCCAA – DNAstem.2.

Results and discussions

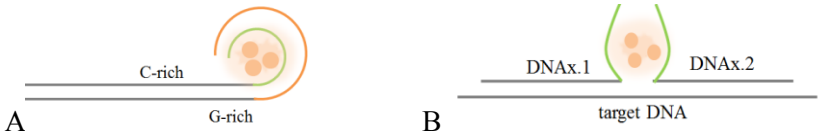

Figure 1. Schemes of DNA/AgNCs complexes: (A) – g-enhancement, (B) – split DNA sensor concept.

At first AgNCs was synthesized using C-rich sequence. After G-rich sequence addition, strong red fluorescence with emission at 630nm appeared. It reached maximum of luminescence intensity in 1h time and then started to decrease. For detailed study of the enhancement mechanism, the nanocluster was synthesized using a G-rich sequence, only after that c-rich was added, and a similar red fluorescence was observed. Thus, the red cluster is observed only in the presence of both strands, and it does not matter in what sequence mix them.

A similar phenomenon is observed with sequences DNAx.1/DNAx.2. The sequences based on split DNA technology [4], were varied. Among all these new developed sequences dna2.1 and dna2.2 are seemed to be optimal for emitting green fluorescent cluster formation in the presence of target molecule. The synthesis conditions: the buffer type, pH and ionic strength were varied. An absorption and luminescence spectra of DNA/Ag complexes were recorded and the fraction distribution of clusters was estimated. There were found clusters of several types: a green cluster with excitation/emission wavelength parameters – 490 nm/560 nm, an orange 560 nm/620 nm cluster and a red 610 nm/700 nm cluster.

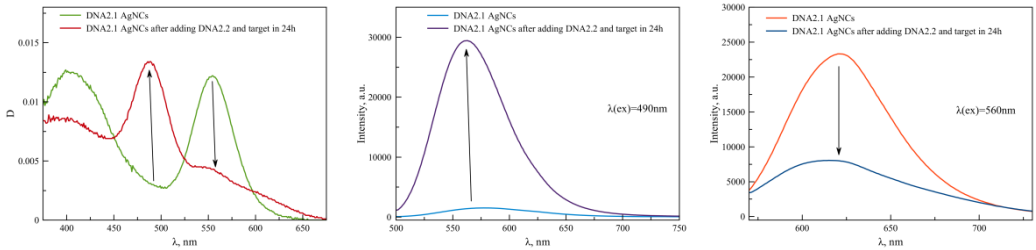

Figure 2. Absorption and luminescence spectra of DNA2.1 AgNCs before and after adding DNA2.2 and target sequences.

Conclusions

We assume that the phenomenon of g-enhancement and the formation of a bright green cluster 490/560nm on DNAx.1/DNAx.2 can be explained by the same mechanism - the rearrangement of the cluster atoms. The optimal conditions for this transformation are found. In the future, this phenomenon can be used as a sensor *in vitro* and *in vivo* for specific sequence of DNA or RNA.

References

[1] Zhiqin Yuan et al., Chem. Comm., 2014, 50(69).
[2] Yuxiang Chen et al., Acc. Chem. Res., 2018, 51, 11, 2756-2763.
[3] Hsin-Chih Yeh et al., Nano Lett., 2010, 10, 8, 3106-3110.
[4] Chen He et al., J. Phys. Chem. C, 2019, 123, 28, 17588-17597

Effect of Ca^{2+} and Mn^{2+} Ions on Formation of Structurally Ordered Nanoscale Complexes of DNA with Nuclear Proteins HMGB1 and H1

D Osinnikova[1], **E Chikhirzhina**[2], **A Polyanichko**[1,2]
[1] Faculty of physics, Saint Petersburg State University, Saint Petersburg 199034, Russia
[2] Institute of Cytology RAS, Saint-Petersburg 194064, Russia

Abstract. The structural organization of DNA in complex with linker histone H1 and non-histone chromosomal protein HMGB1 in presence of calcium and manganese ions have been studied using FTIR and UV circular dichroism spectroscopy. We have demonstrated that the presence of calcium ions leads to the formation of highly ordered DNA-H1-HMGB1 structures, while manganese ions decrease the order in the earlier reported nanoscale complexes.

1. Introduction

Chromatin of the eukaryotic cells comprises of DNA and variety of nuclear proteins. The most abundant nuclear proteins are linker histone H1 and non-histone chromosomal proteins HMGB1/2 **[1, 2]**. Both of these proteins interact with DNA and play critical role in the structural organization of the chromatin. HMGB1/2 proteins have structural functional motif – HMGB-domain, which is responsible for the interactions between HMGB and DNA. HMGB-domain demonstrated ability to form highly ordered complexes with DNA **[3]**. Although the particular role of HMGB proteins remains unclear, they were assigned mostly structural functions in chromatin. Earlier we have demonstrated that HMGB1 co-operate with histone H1 also forming structurally ordered complexes with linker DNA **[4]**. Here we investigate the effect of calcium and manganese ions on the formation and stability of the DNA-HMGB1-H1 complexes reported earlier using UV circular dichroism (CD) and Fourier-transformed infrared absorption spectroscopy (FTIR).

2. Results and Discussion

We have studied the conformational changes of DNA upon the interaction with non-histone chromatin proteins HMGB1 and H1 in presence of manganese and calcium ions. We have shown that the presence metal cations in the DNA-protein system leads to condensation of DNA molecule. The interaction of H1 and HMGB1 with DNA resulted in formation of supramolecular structures different from DNA-H1 and DNA-HMGB1 binary systems. Calcium ions interact with DNA-binding domain of HMGB1 and with phosphate groups of DNA screening their negative changes. Changes in the spectra of the DNA bases at 1693 cm-1 (thymine C2=O2) and 1643 cm-1 (cytosine C=O) show dominant interactions between DNA and HMGB1, which occur in the minor groove. Weaker interactions of the histone H1 in the major groove can also be detected as slight changes in intensities at 1678 cm-1 (guanine C=O) as well as those at 1590, 1572, and 1560 cm-1 (guanine C=N and C-

ND2). Protein binding is also accompanied by considerable DNA unwinding and bending, resulting in distortions in the mutual orientation of the bases. Changes in the sugar-phosphate backbone vibrations indicate intensive binding of the histone H1 with phosphate groups and changes in geometry of the sugar-phosphate backbone.

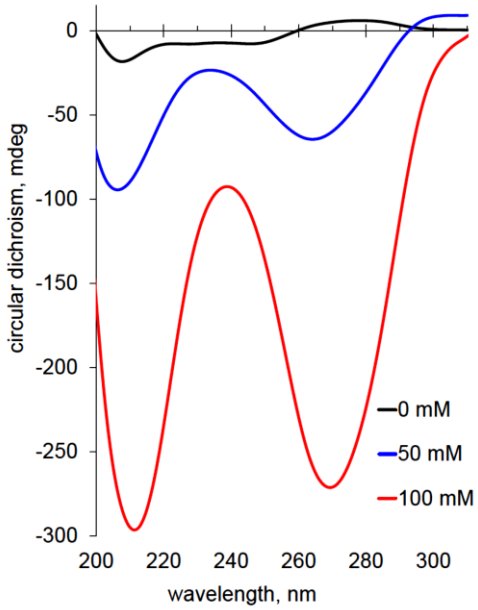

Figure 1. Circular dichroism spectra of DNA complexes with HMGB1 and histone H1 at different concentrations of $CaCl_2$.

The presence of H1 in the Ca^{2+}-containing system increases the affinity of HMGB1 to DNA resulting in 30-50 times higher circular dichroism of DNA in the complex, compared to its unbound state. Similar effect was observed earlier with another HMGB-domain protein, lacking negatively charged C-terminal regulatory fragment of HMGB1 **[3]**. Most likely, Ca^{2+} ions inactivate electrostatic repulsion of the negatively charged groups of DNA and the proteins. Manganese ions in contrast bind not only to phosphate groups of DNA but also to its nitrogen bases. This interplay leads to weakening of the DNA-protein interaction and disrupting the ordered DNA-protein complexes, described earlier **[4]**. At the same time we have observed strengthening DNA-condensation processes and increasing level of interactions between H1 and HMGB1 proteins. Thus, the presence of calcium ions leads to the formation of more ordered structures while manganese ions decrease the order in DNA-H1-HMGB1 complexes.

3. Acknowledgments
The authors acknowledge financial support from the Russian Foundation for Basic Research (RFBR) (grant 18-08-01500).

References
[1] Crane-Robinson C 2016 *Biochim Biophys Acta* **1859** 431
[2] Chikhirzhina E, Starkova T, Polyanichko A 2018 *Biophysics* **63** 858
[3] Polyanichko A, Chikhirzhina E, Skvortsov A, Kostyleva E, Colson P, Houssier C, Vorob'ev V 2002 *Journal of Biomolecular Structure and Dynamics*, **19** 1053
[4] Chikhirzhina E, Romanov N, Polyanichko A 2019 *Journal of Physics: Conference Series* **1410** 012083.

Multichamber hybrid microfluidic chips for nucleic acids detection by qPCR assay

P Afonicheva[1], A Zubik[1], A Bulyanitsa[1], G Rudnitskaya[1], A Evstrapov[1]
[1]Laboratory of Bio-&Chemosensors microsystems, Institute for Analytical instrumentation RAS, Saint Petersburg 190103, Russia

The efficiency of silicon-glass chips for the nucleic acids analysis with a concentration of 10^6-10^2 copies/µl using various algorithms of searching threshold cycles is shown. Hypotheses that explain the observed PCR efficiency decrease for microfluidic chips compared to polymer test tubes are discussed.

1. Introduction

In developing automated systems for the nucleic acids analysis the special attention is paid to systems that provide all stages of nucleic acids extraction from samples with their subsequent analysis by amplification methods [1, 2]. Polypropylene tubes (volume of 25 µl) and microfluidic chips made of different materials, such as silicon or silicon-glass, are commonly used for these purposes [3, 4]. Although such chips are more expensive than polymer ones they exhibit higher thermal conductivity, which is technologically favorable. However, the untreated silicon surface can inhibit the reaction. This can be prevented with various options of protective coating formation by modifying the surface, for example, inorganic layers (silicon oxide) or organic layers (silanizing agents, etc.) [5, 6]. The oxide films deposition is a standard procedure for the microelectronic industry, which is suitable for mass production conditions. Since the literature provides controversial information about the results of PCR in microfluidic chips made of silicon-glass materials we focused on the comparison between the results obtained for hybrid microchips and standard polypropylene test tubes.

2. Materials and reagents

Silicon-glass microfluidic chips with five reaction chambers of 250 µm deep and about 25 µl in volume were manufactured by JSC "Svetlana-electronpribor" (Saint Petersburg, Russia). The system was tested using a kit of reagents to detect the pathogen of potato ring rot «Clavibacter michiganensis subsp. sepedonicus-RT» (cat. No. RN-001, Syntol, Russia) by real-time PCR. Bovine serum albumin (BSA) was added to the reaction mixture at the concentration of 3 µg/µl. A synthetic fragment of DNA *Clavibacter michiganensis subsp. sepedonicus (C.m.s.)* was used as a target. A series of consecutive ten-fold dilutions of the fragment from 10^6 to 10^2 copies/µl were prepared. To prevent evaporation the reaction chamber holes were filled with mineral oil and sealed with adhesive tape. PCR was performed on devices developed at the IAI RAS: in micro-tubes on ANK-32 and in microfluidic chips on the prototype device for microchips. The thermal cycling program was set according to the recommendations of the reagent kit manufacturer. The results were recorded on two FAM and R6G (HEX) fluorescence channels in real time. The threshold cycle was determined in two ways: 1) using the instrument software; 2) by direct comparison of graphs [7].

3. Results

To analyze data we determined the position of the threshold cycle based on finding the inflection point of the amplification curve. Naturally, the threshold cycle value determined by different methods appears to be different. Figure 1 shows the calibration dependences of the threshold cycle on the logarithm of the DNA fragments concentration during PCR in test tubes and microfluidic chip.

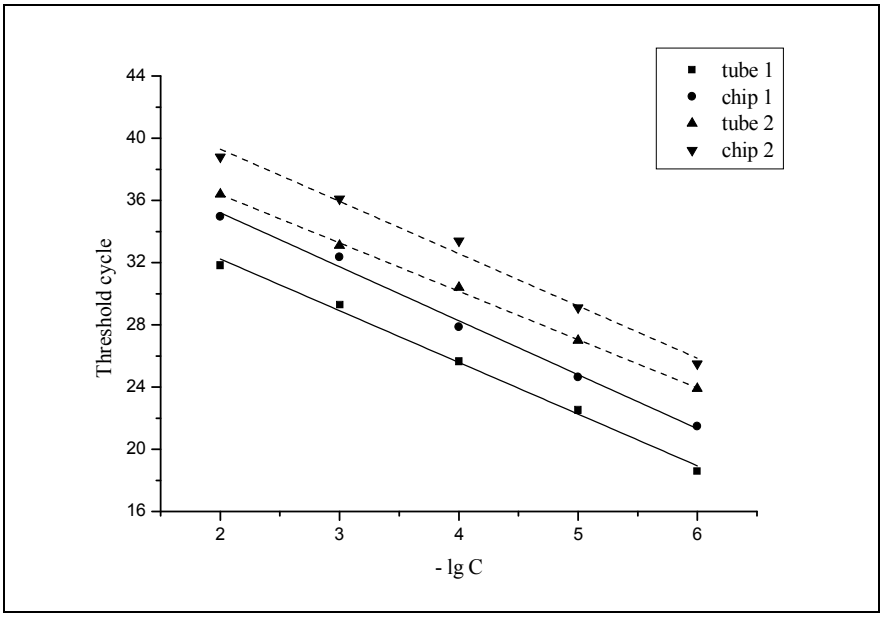

Figure 1. Calibration dependencies obtained during PCR in test tubes and on a microfluidic chip: 1 – software determination of the threshold cycle (solid); 2 – calculated determination of the threshold cycle using the maximum derivative method (dashed)

The obtained results have led us to the following conclusions:

- In all considered cases the error in determining the threshold cycle at concentrations (10^5 and 10^6 copies/μl) lies from a few hundredths to 0.15 of the cycle.
- We revealed a shift in the position of the threshold cycle for chips compared to the test tubes. The shift is estimated as 1.6 – 2.2 cycles at high concentrations and more than 3 cycles at low concentrations. Assuming that the average reaction efficiency for ANK is ~ 100% we get the reduction in efficiency down to 87 – 92 % for the chip.

We suggest that the methods of static (silicon oxide) and dynamic (BSA) modification do not fully compensate the influence of the material on the processes during the reaction. In particular, the ratio of the surface area to the volume in the test tube or the chip differs by more than 5 times. Therefore the role of the surface effects during amplification in the chip is significantly more important, thus it can lead to the reaction inhibition processes. Moreover, it is known that the activity of the Taq DNA polymerase enzyme decreases with overheating [8], thus the efficiency of the reaction with the same thermal cycling program can be also affected due to the difference in the thermal conductivity of polypropylene and silicon with a comparable thickness of the heated layer. Therefore, it is necessary to optimize the thermal cycling program for hybrid chips.

4. Acknowledgments

The research was carried out within the state assignment of Ministry of Science and Higher Education of the Russian Federation (theme No. 075-01073-20-00)

References

[1] Ahrberg C, Manz A, Chung B 2016 *Lab Chip* **16** 3866
[2] Ahmad F, Hashsham S A 2012 *Analytica Chimica Acta* **733** 1
[3] Northrup M, Ching M, White R, Watson R 1993 Int. Conf. on Solid State Sensors and Actuators (Yokohama) vol A43 (New York: IEEE) p 926
[4] Shoffner M, Cheng J, Hvichia G, Kricka L, Wilding P 1996 *Nucleic Acids Res* **24** 375
[5] TaylorT, Winn-DeenE, PicozzaE, WoudenbergT, AlbinM 1997 *Nucleic Acids Res* **25** 3164
[6] Zhang C, Xu J, Ma W, Zheng W 2006 *Biotechnol Adv* **24** 243
[7] Rebrikov D, Samatov G, Trofimov D, Semenov P, Savilova A 2014 Real-Time PCR (Moscow: BINOM) p 223
[8] Lawyer F, Stoffel S, Saiki R, Chang S, Landre P, Abramson R, Gelfand D 1993 *Genome Res* **2** 275

The effect of protein environment on the quantum yield of retinal isomerization in rhodopsins.

V.N. Mironov[1], M.N.Ryazantsev[2], A.A. Shtyrov[2]

[1]Saint-Petersburg State University, Institute of Chemistry, St. Petersburg, Russia
[2]Saint-Petersburg National Research Academic University of the Russian Academy of Sciences, Saint Petersburg, Russia

Corresponding author: vova_mironov_97@mail.ru

Abstract. The isomerization of the retinal protonated Schiff base is the primary event in the photoactivation of visual rhodopsins. This photoactivated isomerization demonstrates a very high quantum yield, about 67%, and occurs on a sub-picosecond timescale. It was proposed that the high value of the isomerization quantum yield is provided both by the protein environment and by the specific modes driving the retinal isomerization, such as hydrogen-out-of-plane motion. In this study, we considered both factors in detail. We demonstrated that the enhancement of the quantum yield occurs in the presence of a negative charge in the vicinity of the NH region of the retinal protonated Schiff base. Also, we derived the new mode of retinal isomerization that can also lead to the enhancement of the quantum yield.

Introduction

Rhodopsins are membrane proteins found in almost all living organisms. They perform many different functions, such as proton pumps in archaea (responsible for proton transfer through the membrane), and animals' vision. Upon photoactivation of rhodopsins, the photoactivated isomerization of the retinal protonated Schiff base, which is the chromophore of rhodopsins, occurs. This isomerization converts the chromophore from the 11-cis conformation to the all-trans conformation (in visual rhodopsins) and from all-trans conformation to 13-cis conformation (in microbial rhodopsins). It was demonstrated both theoretically and experimentally that this isomerization has a very high quantum yield (about 67 %), much higher than observed experimentally for retinal protonated Schiff base in a solvent. In theoretical studies it was shown that two factors are involved in the efficient isomerization: the electrostatic field of the protein environment and the specific modes driving the isomerization [1].

The electrostatic field is formed by the charges of amino acids. Thus, the largest effect on the isomerization efficiency is provided by the charges that are the closest to the chromophore. In rhodopsins, these are the negatively charged glutamic or aspartic acids located in the vicinity of NH chromophore moiety, the so-called counterion residues. For this reason, we decided to investigate the effect of these residues on the isomerization quantum yield.

In previous studies, it is proposed that the isomerization of a retinal chromophore is provided by three modes: the rotation of the reactive bond, the hydrogen-out-of-plane (HOOP) mode and the bond length alteration, which is provided by synchronized contraction of single bonds and elongation of the double bonds in the backbone of the chromophore. Among them, the HOOP mode was shown to enhance the isomerization rate. We analyzed the isomerization trajectories of the retinal chromophore and derived the fourth mode driving the isomerization. It was assumed that the excitation of this fourth mode can lead to the enhancement of the isomerization quantum yield.

1. Physical and mathematic model

To show the influence of the electrostatic field on the isomerization quantum yield the simulation of molecular dynamics trajectories of the retinal protonated Schiff base in the excited state was carried out.

In this case we used the trajectory surface hopping method (TSH) [2], where the wavepacket of molecular vibrations is modelled by a set of independent trajectories. Each trajectory is in the specific state i, the ensemble of trajectories corresponds to the population of the state $a_i{}^2$. The trajectory can jump from one state to another (surface hopping). The Born-Oppenheimer approximation was used, i.e. the nuclei were described by classical molecular mechanics, and electrons by quantum mechanics. To derive the normal modes that are responsible for the retinal isomerisaton, we performed the analysis of energy exchange between normal modes and the phases of modes at the time of isomerization. Energy exchange was characterized by a covariance matrix $COV = EE^T$.
To determine the degree of coupling between the mode and isomerization, the oscillation phases statistics was collected.

2. Numerical modelling

The SHARC software package [3] was used for the molecular dynamics. The BAGEL program [4] was used for quantum calculations of energy and analytical gradients at the caspt2 (6.6) level. 150 trajectories were generated for the chromophore with and without charge. For results processing (quantum yield calculation, decomposition of isomerization into normal modes, normal modes analysis and PCA analysis) home-built scripts were used. All calculations were carried out on the server of Moscow State University.

3. Results

We demonstrated that the increase of the quantum yield value (from 31% to 41%) occurs in the presence of the negative charge (counter-ion) in the vicinity of the NH retinal protonated Schiff base moiety (Table 1).

Conformation	charge, e	number of hops	2-cis	2-trans	3-trans	QY
trans	0.0	71	23	39	9	0.31
trans	-0.4	69	28	39	2	0.41
trans	-0.6	65	28	36	1	0.44
cis	0.0	87	23	64	-	0.73

Table 1. Quantum yield.

A group of normal vibrations was selected that satisfies the criterion of phase matching and weakly exchanging energy: modes 21 (873.5 cm^{-1}), 28 (1071.3 cm^{-1}), 31 (1266.8 cm^{-1}). While mode 21 is a part of HOOP, mode 28 is not a component of HOOP or stretching mode. Thus, our assumption is that if we excite these modes in certain phases using special laser pulses, we can increase the quantum yield of isomerization.

REFERENCES

1. Microbial and Animal Rhodopsins: Structures, Functions, and Molecular Mechanisms. Oliver P. Ernst, David T. Lodowski, Marcus Elstner, Peter Hegemann, Leonid S. Brown, and Hideki Kandori.
2. Nonadiabatic dynamics with trajectory surface hopping method. Mario Barbatti (2011).
3. S. Mai, M. Richter, M. Heindl, M. F. S. J. Menger, A. Atkins, M. Ruckenbauer, F. Plasser, M. Oppel, P. Marquetand, L. González. SHARC2.0: Surface Hopping Including Arbitrary Couplings – Program Package for Non-Adiabatic Dynamics, sharc-md.org (2018).
4. BAGEL, Brilliantly Advanced General Electronic-structure Library, WIREs Comput. Mol. Sci 8, e1331 (2018). DOI: 10.1002/wcms.1331, Shiozaki Group.
5. The ultrafast photoisomerizations of rhodopsin and bathorhodopsin are modulated by bond length alternation and HOOP driven electronic effects. *J. Am. Chem. Soc.* 2011, 133, 10, 3354-3364

Fluorescent Ag-Nanoclusters for Evaluation of Serum Albumin and Immunoglobulin Concentrations in Protein Mixtures

A V Mizintsev, T S Sych, A M Polyanichko, L V Plotnikova, A I Kononov
Department of Molecular Biophysics and Polymer Physics, Physical faculty, Saint Petersburg state University, Saint-Petersburg, 199034, Russia

Abstract. In this work we have designed, synthesized and characterized luminescent metal nanoclusters (NC) on proteins (human serum albumin and immunoglobulins) We have demonstrated that the approach developed allows one to determine the concentrations of albumins and Ig in protein mixtures based on the luminescent properties of the NC.

1. Introduction

Immunoglobulins and serum albumin are two of the most abundant types of proteins in human blood. Albumin performs a transport function for a variety of substances in the blood stream. Among the different types of globulins, there is a group of proteins known as immunoglobulins, representing one of the key elements of the immune system. There are some types of immunoglobulins: IgG, IgA, IgM, IgE and IgD. IgG, also known as antibodies, comprise approximately 75% of all immunoglobulins in serum, while the rest 25% are mainly IgA and IgM. In case of some blood diseases, such as multiple myeloma, the concentration of Ig may increase significantly, which makes very important to have cheap and accurate approach for monitoring concentration of serum proteins.

The aim of this work is to develop a convenient, selective, cheap and very simple luminescent nano-sensor for albumin and immunoglobulin detection. We used silver nanoclusters (AgNCs) as luminescent bio-lables complexed with albumins and immunoglobulins. Being rather bright, having a large absorption cross-section and high quantum yield, the fluorescent AgNCs are excellent candidates for such biolabeling [1]. Earlier, AgNCs have been synthesized on peptides and various proteins including bovine serum albumin and nuclear proteins HMGB and H1 [2].

2. Obtained results

In this work we have synthesized AgNCs, stabilized by human serum albumin (HSA) and IgG matrices. It must be noted, that different matrices provided growth of clusters with different spectral properties. Thus, AgNCs stabilized by HSA emitted in red region of visible spectra (ca. ~1.85 eV), whereas IgG-stabilized AgNCs have emission maximum in near IR region (ca. ~1.6 eV). Spectra of luminescence excitation and emission of the obtained complexes are presented in Fig. 1.

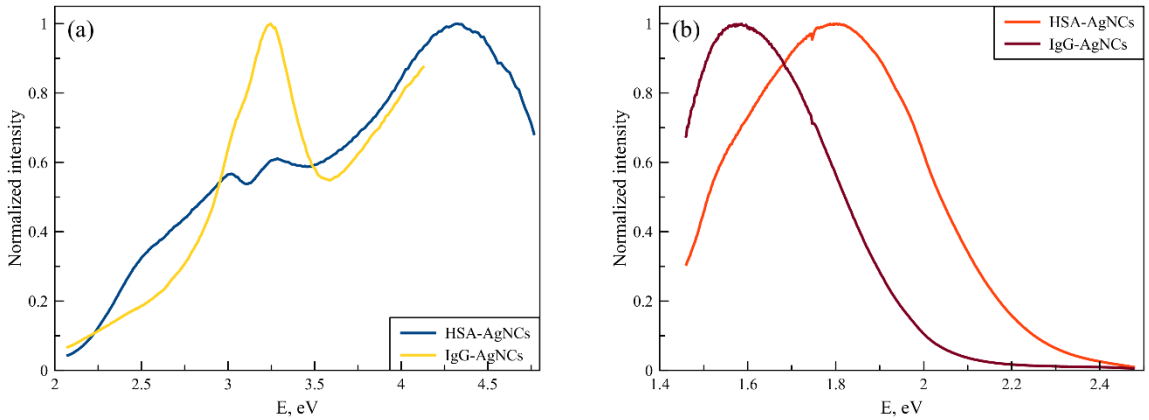

Figure 1(a, b). (a) Normalized excitation spectra of obtained complexes; **(b)** Normalized emission spectra of obtained complexes.

Based on our previous experience [3] we have optimized the synthetic procedure, which allow us to improve sensitivity and accuracy of this approach. We have demonstrated that the approach developed allows one to determine the concentrations of albumins and Ig in protein mixtures. We have analyzed absorption and luminescence spectra, as well as the contribution of each protein in the mixtures to emission spectra. Thus, the combination of all three approaches provides an accurate and reliable method to determine the concentrations of these proteins in their mixture.

Acknowledgments
The work is supported by RFBR project № 19-53-51005.

References

[1] Choi S, Dickson R M, Yu J 2012 *Chem. Soc. Rev.* **41** 1867-1891
[2] Sych T S, Reveguk Z V, Pomogaev V A, Buglak A A, Reveguk A A, Ramazanov R R, Romanov N M, Chikhirzhina E V, Polyanichko A M and Kononov A I 2018 *J. Phys. Chem. C* **122** 29549-29558
[3] Sych T S, Polyanichko A M, Plotnikova L V and Kononov A I 2019 *Anal. Methods* **11** 6153

Determination of the fear coefficient by pupillograms

O L Isaeva[1], M P Boronenko[1], W I Zelensky[1], E S Kiseleva[1]
[1]Oil and Gas Institute, Yugra State University, Khanty-Mansiysk, 628012, Russia

Abstract. Currently, various mathematical models of pupillograms are used to process the results of pupillometric studies. There are also mathematical models of emotions. At the moment, research does'nt combine modeling of pupillograms and modeling of emotions. In our work, an attempt was made to determine the fear coefficient by pupillograms. For research, an optoelectronic installation has been developed. As an example, we give an example of the analysis of pupillograms of people of an older age category. A mathematical model of the pupillogram plot is obtained, obtained in response to fear emotion.

1.Introduction

It is known that the size of the pupils depends on the size of the emotions experienced. However, the existing mathematical models of pupillograms mainly describe the reaction of the pupil to light. Therefore, the search for a mathematical model that describes the pupillary reaction due to emotion is relevant. At the moment, research does'nt combine modeling of pupillograms and modeling of emotions. In our work, an attempt was made to determine the fear coefficient by pupillograms. The purpose of our study: based on experimental data, determine the fear coefficient by pupillograms.

2.Experimental part

The research is based on the dependence of the size of the pupils on the emotions experienced. Information that is significant for a person causes involuntary attention if an individual appears in the field of perception. Before the experiment, a survey was conducted to determine the topic of interest to the subjects. By agreement with the participants, test objects containing the emotion "fear" were selected. For research, an optoelectronic installation was assembled. The components of the optoelectronic installation are shown in Figure 1 (a). A person wearing a helmet is located at a distance at which the change in the illumination of the surface of the eye due to the glow of the monitor becomes insignificant.

a

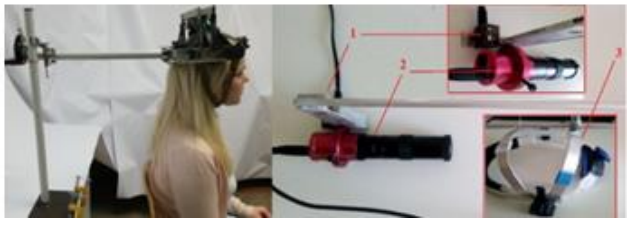

b

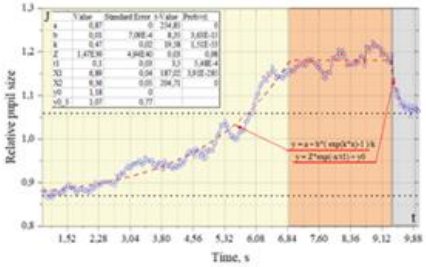

Figure 1 (a, b). (a) Optoelectronic pupil size registration system: 1 - a camera that registers the image of the monitor on which video files were displayed; 2 - a camera recording the size of the pupil; 3 - helmet, creating a rigid coordinate connection with the head; **(b)** Pupillogram-curve of the intensity of emotional experience

As an example, we give an example of the analysis of pupillograms of people of the older age category (50-75 years), in which representatives of different sexes were present. In total, more than 100 people took part in the experiment, including full-time and part-time students. All participants in the experiment were volunteers, and were warned of a possible emotional experience. Basically, all participants have hyperopia, one woman has myopia corrected by glasses. To evoke emotion, we used a video about accidents that were freely available on the Internet.

3.Discussion and main results

The average value of the level of intensity of emotions was considered a normal reaction, since the hypothesis was that most people are mentally balanced and tolerant. Since the size of the pupils depends on the emotions being tested, their intensity can be estimated from the pupillogram. The pupillogram-curve of the intensity of emotional experience is presented in Figure 1 (b). In a time interval of 0-6.84 sec, an increase in the intensity of emotional experience occurs, in a time interval of 6.84-9.5 sec, an emotion saturates, its peak is visible, then the emotion fades [1]. From theory [1], at any time t, the fear coefficient is defined as

$$f(t) = \frac{A}{Q-\frac{I_0}{k}(1-e^{-kt})} = \frac{A}{Q-\frac{I_0}{k}(1-\frac{1}{e^{kt}})} = \frac{A}{Q-\frac{I_0}{k}\left(\frac{e^{kt}-1}{e^{kt}}\right)} \quad (1)$$

From the experiment, a function describing the process of increasing emotion k = -k:

$$F(t) = a - \frac{b}{k}\left(\frac{e^{kt}-1}{e^{kt}}\right) \quad (2)$$

Suppose that the change in the size of the pupil is due to information entering the brain from test objects. Then the intensity of the emotions experienced depends on the coefficient of fear [1]:

$$f(t) = \frac{1}{a-\frac{b}{k}\left(\frac{e^{kt}-1}{e^{kt}}\right)} = \frac{1}{F(t)} \quad (3)$$

Using the attention track, you can determine on which element of the presented test object the reaction occurred. Also, using the track, you can determine that the reaction did not occur to the test object. Emotions should be adequate, that is, average. Any deviation from the norm requires close attention and study. With this, the resulting fear coefficient can help. Proper selection of test objects will expand the capabilities of eye-tracking, as well as improve existing security systems that use artificial intelligence and emotion recognition.

4.Conclusions

A mathematical model of the pupillogram plot is obtained, obtained in response to fear emotion. By the method of equivalent transformations over analytical expressions, the theoretical and experimental functions were converted to a form convenient for comparison. A comparison of the theoretical fear coefficient and the plot of pupillograms constructed on the basis of experimental data showed their syntactic similarity. This allowed us to find the coefficient of fear.

Acknowledgments

The study was carried out with the financial support of the Russian Foundation for Basic Research in the framework of the research project 18-47-860018 p_a

References

[1] Kartvelishvili V M, Lebedyuk E A 2016. Incentives and a mathematical model of the mutual influence of emotions of economic entities // Bulletin of the Russian University of Economics GV Plekhanov. **4 (88)** 113-125

The adaptation of cell-substrate impedance sensing technique for suspension cell lines

A A Abelit,[1,2] D D Stupin[1]

[1]St. Petersburg Academic University, Khlopina 8/3, 194021 St. Petersburg, Russia
[2]Peter the Great St.Petersburg Polytechnic University, Polytechnicheskaya Street, 29, Saint-Petersburg, 195251, Russia

E-mail: anna.abelit@gmail.com, Stu87@ya.ru

Abstract. In this paper, we present modification of the electrical cell-substrate impedance sensing technology which make it applicable for suspension cells and cells with poor adhesion. The key idea of the proposed technique consist in coating electrodes with poly-DL-lysine. We have show that this procedure not only provide negligible influence on the electrode impedance, but also allows to study viability of the suspensions cells k562 in real time.

1. Introduction

Electric impedance spectroscopy (EIS) is a perspective experimental technique that is widely used in experimental biophysics, biosensorics, and medicine [1, 2, 3]. One of the quickstepping area in this field is the development of impedance-based cytosensors [3] — hybrid biodetectors based on the EIS technique. The IS of the electrode covered by cells strongly depends on various factors, such as the morphology of the cells, the degree of coverage of the electrode with cells, their viability, etc. (Giæver-Keese model [4]), therefore, its temporary evolution allows us to assess the state of cells. Up to date, several commercially available impedance cytosensors have been developed, *e.g.* ECIS from Applied Biophysics and xCelligence from ACEA Bioscience. These sensors can be applied to solving different biophysical problems. For example, ECIS-based glucose sensors, toxin sensors [5], and sensors of UV irradiation [6] have been developed. However, despite large progress in this field, the currently available cytosensors have several disadvantages. Particularly, they cannot work with suspension cells and poorly adherent cells. Thus, the aim of this work was to develop and test the EIS-based cytosensors for this type of cells.

2. Material and Methods

For solving the problem of the poor adhesion, we propose to use the poly-DL-lysine coating of the electrodes. This surface preparation does not dramatically change the impedance of the electrodes and at the same time provides good cells capturing on them. For testing this technique we have provided biosensorics experiment, in which we studied the temporal dynamics of the impedance of the treated by poly-DL-lysine and covered by k562 cells electrode under UV radiation. Cells were obtained from the Bank of Cell Culture Institute of Cytology RAS. Cultivation was carried out at 37° C and 5% CO_2. The impedance spectra of the electrodes

were measured using an EIS based on adaptive filtering [7]. A measurement setup diagram is also provided in [7].

3. Results and Conclusion

The obtained results are shown on Fig. 1. On can see, that cells death under UV radiation dramatically affect on the impedance of the covered by them electrode: at beginning the impedance is rising, then it reach the maxima, and finally it fails down to the level of the control electrode. The first two effects are connected with apearence of the UV induced blebs on the cell membrane, and the final phenomena is connected with membrane distortion under UV radiation.

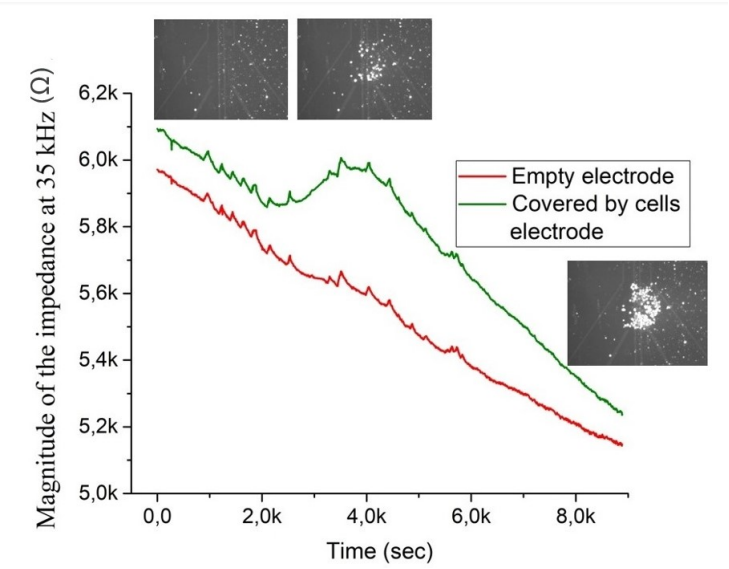

Figure 1. Time evolution of the impedance at 35 kHz.

Thus, the obtained results indicate that the coverage of multielectrodes with poly-DL-lysine allows us to use EIS for studying poorly adherent cells and the suspension cultures. This modification gradually increases the area of bio-EIS applications and paving the way for creating fundamentally new types of cytosensors.

Acknowledgements

The authors acknowledge M.I. Blinova, A.A. Kornev, and M.V. Dubina for comprehensive assistance and support.

References

[1] Barsoukov E and Macdonald J R 2005 *Impedance Spectroscopy: Theory Experiment and Applications* 2nd ed (Wiley-Interscience)

[2] Grimnes S and Martinsen O G 2015 *Bioimpedance and bioelectricity basics* 3rd ed (Academic Press, , Elsevier Ltd)

[3] Ping Wang Q L 2009 *Cell-Based Biosensors: Principles and Applications (Engineering in Medicine & Biology)* 1st ed

[4] Wegener J, Keese C R and Giaever I 2000 *Experimental cell research* **259** 158–166

[5] Stupin D 2017 *Journal of Physics Conference Series* vol 917

[6] Stupin D D 2018 *Semiconductors* **52** 600–601

[7] Stupin D D, Koniakhin S V, Verlov N A and Dubina M V 2017 *Phys. Rev. Applied* **7**(5) 054024

Multimodal approach to reveal the effect of light irradiation on chemical composition of lipofuscin granules of human RPE tissues

A A Gulin[1], A V Aybush[1], A A Vasin[1], A E Dontsov[2], M A Ostrovsky[2]
[1]N.N. Semenov Federal Research Center for Chemical Physics RAS, Moscow 119991, Russia
[2]Emanuel Institute of Biochemical Physics RAS, Moscow 119334, Russia

Abstract. The accumulation of lipofuscin (LF) in tissues is considered as one a hallmark of the aging process. Usually formed in yellow-brown pigment aggregates or granules primarily composed of lipid residues and proteins, the exact chemical composition of LF varies among tissues. LF of the retinal pigment epithelium (RPE) is known to contain byproducts of the visual cycle, including one of the fluorophores in LF bis-retinoid N-retinyl-N-retinylidene ethanolamine (A2E). The last is characterized by high photoreactivity and implicates in age-related macular degeneration. Photoinduced production of reactive oxygen intermediates (ROI) is shown among the main modes of A2E toxicity although particular photochemistry of A2E have yet to be completely identified. In this work we study changes in chemical composition of LF granules of human RPE under light (UV-VIS) irradiation using vibrational spectroscopy (femtosecond broadband CARS) and mass-spectrometry (TOF-SIMS) approach accompanied by measurements of luminescent properties of the LF.

1. Introduction

Lipofuscin (LF) is a result of incomplete lysosomal degradation and represents autofluorescent material of cellular lipids and protein residues, traces of carbohydrates and metals. LF is usually found as water insoluble micrometer-sized particles which cannot be further degraded by lysosomal enzymes or the proteasomes. Up to now, there is no any efficient way to remove LF from living organism. The accumulation of LF in RPE has been associated with the development of retinal diseases, particularly age-related macular degeneration [1]. The constituents of LF, especially A2E, have high photoreactivity leading to ROI and oxidized products (including water soluble ones) under light illumination [2]. Hence one can expect difference of chemical composition of LF samples before and after irradiation; moreover, high variance in this difference from one granule to another can be expected as well. In this work we study chemical profiles of large areas (containing thousands granules) of LP granules of human RPE tissues to deduce averaged effects of light irradiation.

2. Methods and materials

Experiments on tissue isolated from human-cadaver eyes were performed in compliance with officially accepted procedures [3]. Details on isolation of LP from the RPE of human eyes, centrifugation and purification described earlier [4]. Secondary ion mass spectra were collected with a TOF-SIMS 5 mass spectrometer (ION-TOF, Germany) [5]. Femtosecond broadband CARS microspectroscopy (BCARS) is represented as newly built module of the femtosecond laser complex in Semenov Federal Research Center for Chemical Physics [6]. Dried LF thin films were prepared both for TOF-SIMS and BCARS.

High performance characteristics of both methods allowed us to collect large amount (~10^5) of spectra over control and exposed samples to deal with natural sample heterogeneity. Broadband LED (400-760 nm, with band maximums at 450 nm 550 nm, respectively) was used for irradiation.

3. Results and discussion

Luminescence properties of LP samples are essentially dependent on LED irradiation exposure (Fig.1a). Particularly, only 450 nm band of the LED irradiation spectrum leads to the luminescence grow effect. Non-monotonous behavior on irradiation time can be seen for wavelength range ~540-560 nm (Fig.1a) and several bands of TOF-SIMS spectra (Fig.1b) which can be evidence on chemical transformations (including intermediates) in LP samples under the LED irradiation.

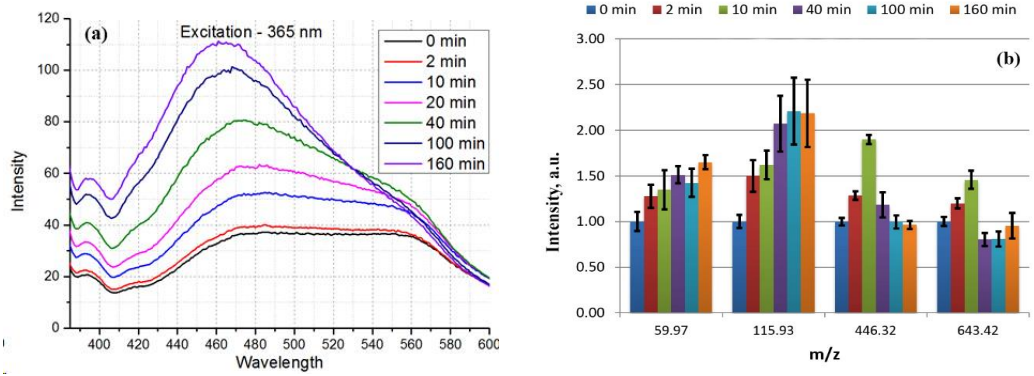

Figure 1. LP luminescence(a) and TOF-SIMS measurements for negative ions (b) for shown light exposure times.

BCARS approach allowed to measure vibrational (Raman) spectra of LP samples for wavelengths free of any LP luminescence. BCARS spectra were collected for fingerprint range ~800-1800 1/cm containing bands (shown in Fig. 2) of the most organic compounds. The bands responsible for lipid oxidation under UV light are aldehydes C=O bands of 1685, 1722 1/cm which can be related to appropriate unchanging bands 1650 1/cm or 1740 1/cm (the bands ratio of 1660/1740 does not change under UV light) [7]. It can be seen from Fig.2 the band ratios 1685/1650, 1685/1740, 1722/1650, 1722/1740 increased up to 40% representing high LP photoreactivity properties under UV light.

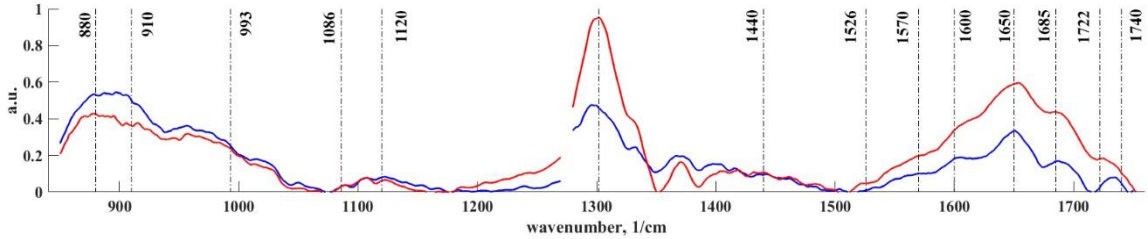

Figure 2. Averaged BCARS spectra (transformed to Raman bands) for control sample (blue curve) and after exposed sample (red curve).

4. Acknowledgments

This work was supported by RFBR (Projects No.18-33-00940, 18-03-01243).

References

[1] Shaw P, Stiles T, Douglas C, Ho D, Fan W, Du H, Xiao X., 2016 *AIMS Mol. Sci.* **3** 196
[2] Lamb L E, Simon J D., 2004, *Photochemistry and Photobiology*, **79** 127
[3] Feldman T B, Ostrovsky M A et al., 2015, *Anal Bioanal Chem*, **407**, 4, 1075
[4] Dontsov A E, Sakina N L, Ostrovsky M, 2012, *Rus. Chem. Bulletin, International Ed.*, **61** 2, 442
[5] Gulin A A, Shakhov A M, Nadtochenko V A et al, 2019 *Applied Surface Science,* **481** 144
[6] Nadtochenko V A, Denisov N N, Aybush A V, Cherepanov D A et al, 2017 *Nanomaterials*, **7**, 371
[7] Muik B.,,Lendl B. et al, 2005, *Chem. and Phys. of Lipids*, **134**, 2, 173

On the possibility of analysis using the wavelet transform of the pulse waveform from the bloodstream

R V Davydov[1,2]**, V Yu Rud**[3]
[1]Peter the Great St. Petersburg Polytechnic University, Saint Petersburg 195251, Russia
[2]Alferov University of the Russian Academy of Sciences, Saint Petersburg 194021, Russia
[3]All Russian Research Institute of Phytopathology, Moscow Region, 143050, Russia

Abstract. A method has been developed using wavelet transform to describe the dynamics of the pulse wave shape during the diagnosis of human health. The pulse wave signal, in contrast to the previously discussed diagnostics, is considered an unsteady signal, in which there may be no periodicity. We found that this method is useful for diagnosing the properties of arterial vessels of patients with coronary heart disease, arterial hypertension and other diseases. Pulse wave research results are presented.

1. Introduction

The blood movement in the vessels is based on the alternation between two processes: relaxation (diastole) and contraction (systole) of the ventricles of the heart. During diastole, the ventricles are filled with blood, and during systole of the ventricular myocardium, blood is expelled from the heart to the aorta and pulmonary artery under pressure [1, 2]. Blood enters the aorta, and it expands until it stops the flow of blood does not stop. The rhythmic contraction of the myocardium causes a contraction of the vascular wall, and the pulse wave propagates from the initial part of the aorta to the arterioles and capillaries. There are several methods used to register a pulse wave. Pulse oximetry (registration of a pulse wave using scattered or reflected laser radiation on blood vessels or veins), unlike others, has gained more extensive application both in clinical diagnostics and for the personal use of various groups of people [3].

For a quantitative analysis in a pulse wave using the method of "one hit". With its use, the position of the maxima and minima on the timeline and their characteristic amplitudes are determined. The shape of the pulse wave depends on the elasticity of the vessel wall, pulse rate, features of the heart and several factors that may be associated with a disease of human organs [1, 3]. The description of the pulse wave shape is often performed only for stationary processes using the Fourier transform. The experiments showed that the Fourier methods for non-stationary processes are challenging to apply. Therefore, we propose to use an algorithm based on the wavelet transform to analyze the pulse wave shape. It will allow developing a system of quantitative parameters for diagnosing the state of arterial vessels and the work of the human heart.

2. The method, results and discussion

Figure 1 shows pulse waves of two people with different health conditions as an example.

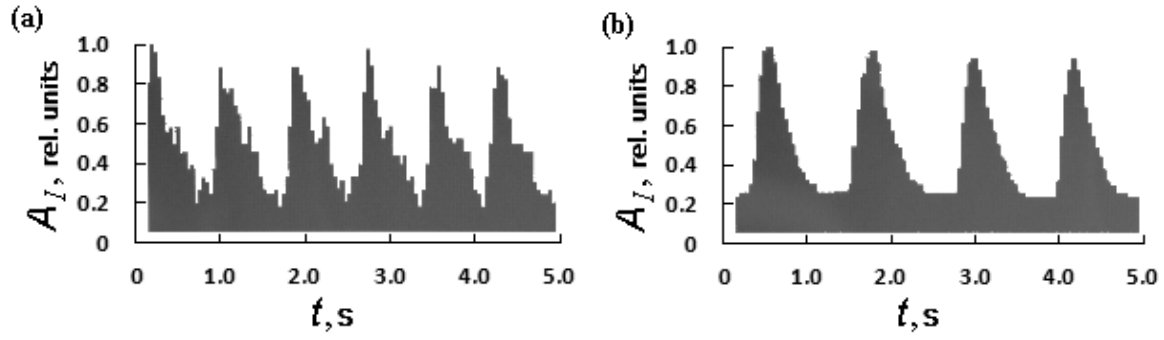

Figure 1. The pulse waveform of men: (a) at the age of 22 years; (b) at the age of 24 years.

Even in the case of a satisfactory state (Fig. 1.a), the formation of a pulse wave is an unsteady process. Therefore, to describe the shape of the pulse wave, the signal (Fig. 1) is proposed to be expanded into basic functions using the operation of compression/extension and shift of some oscillating and location function, which is called the mother wavelet. As a mother wavelet, we propose to use the Morlet function [1, 2]. This function has a zero-mean value. For a quantitative analysis of an unsteady pulse wave signal, we use the integral wavelet transform:

$$V(x,t) = \nu \int_{-\infty}^{+\infty} z(t')\varphi^*(\nu(t'-t))dt' \quad (1)$$

where $\varphi(x)$ – is the mother wavelet.

Expression (1) represents the initial one-dimensional pulse wave signal z(t) in the time-frequency plane. It should also be noted that the mother wavelet φ (x) must be well localized at x = 0, have a unit norm, its average value in the whole interval is zero. Therefore, its following form is proposed:

$$\boldsymbol{\varphi(x)} = \frac{\exp\left(-\frac{x^2}{2}\right)\left(\exp(-i\Omega_m x) - \exp\left(-\frac{\Omega_m^2}{2}\right)\right)}{\sqrt{\sqrt{\pi}\left(1 - 2exp\left(-\frac{3\Omega_m^2}{4}\right) + exp(-\Omega_m^2)\right)}} \quad (2)$$

For values of $\Omega_0 = 2\pi$, the maximum of $|\boldsymbol{V(x,t)}|^2$ for frequency f_1 will correspond to the following relation $f_1 = \nu$. This allows us to use (2) to study unsteady signals that change over time.

3. Conclusion

Using the adaptive Morlet wavelet (2) allows one to obtain a more accurate diagnosis of the frequency and time localization of the signal under study by changing the parameter m in calculating $V(x,t)$. The reliability of the results of diagnosing a person's health condition using a pulse oximeter increases.

References

[1] Bozhokin S V, Lesova E M, Samoilov V O, *et al.* 2018 *Hum Physiol.* **44** 32–40
[2] Bozhokin S V and Sokolov I M 2018 *Tech. Phys.* **63** 1711–1717
[3] Grevtseva A S, Smirnov K J, Davydov V V and Rud' V Yu 2018 *Journal Physics: Conference Series* **1135(1)** 012056

Methods for monitoring oxygen supply of tissues of hazardous occupation specialists based on multichannel integrated analyzer of optical spectra

M S Mazing[1], A Yu Zaitceva[2], Yu Ya Kislyakov[2], V V Davydov[1], N S Kondakov[3], S A Avdyushenko[3]

[1]Peter the Great St. Petersburg Polytechnic University, St. Petersburg 195251, Russia

[2] Institute for Analytical Instrumentation, Russian Academy of Sciences, 190103, St. Petersburg, Russia

[3] S.M. Kirov Military Medical Academy, 194044, St. Petersburg, Russia

Abstract. The studies are aimed at developing a new method of non-invasive control of body tissues oxygen supply for workers of dangerous professions. The proposed method is based on utilizing the differences in the absorption spectra of oxyhemoglobin and reduced hemoglobin, as well as on the analysis of the response of the system using mathematical methods of data processing and image visualization. It is shown that each human subject has his own individual reproducible "image" and can be identified by this "image". During the application of mathematical methods for processing of multidimensional data, the subjects were divided into groups according to the type of reaction to the functional load. Each of the groups has a certain tendency to change the "image" in the presence of the functional load, which is explained by various compensatory-adaptive reactions and the functional state of the subjects. The results of the above studies indicate the high efficiency of the new methodological approach for solving the problems of non-invasive monitoring of human health and organism performance and can be used to create a new generation of diagnostic medical systems.

1. Introduction

Among all causes of death, cardiovascular diseases occupy one of the leading places in the world. The cardiovascular system provides the most important transport function, in particular the respiratory one, consisting in the transfer of oxygen from the lungs to the tissues and carbon dioxide from the tissues to the lungs. This function is due to the presence in the blood of the main respiratory pigment, which is part of the erythrocyte - hemoglobin protein [1]. The reason for the interruption of the oxygen supply to human tissues can be both oxygen deficiency in the external environment and the result of pathological conditions of the cardiovascular system. Early diagnosis of cardiovascular diseases helps to prevent the development and transition of the disease into a chronic form, as well as to minimize possible serious complications. In this work, we develop a spectrophotometric method for monitoring the oxygen supply of body tissues, which is based on different optical properties of the physiological forms of hemoglobin in the blood [2,3].

2. Methods

The system of non-invasive monitoring of the oxygen supply of human tissues consists of two blocks: 1) the sensor and 2) the computation modules. The sensor module is represented by an integrated six-channel spectrum analyzer and a set of optical sensors with cross sensitivity to biologically important

forms of hemoglobin. The computation block includes modules for visualization and pattern recognition.

3. Experiments and results

The experiment is based on readings of the optical spectrum analysers before and after the functional load in 21 human subjects, which is a deep breath-holding. At the same time, heart rate was measured throughout the experiment. The state of rest lasted 60 seconds, after which the subject, after a deep inspiration, held breath for the maximum possible time. Rest time after functional load (recovery) lasted 4 minutes. In addition, each subject filled out a questionnaire. During the application of mathematical methods of multidimensional data processing the subjects were divided into three groups, according to the type of response to the functional load - a group in which there was a change in the oxygen supply of tissues at the time of the start of inspiration and during subsequent recovery, a group that had no changes and a group for which there is a significant change in oxygen status at the time of recovery in relation to the state of rest. Each of the selected groups has a certain tendency to change the “image” while being under the functional load, which is explained by various compensatory-adaptive reactions and the functional state of the subjects. Typical normalized readings of the sensors for subjects from the group with normal indicators of oxygen status restoration are shown in Fig. 1.

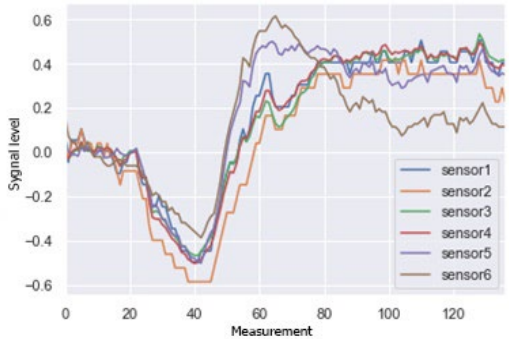

Figure 1. Typical normalized readings of the sensors for subjects from one of the groups.

4. Conclusion

Identified capabilities of the analytical complex to form individual “images” of subjects before the functional load and their individual changes after the load can be used to formulate training algorithms for recognition of the functional state. The results of the studies indicate the high efficiency of the new methodological approach to solving the problems of non-invasive control of human health and work capacity. The measuring control system of the oxygen supply of human tissues allows to get the necessary information about a variety of vascular pathologies and can be used to create a new generation of diagnostic medical systems.

5. Acknowledgments

The study was carried out in the framework of State Assignment No. 075-01073-20-00 on the topic "Microfluidic devices and systems for simulating and studying processes in a living organism" SU NIR 0074-2019-0010

References

[1] Zaitceva A Yu, Kislyakova L P, Kislyakov Yu Ya, Avduchenko S A 2019 Journal of Physics **1400**, 033022
[2] Kislyakova L P, Zaitceva A Yu, Kislyakov Yu Ya 2018 Natural and technical sciences **12**, 318
[3] Anderson R R, Parrish J A 1981 J. Invest. Dermatol **77**, 13

The use of continuous Wavelet transform for the analysis of data obtained on the genetic analyzer NANOFOR-05

Y V Batov[1], D A Puzko[1], V V Davydov[1], A I Petrov[2], V Yu Rud[3]
[1]Higher School of applied physics and space technologies, Peter the Great Saint Petersburg Polytechnic University, Saint Petersburg 195251, Russia
[2]Institute of Analytical Instrumentation of the Russian Academy of Sciences, Riga Ave., 26., St. Petersburg, 190103
[3]All-Russian Research Institute of Phytopathology, Moscow Region 143050, Russia

Abstract. The article discusses a DNA analyzer that determines the sequence of nucleotides. A method for determining the sequence based on a continuous wavelet transform is proposed. The results of experimental studies are presented.

1. Introduction

Currently, to solve many problems, it is necessary to analyze of deoxyribonucleic acid (DNA). For the analysis of DNA using various devices, the principle of which is based on various methods. One among most used instruments for the analysis of DNA is NANOFOR-05 (analysis is carried out according to the Sanger method). The principle of this method is to divide the DNA into fragments, followed by determining the sequence of nucleotides in them. In this analyzer, DNA is separated by an electric field. The device is based on the registration of fluorescence signals from the analyzed sample through 4 channels. Fluorescence is recorded from a specific nucleotide in each channel. The signal is a sequence of fluorescence peaks [1].

The task of data processing is to detect peaks in each channel, their relative position and restoration of the original DNA sequence. The main signal processing problem is the closely spaced fluorescence peaks that overlap each other. This effect increases with time, which is associated with the expansion of the peak.

Most peak detection methods use baseline pre-correction and noise reduction. However, such approaches have two main disadvantages. Firstly, after preliminary processing, the “necessary” peaks of small amplitude, taken as noise, can be removed. Secondly, there are closely spaced peaks in the signals, which leads to an overlay effect, as a result of which information about some peaks may be lost.

2. The method of scalogram based on Continuous Wavelet Transform

In MATLAB, a method was developed for detecting peaks in a signal based on a continuous wavelet transform followed by a scalogram — a function of the absolute value of a continuous wavelet transform versus time and frequency [2]. The appearance of the peak and its location along the time axis are determined by the type of scalogram (Fig. 1).

The preliminary studies showed that the developed method based on the wavelet transform does not require preliminary correction of the baseline and elimination of noise. This increases the probability of detection, since no additional distortions are introduced into the signal during its preliminary processing. In addition, this method is effective in separating several overlapping peaks, since it uses the correlation of the mother wavelet with the signal itself.

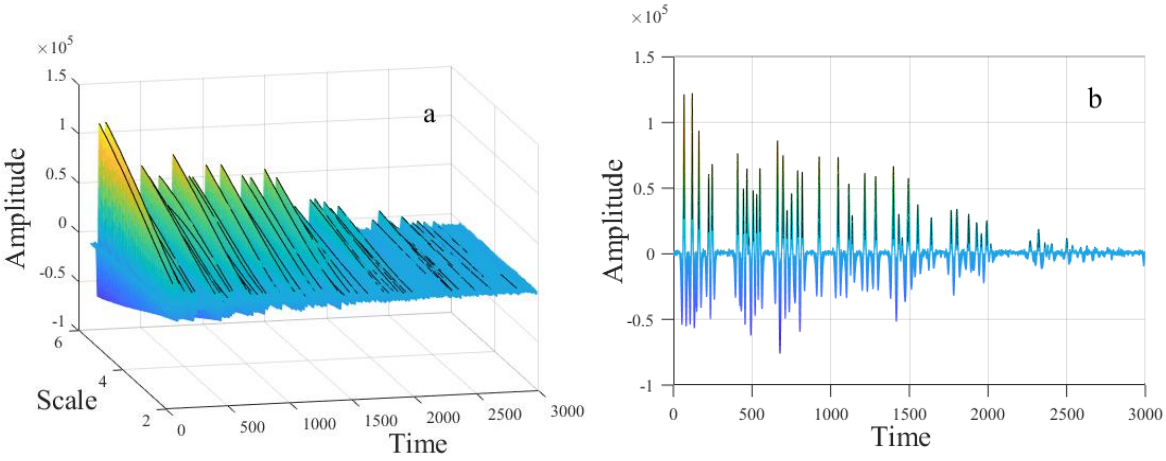

Figure 1 (a, b). (a) Scalogram; **(b)** Scalogram section for scale = 2

Based on this, the mother wavelet is chosen so that its main characteristics are like the desired peak in the signal [3]. The Mexican hat wavelet is most suitable for this study because of the similarity of its shape to the peak, defined as:

$$\psi(t) = \frac{1}{2\pi}(1-t^2)e^{-\frac{t^2}{2}}$$

where t is the process observation time.

3. Conclusion

For model signals that do not have large distortions (for real signals, as a rule, this is true for the first half of the signal), we were able to achieve a peak determination reliability of 0.99. Studies show that for the "good" part of the real signal, in which distortions are not yet very pronounced, this method detects on average more luminescent peaks than other methods. As for the "bad" part of the real signal, the method based on the wavelet transform is not inferior to similar methods.

References

[1] Alekseev Ya I, Belov Yu V, Malyuchenko O P, Monakhova Yu A, Natyrov A N, Orekhov V A, Konovalov S V, Kurochkin V E, Petrov A I 2012 *Scientific instrumentation* **22(4)** 86–92
[2] Misiti M, Misiti Y, Oppenheim G, Poggi J 2019 *Wavelet Toolbox™ User's Guide* (copyright 1997–2019 by the Math Works, Inc.)
[3] Du P, Kibbe W, Simon M. 2006 *Bioinformatics* **22(17)** 2059–2065

Synthesis and characterization of Fe_3O_4@HAp core-shell nanoparticles as potential contract agent for MRI

V V Zheltova, A A Vlasova, N P Bobrysheva, I Abdullin, V G Semenov, M G Osmolowsky, M A Voznesenskiy, O M Osmolovskaya
Institute of Chemistry, St. Petersburg State University, St. Petersburg 199034, Russia

Abstract. Magnetic core-shell Fe_3O_4@HAp nanoparticles with a different HAp amount were synthesized using the original approach based on co-precipitation method combined with hydrothermal treatment at temperatures range from 140 to 240°C.Nanoparticles morphological parameters were characterized using X-ray diffraction, Fourier-transform infrared spectroscopy, transmission electronic microscopy, specific surface area estimation, Mossbauer spectroscopy. As-prepared core-shell NPs demonstrated the narrow size distribution and the presence of magnetite and hydroxyapatite phase. All the samples exhibited superparamagnetic behaviour, blocking temperature values demonstrated the linear dependence on shell thickness. Computer simulation of blocking temperature dependence on shell thickness revealed the impact of the shell on the anisotropy constant and consequently on blocking temperature. To evaluate the efficiency of the core-shell NPs as contrast agents for magnetic resonance imaging, the samples with different HAp amount in agarose matrix were investigated.

1. Introduction

Magnetic Resonance Imaging (MRI) is a non-invasive imaging technique that produces three dimensional detailed anatomical images with high soft tissue contrast and spatial resolution. By now MRI contrast agents have become an indispensable part of MRI procedure for the diagnostic of some diseases, since their addition in many cases improves sensitivity and/or specificity and therefore provide better diagnosis of pathological tissues.

Superparamagnetic and ferromagnetic MRI agents are called negative contrast agents, since diseased tissues that accumulate contrast agents look darker in the images. The main material to produce negative contrast agent is the Fe_3O_4ferrimagnetic (superparamagnetic at the size less than about 20 nm) nanoparticles due to a combination of their superparamagnetic properties, biodegradability and biocompability. Nevertheless Fe_3O_4 magnetic nanoparticles are not widely used in clinical practice probably due to the surface oxidation process which leads to the loss of aggregative stability and magnetic properties. To solve this problem, it was suggested to protect magnetite particle surface with different shells. But almost in all the cases the forming coating may have a thickness greater than the core size, which leads to a significant decrease in the magnitude of the saturation magnetization and the MRI contrast ability.

So creation of the stable and thin shell on a magnetic core is a real challenge to material scientists. We chose hydroxyapatite (HAp, $Ca_{10}(PO_4)_6(OH)_2$) as a material for the shell production, guided by two important factors, namely, biocompatibility and wide use in medicine.

2. Method

In this work magnetic Fe_3O_4@HAp core-shell nanoparticles were synthesized. For that an original three stages approach was developed. The stages are: 1) Fe_3O_4 cores synthesis by co-precipitation method, 2) production of a diffused HAp layer with low crystallinity on core surface, 3) hydrothermal treatment on order to obtain a well-crystalline product. Dependence of the formed shell thickness on synthesis conditions was studied; it was shown that at low temperatures (140°C) of hydrothermal treatment the thickness of the shell grows with the amount of HAp in the reaction media, while at high temperatures (240°C)vice versa the shell thickness decrease with the increase of HAp amount. This is related with differences in the crystallization velocities and leads to formation of shells with different crystallinity.

3. Results

To get the specified properties it is necessary to perform a valid analysis of the obtained results and to be able to predict properties based on the structure.

For detailed study we took samples synthesized at 140°C since the shells of different thickness possess the same crystallinity. All of this samples show typical superparamagnetic characteristics at room temperature. Mossbauer spectroscopy data revealed changes of hyperfine parameters and redistribution of relative areas of magnetic sextets comparing with bare core sample, which could be due to the formation of intermediate magnetic layer during hydrothermal treatment.

Blocking temperatures obtained out of ZFC-FC curves are in linear dependence on the shell thickness. The nanoparticle shell might influence the magnetic moment itself, the dipole interactions of the dipoles by scaling the average distance between nanoparticles, as well as the anisotropy constant. Computer simulations revealed that for “thick” shell (4.5 nm 6.5 nm) the magnetic characteristics is determined by dipole interactions, while for the “thin” shell(3.9 nm)effect of anisotropy is more pronounced.

For core-shell NPs the values of zeta-potential close to -30 mV were observed, which corresponds to the value required for in vivo imaging. Core-shell NPs were tested using a MRI scanning system using an agarose matrix to simulate biological tissues. HAp shell improved the contrast in the case of T1 images, and leads to a decrease in color darkness in T2 mode. The dependence of MRI contrast ability and T2/T1 intensity ratio on shell thickness is not detected. So we can conclude that the shell allow us to protect the magnetite surface from oxidation, to achieve good values of surface charge (acceptable for intravenous injection), and does not greatly affect contrast ability. Thus Fe_3O_4@HAp core-shell nanoparticles could be potential candidates for contrast agent.

4. Acknowledgments

The work is financially supported by the Russian Foundation for Basic Research (RFBR), project no. 18-03-01066.Scientific research was performed using the equipment of the Research Park of St. Petersburg State University: Centre for X-ray Diffraction Studies, Chemical Analysis and Materials Research Centre, Centre for Innovative Technologies of Composite Nanomaterials, Centre for Optical and Laser Materials Research.

5. References

[1] I. Timofeeva, M. Alikina, A. Vlasova, M. Osmolowsky, M. Voznesenskiy, O. Volina, L. Moskvin, O. Osmolovskaya, A. Bulatov, Fe3O4-based composite magnetic nanoparticles for volatile compound sorption in the gas phase: determination of selenium(iv), Analyst, 144(7) (2019) 152-156.

Development of a hydraulic system for bridge amplification

V A Kruglov[1], **V S Reznik**[1], **V V Davydov**[1, 2], **V Yu Rud**[2]
[1]Higher School of applied physics and space technologies, Peter the Great St. Petersburg Polytechnic University, St. Petersburg 195251, Russia
[2]All Russian Research Institute of Phytopathology, Moscow Region, 143050, Russia

Abstract. In this paper, we consider the features of creating a hydraulic system with the goal of conducting bridge amplification, which is part of the Illumin / Solexa method. The result of the work is an automated system with all the necessary functional qualities.

1. Introduction

Currently, biotechnologies that are associated with the study of the genome, including the human genome, have been actively developed in medicine, healthcare and science. The study of the genome is inextricably linked with the study of the sequence of nitrogenous bases that make up deoxyribonucleic acids (DNA).

One such technique is to “read” this sequence or otherwise a sequencing process. [3]

Sequencing methods are constantly being improved and currently the next generation sequencing methods (NGS) are the most relevant. One such method is the Illumina / Solexa method, which is a mass parallel sequencing method. [2]

The advantages of this method are: the ability to obtain a large amount of data in a relatively short period of time, i.e. high sequencing speed, as well as high accuracy achieved by mass. In addition, due to the high speed, the cost per unit of information received is significantly reduced.

One of the components of this method is bridge amplification, an important process which results in DNA segments ready for sequencing, called clusters, fixed on a special surface of the substrate with immobilized oligonucleotides, which act as primers during the reaction.

The process of bridge amplification is based on a sequential increase in the number of segments of the test sample. After passing a special sample preparation, the sample goes through the stage of presynthesis. [1]

2. Hydraulics features

Next, it is necessary to perform several amplification cycles, which consist in a sequential process of linearization of the chain, for which a special linearization mixture is used. After this, it is necessary that the linearized library interact with the mixture for amplification during the experimentally set time. Before carrying out the next cycle, it is necessary to conduct denaturation by feeding formamide. Several cycles are necessary to increase the number of clusters. [1]

Based on the characteristics of the reactions, it became necessary to create an automated system for its implementation. The main requirements that are presented to the system include: the ability to pass reagents through the space in which the substrate with the primers is located, as well as their removal from this space, the ability to automatically select reagents for pumping, the ability to control the pumping and removal process, and the ability to change the temperature at which the reaction

takes place on the substrate. In addition, it is extremely important to be able to verify that the clusters are successfully grown on the surface of the substrate.

The necessary reagents are placed in a tripod, which is connected by flow channels to a hydraulic switch. This switch allows you to connect the flow channels that go to the tanks with reagents, with the flow channel that goes to the reaction cell, in which there is a substrate with primers.

The hydraulic switch has 24 possible positions, which allows the use of up to 24 different reagents for the reaction.

The reaction cell itself is a C-shaped channel, the surface of which is covered with immobilized oligonucleotides. Segments of DNA clinging to these primers undergo an amplification process.

Behind the reaction cell is a series of sensors that allow you to control the quality of the process. One of these sensors is a sensor that detects the rate of fluid flow.

A precision syringe pump is used to pump and remove reagents. In the event of a discharge of the syringe, the reagent fills the flow channels, and then the cell itself together with the pump syringe. [2] When the syringe is empty, the reagents contained in it are sent to the drain tank.

To implement the temperature regime, a thermal cycling system is used.

During the experiment conducted on the developed system, it was possible to successfully carry out bridge amplification, the result of which was the presence of amplified clusters on the surface of the substrate of the reaction cell.

In order to confirm the presence of clusters, an optical detection system was used, the results of which are presented in Fig. 1.

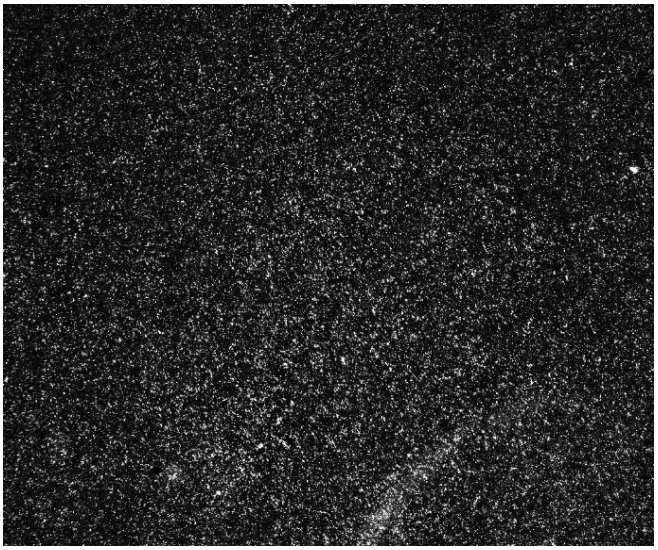

Figure 1. Detected clusters.

3. Conclusion

Thus, the developed automated system allows bridge amplification, which is extremely necessary for sequencing using the Illumina / Solexa method.

References

[1] Gostev A, Dubovik D, Masyutenko N, Nitchenko L, Reznik V, Kruglov V, Davydov R 2019 *IOP Conference Series: Earth and Environmental Science* **390** 012040.

[2] Filatov D L, Galichina A A, Vysoczky M G, Yalunina T R, Davydov V V, Rud' V Yu 2017 *Journal of Physics: Conference Series* **917(8)** 082005

[3] Zarutskii I V, Manoilov V V, Samsonova N S, Petrov A I, Kurochkin V. E, Leont'ev I A, Alekseev Ya I 2018 *Technical Physics* **63** 1364-1369

Modulation *p*-doping as the way to attain multi-state lasing in short-cavity InAs/InGaAs quantum dot lasers

V V Korenev[1,2], A V Savelyev[1], V G Dubrovskii[3], S Breuer[4], M V Maximov[1,2], A E Zhukov[1,2]
[1]St. Petersburg Academic University RAS, St. Petersburg 194021, Russia
[2]Peter the Great St. Petersburg Polytechnic University, St. Petersburg 195251, Russia
[3]ITMO University, St. Petersburg 197101, Russia
[4]Technische Universität Darmstadt, Darmstadt 64289, Germany

E-mail: korenev@spbau.ru

Abstract. The influence of modulation *p*-doping on the lasing threshold current densities of InAs/InGaAs quantum dot (QD) lasers is studied at different levels of acceptor concentrations. It is found that for both undoped and *p*-doped samples, there exists a critical cavity length at which threshold current densities of the lasing via ground- and excited states of QDs become equal so that multi-state lasing can be observed only in samples having longer cavities. It is shown that the usage of modulation *p*-doping is an efficient way to overcome this limitation and to obtain multi-state lasing even in case of sufficiently short samples.

1. Introduction

For many practical applications including ultrafast data transmission and optical coherence tomography, there is a need for stable optical sources emitting near 1.2-1.3 μm corresponding to the transparency window of Si-based waveguides [1 – 2]. Long-wavelength InAs/InGaAs quantum dot (QD) lasers emitting via the QD ground-state (GS) optical transition allow not only to overlap the required spectral range, but also have small threshold currents and high temperature stability [3]. Even if the lasing starts at QD GS around 1.3 μm, further increase in injection usually results in appearance of an additional short wavelength lasing line near at 1.2 μm associated with the first excited-state (ES) optical transition of QDs, the multi-state lasing, i.e. simultaneous lasing via GS and ES of QDs, takes place [4 – 8].

The multi-state lasing can be useful in view of achieving broader lasing spectra [1] and a larger number of optical channels from a single laser source [9]. However, the GS lasing band is quenched with the increase in injection current shortly after the onset of multi-state lasing [7, 10 – 11]. One of the ways to overcome this effect is the usage of *p*-doping that can be an efficient solution particularly in case of the short samples [10]. At the same time, it is also known that *p*-doping may influence not only the output power corresponding to the GS of QDs but also the lasing threshold current [10 – 12]. This result allows one to expect that the *p*-doping can influence a minimal laser cavity length at which multi-state lasing, i.e. simultaneous lasing via GS and ES of QDs, still can be seen. Studying of this question constitutes the key goal of this work.

2. Experimental details

Three series of InAs/InGaAs QD lasers having different levels of *p*-doping of 0, 3 and 5×10^{17} cm^{-3} were grown using molecular beam epitaxy (MBE). The active region of each sample was comprised of 10 layers of InAs/InGaAs QDs separated by 35 nm-thick GaAs spacers. The *p*-doping was implemented by using of carbon atoms embedded into the central areas of barrier layers. The laser diodes were fabricated to have various lengths and the same stripe width of 50 μm. The experimental dependences were derived from the light-current curves and emission spectra measured at different injection currents.

3. Experimental results and their interpretation

To study the influence of *p*-doping level on the critical length of laser cavity at which multi-state lasing still can be seen, the dependence of threshold current densities of undoped and *p*-doped samples on laser cavity length was first measured – see Fig. 1 (a, b, c).

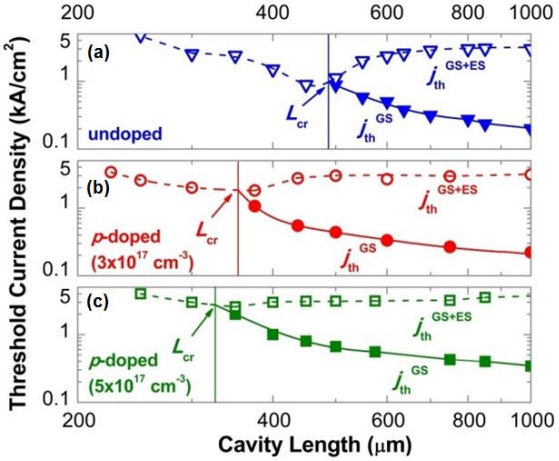

Figure 1. Threshold current density of pure GS-lasing (filled symbols, solid lines) and ES-lasing (empty symbols, dashed lines) vs cavity length. The dopant concentration is 0 (a), 3 (b) and 5 (c) × 10^{17} cm^{-3}. Vertical lines show the minimum cavity lengths (L_{cr}) at which GS-lasing component can be seen.

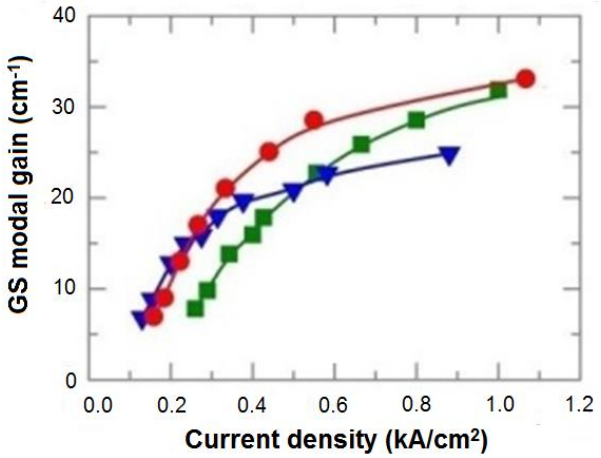

Figure 2. Experimental dependence of the modal gain corresponding to QD GS on the injection current density. Triangles, circles, and squares correspond to The dopant concentrations of 0, 3 and 5×10^{17} cm^{-3}.

As it can be seen in Fig. 1, the decrease in laser cavity length results in the increase in threshold current density of the onset of the lasing via QD GS ($j_{th,GS}$), while threshold current of multi-state lasing ($j_{th,GS+ES}$) decreases. The injection current density interval corresponding to the multi-state lasing, i.e. the interval between $j_{th,GS+ES}$ and $j_{th,GS}$, tends to shrink as cavity length increases. Therefore, there is a critical cavity length (L_{cr}) at which threshold current of GS-lasing and of multi-state lasing become equal – see the vertical lines in Fig. 1. The characteristic feature of L_{cr} is that there is no lasing corresponding to QD GS for the samples shorter than L_{cr}, where pure ES-lasing is only observed. Such a behavior remains true for *p*-doped samples as well – compare Fig. 1a, 1b and 1c. This poses a natural limit on the minimum length of laser cavity at which practically useful GS-lasing can be achieved.

However, the usage of modulation *p*-doping occurs to be a beneficial method to further increase the range of cavity lengths towards shorter cavities, at which simultaneous lasing via QD GS and ES still can be seen. Indeed, in accord with the experimental results shown in Fig. 1, the increase in the dopant concentration from 0 to 3×10^{17} cm^{-3} and to 5×10^{17} cm^{-3} results in the decrease of L_{cr} from 0.49 mm to 0.35 mm and to 0.33 mm respectively. The reason behind is the following: for the same

The effect of graphite coating on the composition, structure and microhardness of the surface of structural chromium-nickel steel during laser pulse processing

V Proskuryakov[1], I Rodionov[1], S Borodina[1]
[1]Yuri Gagarin State Technical University of Saratov, Saratov 410054, Russia

Abstract. In this work, the effect of laser pulsed radiation on the surface of 12Cr18Ni10T stainless steel with a layer of graphite coating previously applied to it was experimentally investigated. It was established that as a result of laser pulsed irradiation, a significant increase in the microhardness of the surface layer of the experimental samples occurs to H=9.56±0.1 GPa. The results of studying the elemental composition of the surface structure showed an increase in the concentration of diffused carbon in the surface layer of steel.

1. Introduction

Along with the traditional methods of chemical-thermal treatment and other various methods of saturating the surface of one metal with others, the most preferred method today is pulsed laser doping.

Currently, methods where the alloying material is applied to the surface to be treated in the form of a previously prepared suspension (coating) are becoming most relevant. Such methods allow, for example, to achieve high hardness of the modified surface layer, to increase corrosion resistance and wear resistance. Often, finely dispersed or nanosized powder materials and a viscous-flowing binder are used as modifying components of the coating. However, despite a large number of experimental works, questions related to the uniform distribution of alloying elements in the modified surface layer remain incompletely studied [1].

2. Methodology

The studies were carried out on stainless steel 12Cr18Ni10T. The experimental samples were plates with dimensions of 10×10 mm and a thickness of 3 mm. Graphite paste (GOST 8295-73) was selected as the alloying material, which was applied to the steel surface with a thin layer of 150±50 μm.

The surface layer was doped in an automated setup for thermophysical coherent surface modification of LRS-50A.

3. Results

Metallographic studies of the structure showed that in addition to the formation of the modified surface layer, a diffusion layer is formed, the microhardness of which is higher than the microhardness of the alloy base. This hardening effect is associated with the saturation of the treated surface with carbon (up to 1.46%), which is contained in large quantities in graphite coating. Figure 1 shows the spectra used to perform elemental analysis and the boundaries of the layers formed as a result of laser doping.

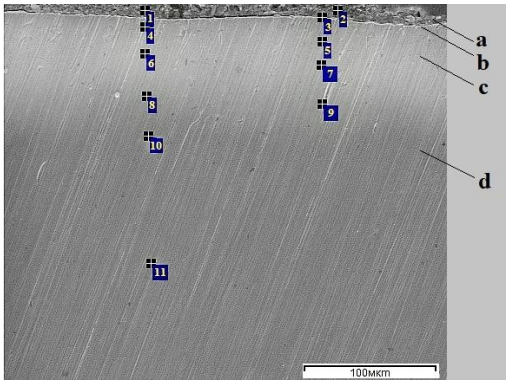

Figure 1. The surface structure of stainless steel samples after laser alloying at a pulse voltage of 300 V: a - epoxy resin; b is a modified surface layer; c is the diffusion layer; d is the basis of the alloy (the numbers indicate the spectra of determination of elemental composition).

Additionally, measurements of the microhardness of the surface showed its significant increase with increasing pulse energy. The maximum value of microhardness H=9.56±0.1 GPa was obtained by treatment with a pulse voltage of U=400 V and a radiation spot diameter of 0.5 mm. It should be noted that the microhardness of the untreated surface of 12Cr18Ni10T steel is in the range 1.4±0.2 GPa. Based on the results obtained, an empirical model of the dependence of the microhardness of the modified surface on the laser treatment regimes was constructed (Figure 2).

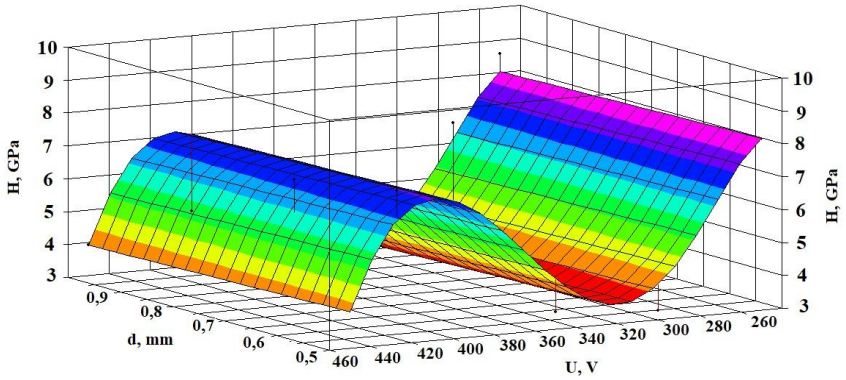

Figure 2. Dependence of the microhardness of the modified surface on the laser doping regimes.

Conclusions

It was established that as a result of laser alloying of 12Cr18Ni10T steel, a layered surface structure with increased microhardness is formed. According to the analysis of elemental composition, the modified surface layer with a thickness of up to 5 μm consists of iron oxides and carbides. The carbon content on the surface of steel samples of the order of 1.4±0.1 at.% Leads to a significant increase in microhardness to 9.56±0.1 GPa and allows you to compare it with carbon tool steel. According to the results obtained, it can be assumed that the surface of stainless chromium-nickel steel alloyed with graphite coating will be more resistant to abrasion and the effect of abrasive particles on it during operation.

Acknowledgments

The studies were carried out in the framework of the RFBR grant (competition for the best fundamental research projects carried out by young scientists studying in graduate school - “Postgraduates”), project No. 19-33-90101.

References

[1] Chi Y, Gu G, Yu H and Chen C 2018 *Optics and Lasers in Engineering* **100** 23-37.

Establishing the applicability of the laser diffraction technique for the graphene oxide platelets lateral size measurements

S D Saveliev [1], M K Rabchinskii [1], S A Ryzhkov [2], E K Nepomnyashchaya [3], S I Pavlov [1], M V Baidakova [2], P N Brunkov [1]

[1] Ioffe Institute, 26 Politekhnicheskaya, Saint-Petersburg 194021, Russia

[2] ITMO University, 49 Kronverksky Pr., 197101 Saint Petersburg, Russia

[3] Peter the Great St.Petersburg Polytechnic University (SPbPU), Polytechnicheskaya, 29, St.Petersburg, 195251, Russia

Abstract. In this paper, basing on the thorough comparison of the size measurement results obtained by Laser Diffraction (LD) and microscopic methods, we demonstrate the LD method to provide reliable and accurate data on the lateral size of two-dimensional graphene oxide (GO) platelets. The features of GO light scattering in aqueous suspensions are studied as well.

1. Introduction

Synthesis of graphene oxide (GO) and its subsequent reduction nowadays is regarded as one of the most prominent techniques for graphene large-scale production due to its low-cost, high yield and simplicity of forming films on various substrates. Within this approach, the lateral size of the GO platelets synthesized via liquid-phase graphite exfoliation, play a crucial role in the determination of the physical and chemical properties of the subsequently formed GO films. [1]. In particular, the electrical conductivity of the film tends to decrease significantly with the reduction of the GO platelets' lateral size due to the increase of the total boundaries length and thus scattering of charge carriers. Therefore, analysis of the GO platelets lateral size in obtained suspensions is one of the crucial stages for their further studying and application.

Several methods are commonly used for GO platelets size determination, such as scanning electron microscopy (SEM) and atomic force microscopy (AFM), although these techniques are rather complicated. On the other hand, laser diffraction (LD) is a widely used simple, rapid and effective method for particle size determination that can be applied to liquid suspensions [2]. However, it is considered to be applicable only for suspensions containing spherical particles, not two-dimensional structures such as GO platelets.

In the presented work, on the base of comparison of the results, obtained by laser diffraction size analysis, with SEM and AFM images, we do demonstrate that this method provides the possibility to determine the size distribution of GO platelets in aqueous suspensions with relevant accuracy.

2. Materials and methods

Four GO suspensions with different lateral sizes of the GO platelets denoted hereinafter as GO#1, GO#2, GO#3, GO#4 were studied. GO#1 and GO#2 suspensions were synthesized by the modified Hummers method [3], using GSM-1 and GO350 graphite as a starting material, respectively. GO#3 and GO#4 were obtained via sonication of the GO#1 suspension in ultrasonic bath (60 kHz, 75 W) for 120 seconds and subsequent centrifugation of the obtained suspension (19200 g, 15 minutes). The GO#3 sample refers to the supernatant, whereas GO#4 corresponds to the sediment rinsed with

the deionized water. GO films were prepared by the Langmuir−Blodgett method on the surface of silicon wafers according to the conventional procedure.

LD size distribution measurements were performed using Mastersizer 2000. The UV-vis absorption spectra of the GO samples were collected by a Shimadzu-2450 spectrophotometer. Surface morphology of the GO platelets was analyzed with a Veeco Dimension 3100 atomic force microscope operating in the tapping mode by using RTESP probes and scanning electron microscope Jeol JSM-7001F. For the light scattering measurements suspensions were placed into quartz cuvette and irradiated with 532 nm diode laser. The scattering pattern was measured using silicon photodiode detector placed on the goniometer. For theoretical calculations MiePlot v4503 software was used.

3. Results and discussion

The size distributions obtained by means of LD measurements have demonstrated progressive reduction of the GO platelets lateral size from GO#1 to GO#4 sample. The outmost platelets' size in the obtained GO suspension is 110 μm (GO#1), whereas the smallest platelets with a diameter of about 0.8-1 μm is demonstrated for the GO#4 suspension. The maximums of the size distribution of GO#2 and GO#3 samples are, respectively, 10 μm and 25 μm. Such difference in lateral dimensions of the GO platelets are both to the use of different graphite precursors having distinct mean size of crystallites and disruption of GO platelets due to the sonication treatment.

Subsequent analysis of the set of SEM and AFM images of the arrays of GO platelets deposited from the studies GO suspensions has allowed us to obtain reference size distribution. The comparison of these distributions has pointed out that LD measurements provide the correct position of the GO platelets size distribution maximum with an error of less than 10%. Moreover, the overall shapes of the distributions obtained from LD measurements and microscopy analysis almost perfectly fit, although in the former case it appears to be narrower. This is most probably due to the limitations of the software used in the Malvern Mastersizer 2000 device.

During the further analysis of the experimentally obtained scattering patterns and their comparison with theoretical calculations, we also found that the pattern of static light scattering for suspensions of graphene oxide is determined mainly by Fraunhofer diffraction. Thus, the light scattering mainly proceeds on the edges of GO flakes, what is additionally verified by the performed UV-Vis measurements. Taking into account also the fact that the illumination of the GO suspensions with laser radiation leads to alignment of all platelets perpendicular to the direction of the beam [4], the obtained data allow us to explain why despite the laser diffraction method is regarded to be applicable only for the spherical particles it can provide correct size distributions of the GO platelets.

4. Conclusion

Summarizing the results, for the first time the possibility of GO platelets' size distribution measurements in aqueous suspensions by the LD method was demonstrated. Taking cue from the experimental study and theoretical calculations of scattering patterns, model accounting for arising of diffraction pattern that can be correctly processed with common LD instrumentation was suggested.

5. Acknowledgments

This work was financially supported by the Russian Foundation for Basic Research (grant no. 18-29-19172).

References

[1] K. E. Lee, J. E. Kim, U. N. Maiti et al. ACS Nano, 2014, 8 (9), 9073−9080
[2] P. Kuchenbecker, M. Gemeinert, T. Rabe. Part. Part. Syst. Charact. 2012, 29, 304–310
[3] W. S. Hummers & R. E. Offeman, J. Am. Chem. Soc., 1958, 80, 1339–1339
[4] R. Wu, Y. Zhang, Y. Yan et al. Nano Lett. 2011, 11, 5159−5164

Resonant tunneling in GaAs/AlGaAs quantum well system for solar photovoltaics

P.S. Klemmer[1,2], **Yu.A. Mityagin**[1], **M.P. Telenkov**[1], **K.K. Nagaraja**[2,3], **D.A. Elantsev**[1], **Sh. Amiri**[1,2]
[1]P.N, Lebedev Physical Institute of Russian Academy of Sciences, Moscow, Russia
[2]National University of Science and Technology «MISiS», Moscow, Russia
[3]Manipal Institute of Technology, Manipal Academy of Higher Education, Manipal 576104, India

Abstract. In this work, we propose a simple and effective method to vary the lowest subband position in a quantum well system. A nearly continuous variation - from the bottom of the quantum well up to a continuous spectrum – can be achieved by inserting a series of thin barriers of host material into a quantum well of fixed width. This technique is technologically simple and promising in a variety of applications, in particular, for aligning the lowest subband position in the sequence of quantum wells in an electric field of an arbitrary configuration, including those typical for p–i–n solar cells.

1. Introduction

The task of controllable variation of the subband position in quantum wells and, correspondingly, the effective bandgap of the structures is of much importance in several optical and optoelectronic applications, in particular, in photovoltaic applications of quantum wells. Introduction of quantum wells into an i-region of p–i–n solar cell is one of the promising methods for improving its efficiency by expanding the absorption spectrum towards the longer wavelengths. The primary problem here is concerned with the efficient extraction of photo-generated carriers if the quantum wells are deep to a continuous spectrum. The tunneling process can be used to extract carriers by having a resonantly aligned lowest subband positions in each well [1, 2]. To provide the resonant alignment of the lowest subband throughout the structure, it is necessary to compensate for the voltage drop between the neighboring quantum wells due to the electric field of the p–i–n junction by adjusting the position of the lowest subband in each quantum well.

Here we present a method to vary the energy of the lowest subband of a quantum well with fixed-width over a wide range - almost from the bottom of the well of the up to the continuous spectrum. It is provided by embedding a set of thin barriers of the host material into a quantum well [3]. The position of the lowest subband is varied by selecting a number and position of the barriers within a quantum well. The method is relatively simple technologically, and can be used in the variety of tasks, in particular, for aligning the lowest subband position in the sequence of quantum wells in an electric field of an arbitrary configuration, including those typical for p–i–n solar cell junction.

Numerical calculations of the subband positions for various configurations of the embedded barrier set showed the possibility to vary the position of the lowest subband over a wide range — practically from the bottom of the quantum well up to the continuous spectrum. The results are shown in Fig.1

We also studied the effect of barrier set imperfection (blurring of the interfaces) on the lowest subband position, and a simple algorithm was proposed for selecting the configuration of the set of the barriers embedded into the quantum well to achieve the requested values of the lowest subband energy.

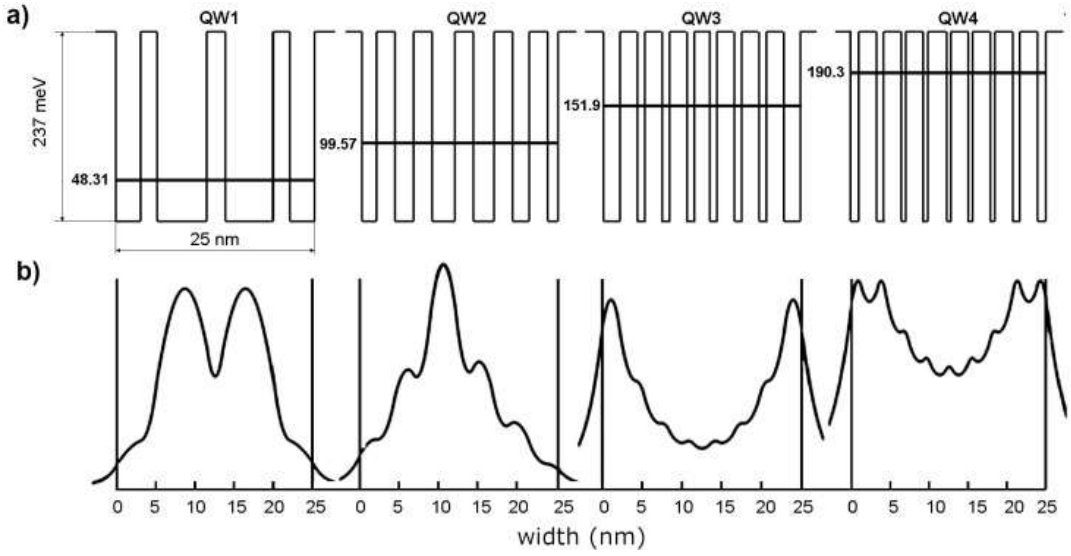

Figure 1. Potential profile of quantum well structures with a different $GaAs/Al_{0.3}Ga_{0.7}As$ configuration of the inserted barriers (a) and distribution of the wave function of the lowest energy subband (b).

Table 1. The calculated energies of the electron lowest subbands for the structures presented in Fig.1a.

Well Number	Number of barriers	E_e, meV	Expected E, meV
0	-	6.81	-
1	3	48.31	50
2	5	99.57	100
3	7	151.9	150
4	8	190.3	200

2. Acknowledgments

The work was carried out with financial support from the Russian Basic Research Foundation (project No. 18-02-00874-a). NKK financial supports from the Ministry of Education and Science of the Russian Federation in the framework of Increase Competitiveness Program of NUST « MISiS» (grant No. K3-2018-020)

References

[1] K. W. J. Barnham and G. Duggan, A new approach to high efficiency multibandgap solar cells, J. Appl. Phys. 67 (1990) 3490.

[2] M.P. Telenkov, Yu. A. Mityagin, Resonant-tunneling structure of quantum wells in the p-in photovoltaic element, Bull. Lebedev Phys. Inst. 40 (2013) 346.

[3] K. K. Nagaraja, M. P. Telenkov, I. P. Kazakov, S. A. Savinov and Yu A.Mityagin, Development of GaAs/AlGaAs quantum well structures providing a resonant tunneling regime in an electric field of p-i-n junction, Materials Today: Proceedings 3 (2016) 2744–2747.

The application of superfast GaAs switch for nanosecond pumping of a semiconductor laser

M.G. Verkholetov[1], V.V. Kopyev[1], V.L. Oleinik[1], I.A. Prudaev[1], Wojciech Knap[2], S.N. Vainshtein[2,3]
[1]Tomsk State University, Tomsk 634050, Russia
[2]Institute of High Pressure Physics PAS, 01-142 Warsaw, Poland
[3]On leave from University of Oulu, FI-90014 Oulu, Finland

Abstract. The results of experimental studies of current switching by an avalanche GaAs S-diode in a semiconductor laser pumping circuit are presented. It is shown that the use of superfast nonlinear switch allows one to generate an optical pulses with a power of up to 140 W, a duration of 1 ns, and a rising edge of 300 ps.

The compact pulsed optical sources of infrared radiation are required for development of modern lidars which are used in unmanned vehicles. The transmitters with pulsed optical power from several tens to hundreds of Watts are of high interest for the development of lidars with a range of several hundred meters. Moreover, reducing the pulse duration to the nano and subnanosecond level is a big challenge for developers of such lidar transmitters. As of today, the best results have been achieved for pulsed emitters, in which MOSFET and HEMT based on GaN structure are used as switch [1, 2]. For them, current pulses up to 30 – 40 A with a duration of 2.4 – 2.5 ns were obtained. These achievements allows one to develop pulsed sources with an optical power of 70 – 120 W (the rising edge of the optical pulses, which determines the resolution of the range finder, is 1 – 1.5 ns). The purpose of this paper is to demonstrate that the use of new principles of switching makes it possible to improve the transient characteristics by 2 – 3 times.

In this work, experimental studies of the electrical and transient optical characteristics of emitting semiconductor microassemblies are presented. The electrical circuit of the microassembly is shown in Fig. 1. The principle of operation of the emitting microassembly is as follows. When a positive pulse is applied, the capacitor is charged to the switching voltage of the S-diode (around 180 V). After switching of S-diode to the ON state, the capacitor starts to discharge, and under ideal conditions the current pulse with a duration of $2.2 \cdot (L \cdot C)^{1/2}$ starts generate. The amplitude of the pumping current pulse is determined by the loop impedance (wave impedance and S-diode resistance in the ON state). The use of miniature semiconductor components made it possible to reduce the length of the circuit down to 1 mm, which ultimately led to decrease in the parasitic inductance of the electric circuit down to 1 nH.

A 905 nm wavelength semiconductor laser chip based on the structure with three InGaAs/GaAs quantum wells was used as an emitter (Osram SPL DS90A_3). The avalanche S-diode was fabricated according to the technology described in [3]: a GaAs structure doped with a deep-level impurity of iron with a total active region thickness of 25 μm was used. It was previously shown that this device operates in superfast switching mode, when the transient time from the closed state to the open one is less than the time of flight of carriers through the active region [3]. The mechanism of such a switching process can be associated with the generation of collapsing field domains [4].

The measurements showed that the low inductance and high switching speed of the S-diode provide the possibility of generating nanosecond current pulses with an amplitude of more than 40 A. The optical pulse measured at a repetition rate of 20 kHz is shown in Fig 2. The duration at half maximum is 1 ns; the rising edge does not exceed 300 ps. The measurements were conducted by using a New Focus 1014 (45 GHz) high-speed photodetector and a Newport power meter. The pulse shape was recorded by using a Tektronix DPO 70804C oscilloscope (8 GHz). Additional measurements and calculations showed that the rising edge of the current pulse was at least 1 ns. The shortening of the optical pulse rise time down to 300 ps can be explained by the gain-switching effect during superfast pumping of a semiconductor laser.

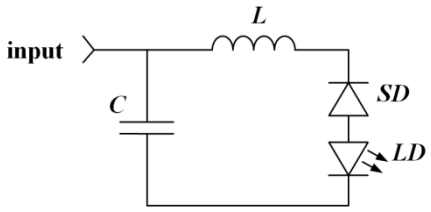

Figure 1. The electrical circuit of the emitting semiconductor microassembly with following elements: storage capacitor *C*=200 pF, total parasitic inductance *L*=1nH, avalanche S-diode (*SD*), laser diode (*LD*)

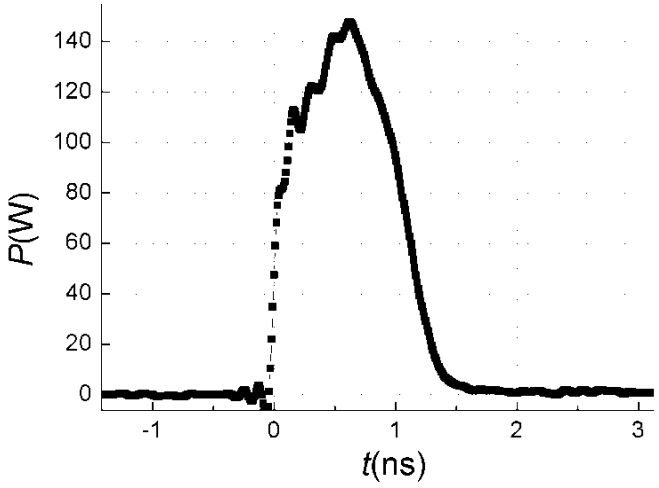

Figure 2. The optical pulse measured at a repetition rate of 20 kHz

Acknowledgement The work was supported by Russian Foundation for Basic Research (Grant # 20-08-00141).

References

[1] https://www.lasercomponents.com/de-en/product/quickswitch-pulsed-laser-diodes/
[2] https://gansystems.com/newsroom/lasers-for-lidar-gan-systems-osram/
[3] I. A. Prudaev, V. L. Oleinik, T. E. Smirnova, V. V. Kopyev, M. G. Verkholetov, E. V. Balzovsky, and O. P. Tolbanov, IEEE Trans. Electron Dev. 65, 3339 (2018).
[4] S. N. Vainshtein, V. S. Yuferev, J. T. Kostamovaara, M. M. Kulagina, and H. T. Moilanen, IEEE Trans. Electron Devices, vol. 57, no. 4, pp. 733–741, Apr. 2010.

Liquid crystals electro-optical modulator with conducting layers modified by carbon nanotubes

A S Toikka[1], **N V Kamanina**[1,2]
[1]Department of Photonics, St. Petersburg Electrotechnical University ("LETI"), 197376 St. Petersburg, Russia
[2]Lab for Photophysics of media with nanoobjects Vavilov State Optical Institute, 199053 St. Petersburg, Russia

Abstract. Due to their unique properties and scalable technology, optical devices based on the liquid crystals are widely used in industry. In optoelectronics, an LC is used to design the optical limiters, switches, and spatial-time light modulators. Response time, electrical consumption and optical transmittance are the most important parameters of an electro-optical modulator. Temporal parameters substantially depends on the level of the applied supply voltage and on the number of layers used in the structure of the LC device. In this paper, it is proposed to compare the reflection loss level of samples with pure ITO and samples with ITO conducting coating modified by carbon nanotubes (CNTs).

1. Introduction

The operation of the electro-optical modulator is based on the birefringence effect. Under external exposure, for example, when an electric field is applied, the LC molecules begin to orient along it, since they have anisotropy of the refractive index. Therefore, the phase difference between the two components is formed, the plane of polarization of the resulting beam is changed, after it modified wave from the LC cell passes through the analyzer. When switching the parameters of the control voltage, it is possible to control the phase shift, as a result, intensity of the modulated signal by analyzer is changing. Structurally, the LC cell consists of an LC mesophase, two conductive coatings (ITO), two orienting layers, and also two quartz or glass substrates. Materials based on polyimide, polyvinyl alcohol, lecithin, and other are used as orienting coatings. These layers have high electrical resistance, many times higher than the resistance of the active LC layer, which is a problem because it is necessary to work with higher voltage values. ITO coatings modified with CNTs simultaneously performs contact and orienting functions, as a result, it isn't necessary to use high resistive orienting layers [1]. In this work, we continued research aimed at studying these nanostructured ITO coatings taking into account reflection losses.

2. Materials and methods

To modify the conducting ITO coating by the CNTs, we used a laser-oriented deposition (LOD) system based on a CO_2 laser (λ = 10.6 μm), which operated in continuous regime with P= 30 W and a beam diameter of 5 mm. The beam moved at a speed of 1-3 $cm \times s^{-1}$ during surface processing. To orient CNTs in the deposition process, an electric field in the range of 100-600 $V \times cm^{-1}$ was used. To avoid chemical interaction with the media, the process took place in a vacuum chamber. This approach, in contrast to the widely used CVD and PVD methods, has the advantage of not requiring a

large amount of substance, and also ensures the purity of the deposited material. The difference between the samples is in the conductive layers. First group has pure ITO films, samples of the second group have the ITO + CNT modification. Notice that the sizes of CNTs with a refractive index of 1.1 are of the order of ten nanometers, and the average ITO film thickness is 0.1 μm. During their interaction, a covalent bond is formed and the optical properties of the conductive layer change significantly [2]. Additionally, the obtained surface topography of the structured ITO contact was investigated by Solver Next AFM.

3. Results

For LC cells, there are two main types of losses: reflection (Fresnel) and absorption (Bouguer-Lambert-Beer). We limit ourselves to Fresnel reflection losses. Nevertheless, the resulting transmission for j interfaces can be divided into the Fresnel ($T_{Fr,total}$) and Bouguer-Lambert-Beer ($T_{BLB,total}$) components:

$$T_{total} = \left[\prod_{i=1}^{j-1} \frac{4n_i n_{i+1}}{(n_i+n_{i+1})^2}\right] \cdot exp\left[-\sum_{i=1}^{j-1} k_{i+1}(\omega) L_{i+1}\right] = T_{Fr,total} \cdot T_{BLB,total} \quad (1)$$

Where n_i, n_{i+1} — refractive and absorption $k_{\lambda,i}$ indices of the respective medias; L_i — medium length. For conductive coatings, a significant dispersion of the refractive index is observed, which affects the spectral dependence of the Fresnel transmission of the LC cell.

Table 1. Transmittance estimation (using the Fresnel losses) for 2 types of the samples

Wavelenght, nm	Pure ITO		ITO+CNTs	
	Refractive index	Total transmittance, %	Refractive index	Total transmittance, %
340	2.10	84.71	1.75	91.46
370	2.31	79.31	1.92	88.69
400	2.03	86.36	1.67	92.29
500	1.40	91.80	1.40	91.80
600	1.42	92.05	1.42	92.05
720	1.49	92.63	1.51	92.71

The resulting transmission, using Fresnel losses taken into account, for the LC cell was obtained from the calculation that n_{air}=1, n_{quartz}=1.46, n_{LC}=1.65. The dispersion of the refractive indices in the considered wavelength range is negligible. Notice that in the violet-blue region of the visible spectrum, the Fresnel transmission for samples with a modified ITO coating is several percent higher. This is due to the fact that CNTs affect the optical properties of the conductive coating via covalent bonding formation, which allows them to be better conformed to the LC mesophase. The procedure proposed leads to decrease significantly the temporal parameters of the current LC up to 1 ms and less.

4. Acknowledgments

Authors would like to thank their colleagues from the Lab for Photophysics of media with nanoobjects for the useful discussions. This study was supported by Vavilov State Optical Institute topic “LC-nanoWS_2”.

References

[1] Toikka A, Kamanina N. International conference on radiation applications (RAP 2019) p.63
[2] Kamanina N.V., Kukharchik A.A., Kuzhakov P.V., Zubtcova Yu.A., Stepanov R.O., Baryshnikov N.V. Liquid crystals and their practical applications. 2015. vol. 15, № 3. p. 109–118

Cathodoluminescence of a multi quantum well heterostructure based on a CdS/ZnSe type-II

M R Butaev[1,2], V I Kozlovsky[1,2], Y K Skasyrsky[2]
[1]National Research Nuclear University «MEPhI», Kashirskoe highway 31, 115409 Moscow, Russia
[2]P.N. Lebedev Physical institute, 53 Leninsky pr., 119991, Moscow, Russia

Abstract. In this work, we studied multi quantum well (MQW) heterostructures based on CdS/ZnSe with discontinuities of zones of the type-II. Laser structures were studied by cathodoluminescence (CL), atomic force microscopy (AFM) and scanning spreading resistance microscopy (SSRM), X-ray diffraction and luminescent microscopy (LM). Here we report one measurement result obtained by the method of low-temperature CL, which is a universal method for rapid diagnostics of any laser structures, in particular A2B6 compounds when working out the technology of their growth. The investigated heterostructures are supposed to be used in semiconductor lasers with longitudinal optical pumping. The paper will also present preliminary results obtained using this heterostructure in a laser with a microresonator and longitudinal optical pumping by a nitrogen laser radiation (337nm). In the future, it is planned to create a semiconductor disk laser (SDL) based on such structures, which is the ultimate goal of the authors of this work.

1. Introduction

The intensive development of optical-pumped SDL is associated with the ability to generate high-power radiation at high beam quality with diffraction divergence in a wide spectral range of wavelengths [1]. The intracavity generation of the second harmonic in such lasers using A2B6 compounds makes it relatively easy to master the actual average ultraviolet range of the spectrum (~240-280 nm). We are currently investigating the possibility of using a heterostructure CdS/ZnSe type-II in SDL. Due to the close refractive indices of the layers of this periodic structure, this heterostructure does not have the effect of displacing the mode beyond the band gap of the photon crystal and from the center of the gain line, which is the main advantage of this heterostructure. Another interest in this heterostructure lies in the small internal absorption during inhomogeneous pumping of QWs, which is related to the peculiarity of the zone diagram of this heterostructure. However, it should be noted that this heterostructure refers to heterostructures with discontinuities of zones of the second type, which leads to spatial separation of the charge carriers generated by pumping, which in turn reduces the rate of radiative recombination and can lead to an increase in the generation threshold in the laser.

2. Experiment

In this work, structures with 10 ZnSe/CdS/ZnSe QWs separated by ZnS_xSe_{1-x} barriers were grown by metal-organic vapor phase epitaxy on GaAs substrate. The thicknesses of the ZnSe and CdS layers varied depending on the desired wavelength available based on this heterostructure. The ZnS_xSe_{1-x} barrier layers had a thickness of about 90 nm. The period of the heterostructure has a thickness of about 100 nm, which is chosen from the condition of resonant periodic gain. Elastic stresses on QWs were compensated by an increase in the composition of sulfur in the barriers. The total thickness of heterostructures with 10 QWs is about 1.2 μm.

3. Experimental results and discussion

Figure 1 shows the spectra of low-temperature CL (T<14 K) of one of the grown structures containing 10 QW in the different excitation depths. The coincidence of the maxima of the emission spectra indicates that all the QWs are almost identical. This in turn means that these heterostructures are less susceptible to solid-state diffusion at epitaxial growth temperatures in contrast to the previously studied Zn(Cd)Se/Zn(Mg)SSe type heterostructures [2, 3], which is associated with stronger sulfur chemical bonds. Based on this heterostructure, firstly we realized a semiconductor laser emitting in the green region of the spectrum both during longitudinal pumping of a microresonator and transverse pumping with a nitrogen laser emission [4]. The conducted research and the obtained results indicate that, despite the discontinuities of zones of the second type, the studied heterostructure is promising for green-band semiconductor lasers with optical pumping.

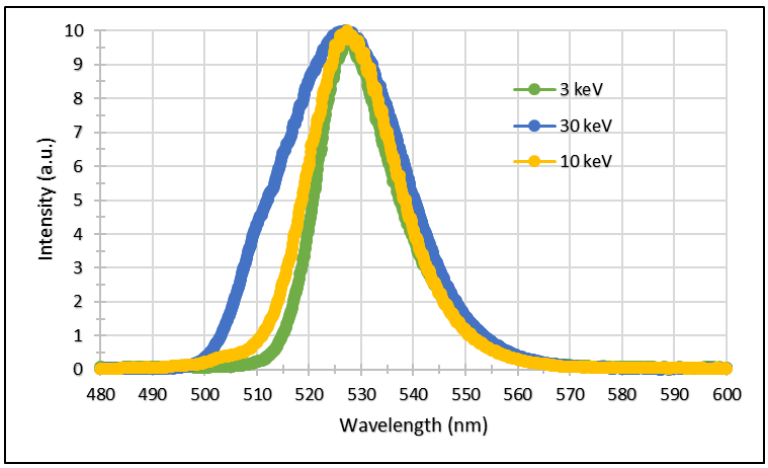

Figure 1. Spectra of the CL of the structure at low temperature (T <14 K) and different excitation depths

4. Acknowledgments

Authors thank V.P. Martovitsky for the X-ray diffraction analysis of the grown structures and P.I. Kuznetsov for his advice on metal-organic vapour phase epitaxy.

References

[1] Okhotnikov O.G. Semiconductor Disk Lasers: Physics and Technology. (Weinheim: Wiley-VCH, 2010).

[2] Ivanov S.V., Sorokin S.V. and Sedova I.V. Molecular Beam Epitaxy of Wide Gap II-VI Laser Heterostructures, in «Molecular Beam Epitaxy», (Elsevier Inc., 25, 571 (2018)).

[3] V I Kozlovsky et al. Quantum electronics, 42(7), 583 (2012).

[4] M R Butaev, V I Kozlovsky, Y K Skasyrsky Optically pumped semiconductor laser based on a CdS/ZnSe type-II multi quantum well heterostructure, Quantum electronics, (2020) to be published

Optical gain in laser heterostructures with active region based on InGaAs/InGaAlAs superlattice

S S Rochas[1], I I Novikov[1], A V Babichev[1], A G Gladyshev[1], E S Kolodeznyi[1], L Ya Karachinsky[2], Yu K Bobretsova[3], A A Klimov[3], A Yu Egorov[1]
[1]ITMO University, 197101 St Petersburg, Russia
[2]Connector Optics LLC, 194292 St Petersburg, Russia
[3]Ioffe Institute of RAS, 194021 St Petersburg, Russia

Abstract. Two laser heterostructures with active region based on seven InGaAs quantum wells and active region based on InGaAs/InGaAlAs superlattice were grown on InP substrates by molecular beam epitaxy. Both active regions were designed for vertical-cavity surface-emitting lasers of 1535-1565 nm spectral range and had total thickness about 80-90 nm. Optical characteristics of stripe lasers fabricated from grown laser heterostructures were studied and compared.

Keywords: molecular beam epitaxy, vertical-cavity surface-emitting laser, heterostructure, quantum well, superlattice

1. Introduction

Strained quantum wells (QWs) are typically used in vertical-cavity surface-emitting lasers (VCSELs) operating in the 1535-1565 nm spectral range to increase the differential optical gain and, as a result, to increase a frequency of small-signal modulation of the VCSELs [1]. Unfortunately, light amplification is absent in potential barriers dividing strained QWs. As an alternative, potential barriers can be used in light amplification in superlattice and modal gain can be increased because of miniband formation in semiconductor layers [2].

2. Experiment

Two laser heterostructures were grown by molecular beam epitaxy (MBE) on InP (100) substrates. Laser heterostructures consisted of an n-type $In_{0.52}Al_{0.48}As$ emitter with a thickness of 1000 nm, an $In_{0.53}Ga_{0.27}Al_{0.2}As$ waveguide with a thickness of 600 nm containing an active region in its center, a p-type $In_{0.52}Al_{0.48}As$ emitter with a thickness of 1500 nm, and a contact layer made of p-type $In_{0.53}Ga_{0.47}As$ with a thickness of 200 nm. Active region of heterostructure H1 consisted of 7 strained $In_{0.74}Ga_{0.26}As$ QWs sandwiched between $In_{0.53}Ga_{0.27}Al_{0.2}As$ barriers [3]. Active region of heterostructure H2 consisted of 29 period $In_{0.60}Ga_{0.40}As/In_{0.52}Ga_{0.27}Al_{0.21}As$ superlattice. Both laser heterostructures were used for 100-um wide stripe laser diodes fabrication.

Fabricated lasers were studied by electroluminescence technique. It was shown that the active region of heterostructure H2 demonstrates a greater gain at equal values of the pump current density compared to the active region of heterostructure H1. For example, when the pump current density is 3000 A/cm^2, which is typical value for the VCSELs lasing threshold, the gain in the heterostructure H2 is 49 cm^{-1}, whereas the heterostructure H1 demonstrates only 33 cm^{-1}, which is about 1.5 times lower. Thus, the obtained results suggest that replacing the active region of VCSELs based on 7 QW

with an active region based on the short-period InGaAs/InGaAlAs superlattice should improve the performance of VCSELs and can reduce the threshold current and increase the frequency of small signal modulation of the VCSELs [4].

Obtained results can be used in designing of compact active regions for VCSELs application.

3. Acknowledgments
This work was supported by the Ministry of Science and Higher Education of Russian Federation, research project no. 2019-1442.

References
[1] M. Ortsiefer et al., *Proc. SPIE* **8276**, 82760A (2012)
[2] A.V. Babichev et al., RF Patent No. 188629 (2019)
[3] E. S. Kolodeznyi et. al. *Opt. Spectrosc*. **125,** 238 (2018)
[4] A. V. Babichev et al., *IEEE J. Quantum Electron*. **53**(6), 1 (2017)

Peculiarities of Manufacturing Technology and Reliability Study of the 808-nm QCW Laser Diode Arrays

E M Filonenko, A V Fomin, E V Smirnov, V V Ivanov, E M Gafurov
FSUE «RFNC-VNIITF named after Academ. E.I. Zababakhin», 456770, Snezhinsk, Russia

Abstract. This work describes design engineering and manufacturing technology used for 808-nm high power quasi continuous wave (QCW) laser diode arrays (LDAs). An optimum composition for the AuSn thin-film solder is selected based on the study and the developed soldering method used to solder the LDAs. Reliability of the manufactured emitters is estimated.

1. Introduction

Innovative solutions in high power semiconductor laser emitters with a spectral range of 790-810 nm offer new potential applications for optical pumping of various diode-pumped solid-state lasers [1]. Wide investigations, focused on the design engineering and the manufacturing technology development for laser emitters based on LDAs, were carried out [2, 3], as part of the process to establish and ramp up domestic manufacturing of diode-pumped solid-state lasers.

2. Results and Discussion

The obtained technological solutions were used to manufacture the LDAs, which are comparable to the world analogues, in terms of their quality (Fig.1).

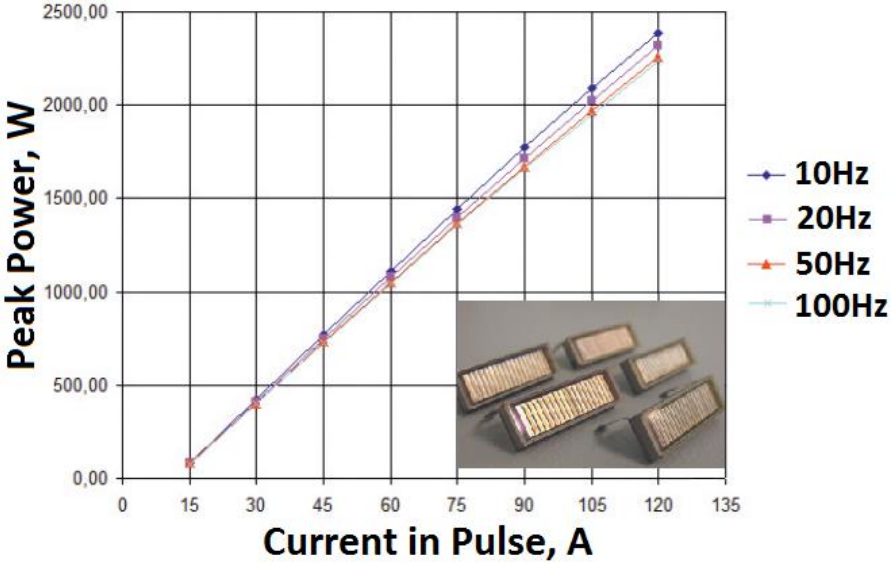

Figure 1. Characteristics of manufactured QCW laser diode arrays.

The engineered LDA design is distinguished by passive heatsinks which are intended for mounting laser bars. The laser bars are mounted as a set of series-connected array elements – laser submodules. At the same time, the materials and the method used to solder the laser bars to the heatsinks were very important from the standpoint of determining long-term stability of the LDAs output characteristics, and as a consequence of this, their reliability. Results of the study and the developed soldering method allowed us to conclude that, the Au(80)Sn(20) solder with the total thickness of 5-7 μm obtained by electron-beam evaporation of alternating thin tin and gold layers, ensure reproducible quality of the soldering due to sufficient wetting of the laser bars metallization by the solder [4] (Fig.2).

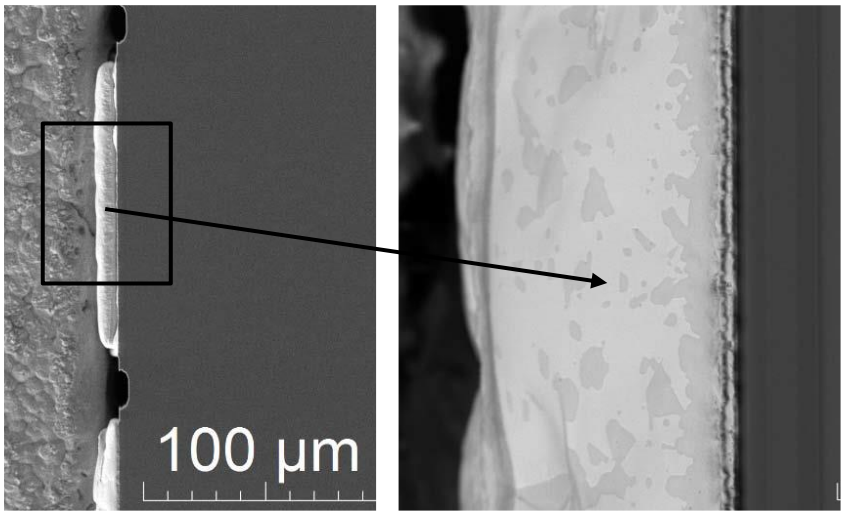

Figure 2. Backscattered electron mode image of the solder joint between the laser bar and the heatsink, with the surfaces sufficiently wet by the solder.

According to the results of the accelerated ageing tests performed to study the degradation rate of high power 808-nm QCW LDAs, in terms of its dependence on the laser-emitter heatset temperature, lifetime of the manufactured emitters in case of nominal operating mode exceeds 10^9 shots.

References

[1] Berk Y. et al. 2009 *Proc. of SPIE* **7198**
[2] Fomin A.V., Smirnov E.V., Milovidov N.I. 2013 *Pat.2544875 Russia*
[3] Filonenko E.M. et al. 2019 *J. Phys.:Conf. Ser.* **1281** 012017
[4] Fomin A.V., Smirnov E.V., Filonenko E.M. 2019 *Pat. 2691152 Russia*

Investigation of the temperature dependences of the I-V characteristics of selective contacts p-Si/MoO_x and n-Si/LiF/Ta

Maksimova A.A. [1], Baranov A.I. [2], Kudryashov D.A. [2], Gudovskikh A.S. [1,2]
[1]Department of Photonics, Saint Petersburg Electrotechnical University "LETI", St. Petersburg, 197376 Russia
[2]St. Petersburg Academic University, St. Petersburg 194021, Russia

Abstract. Symmetrical p-Si/MoO_x and n-Si/LiF/Ta structures were made. The temperature dependences of I–V characteristics of structures with selective contacts based on molybdenum oxide and lithium fluoride were measured. Different behaviour of the I-V characteristics in the wide temperature range up to liquid nitrogen for the structures was shown.

1. Introduction

Currently, there is growing interest in the use of renewable energy sources, including solar energy, the main areas of development of which is the development of new configurations of solar cells in order to increase efficiency and reduce cost. The cost of solar cells manufacturing is strongly influenced primarily by the cost of the substrate and energy costs for technological processes. For example, when creating a back metal contact to the most common silicon solar cells, high-temperature aluminium burning is used (T > 600°C).
Recently, there has been a growing interest in systems of materials with selective properties with respect to the transport of charge carriers of a certain sign, in particular, to selective contacts [1, 2]. So, for example, in [3] it was shown that selective contacts based on molybdenum oxide can be successfully used in the solar cells manufacture, where the efficiency reaches 18%. It is known that measurements of the solar cell efficiency are performed at 25 ° C; however, their operation can also be carried out at low temperatures, where the parameters of the band structure of the silicon / selective contact system may change. The aim of this work is to study carrier transport through selective contacts based on molybdenum oxide and lithium fluoride using silicon substrates of various doping levels and types of conductivity over a wide temperature range.

2. Experiment details

Silicon wafers with doping level of 10^{15}-10^{17} cm^{-3} were used as a substrate. Lithium fluoride was deposited on n-Si(100) by thermal evaporation throw metal hard mask with hole diameter of 0.5 and 1 mm. Prior the deposition the silicon wafer was dipped into HF(1:10) to etch silicon oxide layer. Next tantalum film was deposited onto LiF layer by magnetron sputtering to form metal contact without opening the vacuum chamber. On the bottom side of the wafer the same procedure was performed (excluding the hard mask). Thus, a symmetrical structure was obtained (Fig 1).

Molybdenum oxide (VI) was deposited on p-Si(100) by thermal evaporation throw metal hard mask with hole diameter of 0.5 and 1 mm. Prior the deposition the silicon wafer was dipped into HF(1:10) to etch silicon oxide layer. Next aluminium film was deposited onto MoOx layer by magnetron sputtering to form metal contact without opening the vacuum chamber. On the bottom side of the wafer the same procedure was performed (excluding the hard mask). Thus, a symmetrical structure was obtained.

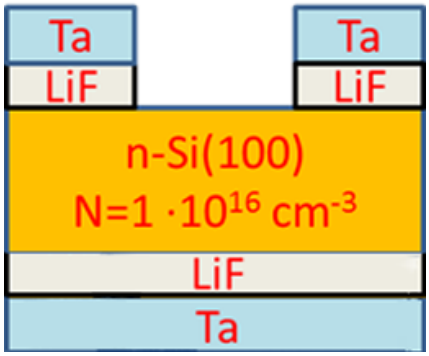

Figure 1. Schematic representation of the n-Si/LiF/Ta structure

3. Results and discussion

Comparative measurements of the current-voltage characteristics showed that with decreasing temperature, the shape of the I–V characteristics changes in the direction of lowering operating currents. In the case of n-Si/LiF/Ta, even at 0°C, the current values decreased by an order of magnitude, while for the p-Si/MoO_x system, the temperature dependence of the I–V characteristic showed a nonlinear character passing through the maximum.

The paper also presents the results of computer simulation of these systems in comparison with the obtained experimental data.

4. Acknowledgments

This work was supported by the Russian Scientific Foundation under Grant No. 18-79-10059.

References

[1] James Bullock et al. // Applied Physics Letters 105, 232109 (2014)
[2] James Bullock et. al. // Adv. Energy Mater. 2016, 1600241
[3] C. Battaglia et. al. // Applied Physics Letters 104 (11), 113902 (2014)

Influence of PEDOT:PSS morphology on performance of bulk heterojunction solar cells

S M Loganchuk[1], A N Yatsenko[1], A V Varnavskaya[1], L G Miroshnichenko[1], S N Chebotarev[1], V A Irkha[1]

[1]Department of Physics and Photonics, Platov South-Russian State Polytechnical University (NPI), Novocherkassk 346421, Russia

Abstract. Influence of morphology of poly(3,4-ethylenedioxythiophene) polystyrene sulfonate (PEDOT:PSS) layer on performance of bulk heterojunction (BHJ) organic solar cells is analysed. Morphology depends on next technological factors: dispersity of PEDOT:PSS solution, substrate treatment, drying, PEDOT:PSS treatment. It is shown that samples with layer roughness less 10 nm have the best performance. Layer roughness was studied by atomic force microscopy (AFM).

1. Introduction

In organic solar cells (OSCs) poly(3,4-ethylenedioxythiophene):polystyrene sulfonate (PEDOT:PSS) is intermediate layer between anode contact made of indium tin-oxide (ITO) and active layer. As the active layer, the blend of poly(3-hexylthiophene) (P3HT) and [6,6]-phenyl-C61-butyric acid methyl ester (PCBM) was used in experiment. PEDOT:PSS reduce the potential barrier during hole injection and provide ohmic contact between anode and active layer [1]. Influence of PEDOT:PSS morphology on performance of OSCs is shown in this paper.

2. Experimental

Glass substrates with size 2.5x2.5 cm and ITO layer with thickness of 150 nm were sonicated in surfactant solution for 15 minutes at 70 °C. After sonication they were washed in deionized water and treated in acetone at ambient temperature. The next steps of preparing substrates were sonication in isopropyl alcohol (IPA) at 65 °C and drying for 10 minutes at 140 °C with further ultraviolet-ozone (UV-Ozone) treatment for 30 minutes.

PEDOT:PSS was spin coated at 2500 rpm. Layer thickness was 80 nm. For better uniformity PEDOT:PSS were treated by ultrasonic disperser and filtered by syringe polytetrafluoroethylene (PTFE) filters.

Blend P3HT:PCBM (concentration 20 mg $\cdot mL^{-1}$, weight ratio 1:1) was prepared in the glove box at nitrogen atmosphere. It was soluted in chlorobenzene and spin coated for 2 minutes at 1000 rpm with further drying for 15 min at 140 °C. The layer thickness was 100 nm.

Aluminum electrode with thickness of 100 nm was deposit in the thermal evaporation chamber.

PEDOT:PSS morphology was studied by nondestructive [2] atomic force microscopy (AFM). For excluding the influence of AFM on OSCs performance, two samples were fabricated with PEDOT:PSS, which was spin coated for each sample in the same way. Before next technological steps the AFM was made on one of them. If performance difference of both samples was more than 10%, these samples were discarded and the results were not used for analysis.

3. Results and discussion

Experiments shows that PEDOT:PSS layer morphology significantly depends on dispersion of solution, as well as substrate preparing, drying and solution treatment. Optimization of these processes allows to reach repeatable PEDOT:PSS layer uniformity with roughness less than 10 nm, that is shown on Fig. 1a. J-V curves of such structure are shown on Fig.2 (blue curve). It is visible that this structure has the best performance.

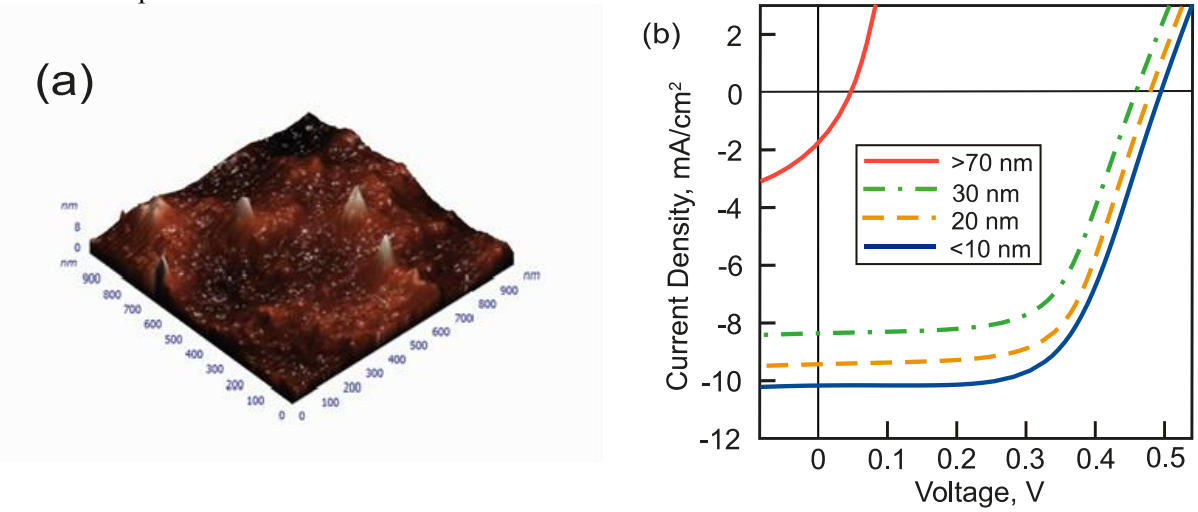

Figure 1 (a,b) (a) AFM-image of PEDOT:PSS layer with roughness less 10 nm **(b)** J-V curves of OSCs with different roughness

J-V curves of devices with PEDOT:PSS roughness 20 nm (orange dashed curve) and 30 nm (green dash-dotted curve) are shown on Fig 1b. It is clearly seen that roughness increasing provides monotonically but not harsh decreasing of OSCs performance. Roughness increasing is due to complicated chain-like chemical structure of PEDOT and PSS molecules. It makes dense packing of molecules in uniform layer difficult.

Another reason for nonuniform PEDOT:PSS layer is large particle agglomeration from aqueous solution. Hydrophobicity of PEDOT is due to this agglomeration. Because of that reason roughness of PEDOT:PSS layer can be 70 nm and more. OSCs with such structure contain many vertical conductive channels and as a consequence leakage currents. On J-V curve this case is shown on Fig 1b (red curve). Open circuit voltage is significantly decreased and current density-voltage characteristic becomes linear.

4. Conclusions

PEDOT:PSS layer morphology significantly affects on performance of OSCs. The best performance is observed with roughness less 10 nm. Performance becomes worse in the values of roughness 10-30 nm. Further increase of roughness make performance much worse because of particle agglomeration with particles size more than 70 nm.

References

[1] Tromholt T and Krebs F C 2015 Polymers, Nanomaterials, and Organic Photovoltaic Devices. In Nanomaterials, Polymers, and Devices, E.S. Kong (Ed.) (Hoboken: John Wiley & Sons, Inc) p 319-340

[2] Horii T, Hikawa H, Katsunuma M, Okuzaki H 2018 Synthesis of highly conductive PEDOT:PSS and correlation with hierarchical structure Polymer **140** 33-38

Optical switching in multilayer structures based on $Ge_2Sb_2Te_5$

N M Tolkach[1,2], N V Vishnyakov[2], P I Lazarenko[1], A A Sherchenkov[1], A U Sudakova[2], D R Nazimov[2]
[1]National Research University of Electronic Technology, Zelenograd 124498, Russia
[2]Ryazan State Radio Engineering University, Ryazan 390005, Russia

Abstract. In this work, we have studied the phase switching in structures based on the $Ge_2Sb_2Te_5$ (GST) composition and their optical parameters of reflectivity and transmissivity at 1550 nm wavelength after exposure to the pulse of 403 nm nanosecond laser. We investigated 24 nm *GST* single-layer structure and found large optical losses due to the reflection and transmission at 1550 nm radiation. To achieve the least optical losses, we added additional SiO_2, Si and Si_3N_4 layers to the structure. This allowed reducing optical losses up to 5% for absorption and 4% for undesirable reflection with the amorphous GST layer, and 16% for absorption and 5% for undesirable transmittance with the crystalline GST layer.

1. Introduction

Currently, systems of integrated optics are actively developing. Their widespread use is limited by high energy consumption, low switching speed, sufficiently large sizes, large-signal delays, double-conversion of information from optical to electric signals and back. The chalcogenide glassy semiconductors of the GST composition have a reversible, fast, and low-energy phase transitions between amorphous and crystalline states with significantly different complex refractive index values [1]. The application of these GST properties in photonic multilayer structures makes it possible to efficiently deflect an optical signal and switch it in predetermined directions. So, in this work, we investigated changes in the optical properties of reflectivity and transmissivity in multilayer optical structures after phase switching of the GST layer from the amorphous to the crystalline state.

2. Theory and experiment

For the normal incidence of an electromagnetic wave, reflectivity $\Re$ and transmissivity $\Im$ of a multilayer structure are determined by the following recurrence Airy relations:

$$\Re = \left| r_{m-1,N+1} \right|^2, \qquad \Im = \left| \tau_{m-1,N+1} \right|^2 n_{N+1} \Big/ n_{m-1},$$

$$r_{m-1,N+1} = \frac{r_{m-1,m} + r_{m,N+1} \cdot e^{i\beta_m}}{1 + r_{m-1,m} \cdot r_{m,N+1} \cdot e^{i\beta_m}}, \qquad \tau_{m-1,N+1} = \frac{\tau_{m-1,m} \cdot \tau_{m,N+1} \cdot e^{i\beta_m}}{1 + r_{m-1,m} \cdot r_{m,N+1} \cdot e^{i\beta_m/2}}, \qquad \beta_m = 4\pi \bar{n}_m h_m / \lambda,$$

where $r_{m,N}$ and $\tau_{m,N}$ are reflection and transmission coefficients, starting with the medium *m-1* and ending with the medium *N+1*; *m, N* are layer numbers ($m < N$); $\bar{n}_m$ is complex refractive index of the medium material *m; h* is layer thickness of the medium material *m;* λ is vacuum wavelength; $r_{m-1,m}$, $r_{m,m+1}$ ... $r_{N-1,N}$, $r_{N,N+1}$ and $\tau_{m-1,m}$, $\tau_{m,m+1}$ ... $\tau_{N-1,N}$, $\tau_{N,N+1}$ are the Fresnel reflection and transmission coefficients, respectively, for adjacent mediums. We performed modeling of multilayer structures, and selected materials and layer thicknesses in such a way that after the phase switching of the GST layer

from the amorphous to the crystalline state, the multilayer structure transmitted or reflected radiation of 1550 nm with the least optical losses. Single-layer 24 nm GST was fabricated by magnetron sputtering. Ellipsometry was used to determine the complex refractive index of layer materials. To change the phase state of the GST layer, we used the nanosecond laser (Cube 403-100C, Coherent) with a 403 nm wavelength. Raman spectroscopy was used to define phase states. Microscopy of the switched areas was performed using the atomic force microscope (Ntegra-Spectra, NT-MDT SIL). Using photodiodes (818-BB-21, 818-BB-30, NewPort), we determined $\Re$ and $\Im$ in switched area.

3. Results and discussion

Modeling of the single-layer *24 nm GST / SiO_2 substrate* structure showed the presence of sufficiently large optical losses for 1550 nm radiation (2% absorption and 22% undesirable reflection for the amorphous GST layer, and 20% absorption and 25% undesirable transmittance for the crystalline GST layer). The measured using photodiodes optical parameters nearly corresponded to the modeled ones. To achieve the least optical losses, we added SiO_2, Si and Si_3N_4 layers to the structure. The resulting structure *100 nm SiO_2 / 110 nm Si / 90 nm SiO_2 / 50 nm GST / SiO_2 wedged substrate / 190 nm Si_3N_4* had the following optical characteristics shown in the Fig. 1(a). As can be seen from the figure, optical losses decreased to 5% for absorption and 4% for undesirable reflection for the amorphous GST layer, and 16% for absorption and 5% for undesirable transmittance for the crystalline GST layer. Reduction of the GST layer thickness to less than 50 nm increases the losses on undesirable transmission in the crystalline state. Enlarging the thickness to greater than 50 nm increases the losses on the absorption at the 1550 nm radiation of the GST layer. Therefore, the optimal option is the GST layer thickness of 50 nm. Absorption optical losses are caused by the fact that GST is not optically transparent at 1550 nm radiation. Full transparency is characterized by a lack of the imaginary component of the complex refractive index $\bar{n}$. For example, Fig. 1(b) shows the case of modeling an ideal multilayer structure with adjusted values of $\bar{n}$. Obtaining of the GST material with such optical parameters is possible using another phase material ($Ge_1Sb_4Te_7$) or modifying impurities (Si, Se).

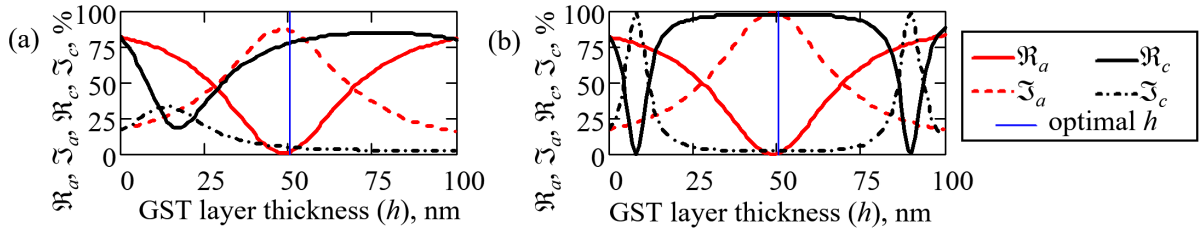

Figure 1(a, b). Dependences of $\Re_a$ and $\Re_c$, $\Im_a$ and $\Im_c$ on the GST layer thickness h in the amorphous and crystalline states at 1550 nm radiation for the modeled 6-layer structure: **(a)** for the real $\bar{n}$ of the GST layer for the amorphous ($\bar{n}$ = 3.8+0.6i) and crystalline ($\bar{n}$ = 6.3+1.2i) states; **(b)** for the unreal $\bar{n}$ of the GST layer for the amorphous ($\bar{n}$ = 3.8) and crystalline ($\bar{n}$ = 9.5) states.

Thus, the model and experimental studies of the multilayer structures based on the GST composition allowed us to select materials, layer thicknesses and reduce optical losses. The construction of complex photonic crystals based on such multilayer structures will make it possible to perform fully optical routing in integrable fiber-optic systems

4. Acknowledgments

The reported study was funded by RFBR according to the research project # 19-37-60023 and used the equipment of Region Centre of probe microscopy of Ryazan State Radio Engineering University named after V.F. Utkin.

References

[1] Wen S, Meng Y, Jiang M & Wang J 2018 *Scientific Reports* **8** 4979

Changing of the dynamic characteristics of the spectral components of the InGaN-based LEDs spectrum during current tests

I V Frolov[1,2]**, O A Radaev**[1]**, V A Sergeev**[1,2]
[1]Ulyanovsk Branch of Kotel'nikov Institute of Radio-Engineering and Electronics of Russian Academy of Sciences, Ulyanovsk 432071, Russia
[2]Ulyanovsk State Technical University, Ulyanovsk 432027, Russia

Abstract. The results of research of changes in the dynamic characteristics of various spectral components of the full electroluminescence spectrum of green InGaN-based LEDs during tests under the pulsed current of increased density are presented. It was found that a decrease in the LED radiation power after 200 hours of testing is accompanied by an increase in the 3dB frequency of modulation of electroluminescence, while an increase in the 3dB frequency of the short-wavelength components of the spectrum is greater than the long-wavelength ones. The results obtained indicate that the process of defect formation during testing proceeds more intensively in the areas of the heterostructure with a low In concentration.

Despite the improvement of manufacturing technologies for LEDs based on group III nitrides, changing their electrophysical and optical characteristics during operation remains one of the key problems. A number of studies [1] showed that significant changes in the characteristics of LEDs occur at the run-in stage in the first 100 – 1000 hours of operation at rated direct current and are usually associated with processes in the heterostructure, which cause, inter alia, changes in the parameters of the radiative and non-radiative recombination and, as a consequence, a change in the dynamic characteristics of electroluminescence. Of practical interest is the investigation of the possibility of reducing the duration of the run-in stage of LEDs by conducting their accelerated tests. The purpose of the work was to research changes in the 3dB frequency of various spectral components of the electroluminescence spectrum of InGaN-based LEDs when tested under the pulsed current of increased density.

We studied commercial green InGaN-based LEDs produced by Cree with a central wavelength of the emission spectrum of 525 nm and a rated operating current of 20 mA. LEDs were tested at an ambient temperature of 25 °C for 200 h at the following values of pulsed current parameters: amplitude current value is 300 mA, pulse duration is 100 μs, period is 10 ms. The temperature of the active region of the LEDs during testing did not exceed 30 °C.

The 3dB frequency of separate spectral bands of the LED electroluminescence spectrum was measured on a hardware-software complex that included a DG4162 functional generator, an Ocean Optics USB2000+ spectrometer, and a computer with LabView software [2]. The principle of the complex's operation is to measure the LED electroluminescence spectra when the pulse current frequency increases from 1 kHz to f_{3dB}, at which the optical signal level drops 1.19 times relative to the level at the lower modulation frequency. A computer program extracts from the general spectrum the separate components of the spectrum with a step of 1.5 nm, saves their amplitude-frequency characteristics to the text file and calculates the 3dB frequency.

In fig. 1, the solid line shows the characteristic dependence of the 3dB frequency on the electroluminescence wavelength before testing one of the investigated LEDs, measured at a current of 500 μA, which corresponds to the maximum of the external quantum efficiency. The dashed line shows the normalized emission spectrum of the LED. The dependence $f_{3dB}(\lambda)$, which is characteristic of all 15 pieces of LEDs of the studied sample, has a nonmonotonic character. The most significant changes in the power *P* of the optical radiation of the LEDs and the 3 dB frequencies occur in the first 100 hours of accelerated testing. With further testing, the rate of change in performance decreases.

It was determined that an increase in the emission power P is accompanied by a decrease in the 3dB frequency, and a decrease in *P* is accompanied by an increase in f_{3dB}. In fig. 2, the solid line shows the relative change in the 3dB frequency after 100 h of testing the afore-referenced LED. The graph shows that an increase in the 3dB frequency of the short-wavelength components of the emission spectrum is 2–3% more than an increase in the 3 dB frequency of the long-wavelength components. As a result of tests, the LED emission power decreased by 10%, and the shape of the spectrum practically unchanged.

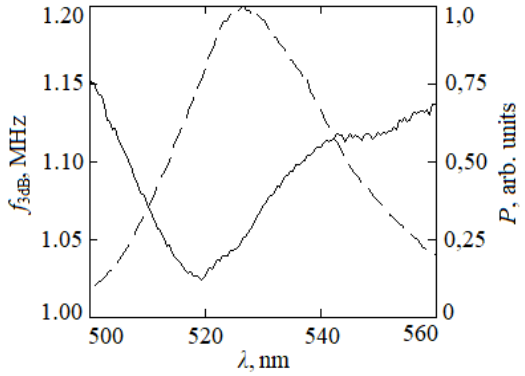

Figure 1. The dependence of the 3dB frequency on the emission wavelength, measured at a current of 500 μA

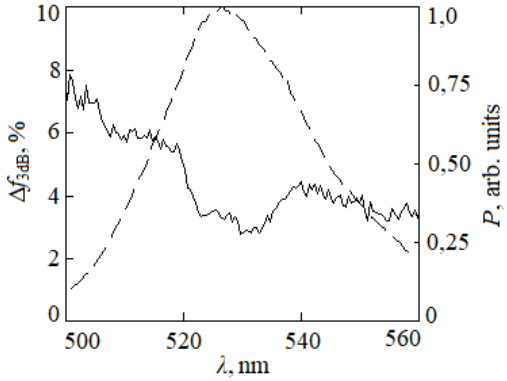

Figure 2. The relative change of the 3dB frequency after 100 hours of testing

An increase in the 3dB frequency indicates a decrease of the charge carriers lifetime during nonradiative recombination due to an increase in the defects density in the structure [3, 4]. According to the model of the inhomogeneous distribution of the In concentration over the active area of the heterostructure [5], the short-wavelength wing of the emission spectrum is formed by local areas of the heterostructure with a low In concentration, and the long-wavelength wing is formed by local areas with a high In concentration. Thus, the results obtained indicate that the process of defect formation during testing proceeds more intensively in areas of the structure with a reduced In concentration, characterized by large values of the band gap and current density. The results will be used to develop a methods for stabilizing changes of the LEDs characteristics in the first hundreds of hours by reducing the stage of rapid degradation due to accelerated tests under the pulsed current of increased density.

The reported study was funded by RFBR and Ulyanovsk region, project number 19-47-730002.

[1] Seong T-Y, Han J, Amano H, Morkoç 2017 H *III-Nitride Based Light Emitting Diodes and Applications* (Springer Nature Singapore Pte Ltd.)
[2] Radaev O A, Sergeev V A, Frolov I V 2019 *Measurement Techniques*, **62 (8)**, 708
[3] Schubert E F 2006 *Light Emitting Diodes* (Cambridge University Press)
[4] Sergeev V A, Frolov I V, Shirokov A A, Radaev O A, 2018 *Semiconductors*, **52 (15)**, 1976
[5] Manyakhin F I 2018 *Physics of Semiconductor Devices* **52**, 359

High-efficient InGaAs metamorphic laser power converters with distributed Bragg reflector for wavelengths 1-1.1 μkm

N A Kalyuzhnyy[1], V M Emelyanov[1], S A Mintairov[1], M V Nahimovich[1], R A Salii[1], M Z Shvarts[1]
[1] Photovoltaic Laboratory, Ioffe Institute, St. Petersburg 194021, Russia

Abstract. The laser power converters (LPC) for high power monochromatic light, based on metamorphic InGaAs heterostructures and included distributed Bragg reflector (DBR) have been investigated. Such LPCs cover the atmospheric transmission window (λ=1-1.1 μkm) and can be practically used for wireless energy transmission systems. The DBR stabilised high level of LPC quantum efficiency (spectral response) at the $In_{0.18}Ga_{0.82}As$ absorption edge that with combination of maximal operating voltage allowed achieving energy conversion efficiency about 52% at λ = 1.06 μm and 55% at 1.02 μm.

1. Introduction

The laser power converters (LPCs) for the radiation with λ=1–1.1 μm (atmospheric transparency window) are needed for wireless energy transmission systems, for example, for recharge household unmanned aerial vehicles. In our work [1] the $In_{0.23}Ga_{0.77}As$ LPC with efficiency more than 50% (λ=1064 nm) was obtained. The composition of the active region («x»=0.23) allows obtaining a good collection of charge carriers from the base region and a high value of the external quantum efficiency. However from the voltage optimization viewpoint, the indium composition should be reduced more.

2. Experimental details

LPC structures were grown by MOVPE (metal-organic vapour phase epitaxy) and based on InGaAs solid alloys grown over metamorphic buffer on GaAs-n substrates [2]. The composition of $In_xGa_{1-x}As$ active area was varied from x=0.23 to 0.18 in order to increase the operating voltage due to band gap energy increasing.

Based on the refractive indices we obtained earlier [3] for $In_xGa_{1-x}As$ materials with various compositions "x", we calculated the $In_xGa_{1-x}As/In_xAl_{1-x}As$ DBRs centring at wavelengths in the range λ=1-1.1 μm. The main technological difficulty in using DBR is doping of super lattice which includes aluminum-based wide band-gap layers (InAlAs). In case silicon doped DBR, noticeable resistive losses are observed [4], which can be caused by energy barriers near the heteroboundaries, which arise due to discontinuity of valence or conduction bands. We have used tellurium as a shallow donor that allw reducing the series resistance of DBR to five orders of magnitude.

The LPCs were manufactured with size 3×3.4 nm. The LPC *I-V* characteristics were measured at in the two regimes: high-power fiber-guided pulsed laser (λ=1.064 μm) with 1.5 msec pulse duration laser and Xe flash lamp (uniform illumination over sample surface and absence of the overheating at IV curve recording) that allow estimating efficiency of monochromatic radiation conversion in the range λ=1-1.1 μkm.

3. Results and discussion

Fig. 1 a shows a comparison of the V_{oc}-P (open circuit voltage – laser power) dependences for the $In_{0.23}Ga_{0.77}As$ and $In_{0.18}Ga_{0.72}As$ LPCs. The composition of $In_{0.18}Ga_{0.72}As$ is almost boundary for the conversion of radiation with a wavelength of λ = 1064 nm, but still can be used due to Urbach tail [5]. The difference in open circuit voltage for LPCs with these compositions is about 0.067 eV in the all laser power range that correlates with theoretical difference between the $In_{0.23}Ga_{0.77}As$ and $In_{0.18}Ga_{0.72}As$ band gaps (0.0675 eV). It means that the operating voltages for both LPCs are maximal and are determined mainly by band gaps of ternary alloys. The $In_{0.18}Ga_{0.72}As$ LPC with embedded DBR consisting of 12 pairs of $In_xGa_{1-x}As$/ $In_xAl_{1-x}As$ layers allows additionally improved the V_{oc}. It can be explained by the following. The using DBR allow reducing the thickness of $In_xGa_{1-x}As$ active area (base and emitter) two times, because of double optical path of photons in the spectral range where DBR have maximal coefficient of reflection. In this case the operating voltage is determined only by $In_{0.18}Ga_{0.72}As$ band gap. Moreover, DBR improve the external quantum response of LPC practically at the absorption edge. In our case DBR had the maximal reflection in the range λ=1.02-1.06 μkm and as a result the LPC spectral response was stabilised at the high level in this spectral range (Fig.1 b). The high SR in the long wavelength region proves that technological conditions were found under which the negative effects of tellurium (the memory effect and the segregation of large radius atoms [6]) were suppressed.

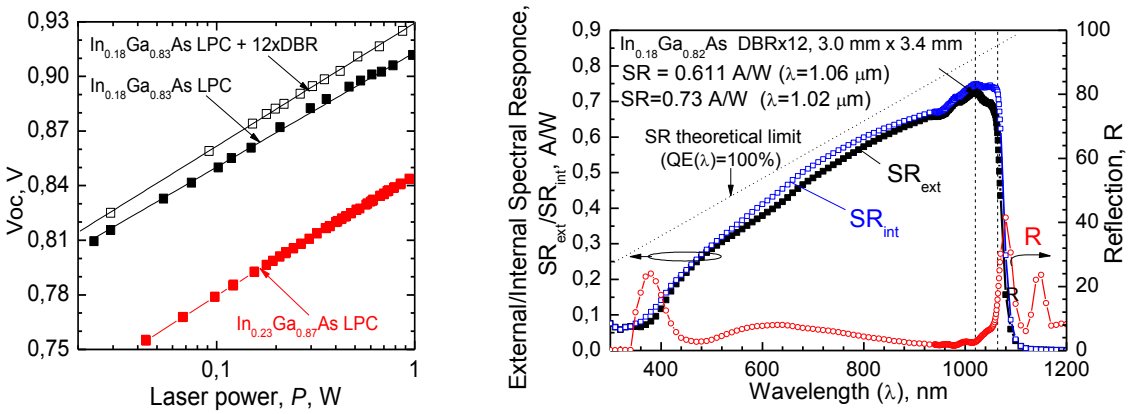

Figure 1. Dependences of the open circuit voltage (V_{oc}) on the laser power radiation (P) for $In_xGa_{1-x}As$ LPCs with different indium composition (a); and the spectral response of $In_{0.18}Ga_{0.72}As$ with DBR consisting of 12 pairs of $In_xGa_{1-x}As$/ $In_xAl_{1-x}As$ layers.

As a result of the voltage increase (due to the minimum concentration of indium in the LPC with $In_{0.18}Ga_{0.72}As$ active region) and the use of InGaAs/InAlAs DBR, which allow stabilized spectral high response at the InGaAs absorption edge, the record efficiency (for such type of LPC) for monochromatic light conversion was achieved: about 52% at λ = 1.06 μm and 55% at 1.02 μm.

Acknowledgements

The work has been supported by the Russian Science Foundation (grant № 17-79-30035).

References

[1] Kalyuzhnyy N A, et al., 2019 *AIP Conf. Proc*, **2149** 050006
[2] Kalyuzhnyy N A, et al. 2017 *Electron. Lett.* **53** 173
[3] Emelyanov V M, et al, 2018 *Opt. Express* **26** A832
[4] Emelyanov V M, et al, 2020 Semiconductors **4** *in press*
[5] T. S. Moss, G. J. Burrell and B. Ellis, 1973 *Semiconductor Opto-Electronics* (Butterworth & Co)
[6] Yu-Min Houng, T. S. Low, 1986 *J. Cryst. Growth* **77** 272

Photoelectric properties of heterostructures based on $InAsSb_x$ solid solutions (0.3 <x <0.35).

R.E. Kunkov, A.A. Klimov, N.M. Lebedeva[1], T.C. Lukhmyrina[1], B.A. Matveev[1], M.A. Remennyi[1,2]

[1]IR Optoelectronics Laboratory, Ioffe Institute RAS, Saint Petersburg 194021, Russia
[2] LLC "IoffeLED", Saint Petersburg 194021, Russia

Abstract. The results of a study of multilayer p-n heterostructures based on $InAsSb_x$ solid solution (0.3 <x <0.35), with a long-wavelength photosensitivity boundary of $\lambda_{0.1}$≈9.5 μm at room temperature are presented. The volt-ampere and spectral characteristics of photosensitivity and electroluminescence were analyzed in the temperature range 80-300 K. It is shown that the photoelectric properties are determined by the diffusion mechanism of current flow, and experimental samples of photodetectors based on them are characterized by a quantum efficiency of Si≥1 A / W.

1. Introduction

InAsSb solid solutions are used to create photodetectors based on structures with homo and hetero p-n junctions, barrier structures with bulk layers and superlattices, photosensitive in the MWIR spectral range, operating in a wide temperature range [1]. Such photodetectors are used in gas analysis instruments, low-temperature high-speed pyrometry and thermal imaging systems.

The use of $InAsSb_x$ solid solution in the composition region x≥0.3 opens up the possibility of using the already developed technological approaches for creating photodiode photodetectors operating in the long-wavelength region of the spectrum λ = 8-14 μm [2]. n this paper, we study the photoelectric properties of p-n heterostructures with a photosensitive $InAsSb_x$ region in the composition range 0.3 <x <0.35 with a long-wavelength photosensitivity boundary $\lambda_{0.1}$≈9.5 μm at room temperature..

2. Experimental results

Epitaxial structures were obtained by LPE on InAs (100) substrates, and contained: N-InAsSb buffer layers with a total thickness of 4 μm, a photosensitive InAsSbX layer (x ≈ 0.35) 2-3 μm thick, a P-InAsSb (P) contact layer, 2 microns thick. Using multi-stage photolithography and plasma-chemical etching, we fabricated "flip-chip" samples with a photosensitive region D = 40, 90, 180, and 270 μm. For research, the samples were mounted on subcrystal boards and docked with immersion lenses made of Ge with a diameter of 3.5 mm. The study of electroluminescence and photoelectric characteristics was carried out using a pumped cryostat in the temperature range 77-350 K and a VERTEX 70v Fourier spectrometer, a HgCdTe (77 K) photodetector and a Keithley SourceMeter 6430 source meter and a LCR E4980A precision meter.

An analysis of the current – voltage characteristics showed that as the temperature decreases from room temperature to 150 K, the characteristic acquires a pronounced diode character, while the temperature dependence of the dark current has an exponential character $J_{sat} \sim 1 / \exp(E_a / kT)$ with an activation energy of E_a = 200 meV close to the band gap of the photosensitive region, which indicates the diffusion mechanism of current flow in the studied temperature range. The dependence of the dark current density on the band gap of the photosensitive region at room temperature, made using data obtained on photodetectors with $InAsSb_x$ photosensitive regions in the composition region x <0.3, has an exponential character $J_{sat} \sim 1 / \exp(h\nu_{0.5} / kT)$ with energy activation close to the band gap of the photosensitive region, which also indicates the diffusion mechanism of current flow and the insignificant contribution of the generation-recombination mechanism to the dark current. An analysis of the current – voltage characteristics depending on the size of the photosensitive region and the modulation frequency shows the absence of a noticeable contribution of surface states to current flow, but may indicate the presence in the dark current, a small (within 10–15%) component associated with carrier generation through deep levels. The photoresponse spectra are characterized by a long-wavelength photosensitivity border $h\nu_{0.5}$,

close to the band gap of the photosensitive region, and the temperature dependence $h\nu_{0.5} = f(T)$ is well approximated by the function $h\nu_{0.5} = 205\text{-}0.6 \times T2 / (T + 500)$, with coefficients corresponding to the coefficients of temperature change in the InSb band gap [3].
A comparison of the experimental data on the long-wavelength photosensitivity boundary and the photosensitive ones calculated along the band gap of the photosensitive region [4] shows the participation of both interband transitions and transitions to acceptor levels in the formation of the photoresponse spectrum, most likely related to doping of the photosensitive Zn region. The short-wavelength photosensitivity boundary is determined by the absorption in the undoped n-InAs substrate, and the shape of the spectrum is characterized by an almost constant value of quantum efficiency. The absolute values of quantum efficiency are 1 A / W at T = 200 K and practically do not change with a further decrease in temperature, which, apparently, is due to reaching its maximum value for a given thickness of the structure. With increasing temperature, the quantum efficiency decreases, which is associated with a decrease in the resistance of the pn junction and the deterioration of the conditions for the efficient separation of carriers.

3. Conclusions

The photoelectric properties of multilayer pn heterostructures with a photosensitive region based on an $InAsSb_x$ solid solution (x = 0.35) with a long-wavelength photosensitivity boundary of $\lambda_{0.1} \approx 9.5$ μm at room temperature were studied, which showed the possibility of creating high-performance photodetectors based on them for the long-wavelength region of the spectrum, the parameters of which are determined diffusion mechanism of current flow in the temperature range 200 ÷ 300 K, and the values of current sensitivity reach more than 1 A / W at temperatures achievable using thermoelectric cooling.

4. References

[1] Rogalsky A, Kopytko M, Martyniok P 2017 Antimonide-based infrared detectors (Bellingham: SPIE press)
[2] N.D. Il'inskaya, S.A. Karandashev, A.A.Lavrov, B.A. Matveev, M.A. Remennyi, N.M. Stus', A.A. Usikova, "Mid-IR $InAs_{0.7}Sb_{0.3}$ ($\lambda_{0.1}$=8.5 μm) bulk photodiodes operating at near room temperature», Physica Status Solidi A: Applications and Materials Science, 2018, 1700694
[3] http://www.matprop.ru/InSb_bandstr#Temperature
[4] Ponomarenko V P 2018 Quantum photosensory, (Moscow: Orion)

The study of turn-on delay in quantum cascade lasers under pulsed electrical pumping with non-zero rise-time

E D Cherotchenko[1], V V Dudelev[1], D A Mikhailov[1], A V Babichev[2], A G Gladyshev[2], I I Novikov[2], A V Lyutetskiy[1], S O Slipchenko[1], N A Pikhtin[1], L Ya Karachinsky[2], A Yu Egorov[3], A N Baranov[4], G S Sokolovskii[1]

[1]Ioffe Institute RAS, Saint Petersburg 194021, Russia
[2]Connector Optics LLC, Saint-Petersburg, Russia
[3]ITMO University, Saint-Petersburg, Russia
[4]IES, University of Montpellier, CNRS, F-34000 Montpellier, France

Abstract. We study the turn-on delay of quantum cascade lasers as a function of the amplitude of pulsed electrical pumping with non-zero rise-time. Although observed QCL dynamics is much slower than the theoretical predictions, our numerical simulations qualitatively agree with experiment. The quantitative discrepancy comes from the difference in the laser parameters.

1. Introduction

Quantum cascade lasers (QCLs) are very attractive for a large variety of cutting-edge applications including free-space communications, gas sensing and hyper-spectral imaging. Adequate understanding of carrier dynamics in QCLs is necessary to reach laser performances perfectly meeting requirements of many applications, from communications to imaging and spectroscopy in general. Considering short intersubband relaxation times [1], well-established theoretical models of the laser dynamics for mid-IR QCLs [2,3] predict figures of 10s picoseconds for the turn-on delay under pulsed pumping with zero rise-time. Such a fast dynamics may be extremely beneficial for many applications.

2. Experiment

In this work, we present the results of our theoretical and experimental investigations of the turn-on delay of QCLs under pulsed pumping with non-zero rise-time. The experimental study of the turn-on delay was carried out on two sets of QCLs emitting at the 8 μm wavelength. The active regions contained 25 and 50 cascades correspondingly [4]. The electrical pumping was 150 ns duration with approximately 20 ns rise-time and 25 kHz repetition frequency. In our measurements the turn-on delay was registered as the time from the moment when pumping reaches the threshold ($t_{threshold}$) to the front edge of the optical pulse. Figure 1 represents the experimental turn-on delay curves.

3. Modelling

To simulate the results, shown in Figure 1 we numerically solved the system of rate equations and basic parameters adopted from Ref. [2]. Rising edge of the pump pulse was taken from the experimental measurements. Simulations of the QCL turn-on dynamics at different pumping amplitudes yield the dependence of the turn-on delay on the normalized pump current density (Figure 2a). Turn-on delay is calculated as the time from the moment when pumping reaches the threshold

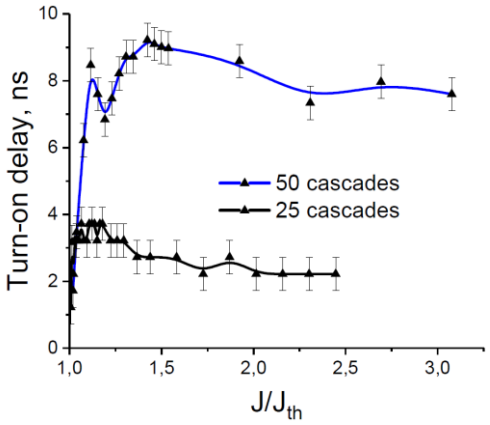

Figure 1. Experimental measurements of the turn-on delay in the two sets of QCL samples

to the laser turn-on time. The last is defined in three different ways: the moment when number of photons reaches 0.1% (black curve), 1% of maximum photon density (blue curve) or as a tangent (red curve in Figure 2a). the definition of $t_{tangent}$ is shown in Figure 2b.

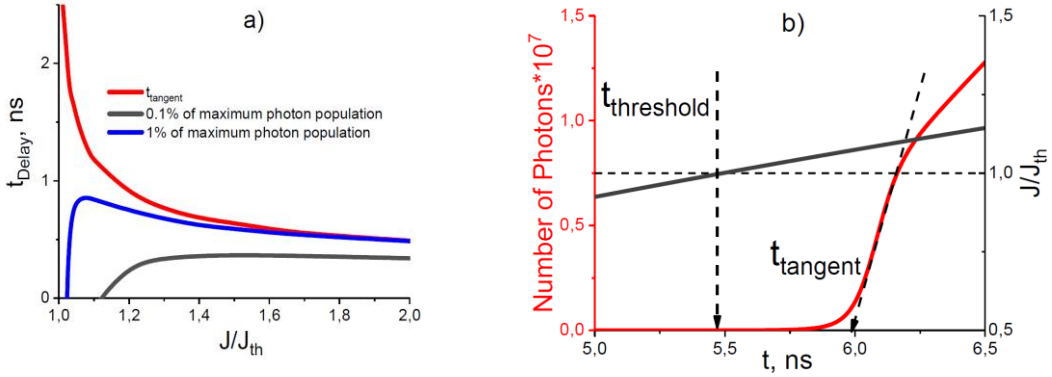

Figure 2. Numerical modelling: a) turn on delay calculated with three different ways: the difference between the threshold and the time, when the photon number reaches 0.1% (grey curve) and 1%(blue curve) of its maximum population and the interval between the threshold and the time $t_{tangent.}$ b) the simulation of photon and pumping dynamics, showing the definition of $t_{tangent}$.

4. Summary

The results of our measurements are shown in Figure 2 and demonstrate qualitative agreement with numerical simulations (blue curve in Figure 1a). However, the quantitative discrepancy between the theory and experiment can hardly be explained only by choice of the structural parameters. We also note that the turn-on delay seems to dramatically increase with the number of cascades in the active region. This effect is not predicted by our simulations.

Acknowledgments

The authors acknowledge the support from the Ministry of Science and Higher education of the Russian Federation (project identifier RFMEFI61619X0111).

References

[1] Choi H et al., 2008 Phys. Rev. Lett. **100** 167401
[2] A.Hamadou, S.Lamari, J. L.Thobel, 2009 J. Appl. Phys. **105** 093116
[3] K.S.C.Yong, K.Haldar, J.F.Webb, 2018 J. Mod. Opt. **65** p.406
[4] V.V. Dudelev, S. N. Losev, V. Yu. Mylnikov et al., 2018 Optics and Spectroscopy 125, pp. 402-404

The study of voltage loss reasons in GaAs solar cells with embedded InGaAs quantum dots

R A Salii[1,2], V V Evstropov[1], S A Mintairov[1], M A Mintairov[1], M V Nakhimovich, M Z Shvarts[1] and N A Kalyuzhnyy[1]

[1] Ioffe Institute, Russia, Polytechnicheskaya str. 26, 194021, St.-Petersburg

[2] E-mail: r.saliy@mail.ioffe.ru

Abstract. In the work the effect of the number of $In_{0.8}Ga_{0.2}As$ stacked quantum dots (QDs) embedded in a single-junction GaAs solar cell (SC) matrix on its photoelectric characteristics has been studied. A series of GaAs SC structures, which differed by a number of embedded QD rows, were grown via organometallic gas-phase epitaxy. By analyzing the electroluminescence spectra and the current–voltage characteristics of the obtained structures, the main reason for the voltage loss in SC with QDs has been established: an increase in recombination through the QD levels with an increase the number of QD rows in the SC matrix.

1. Introduction

Today, one of the factors limiting the efficiency of solar cells (SC) based on the triple-junction GaInP/GaAs/Ge structure is the current mismatch between subcells of such a SC [1]. Recently, an approach that can provide an increase the photogenerated current of the middle GaAs subcell by embedding quantum dot (QD) arrays into its matrix has been actively developed [2]. An increase in the photogenerated current can be achieved due to the absorption of subbandgap photons by a QD array, which will make it possible to achieve the current balance and increase the efficiency of the whole SC structure [3]. However, several studies devoted to the introduction of QDs in a matrix of single-junction GaAs SC showed that, along with an increase in photogenerated current the open-circuit voltage (V_{oc}) loss occurs, which minimize the achieved advantage [4, 5]. The aim of this work is to establish the main reason for V_{oc} loss in GaAs SC with embedded $In_{0.8}Ga_{0.2}As$ QD arrays.

2. Experimental procedure

To study the effect of QD arrays on the photoelectric characteristics of GaAs SC, the organometallic gas-phase epitaxy tecnique have been used to grow a series of samples of single-junction GaAs SC with embedded $In_{0.8}Ga_{0.2}As$ QD arrays. The samples in the series differed in the number of QD rows in the array in a wide range (from 1 to 20 rows). To study the current flow mechanisms in a p-n junction with embedded QDs current-voltage characteristics and electroluminescence (EL) spectra of SC structures were obtained.

3. Results and discussion

The obtained EL spectra (figure 1) demonstrate a noticeable effect of the number of QD rows on the spectrum shape. As the number of QD rows increases, the redistribution of the EL peak intensities occurs, associated with a decrease in the contribution of radiative recombination of the GaAs matrix and an increase in the contribution of the QD array.

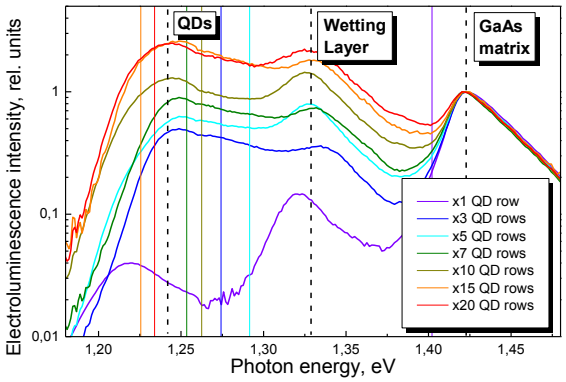

Figure 1. EL spectra for GaAs SCs with different numbers of $In_{0.8}Ga_{0.2}As$ QDs rows, normalized to GaAs matrix (solid curves) and calculated E_a of diffusion current flow mechanism (energies shown as vertical lines).

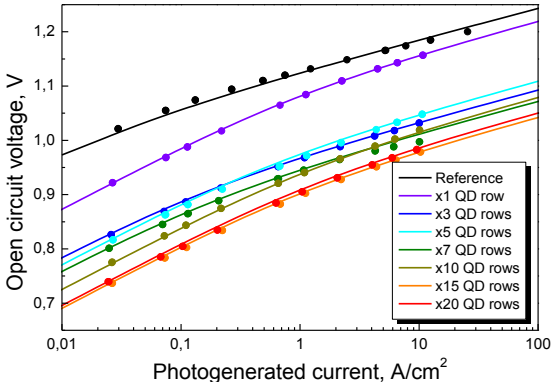

Figure 2. V_{oc}-J_g characteristics for GaAs SCs with different numbers of $In_{0.8}Ga_{0.2}As$ QDs rows and of a reference solar cell (without QDs): symbols – experimental characterisitcs, lines – two diode model approximation.

The dependences of the open circuit voltage (V_{oc}) on the photogenerated current (J_g) demonstrate (figure 2) a voltage loss with an increase in the number of QD rows, which is consistent with the measured EL spectra. It is known that a change in V_{oc} (ΔV_{oc}) indicates a change in the band gap of the material [6]. This is due to the fact that the saturation current J_0, which determines V_{oc}, depends on E_g. In turn, J_0 is determined by the rate of carrier recombination. In p-n junctions with QDs carriers can recombine both in the matrix and in the QDs. Since these objects have different E_g, ΔV_{oc} characterizes which part of the carriers recombines in the matrix and which in the QDs. Thus, in p-n junctions with QDs ΔV_{oc} characterizes the average (E_a) energy of carrier recombination. To calculate ΔV_{oc} we determined the values of the saturation current J_0 for each of the samples by approximating the V_{oc}-J_g dependences using the two-diode model. The calculation has been made for the diffusion component of the photogenerated current. Using the obtained values E_a were found as the difference between the E_g of the matrix and ΔV_{oc}. In figure 1 these values marked as vertical lines. It is seen that with an increase in the number of QD rows E_a shifts to the low-energy region, i.e. into the QD absorption region. Thus, the obtained data show that the main mechanism affecting the V_{oc} loss in GaAs SC with QD arrays is an increase in recombination through QD levels caused by an increase in the number of QD rows in the array. The result should be taken into account for the structural design of both single and multi-junction solar cells.

Acknowledgements
The work has been supported by the Russian Science Foundation (Grant №17-72-20146).

References

[1] Algora C. and Rey-Stolle I. 2016 *Handbook of concentrator photovoltaic technology* (John Wiley & Sons, The Atrium, Southern Gate, Chichester, West Sussex, UK)
[2] Luque A and Marti A 1997 *Phys. Rev. Lett.* **78** pp 5014–5017
[3] Kerestes C., Polly S., Forbes D., Bailey C., Podell A., Spann J., Patel P., Richards B., Sharps P. and Hubbard S., 2016 *Progr. Photovolt.* **22** 1172
[4] Sogabe T., Shen Q., Yamaguchi K., 2016 *J. Photon Energy* **6**(4) 040901
[5] López N., Martí A., Luque A., Stanley C., Farmer C., Diaz P. 2007 *Journal of Solar Energy Engineering* **129** p 319
[6] King R. R. et. al. 2011 *Prog. Photovolt: Res. Appl.* **19**

The influence of quantum well geometry on wavelength of AlInGaAs/InP laser diodes

A Chelny[1], Yu Akhmerov[1], A Savchuk[1,2], A Zharkova[1,2], O Rabinovich[2], M Mezhenny[1], , A Aluyev[1], M Zakusov[1], M Orlova[2], V Murashev[2], S Didenko[2]

[1]Optron JSC, Moscow 105187, Russia
[2]National university of science and technology "MISiS" Moscow, 119049, Russian Federation

Abstract. The AlGaInAs structure was successfully grown on the InP substrate by MOCVD method. The active region was studied by Auger spectroscopy. The thicknesses and compositions of the quantum wells did not coincide with the theoretical ones. The mathematical model which correlates with investigation results was proposed.

AlGaInAs/InP laser structure was grown by MOCVD. Active region composition and thickness were designed by a mathematical model describing the energy levels distribution in finite square well [1]. Based on the laser structure, laser diodes with ridge geometry were manufactured. In the Figure 1 it is shown the laser structure draft

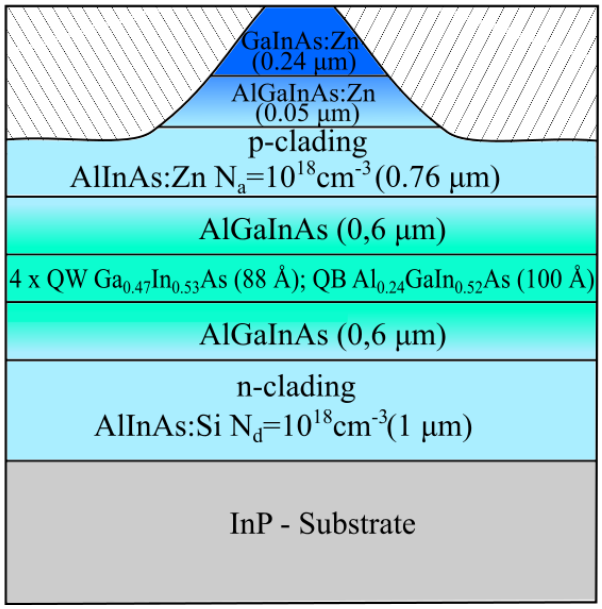

Figure 1. Laser structure.

Electroluminescence measurement showed that the wavelength does not correspond to the calculated one, and several emission peaks were also visible on the spectrum. One of the most likely explanations for this result may be the heterogeneity of the quantum wells geometry [2, 3], which arises due to transient process that occurs because of switching gas flows during the growth of the structure. The main influence of transient process [4] in case of this structure is blurring of aluminum concentration profile in barriers and wells, as a result the quantum wells geometry could spread from finite square well [5].

To determine the effect of transient process on the geometry of quantum wells, an active region was studied. The composition of the active region of the sample was studied using an Auger spectrometer; sample was prepared by oblique etching.

The thicknesses and compositions of the quantum wells did not coincide with the theoretical ones; therefore, a mathematical model was compiled that described the distribution of energy levels in accordance with the investigation results. In this mathematical model the deviation of the quantum well geometry from the finite square well was considered, as well as the mutual influence of quantum wells and barriers of different thickness and depth. However, for more accurate modeling of other characteristics of laser diodes and further refinement of the model, it is necessary to take into account such factors as: electric transport, mode distribution and etc.

References:

[1] Ebbens A T 2018 Phys. Educ. 53 045018
[2] Yu H, Roberts C, Murray R 1995Appl. Phys. Lett. 66 2253
[3] Ozturk O, Ozturk E, Elagoz S 2018 Journal of Molecular Structure 1156 726
[4] Pankratov E L, Boldyrevskiy P B 2017 Physics and mathematics sciences. Physics 42 91
[5] Ozturk E 2016 Laser Phys. 26 096102

Study of SiN_x based antireflection coating for GaP/Si heterojunction solar cells

E V Anokhina[1], A V Uvarov[2], A S Gudovskikh[1,2]
[1]Department of Photonics, Saint Petersburg Electrotechnical University 'LETI', Saint Petersburg 197022, Russia
[2] Renewable Energy Lab, St. Petersburg Academic University, St. Petersburg 194021, Russia

Abstract. This paper presents the results of a research the optical properties of SiN_x layers with various compositions obtained by plasma-enhanced chemical vapor deposition (PECVD) and used as antireflection coatings for GaP/Si solar cells. Also a strong dependence of the optical properties of SiN_x on concentration of silane in the gas mixture during deposition was demonstrated.

Introduction

Solar power is very promising area of alternative renewable energy source. The further development of photovoltaics requires increasing the efficiency of solar cells (SC) – devices that convert light energy into electric energy. [1]. One of the factors determining the low efficiency of SC is the presence of optical losses, mainly by reflection. The conversion efficiency can be increased by optimizing the structure, in particular, the usage of silicon-based heterostructures. Recently the significant capability of a-Si:H/c-Si heterostructure SC was demonstrated, which reached a record efficiency value of 24.7% for the classic design with contacts on the both side. However, the a-Si:H layer absorbs a part of optical radiation and a further increase of the efficiency of heterostructure SC is possible due to the use of wide band gap emitter materials, in particular, GaP. Development and optimization of the structure is required for new GaP/Si structures to reduce optical reflection losses, in particular, by applying antireflection (AR) coatings. AR coating is a film that has a lower refrective index than the material that has to be coated. The enlightenment process is carried out by the interference of reflected rays at the boundaries: layer-air, layer-semiconductor. The point of applying an AR coating to create a dual interface using a thin film that produces two reflected waves. There are many ways to form AR coatings but plasma-enhanced chemical vapor deposition (PECVD) is the most suitable one from a technological point of view. In this method deposition is achieved by introducing gases - the sources of atoms into reaction chamber, which are decomposed in a glow discharge plasma. In this paper the researches were carried out to determine the possibility of using SiN_x layers with various compositions deposited by PECVD [2] for bleaching of GaP/Si photoconversion structures.

1. Experimental conditions, materials and results

The researches included the following steps:

- The depositions of SiN_x layers with various compositions of the gas mixture (nitrogen N_2 and silane SiH_4) using Oxford Plasmalab 100 PECVD installation.

- The study 0f the optical properties of SiN_x layers with various compositions using ellipsometry (at a wavelength of 632 nm), measurement of reflection and transmission spectra (200-1200 nm) of the layers deposited on silicon and quartz substrates.
- Modeling and developing SC structures with an AR coating using AFORS-HET software.
- Formation and study of the optical properties of a GaP/Si SC structure with an AR coating on planar polished and textured silicon substrates. The measurements were carried out using an integrating sphere to measure the spectra of total reflection from the textured surface [3].

The results demonstrate that an increase of the SiH_4 concentration, on the one hand, leads to an increase in the refraction index of SiN_x layers but, on the other hand, their absorption edge shifts to the visible area (Figure 1) leading to an increase in optical losses in this layer. The optimal deposition conditions and the design of SC with minimal optical loss have been found.

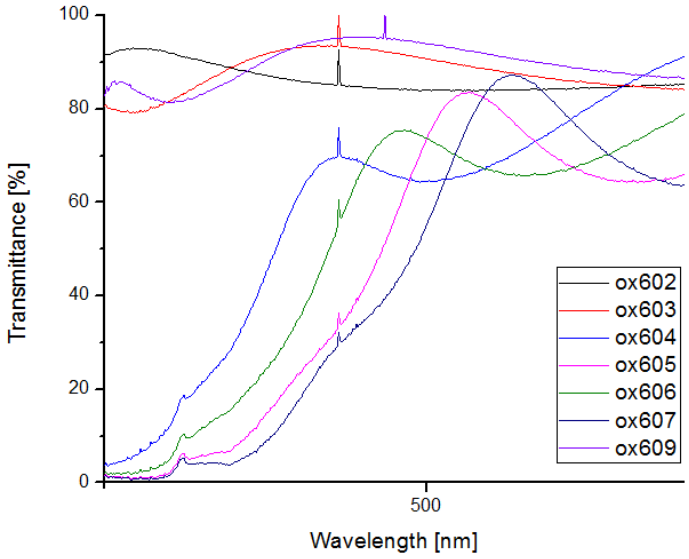

Figure 1. Transmission spectra of SiN_x layers in the short-wavelength region of the spectrum

Acknowledgments

The reported study was partially supported by Ministry of Science and Higher Education of the Russian Federation (research project FSRM-2020-0004).

References

[1] Lukutin B.V., Surzhikova O.A., Shandarova E.B. Renewable energy in decentralized power supply. - M.: Energoatomizdat, 2008. - 231 p.

[2] Ay and Aydinli. Comparative investigation of hydrogen bonding in silicon based PECVD grown dielectrics for optical waveguides. Optical Materials (2004) vol. 26 (1) pp. 33-46

[3] Jacquez J.A., Kuppenheim H.F. Theory of the integrating sphere. // J.Opt.Soc.Am., 1955. – Vol.45. – P.460-470.

Development of front contact grid for GaP/Si solar cells

M V Bogdanova[1], **I A Morozov**[2], **A S Gudovskih**[1,2]
[1]Department of Photonics, St. Petersburg Electrotechnical University ("LETI"), 197376 St. Petersburg, Russia
[2]St. Petersburg Academic University of RAS, 194021 St. Petersburg, Russia

Abstract. Currently, a search is being made for a scalable technology for applying metallization to GaP/Si photovoltaic structures for mass production. The study of Ag-based contacts, which are obtained by screen-printing with subsequent annealing, are presented in this paper. Contact resistance measurements are done using the TLM method. The developed contacts have demonstrated excellent performance even in comparison with the vacuum deposition technology, which is the basis for using the developed technology of forming contacts in industry.

1. Introduction

In recent years, the task has been set to search, develop and improve photovoltaic semiconductor structures with a small quantity of optical and electrical losses, providing the highest efficiency of solar energy conversion. A perspective way to reach the lowest optical losses is to use the wide band gap emitter layers, in particular a growth of GaP on Si substrate could provide several advantage compared to conversional Si based solar cells design. The mismatch of lattice constants between GaP and Si is 0.37% [1], as a result layer-by-layer growth of structures with fewer defects is possible. At the same time, the influence of defective levels is reduced and the thermal stability of such structures is improved. However, the important task is to find the optimal material and technology for the front contacts to GaP/Si, which should exhibit the lowest level of losses due to contact resistance and can be applied in mass production. In the current work, the properties of the contacts obtained by different metallization technologies on GaP are explored.

2. Experimental conditions, materials and results

The study compared two groups of samples that differ in metallization application technology. The contacts of the first group of samples were formed by screen-printing using conductive paste based on Ag and subsequent annealing. Samples with contacts formed by vacuum deposition of Ag/Ti are also considered. Samples made using screen-printing technology with a set of contact pads measuring 2.85×0.85 mm were annealed in N_2 atmosphere using the Jipelec JetFirst 100 rapid thermal annealing setup at a temperature of 700-800°C for 1 minute. Alternatively, Ti/Ag non-alloyed ohmic contacts (area of 1.5×0.2 mm) were formed on the top of GaP/Si structures using lithography and vacuum evaporation (Boc Edwards Auto 500).

During the experiment, the specific contact resistance ρ_c of the samples was determined. The transmission line method (TLM) was used, which considers the dependence of the total resistance R_T between two contacts as a function of the distance between them. During the measurements a set of distances L was used and for each position of the measuring contacts a current-voltage (I-V)

characteristics were measured, which determined the total resistance. Figure 1 (a,b) presents examples of obtained dependencies.

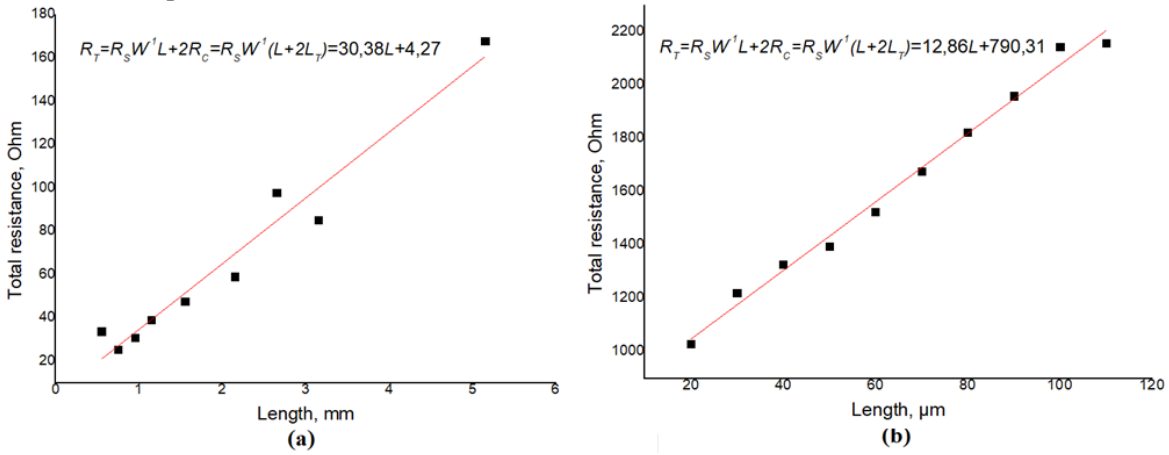

Рисунок 1(a, b). (a) Total resistance of the screen- printed sample **(b)** Total resistance of the sample with vacuum deposition

The specified dependence is approximated by a straight line [2]:

$$R_T = \frac{R_S}{W}L + 2R_C = \frac{R_S}{W}(L + 2L_T) \quad (1)$$

Where R_S— semiconductor volume resistance, W— contact width, R_C—contact resistance, L_T— transfer length. These parameters can be derived from experimental data. By them, we can determine the value of the specific contact resistance:

$$\rho_C = R_C L_T W \quad (2)$$

For Ag/GaP/Si samples obtained by screen-printing method and annealed at T=700°C and 800°C, the specific contact resistance values are $4.2 \cdot 10^{-3}$ Ohm·cm^2 и $1.8 \cdot 10^{-5}$ Ohm·cm^2 respectively. For the Ag/Ti/GaP/Si sample obtained by vacuum deposition technology, the specific contact resistance value is 0.18 Ohm·cm^2.

Thus, we can conclude that for samples with metallization formed by screen printing, the specific contact resistance is several orders of magnitude lower than for samples with vacuum metallization. This allows to reduce ohmic losses and improve the operational properties of the samples. Note that this method of forming contacts is scalable and can be released for mass production.

3. Acknowledgments

The reported study was partially supported by RFBR research project #20-08-00870.

References

[1] Adachi S. Properties of Group-IV, III-V and II-VI Semiconductors. Chichester, UK: John Wiley & Sons, Ltd, 2005. — 422 p.

[2] Reeves G.K. Obtaining the specific contact resistance from transmission line model measurements. IEEE Electr. Dev. Leter. 1982. No. 5. p 111—113.

Investigation of the elimination kinetics of low and middle molecular weight uremic markers during hemodialysis treatment with the optoelectronic multispectral sensor

G A Konoplev [1], O S Stepanova[1], G A Zemchenkov[2], V Korsakov[3], A Kuznetsov[3], A Frorip[3]

[1]Department of Photonics, St. Petersburg Electrotechnical University, St. Petersburg, 197376, Russia

[2]Nevsky Nephrology Center, St. Petersburg, 193318, Russia

[3]LDIAMON AS, Tartu, 51014, Estonia

Abstract. The elimination kinetics of conventional low-molecular weight uremic markers and advanced glycation end products (AGE products), which are considered as a possible middle molecular weight marker of uraemia in hemodialysis (HD) patients, was investigated by continuous monitoring of ultraviolet (UV) absorption of effluent dialysate in the outlet of a dialysis machine. Optoelectronic multispectral sensor based on deep UV LEDs as the source of UV radiation at the wavelengths 285 nm (associated mainly with uric acid and other low-molecular weight substances) and 365 nm (associated with AGE products) was used as a monitoring tool. The time profiles of effluent dialysate UV absorption during HD treatment sessions for a group of patients were measured and analysed according to the double-pool kinetic model. It was shown that the elimination kinetics of AGE products in general is very similar to the kinetics of conventional low-molecular weight uremic markers.

1. Introduction

Hemodialysis (HD) is the most widely used method of renal replacement therapy. As a life supporting treatment it provides elimination of various low and middle molecular weight metabolic waste products, e.g. urea, creatinine, uric acid, phosphates, advanced glycation end products (AGE products) from blood to dialysis fluid (dialysate) via semi-permeable membranes. The membrane works as a molecular sieve: small and partially middle molecules easily pass through pores while higher molecular weight substances and blood cells remain intact [1].

According to KDOQI Clinical Practice Guideline for HD Adequacy [2] the fractional urea clearance (Kt/V) is the most precise and tested measure of the dialyzer effect on patient survival and is the most frequently applied measure of the delivered dialysis dose, but according to some newer reports this approach is outdated and do not give the full picture [3]. Multiple alternative dialysis adequacy markers have been suggested, for example β-2-microgloubuline or Cystatin C [4].

Advanced glycation end products (AGE) belong to the factors of high mortality among end stage renal disease patients [5-7]. There had been no reliable methods for assessing and monitoring AGE elimination during HD until optical monitoring based on characteristic absorption of AGE is in the region 360-370 nm was introduced [8].

The aim of this work is to investigate the elimination kinetics of conventional uremic markers and AGE products simultaneously by continuous monitoring of ultraviolet (UV) absorption of effluent

dialysate in the outlet of a dialysis machine and to evaluate the perspectives of AGE products as a marker substance for assessing HD adequacy.

2. Experiment and results

Optoelectronic multispectral sensor based on deep UV LEDs as the source of UV radiation (designed by Ldiamon AS) for monitoring optical absorption at the wavelengths 285 nm and 365 nm was connected to the outlet of a dialysis machine. Monitoring of more than 70 HD sessions was conducted for a group of 20 patients with end-stage chronic kidney disease. The results reveal that normalized absorption curves for both wavelengths are in good concordance with each other. For majority of HD treatment sessions the curve for 365 nm lies slightly higher than the curve for 285 nm. The parameters of the double-pool model of solute kinetics [9] which was applied to the temporal dependences of normalized optical absorbance at 285 nm and 365 nm were estimated. The mean values of the time constants of the "fast" exponent (responsible for a dialyzer clearance) for 285 nm (associated mainly with uric acid and other low-molecular weight substances) and 365 nm (associated with AGE products) were 144 min and 136 min respectively; for the «slow» exponent (responsible for intercompartment transport) the mean time constants were 18 min and 15 min respectively. The mean values of both time constants for the 365 nm absorbance curves is slightly lower than time constants for the 285 nm absorbance curves, but the difference (8 min for the "slow" exponent and 3 min for the "fast" exponent) is less than the standard deviations of the respective time constants in the group. The clinical significance of these variations remains unclear; more in-depth research involving larger groups of patients and thorough analysis of clinical data is needed.

3. Conclusion

It was shown that the elimination kinetics of AGE products during HD treatment in general is very similar to the kinetics of conventional low-molecular weight uremic markers. Optical monitoring of effluent dialysate UV absorption at the wavelength of 365 nm potentially may be used as an alternative technique for assessing HD adequacy.

4. Acknowledgments

Authors wish to express their gratitude to the nursing and technical staff of Nevsky Nephrology Center for invaluable help in collecting experimental data.

References

[1] Hörl W H, Koch K M, Lindsay R M, Ronco C, Winchester J F 2004 *Replacement of Renal Function by Dialysis* (Springer)
[2] National Kidney Foundation. KDOQI clinical practice guideline for hemodialysis adequacy: 2015 update 2015 *Am. J. Kidney Dis.* **66** 884
[3] Neirynck N, Vanholder R, Schepers E, Eloot S, Pletinck A, Glorieux G 2013 *Int. Urol. Nephrol.* **45** 139
[4] Maheshwari K U, Santhi S, Malar R J 2015 *Indian J. Nephrol.* **25** 143
[5] Papanastasiou P, Grass L, Rodela H, Patrikarea A, Oreopoulos D, Diamandis E P 1994 *Kidney Int.* **46** 216
[6] Schmitt A, Gasic-Milenkovic J, Schmitt J 2005 *Anal. Biochem.* **346** 101
[7] Dolhofer-Bliesener R, Lechner B, Deppisch R, Ritz E, Gerbitz K D 1995 *Nephrol. Dial. Transplant.* **10** 657
[8] Kuznetsov A, Frorip A, Gerasimchuk R, Konoplev G 2016 *Nephrol. Dial. Transplant.* **31 (S1)** 1500
[9] Burgelman M, Vanholder R, Fostierx H, Ringoir S 1997 *Med. Eng. Phys*. **19** 69

Drift-diffusion simulation of photodetector with controlled relocation of carrier density peaks

I V Pisarenko[1], **E A Ryndin**[2], **I D Isakov**[2]
[1] Southern Federal University, Institute of Nanotechnology, Electronics and Electronic Equipment Engineering, Department of Electronic Apparatus Design, 2 Shevchenko St., Taganrog 347922, Russia
[2] Saint Petersburg Electrotechnical University "LETI", Faculty of Electronics, Department of Micro- and Nanoelectronics, 5a Professor Popov St., Building 5, Saint Petersburg 197376, Russia

Abstract. This paper continues the theoretical research of the photodetector with controlled relocation of carrier density peaks using physical and topological models. Previously, we performed the quantum-mechanical simulation of the device, but multiple semiclassical effects were neglected. To complete the analysis of physical processes in the photodetector structure, we propose a two-dimensional drift-diffusion model that is based on the continuity and Poisson differential equations. We develop a technique of non-stationary drift-diffusion simulation and corresponding applied software. The results of numerical simulation allowed for the modification of the photodetector structure in order to improve its functional characteristics.

Modern electronics faces the degradation of metal interconnection performance in integrated circuits with nanoscale feature dimensions of transistors. The utilization of constructively and technologically integrated optical links instead of metal wires is a promising way of the problem solution. Previously, we proposed an advanced design of an on-chip injection laser with an $A^{III}B^{V}$ nanoheterostructure and a functionally integrated optical modulator [1]. To implement the efficient laser-modulator-based optical interconnections, technologically compatible photodetectors with subpicosecond response time are required.

In paper [2], we introduced the concept and design method for a photodetector with controlled relocation of carrier density peaks within specially arranged quantum regions. The device includes a traditional *p-i-n* photosensitive junction and an orthogonally oriented control heterostructure. The transverse electric field displaces the peaks of electron and hole densities into the regions with low carrier mobilities and lifetimes during the back edge of an optical pulse. This relocation results in the fast decline of photocurrent that does not depend on the longitudinal transport of electrons and holes.

To estimate the back-edge performance of the photodetector with controlled relocation of carrier density peaks, we implemented a quantum-mechanical combined model [2] based on the Schrodinger-Poisson equation system. The model allowed for due regard to important features of transverse relocation of charge carrier wavefunctions in the quantum-well regions of the control nanoheterostructure. However, the developed quantum-mechanical model omits multiple semiclassical aspects of the device operation such as longitudinal transport of charge carriers in non-uniform electric field of a *p-i-n* structure, electron and hole diffusion, flowing of displacement current through the supply circuit, leakage of photogenerated charge carriers to the control contacts and others.

This paper is aimed at the development of a two-dimensional drift-diffusion model of the photodetector with controlled relocation of carrier density peaks, which addresses the aforementioned semiclassical effects properly. The realization of the drift-diffusion model is provided by a designed numerical simulation technique and corresponding applied software. The obtained simulation results indicate and solve several challenges caused by the specific operation mode of the photodetector with controlled relocation of carrier density peaks.

The activation of the control voltage during the back edge of an optical pulse results in a current surge that worsens the measuring signal of the photodetector with controlled relocation of carrier density peaks. To deal with this challenge, we propose the application of the differential principle for the detection of optical signals by on-chip optical interconnections.

Another important problem is connected with the shutdown of the control voltage after the end of the relocation process: the disappearance of the transverse electric field leads to the return of non-equilibrium electrons and holes to the absorbing region. Hence, undesired current pulses occur in the supply circuit of the photodetector. We suggest to modify the device structure in order to hold and accumulate previously relocated electrons and holes in the absorbing region at different values of the control voltage.

References

[1] Konoplev B G, Ryndin E A and Denisenko M A 2015 *Russian Microelectronics* **44** 190–6
[2] Pisarenko I V and Ryndin E A 2020 *Photonics* **7** 21

InGaAs photodiode with InGaAsP gradient metamorphic buffer layer grown on Si/Ge (001) substrate

I.V. Samartsev. S.M. Nekorkin, B.N. Zvonkov, N.V. Baidus, A.V. Rykov, V.G. Shengurov, V.Y. Chalkov, A.V. Zdoroveyshchev
Research Institute of Physics and Thechnology, Nizhny Novgorod State University, Nizhniy Novgorod 603950, Russia

Abstract. Opportunity of growing InGaAs photodiode at a wavelength 1.44 μm on Si/Ge (001) substrate using InGaAsP gradient metamorphic buffer layer has been shown. Photoluminescence and photosensitivity were investigated. The dark current for this diodes was 0.1 mA at voltage -5 V.

1. Introduction

At present, important research area is integration of A3B5 and silicon technologies. Perspective way [1] is related to fabricating hybrid structures on exactly oriented (noninclined) Si(001) substrates. However, achievements in this direction were mostly related to using molecular beam epitaxy (MBE), which is a low-productivity method in comparison to metal-organic chemical vapor deposition (MOCVD). MOCVD is the technology that is commonly used for fabrication of the majority of commercial semiconductor heterostructures. Therefore, the production of hybrid structures for mass market applications poses the task of fabricating laser and photodiodes on silicon substrates using exact the MOCVD technology.

In this paper, the results of studies of p-i-n photodiode with photosensitive area at a wavelength 1.44 μm. InGaAsP metamorphic buffer layer of gradient composition are presented. This wavelength is achieved by using the metamorphic buffer InGaAsP and InGaAs with a high content of In (58%) as the active area.

2. Experimental samples

The photodiodes were grown on noninclined Si (001) substrates (with misorientation below 0.5°) using a three-stage procedure [2]. At the first stage, using MBE system was prepared “virtual” Ge/Si (001) substrate [3]. Then, a GaAs(50 nm)/AlAs(10 nm) buffer structure and layer GaAs (1000 nm) were grown on this “virtual” Ge/Si (001) substrate at reduced pressure in MOCVD system [4]. After growing the buffer structure by MOCVD at atmosphere pressure InGaAsP metamorphic buffer layer and p-i-n structure were grown. The composition of the quadruple solution was changed in a stepwise way. Such a buffer layer makes it possible to change the lattice constant from the GaAs to a value consistent with the lattice constant of the $In_{0.58}Ga_{0.42}As$ solid solution p-i-n structure. The design of the grown structure is shown in table1.

Based on the obtained structures, photodiodes were fabricated. On the side of the structure, AuGe ohmic contacts were deposited by thermal evaporation in vacuum, photolithography and etching formed contacts in the form of a ring with external and internal diameter of 0.55 mm and 0.35 mm, respectively. Then a mesa structure with a diameter of 0.6 mm was etched. On the side of the substrate, continuous AuGe ohmic contact is deposited by thermal evaporation in a vacuum.

Table 1. The design of structures.

	Layer	Thickness, nm
	Substrate n-Si/Ge	
1	n-AlAs	10

2	n-GaAs	50
3	n-AlAs	10
4	n-GaAs	50
5	n-AlAs	10
6	n-GaAs	1000
7	n-InGaP	150
8	n-InGaAsP gradient composition (6 layers)	450
9	i-InGaAs	900
10	p-InGaAs	300

3. Results and discussion

The Photoluminescence spectrum (PL) at temperature 77 K has two peaks; the longer wavelength peak (λmax ~ 1.33 μm) corresponds to the emission of the InGaAs photosensitive region, and the shorter wavelength (λmax ~ 1.05 μm) to the emission of the InGaAsP buffer layer, the PL intensity from the photosensitive region exceeds the PL intensity from the buffer layer.

In order to study the spectral dependence of the absorption of photodiodes fabricated on the grown structures, the photovoltage spectrum was obtained at room temperature (Fig. 1).

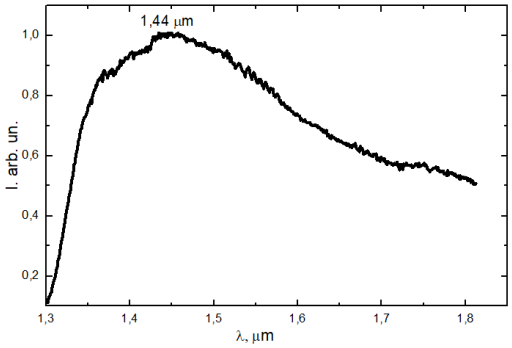

Figure 1. The photovoltage spectrum of photodiodes with a metamorphic InGaAsP layer on a Si / Ge substrate at room temperature.

The values of the dark current of photodiodes made from structures with a metamorphic buffer layer of InGaP were 0.1 mA at a voltage of -5 V.

Thus, the possibility of creating InGaAs photosensitive structures at a wavelength of 1.44 μm on a Si / Ge substrate using an InGaAsP metamorphic layer has been experimentally shown.

This project is supported by government task №16.7443.2017/БЧ and grant of president *РФ № МК-1004.2019.2*

References

[1] Sun C., Wade M.T., Lee Y. et al // Nature. 2015. V. 528. P. 534 – 538.
[2] V. G. Shengurov, S. A. Denisov, V. Yu. Chalkov, Yu. N. Buzynin, M. N. Drozdov, A. N. Buzynin, P. A. Yunin // Technical Physics Letters. 2015. V. 41 (1). P. 36–39.
[3] Sun C., Wade M.T., Lee Y. et al // Nature. 2015. V. 528. P. 534 – 538.
[4] Байдусь Н.В., Алешкин В.Я., Дубинов А.А. и др. // ФТП. 2017. Т. 51. В. 11. С. 1579 - 1582.

Application of selective contacts for study of silicon surface degradation

Kudryashov D.A.[1], Maksimova A.A.[2], Baranov A.I.[1], Uvarov A.V.[1], Morozov I.A.[1], Gudovskikh A.S.[1,2]

[1]St. Petersburg Academic University, St. Petersburg 194021, Russia

[2]Department of Photonics, Saint Petersburg Electrotechnical University "LETI", St. Petersburg, 197376 Russia

Abstract. In this work an application of selective contacts p-Si/MoO_x for evaluation of silicon sufrace degradation is shown. Using a method of I-V measurements the effect of silicon surface degradation during SiO_2 magnetron deposition was demonstrated.

1. Introduction

Silicon (Si) is the second most common element in the Earth's crust. Being also a semiconductor Si had been applied extensively in different electronic devices: transistors, microprocessors, sensors, solar cells. Earlier, the most of deviced based on silicon were being produced with using of high-temperature diffusion processes to form p-n junction or conctact areas. Such technology is quite simple, however requires sufficient energy consumption. Nowadays a low-temperature approach for electronic devices is actively developed. It is connected with heterojunction technology. It is well known that the transistors based on heterojunctions have enhanced characteristics in comparison to diffuse p-n junction ones. Silicon solar cells based on heterojunction also show the highest efficiency where the world record of 26% was reached [1]. The main problem that is still remained is a heterointerface quality. Charge carriers must pass throw it without significant recombination. In the same time surface defects such as impurities incorporation, surface roughening could significantly degrade the hetejunction properties and finally - the performance of electronic device. There are some methods to reveal or estimate a silicon surface degradation: space charge capacitance methods and optical methods based on photoluminescence decay measurement. The first one is quite complicated and requires high perfomance technique to detect response from the defects. The second method is based on the effect of an increase of recombination rate at the silicon surface if it has a lot of defects and is evidenced by low photoluminescence intensity and/or decay time.

In recent years, considerable attention has been given to the selective conctacts [2,3]. It is a kind of electric contact where charge carriers of one type may pass throw it whereas the others are blocked. For p-type silicon the most investigated selective contacts are formed with MoO_3, WO_3, V_2O_5. For n-type silicon LiF, MgF_2 with low work function metals are usually used. The transport properties of selective contacts are highly depended on the Fermi level position in silicon. Semiconductor surface degradation may lead to Fermi level shifting or even pinning, which in turn in the worst case may block the transport of the both types of charge carriers. This results in current-voltage (I-V) characteristics behaviour changing – from linear to Schottky type. Measuring of I-V characteristics is

more easier and faster than capacitance or optical-based methods and potentially the investigations may become faster.
The aim of this work is to study the effect of different silicon surface degration on carrier transport behaviout through selective contacts based on molybdenum oxide and lithium fluoride using silicon substrates.

2. Experiment details

N-type silicon wafers with doping level of 10^{16} cm^{-3} were used as a substrate. Molybdenum oxide (VI) was deposited on the wafers by thermal evaporation (throw metal hard mask with hole diameter of 0.5 and 1 mm on top side and without mask on the bottom side). Prior the deposition the silicon wafer was dipped into HF(1:10) to etch silicon oxide layer. To investigate the effect of silicon surface degradation on I-V characteristics magnetron plasma was used. A series of silicon samples with different plasma exposion during SiO_2 deposition was made. Silicon oxide after the deposition is etched in HF(1:10) solution leaving the degraded surface for subsequient selective contact deposition. I-V curves were recorded by Keithley 2400 source meter at 25 °C.

3. Results and discussion

Current-voltage characteristics measured for the degradated and the reference silicon wafers showed a significant (more than 3 orders) decrease of operational currents for the plasma exposed silicon sample. Variations of different plasma power and exposion time will be presented as well as the results of computer simulation of these systems in comparison with the obtained experimental data.

4. Acknowledgments

This work was supported by the Russian Scientific Foundation under Grant No. 18-79-10059.

References

[1] C. Battaglia, A. Cuevas and S. De Wolf // Energy & Environmental Science 9(5), 1552 (2016)
[2] James Bullock et. al. // Adv. Energy Mater. 2016, 1600241
[3] C. Battaglia et. al. // Applied Physics Letters 104 (11), 113902 (2014)

Optical properties of dry etched vertically aligned silicon structures with different geometry

I.A. Morozov[1], A.S. Gudovskikh[1, 2], A.V. Uvarov[1], A.I. Baranov[1], K.A. Vyacheslavova[1, 2], D.A. Kudryashov[1]

[1]Alferov University RAS, 194021, St.-Petersburg, Russia
[2]Saint-Petersburg Electrotechnical University "LETI", 197376, St.-Petersburg, Russia

Abstract. Nowadays Silicon is predominantly used in solar cells manufacturing due to its availability and relatively low cost. Further development of photovoltaics requires to increase the photovoltaic conversion efficiency and to decrease the price of the produced energy. Thus, new concepts and approaches should be explored. One of the key factors affecting the efficiency of solar cells is the optical losses related with reflection and incomplete absorption in the active layers of a semiconductor material. One of the promising paths to reduce optical losses is the usage of micro-and nano-structured surface of Si. In this paper, we consider vertically oriented structures on silicon obtained by cryogenic deep etching. The feature of this method is that the silicon substrate is hold at a low temperature from -80°C to -150°C during the process. At these temperatures, the side surface is passivating due to the formation of a non-volatile SiOF compound. This process allows one to adjust the angle of slope of the etching walls with a high accuracy additionally providing a possibility to increase the resistance of the mask to etching due to low temperature. A large variation of the process parameters (pressure, SF6/O2 ratio, RF and ICP power, temperature) will be performed to obtain low defect and low reflectance conditions. Dependence of optical and electrical properties on the length and diameter of silicon wires will be presented.

Experimental

At the beginning, 500 nm of SiO_2 were deposed on 4-inch (100) silicon substrate in Oxford Instruments PlasmaLab 100 PECVD. Initial polystyrene solution was 10 wt. % 0.89μm and 2 μm spheres in water. Spin coating was used for nanosphere lithography. Before deposition polystyrene spheres was dried in centrifuge and diluted in isopropyl/water/ propylene glycol solution. Then Sphere was etched in oxygen plasma to reduce diameter. Silicon oxide was etched in CHF3 plasma through sphere mask to form SiO2 mask for cryogenic etching. variation of the process parameters (pressure, SF6/O2 ratio, RF and ICP power, temperature) will be performed to obtain low defect and low reflectance conditions.

Acknowledgements

This work was supported by the Russian Scientific Foundation under grant 19 no. 18-79-10059.

Carbon nanotubes and wolfram oxide nanoparticles spray coating on polymer photoactive layer

A V Romashkin, Yu A Polikarpov, E V Alexandrov, V K Nevolin
Center of Probe Microscopy and Nanotechnology, National Research University of Electronic Technology, Moscow 124498, Russia

Abstract. Carbon nanotubes (CNT) and tungsten oxide nanoparticles (nWO_3) were spray-coated on the MEH-PPV photoactive layer. The effect of the neighboring layers mixing on the electrical characteristics of an organic solar cell layers and methods to minimize that mixing by optimization of solvents and deposition parameters was investigated. Mixing was controlled by measuring surface resistance (for CNT) and particle diameter on the surface (for nWO_3).

1. Introduction

Current coating techniques used in organic photovoltaics involve the use of vacuum, which increases the cell production cost and indium tin oxide (ITO) part of the total cost (material and production process) can be up to 87% [1]. Spray-coating is one of the alternative coating methods that does not significantly affect quantum efficiency, but has a great production worth due to the scaling possibility and low cost [2]. However, the use of solution process leads to the underlying layers dissolution and residual solvent evaporation problems from the layer, which can lead to an electroluminescence and quantum efficiency decrease, changes on spectral characteristics, which demonstrated by samples comparison before and after annealing [3] and significant cell efficiency increase with optimal deposition temperature [4]. Thus, the aim of this work is the selection of optimal deposition parameters and solvents with optimal solvent removing rate for spray coating transparent conductive layers based on CNT and buffer layers based on metal oxide nanoparticles on the photoactive layer surface without dissolving while maintaining electrical and photovoltaic characteristics.

2. Results and discussions

CNT (P3-SWNT, Carbon Solutions Inc., USA) and tungsten oxide nanoparticles (nWO_3, <50 nm, Sigma Aldrich, USA) were used for deposition transparent conducting and buffer layer. In addition, a mixture of CNT and polyaniline (PANI, 5 kDa, Sigma Aldrich, USA) in a 5:1 ratio was used. Poly[2-methoxy-5-(2-ethylhexyloxy)-1,4-phenylenevinylene] (MEH-PPV, 40-70 kDa, Sigma Aldrich, USA) was used as a test photoactive layer. The structure of test structures was: A) Ti/TiO_2/MEH-PPV/CNT, B) Ti/TiO_2/MEH-PPV/PANI-CNT, C) Ti/TiO_2/MEH-PPV/nWO_3/CNT. Titanium foil (Ti) with naturally occurring oxide was used as the substrate. MEH-PPV with thickness ~900 nm was deposited by drop-coating from o-xylene, due to the presence of Ti microdefects with height ~500 nm. Solutions with 1 mg/ml MEH-PPV in 15 different solvents were prepared to determine minimally dissolving MEH-PPV solvents or mixtures. After 1 day storage and heating at 90 °C for 3 minutes (which simulated conditions during deposition) the least solubility of MEH-PPV inherent for 2-propanol, ethylene glycol, propylene carbonate, propylene glycol (PG) and n-butanol. Cyclohexanol (CHL), n-decane and PGMEA also demonstrated low solubility. However, the optimal solvent should have the low MEH-PPV solubility and on the other hand the stability of the colloidal dispersion nWO_3 or CNT

as well as an optimal evaporation rate to obtain uniform spray-coating; therefore, 1:1 mixture of PG:CHL was chosen as the most optimal solution. The deposition of nWO_3 and CNT was carried out by own designed spray-coating system (Fig. 1a,b). The average diameter nWO_3 was 19.5 nm and 17 nm for MEH-PPV and glass substrate due to the smaller amount of 2-4 nm particles on MEH-PPV (Fig. 1c), which apparently indicates a partial (insignificant, less than 4 nm) nanoparticles dipping in MEH-PPV. However, this is caused not only by the dissolution of MEH-PPV itself during deposition as by the dipping due to presence of residual solvent in MEH-PPV before deposition due to the absence of layer annealing [3]. The optimal solvent mixture provides to neutralize the dissolving effect and significantly reduce the resistance of the CNT network used as upper electrode (from 106.5 kΩ/□ to 1.4 kΩ/□ when changing the solvent from NMP to the PG and CHL mixture). Due to the absence of annealing (and the presence of residual solvent, which was confirmed by fluorescence spectra), as well as the excess MEH-PPV thickness (optimum active layers thickness is not more 200 nm [5]), investigated structures photoresponses were low with slow photocurrent increasing at -3 V (up to 10 minutes) - 500 nA, 283 nA for structures A, C and 50 nA in few seconds for B. Also, used materials do not provide the required charge separation (for example, WO_3 is an electron transport layer in some cases [6]). I–V characteristics hysteresis also showed a significant contribution of charge trapping and recombination to the charge collection efficiency decrease. On the other hand, the obtained resistance with transparency ~82 % is sufficiently high for using the CNT network as a solar cell electrode, but it is typical for these CNT [7] and can be reduced by doping or compositing with metal nanowires. CNT layer resistances on PET and MEH-PPV are practically similar (1.5 kΩ/□ and 1.4 kΩ/□), which also indicates an absence of mixing with the MEH-PPV during spray-coating.
Thus, we propose the method for estimation thickness layer at the interface, where materials are mixed, using statistical analysis of the nanoparticles sizes of interested material deposited on studied layers, which is difficult to detect even by SEM. Also, it was demonstrated that the developed spray coating technique can be used to form transparent conducting and buffer layers from solutions on various active layers of solar cells.

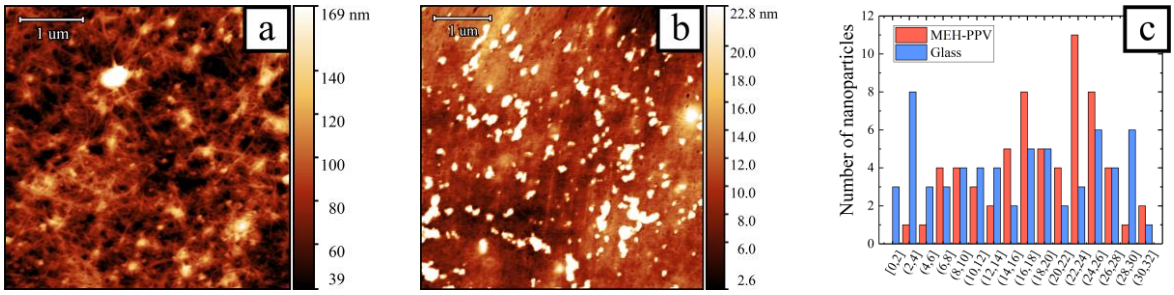

Figure 1(a, b, c). AFM-images of **(a)** CNT and **(b)** nWO_3 spray-coated on MEH-PPV, **(c)** distribution of nWO_3 diameter from AFM data.

3. Acknowledgments

This work was supported by grant of President of the Russian Federation for young Russian scientists support (grant № МК-1024.2020.8)

References

[1] Espinosa N, Garcia-Valverde R, Urbina A, Krebs F C 2011 *Sol. Energy Mater. Sol. Cells* **95** 1293
[2] Kang M H, Heo D K, Lee M, et al 2019 *IEEE Journal of the Electron Devices Society* **7** 1129
[3] Chou H L, Lin K F, Fan Y L, Wang D C 2005 *J. Polym. Sci. Part B: Polymer Physics* **43** 1705
[4] Cai C, Zhang Y, Song R, et al 2017 *Sol. Energy Mater. Sol. Cells* **161** 52
[5] Nam Y M, Huh J, Jo W H 2010 *Sol. Energy Mater. Sol. Cells* **94** 1118
[6] Gheno A, Pham T T T, Bin C D, et al 2017 *Sol. Energy Mater. Sol. Cells* **161** 347
[7] Emelianov A V, Akhmadishina K F, Romashkin A V, et al 2015 *Technical Physics Letters* **41** 94

Development of a method for adjusting the coordinates of the center of attention in the absence of fixation of the head

E S Kiseleva[1], **O L Isaeva**[1], **M B Boronenko**[1], **V I Zelensky**[1]
[1]Laboratory of Integrated Engineering, Yugra State University, Khanty-Mansiysk 628012, Russia

Abstract. In this paper, the movement of the pupils is a biometric indicator that analyzes the emotional state of a person. Aitracking using infrared illumination based on the determination of the displacement vector between the centers of the pupil and the shine of the cornea gives results with high accuracy, provided that the human head is fixed. A method for determining the coordinates of the center of attention in the absence of fixation of the head without the use of infrared illumination is proposed. Improving the accuracy of determining the coordinates of the center of attention is carried out by moving from a coordinate system associated with a fixed head to a coordinate system associated with a moving center of the pupil.

1. Introduction

By registering the time of fixation and the density of the trajectory of the gaze, one can judge the significance of the elements visible to a person. [1]. Eyetracking is minimally invasive and analyzes the movement of the pupil, which is a subconscious mechanism that is difficult to fake or control [2]. At the same time, the drawback of such systems is the use of a large amount of equipment, the use of special glasses, the complex process of projecting an image on the screen, the pupil, the increased number of images themselves, and the use of rigid fixation of the subject's head [3-5]. In real shooting conditions, you can increase efficiency by using non-rigid fixation of the head, while maintaining the reliability of the data. This article describes a method for improving the accuracy of tracking the pupil's focus of attention regardless of the position and movement of the subject's head. The aim of the study was to develop a method to increase the accuracy of tracking the pupil's center of attention in the absence of a rigid connection between the subject's head and the optoelectronic system. To do this, it is necessary to obtain a track of attention without distortion (angle of rotation of the head 0º), to obtain a deliberately distorted track (rotation of the head to a certain angle), to test the correction method at coordinate points.

2. Experimental

The installation mechanism (Fig. 1) consisted of an optoelectronic system.

Figure 1. Experimental setup.

T7 Astro Camera Astronomical, 1X-100X optical zoom microscope lens. A helmet that creates a rigid coordinate connection between the camera and the head. The frame provides for the adjustment of the helmet on a horizontal axis with a range of 180 degrees. Video mode 30 frames per second. To obtain a pupil movement track without distortion, a helmet is put on the subject's head. The swivel mechanism is set to 0 degrees. Next, using the optoelectronic system, video recording of the movement of the pupil is performed. To obtain a distorted track of the center of attention with the help of a rotary mechanism, the subject's head is rotated by a fixed angle from 0 to 15 degrees. All things being equal. Further, the obtained tracks are superimposed on the calibration grid (Fig. 2a, b).

3. Result and Discussion

During testing, the subject observed images of black dots on the slide, while the tilt of the head was not limited by anything. Fig. 2 (a) shows the pupil movement track, which requires adjustment, Fig. 2 (b) the same track after adjustment.

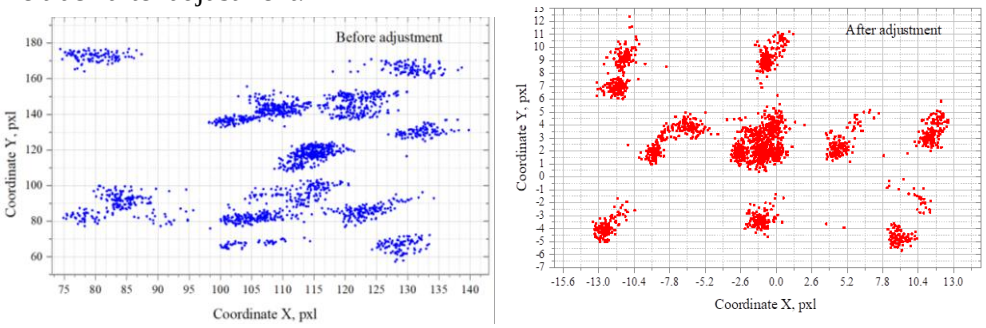

Figure 2. Pupil movement track before (a) and after (b) adjustment.

First, the pupils are contoured and separately the image from the monitor on the cornea, while the accuracy of the method depends on its quality. Next, the coordinates of the center of mass of the pupil and the reflection of the monitor on the pupil are determined. Then, the offset is calculated relative to the coordinate of the image of the monitor from the center of mass of the pupil. This adjustment allows you to more accurately track the trajectory of the pupil's attention, even in the absence of a rigid connection with the subject's head.

4. Conclusion

In the course of the study, it was found: 1. a shift in the focus of attention by 8 ° 0'30 "leads to a change in the size Δs / s of the pupils ± 0.02; 2. rotation of the head 15 degrees horizontally leads to distortion of the track of the center of attention, which makes it impossible to correctly track The proposed method allows you to move from the coordinate system associated with the center of the pupil to the system associated with the center of attention, thereby reducing the distortion of tracking the trajectory of a person's gaze, which can be used in optoelectronic security systems. The study was carried out with the financial support of the Russian Foundation for Basic Research in the framework of the research project 18-47-860018 p_a.

References

[1] Fazylzyanova, G.I., & Balalov, V.V. 2014. *Aitracking. Bulletin Rus. Univ. Math.*, **19 (2).**
[2] Lebedenko, Yu. I. 2013, *Biometric security syst*. (Directmedia) p 159.
[3] Deryushev, A.A., Kukin, D.P., & Sweeto, I.L. 2008. *Methods for displaying three-dimensional information.* Proc Belarus. St. Univ. of Inform & Radioelec., **2 (32)**.
[4] Sergeev, S.F. 2013. *Testing methods and optimization of information systems interfaces,* p 32-64.
[5] Falikman, M.V., & Devyatko, D.V. 2008, Thesis. *Psychological mechanisms of visual disappearance*, p 11-28.

An optical method for studying a magnetic track using speckles of the structure of scattered laser radiation

S E Logunov[1], V V Davydov[1, 2], V Yu Rud[2]
[1]Higher School of applied physics and space technologies, Peter the Great Saint-Petersburg Polytechnic University, Saint Petersburg 195251, Russia
[2]All-Russian Research Institute of Phytopathology, Moscow Region 143050, Russia

Abstract. A new method for detecting a magnetic track from a moving magnetic object is presented. A technique has been developed to study the nature of changes in the magnetic field in a magnetic track using ferromagnetic fluid. The results of experimental research are presented.

1. Introduction

The development of science in the modern world allows scientists to start researching complex physical phenomena, which contain a lot of useful information, both about the structure of the Earth and about the processes taking place in the surrounding world. In this case, the leading role is played by applied physics [1]. A large number of phenomena associated with processes occurring in the environment are investigated using measurements of magnetic field parameters [1, 2]. Magnetic fields are also used to conduct studies of various condensed matter, for example, NMR or EPR spectrometers.

One of the least studied phenomena in the physics of magnetic phenomena is the magnetic track. Particularly great difficulties arise with the study of this phenomenon during its formation from the motion of a moving object. It should be noted that the studies carried out by various scientists of magnetic tracks made it possible to establish the physical principle of its formation and some features. Our studies have shown that the features of the formation of a magnetic track depend on many factors. In some cases, for example, in air, a magnetic track exists for a time of the order of several seconds. At sea depths (more than 550 m), depending on the parameters of the marine object, the boundaries of the magnetic track are more pronounced, compared with the air, the magnetic field variations in the magnetic track at the sea depth are more significant. The study of the magnetic track at sea depths is a very expensive and complex process. Before full-scale tests, it is necessary to study the processes associated with the formation of a magnetic track in laboratory conditions, so that in full-scale studies under conditions of a time limit, the process of measuring magnetic field variations can be correctly constructed. Therefore, the development of various methods for conducting studies of the magnetic track in laboratory conditions is relevant for solving this problem of applied physics.

2. The method of studying the magnetic track and the method of its detection

To conduct studies of the magnetic track in laboratory conditions, we propose using the optical method that we previously developed to study the structure of magnetic field lines using scattered laser radiation and a ferrofluidic cell [3].

Based on previously obtained results on the study of the structure of magnetic field lines, we developed an experimental setup for studying a magnetic track from a moving object. Laser radiation

with λ = 632.8 nm enters through the diaphragm and lens onto the transparent surface of a quartz glass ferrofluidic cell in which magnetic fluid is placed (an aqueous solution of hematite with a surfactant - oleic acid). The ferrofluidic cell is in the field of an electromagnet with induction B_0 = 86 μT - the average magnetic field of the Earth at the considered depths. Hematite nanoparticles are located in the region of the lines of force of the magnetic field B_0. Scattered laser radiation from hematite nanoparticles, which formed agglomerates in the vicinity of magnetic field lines, is detected by a CCD camera as speckle structures. With a high uniformity of the magnetic field B_0, the recorded diffraction image is symmetric with respect to the central maximum.

After the appearance of a moving magnetic object in the area of the magnetic field lines B_0 of the magnetic field B_0, the field lines are closed on its structure. The destruction of agglomerates begins. The recorded speckle structure changes. This destruction depends on the speed of the object and its magnetic field. Figure 1 shows as an example the diffraction patterns of speckle images corresponding to the cases considered.

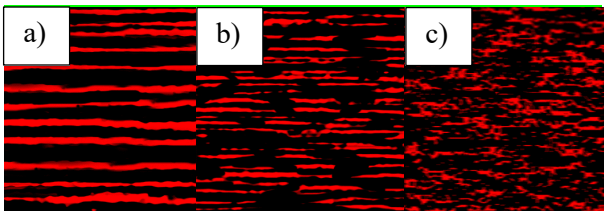

Figure 1. The diffraction pattern of the laser radiation in the case of the magnetic liquid placing: (a) in a uniform magnetic field; (b) a magnetic field force lines are closed on the body; (c) 2 minutes passed after the closure of all the magnetic field lines on the body.

We have established the dependences of the rate of change of the amplitude of the maxima and minima in the recorded diffraction image, their relative position and width, as well as their number on the speed and direction of movement of the magnetic object, as well as its magnetic field.

3. Conclusion

An analysis of the obtained diffraction images shows that the optical method we developed allows us to determine the presence of a magnetic track at a depth and to study its parameters depending on various factors. Using the method developed by us allows us to estimate the time of formation of a magnetic track from a moving object with an error of no more than 30 %.

References

[1] Vershovskii A K, Dmitriev S P and Pazgalev A S 2013 Technical Physics Journal **83** 879
[2] Aleksandrov E B and Vershovskii A K 2009 Physics-Uspekhi 52 573-601
[3] Logunov S.E., Koshkin A.Yu., Davydov V.V., Petrov A.A. Visualizer of magnetic fields // Journal of Physics: Conference Series 741(1) (2016) 012092
[4] Logunov S E, Davydov V V, Vysoczky M G and Mazing M S 2018 Journal of Physics: Conference Series 1038(1) 012093

Capacitance characterization of silicon nanowires formed by cryogenic dry etching

A I Baranov[1,2], D A Kudyashov[1], L N Dvoretckaia[1], I A Morozov[1], A V Uvarov[1], K Yu Shugurov[1], A S Gudovskikh[1,2]
[1]Alferov University, 194021 St Petersburg, Russia.
[2]St Petersburg Electrotechnical University "LETI", 197376 St Petersburg, Russia.

Abstract. Arrays of vertical aligned nanowires with height of 3-10 μm and aspect ratio of 5 with smooth side surface of NWs and between them were formed by cryogenic dry etching. The post-processing technology was developed to fill arrays of NWs by dielectric layer and form Schottky diodes by metal evaporation or passivation by amorphous silicon deposition on different part of wafers to study their properties by capacitance methods. Deep defect with an activation energy of 0.68-0.74 eV was observed in arrays of NWs, and its concentration grows with increase of time etching. However, its concentration can be partially reduced by wet etching in KOH.

1. Introduction

Nowadays, there is movement from classical planar solar cells to structures with layers of low dimension, which allows to vary the geometry and electronic properties of the materials. For example, it is using of vertically aligned nanostructures (nanowires, nanorods) to enhance the absorption of radiation and double-junction production based on them, since it allows the use of cheap silicon wafers and technologies of the silicon industry as the most developed in micro- and nanoelectronics. It was demonstrated experimentally in microcrystalline silicon solar cells grown on silicon nanowires (SiNWs) [1,2]. However, its effective development is hampered by the imperfection of the applied technologies like metal-assisted chemical etching of silicon wafer or vapour-liquid-crystal for the formation of nanowires, and also by the limitations of the methods allowing the detection and description of the properties of defect levels in the bulk of nanowires and on their surface rising during this methods. Recently, SiNWs are formed by new method of dry etching of silicon wafer in inductively-coupled plasma (ICP) at cryogenic temperature [3]. However, influence of cryogenic etching process on properties of SiNWs were not studied in details unlike Si wafer surface. Therefore, in this work defect properties of arrays of SiNWs will be studied.

2. Experiments and results

Silicon wafers ($n=1\times10^{15}$ cm^{-3}) were etched in ICP mode in mixture of gases SF_6 and O_2 during 3-5 minutes in equipment Oxford Plasma Lab ICP 380 at -140 °C to form arrays of vertical aligned nanowires with height of 3-10 μm and aspect ratio of 5 with smooth side surface of NWs and between them. To explore influence of cryogenic etching process on properties of silicon NWs the post-processing technology was developed to fill arrays of NWs by dielectric layer and form Schottky diodes by metal evaporation or passivation by amorphous silicon deposition on different part of wafers: on top of Si NWs, on side of Si NWs and between them. Admittance spectroscopy were

performed using a precision E4980A Keysight (former Agilent) LCR-meter and capacitance deep-level transient spectroscopy were performed using an automated installation based on a Boonton-7200B capacitance bridge in the temperature range of 80-360 K to study interface in different area of wafers and its defect properties.
In result, deep defect with an activation energy of 0.68-0.74 eV was observed in arrays of NWs, and its concentration grows with increase of time etching. However, its concentration can be partially reduced by wet etching in KOH. More detailed information will be presented on conference.

3. Acknowledgments
The work is supported by the Russian Scientific Foundation under Grant No. 19-79-00338.

References

[1] Gudovskikh A S et al. 2017 *Mater. Today Proc. Elsevier Ltd* **4** 6797–6803

[2] Kelzenberg M D et al. 2010 *Nat. Mater. Nature Publishing Group* **9** 239–44

[3] Morozov I A et al. 2019 *Phys. Stat. Sol. (a)* 1900535

Long–range night vision camera based on SWIR photocathode

K J Smirnov[1], V V Davydov[2], V Yu Rud[3]
[1]Bonch-Bruevich Saint Petersburg State University of Telecommunications, Saint Petersburg 193232, Russia
[2]Peter the Great Saint Petersburg Polytechnic University, Saint Petersburg 195251, Russia
[3]All-Russian Research Institute of Phytopathology, Moscow Region 143050, Russia

Abstract. Technological aspects of manufacturing SWIR sensitive detector on the basis of InP/InGaAs/InP photocathode and electron-bombarded CCD are given. Scheme of the digital camera for long distance detection is represented. SWIR camera operating mode and properties in case of implementation of impulse laser source are discussed.

1. Introduction

The problem of creation observing and location systems which operate in low and zero visibility conditions is extremely relevant for military and civilian tasks. Requirements for maximum detection range, as well as the possibility to easy interpret an object could not be achieved by common night vision devices, such as thermal detectors based on microbolometers as well as photon detectors based on electron-optical converters with GaAs photocathode. At present time the most perspective way to realize night vision system it is creation of photodetector which is sensitive in eye-safe short-wave infrared spectral range (SWIR). The readout and conversion scheme of such devices are similar to visible and near-infrared devices. However, application of SWIR allows to achieve significantly better parameters of detection characteristics due to decrease of the Rayleigh scattering, presence of atmospheric window and the peak of night lighting.

The additional improvement of detection characteristics could be achieved by realizing of complex active night vision scheme. It consists impulse-mode laser source (1.54 μm. Nd:YAG shifted laser) and synchronized gated-mode SWIR camera. To achieve the pulse duration below 100 ns the main part of gated camera – photosensitive sensor should include SWIR-photocathode [1]. The purposes of the work were to develop SWIR-sensitive photodetector based on photocathode and to implement it in gated night-vision camera.

2. Experimental

Requirement of implementation photocathode technology and spectral range of photosensitive device could be fulfilled by implementation of InP/InGaAs/InP heterostructure activated with Cs and O_2. It based on the principle of inter–valley electron transfer (transfer electron photocathodes – TEP) and sensitive in 0.9–1.7 μm spectral range [2-3]. The device design is shown in figure 1(a). In vacuum photoelectronic device the electron-bombarded charge-coupled device (EBCCD) should be used as the photoelectron converter [4]. Applying of high voltage between photocathode structure and EBCCD allows to accelerate existing photoelectrons and to achieve the electron-bombarded gain (EBS) process in the structure of CCD. The principal scheme of camera with InP/InGaAs/InP based photodetector is shown in figure 1(b).

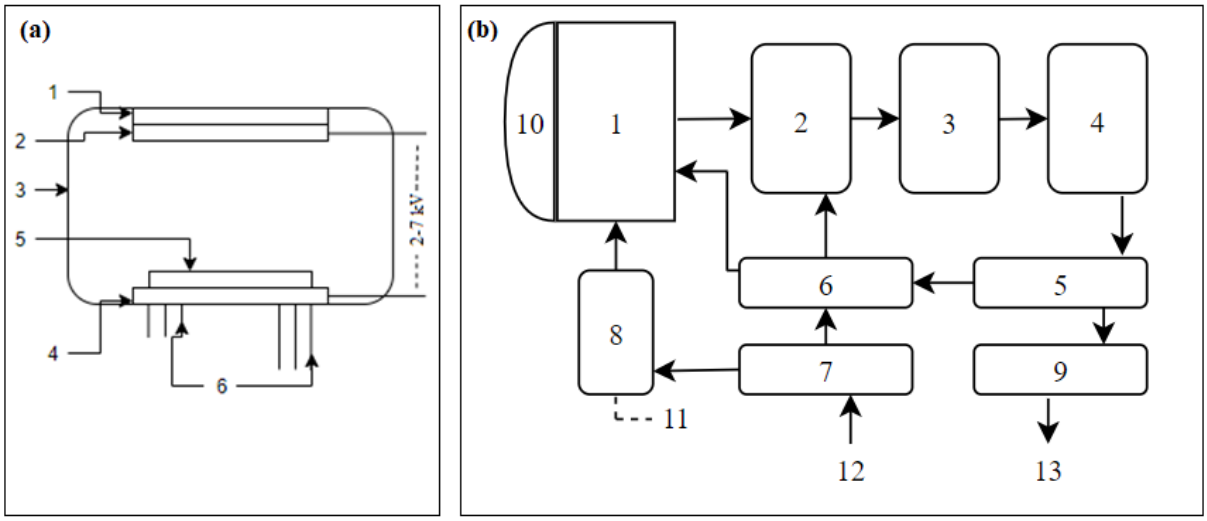

Figure 1(a, b). (a) Device design: 1 – input window, 2 – InP/InGaAs/InP photocathode structure, 3 – device body, 4 – photoelectron converter holder board, 5 – EBCCD, 6 – inputs and outputs; **(b)** Functional scheme of SWIR gated camera: 1 – photosensitive detector with TEP and EBCCD, 2 – amplifier, 3 – filter, 4 – analog-digital converter, 5 – synchrogenerator, 6 – level converters, 7 – voltage driver, 8 – high-voltage power supply 9 – USB interface, 10 – focusing lens, 11 – synchronizing to laser supply, 12 – 27 V. camera power supply, 13 – video out.

As the result of manufacturing process photoelectronic vacuum device was created. In passive transparent mode (photocathode illuminated from the InP substrate side) and room temperature conditions the 5% quantum efficiency was achieved. In case of cooling photocathode to 278 K the QE increases more than 2 times by the opportunity to apply higher supply voltage [3,5]. In consequence of using proximity-focusing technology the active surface of the photocathode structure should be 1.4x1.0 cm in case of 1,38x9,8 cm CCD size. Therefore, the uniformity of InP/InGaAs/InP structure is the most significant problem.

The suggest design of SWIR camera allows to use it in passive (detection of only natural radiation without additional laser source), active (camera detects reflected radiation from object illuminated by SWIR laser source) and active-impulse mode (in addition to common active mode the high voltage power supply connected to TEP synchronized to laser pulse duration). Active-impulse mode allows to collect only the radiation reflected from the target area of interest. In this way, only the objects in a volume defined by the area covered by the laser beam and a depth of field set by the gate time width are presented in the image [1].

3. Conclusion

Development of SWIR-sensitive gated photodetector systems allows to exceed characteristics of existing night vision cameras based on Gen 3 photocathodes and also uncooled InGaAs-FPA cameras. Sensitivity in 0,9–1,7 μm. spectral range is obtained with the help of InP/InGaAs/InP heterostructure. Photoelectron to electric signal conversation and internal amplifying are accomplished by EBCCD. Applying of laser-gated imaging technology allows to meet the challenges of tactical targeting and target identification (ID) in exceptionally long range (>20 km).

References

[1] Aebi V W, Vallianos P 2000 *Laser Focus World*, **9** pp 147–150
[2] Aebi V W, Sykora D F, Jurkovic M J, Costello K A 2011 *Proc. of SPIE*, **8033** 80330T
[3] Smirnov K J, Medzakovskiy V I, Davydov V V, Vysoczky M G, Glagolev S F 2017 *J. of Phys: Conference Series* **917(6)** 062019
[4] Williams G M, Rheinheimer A L, Aebi V W; Costello K A 1995 *Proc. of. SPIE*, **2415**
[5] Junkai X, Xiangyan X, Jinshou T, Duan L, Dandan H 2016 *Infrared Technology and Applications, and Robot Sensing and Advanced Control Proceedings* **10157** 101573

Heating Dynamics Measurements in QCL emitting at 8 μm wavelength

V V Dudelev[1], D A Mikhailov[1], A V Babichev[2], V Yu Mylnikov[1], A G Gladyshev[2], S N Losev[1], I I Novikov[2], A V Lyutetskiy[1], S O Slipchenko[1], N A Pikhtin[1], L Ya Karachinsky[2], A Yu Egorov[3], G S Sokolovskii[1]

[1]Ioffe Institute, Saint-Petersburg, Russia
[2]Connector Optics LLC, Saint-Petersburg, Russia
[3]ITMO University, Saint-Petersburg, Russia

Abstract. In this work we present a technique for heating dynamics measurements of quantum cascaded lasers active region under short pulse pumping.

1. Introduction

Recently quantum cascade lasers emitting in the mid-infrared range undergo very active development due to broad area of their possible applications in modern gas analysis, environmental monitoring, and safety systems. One of the most critical factors that lead to a degradation of any semiconductor device is overheating. That is why any high-power device requires control of temperature. Therefore, precise control of temperature and heating dynamics is a key to the improvement of reliability and lifespan of QCLs.

2. Experiment and simulations

In our experiment, the QCL sample emitting near 8 μm [1,2] is operating under pumping by short (about 100 ns duration) current pulses with 25 kHz repetition rate. The pumping current densities are 6.7 kA/cm^2 and 15 kA/cm^2. The technique of measuring the heating dynamics in the active region is based on the analysis of the dynamics of QCL spectra and measurement of the Fabry-Perot (FP) modes chirp [3]. Figure 1a represents the time-resolved spectra of the QCL sample under pumping with 15 kA/cm^2 current density. Figure 1b shows the section of the spectrum inside the white rectangle in Figure 1a. From the plot, one can see that FP modes undergo a significant redshift. The linear chirp of FP modes designates an increase in the temperature of the active region during the pump pulse. The heating rate of the active region of QCL can be estimated by the simple expression:

$$V_T = \frac{\partial T}{\partial t} = \frac{\partial n}{\partial t}\left(\frac{\partial n}{\partial T}\right)^{-1} = \frac{n}{\lambda_m}\frac{\partial \lambda_m}{\partial t}\left(\frac{\partial n}{\partial T}\right)^{-1},$$

where $\partial n/\partial T$ is the refractive index thermal coefficient, $\partial \lambda_m/\partial t$ is FP mode chirp. The measured FP mode chirp for current densities 6.7 kA/cm^2 and 15 kA/cm^2 was 0.33 Å/ns and 0.88 Å/ns correspondingly. Knowing the expression for FP modes spacing $\Delta\upsilon = c/(2nL)$ we can determine $\partial n/\partial T$. Here c is the speed of light in vacuum, n is the effective refractive index, L is the length of FP cavity. From the data taken from the spectra measured at pumping current 6.7 kA/cm^2 and heatsink temperature 288 K and 323K,

we find $\partial n/\partial T=2.2\cdot10^{-3}$ K^{-1}. Thus, the heating rate is determined as 6.2 mK/ns at 6.7 kA/cm^2 and 16.4 mK/ns at 15 kA/cm^2.

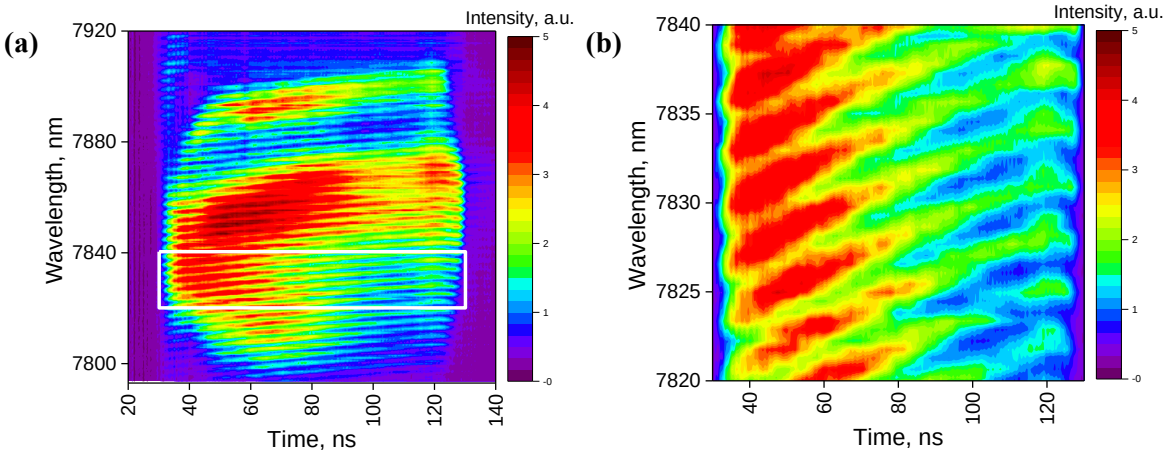

Figure 1. (a) Measured time-resolved QCL spectrum at pump current density J=15 kA/cm^2 (b) The enlarged region selected in Figure 1(a).

In previous studies [4] with the pulse duration of 20 μs the demonstrated heating rate was more than 3 times lower than in present research. This indicates saturation of the heating process of the QCL active region at pumping by longer pulses, as shown in ref. [5].

3. Summary

In conclusion, we have shown the technique that allows to determine the heating rate of the active region of QCL under short pulsed pumping. It is shown that heating of the QCL active region is present even under pulse pumping with durations of ~ 100 ns and duty cycle below 0.2%.

Acknowledgment

This research is supported by Ministry of Science and Higher education of Russian Federation (project identifier RFMEFI60719X0318).

References

[1] A V Babichev et al., 2019 Technical Physics Letters **45** 735–738
[2] V V Dudelev et al., 2018 Optics and Spectroscopy **125** 402-404
[3] V V Dudelev et al, 2019 Proc. of CLEO/Europe-EQEC 2019 p 8872297
[4] D Pierciska, 2018 J. Phys. D: Appl. Phys. **51** p. 013001
[5] J Altet, W Claeys, S Dilhaire, A. Rubio, 2006, Proc. of the IEEE, vol. 94, pp 1519-1533
[6] Caplar R and Kulisic P 1973 Proc. Int. Conf. on Nuclear Physics (Munich) vol 1 (Amsterdam: North-Holland/American Elsevier) p 517

Design and Assembly of an Optical System for the Fiber-Coupled Output Laser Module Based on Continuous-Wave Laser Diodes

A N Ignatev, S R Usmanov, E V Kadigrob
FSUE «RFNC-VNIITF named after Academ. E.I. Zababakhin», 456770, Snezhinsk, Russia

Abstract. Laser modules based on semiconductor laser emitters currently have found wide application as pumping sources for fiber lasers. They are relatively less expensive, small-size, and are characterized by high brightness, reliability and efficiency. In this work, we describe the design engineering and manufacturing of compact laser modules based on spatial combination of continuous-wave laser diodes and subsequent beam coupling into a multimode optical fiber with the diameter of 105/125 μm and numerical aperture of 0.15.

1. Introduction

Continuous-wave (CW) laser diodes (LDs) are used as an emitter source in laser modules (LMs) with fiber-coupled output. They designed as a common pumping source for high-power fiber lasers. One of the LM key parameters associated with its effective use is intended for achieving the ultimate output power. To do this, the LM is designed involving the schemes of spatial, polarization, and spectral combination of several laser-diode beams. In this work, the LM design based on the spatial combination of high-power laser diodes with 975-nm center wavelength is considered. We focused on achieving the maximum output power, as well as, reproducible L-I characteristics while maintaining the system reliability.

2. Results and Discussion

Densely packed LDs, as part of the LM design, increase the output power. Maximum quantity of LDs, as well as their emission that can be efficiently combined and coupled into the LM optic fiber are constrained by the emitting area (width) and the beam intensity divergence in two planes, perpendicular to p-n boundary (fast axis), and parallel to p-n boundary (slow axis) [1,2]. Table 1 summarizes the LD parameters used in this work.

Table 1. Laser Diode Parameters.

Parameter	Value
LD Emitter width	90
Fast axis divergence leveled at 95% of the maximum ° (I=12A, t=25°C)	58
Slow axis divergence leveled at 95% of the maximum, ° (I=12A, t=25°C)	10.5

Compensation of the LD's beam intensity divergence requires using some optical elements. For example aspherical lens with the working distance of ~ 80 μm. They require micron-accurate positioning and assembly [3] and minimum-shrinkage adhesion material.

In this work, we made a laser module to combine the beams of seven LDs. The output power at the pumping current of 12 A was 55 W. The L-I characteristics reproducibility was demonstrated with several samples (Fig.1). Burn-in tests were performed to confirm stability of the output performance and the spectral characteristics. Future work can be focused on further multiplication of the LM output power.

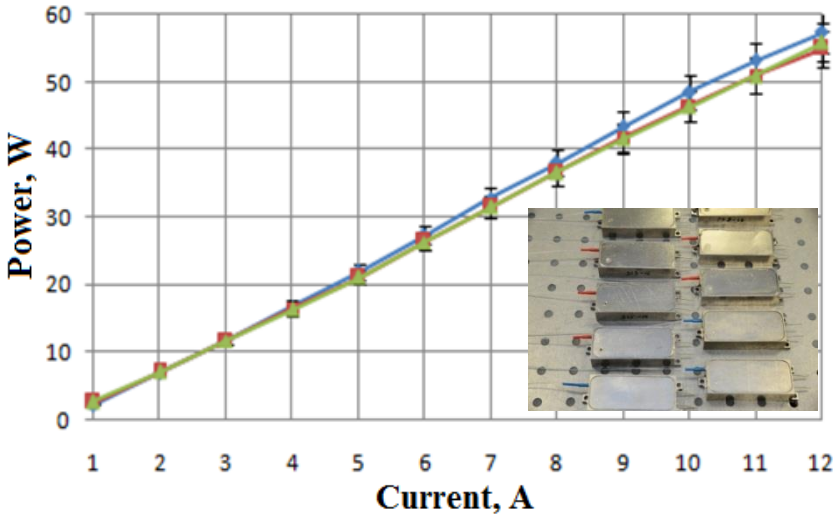

Figure 1. L-I curves of laser modules

References

[1] Liu X. et al. 2015 *Packaging of high power semiconductor lasers* (Springer New York)
[2] Liu R. et al 2015 *Proc. of SPIE* **9348**
[3] Werner M. et al 2009 *Proc. of SPIE* **7198**

Isotype barriers in the connecting part of multi-junction solar cells

M.A. Mintairov[1], V.V. Evstropov[1], S.A. Mintairov[1], M.Z. Shvarts[1] & N.A. Kalyuzhnyy[1]
[1] Photovoltaics Lab, Ioffe Institute, Saint Petersburg 194021, Russia

Abstract. The characteristics of previously found not optimized isotype barriers (on heterointerfaces) in the bottom connecting part of triple-junction *GaInP/GaAs/Ge* solar cell has been investigated. It has been shown that it is possible to obtain the IV characteristics of such barriers in various ways, including by creating structures containing only an isotype substrate and layers forming the heterointerface. It has been found that if heterointerface contact with the p-n junction layers its direct IV characteristic shape depends on the incident light intensity.

1. Introduction

Some triple-junction *GaInP/GaAs/Ge* solar cells (SCs), IV characteristics have a distortion [1-3] – kink in the vicinity of open circuit point. The presence of an inflection correlates with an increase in series resistance. The properties of the inflection gave reason to assume its origin – these are isotype complex barriers that arise between the *p-AlGaAs/p-AlGaInP* structure fragment and the boundaries (on the one side) with p^{++}*-AlGaAs* (p-layer of tunnel heterojunction) and *p-GaAs* (base layer of middle subcell) on the other side [3]. In this paper, to substantiate this assumption, two similar structures has been created by metal-organic epitaxy. In one structure, the barrier is connected with in the p-region of a single-junction *GaAs* solar cell and in another, barrier grown as an independent device. In both structures, the studied fragment connection with the p^{++}*-AlGaAs* layer was changed to connection with the *p-GaAs* substrate.

2. Results and discussion

Figure 1 shows the IV characteristics of isotype barriers. Some characteristics (circles) have been obtained by extraction [2-3] from the light IV curves of a single junction SC, the other has been measured directly on an independent barrier device (triangles). Both characteristics have a similar form and closely coincide in negative bias. It should be noted that the shape of the extracted IV characteristics depends on the solar radiation. Both characteristics could be described by a two-exponential curve presented in [3].

Thus, the possibility of studying the heterointerfaces (barriers) included in the structure of multi-junction solar cells has been shown. Both using the previously proposed methods of IV curve extracting and using of the special structures with separate barriers are reliable for such investigations. The possibility of such studies is in great interest, since there is tendency to an increase the number of multy-juction subcells, so the number of heterointerfaces, including those requiring optimization, will be also increasing.

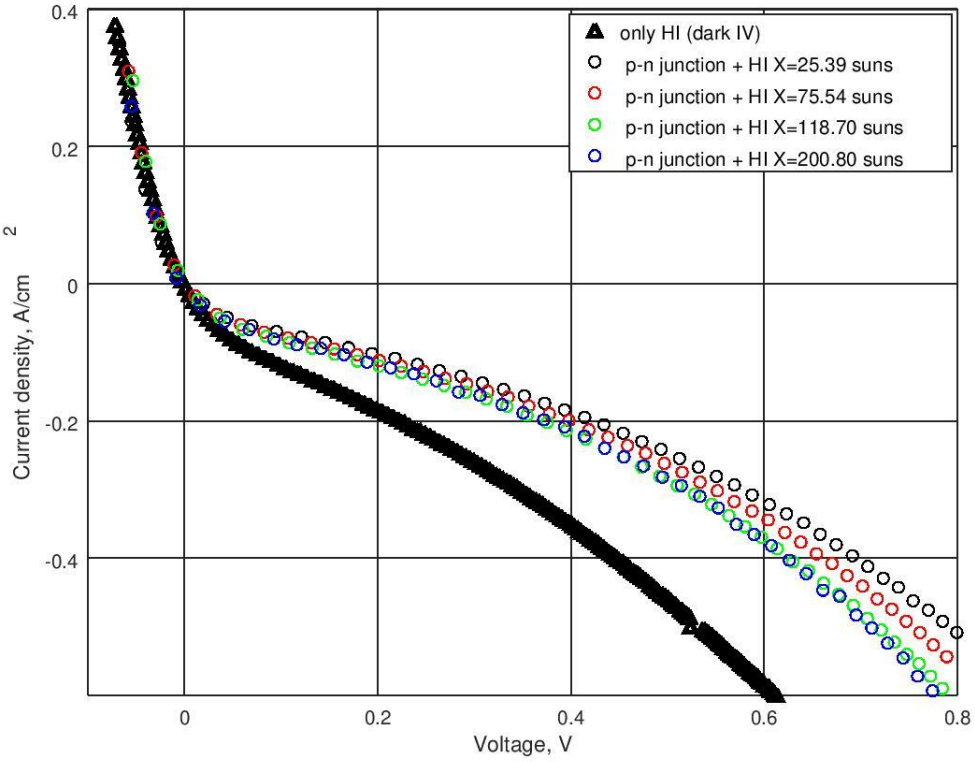

Figure 1. IV characteristics of non-optimized barriers in GaInP/GaAs/Ge solar cell. Circles – extracted form single junction GaAs device, triangles – measured from special device with only barriers layers.

References

[1] J. F. Geisz, M. A. Steiner,N. Jain, K. L. Schulte, R. M. France, W. E. McMahon, E. E. Perl , and D. J. Friedman, Building a Six-Junction Inverted Metamorphic Concentrator Solar Cell, IEEE J. Of PV, 2018, 8 (2)

[2] M.A.Mintairov, V.V.Evstropov, N. A. Kalyuzhnyy, S. A. Mintairov, N.Kh.Timoshina, M.Z.Shvarts, Heterointerfaces in MJ SC: IV Curves and Their Peculiarities, AIP Conference Proceedings, Aix-les-Bains (France) 2015, 1679, 050007

[3] M.A.Mintairov, V.V.Evstropov, N. A. Kalyuzhnyy, S. A. Mintairov, N.Kh.Timoshina, M.Z.Shvarts , Heterointerfaces in the bottom tunnel part of GaInP/GaAs/Ge solar cells, JOP Conference Series 2018, 1124(4):041028

The dependence of recombination in GaAs solar cells on the number of included GaInAs quantum objects

M.A. Mintairov[1], V.V. Evstropov[2], S.A. Mintairov[2], Mariia V. Nakhimovich[2], M.Z. Shvarts[2] &N.A. Kalyuzhnyy[2]

[1] Submicron Heterostructures for Microelectronics, Research & Engineering Center, 194021, St. Petersburg, Russia

[2] Photovoltaics Lab, Ioffe Institute, Saint Petersburg 194021, Russia

Abstract. The experimental characteristics of GaAs p-i-n structures with hybrid GaInAs quantum objects (QOs) has been investigated. The study of electroluminescence spectra show that an increasing of QOs number leads to relative increase in electroluminescence intensity from QOs and decrease it from the GaAs matrix. Increase of QOs recombination leads to a open circuit voltage drop. It has been shown that recombination through deep levels in the QOs begins to dominate recombination in the matrix at lower QOs number than it does with inter-band recombination.

1. Introduction

One of the ways to improve the widely used triple-junction (TJ) *GaInP/GaAs/Ge* solar cells (SCs) is the introduction of hybrid *InGaAs* quantum objects [1] to a middle *GaAs* subcell. This allows increasing middle subcell photogenerated current and improving the photogenerated currents balance of the SC [2]. Note that it was experimentally discovered [3, 4] that the introduction of quantum objects in p – n junction always leads to an increase in the saturation current and, consequently, to an open circuit voltage drop. At the same time, the improvement in the photogenerated current balance will be able to outweigh these losses. As a result, the introduction of quantum objects (QO) in the middle subcell is a one of the promising way to enhance the TJ SC performance. In the work we studied the change in the recombination processes in the p-n junction with the introduction of quantum objects.

2. Results and discussion

The photovoltaic and electroluminescent characteristics of solar cells with a different number of hybrid QOs rows has been investigated. One can see on Fig.1b that the increasing of quantum objects number changes the electroluminescence spectrum. With an QOs rows increasing the ratio between the peak intensities from the *GaAs* matrix (peaks in the region of 1.42 eV) and from hybrid QOs is changing. Note that all the spectra shown has been obtained at same current (10 mA) through the SC. Thus, the increasing of QOs rows reduces the relative contribution of recombination from the matrix and increases the contribution from hybrid QOs.

This effect on the electroluminescence spectrum is consistent with the effect on the V_{oc}-J_g (open circuit voltage vs photogenerated current) characteristics (Fig. 1a). It can be seen that with an increase in the number of rows, the open circuit voltage drops, in other words, the p-n junction saturation current (J_0) increases. A two-diode model has been used (lines on Fig. 1a) to describe the experimental characteristics (symbols on Fig. 1a) and J_0 values have been obtained for a unary (diffusion) and

binary (recombination) current components. These values have been used to calculate the open-circuit voltage drop. According to [5], a change in V_{oc} also indicates a change in the energy gap. In our case there are two type of recombination centers (in matrix and in OQs) with different energy gaps, so this energy characterize the average recombination energy. In Figure 1b, we shown this energy by vertical lines.It has been calculated by using unary and binary saturation currents. It can be seen that with an increase in the dominance of QOs recombination, the average recombination energy (calculated from the V_{oc}-J_g characteristics) shifts toward the main peak of QOs (in the region of 1.2 eV).
Note, that the energy calculated by unary current do not reach the QOs effective band gap while energy calculated by binary component reaches it. The unary saturation current determined by inter-band recombination and binary one by a recombination thought a deep layers. The equality of binary average recombination energy with QOs effective band gap at 20 QOs rows means that recombination through deep levels in QOs begin to dominates at such QOs row numbers inter-band recombination is till presented in GaAs matrix.

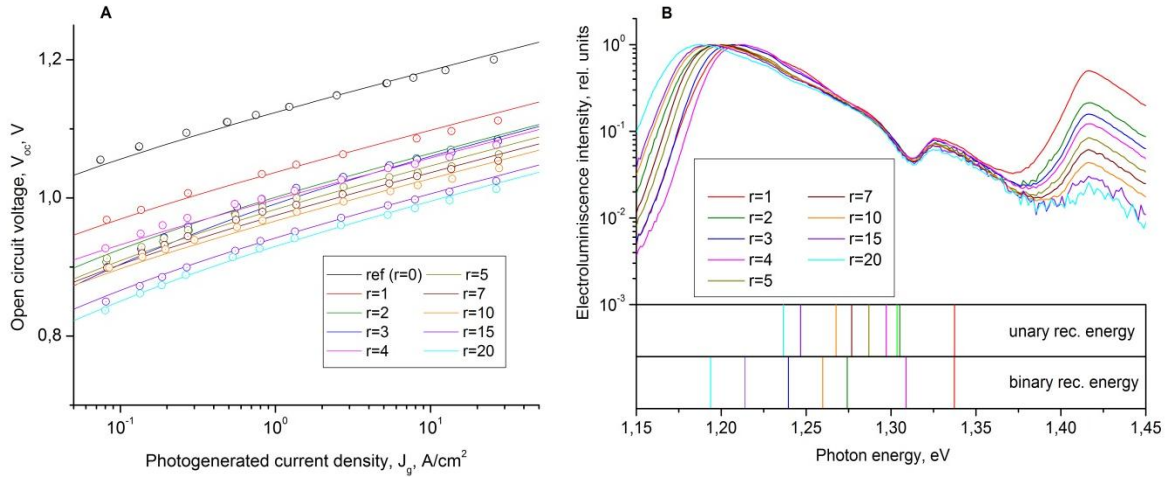

Figure 1(a, b). (a) Open circuit voltage vs photogenerated current (V_{oc}-J_g) characteristics of GaAs solar cells with GaInAs hybrid quantum objects and of a reference solar cell (without quantum objects): symbols – experimental characteristics, lines – two diode model fit**. (b)** Electroluminescence intensity spectra for *GaAs* solar cells with *GaInAs* hybrid quantum objects (solid lines) and calculated average recombination energy of unary (diffusion) and binary(recombination) current flow mechanisms (energies shown as a vertical lines).

Acknowledgments
The work has been supported by the Russian Science Foundation (Grant №17-72-20146).

References
[1] S. A. Mintairov, et.al., Electron. Lett. 51 1602–4, 2015
[2] H. Fujii., et. al., Prog. Photovolt: Res. Appl. 2014; 22:784–795.
[3] M.A. Mintairov, et.al., Semiconductors, 2018, v52, p. 1244
[4] M.A. Mintairov, et.al., AIP Conf. Proc., St. Petersburg (Russia), 2016, v. 1748, p. 050003
[5] R. R. King, et. al., Prog. Photovolt: Res. Appl. 2011, 19

Electrically pumped microdisk lasers with semitransparent conducting pyrolytic carbon film

E I Moiseev[1], Yu S Polubavkina[1], N V Kryzhanovskaya[1], M M Kulagina[2], Yu M Zadiranov[2], M V Maximov[1], T Kaplas [3], Yu Svirko[3], A A Lipovskii[1,4], F I Zubov[1], A E Zhukov[1]

[1] St Petersburg Academic University of RAS, Khlopina 8(3), St Petersburg 194021, Russia

[2] Ioffe Physical Technical Institute of RAS, St Petersburg, Russia

[3] University of Eastern Finland, Joensuu, Finland

[4] Peter the Great St Petersburg Polytechnic University, St Petersburg 195251, Russia

Abstract. Electrically driven microdisk lasers with top contacts made of a semitransparent conducting pyrolytic carbon film are developed. Electrical properties of the pyrolytic carbon contact to p-type doped GaAs epitaxial layer are studied. Room temperature electroluminescence spectra from the array of the microdisk lasers are demonstrated.

Introduction

There has been significant work on the miniaturizing semiconductor lasers. Recently semiconductor WGM microlasers based on ring/disk cavities with low threshold (2 uW) [1] and high quality factor (Q) up to $7x10^5$ [2] have been demonstrated. Under optical pumping, lasing operation at 100°C of microring laser as small as 2 μm has been recently reported [1]; room temperature lasing was reported in 1.16 μm GaInAsP microdisk laser [3] and in 1μm InAs/GaInAs quantum dot (QD) microdisk laser [4]. At the same time, the smallest diameter of the microdisk laser with current injection is 6.5 μm with room temperature operation [5]. Further reduction of the injection microdisk laser requires electron beam lithography, planarization stage or air-bridge technology to form an electrical contact to upper p-doped layers. In this work we study the possibility to use the pyrolytic carbon (PyC) film to make an electric contact to the p-doped GaAs cap layer. Room temperature electroluminescence spectra of the microdisk lasers with diameters 15-30 μm, which are electrically pumped through the semitransparent PyC layer are demonstrated.

Experiment

Epitaxial structures were grown by molecular beam epitaxy on an *n*+ GaAs(100) substrate. Ten layers of InAs/$In_{0.15}Ga_{0.85}As$ QDs were deposited in the middle of a 0.44 μm thick GaAs waveguiding layer confined with $Al_{0.25}Ga_{0.75}As$ claddings. Microdisk resonators were formed by means of chemical plasma etching to have diameters of 15…31 μm. Etch depth was about 7μm. AgMn/NiAu (AuGe/Ni/Au) metallization was used to form ohmic contacts to *p*+ GaAs cap layer (*n*+ substrate, respectively). PyC films were deposited in CVD quartz chamber using CH_4:H_2 gas mixture on the transferring PMMA layer. In our work we used 20-25 nm-thick PyC films with app. 50% transparency at 1.3 μm. To make an electrode to p-type contact, the PyC film was attached to the top of the array of the microdisk lasers. Owing to mechanical strength the film did not show any sagging. Current was

injected thought the PyC film to the array of the microdisk lasers using a copper tape. The schematic of the microdisk lasers with PyC contact is shown in Fig.1. Lasers were mounted on a copper heatsink and tested at room temperature without external cooling. In-plane emitted light was collected with a piezoelectrically adjustable x100 Olympus LMPlan IR objective.

Results

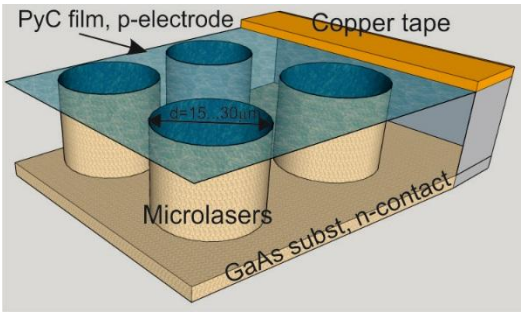

Fig.1 3D achematic illustration of the array of microdisk lasers with top PyC electrode.

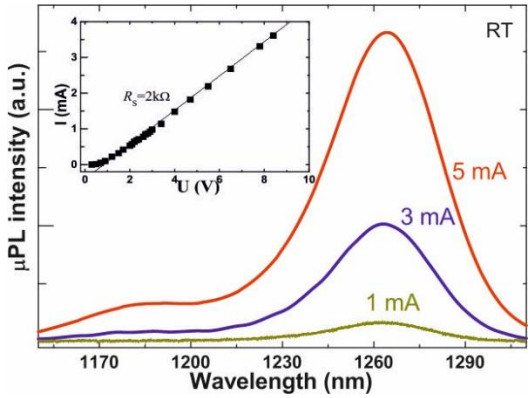

Fig.2 Electroluminescence spectra of the microdisk array with PyC electrode at room temperature. Inset: current–voltage characteristics of the microlasers.

The microlasers demonstrate well pronounced turn-on behavior of current-voltage characteristic with an opening voltage under forward bias of U_0 ~1 V and series resistance R_S =2kOhm. Figure 2 shows the electroluminescence spectra of the microdisk array with diameters of 15-30 μm recorded at different currents. The emission spectrum has the typical form of the spontaneous emission of self-organized InAs/InGaAs QDs with 1.26 μm maxima at low pump power. We did not obtain any WGM lasing due to the spread of the current between the different lasers. With increasing pump current, the electroluminescence maxima demonstrates red shifts caused by the heating of the structure (0.8nm/mA). From this shift we can estimate the structure overheating to be 60°C at 15mA, which is nearly the same obtained for the single microlaser pumped directly without PyC film.

Acknowledgments
The work is supported in different parts by RFBR projects 15-32-20238 and 15-02-03624.

References

[1] Maximov M V, Kryzhanovskay N V, Nadtochiy A M, Moiseev E I, Shostak I I, Bogdanov A A, Sadrieva Z F, Zhukov A E, Lipovskii A A, Karpov D V, Laukkanen J and Tommila J 2014 *Nanoscale Research Lett*. **9** 657.
[2] C.P.Michael, K.Srinivasan, T.J.Johson, O.painter, K.H. Lewe, K.henessy, H.Kim, E.Hu, *Appl.Phys. Lett*. 90, 051108 (2007).
[3] R.Perahia, T.P.Mayer Alegre, A.H.Savafi-Naeini, O.Painter, *Appl.Phys. Lett,* 95, 201114 (2009).
[4] N.V. Kryzhanovskaya, A.E. Zhukov, M.V. Maximov, E.I. Moiseev, I.I. Shostak, A. M. Nadtochiy, Yu.V. Kudashova, A.A. Lipovskii, M.M. Kulagina, S.I. Troshkov, IEEE JSTQE, 21, 1-5 (2015).
[5] Mao M-H, Chien H-C, Hong J-Z and Cheng C-Y 2011 *Opt. Exp.* **19** 14145.
[6] T.Kaplas, Yu.Svirko, *Journal of Nanophotonics*, **6**, 061703, 2012.

Lasing in microdisc resonators with InAs/InGaAs quantum dots transferred on a silicon substrate

E I Moiseev[1], N V Kryzhanovskaya[1], A M Nadtochiy[2] , M V Maximov[1], A E Zhukov[1], I I Shostak[1], M M Kulagina[3], AV Savel`ev[1,2], K A Vashanova[3], A A Lipovskii [2,1]

[1] St. Petersburg Academic University, Nanotechnology Center for Research and Education, Russian Academy of Sciences, St. Petersburg, 194021 Russia
[2] St. Petersburg Polytechnic University, St. Petersburg, 195251 Russia
[3] Ioffe Physical–Technical Institute, Russian Academy of Sciences, St. Petersburg, 194021 Russia

moiseeveduardne@gmail.com

Abstract. Room temperature lasing in 6 μm microdisks laser with InAs/InGaAs quantum dots transferred on a silicon substrate is demonstrated. Immersing of the microdisc into glue does not lead to deterioration of surface quality or to significant increase in radiation loss. Quasi single mode lasing is observed at 78 K.

1. Introduction

Currently there is a need to develop radiation sources for optoelectronic integrated circuits with small size, low power consumption, planar design and high temperature stability [1, 2]. Semiconductor ring and disk microcavities with active region of InAs/InGaAs quantum dots (QDs) satisfy these requirements. The non-direct gap energy structure of silicon, which is dominant in electronics, is significantly hampering the development of silicon microlasers. Thus, the problem of integration high performance III-V radiation sources with silicon chips remains topical. Recently were demonstrated microring and microdisk lasers based on InAs/InGaAs QDs with outstanding characteristic and lasing up to 107 ^{0}C [3]. In this work we develop the simple technology of transferring of microdisk laser with InAs/InGaAs QDs on a silicon substrate and get it characterization in 78-300K temperature range.

2. Experiment

The structure was grown by molecular beam epitaxy with Riber 49 setup with a solid-state As source on a semiinsulating GaAs (100) substrate. For selective etching, a buffer GaAs layer was deposited and then $Al_{0.98}Ga_{0.02}As$ stoplayer was grown. The InAs/InGaAs QDs layers were inserted into a 0.2-μm thick GaAs waveguiding layer. Microdisc resonators with 6 μm diameter were formed using photolithography and etching by an Ar+ ion beam (figure 1, a). The epitaxial side of the structure was then fixed to the Si substrate by glue (figure 1, b). The GaAs substrate and buffer layers and $Al_{0.98}Ga_{0.02}As$ stop-layer were subsequently removed using an etching agents (figure 1, c). Microphotography of microdisk (D=6μm) is shown at figure 1, d. The structures were investigated under optical pumping with YAG: Nd laser (λ = 532nm).

3. Results

Microphotoluminescence spectra of the microdisk transferred on Si substrate obtained at 300 K is shown at figure 2. The narrow lines in the spectra correspond to the whispering gallery modes with different radial and azimuthal numbers. The intensity-pump curve for dominant line (λ=1296 nm) has a pronounced threshold (see inset in figure 2). The quality factor of the dominant line $Q=\lambda/\Delta\lambda$ exceeds 3.4×10^4 at 300 K. This value is the same for initial microdisks measured before transferring. This is allows us to conclude that developed technology of transferring and immersing of the microdisc into the glue do not lead to deterioration of microdisk surface quality or to a significant increase in radiation losses due to decrease in the contrast of the refractive index. At low temperatures the dominant wavelength line is shifted to λ= 1237 nm due to the temperature driven active region band-gap shrinkage. Decrease of temperature to 78 K results in slight decrease of lasing threshold by 2 ($P_{th}^{300K}=2\ P_{th}^{78K}$) due to suppression of nonradiative recombination processes. The side mode suppression ratio at 78K is 14 dB. Thus, the microdisc exhibits quasi single mode lasing.

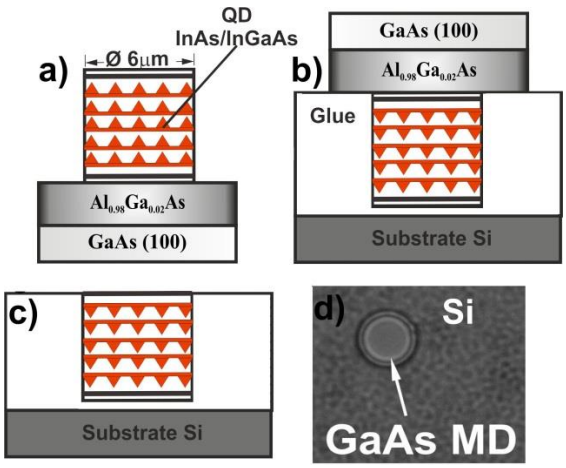

Figure 1. Schematic sequence of microdiscs transfer technology: (a) photolithography and etching by an Ar+ ion beam, (b) gluing of microdiscs to a Si substrate, (c) removal of a sacrificial layers; (d) microphoto of disc microresonator on silicon.

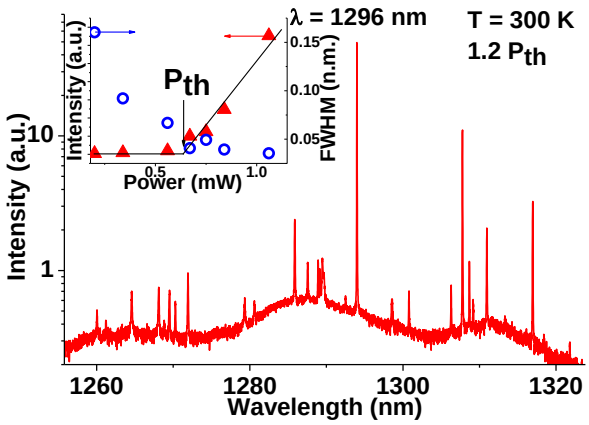

Figure 2. Spectra of microdisks at 300 K. Insert: intensity-pump curve of the microdisk.

4. Conclusion

The method of transfer of microdisc resonators with InAs/InGaAs QDs on the silicon substrate has been developed. Room temperature lasing in 6 μm microdisks laser is demonstrated.

Acknowledgments

The work is supported in different parts by «Foundation for Development of the Center for Elaboration and Commercialization of New Technologies».

References

[1] Levi A F J, Slusher R E, McCall S L, Tanbun-Ek T, Coblentz D L and Pearton S J 1992 *Electron. Lett.* **28** 1010-12

[2] Baba T and Sano D 2003, *IEEE J. Sel. Top. Quantum Elecctron* **9** 1340-46

[3] Kryzhanovskaya N V, Zhukov A E, Nadtochiy A M, Slovinskii I A, Maximov M V, Kulagina M M, Savel'ev A V, Arakcheeva E M, Zadiranov Yu M, Troshkov S I and Lipovskii A A **46**(8), 1040-43

Investigations of the share of laser radiation in injection microdisk lasers based on InGaAsN quantum wells

S A Kadinskaya[1], M V Maximov[1], N V Kryzhanovskaya[1,2], O I Simchuk[1], M M Kulagina[2], E I Moiseev[1], M Guina[4], A E Zhukov[1,2,¶]

[1] St Petersburg National Research Academic University of RAS, St Petersburg, Russia
[2] Peter the Great Polytechnic University, St Petersburg, Russia
[3] Ioffe Physicotechnical Institute, Russian Academy of Sciences
[4] Tampere University of Technology, Tampere, Finland

Abstract. The results of a comparative analysis of the spectral and threshold characteristics of injection microdisk lasers operating at room temperature with a spectral range of 1.2xx μm with an active region of InGaAsN / GaAs quantum wells for the results obtained in this and earlier studies are presented. It was found that the microlasers studied for this work have better characteristics in comparison with the microlasers studied in earlier works.

1. Introduction

Microdisk lasers are promising as ultra-small radiation sources [1]. The advantages of such lasers are ease of manufacture, small size, low threshold currents, and radiation directivity in the cavity plane. Using quantum dots (QDs) as active region in such lasers have advantages of low threshold and high thermal stability of characteristics [2]. However the ground state QDs optical gain is limited [3] due to the finite number of the QDs what leads to lasing via excited states of QDs. Quantum well (QW) active region provides higher gain as compared to QDs. Therefore, using QW active region may help to overcome the problem of gain saturation.

2. Experiment

The heterostructures used to create microdisk lasers were synthesized by molecular beam epitaxy on n^+ GaAs (100) substrates. Its active region consisted of 3 strained $Ga_{0.7}In_{0.3}N_{0.02}As_{0.98}$ QWs, separated from each other by 10 nm thick GaAs layers and placed in a 0.4 μm thick undoped GaAs waveguide layer. The structure was made as semiconductor p-n diod, with p-side on top, and n-side is substrate. On the top structure has 200-nm-thick p-GaAs layer, in the bottom, between barrier and substrate is 500-nm-thick layer of n-GaAs. Microdisks were fabricated using photolithography and wet etching. The structures were investigated under different impulse injection pumping at the room temperature. Microelectroluminescence signal (μEL) was measured by an Optical Spectrum Analyzer AQ6370. Diameter micodisk was in the range from 11 to 30 μm.

3. Results

μEL spectra and the dependence of the intergal intensity on the pump current were obtained for all available dimensions. You can see one of them on Figure 1. A comparison of the dependences of the threshold pump current on the diameter of the microdisk laser for the results obtained in this and

earlier studies [4] is presented in Figure 2. A decrease in the threshold pump current for new structures is observed by optimizing epitaxial structure growth. Shares of laser radiation to total optical power depending on the pump current normalized to the threshold pump current were also obtained. In Figure 2, you can see that the resulting laser radiation fraction is more than 60%, which is much larger than for structures with QD (~2.8%) [5].

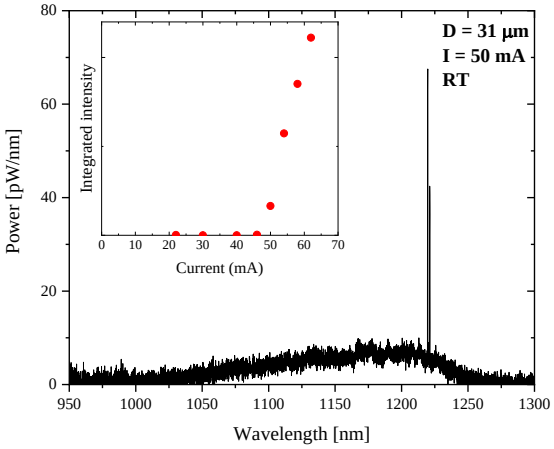

Figure 1. μEL spectra of a 30 μm in diameter microdisk laser at RT

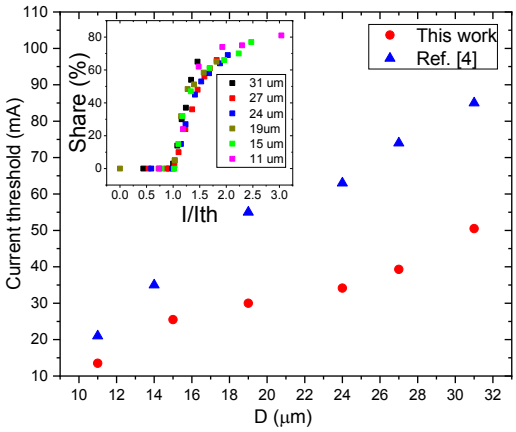

Figure 2. The dependence of the threshold pump current on the diameter of the microdisk laser

Acknowledgments

The work is supported by FRBR (16-29-03127), Ministry of Higher Education and Science of the Russian Federation (project No 3.9787.2017/8.9).

References

[1] Srinivasan, Kartik, et al. "Cavity Q, mode volume, and lasing threshold in small diameter AlGaAs microdisks with embedded quantum dots." Optics Express 14.3 (2006): 1094-1105.

[2] Arakawa, Y., and Hiroyuki Sakaki. "Multidimensional quantum well laser and temperature dependence of its threshold current." Applied Physics Letters 40.11 (1982): 939-941.

[3] Bimberg, D., et al. "InGaAs-GaAs quantum-dot lasers." IEEE Journal of selected topics in quantum electronics 3.2 (1997): 196-205.

[4] Moiseev, E. I., et al. "Room temperature lasing in injection microdisks with InGaAsN/GaAs quantum well active region." Journal of Physics: Conference Series. Vol. 1124. No. 8. IOP Publishing, 2018.

[5] Zubov, F. I., et al. "Laser characteristics of an injection microdisk with quantum dots and its free-space outcoupling efficiency." Semiconductors 50.10 (2016): 1408-1411.

Terahertz waves polarization rotation in photoexcited single-wall carbon nanotube thin film

A Kvitsinskiy[1], P Demchenko[1,2], M Novoselov[1,2], I Anoshkin[1], K Bogdanov[3], A Baranov[3] and M Khodzitsky[1,2]

[1] Terahertz Biomedicine Laboratory, ITMO University, 3 Kadetskaya Liniya, Building 2, Saint Petersburg 199034, Russian Federation
[2] Center for Bioengineering, ITMO University, 49 Kronverksky Prospekt, Saint Petersburg 197101, Russian Federation
[3] Center of Information Optical Technology, ITMO University, 14 Birzhevaya Liniya, Saint Petersburg 199034, Russian Federation

E-mail: anatolykvitsinskiy@gmail.com, khodzitskiy@yandex.ru

Abstract. Terahertz time-domain spectroscopic polarimetry (THz-TDSP) method was used to experimental study polarization properties of unaligned single-wall carbon nanotube thin films with different geometric parameters on transparent float glass substrates in a frequency range from 0.2 THz to 0.8 THz (corresponding to a wavelength range from 1.50 mm to 0.37 mm) at controlled room temperature. Frequency dependencies of azimuth and ellipticity angles of a polarization ellipse (PE) of the electromagnetic waves transmitted through the samples, and the PEs at various frequencies were obtained for various values of an external near infrared optical pumping with an external static magnetic field acting the samples. Polarization properties were calculated from temporal waveforms of signals transmitted through the samples at two positions of a transmission direction of polarizers. The results show that using nanomaterials-based structures it is possible to devise efficient magneto-optically tunable polarization modulators that can be used in the advanced fields of terahertz nanophotonics.
Keywords: terahertz time-domain spectroscopic polarimetry, unaligned single-wall carbon nanotubes, polarization rotation, polarization properties, Stokes parameters, Faraday effect.

1. Introduction

Terahertz (THz) frequency range is widely used in physics and astronomy, chemistry and medicine, security and telecommunication systems, and other fields of science and technology. Currently, one of the relevant problems for development in THz photonics is the lack of efficient and affordable tunable under external influences devices for modulating the polarization of an electromagnetic (EM) radiation in the THz frequency range. A promising solution to the foregoing problem is a study of carbon nanomaterials-based structures (CNBSs) for use as a functional medium in polarizers due to unique optical and electronic properties of this materials. For experimental studies of polarization properties of materials, and the magneto-optic Faraday effect (MOFE) and the magneto-optic Kerr effect (MOKE), THz time-domain spectroscopic polarimetry (TDSP) and THz time-domain spectroscopic ellipsometry (TDSE) methods are widely used.

The goal of this work was an experimental study of unaligned single-wall carbon nanotubes (U-SWCNTs) with different geometric parameters using the THz-TDSP method with an external near infrared (NIR) optical pumping (OP) system to obtain their polarization properties.

2. Materials and methods

Two U-SWCNT thin films samples on transparent float glass (TFG) substrates were studied. The U-SWCNTs were synthesized by the chemical vapor deposition at KTH Royal Institute of Technology's Microsystem Technology Laboratory (Sweden) on a nitrocellulose micropore filter (NCMF) using ethanol gas without adding the hydrogen [1]. Then the carbon nanotubes (CNTs) were transferred from the NCMF to the TFG substrates. The diameters of CNTs were calculated using the Kataura plot, and were 1.1–1.4 nm. The length of the CNTs was visualized by the transmission electron microscopy, and was 0.3–15 µm. To study the polarization properties of the experimental samples using the THz-TDSP method, a system based on a THz time-domain spectrometer [2], three wire grid polarizers, a 980 nm laser for creating the external OP of 0.2–1.0 $\mathrm{W cm^{-2}}$, and a NdFeB axially magnetized magnet for creating an external static magnetic field (MF) of ∼0.3 T were used. Temporal waveforms of the THz signals transmitted through the experimental samples were recorded at the parallel and the crossed by 45° positions to a transmission direction of the polarizers, under a controlled room temperature of 291–293 K.

3. Results and conclusion

Experimental frequency dependencies of an azimuth angle ψ and an ellipticity angle χ of a polarization ellipse (PE) of the EM waves transmitted through the samples in the range 0.2–0.8 THz and the PEs at various frequencies were calculated. Results are shown in **Figure 1**.

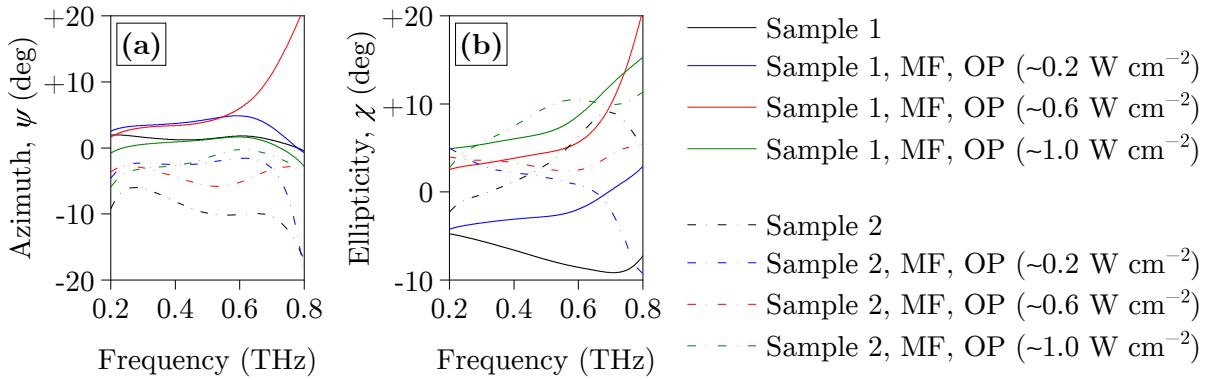

Figure 1. Frequency dependencies of **(a)** the azimuth angle ψ, and **(b)** the ellipticity angle χ of the PE of the EM waves transmitted through the samples.

According to the obtained experimental results, it is seen that, under the NIR OP of ∼0.6 $\mathrm{W cm^{-2}}$, the azimuth angle changes up to 20° and the ellipticity angle changes up to 10° relative to the U-SWCNT thin films without influences. As a result of this work, the polarization properties of the U-SWCNT thin films in the THz frequency range were studied. It can be seen that the U-SWCNTs is an efficient nanomaterial for devise magneto-optically tunable polarizers, which are necessary in cutting-edge THz nanophotonics.

Acknowledgments

The reported study was funded by the Government of the Russian Federation, Grant Number 08–08, and by the Russian Science Foundation (RSF), Grant Number 19–72–10141.

References

[1] Tonkikh A A *et al.* 2012 *J. Nanoelectron. Optoelectron.* **7**(1) 99–101 URL https://doi.org/10.1166/jno.2012.1226

[2] Kvitsinskiy A *et al.* 2019 *SN Appl. Sci.* **1**(12) 1714 URL https://doi.org/10.1007/s42452-019-1748-x

Photoionization of polarized argon atoms in a magnetic field

E.A.Viktorov[1], N.N.Bezuglov[1], A.N.Klyucharev[1], A.A.Pastor[1], P.Yu.Serdobintsev[1], M.A.Khodorkovskii[2]

[1] Department of Optics, Faculty of Physics, St. Petersburg State University, 198504, Russia

[2] Peter the Great St. Petersburg Polytechnic University, St. Petersburg, 195251, Russia

Abstract. Analyzing of fluorescence signals after exciting atomic states by polarized light is an important brunch of modern spectroscopy. Observation of magnetic resonances in polarized gas media is the basis of construction and realization of sensitive magnetometers. External magnetic fields result in diverse types of oscillating structures in detected signals that allow making precision measures of atomic state parameters beyond limitations due to Doppler broadening. Traditional methods of spectroscopy are associated mainly with bound-bound optical transitions [1]. In the present report, we demonstrate, both experimentally and theoretically, a possibility to examine photocurrent oscillations upon photoionization of argon atoms in a supersonic beam.

1. Experiment

Three-photon excited states $3s^2 3p^5(^2P_{3/2})3d[5/2]_3$ (jl-coupling [2]) of Ar atoms having the azimuthal quantum number M=3 were produced by titanium–sapphire femtosecond laser light ($\lambda = 263.8$ nm) of the right circular polarization (see Fig. 1). Photoionization of polarized atoms in the state J=3, M=3 was operated as well by right-circularly polarized light of the second harmonic of titanium–sapphire laser ($\lambda = 400$ nm). Photoelectrons were trapped in an inhomogeneous magnetic field of a magnetic-bottle time-of-flight electron spectrometer. The pump (exciting) and probe (ionizing) pulses duration were 50 fs; the delay time t between them was varied in the range of 0 – 650 ps. With varying t, periodical oscillations of photocurrent intensity were arising (Fig. 2), as a result of Larmor precession of optically polarized argon atoms in the magnetic field.

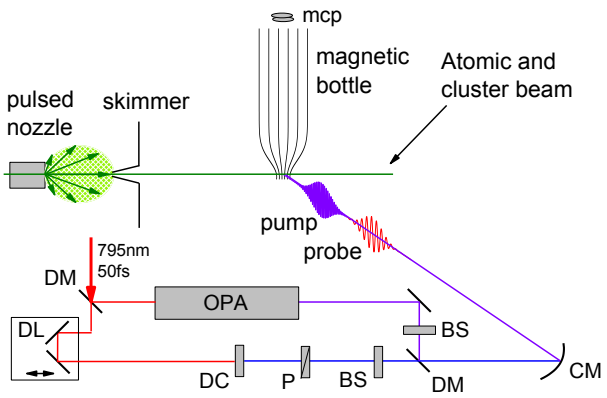

Figure 1. Experimental setup: OPA – optical parametric amplifier; DL – delay line; DM – dichroic mirrors; DC – doubling crystal; P – polarizer; BS – Babinet-Soleil compensators; CM – concave mirror.

2. Equations

We performed a theoretical analysis of the oscillating structure of integral photocurrents $I_{l'}(t)$ when one of two possible values of photoelectron orbital moment $l \rightarrow l' = l \pm 1$ is fixed. The irreducible tensor

operators technique for atomic and photon polarization moments ρ_q^κ, Φ_q^κ [1] along with the sum rules [2] allow one to derive the following formula for the partial photocurrents:

$$\frac{I_{l'}(t)}{I_{pr}} \sim \rho_0^0 \Phi_0^0 D_0 M_0 + \rho_0^1 \Phi_0^1 D_1 M_1 \cos(\omega_L t) + \rho_0^2 \Phi_0^2 D_2 M_2 (1 + 3\cos(2\omega_L t))/4 \qquad (1)$$

where I_{pr} is the intensity of the ionizing laser light. The first atomic polarization moments ρ_q^κ with $\kappa = 0$ (population), $\kappa = 1$ (orientation) and $\kappa = 2$ (alignment) determine the oscillation of the observed signal on the Larmor frequency overtones $\kappa\omega_L$. Coefficients D_k and M_k

$$D_\kappa = (-1)^{l'+l} \begin{Bmatrix} 1 1 \kappa \\ l l l' \end{Bmatrix} \quad M_\kappa = (2J+1)(2K+1) \begin{Bmatrix} K K \kappa \\ J J \frac{1}{2} \end{Bmatrix} \begin{Bmatrix} l l \kappa \\ K K j \end{Bmatrix} (-1)^{2K-l-J-0.5-j} \qquad (2)$$

are expressed via *6j*-symbols [1], which contain quantum numbers of the bound atomic state $3s^2 3p^5(^2\mathrm{P}_j) nl[K]_J$ in the initial channel and the free electron orbital moment $l' = l \pm 1$ in final (ionization) channel.

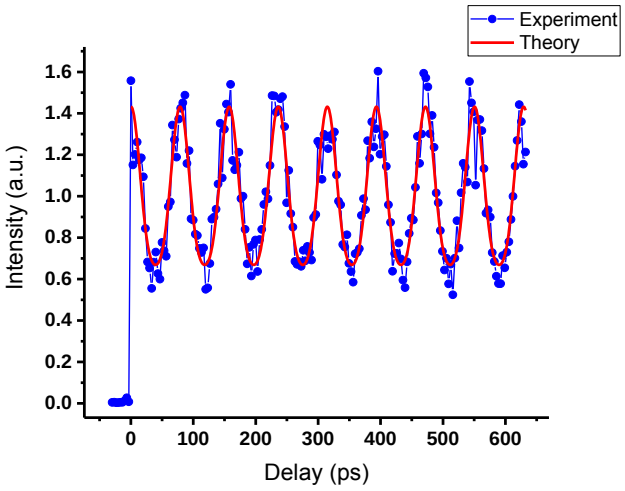

Figure 2. Delay dependence of photoionization intensity I(t) for the polarized Ar state $^2\mathrm{P}_{3/2}\,3\mathrm{d}[5/2]_3$, M=3 (113 716.555 cm^{-1}) (dots – experiment, solid curve – theory).

3. Conclusions

The aggregated intensity *I(t)* of photocurrent

$$I(t) = \sum_{l'=l\pm1} g_{l'} I_{l'}(t) + I_{l'}(t); \qquad g_{l'} = (nl \,||\, D \,||\, \varepsilon' l')^2 \qquad (3)$$

is calculated from the partial intensities (1) with statistical weights $g_{l'}$ equal to reduced matrix elements of bound-free optical transitions (ε' is the photoelectron energy). Figure 2 demonstrates close agreement between experiment and theory provided the ratio of statistical weights $g_{l'=3} / g_{l'=1} = 3.98$. The latter value corresponds to the Bethe rule [2], which states that the dominant photoprocesses occur with increasing photoelectron orbital moments.

References

[1] Aleksandrov, E. B., Chaika, M. P. and Khvostenko, G. I. (1993). Interference of Atomic States. Springer Series on Atoms and Plasmas; 7, Springer-Verlag, Berlin.
[2] Sobelman, I. I. (1992). Atomic Spectra and Radiative Transitions. Springer, Berlin.

Orientation and alignment of $O(^1D_2)$ atoms in ozone photodissociation via the Hartley band

B. V. Semak[1], A.A. Semenov[1], and O. S. Vasyutinskii[1]
[1]Physical gasdynamics Laboratory, Ioffe Institute RAS, Saint Petersburg 194021, Russia

Abstract. We theoretically derived symmetry properties of the anisotropy transforming coefficients describing angular momentum polarization of photofragments produced in photodissociation of planar triatomic molecules with polarized light. The full quantum mechanical approach was used throughout the paper. We have shown that orbital orientation of O(1D2) atoms produced in photolysis of ozone can be described by three independent incoherent and coherent excitation mechanisms described by corresponding anisotropy transforming coefficients that have either real, or pure imaginary values. The theory was used for describing ozone photolysis at 266 nm.

1. Introduction

As known [1,2] vector correlation in molecular photodissociation can be effectively described by a set of anisotropy transforming coefficients (ATC) related to several independent mechanisms of production of photofragment orientation and alignment. The ATC contain detailed information on photolysis dynamics and can be either determined directly from experiment, or calculated (at least in principle) from quantum mechanical theory. In particular, ATC allow researcher to obtain information on molecular excited states symmetry and on nonadiabatic interactions between different potential energy surfaces (PES). Ozone is a planar molecule that plays an important role in the atmospheric processes on the Earth and in various industrial devices. In particular, ozone photolysis is responsible for protection of all living organisms on Earth from harmful UV radiation from space. Therefore, detailed understanding of the mechanisms of ozone photolysis is very important as it can provide deep insight into the physical and chemical processes in the Earth atmosphere. In this paper full quantum mechanical calculations on the photofragment orientation and alignment produced in photolysis of ozone with polarized light have been made using the irreducible tensor representation of the density matrix and the first-order time-dependent perturbation theory. Dissociation wave function has been expanded as a Wigner D-function series and the symmetry of ATC have been analysed.

2. Theoretical approach

The expression describing the polarization cross-section of the photofragments produced in molecular photolysis was presented in the form [2]:

$$\sigma_{KQ}(\boldsymbol{k}) \sim \sum D^{k_d}_{q_d q_k}(\boldsymbol{k}) D^{K^*}_{Q q_k}(\boldsymbol{k}) E_{k_d q_d}(\boldsymbol{e}) c^K_{k_d q_k}, \qquad (1)$$

where $D^J_{MM'}(\boldsymbol{k})$ are Wigner D-functions, $\boldsymbol{k}$ is the recoil direction, $E_{k_d q_d}(\boldsymbol{e})$ is a light polarization matrix, and $c^K_{k_d q_d}$ are ATC. Summation over the indices k_d, q_d, q_k is assumed in eq. (1).

The rank K in eq. (1) can take the values K=0,1 and 2 describing the photofragment number, angular momentum orientation, and alignment, respectively, and Q is the component of K onto the recoil direction k. The rank k_d in eq. (1) can be equal to 0,1,2 where k_d = 1 and 2 refer to circular and linear polarization of the incident photolysis light [1].

3. Results

The symmetry properties of the ATC $c^K_{k_d q_d}$ in case of a planar triatomic molecule have been derived explicitly by considering symmetry properties of Clebsch-Gordan, 6-j symbols and photofragment's asymptotic wave functions.

We have shown that ATC obey the following symmetry properties:

$$c^{K^*}_{k_d q_k} = c^K_{k_d - q_k} \tag{2}$$

$$c^K_{k_d - q_k} = (-1)^{K+k_d} c^K_{k_d q_k} \tag{3}$$

As resulted from eqs. (2) and (3) the ETC with odd $K + k_d$ values are all purely imaginary and those with even $K + k_d$ are real. A model using the symmetry properties in eqs. (2) and (3) have been built that explains earlier reported experimental results on vector correlations in ozone photolysis at 266 nm [3].

4. Acknowledgments

We acknowledge the financial support from the Foundation for the Advancement of Theoretical Physics and Mathematics "BASIS".

References

[1] A.G. Suits and O.S. Vasyutinskii, Chem. Rev. 108, (2008) 3706.
[2] P. S. Shternin and O. S. Vasyutinskii, J. Chem. Phys. 128, 194314 (2008).
[3] S. K. Lee, D. Townsend, O. S. Vasyutinskii, A. G. Suits, Phys. Chem. Chem. Phys. 7, (2005) 1650.

Laser-Induced Crystals on a Stainless Steel Surface

A A Burtsev[1], **D N Bukharov**[2], **O Ya Butkovskii**[2]
[1]Nanophotonics and Nanoplasmonics Laboratory, Institute on Laser and Information Technologies - Branch of the Federal Scientific Research Centre "Crystallography and Photonics" of Russian Academy of Sciences, Shatura, Moscow Region 140700, Russia
[2]Department Physics and Applied Mathematics, Vladimir State University named after Alexander and Nikolay Stoletovs, Vladimir 600000, Russia

Abstract. It is demonstrated that laser irradiation causes formation of complicated fractal crystals (classical dendrites, spherulites) on a steel surface. The distribution of these structures over the irradiated region can be controlled using variations in the profile of the incident laser beam. Electron microscopy is used to evaluate the size distributions of crystals and the surface distribution density. The chemical composition of various types of crystals was established by energy dispersive Xray spectroscopy. Cellular automata are used for modeling of crystal growth and crystals distribution.

1. Introduction

Surface modification by laser radiation has occupied an important place in science and technology. These methods have high flexibility, since the laser beam can be controlled in time and space, as well as accurately dose and adjust the radiation energy. The use of lasers with different wavelengths determines a wide range of studied and modifiable materials, as well as different methods for a single material. From the point of view of technological applications, an important problem is a possibility to obtain morphology with specified physical and physicochemical properties, thereby ensuring the required quality of laser processing, for example, during welding and cladding [1, 2].

On the other hand, laser heating can lead to highly nonequilibrium conditions under which new forms of crystallization of substances can be observed. In particular, when exposed to laser radiation, fractal types of crystalline structures can grow. As shown in [3-5], fractal dimension can serve as a universal characteristic of morphology and is associated with properties that are often impossible to obtain by traditional methods. In this paper there are results of experimental study of the steel surface morphology after interaction by pulsed laser radiation, an analysis of the emerging types of fractal clusters.

2. Experimental and Modeling

In experiments, it was employed a pulsed Nd: YAG laser that is used for spot welding of various metals and alloys with a thickness of up to 2 mm. Stainless steel samples (AISI 304 and AISI 201) 1 mm thick are irradiated at different pulse energies and a spot size and studied using electron microscopy with energy dispersive analysis.

Experimental results demonstrate that at more long-term heating in the peripheral regions there is a greater number of stable crystallization centres. Moreover, the fractal structure indicates an uneven

distribution of temperature during the phase transition [6]. The crystals formed differ in shape: at the very edge of the area of influence, spherulites ("needle-like" formations) are visible, closer to the centre; the crystals acquire a shape similar to the classical stochastic fractal (dendrites). Each type of crystals has particular chemical composition. Modeling of crystallization centres distribution and stabilized growth were simulated by cellular automata (Conway's "Life" [7] and diffusion-limited aggregation [8]). These models can be used for simulation of different distribution and particular crystal growth.

3. Acknowledgments

This work was supported by the Ministry of Science and Higher Education within the State assignment FSRC "Crystallography and Photonics" RAS and Russian Foundation for Basic Research (Project No. 18-07-00943-a).

4. References

[1] Katayama S 2013 *Handbook of laser welding technologies* (Cambridge: Woodhead Publishing Limited) p 654
[2] Toyserkani J E, Khajepour A, Corbin S 2005 *Laser cladding* (Boca-Raton: CRC Press) p 263
[3] Andreeva L V, Novoselova A S, Lebedev-Stepanov P V, et al. 2007 *Technical Physics* **52** 164
[4] Antonov D N, Burtsev A A, Butkovskii O Ya 2016 *Technical Physics* **61** 108
[5] Haque N, Cochrane R, Mullis A 2016 *Intermetallics* **76** 70
[6] Burtsev A A, Butkovskii O Ya 2019 *Physical and chemical aspects of the study of clusters, nanostructures and nanomaterials* **11** 107
[7] Bays C, Adamatzky A 2010 *Game of Life Cellular Automata* (London: Springer-Verlag) p 579
[8] Witten T A, Sander L M 1983 *Physical Review B* **27** 5686

Physico-mechanical properties and SEM of sol-gel plates based on chitosan L-(D-)ascorbate

Yu Yu Zhuravleva, O N Malinkina, I V Zudina, A B Shipovskaya
Department of High Molecular Compounds, Saratov State University, Saratov 410012, Russia

Abstract. A comparative analysis of the physico-mechanical properties and SEM of the surface morphology of sol–gel plates based on chitosan L-(D-)ascorbate was carried out. It has been established that the AscA isoform has a significant effect on the elastoplastic characteristics of the samples and the surface relief of their solid phase.

1. Introduction

In our previous studies, it was shown that the isomeric form of ascorbic acid (L- or D-AscA) used to obtain the salt form of chitosan had a significant effect on the total space charge, size and general chirality of chitosan ascorbate macromolecules in solution, their stereomeric ordering in lyophilically isolated solid phase, as well as the kinetics of sol–gel synthesis of materials based thereon [1–4]. This study examines the effect of L- and D-AscA on the physico-mechanical and morphological properties of thin-film sol–gel plates based on chitosan L- or D-ascorbate without and with Aloe Vera juice (AV) added.

2. Methodology

Sol–gel plates were prepared from water–glycerol solutions of chitosan L-(D-) ascorbate (CS · L-(D-)AscA), polyvinyl alcohol and silicon tetraglycerolate (Si(OGly)$_4$) without and with AV added in mass ratios of components of 4:2:2:2. The solid phase (xerogels) was isolated by exhaustive extraction with ethyl alcohol in combination with cryoprocessing.

The elastoplastic properties were evaluated on an Instron 3342 tensile testing machine (Germany) in uniaxial tension mode at a speed of 10 mm/min, a loading cell of 500 N. The surface morphology was evaluated on a scanning microscope MIRA/LMU (Tescan, CZ).

3. Results and discussion

The physico-mechanical studies showed that for all the sol–gel plates obtained, such stress–strain curves were realized, which were characteristic of soft plastic polymeric materials not reaching the yield strength under tensile conditions. It was found that the plates with the AV additive were characterized by higher values of Young's modulus and elongation at break than those without the additive. The elastoplastic properties of the CS · L-AscA-based plates were slightly worse in comparison with those based on CS · D-AscA.

It was also found that the AV addition in the composition of the source solution increased the hydrophilicity of the sol–gel plates, their mucoadhesive properties and resistance to UV radiation.

The revealed differences in physicochemical properties are also reflected in the surface morphology of xerogels isolated from the corresponding plates (Fig. 1). The degree of roughness and the surface relief are determined by both the addition of AV and the AscA isoform.

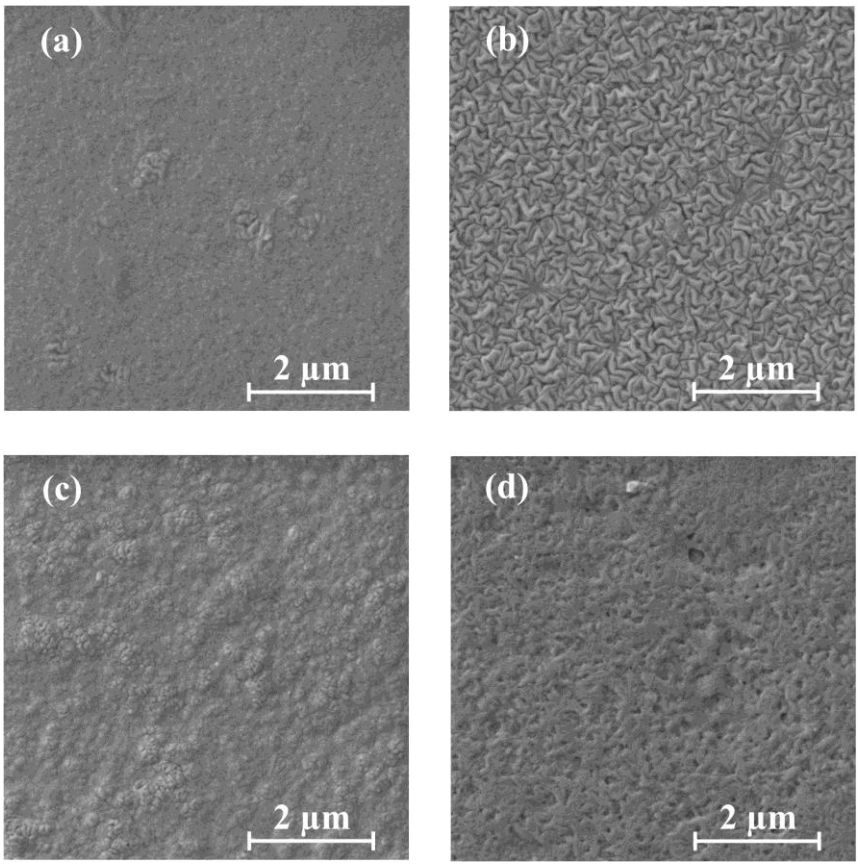

Figure 1(a-d). SEM images of the morphostructure of the xerogels isolated from sol–gel plates based on CS · L-AscA (a, b) and CS · D-AscA (c, d) without (a, c) and with the addition of AV (b, d).

The solid phase of CS · L-AscA is characterized by a more uniform structure than CS · D-AscA (Fig. 1 a and c). The addition of AV leads to significant texturing of the surface relief. E.g., the CS · L-AscA-based xerogels acquire a 3D-ordered orientation of the folded-type supramolecular structural elements (Fig. 1 b). The morphostructure of the samples based on CS · D-AscA is transformed into a 2D ordered developed structure (fig. 1 d).

Thus, the sol–gel plates obtained from CS solutions in D-AscA have the best properties compared to those of L-AscA. The AV additive not only improves the physico-mechanical characteristics of the samples, but also significantly affects the supramolecular ordering of the material. The latter could be used to design specific optical sensors and optodes of medico-biological purposes.

References

[1] Malinkina O N, Gegel N O, Shipovskaya A B 2019 J. Mol. Liq. 3 164.

[2] Malinkina O N, Zhuravleva Yu Yu, Zudina I V, Shipovskaya A B 2019 In IOP Conference Series: Journal of Physics 1410 012056.

[3] Zudina I V, Malinkina O N, Shipovskaya A B 2018 Microbiology 87 732.

[4] Gegel N O, Zhuravleva Yu Yu, Shipovskaya A B et al 2018 Polymers 10(3) 259.

Optical spectra of titanium laser-modificated surfaces with gold nanoparticles

A Tcibulnikova[1*], A Khankaev[1*], I Samusev[1*], M Demin[1], I Lyatun[1].
[1]Immanuel Kant Baltic Federal University, [*]SEC Fundamental and Applied Photonics.Nanophotonics, Kaliningrad 236016, Russia

Abstract. This paper presents the reflection spectra of s - and p-polarized light and the refractive index spectra of anodized titanium surfaces modified by laser-induced periodic structures with gold nanoparticles. It is shown that these surfaces generate surface plasmons in the visible region of the spectrum, which leads to the formation of a negative values region in the refractive index.

1. **Introduction.**

Laser-induced periodic surface structures (LIPPS) have been widely studied recently [1,2]. The formation of LIPPS occurs under femtosecond laser exposure, and the properties of theses structures depend on the laser parameters such as laser polarization, pulse energy, angle of incidence, and the properties of the medium and material. LIPPS allow to change the optical, biological, mechanical properties and wettability of the modified surfaces. The possibility of using LIPPS in physics, chemistry, medicine and biology makes these structures a promising area of research [3]. This paper presents a study aimed to the investigate the formation of LIPPS on the anodized titanium surface with gold nanoparticles (NPs) and changes in its optical properties.

2. Results and discussion

Figure 1 shows the results of scanning electron microscopy of a titanium anodized surface without LIPSS (a) and with LIPSS (b).

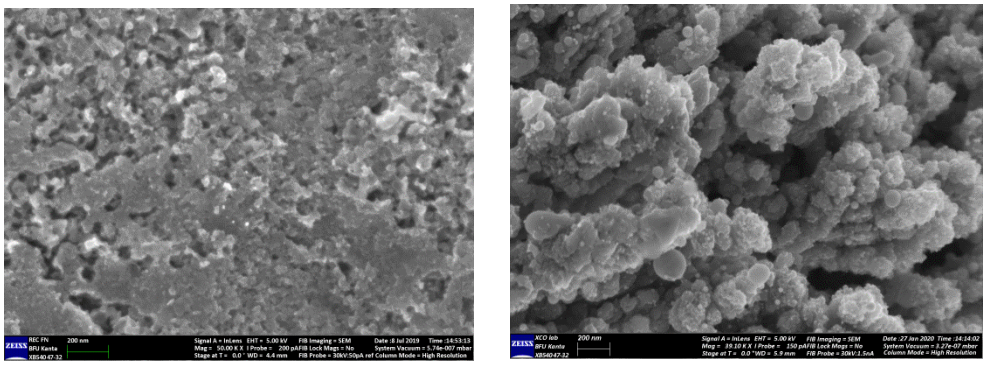

Figure 1. SEM images of titanium anodized surface without LIPSS (a) and with LIPSS (b).

Figure 2 shows the reflection and refractive index spectra of titanium nanostructured surfaces with gold nanoparticles.

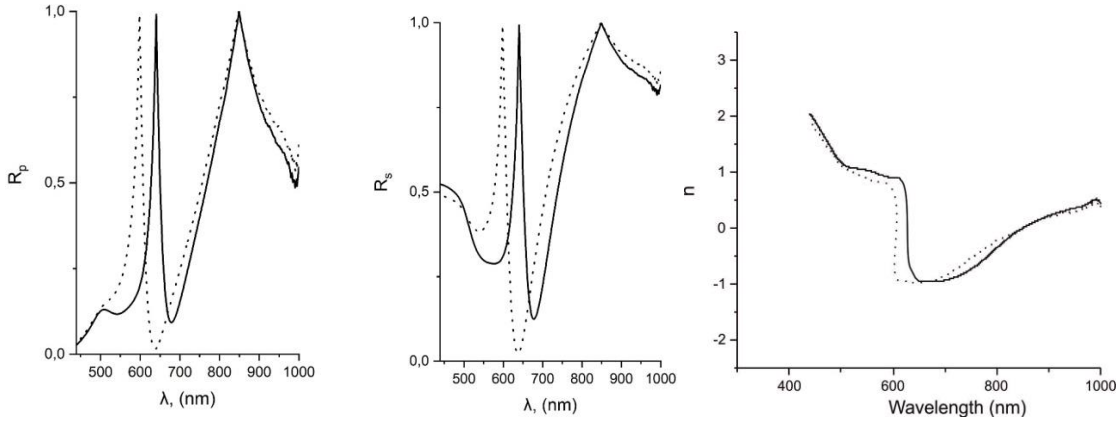

(a) (b) (c)

Figure 2. Reflectance spectra (a,b) and refractive index spectra (c) of titanium surface modified by gold nanoparticles without LIPSS (solid curves) and with LIPSS (dot curves).

As can be seen from figure 2(a,b), two minima are observed in the reflection spectra. The first minimum, located in the region of 550-600 nm, is due to the plasmon resonance of gold nanoparticles. The second minimum in the region of 650-700 nm is due to the plasmon resonance generated on the laser-structured surface of titanium. Minima of the reflection spectrum of p-polarized radiation of the titanium anodized surface with deposited gold nanoparticles are located at the wavelength of 540 nm and 679 nm. For s-polarized radiation, a broadening of the spectrum is observed in the plasmon resonance region of nanoparticles. The value of the reflection coefficients of s-polarized radiation for the plasmon resonance of gold NPs on a surface without LIPSS and with LIPSS is 0.26 and 0.35, respectively. Note that the position of the minima of the absorption spectrum of the titanium surface does not change and is shifted to the blue region after laser structuring. The values of the coefficients Rp and Rs at λ=650 nm (for the surface of titanium structured by a laser and the LF of gold) are the same.

As can be seen from figure 2c, a region of negative refractive index values is observed in the refractive index spectrum (600-800 nm). The negative refractive index coincides with the region of strong reflection and is caused by plasmon gerenation on these surfaces.

3. Acknowledgments

The reported study was funded by Russian Foundation for Basic Research and the government of the Kaliningrad region according to the research project № 19-42-390002.

References

[1] Gräf S, Kunz C, Müller F 2017 Materials **10(8)** p 933
[2] Senegačnik M, Hočevar M, Gregorčič P 2019 Procedia CIRP **81** p 99–103
[3] Bonse J, Kirner S.V, Höhm S, Epperlein N, Spaltmann D, Rosenfeld A, Krüger J 2017 Laser-Based Micro- and Nanoprocessing XI (San Francisco)

A polarization-independent highly sensitive hybrid plasmonic waveguide structure

M A Butt[1], **S A Fomchenkov**[1,2]
[1]Samara National Research University, Samara, Russia
[2]Image Processing Systems Institute of RAS-Branch of the FSRC "Crystallography and Photonics" RAS, Samara, Russia

Abstract. We proposed a novel design of a polarization-independent hybrid plasmonic waveguide. The transverse magnetic (TM) hybrid mode is confined in the low index material sandwiched between the silicon core and top gold layer whereas the transverse electric (TE) hybrid mode is supported in a narrow air gap on both sides between the silicon core and a gold layer. For sensing applications, two vital parameters such as the sensitivity of the hybrid mode (S_{mode}) and evanescent field ratio (*EFR*) are studied which depends on the geometric parameters of the waveguide. The geometric parameters of the waveguide are optimized using the finite element method. The highest S_{mode} *and EFR* for both polarizations is greater than 0.91 and 0.6, respectively. This study shows that polarization-independent highly sensitive refractive index sensors or evanescent field absorption gas sensors can be realized by utilizing the proposed hybrid plasmonic waveguide design.

1. Introduction

In this work, we proposed a novel scheme of a polarization-independent hybrid plasmonic waveguide which requires two metal-dielectric interfaces capable of supporting both TE and TM guided modes. The waveguide structure consists of a vertical hybrid plasmonic waveguide structure, besides, a thin layer of gold is deposited on both sides of the core separated by a small air gap. This arrangement of layers provides a TM mode confinement in the central part and TE mode is supported in a nano-slot on both sides of the waveguide core. The waveguide geometry is optimized at 1550 nm to obtain high mode sensitivity and evanescent field ratio. The numerical investigations showed that the obtained values are quite high which makes this waveguide an ideal candidate to be employed in evanescent field absorption gas sensors or refractive index sensing applications.

2. Waveguide geometry

The schematic of a hybrid plasmonic waveguide[1, 2] is shown in figure 1. The central core consists of three layers such as silicon (*Si*), silicon dioxide (SiO_2) and gold (*Au*) deposited on a silica substrate. The width of the waveguide core, the height of the silicon core, the height of silicon dioxide and height of the top gold layer is represented as W_{Core}, H_{Core}, H_{SiO2} and $H_{top\text{-}Au}$, respectively. This configuration facilitates the propagation of transverse magnetic (TM) hybrid mode in H_{SiO2} layer. A thin layer of gold of height ($H_{rail\text{-}Au}$) equivalent to H_{Si} is deposited on both sides of the central core separated by a gap (g). Throughout the paper, the parameters such as H_{SiO2}, $H_{top\text{-}Au}$ and g is fixed at 50 nm, 80 nm and 50 nm, respectively.

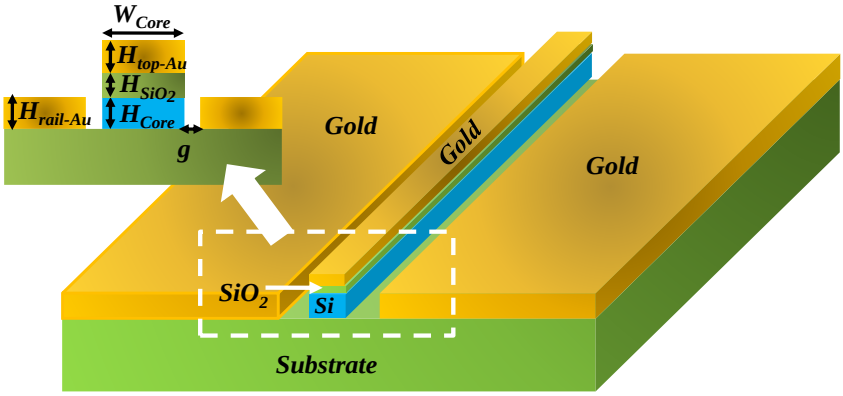

Figure 1. Schematic of a polarization-independent hybrid plasmonic waveguide structure

3. Mode sensitivity analysis

For sensing applications, mode sensitivity (S_{mode}) is an essential parameter which should be taken into consideration while designing optical waveguides. We evaluated S_{mode} concerning the geometric parameters of the waveguide. S_{mode} is calculated with the help of the following expression:

$$S_{mode} = \frac{n_{eff2} - n_{eff1}}{n_2 - n_1}$$

where n_{eff2} is the effective refractive index at the refractive index of the analyte (n_2) and n_{eff1} is the effective refractive index at the refractive index of air (n_1). In this analysis, n_2=1.35 is used to calculate the sensitivity of TE and TM hybrid modes. For TE hybrid mode, H_{Core} plays an important role in enhancing the S_{mode} but H_{Core} > 150 nm makes the mode highly vulnerable which decreases S_{mode} drastically when W_{core} > 250nm. S_{mode} for TM hybrid mode shows the same behaviour with increasing core dimensions which is more vulnerable as H_{Core} increases. For instance, at H_{Core} and W_{Core}=150 nm, the S_{mode} of 0.87 and 0.764 is obtained for TE hybrid mode and TM hybrid mode, respectively.

4. Conclusion

We proposed a novel design of a hybrid plasmonic waveguide which is capable of supporting both transverse electric (TE) and transverse magnetic (TM) hybrid modes at 1550 nm. This waveguide structure can be utilized in integrated sensors where strong light-matter interaction is required. For sensing applications, the waveguide geometry should be optimized taking into account the mode sensitivity (S_{mode}) and evanescent field ratio (*EFR*) of the hybrid mode. For TE hybrid mode, the highest S_{mode} and *EFR* of 0.98 and 0.68 is obtained by optimizing the geometric parameters of the waveguide, respectively. Almost the same modal characteristics are obtained for TM hybrid mode where S_{mode} is 0.92 and *EFR* is 0.6. This study shows that polarization-independent highly sensitive refractive index sensors or evanescent field absorption gas sensors can be realized by utilizing the proposed hybrid plasmonic waveguide design.

Acknowledgements

This work was financially supported by the Ministry of Science and Higher Education within the State assignment FSRC "Crystallography and Photonics" RAS (No. 007-GZ/Ch3363/26) and RFBR (No. 18-58-14001).

References

[1] Butt MA, Kazanskiy NL, Khonina SN 2019 *Laser Physics* **30** 016202.
[2] Butt MA, Khonina SN, Kazanskiy NL 2018 *Journal of Modern Optics* **65** 1135.

IR-phonons and spin-phonon interaction in multiferroic $LiNiPO_4$

M S Radionov[1,2], A V Peschanskii[3], N N Novikova[1], V A Yakovlev[1], S A Klimin[1]

[1]Institute of spectroscopy RAS, Troitsk, Moscow 108840, Russia
[2]Moscow Institute of Physic and Technology, Dolgoprudny 141701, Russia
[3]B.Verkin Institute for Low Temperature Physics and Engineering NASU, Kharkov 61103, Ukraine

Abstract. Results on the experimental study of the $LiNiPO_4$ single crystal are presented by means of IR spectroscopy. Spectroscopic parameters of the room-temperature IR phonons are obtained. Frequency shifts of the specific lines in the absorption spectra in the vicinity of the Néel temperature indicate the presence of significant spin-phonon and spin-electron interactions in a crystal under study.

Introduction

There are two reasons, why a $LiNiPO_4$ crystal is of interest for scientific research. Firstly, it is a promising material for using as a cathode in lithium-ion batteries [1, 2]. Secondly, it is low-temperature magnet [3, 4] with interesting phase diagrams and multiferroic properties. Literature information on IR vibrational properties is scarce. Only Raman-active phonons have been studied in detail [5]. In this paper, the spectra of IR-phonons have been studied at room temperature, as well as the transmission spectra of electronic and overtone absorption upon cooling down to helium temperatures.

Aims, methods and results

The aims of this work are an experimental study of IR-phonons in polarized light and a search for the features associated with typical for multiferroics interactions of various crystal subsystems, namely, the lattice and magnetic ones.

Polarized reflection spectra were measured using a Bruker IFS66 Fourier spectrometer. Low-temperature transmission spectra in a wide spectral range (1200-20000 cm^{-1}) were obtained using a Bruker IF125HR Fourier spectrometer, which was equipped with a helium closed-cycle Cryomech PT403 optical cryostat.

As a result of studying the reflection spectra and further model fitting, the parameters of IR-phonons, including their frequencies, oscillator strengths and damping constants, were obtained. Also, the symmetries of each phonon were determined. An amplification of the overtone intensity due to the Fermi effect was detected for the B_{2u} phonon with a frequency near 999 cm^{-1}. It was found that two absorption lines (1825.3 and 1833.0 cm^{-1}) in the overtone spectral region are sensitive to a magnetic ordering. At temperatures near 21^o K, an abrupt shift of these two lines was detected to the frequencies of 1824.3 and 1832 cm^{-1} (Fig 1a, b), respectively. At the same temperatures, an abrupt shift was detected in the region of Ni^{2+} electronic absorption frequencies (Fig 1c, d).

These facts unambiguously indicate a noticeable interaction of the magnetic, lattice and electronic degrees of freedom in the $LiNiPO_4$ crystal. A possible explanation for the shifts of the absorption lines could be the magnetostriction arising due to the magnetic ordering.

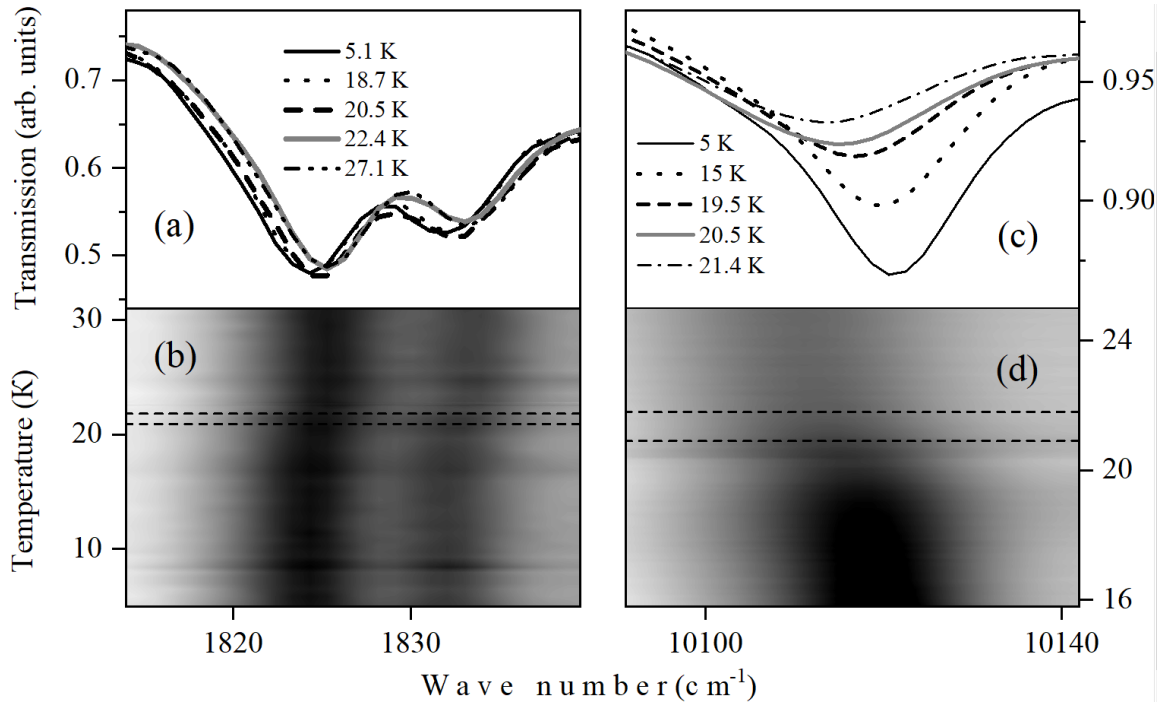

Figure 1(a,b,c,d). (a,c) Transmission spectra at low temperature and (b,d) intensity maps. (a,b) Overtone region; (c,d) Electronic absorption region.

References

[1] S. Karthickprabhu, et. al. // Mater. Lett. 2019. V.237. P.224-227.
[2] A. Ornek // Chem. Eng. J. 2018. V. 331. P.501-509.
[3] S. Lewinska, et. al. // Phys. Rev. B. 2019. V. 99. P.214440.
[4] L. Peedu, et. al. // Phys. Rev. B. 2019. V.100 P.024406.
[5] V. I. Fomin et. al. // Low Temp. Phys. 2002. V.28 P.288-296.

Raman scattering in strained gallium phosphide nanowires.

V Sharov[1, 2], P Alekseev[2], A Bolshakov[1], V Fedorov[1] and I Mukhin[1]
[1] Alferov university, Saint-Petersburg 194021, Russia
[2] Ioffe institute, Saint Petersburg 194021, Russia

Abstract. A complex study of the single bent GaP NWs based on micro-Raman mapping is introduced. We discuss strain-induced changes in Raman spectra of bent GaP NWs with respect to strain rate and polarization in terms of deformation potential theory. Analysis of obtained spectra revealed the removal of a degeneracy and spectral shift of the Raman modes arising from the linear strain distribution across the NW. Introduced subwavelength technique is a powerful tool for the investigation of the structural and optoelastic properties of the nano-sized objects without the use of tip-enhanced effects.

1. Introduction

Semiconductor nanowires (NWs) are prospective building blocks for next generation nanoscale electronic devices [1]. Among NW unique properties, great mechanical strength is remarkable. In this case, utilizing mechanical stress for NW-based devise performance expansion through energy band diagram changing is of interest. Successful tuning or enhancement of NW optical and transport properties was recently showed in numerous papers [2-5]. The research interest around strain engineering stimulates studies of strain-induced effects in NWs. Raman spectroscopy is a conventionally used for strain analysis in semiconductors. In this work we show a simple way for creating large bending strains in MBE-grown GaP NWs and investigate stress-induced spectral changes with micro-Raman spectroscopy.

2. Results and discussion

GaP NWs were grown in self-catalytic vapour-liquid-solid regime on (111) Si using solid-source molecular beam epitaxy. NW average length exceeded 25μm. For subsequent study NWs were dispersed on glass by mechanical rubbing. As a result, some of them were randomly bent. Optical measurements were carried out using Horiba LabRam HR 800 confocal Raman microscope. First, we conducted Raman study of a straight NW in four polarization geometries (figure 1, a). Pronounced TO and LO modes appear at 366 and 400 cm^{-1} respectively. TO Raman intensity is strongest for both $\bar{z}(xx)z$ and $\bar{z}(yy)z$ cases while LO intensity weakly depends on polarization. Thus, Raman selection rules are not fully masked by antenna effect as NW diameter (around 140 nm) is large enough. Full width on half maximum (FWHM) of TO mode doesn't exceed 4 cm^{-1}. Raman spectra from the central region of bent NW are presented in figure 1, b. The NW curvature radius in the most strained region was approximately 2.5 μm according to optical image. TO FWHM increased due to red shift in tensed region and blue shift in compressed region arising from strain-induced energy band changes. The increase is most significant (up to 16 cm^{-1}) in case of $\bar{z}(xx)z$ polarization that may be attributed to stronger stress along NW growth direction (111). According to recently published TEM+Raman strain mapping study of GaP NWs [7] we estimate that the bending strain rate in studied NW exceeds 3.5%.

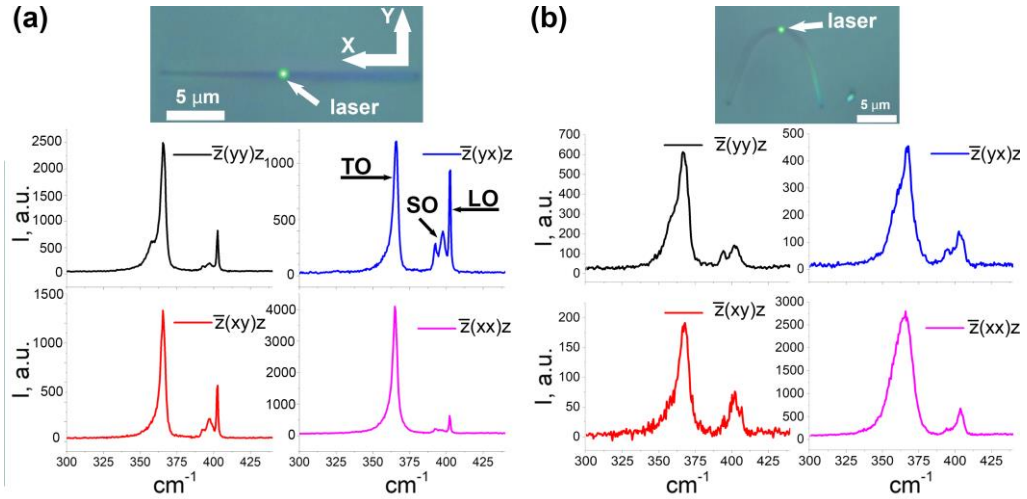

Figure 1. Polarized Raman spectroscopy of individual horizontal straight (a) and bent (b) nanowire.

We further obtained three Raman spectra with different pumping spot Y coordinate (see figure 3). First, the spot mostly illuminates NW compressed side, the impact from compression-induced blue TO shift is dominant. TO peak has steep right shoulder and the maximum value at 369 $cm^{-1}$and FWHM value is 20 cm^{-1}. Second, the spot is located at the middle of NW cross section, the impact from tensed and compressed regions is equal. TO mode is uniformly broadened (FWHM 16 cm^{-1}), with the maximum value 366 cm^{-1}. Third, the spot is located on the tensed NW side, the impact of tensed region leading to red TO shift is dominant. TO maximum value is 362 cm^{-1} and FWHM is 20 cm^{-1}. Peak shift across NW is considered linear, that is in agreement with linear strain distribution.

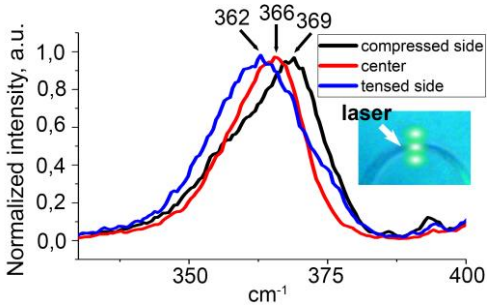

Figure 2. Raman spectroscopy of bent nanowire.

3. Conclusion

To conclude, we provided polarization-dependent Raman study of individual self-catalytic MBE-grown GaP nanowire. Simple yet efficient method of mechanical rubbing was utilized to create 3.5% strains. Stress-induced non-uniform broadening and linear shift of TO mode were observed. The shift originates from the impact of highly strained regions across NW which size is much smaller than the resolution of our optical system. Our approach allows characterization of local optomechanical properties of nanosized objects without using tip-enhanced techniques.

References

1. M. Meyyappan and M. K. Sunkara (CRC Press, 2018).
2. R. Chen, Q.-L. Ye, T. He, T. Wu, and H. Sun, *Applied Physics Letters* **98**, 241916 (2011).
3. G. Signorello, S. Karg, M. T. Björk, B. Gotsmann, and H. Riel, Nano letters **13**, 917–924 (2013).
4. Y.-M. Niquet, C. Delerue, and C. Krzeminski, *Nano letters* **12**, 3545–3550(2012).
5. P. A. Alekseev, V. A. Sharov et. al, *Nano letters* **19**, 4463–4469 (2019).
6. H. S. Im, K. Park et. al, *ACS omega* **3**, 3129–3135 (2018).

Influence of impurity compensation on terahertz photoluminescence of the donor doped GaAs/AlGaAs quantum wells

A D Kurnosova, I S Makhov and D A Firsov
Peter the Great St. Petersburg Polytechnic University, 195251 St. Petersburg, Russia

Abstract. The results of the experimental studies of terahertz photoluminescence of the nanostructures with donor doped GaAs/AlGaAs quantum wells with different compensation degree of donors with acceptors are presented. The optical transitions of charge carriers through the donor and acceptor states are observed in the terahertz photoluminescence spectra of the nanostructures. It is demonstrated, that the compensation of donors by acceptors in quantum wells leads to an increase in the terahertz photoluminescence intensity. The spectra of terahertz photoconductivity and near-infrared photoluminescence with the participation of shallow impurity states were also investigated.

1. Introduction

Terahertz photoluminescence (PL) associated with the optical transitions of nonequilibrium electrons from the first electron subband and excited donor states to the donor ground states was earlier observed under conditions of interband optical excitation of nanostructures with silicon doped GaAs/AlGaAs quantum wells (QWs) [1]. Observation of such impurity-assisted optical electron transitions became possible due to the depopulation of the ground donor state by radiative electron-hole recombination between donor ground state and first heavy hole subband in QW. This work is devoted to the studies of possibility to increase an intensity of impurity-assisted terahertz luminescence in nanostructures with doped QWs due to the significant compensation of donors with acceptors. Such compensation results in a decrease of equilibrium population of donor states in QWs as well as in the emergence of additional depopulation of ground donor states via "donor-acceptor" optical transitions.

2. Samples and experimental setups

Samples under study were MBE grown on a semi-insulating GaAs substrate on a 0.5 μm thick GaAs buffer layer and contained 50 periods of 7.6 nm wide GaAs/$Al_{0.3}Ga_{0.7}As$ QWs. QWs in nanostructures were doped with silicon only or with both silicon and beryllium. The surface concentration of each impurity was $3 \cdot 10^{10}$ cm^{-2}. For the electrical and photoelectrical studies, an indium contacts were deposited on the surface of the samples and annealed in the N_2 atmosphere (400°C, 5 minutes).

Samples were mounted in a Janis PTCM-4-7 closed cycle optical cryostat (T = 4-320 K). Terahertz PL and photoconductivity (PC) spectra were studied using a Bruker Vertex 80v vacuum FTIR spectrometer operating in a step scan regime and Mylar multilayer beamsplitter. Liquid He cooled Si bolometer was used as a terahertz sensitive detector. Nd:YAG solid state CW laser (λ = 532 nm, 0.5 duty cycle, 80 Hz frequency) was used as a source of pumping radiation. Photoconductivity

measurements were carried out under a 5 V bias voltage applied to the sample using a SR-570 current preamplifier. A mercury lamp was used as a source of broadband terahertz radiation.

3. Results and discussion

Terahertz PL spectra of both nanostructures are consisted of several emission bands related to the optical transitions of charge carriers involving impurity states in QWs. A broad emission band in the photon energy range of 3-28 meV observed for both compensated and uncompensated nanostructures is associated with optical electron transitions from the first electron subband $e1$ and excited donor states $2p_{x,y}$ to the ground donor state $1s$ in QWs. Spectral position of this emission band is in a good agreement with a PC spectrum of donor doped QWs, which is consisted of broad photocurrent band related to the $1s$-$e1$ and $1s$-$2p_{x,y}$ optical electron transitions. Another emission band in the photon energy range 34-40 meV is observed for the compensated QWs only and could be associated with optical electron transitions from the ground acceptor state to the first heavy hole subband.

The near-infrared PL spectra of both nanostructures measured at a $T = 8$ K show emission bands related to radiative recombination of free and impurity-bound excitons as well as radiative electron-hole recombination through the donor states in QWs. The near-infrared PL spectrum of nanostructure with compensated QWs also shows emission bands associated with optical transitions of charge carriers between the first electron subband e1 and ground acceptor states as well as with "donor-acceptor" optical transitions.

Comparing the terahertz PL intensity integrated in the photon energy range of 9-30 meV for two nanostructures (see Figure 1) one can see that compensated QWs show an order of magnitude larger emission intensity than donor doped ones in the wide range of optical pumping powers.

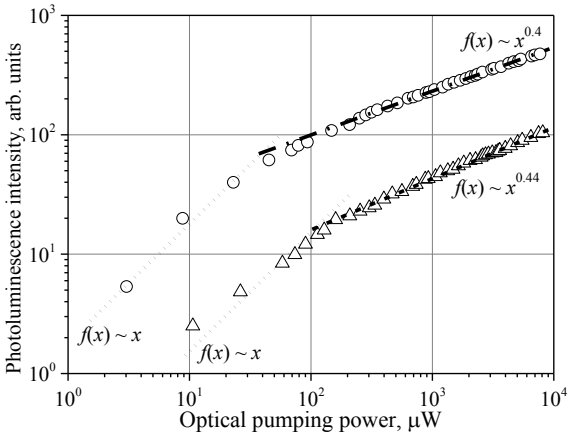

Figure 1. Dependencies of integrated terahertz PL intensity on the pumping power of the nanostructures with donor doped (triangles) and compensated (circles) QWs measured at the $T = 8$ K. Dashed, dotted and dash-dotted lines show the approximation of experimental data.

Conclusion

The low-temperature near-infrared PL, terahertz PL and terahertz PC are investigated in nanostructures with doped compensated and uncompensated QWs. The optical transitions of charge carriers involving impurity states in PL and PC spectra of nanostructures are revealed. It is shown that compensation of impurities in QWs allows to increase the impurity-related terahertz PL intensity.

Acknowledgments

This work was supported by the Russian Foundation for Basic Research (grant 18-32-00122) and the Ministry of Science and Higher Education of the Russian Federation (state assignment).

References

[1] Firsov D A, Vorobjev L E, Panevin V Yu et al 2015 *Semiconductors* **49**(1) 28

Long-lived spin echo from trions in InAs quantum dots in microcavity

I. I. Yanibekov[1], A.V. Trifonov[1,2], S. V. Poltavtsev[1,2], S. E. Scholz[3], C. Sgroi[3], A. Ludwig[3], A. D. Wieck[3], I.A. Akimov[2,4], M. Bayer[2,4]

[1]Saint Petersburg State University, 198504 Saint Petersburg, Russia
[2]Experimentelle Physik 2, Technische Universität Dortmund, 44221 Dortmund, Germany
[3]Angewandte Festkörperphysik, Ruhr-Universität Bochum, 44780 Bochum, Germany
[4]A.F. Ioffe Physical-Technical Institute, Russian Academy of Sciences, 194021 St Petersburg, Russia

Iskander1331@mail.ru

Abstract. Coherent dynamics of trions in InAs quantum dots (QDs) in microcavity was investigated using time-resolved photon echo (PE) and stimulated photon echo (SPE) techniques. Temporal profiles and polarization properties of PE and SPE signals shows that the system under study is the model trion system. The trion population decay time and irreversible optical phase relaxation decay time, were determined at low power excitation regime at low temperature. Long spin relaxation time allows us to observe the mode-locking effect in SPE signal.

1. Introduction

Nowadays, time-resolved four-wave mixing (FWM), photon echo (PE) and stimulated photon echo (SPE) spectroscopy are one of the most prospective methods of investigation optical and spin coherent dynamics. The reason for the wide interest in these effects is determined by the broad potential of their application in the field of optical information processing [1]. Combination of time-resolved methods and polarimetry technique allows not only distinguish type of quasiparticle under study, but also obtain fundamental characteristics, such as phase and energy relaxation times. In this work, coherent and polarimetry properties of trions in semiconductor QDs in microcavity was studied.

2. Experiment and results

The sample under study (#14833) contains 4 layers of InAs QDs embedded in antinodes of the standing wave of the microcavity, which consist of 11 and 14 pairs of GaAs/AlAs distributed Bragg reflectors (DBRs). The sample was annealed at a temperature 850 °C to achieve the coincidence of the energies of QDs trion resonances and photon mode of the microcavity. The sample scheme is

presented in Figure 1 (a). In order to minimize phonon scattering of trions, the sample was immersed in liquid helium at a temperature 1.4 K. Optical excitation was performed by picosecond laser at wavelength 863.2 nm.

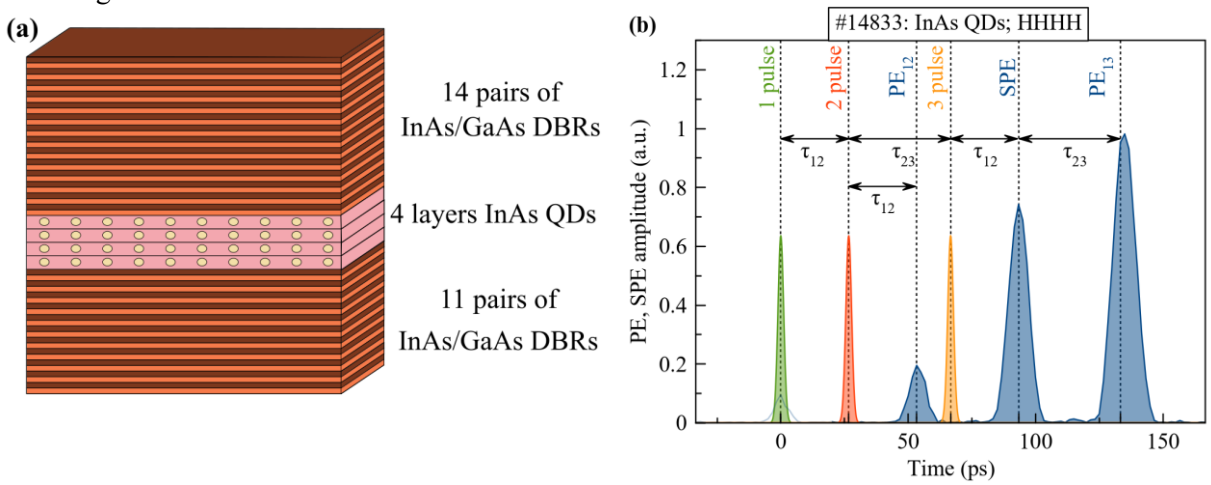

Figure 1 (a,b). (a) Sample scheme; **(b)** Experimentally obtained PE and SPE temporal profiles and schematically illustrated exciting picosecond pulses.

The experimental PE and SPE signal temporal profiles are presented in **Figure 1 (b)**. Two-pulse PE signal appears after the action on the sample of two optical pulses, delayed in time by τ_{12}. In this case, PE_{12} has a maximum at $2\tau_{12}$ after the action of the first pulse. For SPE third pulse, which comes at $\tau_{12}+\tau_{23}$, is needed. As a result, one can see the maximum of SPE signal at time $2\tau_{12}+\tau_{23}$. There is also PE_{13} signal, and its origin is similar to PE_{12}, because this is a PE from first and third pulses.
$P_{PE_{12}}(\tau_{12})$ and $P_{SPE}(\tau_{23})$ exponentially decays with T_2 and T_1 characteristic times, which are the optical and population irreversible phase relaxation times accordingly (**Figure 1 (b)**). This behaviour can be described by formulas:

$$P_{PE_{12}} \propto \exp\left(-\frac{2\tau_{12}}{T_2}\right) \qquad (1)$$

$$P_{SPE} \propto \exp\left(-\frac{2\tau_{23}}{T_1}\right) \qquad (2)$$

The polarimetry behaviour of PE signal amplitude in excitonic and trion systems was investigated in [2]. By changing of mutual polarization of the second laser pulse and polarization of signals detection, one can measure polar rosette-like patterns. In **Figure 2 (a)** in polar coordinates the dependencies of PE amplitude on the angle between first and second pulses are presented. First pulse excites the sample with horizontal polarization (H), linear polarization of the second pulse rotates (R), and then horizontal and vertical (H and V) polarization of PE was detected. The behaviour of the shown experimental patterns corresponds to trion system [2].

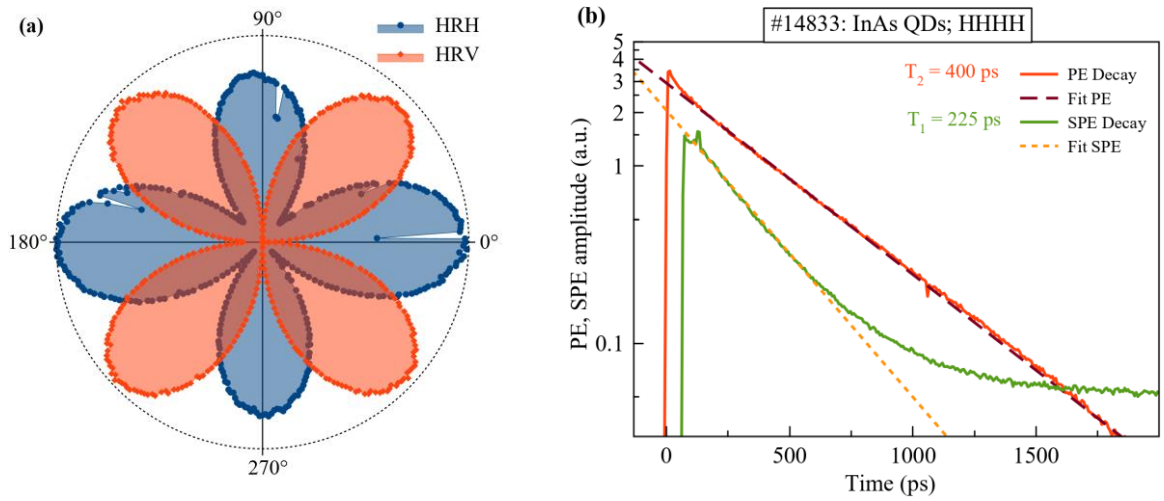

Figure 2 (a,b). (a) Polar rosette-like patterns, which correspond to trion; **(b)** PE and SPE decays.

Dependence of PE and SPE signal amplitudes on the delay between excitation pulses allows one to extract the population decay time and irreversible optical phase relaxation decay time (see Eq. (1) and (2)). **Figure 2 (b)** shows time decays of SPE and PE signals for the system under study corresponding to T_1=225 ps and T_2=400 ps. The fact that $T_2/T_1 \approx 2$ allows one to conclude that under experimental conditions were no effects of polarization and population scattering.
The experimental results of investigation mode-locking effect [3], which manifest itself in SPE under the action of magnetic field, will be presented at the conference report.

3. Acknowledgements

This research was supported by the Deutsche Forschungsgemeinschaft through the International Collaborative Research Centre TRR 160 (Project A3) and the Russian Foundation for Basic Research (Project No. 19-52-12046)

4. References

[1] L. Langer, S. V. Poltavtsev, I. A. Yugova, M. Salewski, D. R. Yakovlev, G. Karczewski, T. Wojtowicz, I. A. Akimov, M. Bayer, *J. Nat. Phot*, **8**, 851-857 (2014)
[2] S. V. Poltavtsev, Yu. V. Kapitonov, I. A. Yugova, I. A. Akimov, D. R. Yakovlev, G. Karczewski, M. Wiater, T. Wojtowicz, M. Bayer, *J. Scientific Reports*, **9**, 5666 (2019)
[3] A. Greilich, D. R. Yakovlev, A. Shabaev, Al. L. Efros, I. A. Yugova, R. Oulton, V. Stavarache, D. Reuter, A. Wieck, M. Bayer, *J. Nature*, **313**, 341-345 (2006)

8-Sectorial Dichroic Plates for Radially Polarized Beams Forming

S A Degtyarev[1,2], **S V Karpeev**[1,2], **S A Fomchenkov**[1,2]
[1]Image Processing Systems Institute - Branch of the Federal Scientific Research Centre "Crystallography and Photonics" of Russian Academy of Sciences, Samara 443001, Russia
[2]Samara National Research University, 34, Moskovskoye Shosse, Samara, Russia, 443086

Abstract. We propose to create radially polarized beam with 8-sectorial polarizer. Simulation is provided with Comsol multiphysics software. We show that the plate can create the radially polarized beam with the vortex phase.

1. Introduction

Cylindrical vector beams of various orders [1-7] are of practical interest in a wide list of areas. Many applications can be based on the phenomenon of the so-called reverse flow [8], which occurs when focusing high-order radially polarized beams. Thus, the formation of cylindrical beams is an urgent task.

A significant number of works have been devoted to the study of methods for producing cylindrical vector beams, including high orders, in recent years. The main approaches include the polarization transformations of the initial beam using liquid crystal polarization modulators (LCMs) [9], using a superposition of vector beams [10], using subwave gratings [11-13], and also using crystal [14-16] and film [14, 17] sector plates. A continuous analogue of sector plates is the use of an interference polarizer [18, 19]. All methods have their pros and cons. LCMs convert the polarization of only part of the transmitted light, thereby reducing the polarization instinction ratio. For a converter based on subwavelength gratings, the efficiency and, therefore, the polarization contrast change depending on the angle of rotation of the plane of polarization. True, the minus of the subwavelength polarization gratings, which consists in the unevenness of Fresnel reflections, can be circumvented by combining subwavelength gratings with orthogonal strokes in neighboring Fresnel zones [20]. It should also be noted that for the infrared range the technology of manufacturing subwavelength gratings is somewhat simpler due to the longer wavelength.

The main advantage of all types of sector converters is the lowest cost per unit area and ease of use.

The so-called "pseudo-radial" polarization is obtained and it can be corrected with additional phase conversion using phase plates [7].

2. Radial polarization formation with sectorial polarizer

Here we propose to create radially polarized beam with 8-sectorial polarizer which is illustrated in fig. 1a. The transmissive axis is radially oriented from the center to the periphery of the element. There are the results of simulation of the element working in Fig. 1. Circularly polarized beam passes through

the element and loses one of the John's vector component due to the dichroic absorption. Simulation is provided with Comsol multiphysics software.

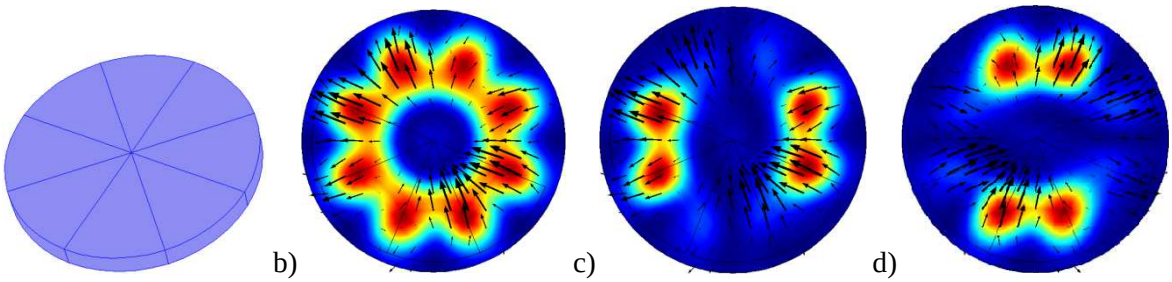

Figure 1(a, b, c, d). (a) General view of dichroic sectorial plate; **(b)** Electric field amplitude after that the circular polarized beam passes through the element; (**c**) Horizontal component of the electric field; (**d**) Vertical component of the electric field; black arrows show the polarization

3. Conclusions

Operation of 8-sectorial plate is numerically simulated. We show that the plate can create the radially polarized beam with the vortex phase.

4. Acknowledgments

This work was financially supported by the Russian Foundation for Basic Research (grant 18-29-20045 mk) for numerical simulation and by the Ministry of Science and Higher Education within the State assignment FSRC "Crystallography and Photonics" RAS (No. 007-GZ/Ch3363/26) for theoretical results.

References

[1] Zhan Q 2009 *Adv. Opt. Photon.* **1**, 1
[2] Millione G, Nguyen Th, Leach J, Nolan D, Alfano R 2015 *Optics Letters* **40,** 4887
[3] Zhou Z, Zhu L 2015 *Opt. Quant. Electron.* **48** 1
[4] Saenz J 2011 *Nat. Phot.* **5** 514
[5] Lan C, Yang Y, Geng Z, Li B, Zhou J 2015 *Scientific Reports* **5** 16416
[6] Mawet D, Riaud P, Surdej J, Baudrand J 2005 *Appl. Opt.* **44** 7313
[7] Mawet D, Serabyn E, Liewer K, Burruss R, Hickey J, Shemo D 2010 *ApJ* **709** 53
[8] Khonina S, Ustinov A, Degtyarev S 2018 *Phys. Rev. A* **98** 043823
[9] Hsu W, Balakrishnan K, Ibn-Elhaj M, Pau S 2014 *Applied Optics* **53** 5252
[10] Maurer C, Jesacher A, Fürhapter S, Bernet S, Ritsch-Marte M 2007 *New J. Phys.* **9** 78
[11] Niv A, Biener G, Kleiner V, Hasman E 2004 *Optics Letters* **29** 238
[12] Bomzon Z, Biener G, Kleiner V, Hasman E 2002 *Opt. Lett.* **27** 285
[13] Stafeev S, Kotlyar V, Nalimov A, Kotlyar M, O'Faolain L 2017 *Photonics and Nanostructures - Fundamentals and Applications* **27** 32
[14] Alferov S, Karpeev S, Khonina S, Moiseev O 2014 *Computer Optics* **38** 57
[15] Karpeev S, Podlipnov V, Khonina S, Paranin V, Reshetnikov A 2018 *Computer Optic* **42** 401
[16] Machavariani G, Lumer Y, Moshe I, Meir A, Jackel S 2007 *Opt Lett* **32** 1468
[17] Man Zh, Min Ch, Zhang Y, Shen Z, Yuan X-C 2013 *Laser Phys* **23** 105001
[18] Karpeev S, Paranin V, Khonina S 2017 *J Opt* **19** 055701
[19] Paranin V, Karpeev S, Khonina S 2015 Computer Optics **39** 492
[20] Degtyarev S, Volotovsky S, Khonina S 2018 *Journal of the Optical Society of America B: Optical Physics* **35** 1963

Investigation of the optical properties of a metasurface based on silicon nanocylinders in a hybrid anapole state

A V Kuznetsov[1,2], **A Canos Valero**[1], **A S Shalin**[1]
[1]International Laboratory Nano-optomechanics, ITMO University, Saint Petersburg 197101, Russia
[2]Faculty of Laser Photonics and Optoelectronics, ITMO University, Saint Petersburg 197101, Russia

Abstract. In this work, we utilized COMSOL Multiphysic package to study the optical properties of hybrid anapole states supported by individual silicon nanocylinders and their metasurfaces.

1. Introduction

In recent years, studies in the field of dielectric nanophotonics are gaining more and more popularity. This interest is largely due to the emerging possibilities of applying the anapole state of dielectric nanoparticles in practice [1]. Due to the fact that the anapole states in dielectric nanoparticles are practically invisible at a certain wavelength [2], they, for example, can be used to hide objects, making them invisible [3]. The anapole state also has enormous potential for use in metamaterials for various optical problems [4]. Great prospects appeared after a detailed examination of high-order toroidal moments, with the help of which one can explain the interference of the far fields of the high order basic multipole moments and their toroidal counterparts [5]. In the future, the hybrid anapole state will make possible to tune the light behavior, which will contribute to the creation of new photonic elements, and will also finds its application in radiation generation, sound engineering, and nonlinear optics [6].

2. Results

First of all, the anapole state for a silicon nanocylinder was found by optimizing its geometric dimensions to obtain a minimum scattering cross section at a specific wavelength.

Then, a metasurface consisting of these nanocylinders having a hybrid anapole state at a wavelength of λ = 789 nm was developed, and its optical properties depending on the wavelength of the incident radiation were considered (figure 1).

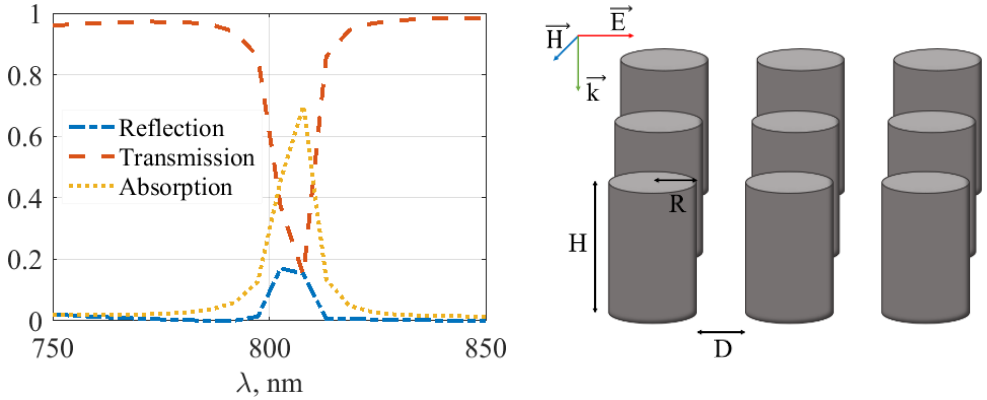

Figure 1. Graphs of the dependence of the transmission, reflection and absorption of radiation with a wavelength of λ = 789 nm metasurface consisting of silicon nanocylinders with a radius of R = 128 nm and a height of H = 369 nm, on the wavelength of the incident radiation.

Our simulations prove that such a metasurface has a high transmittance and low reflection coefficient, which makes it practically invisible at the wavelength of the hybrid anapole state.

3. Conclusions

Thus, in this work, the hybrid anapole state for silicon nanocylinders was found by optimizing their geometrical parameters. In a periodic arrangement of the optimized structures (a metasurface), the novel effect was shown to lead to almost complete transparency, paving the way towards exciting new paths to create photonic devices for control light at the nanoscale.

4. Acknowledgements

The work has been supported by the Russian Fund for Basic Research within Projects No. 18-02-00414 and No. 18-52-00005. Numerical simulations have been supported by the Russian Science Foundation (Project No. 18-72-10127).

References

[1] Kseniia V. Baryshnikova, Daria A. Smirnova, Boris S. Luk'yanchuk, and Yuri S. Kivshar 2019 Optical Anapoles: Concepts and Applications // Advanced optical materials.
[2] Andrey E. Miroshnichenko, Andrey B. Evlyukhin, Ye Feng Yu, Reuben M. Bakker, Arkadi Chipouline, Arseniy I. Kuznetsov, Boris Luk'yanchuk, Boris N. Chichkov & Yuri S. Kivshar 2015 Nonradiating anapole modes in dielectric nanoparticles // Nature Communications.
[3] Anar K. Ospanova, Giuseppe Labate, Ladislau Matekovits & Alexey A. Basharin 2018 Multipolar passive cloaking by nonradiating anapole excitation // Scientific Reports volume.
[4] Pavel D. Terekhov, Viktoriia E. Babicheva, Kseniia V. Baryshnikova, Alexander S. Shalin, Alina Karabchevsky, and Andrey B. Evlyukhin 2019 Multipole analysis of dielectric metasurfaces composed of nonspherical nanoparticles and lattice invisibility effect // Physical review.
[5] Gurvitz E.A., Ladutenko K.S., Dergachev P.A., Evlyukhin A.B., Miroshnichenko A.E., Shalin A.S. 2019 The High-Order Toroidal Moments and Anapole States in All-Dielectric Photonics // Laser & Photonics Reviews.
[6] Yuanqing Yang, Sergey I Bozhevolny 2019 Nonradiating anapole states in nanophotonics: from fundamentals to applications // Nanotechnology.

The study of radiation attenuation in disordered silver nanoparticles arrays formed by dry aerosol printing

K M Khabarov[1], **V V Ivanov**[1]
[1]Moscow Institute of Physics and Technology (National Research University), Dolgoprudny 141701, Russia

Abstract. The processes of interaction of continuous laser radiation with wavelengths 527 and 980 nm with spherical silver nanoparticles arrays formed by dry aerosol printing are studied. The arrays were deposited in the form of flat layers with different thicknesses and were differed by nanoparticles sizes. It is shown that the radiation attenuation by nanoparticles arrays with disordered structure depends on resonant effects arising both on individual spherical nanoparticles and nanoparticles agglomerates.

1. Introduction

The interaction of laser radiation with disordered metal nanoparticles (NP) arrays is described by absorption and scattering processes on array elements. Resonant effects that occur on individual NPs and their ensembles caused by NPs collective interaction may cause a significant impact on the propagation of radiation in such systems. The arrays formed by dry aerosol printing are interesting due to the complex disordered structure of dendrite-like NPs agglomerates characterized by collective electrical conductivity. In this case, the interaction of laser radiation with such structures may be described by the excitation of plasmon modes on individual NPs and their ensembles [1], as well as by the excitation of radiative modes of nanoantennas in the form of NPs agglomerates [2].

2. Experiment

In this paper we studied the dimensionless radiation attenuation coefficients of disordered spherical silver NPs arrays formed by dry aerosol printing on glass substrates. In the experiments we varied the thickness of flat arrays and the average diameter of NPs, which were controlled by optical profilometer and transmission electron microscope (TEM) respectively. The NPs agglomerates size distribution was also measured directly in the gas flow by the electrodiffusion method.

The dimensionless attenuation coefficient dependences for NPs arrays from their thickness were obtained from the measurements of the intensity of incident and transmitted coherent linearly polarized continuous (CW) laser radiation with wavelengths 527 and 980 nm (Fig. 1 (c, d)). The studied value was being averaged over a large area of the sample with the selected laser beam diameter 1.5 mm. The dependences were interpolated by an exponential function with the k_λ index reflecting the dimentional radiation attenuation coefficient for the array consisting of NPs and NPs agglomerates with a given average diameter and size spectrum respectively.

According to the results, the arrays with NPs and agglomerates with the average size about 20 and 160 nm respectively attenuate incident radiation more effectively than the arrays with NPs and agglomerates with the average size about 60 nm for both, although the radiation absorption efficiency at these wavelengths increases with the rise of NPs diameter [3]. This effect may be explained by the fact that the NPs in the agglomerates work as a whole, exhibiting properties of the extended dendrite-like plasmon nanoantennas. In this case, the radiation attenuation coefficients proximity for both lasers for each medium may be a result of a wide size distribution of NPs and agglomerates in the array that includes the particles sizes with similar radiation absorption efficiencies for both wavelengths.

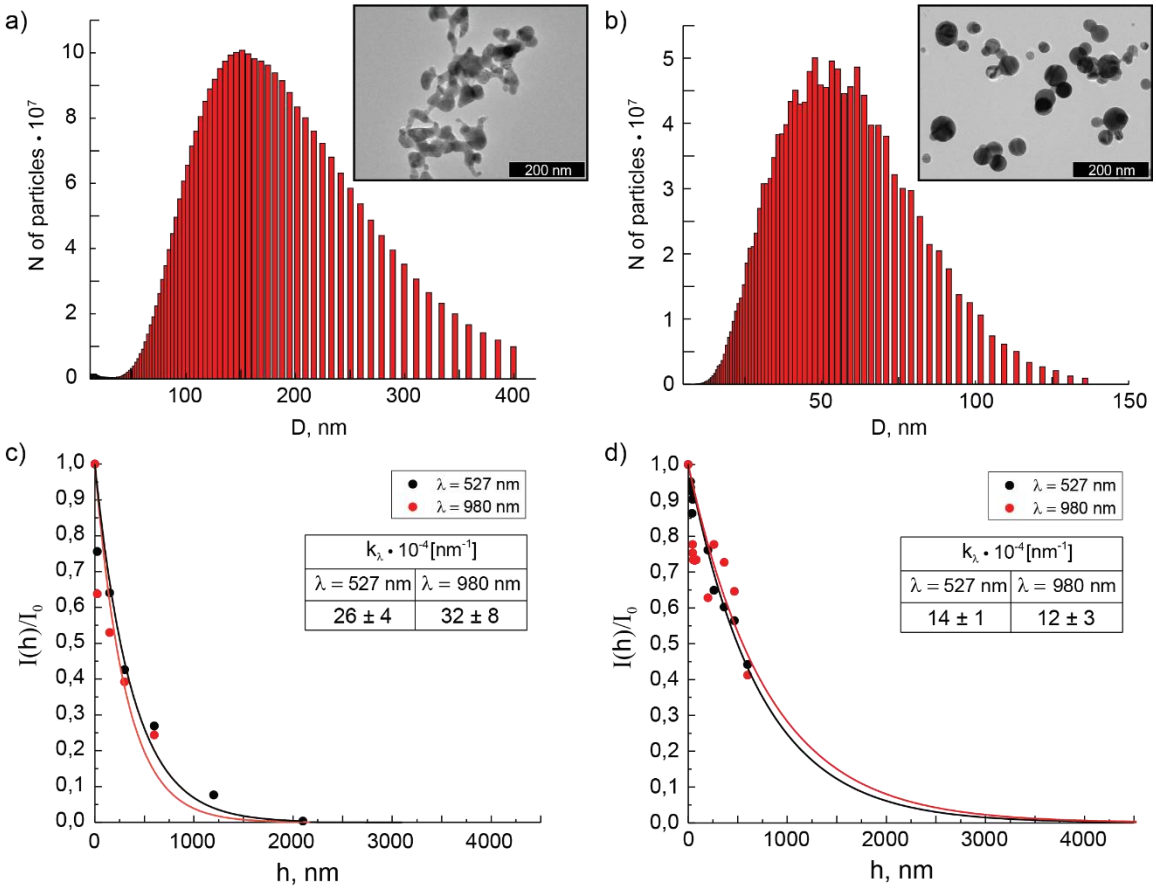

Figure 1(a – d). (a, b) The size distribution histograms of NPs agglomerates (electrodiffusion method) forming the studied arrays (embedded TEM images of primary NPs for the corresponding cases); **(c, d)** The dependencies of the dimensionless radiation attenuation coefficients for arrays of silver nanoparticles with average diameters 20 and 60 nm respectively from the array thickness for laser wavelengths 527 and 980 nm.

3. Conclusion

The interaction of CW laser radiation with wavelengths 527 and 980 nm with the spherical silver NPs arrays formed by dry aerosol printing is determined by the radiation absorption and scattering processes both on individual NPs and on their agglomerates. The radiation attenuation coefficients for arrays with NPs and agglomerates with an average size about 20 and 160 nm respectively are two times higher than for arrays NPs and agglomerates with an average size about 60 nm for both.

Acknowledgments

The reported study was funded by RFBR, project number 19-33-90202.

References

[1] Maier S. A. Plasmonics: fundamentals and applications. – Springer Science & Business Media, 2007.
[2] Cubukcu E. et al. Plasmonic laser antennas and related devices //IEEE Journal of Selected Topics in Quantum Electronics. – 2008. – Т. 14. – №. 6. – С. 1448-1461.
[3] Bilankohi S. M. Optical scattering and absorption characteristics of silver and silica/silver core/shell nanoparticles //Oriental Journal of Chemistry. – 2015. – Т. 31. – №. 4. – С. 2259-2263.

Photoemission from *p*-GaAs(Cs,O) under transition from negative to positive electron affinity

D E Protopopov[1,2], **V S Khoroshilov**[1,2], **A G Zhuravlev**[1,2], **D M Kazantsev**[1,2], **V L Alperovich**[1,2]
[1]Rzhanov Institute of Semiconductor Physics, 630090 Novosibirsk, Russia
[2]Novosibirsk State University, 630090 Novosibirsk, Russia

Abstract. The dependences of the electron escape probability from *p*-GaAs(Cs,O) in vacuum were measured under the transition from negative to positive electron affinity. The transition was induced by the deposition of excess cesium or oxygen on the *p*-GaAs(Cs,O) surface activated to the state of negative electron affinity. Under deposition of excess cesium, the escape probability was significantly lower as compared to excess oxygen, presumably, due to reflection and scattering of electrons on two-dimensional cesium metal clusters. A new peak was observed below the band gap in the photoemission quantum yield spectra at positive values of affinity.

1. Introduction

The deposition of thin (subnanometer) layers of cesium and oxygen to the atomically clean *p*-GaAs surface leads to the reduction of the surface potential barrier for electron emission into vacuum and the formation of the state with negative effective electron affinity (NEA) $\chi^* \approx -0.2$ eV at which the vacuum level is below the bottom of the conduction band in the bulk of GaAs [1]. NEA photocathodes based on *p*-GaAs(Cs,O) are widely used in various photoemission devices. Interest in semiconductors with relatively small positive electron affinity (PEA) $\chi^* \sim 0.2$-0.4 eV is due to the possibility of increasing the efficiency of solar energy conversion using photon-enhanced thermoelectronic emission (PETE) [2,3]. Earlier, in experiments on the transition from the state with PEA to the state with NEA and back, from NEA to PEA, a nonmonotonic dependence of the escape probability of thermalized electrons in vacuum P_t on the effective electron affinity was observed, with a deep minimum near $\chi^* \approx 0$ [4, 5]. It has been suggested that the minimum is due to a change in the mechanism of emission at the transition from a positive to a negative affinity. However, the experimental data obtained in [5] are not sufficient to explain the significant differences in $P_t(\chi^*)$ dependences in the transitions from NEA to PEA induced by excess Cs and O_2, because in these experiments the initial values of NEA χ^* differed significantly. The aim of the present study is to fill this gap by performing additional experiments by depositing excess cesium and oxygen on optimally activated surfaces *p*-GaAs(Cs,O) with close initial values of a quantum yield and affinity. A substantial increase in the signal/noise ratio allowed us to resolve a new Cs-induced sub-bandgap feature in the photoemission quantum yield spectra.

2. Experimental

The experiments were done on epitaxial layers of heavily doped *p*-GaAs(001). The photoemission quantum yield spectra were measured in the ultra-high vacuum set-up, during cesium or oxygen deposition on the GaAs(Cs,O) surface activated to the NEA state. The details of preparing atomically

clean surface of GaAs(001), activating the surface by Cs and O_2 and measuring photoemission spectra are described earlier [3-5].

3. Results and discussion

The evolution of photoemission quantum yield spectra measured by Cs deposition on the *p*-GaAs(Cs,O) surface activated to the state of NEA is shown in figure 1. The affinity χ^* increases from top to bottom. The spectra contain contributions of direct photoemission (of hot photoelectrons) and PETE (thermalized electrons). Under Cs deposition we also observed an additional peak at 1.365 eV below the band gap ε_g. The origin of this peak is not yet clear. It may stem from the sub-bandgap absorption in the band bending region due to Franz-Keldysh effect in the surface electric field.

The electron affinity and escape probability was determined by comparing the measured and calculated spectra [3]. The dependences $P_t(\chi^*)$ determined for O_2 and Cs depositions on the activated *p*-GaAs(Cs,O) surface with NEA are shown in figure 2. It is seen that the shape of both dependencies are qualitatively the same, with a deep minimum at $\chi^* = 0$. Unlike [5], the initial values of the affinity and escape probability are approximately the same. However, P_t values in the "cesium" experiments are considerably (by 3-5 times) lower than in the "oxygen" experiments. This difference is presumably explained by reflection and scattering emitted electrons on two-dimensional cesium clusters, which reduce the escape probability and photoemission quantum yield.

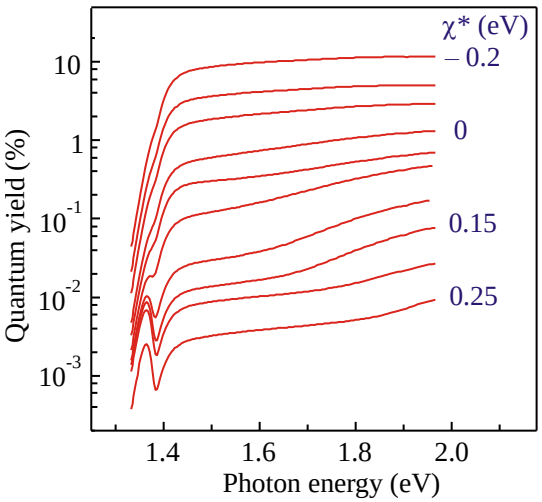

Figure 1. Evolution of photoemission quantum yield spectra measured under the deposition of excess Cs on the NEA *p*-GaAs(Cs,O) surface. The affinity χ^* increases from top to bottom.

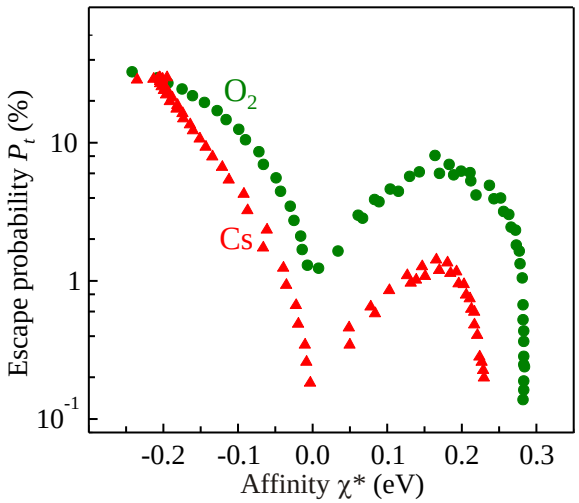

Figure 2. Electron escape probability P_t versus χ^* measured for the excess oxygen (circles) and cesium (triangles) depositions on the activated *p*-GaAs(Cs,O) surface with the state of NEA.

4. Acknowledgments

This work was supported by the Russian Foundation for Basic Research (grant 20-02-00355 A).

References

[1] Bell R L 1973 Negative Electron Affinity Devices (Oxford: Clarendon)
[2] Schwede J W et al. 2010 *Nat. Mater.* **9** 762
[3] Zhuravlev A G, Romanov A S and Alperovich V L *Appl. Phys. Lett.* **105** 251602
[4] Zhuravlev A G, Khoroshilov V S and Alperovich V L 2017 *JETP Lett.* **105** 686
[5] Zhuravlev A G, Khoroshilov V S and Alperovich V L 2019 *Appl. Surf. Sci.* **483** 895

Manufacture of optical ceramics based on two solid solutions of the AgBr – ($TlBr_{0.46}I_{0.54}$) system

L V Zhukova[1], A E Lvov[1], D D Salimgareev[1], A A Yuzhakova[1], D A Belousov[1], M S Korsakov[1]

[1]Department of chemical technology, Ural federal university named after the first President of Russia B. N. Yeltsin, Ekaterinburg 620002, Russia

Abstract. This work is devoted to the synthesis and the optical properties study of a new multicomponent heterophase ceramic based on two solid solutions of the AgBr – ($TlBr_{0.46}I_{0.54}$) system. Ceramics are transparent in the infrared range from 1.0 to 40.0 ÷ 50.0 μm, non-hygroscopic, are photo- and radiation-resistant, flexible, as a result of which various optical products are made from it by hot embossing.

1. Introduction

Today, there is a wide development of the mid-infrared range, since it is deficiently studied and poorly developed. This is evidenced by a very limited number of existing solid-state and fiber laser systems capable of generating radiation in this range. Therefore, a popular area is the creation of multifunctional elements based on crystalline ceramics for the generation, transmission, recording and control of infrared (IR) radiation in a wide spectral range from 1.0 to 50.0 microns. However, the known ceramic materials have complex manufacturing techniques and require special expensive equipment. In addition, their transparency range is limited by the visible and near infrared ranges.

2. Optical properties

To date, the article's authors for the first time synthesized a multicomponent, highly transparent, without absorption windows in the range from 1.0 to 40.0 ÷ 50.0 μm (Fig. 1) heterophase ceramic based on cubic and rhombic phases two solid solutions. The ceramic is based on the cubic phase of the AgBr – ($TlBr_{0.46}I_{0.54}$) system with a $TlBr_{0.46}I_{0.54}$ content in AgBr from 1.0 to 42.0 wt. % and from 85.0 to 97.0 wt. %, which follows from the previously studied diagram of the system' melting point [1]. For the first region, the rhombic phase has the composition Tl_2AgBr_2I, and for the second, $AgTl_2BrI_2$, which is confirmed by studies. It should be noted that the obtained ceramics' quality and the ratio of solid crystalline phases in it depend primarily on the degree of starting components' homogenization, and to a much lesser extent on the growth rate.

The main optical materials characteristic is their transparency range. The spectral range of the new ceramics was studied on plane-parallel plates from 300 to 1000 nm thick, manufactured on a Specac 15 ton manual hydraulic press by hot embossing. The plates corresponded to different compositions of AgBr – ($TlBr_{0.46}I_{0.54}$) system' solid solutions. The ceramics spectral transmission was determined using IR-Fourier spectrometers IRPrestige-21 (Shimadzu) operating in the spectral range 7800 – 240 cm^{-1} (1.28 – 41.70 μm) with various combinations of detectors and dividers, VERTEX 80 (Bruker) with an expanded IR range 680 – 165 cm^{-1} (from 14.7 to 60.6 μm).

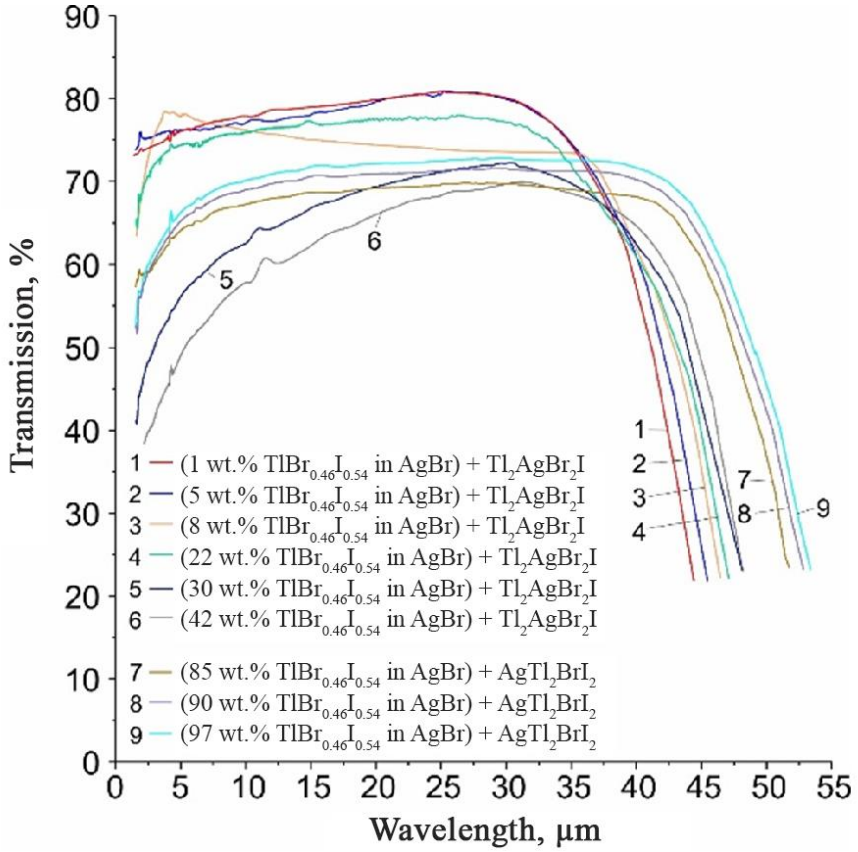

Figure 1. Transmission spectra of multicomponent heterophase ceramics based on two solid solutions of the AgBr – ($TlBr_{0.46}I_{0.54}$) system.

The synthesized ceramics are highly transparent, flexibility, non-hygroscopicity, photo- and radiation-resistant [2, 3], while the method for its preparation consists one step (the vertical method of directional crystallization), therefore it is an economical and practically waste-free process. The targeted synthesis of heterophase optical ceramics based on the AgBr – ($TlBr_{0.46}I_{0.54}$) system can significantly simplify and reduce material and time costs, in comparison with the growing crystals' process of the same system. In addition, due to the ceramics flexibility, it is suitable for the manufacture by hot embossing of various optical products [4].

3. Acknowledgments
This work was supported by the Russian Science Foundation under grant No. 18-73-10063.

References

[1] Salimgareev D D, Lvov A E, Korsakova E A, Korsakov A S, Zhukova L V, 2019, *Mater. Today Commun.* **20** 100551
[2] Korsakov A, Salimgareev D, Lvov A, Zhukova L, 2016, *Opt. Mater.* **62** 534-537
[3] Korsakova E, Lvov A, Salimgareev D, Korsakov A, Markham, S, Mani A, Silien C, Syed T A M , Zhukova L, 2018, *Infrared Phys. and Tech.* **93** 171-177
[4] Korsakov A S, Vrublevsky D S, Korsakov V S, Zhukova L V, 2015, *Appl. Opt.* **54** (26) 8004-8009

Near-infrared photoluminescence and micro-Raman study of spark discharge germanium nanoparticles

D Malo[1,2], A A Lizunova[1], A A Ramanenka[3], B I Masnaviev[1], V R Solovey[1], V V Ivanov[1]

[1]Phystech School of Electronics, Photonics and Molecular Physics, Moscow Institute of Physics and Technology, Dolgoprudny, 141701, Russia

[2]Biomedical Engineering Department, Faculty of Mechanical and Electrical Engineering, Damascus University, Damascus, Syria

[3]B.I. Stepanov Institute of Physics NASB, 220072 Minsk, Belarus

Abstract. We report the investigation of near-infrared (NIR) photoluminescent and structural properties of aerosol germanium nanoparticles, synthesized by spark discharge method followed by sintering in a tube furnace at different temperatures varying from 25 to 775 °C. We demonstrate a growth of mean primary particle size from 7 to 51 nm and change in crystal structure from agglomerates of germanium nanocrystals in amorphous matrix to individual pure crystal germanium nanoparticles with temperature increase. Pure germanium nanoparticles are prepared at temperatures above 600 °C and distinguished by absence of near-infrared photoluminescence. However, according to Raman spectroscopy the presence of amorphous germanium in the samples, sintering at 25 to 475 °C, leads to the luminescence intensity increase from 1100 to 1550 nm.

1. Introduction

Germanium nanoparticles (NPs) continue to be a subject of interest for achieving enhanced properties of light emitters in various quantum technologies especially for biomedical applications and optoelectronic devices due to its unique photoluminescent properties, in particular, the possibility of emission in wide range, from UV through the visible to the near-infrared (~ 1.7 mkm) [1]. The aim of our work is to study the size, structural properties and NIR luminescence of aerosol Ge NPs produced in a gas discharge.

2. Materials and Methods

Ge nanoparticles were synthesized using the aerosol spark discharge generator [2], which was supplemented by a tube furnace for NPs sintering at different temperatures directly in gas flow. Five samples were produced at various temperatures: 25, 325, 475, 625 and 775 °C. Cylindrical n-type germanium was used as electrodes for electrical erosion. Spark processing was performed in argon gas of 99,9999 purity, the pressure was maintained at 1.5 bar. The frequency of the discharges and the capacitor voltage were 370 Hz and 1,5 kV, respectively. Aerosol NPs were collected on a cellulose filter and TEM copper grids with carbon film directly in the setup chamber.

Fluorescence measurements in the IR region were performed on the Fluorolog-3 spectrofluorometer (Horiba Scientific) with laser excitation at 532 nm. Micro-Raman spectroscopy studies was carried out

with a LabRAM HR Evolution (Horiba Scientific) using the 532 nm excitation wavelength of the He-Ne laser (0.1mW). The particle size properties and crystal structure of the samples were analyzed with the aid of transmission electron microscopy (TEM) Jeol JEM 2100 (200 kV).

3. Results and Discussion

According to the analysis of TEM images, the mean size of primary nanoparticles increased with raising of sintering temperature from 6.8 ± 5.2 for 25 °C sample to 51.3 ± 31.8 nm for 775 °C, the width of the particle distribution by size and the proportion of large particles also increased. The particles sintered at temperatures from 25 to 475 °C formed agglomerates, at 775 °C individual Ge particles were observed.

Raman spectra of germanium nanoparticles synthesized at different temperatures (Figure 1a) shows that for 25, 325, 475 °C samples there were two peaks at ~ (275 – 280) cm^{-1} and 298 cm^{-1}, while for 625, 775 °C samples was detected one peak at 298 cm^{-1}. Figure 1b shows absence of near-IR luminescence for Ge NP, sintered at 625, 775 °C, while for 25, 325, 475 °C samples photoluminescence intensity increased from 1100 to 1550 nm.

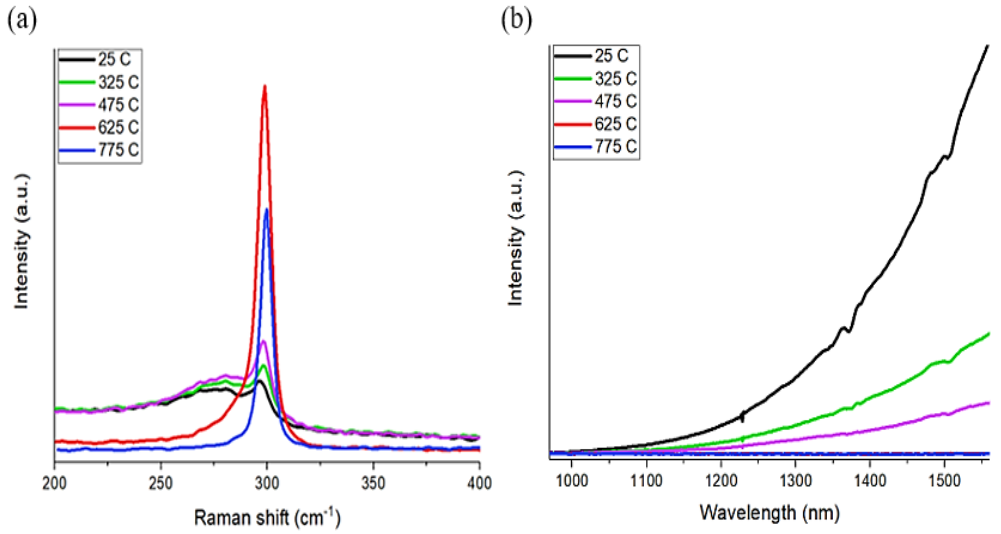

Figure 1(a, b). (a) Raman spectra; **(b)** Near-IR luminescence of Ge NPs, sintered at various temperatures.

The Raman peak at 298 cm^{-1} refers to a crystalline germanium with a cubic lattice characteristic of bulk germanium. The presence of a wide peak with a maximum of about 275 cm^{-1} is associated with the presence of amorphous germanium in samples synthesized at low temperatures from 25 to 475 °C.

By comparing the data of Raman spectroscopy and NIR luminescence, it can be assumed that luminescence occurs either in amorphous Ge or on the interface of the crystal – amorphous germanium.

4. Acknowledgments

This work was financially supported by Russian Science Foundation (project No. 19-79-00337).

References

[1] Vaughn D D, Schaak R E 2013 *Chem. Soc. Rev.* **42** 2861

[2] Ivanov V V, Efimov A A, Mylnikov D A, Lizunova A A, Bagazeev A V, Beketov I V, Shcherbinin S V 2016 *Tech. Phys. Lett.* **42** 876

Thermal poling of glasses to fabricate masks for ion-exchange

E Babich[1], **I Reduto**[2], **A Redkov**[3], **I Reshetov**[1], **V Zhurikhina**[1,4], **A Lipovskii**[1,4]
[1] Peter the Great St. Petersburg Polytechnic University, St. Petersburg, 195251, Russia
[2] University of Eastern Finland, Joensuu, 80101, Finland
[3] Institute of Problems of Mechanical Engineering, St. Petersburg, 199178, Russia
[4] Alferov University, St. Petersburg, 194021, Russia

Abstract. It has been demonstrated that thermally poled regions of silicate glasses are capable of blocking penetration of silver ions into the glasses in the course of ion-exchange processing. This allows using locally poled regions of the glass surface as thick dielectric masks in the ion exchange formation of optically waveguiding structures in glass substrates. This approach provides easy multiplication of the structures and, being based on the thermal electric field imprinting, allows avoiding both lithography with the use of liquid chemicals and the influence of metal masks potential on the flux of the ions penetrating the glass in the ion-exchange.

1. Introduction

Integrated optical structures based on optical glasses are presently in use as elements of fiber optics circuits, in integrated lasers and in sensors. A common manufacturing technique of these structures is based on purely thermal or electrically stimulated ion-exchange processing of glasses in the melts of salts containing monovalent metal ions. This process usually results in local increase of the glass index, and thus leads to the formation of optically waveguiding structures. Ion-exchange fabrication of micron-scale integrated optical schemes with channel optical waveguides in glasses requires the use of masks deposited onto the glass surface. Conventionally, lithography-formed dielectric or, more often, metal masks are in use. In general, dielectric masks look preferable, because they do not induce contact voltage influencing ionic fluxes in the ion-exchange, however conductive metal masks are in widely exploited because of technological reasons. Here we present a novel approach to dielectric masking of the ion-exchange, which does not require lithographic processing of glass substrates and allows easy multiplication of masks exceeding in thickness deposited metal or dielectric layers. The approach is based on thermal poling of silicate glasses with pressed profiled anodic electrodes [1]. As known, thermal poling results in the removal of contained in the glass metal ions from the subanodic region and in the restructuring of that region, which brings it closer to silica glass [2]. Recently it has been shown that poled regions of silicate glasses have better durability in acidic etchants and worse durability in standard reactive ion etching as compared to unpoled regions [3]. Such behaviour is very similar to the one of silica glass. In this study, we compared ion-exchange processing and optical characteristics of the poled and unpoled regions of a silicate glass.

2. Experiments and results

In the experiments, we poled soda-lime glass microscope slides (Menzel glasser) in ambient atmosphere with pressed profiled anode and planar cathode electrodes as reported elsewhere [4]. The anode presented a glassy carbon plate with the set of differently wide and 400 nm deep grooves, the size of the 3 mm thick anodic electrode being 2×2.5 cm^2. The poling was performed at 300 °C DC

during 30 min under 300 V. This processing resulted in the thickness of the poled region ~600 nm [4]. As known, the index of poled soda-lime glass regions is below the one of the virgin glass by ~0.01-0.02 [5]. Thus, the processing resulted in the strips of the virgin glass surrounded by ~600 nm thick flat regions of the poled glass with decreased index. To test ion-exchange properties of the fabricated structures we immersed them into the melt of $Ag_{0.05}Na_{0.95}NO_3$ at 325 °C for 30 and 60 min for silver-to-sodium ion-exchange.

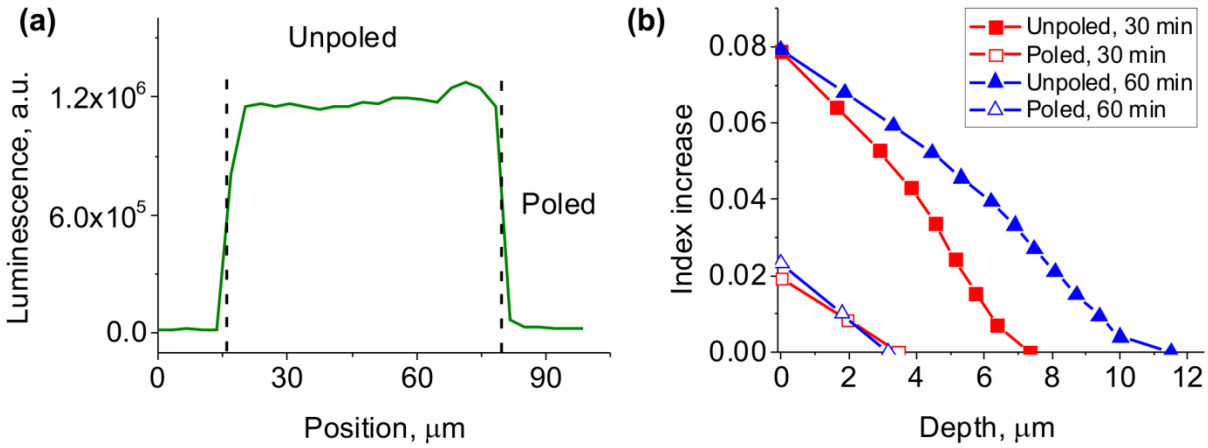

Figure 1(a, b). (a) Intensity of silver luminescence background (1500-3800 cm^{-1}) and **(b)** depth profiles of the glass index increase in ion-exchanged for 30 and 60 min (duration is marked in the legend) poled and unpoled regions of the glass.

To characterize masking properties of the poled regions of the glass we compared the silver luminescence background in the poled and unpoled regions after the ion-exchange (Fig. 1a) and found that the luminescence profile properly corresponds to the mask opening that is unpoled glass region, while the luminescence in the poled glass regions is essentially weaker. The luminescence was excited by 530 nm laser radiation. The depth profiles of the refractive index change (Fig. 1b) also demonstrate essential difference in the penetration of silver ions into the poled and virgin glass regions and in the increase of the glass refractive index. The refractive index profiles were deduced with Heidrich-White algorithm [6] from the mode spectra of optical waveguides measured using standard prism coupling technique.

Thus, it is shown that thermal poling of glasses allows the formation of resistive to ion-exchange processing dielectric masks, which can be used in easy fabrication of integrated optical circuits.

3. Acknowledgments

The study was supported by the Ministry of Science and Higher Education of Russian Federation, project FSRM-2020-001. I.R. thanks the Academy of Finland Flagship Programme (PREIN): Photonics Research and Innovation (#320166).

4. References

[1] Brunkov P N, Melekhin V G, Goncharov V V, Lipovskii A A, Petrov M I 2008 *Techn. Phys. Lett.* **34** 1030
[2] Redkov A V, Melehin V G, Lipovskii A A 2015 *J. Phys. Chem. C* **119** 17298
[3] Reduto I, Kamenskii A, Zhurikhina V, Svirko Yu, Lipovskii A 2019 *Opt. Mater. Express* **9** 3059
[4] Babich E S, Gangrskaya E S, Reduto I V, Beal J, Redkov A, Maurer T and Lipovskii A A 2019 *Current Appl. Phys.* **19** 1088
[5] Ziemath E C, Araújo V D, Escanhoela Jr C A 2008 *J. Appl. Phys.***104** 054912
[6] White J M, Heidrich P F 1976 *Appl. Opt.* **15** 151

Formation and SERS efficiency of periodic metal-dielectric nanostructures

E Gangrskaia[1], E Babich[1], S Scherbak[2,3], I Reduto[4], A Redkov[2,5], A Lipovskii[1,2]

[1] Institute of Physics, Nanotechnology and Telecommunications, Peter the Great St. Petersburg Polytechnic University, St. Petersburg 195251, Russia

[2] Department of Physics and Technology of Nanostructures, Alferov University, St. Petersburg 194021, Russia

[3] International Laboratory of Quantum Optoelectronics, High School of Economy, St. Petersburg 194100, Russia

[4] Institute of Photonics, University of Eastern Finland, Joensuu 80101, Finland

[5] Laboratory of Phase Transitions, Institute for Problems in Mechanical Engineering RAS, St. Petersburg 199178, Russia

Abstract. Gratings on a glass surface with silver nanoparticles at the bottom of the gratings' grooves were studied. The gratings and nanoparticles were fabricated by selective etching of the glass slide patterned by thermal poling and out-diffusion technique, correspondingly. Obtained nanostructures provided both plasmonic and grating optical resonances and demonstrated SERS enhancement two times higher than one of a common plasmonic structure.

1. Introduction

Surface-enhanced Raman scattering (SERS) spectroscopy is the analytical tool widely used in chemical biology and medical diagnostics to identify molecular species down to the lowest analyte concentrations. The SERS phenomenon is mainly attributed to strong enhancement of local electric field by metal nanoparticles at surface plasmon resonance wavelength. Therefore, metal nanostructures-based SERS substrates providing high-quality Raman signal from analytes absorbed on their surface are being actively developed [1]. However, additional enhancement of Raman signal can be achieved by using so-called biresonant nanostructures [2], which support two optical resonances and can enhance both exciting and inelastically scattered radiation. This study is devoted to the fabrication and SERS application of biresonant structures which are periodic grooves (gratings) on a glass surface with silver nanoparticles at their bottom.

2. Experiments

We used the four-step technique of soda-lime glass modification described in detail in our previous work [3] to fabricate the metal-dielectric nanostructures. Firstly, the glass slides were enriched with silver ions by silver-to-sodium ion-exchange. Then we thermally poled the samples at 300V and 300°C for 5 min using an anodic electrode with grooves to form accordant silica-like pattern in the subsurface region of the glass. The pattern was acid resistant, and the following etching for 10 min in 0.1wt.%HF-11.1wt.%NH_4F-88.8wt.%H_2O solution resulted in the formation of a grating relief on the glass surface. The last step was annealing in H_2 atmosphere at 400°C for 10 min. Hydrogen reduced the silver ions, and silver nanoparticles were formed via out-diffusion process, partly in the glass bulk,

but mainly at the bottom of the grooves. The optical studies of the prepared nanostructures were performed using the normally incident light polarized parallel and perpendicular to the grating grooves. SERS efficiency of the nanostructures was evaluated using the test analyte, BPE (1,2-Di(4-pyridyl)ethylene 97%), under excitation at 532 nm laser wavelength. The droplet of the analyte was dried on the surface of the nanostructures forming thin layer of molecules with surface concentration ~10 nmol/mm^2.

3. Results and discussion

According to the modelling [4], the highest enhancement of Raman BPE band at 1640 cm^{-1} by a biresonant metal-dielectric structure should be provided by the structure with the grating period P=510 nm and the silver nanoparticles' radius R=50 nm. Used electrode and the fabrication mode allowed us to obtain the sample with P=590±20 nm and average nanoparticles radius R=35±3 nm. One can see two peaks in the extinction spectrum of the sample in Fig. 1(a). The spectrum is the difference of the spectra collected under the sample illumination with light polarized perpendicular to the grating grooves and parallel to the grooves. The two peaks correspond to two optical resonances: the peak at 496 nm corresponds to the surface plasmon resonance of the silver nanoparticles on the glass surface (at the bottom of the grooves), while one at 618 nm is attributed to the grating resonance [5]. The comparison of two SERS spectra of BPE measured under excitation by perpendicular and parallel polarized laser radiation in Fig. 1(b) shows that signal-to-noise ratio is higher for the perpendicular polarization, and the integral Raman intensity is 2 times higher. Thus, nanostructures under discussion, which provides both plasmonic and grating optical resonances, are two times more efficient for SERS applications than a similar one-resonance plasmonic system.

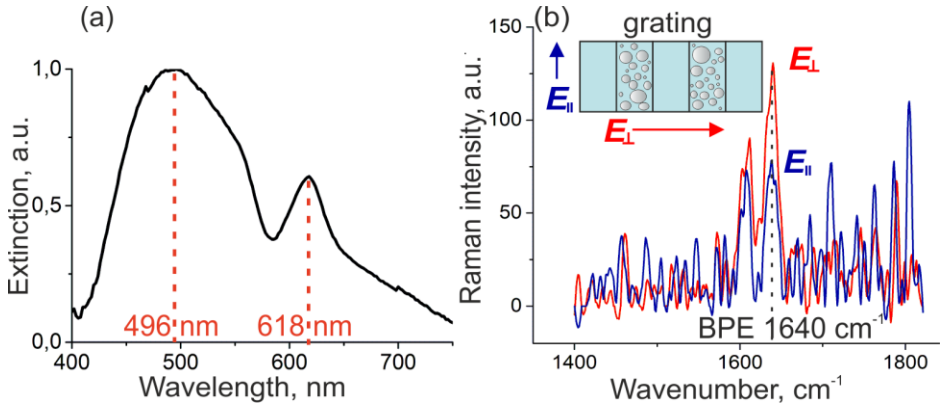

Figure 1. (a) Optical extinction spectrum of the biresonant metal-dielectric nanostructure. (b) SERS spectra collected using light polarized parallel (blue line) and perpendicular (red line) to the grating grooves, excitation wavelength is 532 nm. Inset: scheme of electric field orientation relative to grating.

4. Acknowledgments

The study was supported by the Ministry of Science and Higher Education of Russian Federation, project FSRM-2020-001. I.R. thanks the Academy of Finland Flagship Programme "Photonics Research and Innovation" (PREIN, #320166); and Academy of Finland and Business Finland project "Laser processing of dielectric materials" (LaPro, #247159).

References

[1] Zhong L, Yin J, Zheng Y, Liu Q, Cheng X and Luo F. 2014 *Anal. Chem.* **86** 6262
[2] Scherbak S A and Lipovskii A A 2018 *J. Phys. Chem*. C **122** 15635–45
[3] Babich E S, Gangrskaia E S, Reduto I V, Beal J, et al. 2019 *Curr. Appl. Phys.* **19** 1088
[4] Scherbak S A, Babich E S, Reduto I V and Lipovskii A A 2019 *J. Phys. Conf. Ser.* **1410** 012185
[5] Zou S and Schatz G C 2006 *Nanotechnology* **17** 2813–20

Optical method for determination of fatigue damage in organic glass

E A Sinicyna[1], V.V. Davydov[1, 2], V Yu Rud[2]

[1]Peter the Great Saint-Petersburg Polytechnic University, Polytechnicheskya street 29, Saint Petersburg, Russia, 195251
[2]All-Russian Research Institute of Phytopathology, Moscow Region 143050, Russia

Abstract. The features of nucleation, start, and propagation of a crack inside a transparent organic sample are investigated. The distribution of the refractive index and density around the crack was studied by changing of speckle images and ellipsometry method. It was found that the maximum value of the relative change in density is near the crack. This value before the crack start is greater than 0.003. It is proved that the speckle method we offer can be the basis for the creation of various techniques. Using these techniques will allow us to estimate the time before the crack start by the rate of change of physical quantities in small areas of the order of 50 μm and their limiting values. The results of experimental investigations are presented

1. Introduction

The fatigue of the material is the dominant factor in the destruction for organic glasses with a large cyclic load [1, 2]. At present, there are not the adequate physical models for the fatigue fracture of organic glasses. For this reason, the simple and reliable methods that unambiguously were interpreting the results of fatigue damage processes investigations inside organic glasses are not developed [1, 2]. The active use of speckle images for the investigations of surface defects in the form of cracks, as well as their application for other tasks [3], allowed us to propose a new technique for detecting and research the expansion of cracks inside glasses.

2. Experimental setup and research method

In fig. 1 shows an experimental setup for studying internal fatigue fracture cracks.

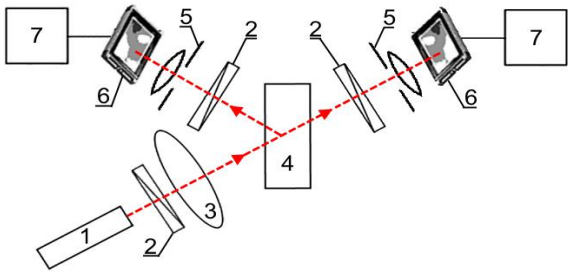

Figure 1. Block diagram of experimental setup for registering a speckle structure: 1-semiconductor laser; 2-polarizer; 3- lens; 4 - glass with crack; 5 - lens of tv camera; 6- photosensitive elements of tv camera CCD matrix; 7- processing device.

The speckle pattern was recorded in the image plane of the sample. To ensure a high degree of contrast when recording speckles, the diameter of the aperture of the lens of the camera 5 was set so that the minimum size of the speckles was slightly larger than the pixel size of the CCD of the camera matrix.

3. Result of experimental investigations

In fig. 2 shows the speckle images in the transmitted scattered laser radiation in the presence of a crack inside the organic glass.

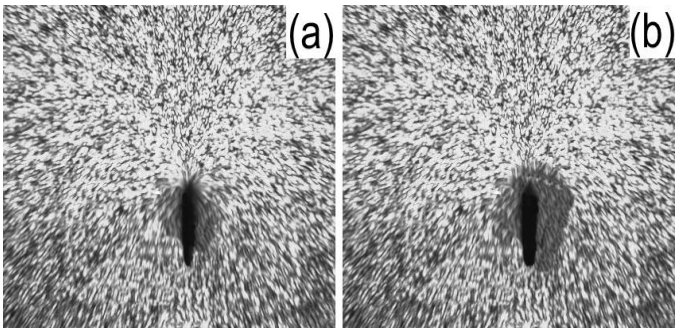

Figure 2. The speckle image from the scattered laser radiation passing through the glass with an internal crack: (a) before the cyclic load, (b) after it.

In fig. 2.b an increase in crack after loading is observed. In the direction of the crack growth, intensified darkening of speckle images is observed. This blackout is less intensely present in fig. 2.a. with a pronounced direction. In case are detected of speckles in reflected scattered laser radiation from a crack, dimming is also present. The contrast of his image will be much less (more than an order of magnitude).

3. Conclusion

The obtained results showed that used the analysis data of speckle images it possible to determine the crack start time with high probability. The method we developed using speckle images in spatial resolution (less than 40 nm) and sensitivity significantly exceeds the traditional coherent-optical measurement and control methods used. This is due to the fact that already in the early stages of fatigue, as a result of the breaking of atomic bonds, disc-shaped defects with diameters of tens of nanometers are formed in organic glass.

The obtained data in during the experiments are extremely useful for creating new methods that allow one to determine the time before the crack start with multi-cycle fatigue of transparent dielectric materials.

References

[1] Vladimirov A P, Kamantsev I S , Veselova V E, Gorkunov E S, Gladkovskii S V 2019 *Technical Physics* **61(4)** 563-568

[2] Logunov S E, Davydov V V, Yalunina T R 2018 Proceedings - International Conference Laser Optics 2018, ICLO 2018 (Russia. St. Petersburg) vol. 8435501 p. 149

[3] Vladimirov A P 2016 *Optical Engineering* **55(12)** 121727

Simulation of the super-Gauss beam abrupt focusing in the near diffraction zone using high-performance computer systems

D A Savelyev[1,2]**, S G Volotovskiy**[2]
[1]Samara National Research University, 34, Moskovskoye Shosse, Samara, Russia, 443086
[2]Laboratory of Laser Measurements, Image Processing Systems Institute - Branch of the Federal Scientific Research Centre "Crystallography and Photonics" of Russian Academy of Sciences, Samara 443001, Russia

Abstract. We investigated the change in the type of focal spot when laser radiation passed through the diffraction axicon and the optical element matched with the circular Airy distribution having abrupt focusing properties. Modelling of near zone diffraction is numerically investigated by the finite difference time domain (FDTD) method. The abrupt formation of a light needle was shown for the optical element matched with the circular Airy distribution.

1. Introduction

The formation of light fields with a given structure of amplitude, phase, and polarization (the so-called structured light) is currently necessary to solve many pressing problems in various fields - optical manipulation [1-3], imaging optics [4], optical and quantum communications [5, 6] and other applications [7]. To form such structured fields, elements of diffraction optics, photonic crystals, and all kinds of metamaterials and metasurfaces are widely used.

One of the main driving forces of technological change in the XXI century became a miniaturization of technical systems and devices, a tendency to the development of information, sensor components, combined on the basis of nano-and microsystem technology. The development of such a technique has led to the need for the development and development of elements of nano- and micrometer sizes that could be used to control light at appropriate scales. The possibility of manufacturing microaxicons [8, 9] expanded the range of application of axicons and allowed them to occupy an important place in micro- and nanooptics [10-12]. Another interesting type of a laser distribution is the Airy circular beam which have the property of sharp autofocusing [13, 14] which is also in demand in many applications.

We compared the focusing of super Gauss through the diffraction axicon and the optical element matched with the circular Airy distribution. The FDTD method using high-performance computations is applies to numerically simulate the diffraction of the laser radiation [15] with using the Meep software package. Calculations were made on the computational cluster with power of 850 GFlops.

2. Investigation of focusing short pulses

Simulation parameters: the wavelength $\lambda = 0.532$ microns, the size of the computational domain x, y, z $\in [-3.8\lambda; 3.8\lambda]$. The thickness of the absorbing layer PML ~ 1.3λ, the sampling step of space – $\lambda/21$,

the sampling step of time – λ/(42c), where c is the velocity of light. The Super-Gauss with circular polarization was considered as the input laser radiation. The refractive index of the axicon and the optical element matched with the circular Airy distribution are n = 1.5. The numerical aperture (NA) of the focusing binary axicon was 0.95. The results of numerical simulation in the xz plane and input beam are shown in figure 1.
It should be noted that the focusing of laser radiation for the axicon occurs in the immediate vicinity of the optical element. The formation of a strong light needle is observed for an optical element with a radial Airy function

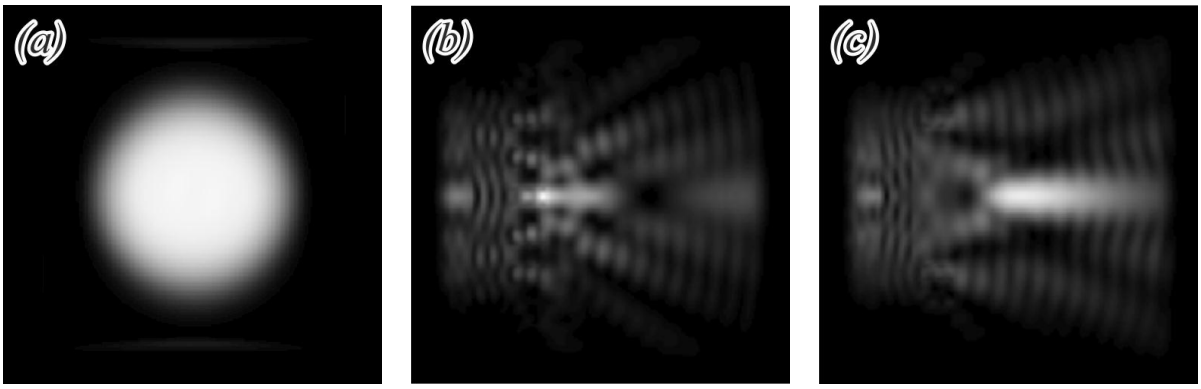

Figure 1. The longitudinal cross section (xz) of propagation laser radiation: (a) the input beam, (b) laser propagation through the axicon, (c) laser propagation through the optical element matched with the circular Airy distribution.

3. Conclusion

The formation of the Super-Gauss radiation with circular polarization passed through the diffraction axicon and the optical element matched with the circular Airy distribution were investigated. It should be noted the abrupt formation of strong light needle was shown for the Airy-matched optical element.

4. Acknowledgments
This work was financially supported by the Russian Foundation for Basic Research (grant 20-07-00505) and by the Ministry of Science and Higher Education of the Russian Federation.

References
[1] Padgett M and Bowman R 2011 *Nat. Photonics* **5** 343
[2] Dholakia K and Čižmár T 2011 *Nat. Photonics* **5** 335
[3] Smalley D E et. al. 2018 *Nature* **553** 486
[4] Geng J 2011 *Adv. Opt. Photon.* **3** 128
[5] Wang J et. al. 2012 *Nat. Photonics* **6** 488
[6] Wang J 2016 *Photon. Res.* **4** B14
[7] Rubinsztein-Dunlop H et. al. 2017 *J. Opt.* **19** 013001
[8] Grosjean T et. al. 2007 *Appl. Opt.* **46** 8061
[9] Kuchmizhak A, Gurbatov S, Nepomniaschii A, Vitrik O and Kulchin Y 2014 *Appl. Opt.* **53** 937
[10] Khonina S N et. al. 2013 *Journal of Optics* **15** 085704
[11] Khonina S N, Degtyarev S A 2016 *Journal of Optical Technology* **83** 197
[12] Khonina S, Degtyarev S, Savelyev D and Ustinov A 2017 *Optics Express*, **25** 19052
[13] Efremidis N K and Christodoulides D N 2010 *Opt. Lett.* **35** 4045
[14] Porfirev A P, Khonina S N 2017 *Journal of the Optical Society of America B* **34** 2544
[15] Savelyev D A and Khonina S N 2014 *Journal of Physics: Conference Series* **490** 012213

Investigation of energy transitions in MoS_2 by photoreflectance spectroscopy method

A O Mihin[1], D D Firsov[1], O S Komkov[1]
[1]Photonics Laboratory, Micro- and nanoelectronics department, St. Petersburg Electrotechnical University, St. Petersburg 197376, Russia

Abstract. Photoreflectance spectroscopy was used to study the energy spectra of natural molybdenum disulfide samples at various temperatures. The observed spectral features imply a transition from the H-point of the Brillouin zone, in addition to the generally accepted K-point. The H-exciton binding energy obtained from our experiments is 77 meV, which is consistent with the available theoretical data.

1. Introduction

Molybdenum disulfide is a layered semiconductor compound with strong covalent bonds within the plane, and weak van-der-Waals bonds between the tetralayers. Today MoS_2 is one of the most studied graphene-like materials, however it did not lose its relevance for research [1]. It is also a good model object, which can be used for refinement of the experimental techniques intended for further characterization of less studied layered semiconductors. In this work, we apply the photoreflectance (PR) spectroscopy method to probe the weak features of MoS_2 band structure.

2. Experiments

The current study has been conducted on natural MoS_2 crystals obtained from "2D Semiconductors" (USA). PR spectroscopy is an optical method that provides information about the main transitions in the energy spectrum of a semiconductor material. Typically, the PR spectra consist of derivative-like features, from which the values of the transition energies can be obtained using the transformation method described by Hosea in [2]. An example of the measured photoreflectance spectra of MoS_2, as well as the result of its transformation, are shown in Fig. 1 (a, b). A total of seven spectral features have been observed in each of the PR measurements at various temperatures.

To interpret the transitions observed in the PR spectra, we have considered two approaches, described in refs. [3] and [4]. Both hypotheses identify E_1 as the first ground state exciton (A_1) at the K-point of the Brillouin zone [5]. This state has a spin-orbit split valence band, which is also exhibited in the spectrum (the E_6 peak in Fig. 1b). However, the two hypotheses considered provide a different interpretation of the remaining extrema.

According to the first model [3], features with energies from E_2 to E_4 relate to the excited states of the K-exciton. The exciton energy levels were estimated according to the well-known expression: $A_n = E_g - R/n^2$. Therefore, it is possible to obtain the effective Rydberg (R) value, which in this case turns out to be 56 meV. In addition, we obtained the band gap (E_g= 1.986 eV) from this expression and then substituted it to calculate the energies of the excited states series (A_n). The obtained values are the following: A_1= 1.930 eV, A_2= 1.972 eV, A_3= 1.980 eV, and A_4= 1.982 eV. This is sufficient to describe four of the observed extremes, but not the last one, the E_5 energy peak. Its remoteness from the E_4 feature

suggests that the E_5 maximum does not apply to the excited states of the K-exciton and the nature of its appearance is different.

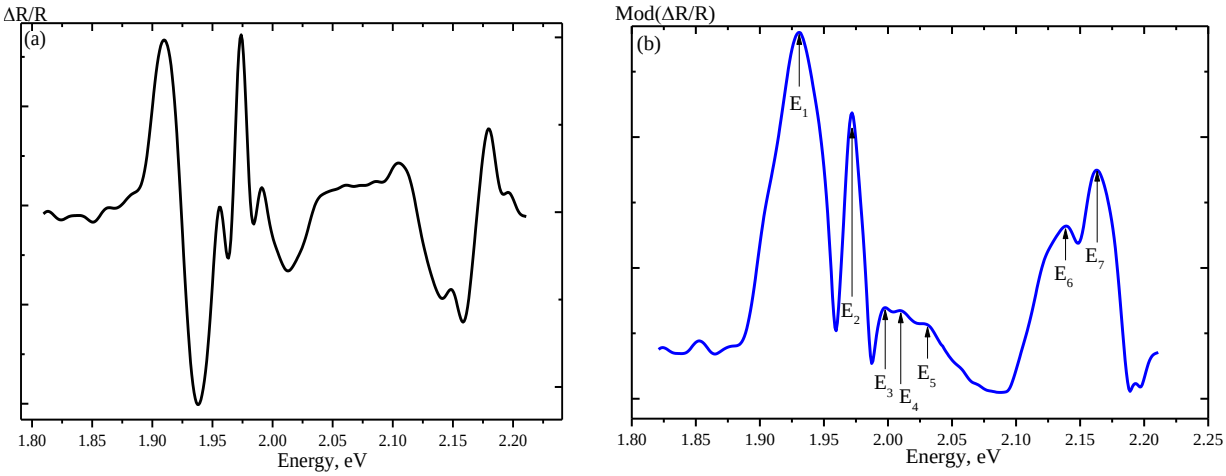

Figure 1. The photoreftectance spectrum (ΔR/R) of natural MoS_2 measured at 80 K **(a)**, and the transformed [2] PR spectrum Mod(ΔR/R) with seven energy transitions marked by arrows **(b)**.

The other model, which has been put forward by Saigal and Ghosh [4], is able to explain the existence of the E_5 feature. The authors describe the E_2 energy peak as the exciton ground state transition, but at the H-point of the Brillouin zone instead of the K-point. Our observed difference between the transition energies at K- and H-points of the valence band is equal to 42 meV, whereas the spin-orbit splitting is 209 and 191 meV for K- and H-points, respectively. The obtained values are close to the data that was published in [4], but the E_5 peak was not resolved in their spectra. We assume that this peak corresponds to the first excited state of the H-point exciton. This makes it possible to obtain the exciton binding energy from the PR spectrum, which is found to be 77 meV. In the work [6], the authors estimated that the exciton binding energy should be 84 ± 8 meV from the absorption spectrum simulation. It can be seen that our experimental result falls within the predicted range. Therefore, we can confirm the existence of an H-point transition, and conclude that E_2 is indeed the exciton ground state at the H-point, while the observed E_5 peak corresponds to its first excited state.

3. Conclusions

As a result, we were able to describe the E_5 feature in the PR spectrum of MoS_2 for the first time, which is the excited level of the exciton ground state (E_2). Its presence in the PR spectrum confirms an existence of an optical transition at the H-point of the Brillouin zone. This fact enabled us to experimentally determine the exciton binding energy, which turned out to be 77 meV. The obtained value is in good agreement with the theoretically predicted range.

4. Funding

The work was partially supported by the Russian Science Foundation (RSF), project #18-79-10161.

References

[1]. C. Robert et al., 2018 Phys. Rev. Mat. **2**, 011001(R)
[2]. T. J. C. Hosea 1995 Phys. Stat. Sol. (b) **189**, 531
[3]. B. Evans, P. Young 1965 Lond Proc. Roy. Soc. A **284,** 402
[4]. N. Saigal, S. Ghosh, 2015 Appl. Phys. Lett. **106**, 182103
[5]. R. V. Kasowski 1973 Phys. Rev. Let. **30**, 1175
[6]. N. Saigal, V. Sugunakar, S. Ghosh, 2016 Appl. Phys. Lett. **108**, 132105

Possibilities of using spectral analysis in the method of nuclear magnetic spectroscopy for the study of condensed matter

S S Makeev[1], V V Davydov[1, 2], V Yu Rud[2]

[1]Higher School of applied physics and space technologies, Peter the Great Saint Petersburg Polytechnic University, Saint Petersburg 195251, Russia
[2]All-Russian Research Institute of Phytopathology, Moscow Region 143050, Russia

Abstract. The necessity of developing a mathematical model for converting the recorded NMR signal using a modulation technique into the spectrum for conducting the composition of the medium under study is substantiated. A mathematical model has been developed to represent the NMR signal in the form of a spectrum, taking into account the features of its registration from condensed matter. Spectra of calculated and experimental NMR signals are presented. Their comparison is completed..

1. Introduction

In recent years, the need to use rapid control methods to determine the state of a condensed medium has been constantly increasing [1, 2]. The most promising among the developed devices for express control are considered devices in which the phenomenon of nuclear magnetic resonance (NMR) is used. Measurements using NMR do not introduce changes in the physical structure and chemical composition of the test medium [3]. This allows you to receive confirmation of the detected deviations in the studied samples in stationary laboratories on high-resolution devices [3]

The experimental studies made it possible to establish that during express control, the NMR signal from the condensed matter is most expediently recorded using a modulation technique in a weak magnetic field. Other methods for registering an NMR signal do not provide the necessary measurement error. Our experimental results of the study of various condensed matter showed that the previously proposed method in [3] for determining the composition of the matter has several disadvantages. These deficiencies degrade accuracy and increase measurement time. Therefore, we developed a new technique for determining the composition of a condensed matter using a registered NMR signal during express control of its state.

2. The technique of constructing a spectrum of NMR signals and comparing the calculation results with experiment.

When using a modulation technique to record an NMR signal, its shape is a superposition of absorption and dispersion signals. If the medium contains several media that did not enter into a chemical reaction (for example, gasolines, oil, and kerosene), the recorded signal is the sum of all absorption and dispersion signals from each of the components of the medium under study. In [3], a method was proposed for describing the line shape of the recorded NMR signal using the calculated absorption and dispersion signals that correspond to the experiment. The absorption and dispersion signals were obtained by numerically solving the Bloch equations. The phase in constructing the line shape was selected empirically. With a large number of components in the mixture, this created a number of problems. To solve them, we propose to use a spectral analysis of experimental and calculated NMR signals. Compare the spectra of the experimental signal with the spectra of the calculated absorption and dispersion signals.

Studies have shown that to construct the spectra of NMR signals it is most appropriate to use the discrete Fourier transform, since these signals cannot be described by any periodic function:

$$y_k = \sum_{n=0}^{N-1} x_n e^{-j2\pi kn/N} \tag{1}$$

where n = 0, 1, 2, …, N–1, x_n - is the input data sequence, N – is the number of elements of the input data sequence x_n,

$$y_k = \begin{cases} y_0 & k = 0 \\ \sqrt{2}\,\dfrac{y_k}{N} & k = 1,2,\ldots\left\lfloor \dfrac{N}{2} - 1 \right\rfloor \end{cases} \tag{2}$$

In relation (2), the operation in brackets [N / 2 -1] means rounding to the nearest smallest integer. Accordingly, the amplitude spectrum $S(f) = |y_k|$ – is the modulus of the one-sided complex spectrum, phase spectrum P(f) = arg y_k - is its argument, where f = k Δf.

In fig. 1 as an example, the phase spectra of the experimental NMR signal recorded from a water sample and the spectra from the calculated absorption and dispersion signals are presented.

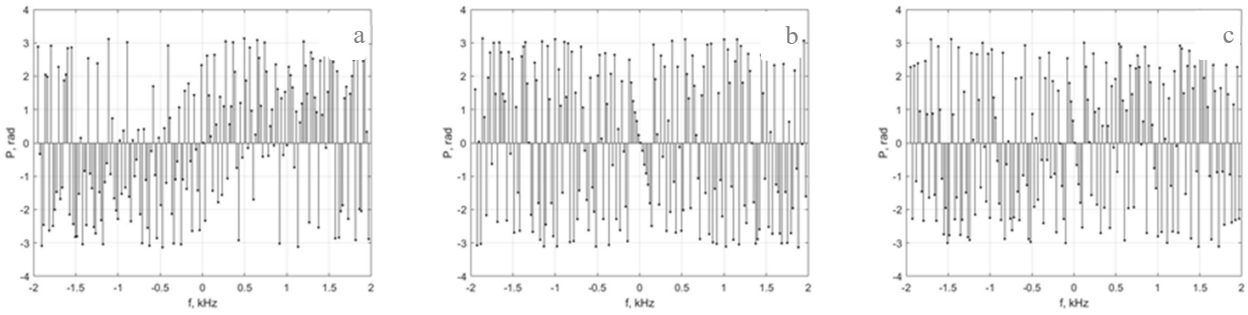

Fig. 1 Phase spectra of NMR signals: (a) experimental; (b) absorption; (c) dispersion.

Analysis of the results in Fig. 1 shows that the nature of the change in harmonics in the spectra from the calculated signals corresponds to the nature of the change in harmonics in the experimental spectrum. This allows, when choosing the coefficients that determine the contributions of the absorption and dispersion signals to the recorded signal, to obtain a match in the amplitude of the harmonics in the spectra.

3. Conclusion

The results obtained confirmed the possibility of determining, using spectral analysis, the contributions of absorption and dispersion signals to the recorded NMR signal. This allows, using spectral analysis, also to describe the experimental signal for the matter with weight coefficients for each of the components and to calculate the composition of the components in the mixture and their concentration.

References

[1] Myazin N S, Davydov V V, Yushkova V V, Davydova T I and V Yu Rud' 2017 *Journal of Physics: Conference Series* **917** 042017

[2] Karseev A Yu, Cheremiskina A V, Davydov V V, Velichko E N 2014 *J. of Physics: Conference Series* **541** 012006

[3] Myazin N S and Davydov V V 2018 *Journal of Physics: Conference Series* **1124(1)** 031004

Laser-induced graphene on polyimide film: photon drag effect observation

A E Fateev, K G Mikheev, R G Zonov, D L Bulatov, G M Mikheev
Institute of Mechanics, Udmurt Federal Research Center of the UB RAS, Izhevsk 426067, Russia

Abstract. Porous graphene film structures were produced by irradiation of polyimide film with focused continuous wave CO2 laser. Generation of nanosecond pulses of photocurrent was observed in the obtained structures upon excitation by nanosecond laser pulses in a wide range of wavelengths. It is shown that the photocurrent linearly increases with pulsed laser power and its dependence on the angle of light incidence on the film is symmetric about the origin. Wavelength dependence of light-to-photocurrent conversion coefficient was measured. The obtained results are explained by photon drag effect photocurrent generation.

1. Introduction

Recently, it was shown in article [1] that it is possible to produce porous graphene (3D graphene), called laser-induced graphene (LIG), using decomposition of a polymer film using pulsed irradiation by CO_2 laser. LIG have various perspective applications [2] (microsupercapacitors, various sensors, electrocatalysts and microfluidic systems). Meanwhile, it is known that photon drag effect (PDE) [3] photocurrent with dependence on the angle of film incidence can be observed in graphene and nanographite films [4,5].The purpose of this work is to investigate PDE in LIG, obtained on the surface of polyimide (PI) film using continuous wave CO_2 laser.

2. Experimental

In our experiments, commercial PI films with thicknesses of 40, 80, 120 μm and a CO_2 laser at a wavelength of 10.6 μm, generating continuous wave radiation with a power of up to 50 W, were used to synthesize LIG. The LIG was formed during scanning by a focused laser beam. The LIG in the obtained films was identified using a Raman spectrometer Horiba HR800 with excitation radiation at a wavelength of 632.8 nm. The morphology of the obtained films was studied using a scanning electron microscope.

To study the generation of photocurrent, the obtained films were placed on a special goniometric device, which is capable of performing smooth changes of the angle of incidence of light α on the film. Measuring electrodes were attached to the film along the short sides. The first, second, third, and fourth harmonics of a single-mode YAG:Nd^{3+} laser with passive Q-switching at wavelengths λ = 1064, 532, 354.7, and 266 nm, respectively, were used.

The experiments have shown that photocurrent pulses with nanosecond duration are generated in the synthesized film structures under irradiation with obliquely incident nanosecond laser pulses. Upper insert in fig.3 shows the linear dependence of the i_x transverse photocurrent on the pulsed power P_{in} of a laser at a wavelength of 1064 nm. The linear dependence of i_x on P_{in} is retained upon excitation of the photocurrent by radiation at 532, 354.7, and 266 nm. Figure 3 shows the dependence of conversion

efficiency η on the angle of incidence α at a wavelength of 1064 nm for *p*- and *s*-polarizations of the incident radiation.

The bottom left inset in fig. 3 shows the experimentally obtained dependence of η (α= 45°) on the wavelength λ of the exciting laser. The nature of the obtained dependence η(λ) indicates the possibility of using LIG to detect laser radiation pulses in a wide spectral range. The photocurrent can be explained by PDE as the aforementioned dependences are characteristic of photon drag effect.

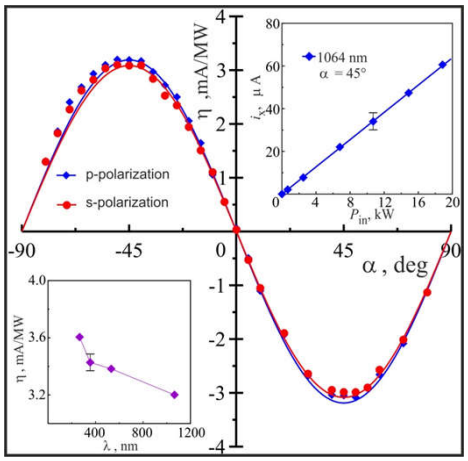

Figure 1. Dependence of the laser-to-photocurrent conversion efficiency η on the incidence angle *α* at the wavelength of 1064 nm at p- and s-polarizations of the laser beam irradiating LIG. Upper inset: dependence of LIG photocurrent on the power of p-polarized laser radiation at wavelength of 1064 nm and incidence angle of 45°. Lower inset: dependence of the laser-to-photocurrent conversion efficiency η in LIG on wavelength of laser radiation at incidence angle of 45°.

3. Conclusions

Porous graphene film structure can be formed on polyimide films using continuous wave CO_2 laser at wavelength of 10.6 μm with power density of 8 W/cm^2 and scanning speed of 255 mm/s. Nanosecond laser irradiation of laser-induced graphene at a wavelength range of 266 - 1064 nm leads to photon drag effect photocurrent generation. Laser-induced graphene can be used to manufacture fast reacting photodetectors working in a wide spectral range.

4. Acknowledgments

The work was performed with the support of the Russian Science Foundation (Project No. 19-72-00071). The measurements were performed using equipment of the Shared Use Center “Center of Physical and Physicochemical Methods of Analysis and Study of the Properties and Surface Characteristics of Nanostructures, Materials, and Products” UdmFRC UB RAS.

References

[1] Lin J, Peng Z, Liu Y, Ruiz-Zepeda F, Ye R, Samuel E L G, Yacaman M J, Yakobson B I and Tour J M 2014 *Nat. Commun.* **5** 5–12

[2] Ye R, James D K and Tour J M 2019 *Adv. Mater.* **31** 1–15

[3] Kovalev V M, Miroshnichenko A E and Savenko I G 2018 *Phys. Rev. B* **98** 165405

[4] Obraztsov P A, Mikheev G M, Garnov S V, Obraztsov A N and Svirko Y P 2011 *Appl. Phys. Lett.* **98** 091903

[5] Zhu L, Huang Y, Yao Z, Quan B, Zhang L, Li J, Gu C, Xu X and Ren Z 2017 *Nanoscale* **9** 10301–11

Performance of an optical non-volatile storage element based on $Ge_2Sb_2Te_5$

M. Makarov[1, 2], **A. Sapegin**[1, 3], **A. Italyantsev**[1]
[1]JSC Molecular Electronics Research Institute, Moscow 124460, Russia
[2]Institute of Microelectronics Technology and High-Purity Materials of Russian Academy of Sciences, Chernogolovka 142432, Russia
[3] Moscow Institute of Physics and Technology, Dolgoprudny 141701, Russia

Abstract. Considerable growth in data exchange leads to enhanced requirements for computing, storage and transmitting devices. Promising solutions to this challenge can be found in the use of phase-change materials. This paper is devoted to evaluating the operating speed of a non-volatile storage element with optical recording and readout. The evaluation shows that it is possible to reduce the operating cycle time of the device and thus improve its performance.

1. Introduction

Today there is a great demand for high-speed devices in various areas. The requirements for devices are increasing with the volume of data being transmitted. However, common solutions to this problem by the microelectronics methods are reaching a physical limit. Therefore, some major corporations, such as IBM, Intel, and Fujitsu, are applying photonic technologies in integrated circuits. The validity of this approach is confirmed by several works in scientific periodicals [1, 2]. Another way to improve device speed is by applying non-volatile storage devices [3, 4] and the neural architecture [5]. This paper presents a theoretical and numerical estimation of an optical non-volatile storage element performance. The logical state of the structure is stored in the thin $Ge_2Sb_2Te_5$ (GST) layer which is located on a Si strip waveguide. Different optical transmittance of the GST layer in the amorphous and crystalline states corresponds to “1” and “0” in binary notation. Recording, readout and erasing operations of the storage element are performed by laser pulses with different energy and duration.

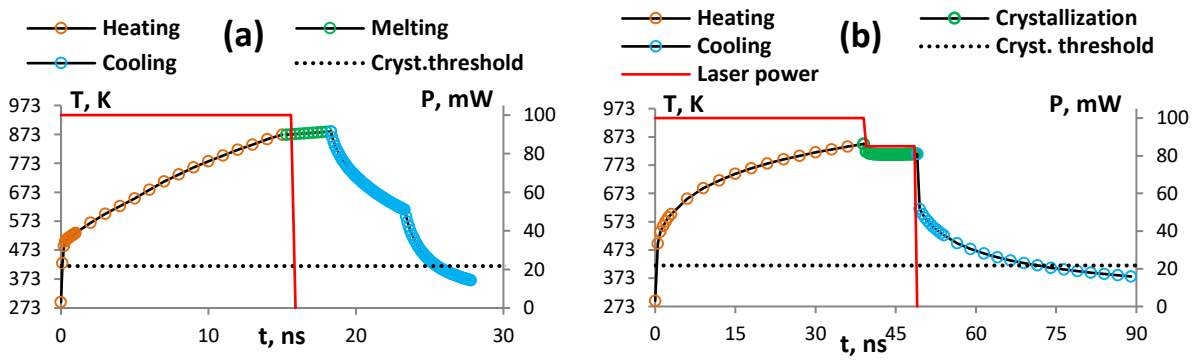

Figure 1(a, b). Temperature dependence during **(a)** the recording operation; **(b)** the erasing operation

2. Device simulation and discussion

An analytical model of GST crystallization kinetics [6] was chosen to describe phase transitions. The model provides a dependence of a crystalline phase growth on temperature and time. It's worth mentioning that the phase transition time has an extremum in the temperature range near the GST melting point. In practice, many different factors affect the duration of switching between GST phase states. Respectively, the total time interval depends on the guided light power, the absorption coefficient of the specific GST layer, heat transfer in solid media, the cooling rate and phase transition time described in [6]. Complex numerical calculations that consider all these factors have shown that there is an optimal regime of laser irradiation **(Fig. 1)**. The regime provides an opportunity to achieve a significant increase in performance compared to similar devices [7, 8] because of two facts. Firstly, short high-power laser pulses provide a shorter time to reach a suitable temperature regime. The second fact is the correct choice of temperature conditions for the crystallization process exponentially shortens its duration. Thus, the duration of the recording/erasing cycle in the first approximation is 100 ns for the device in question.

3. Conclusion

This work represents a comprehensive theoretical and numerical analysis of the operating speed of the optical non-volatile storage element. The calculations show that it is possible to reduce the erasing time of the storage element by providing the optimal operating regime based on the use of the GST crystallization rate extremum.

4. Acknowledgments

The reported study was funded by RFBR according to the research project № 19-21-00001.

References

[1] E. Kuramochi, K. Nozaki, A. Shinya, K. Takeda, T. Sato, S. Matsuo, H. Taniyama, H. Sumikura and M. Notomi 2014 *Nature Photonics* **8** 474
[2] C. Ríos, M. Stegmaier, P. Hosseini, Di Wang, T. Scherer, C. D. Wright, H. Bhaskaran and W. H. P. Pernice 2015 *Nature Photonics* **9** 725
[3] G. Y. Krasnikov, N. A. Zaytsev, A. G. Krasnikov 2015 *Nano- and microsystems technology* **4** 60
[4] H.-S. Philip Wong, S. Salahuddin 2015 *Nature Nanotechnology* **10** 191
[5] M. A. Zidan, J. P.Strachan and W. D. Lu 2018 *Nature Electronics* **1** 22
[6] C. D. Wright, M. Armand and M. M. Aziz 2006 *IEEE Transactions on Nanotechnology* **5** 50
[7] C. Rios, N. Youngblood, Z. Cheng, M. Le Gallo, W. H. P. Pernice, C. D. Wright, A. Sebastian and H. Bhaskaran 2019 *Science Advances* **5**
[8] X. Li, N. Youngblood, C. Rios, Z. Cheng, C. D. Wright, W. HP Pernice and H. Bhaskaran 2019 *Optica* **6** 1

The Simulation of Gold Nanoparticle in a TiO_2 Matrix Absorption and Reflection Spectra

Y Enns[1,2], A Kondrateva[1,2], M Mishin[1]

[1]St. Petersburg Academic University, St. Petersburg, Russia
[2]Peter the Great Saint-Petersburg Polytechnic University, St. Petersburg, Russia

Abstract. In this work results of a theoretical analysis of the nanocomposite structures optical parameters is presented. The variable parameters are: shape of nanoinclusions, matrix width and angle of incident radiation. In this work quasiperiodic nanocomposite structures consisting of a matrix of titanium dioxide and gold nanoparticles hemisphere were simulated. A spectral analysis of these structures showed the nonlinear nature of the change in the absorption and reflection peaks from the nanoparticles shape.

1. Introduction

A steady interest in the optical properties of complex structures has been observed for more than 35 years [1]. The nanocomposite structures in which excitation of surface plasmon polaritons (SPPs) is possible are widely studied [2]. Moreover, a significant local increase in the fields can be observed depending on the shape and size of the nanoinclusions [3]. Due to the quasiperiodic arrangement of nanoparticles, surface plasmon polaritons are excited in the nanocomposite layer. This effect affects the passage of light through the structure. Both a significant increase in the transmitted light flux and its decrease are possible depending on the relative position of the nanoparticles. This allows to design both passive [4,5,6] and active optical elements [7-9]. So, in addition to studying fundamental optical properties, research are under way to create a highly efficient optoelectric systems, including MEMS [10, 11]. The introduction of SPP-based optical elements will significantly reduce the size of integrated circuits and increase their efficiency [12].

One of the first steps in the manufacture of optoelectronic components of integrated circuits is the modeling of their optical and electrical characteristics. This is important in terms of creating nanocomposite quasiperiodic structures, since it is possible to evaluate the effect of the parameters of the matrix and nano inclusions.

2. Results

In this work, the optical characteristics of nanocomposite structures consisting of a matrix of titanium dioxide containing gold hemispheres (Fig. 1a) were simulated. A detailed technology for the formation of such structures is given in [13].The aim of the work was to determine the influence of the geometric parameters of the structure on its optical characteristics. Spectral optical characteristics were obtained for nanocomposite structures with a diameter of gold nanoparticles from 5 nm to 100 nm. The obtained simulation results are consistent with published experimental data for particles with a diameter of 10–20 nm [14]. The results show that increasing the diameter of the hemispheres leads to a nonlinear character of the shift of the absorption and reflection peaks (Fig. 1b).

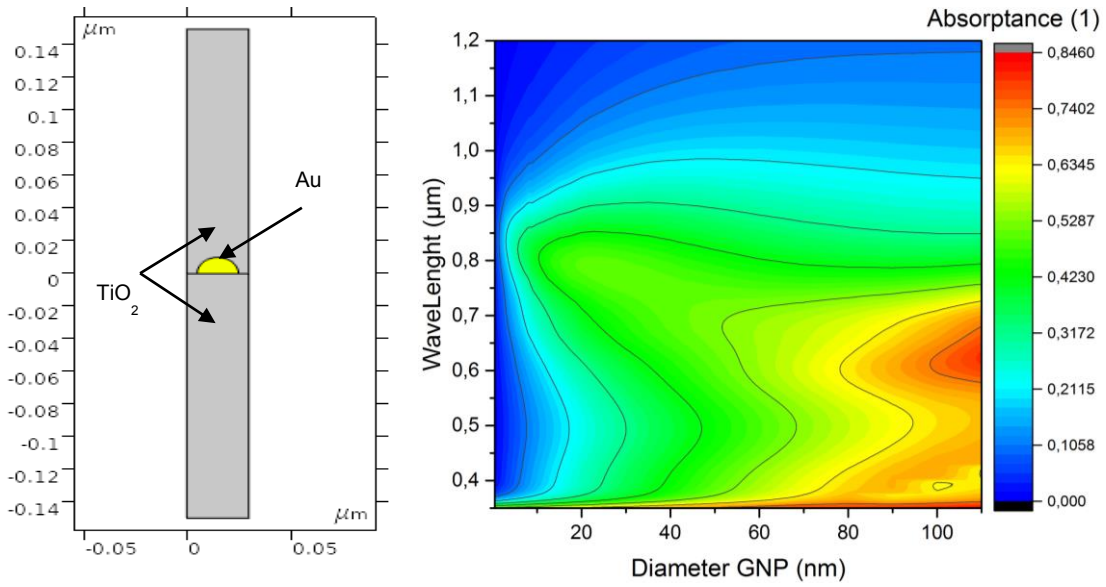

Figure 1(a, b). (a) Schematic of cross section of TiO2 / GNP nanocomposite (diameter GND 20 nm; **(b)** Absorption topography in space wavelength /diameter GNP.

3. Acknowledgments

Authors wishing to acknowledge the Ministry of Education foundation for financial support assistance (№ FSRM-2020-009).

References

[1] Berthold K, Höpfel R A, Gornik E 1985 *J. Appl. Phys. lett.* **46** (7) 626

[2] Raether H 1988 (Springer) 4-39

[3] Shaaran T., Ciappina M. F., Lewenstein M 2012 *J. Phys. Rev. A.* **86(**2) 023408

[4] Charbonneau R, Scales C, Breukelaar I, Fafard S, Lahoud N, Mattiussi G, Berini P J. 2006 Lightwave Tech. **24** (1) 477-494.,

[5] Fan H, Buckley R, Berini P 2012 *J. Appl. opt.* **51** (10) 1459-1467

[6] Steinberger B, Hohenau A, Ditlbacher H, Aussenegg F R, Leitner A, Krenn J R 2007 *J. Appl. Phys. Lett* **91**. – №. 8. – С. 081111.

[7] Krasavin A V, Zayats A V 2010 J. *Appl. Phys. lett.* **97**(4) 041107

[8] Jorgenson R C 2001 *Sens. and Act. B: Chem.* **73**(2) 236-248

[9] Cao J, Sun T, Grattan K T V 2014 *Sens. and Act. B: Chem.* **195** 332-351.,

[10] Kanamori Y, Hokari R, Hane K 2015 *J. Sel. Top. in Quant. Electr.* **21**(4) 137-146

[11] Zhang X M, Zhu W M, Cai H, Liu A Q 2008 IEEE 21st International Conference on Micro Electro Mechanical Systems. 778-781

[12] Flynn R A, Vurgaftman I, Bussmann K, Simpkins B S, Kim Ch S, Long J P 2010 *J. Appl. Phys. lett.* **96(**11) 111101.

[13] Mishin M V , Vorobyev A A, Kondrateva A S, Koroleva E Y, Karaseov P A, Bespalova P G, Shakhmin A L, Glukhovskoy A V, Wurz M C and Filimonov A V 2018 *Semiconductor Science and Technology* **33(**7)

[14] Kostrova A N, Aybusha A V, Gosteva F E, Shelaeva I V, Titova A A, Nadtochenkoa V A 2019, *Rus. J. of Phys. Chem. B* **13(**3) 539–542

Developing of NbN films for superconducting microstrip single photon detector

N.N. Manova[1], N.O. Simonov[1], Yu.P. Korneeva[1], A.A. Korneev[1,2]
[1]Institute of Physics, Technology, and Information Systems, Moscow State Pedagogical University, Moscow 119991, Russia
[2] National Research University Higher School of Economics, Moscow 101000, Russia

Abstract. We optimized NbN films on a Si substrate with a buffer SiO_2 layer to produce superconducting microstrip single photon detectors (SMSPD) with saturated dependence of quantum efficiency (QE). We varied thickness of films and observed the maximum QE saturation for device based on the thinner film with the lowest ratio $R_{s\,300}/R_{s\,20}$.

1. Introduction

In [1] the first time new type of single photon detectors that based on the effect of appearance resistance area in the superconducting nanowire after photon absorption was demonstrated. This detector was named superconducting single photon detector (SSPD). Typically SSPD produced as a stripe about 100 nm wide patterned on the meander, covering the aria about 250 μm to well couple with single mood fiber. Today they are used in many science applications. The further enlargement of its application sphere requests increase of SSPD sensitive area to the value comparable to multimode fiber core. But increase of nanowire length leads to increase of kinetic inductance and as circumstance to reduction of count rate, increase of jitter and significant technology process complication. In [2] it was theoretically predicted ability to detect single photon by wide (till 100 μm) superconducting stripe in the case when the film used for detector fabrication let through the current close to depairing current (I_{dep}). In [3] was demonstrated the first SMSPD. SMSPD get opportunity to produce detectors with large work area. The goal of this work is investigation of film characteristics to produce SMSPD with saturated QE. QE saturation means 100% internal QE of devise.

2. Methods and experimental results

To choose the best film for superconducting microstripe single photon detector (SMSPD) we produced a set of NbN films with different thicknesses. We used Si substrate with an additional SiO_2 layer as λ/4 optical cavity. The films were deposited by DC reactive magnetron sputtering of Nb target in nitrogen atmosphere. The partial pressure of N_2 and the temperature of substrate were constant at all processes. We only changed the deposition time, so we got films with thicknesses h ranging from 3.5 nm to 6.4 nm. We estimated thickness value by multiplying deposition rate and time of deposition. In order to obtain superconducting transition temperature (T_c) and residual-resistance ratio ($R_{s\,300}/\,R_{s\,20}$) we measured the temperature dependences of resistance for each film (figure 1(a)). The main parameters of the films are summarized in table 1.

Table 1. Main parameters of studied films.

	h, nm	$R_{s\,300}$, Ω/□	$R_{s\,300}/R_{s\,20}$	T_c, K
2314	7.28	407	0.59	9.88
2362	6.44	614	0.68	9.15
2347	5.39	753	0.57	8.01
2316	3.5	1027	0.61	6.85

For each film we fabricated the set of 1-μm-wide and 10-μm-long straight strips. We used our standard technology based on electron beam lithography and reactive ion etching [3]. Then we measured critical current (I_c) for all strips. For each film we chose one strip with the biggest I_c and measured it's QE at 1.7K (figure 2(b)). The I_c and QE measurements technique was described in detail in [3]. In figure 2(b) there is no QE dependence for strip based on film 2316, because we did not observe photo response for this devise at all.

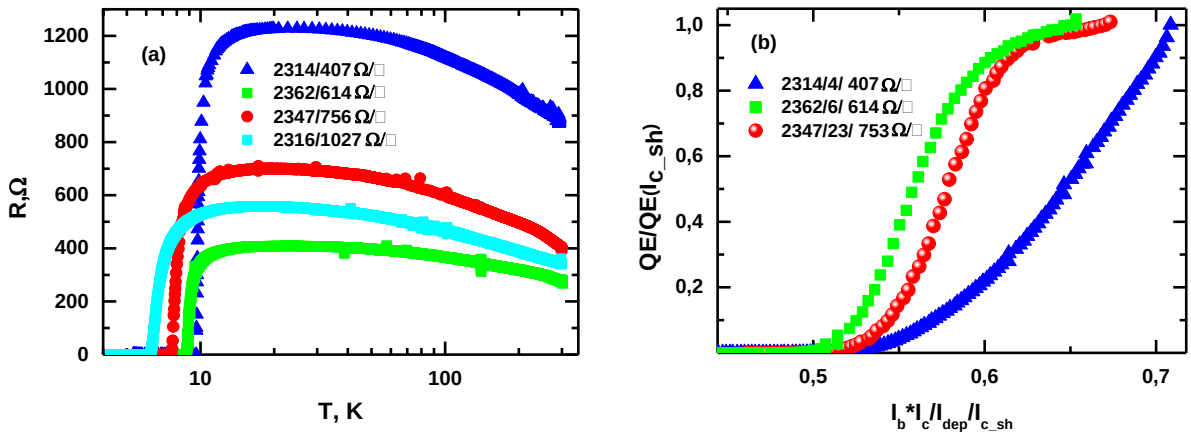

Figure 2(a, b). (a) The experimental dependence of resistance R on temperature T for NbN films; **(b)** Normalized QE as a function of relative bias current.

Having analyzed QE dependence we done following conclusions: (1) The best film is 2347 with the lowest value of $R_{s\,300}/R_{s\,20}$. This result is well agreed with [4]. (2) We did not reach QE saturation even for dives based on the best film. In our future work we will change other parameters of film deposition (concentration of N_2, temperature of substrate). (3) The worse devise have the biggest ratio I_b/I_{dep}. This fact can be explained by using one diffusion coefficient (0.4 cm^2/s) for I_{dep} calculation for all devises. In future, we will measure diffusion coefficient for each devise and recalculate I_b/I_{dep}.

This work is supported by the Russian Foundation for Basic Research grant No. 18-29-20100.

References

[1] Goltsman G, at all 2001 *Appl. Phys. Lett.* **79** 705
[2] Vodolazov D 2017 *Phys. Rev. Applied* **7** 034014
[3] Korneeva Yu, Vodolazov D, Semenov A, Florya I, Simonov N, Baeva E, Korneev A, Goltsman G, Klapwijk T 2018 *Physical Review Applied* **9(6)** 064037
[4] Smirnov K, Divochiy A, Vakhtomin Yu, Morozov P, Zolotov Ph, Antipov A, Seleznev V 2018 *UK Supercond. Sci. Technol.* **31** 035011

Study of microheater's phase modulation for on-chip Kennedy receiver

I O Venediktov[1], M S Elezov[1], A I Prokhodtsov[1,2], V V Kovalyuk[1,3], P P An[1,3], A D Golikov[1], M L Shcherbatenko[1], D V Sych[1,4,5], G N Goltsman[1,2]

[1]Department of Physics, Moscow State Pedagogical University, 119992, Russia

[2]National Research University Higher School of Economics, Moscow, 101000, Russia

[3]Zavoisky Physical Technical Institute of the Russian Academy of Sciences, 420029, Russia

[4]P.N.Lebedev Physical Institute, Russian Academy of Sciences, Moscow, 119333, Russia

[5]JCS "QRate", Skolkovo, Moscow 143025, Russia

Abstract. In this work we describe phase modulators for several Mach-Zehnder interferometers (MZI) on silicon nitride platform for telecomm wavelength (1550 nm). We obtained IV and phase-voltage curves for these modulators. These MZI are needed for Kennedy receiver, which used to distinguish coherent states of light of small intensity, which is the main purpose of the work in the future. Thermo-optical (TO) modulation is ensured by microheaters on one of the arms MZI, which give us that refractive index of the material is changing with temperature. This approach allows you to apply the necessary voltage to the gold microheaters to see the phase change. For the on-chip microheaters we demonstrate the dependence of the phase shift on the applied voltage of our on-chip microheaters.

1. Introduction

Mach-Zehnder interferometers with microheater phase modulators are main parts in the realization of Kennedy receiver, which is used to distinguish coherent states of single photons [1] or discrimination between two phase-modulated coherent states [2]. The main task of a receiver is to make some measurement of the signal and find out the actual binary signal state. The main idea of any quantum receiver is to produce some scaling of the signal to determine its ground state. Also, such receivers were demonstrated in free space and in fiber optics [3]. On-chip realization allows us to has advantages like small footprint, which leads to higher stability of device, including temperature fluctuations along the surface, and also it has shorter waveguides which leads to less phase fluctuations. As a waveguide material we used silicon nitride (Si_3N_4) platform, which combines low optical absorption in the infrared (IR) and good mechanical properties [4]. For phase modulation we used thermo-optical (TO) effect, due to dependence of refractive index on temperature. This change of refractive index leads to difference of optical paths in different arms of interferometer, which give us a phase shift between them. For operating Kennedy receiver we need from 0 to 180 degrees phase shift.

2. Device design and fabrication

We used several stages of nanophotonic fabrication processing on commercially available Si wafers with a 450 nm Si_3N_4 waveguiding and 2600 nm SiO_2 cladding layers. At the first stage, using electron-

beam (e-beam) lithography and dry etching in CHF_3 atmosphere, we fabricated waveguiding scheme, consisting of several Mach-Zehnder's interferometers and focusing grating couplers for input/output light from a chip. At the second stage, e-beam deposition of 1 µm thick SiO_2 on the top waveguide layer was made. Finally, we used laser lithography to form Ti/Au -contact pads and microheaters by standard lift-off technique in acetone. Figure 1 shows an optical image of a fabricated device. There are 5 phase modulators (PM), electrical contacts for applying voltage, optical input (port 1) and outputs (ports 2 and 3).

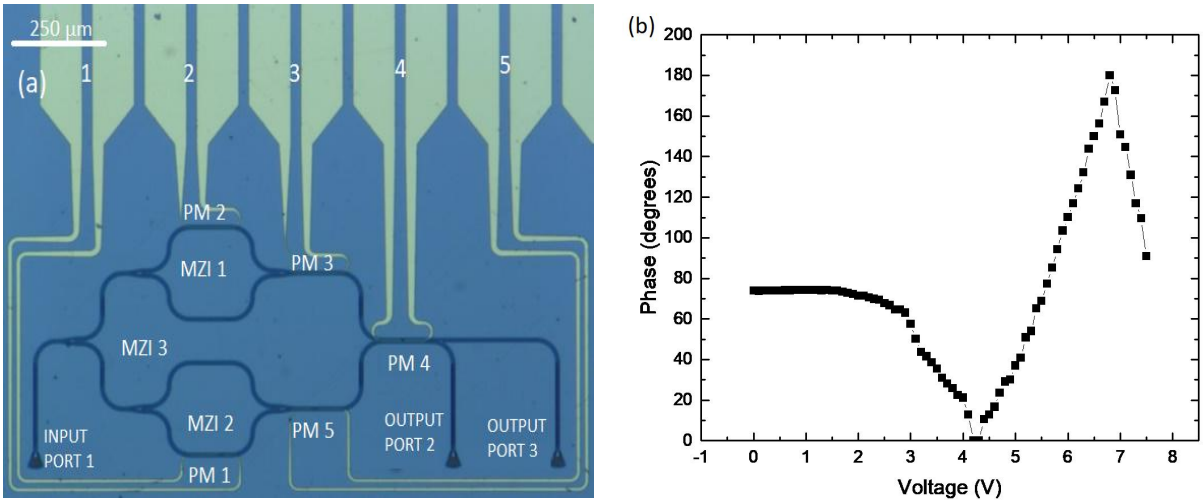

Figure 1 (a,b); (a) optical image of fabricated device, **(b)** phase-voltage dependence**;**

3. Experimental results

Using the tunable voltage source applied on the each heater separately we measure the optical transmission on the 1596 nm wavelength (from port 1 to port 2). The obtained phase-voltage dependence for one of the microheater (1) is shown in figure 1. From the graph it can be seen that maximum voltage before burnout is 8V, and that full phase shift for 180 degrees corresponds to voltage change 3V.

4. Conclusion

We fabricated on-chip Kennedy receiver scheme, consisting of several MZIs with microheaters and focusing grating couplers on silicon nitride platform. We studied phase-voltage curves, which demonstrates, that phase changes from 0 to 180 degrees, which is enough for Kennedy receiver. Our results have a great potential for fabrication on-chip Kennedy receiver.

5. Acknowledgments

We acknowledge support of the Russian Science Foundation grant No. 19-72-10156 (waveguide fabrication), grant No. 16-12-00045 (experimental study).

References

[1] R. S. Kennedy 1973 "A Near-Optimum Receiver for the Binary Coherent State Quantum Channel." *MIT Research Laboratory of Electronics Quarterly Progress Report* 108: 219-225
[2] M.L. Shcherbatenko, M.S. Elezov, D.V.Sych, G.N. Goltsman - "Sub-shot-noise-limited fiber-optic quantum receiver" 2020 Phys Rev A 101
[3] Mikhail Elezov, Mikhail Scherbatenko, Denis Sych, Gregory Goltsman - "Towards the fiber-optic Kennedy quantum receiver" 2019 EPJ Web of Conferences 220, 03011
[4] A P Ovvyan, N Gruhler, S Ferrari and W H P Pernice 2016 J. Opt. 18

Silicon nitride Mach-Zehnder interferometer for on-chip quantum random number generation

A Prokhodtsov[1,2], V Kovalyuk[2,3], P An[2,3], A Golikov[2,4], R Shakhovoy[5,6], V Sharoglazova[5,6], A Udaltsov[5,6], Y Kurochkin[5,6,7], G Goltsman[1,2,3]

[1]National Research University Higher School of Economics, Moscow 101000, Russia
[2]Department of Physics, Moscow State Pedagogical University, 119992, Russia
[3]Zavoisky Physical-Technical Institute of the Russian Academy of Sciences, 420029, Russia
[4]Moscow Institute of Physics and Technology (State University), 141700, Russia
[5]Russian Quantum Center, 45 Skolkovskoye shosse, Moscow, Russia
[6]QRate, 100 Novaya str., Skolkovo, Russia
[7]NTI Center for Quantum Communications, National University of Science and Technology MISiS, 4 Leninsky prospekt, Moscow, Russia

Abstract. In this work, we experimentally studied silicon nitride Mach-Zehnder interferometer (MZI) with two directional couplers and 400 ps optical delay line for telecom wavelength 1550 nm. We achieved the extinction ratio in a range of 0.76-13.86 dB and system coupling losses of 28-44 dB, depending on the parameters of directional couplers. The developed interferometer is promising for the use in a compact random number generator for the needs of fully integrated quantum cryptography system, where compact design as well as high generation speed are needed.

1. Introduction

Quantum random number generator (QRNG) is an essential ingredient for quantum key distribution (QKD) systems. There have been demonstrated a number of optical QRNGs based on various quantum effects, including phase fluctuation in a laser diode [1,2], photon-pair interference [3], spontaneous Raman scattering [4]. Among all of these schemes, the QRNGs based on laser phase fluctuations could provide the highest generation rates, up 68 Gbps. To date, most of the QRNGs were implemented in free space or using optical fiber and suffer from limitations due to their size and stability, which strongly limits their practical use. To reduce physical dimensions, such generators have been demonstrated on various substrates like silicon-on-insulator (SOI) [5], indium phosphide (InP) [6], lithium niobate (LN) [7]. Different platforms have pros and cons, for example LN provides increased generation speed but the relatively large waveguide of LN can limit the dimensions of the on-chip integration, SOI suffers from the two-photon absorption, while InP suffers from large optical losses. Here we used silicon nitride (Si_3N_4) platform which combines low optical absorption in the infrared (IR) and good mechanical properties [8] for the fabrication and study of the main element of QRNG is Mach-Zehnder interferometer (MZI) with delay line in one of the arm.

2. Device design and fabrication

In order to fabricate an MZI interferometer with a delay line of 400 ps in one of the arms, the delay lines were studied separately [9]. For a half etched rib waveguide cross section of 0.45×1μm we founded the group index of n_g = 2.037 @ λ = 1.55 μm, which corresponds of 5.8635 cm long delay line [10]. The commercially available wafers on a silicon (Si) substrate with a thickness of 450 μm had 2.6 μm silicon buried oxide (SiO_2) and 450 nm silicon nitride (Si_3N_4) layer atop. For fabrication process, we use one step of e-beam lithography and dry reactive-ion-etching (RIE) in CHF_3-Ar mixture. Figure 1(a) shows an optical micro-photo of a MZI with spiral delay line two focusing grating couplers for input/output light, two directional couplers with equal parameters (interaction length and gap) and one short arm.

3. Experimental setup and results

For MZI experimental study with two different parameters of directional couplers we characterize the transmission of MZI in the wavelength range of 1510-1620 nm. The transmitted power was measured by a low-noise photodetector and recorded by Ni-DAQ system. Figure 1(b) shows the measured MZI

transmission spectra for the one of the fabricated device with directional couplers parameters equal to gap = 1.65 μm, interactional length =110 μm. ER was calculated as the ratio of the maximum (T_{max}) to the minimum (T_{min}) of optical transmittance (Fig.1c).

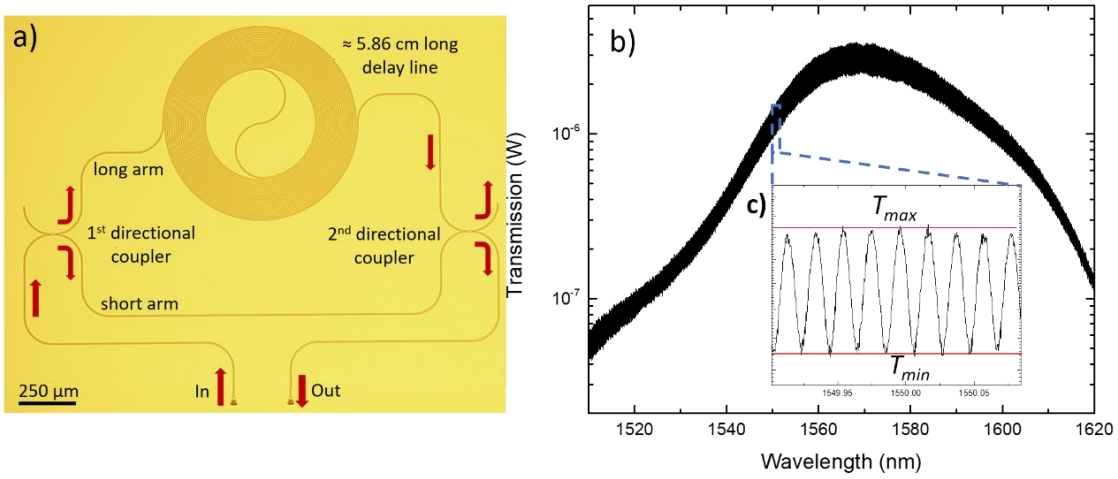

Figure 1. (a-c). (a) Optical micrograph of the MZI with spiral delay line; **(b)** The measured transmission spectra of MZI together with focusing grating couplers; **(c)** Enlarged transmission spectrum of MZI.

Our numerical estimation and preliminary experimental results show that for the efficient operation of the QRNG it is necessary to have input/output losses < 33 dB, and ER > 3 dB. For several of the fabricated devices, experimentally obtained losses are equal to ≈ 30 dB, as well as ER ≈ 3.14 simultaneously, that make it possible to use its for further measurement as a QRNG and promising application of quantum communication technologies.

4. Conclusion

We fabricated silicon nitride on-chip MZI with two directional couplers and spiral delay line integrated in one of the arm. We the system losses ≈ 30dB and extinction ratio ≈ 3.14 dB as well. Further work will be devoted to testing this MZI and laser diode for generating random numbers, as well as improving the coupling efficiency.

5. Acknowledgments

We acknowledge support of the Russian Science Foundation grant No. 19-72-10156 (waveguide fabrication), grant No. 16-12-00045 (experimental study), as well as grant No. 17-71-20146 (theoretical and numerical calculations).

References

[1] Nie Y-Q, Huang L, Liu Y, Payne F, Zhang J, and Pan J-W 2015, *Rev. Sci. Instrum* **86**
[2] Shakhovoy R, Sych D, Sharoglazova V, Udaltsov A, Fedorov A, and Kurochkin Y 2020 *Optics Express* **28** 6209
[3] Rarity J G, Owens P C M, and Tapster P R, 1994 *J. Mod. Opt* **41**, 2435
[4] Collins, M. J., Clark, A. S., Xiong, C., Mägi, E., Steel, M. J., and Eggleton, B. J. 2015 *Applied Physics Letters* **107**, 141112
[5] Raffaelli F, Sibson P, J E Kennard, Mahler D H, Thompson M G and Matthews J C F 2018 *Optics Express* **26** 328578
[6] Abellan C, Amaya W, Domenech D, noz P M, Campany J, Longhi S, Mitchell M W and Pruneri V 2016 *Optica* **3** 989
[7] Haylock B, Peace D, Lenzini F, Weedbrook C and Lobino M *Quantum* 2019 **3** 141
[8] Ramelow S, Farsi A, Clemmen S, Orquiza D, Luke K, Lipson M, and Gaeta A L 2015 ArXiv:1508.04358v1
[9] Prokhodtsov A, An P, Kovalyuk V, Zubkova E, Golikov A, Korneev A, Ferrari S, Pernice W, Goltsman G 2018 *Journal of Physics: Conf. Series* **1124** 051052
[10] Bakhvalova T., Belkin M E, Kovalyuk V V, Prokhodtcov A I, Goltsman G N, Sigov A S, 2019 *IEEE Xplore* 745-751

Intercept-resend attack on passive side channel of the light source in BB84 decoy-state protocol

D Babukhin[1,2,3]**, D Sych**[3,4,5]
[1]Dukhov Research Institute of Automatics (VNIIA), Moscow 127055, Russia
[2]Russian Quantum Center (RQC), Moscow 143026, Russia
[3]QRate LLC, Moscow 121353, Russia
[4]Moscow State Pedagogical University, Moscow 119992, Russia
[5]P.N. Lebedev Physical Institute, Moscow 119991, Russia

Abstract. Quantum key distribution (QKD) promises unconditionally secure communication based on fundamental laws of physics, though practical realizations of QKD may have loopholes and side channels, thus their security can be compromised. We analyze the intercept-resend attack on the BB84 decoy-state protocol under the presence of a passive side channel of the light source. We derive an upper bound for the secret key rate and show that it does not significantly deviate from the ideal side-channel-free case.

1. Introduction

Among the emerging quantum technologies, QKD is the most developed branch up to date. The security of QKD is based on the fundamental laws of quantum physics and the constraints imposed on the ability of an eavesdropper to obtain the exact copy of a quantum signal. The problem with the QKD security appears when the eavesdropper attacks the real-world QKD implementations. In practice, all devices differ from their ideal models. For example, quantum communication signals emitted by different lasers may have slightly different spectral, temporal, or spatial modes. These differences, called passive side channels of the light source, allow the adversary to obtain additional information about the quantum signals. The question of how to estimate and properly account for side channels is an active research subject [1]. Since the original proof of unconditional security of the BB84 protocol for ideal devices [2], there were a number of works on the QKD security with imperfect devices [3-5].

In this work, we take into account the overall photonic mode mismatch as a side channel, estimated via the Hong-Ou-Mandel (HOM) interference [1], and show an explicit intercept-resend attack on the BB84 decoy state protocol which makes use of this side channel. The obtained secret key rate serves as an upper bound on the possible secret key rate in the presence of passive side channel of the light source for an arbitrary attack.

2. Methods

We use auxiliary degrees of freedom of phase-randomized weak coherent states of light, employed as signal states in BB84 decoy-state protocol, as a model of the passive side channel. The degree of distinguishability of quantum states is estimated from the HOM interference visibility. We numerically calculate secret key rate under the intercept-resend attack on the BB84 protocol for different values of the HOM interference visibility

3. Results and discussion

The calculated secret key rate for several values of HOM interference visibility (0.2,0.3,0.4,0.5) is shown in Fig. 1. We note that the modern laser sources used in QKD typically have HOM interference visibility values above 0.45. Thus we can say that there is almost no influence of realistic laser source imperfections on the upper bound of the secret key rate. The study of tighter bounds on the secret key rate requires analysis of more advanced eavesdropping strategies, which is currently in progress.

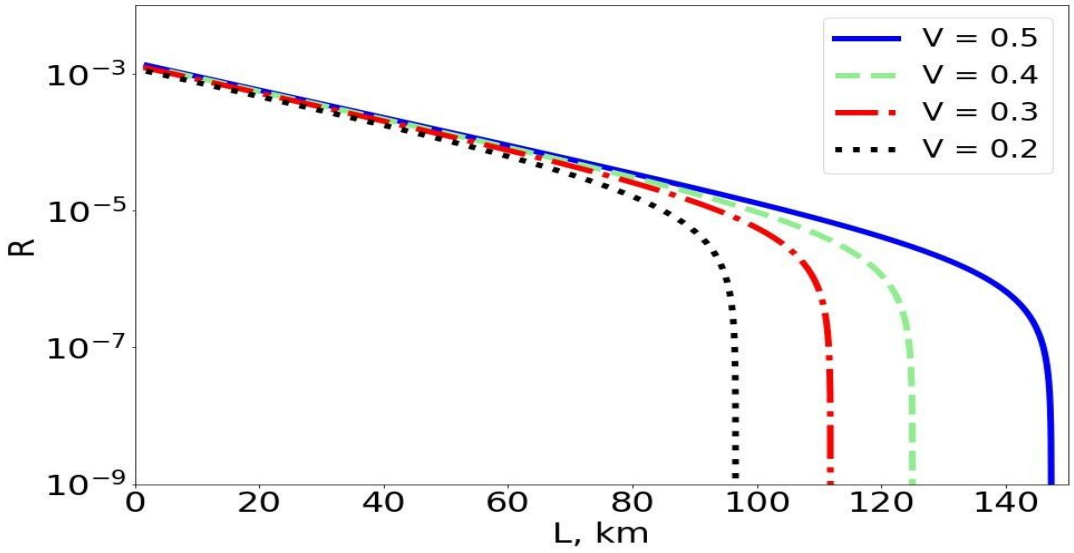

Figure 1. Secret key rate R as a function of fiber-optic communication distance L for different values of Hong-Ou-Mandel interference visibility V, under the intercept-resend attack on the BB84 decoy-state protocol. We assume the standard single-mode optical fiber loss of 0.2 dB/km.

References

[1] A. Duplinskiy, D.V. Sych arXiv:1908.04703
[2] P.W. Shor and J. Preskill 2000 Phys. Rev. Lett. **85** 2
[3] D. Gottesman, H.-K. Lo, N. Lutkenhaus, J. Preskill 2004 Quant.Inf.Comput. 5 325-360
[4] M. Koashi, J. Preskill 2003 Phys.Rev.Lett. 90 057902
[5] M Koashi 2009 New J. Phys. **11** 045018

Features of the construction of fiber-optic communication lines with code division multiplexing

N I Popovskiy[1], V V Davydov[2, 3], V Yu Rud[3]

[1]The Bonch-Bruevich Saint-Petersburg State University of Telecommunication, Saint Petersburg 193232, Russia
[2]Peter the Great Saint Petersburg Polytechnic University, Saint Petersburg 195251, Russia
[3]All-Russian Research Institute of Phytopathology, Moscow Region 143050, Russia

Abstract. The necessity of studying fiber-optic communication lines with code division multiplexing. Structural diagrams of transmitters and signal receivers of fiber-optic communication lines with code division multiplexing. The features of their construction are established. Research results are presented.

1. Introduction

To meet the growing demand for high-speed communications in optical networks, it is necessary to use multiple access methods that allow multiple users to share the common bandwidth of the optical fiber. There are three main methods of multiple access: the user is allocated a specific time interval in time division multiple access (TDMA) or a specific frequency (wavelength) slot in a wavelength division multiple access (WDMA) system. Both methods have been widely studied and are currently used in optical communication systems. An alternative method is optical code division multiple access (OCDMA), which is currently gaining ground as it improves information security, simplifies network management, improves spectral efficiency, and increases flexibility in bandwidth allocation [1]. On the other hand, when using this method when constructing the fiber optic design, a number of features arise that must be taken into account when transmitting information in communication channels.

2. The method of phase difference influence estimates between channels at peleng accuracy

The method with code division multiplexing has a number of features that will affect the design of the fiber optic link. Therefore, in our work it is necessary to consider some of them. In OCDMA, different users share a common communication environment in which signals from different transmitters can overlap in both time and frequency. Multiple access is achieved by assigning different code sequences to different transmitters, which are subsequently detected at the receiver in the presence of multiple interference from other users [1, 2].

Statistical distribution of network bandwidth: any particular OCDMA receiver perceives other users' signals as noise. This means that you can continue to add channels as long as the signal-to-noise ratio (SNR) remains low enough and the number of bit errors remains at a constant level. So many active connections can be allocated per connection so that the total data traffic remains below the channel bandwidth [1]. For example, if several hundred voice channels are transmitted using OCDMA, and average power is the channel limit, then many more voice connections can be controlled than using TDMA or WDMA methods.

In OCDMA, there is another feature associated with a high frequency optical carrier. For this reason, at a high data transfer rate, for example, of several Gbit/s per user, the limit of electronic information processing can be reached [2].

The structure of a coherent homodyne transmitting module with an external Mach – Zehnder optical modulator is shown in Fig. 1. The input data is first encoded by a BPSK modulator to generate in-phase and quadratic phases, and then the generated electrical signal is fed to the optical modulator drive. Finally, several CDMA standard light streams encoded using a group of code sequences and multiplexed through couplers are transmitted to the optical network [1].

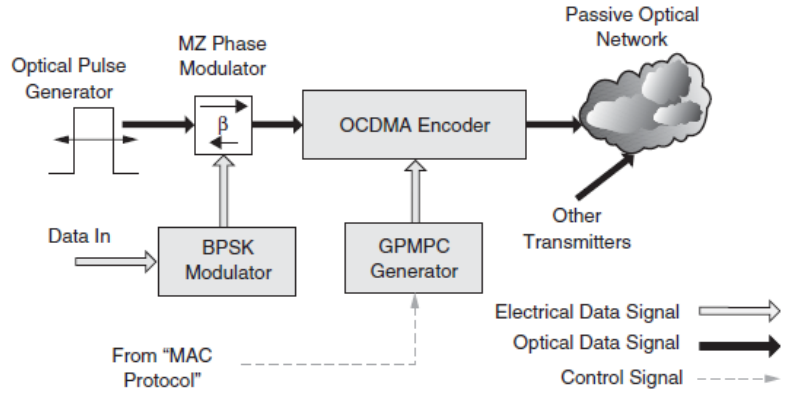

Figure 1. Structure of the transmission module for a fiber- optic communication line.

A local oscillator is installed on the optical receiving module (Fig. 2), which is modulated using a pre-reserved code sequence. As a result, the generated signal is mixed and correlated with the received OCDMA signal. Coherently mixed optical signals are coupled to a two balanced detector, whose electrical output stores phase information. The generated bipolar electrical signal is integrated through a bit interval and the result is compared with a reference to form the final bit estimate [2].

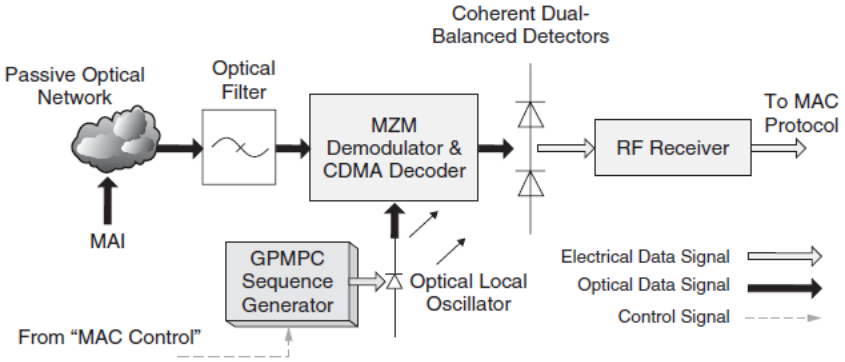

Figure 2. Structure of an optical receiving module for a fiber- optic communication line.

Such a construction of channels makes it possible to reduce the influence of interference noise, the intensity of which increases with increasing number of channels, on optical signals that carry information.

3. Conclusion

The obtained experimental results showed that the most appropriate direction of research for solving this problem is the development of new orthogonal optical code sequences. Their use will reduce the influence of interference interference arising from the transmission of signals at the time of separation between different users.

References

[1] Shiraz H G and Karbassian M M 2012 *Optical CDMA Networks Principles, Analysis and Applications* (Chichester: John Wiley & Sons Ltd.)
[2] Kitayama K I 2014 *Optical code division multiple access: a practical perspective* (New York: Cambridge University Press)

Formation of silver nanoparticles in ion-exchanged glass with nanosecond laser irradiation

O Morozova[1], E Babich[1], V Kaasik[1], A Raskhodchikov[2], D Raskhodchikov[2], V Zhurikhina[1,2], A Lipovskii[1,2]

[1] Institute of Physics, Nanotechnology and Telecommunications, Peter the Great St. Petersburg Polytechnic University, St. Petersburg 195251, Russia

[2] Department of Physics and Technology of Nanostructures, Alferov University, St. Petersburg 194021, Russia

Abstract. Irradiated a soda lime glass slides subjected to silver-to-sodium ion exchange by 6 nanoseconds pulsed laser at the wavelengths of 1064, 532 and 355 nm. Both pulses intensity and frequency were varied. Microscopic images, surface profiles and extinction spectra of the irradiated glass regions after the laser exposition and after 15, 45 and 90 s reactive ion etching were studied. Independently on the wavelength, the exposition resulted in the formation of silver nanoparticles demonstrating localized surface plasmon resonance, which gradually disappeared with the etching of the samples. The spectral position and amplitude of the resonance, size of the nanoparticles-containing region and depths of etching of differently irradiated regions were compared.

1. Introduction

Studies of glasses embedded with silver nanoparticles (SN) and containing the nanoparticles on their surface are being carried out during last decades. The reason of this interest is the possibility to use SN in multiple applications: as nucleation agent in glass ceramics formation, as Raman scattering and luminescence enhancing agents, as elements of optical polarizers and masks, in nonlinear optics, etc. In all cases, silver should be either introduced in the glasses or deposited onto their surface. Except the synthesis of silver-contacting glasses, a powerful tool to dope glasses with silver is their ion exchange processing resulting in the replacement of sodium or other alkaline ions from the glass composition by silver ions from the melt of a silver-containing salt. These ions can be reduced to metal silver forming nanoparticles in the bulk and on the surface of the ion-exchanged glasses via the phase decomposition of the silver-glass solid solution. The reduction can be induced either by a reducing agent, like hydrogen penetrating in the glasses, or by ions of variable valence, which can be introduced in glasses in their synthesis. Another approach to SN formation is the irradiation of silver-containing glasses with powerful lasers [1]. Besides, except arising and growth of SN [1], their laser modification [2], dissolution [3] and structuring of glasses with formed SN [4] were reported. In the present study, we have compared the effect of different expositions of a silver-doped glass by the fundamental, the second and the third harmonic of a neodymium nanosecond laser radiation on the formation of SN, surface relief of the irradiated glass regions and reactive ion etching (RIE) of these regions.

2. Experiments

We used a soda-lime glass containing 14.3 wt.% of sodium oxide. 1 mm thick glass slides were ion-exchanged in the melt of $Ag_{0.05}Na_{0.95}NO_3$ at 325 ^{o}C for 20 min. This resulted in the enrichment of the

glass with silver ions, maximal depth of their penetration (zero concentration level) being ~8 μm. Maximal silver oxide concentration at the glass surface was ~10.5 wt.%. The ion-exchanged glass samples were irradiated with a Nd:YAG laser providing 6 ns pulses with the maximal energy of 14 mJ at 1064 nm wavelength. Doubler and tripler of the radiation frequency provided pulses at 532 and 355 nm with the maximal energies of 3.6 and 1.4 mJ, respectively. The radiation was focused on the sample surface: at 1064 and 532 nm to the spots of 130 and 70 μm in diameter, respectively, and at 355 nm to the 2 μm spot. Using a computer-driven platform, we moved the samples perpendicularly to the laser beam at a speed of 200 μm/s to draw "lines" on their surface using different wavelength, pulse energies and frequencies. Besides, some overlapping of the spots of the glass surface was provided. We characterized local optical extinction of the irradiated glass regions using a spectrometer equipped with 50 μm optical fiber and 5x/0.13 objective. RIE of the samples was performed in Plassys mu400 station using 10Ar:20CF_4 gas composition at 6mTorr during 15, 45 and 90 s. Surface profiles of the laser-modified regions before and after RIE were characterized with 2-μm stylus profilometer.

3. Results and discussion

The results are illustrated with Fig. 1. Fig. 1a shows the temporal behavior of the maxima of extinction spectra of the regions irradiated at different wavelength in RIE and the extinction spectrum after 1064 nm irradiation. Fig. 1b presents the surface profiles of these regions subjected to RIE for 90 s.

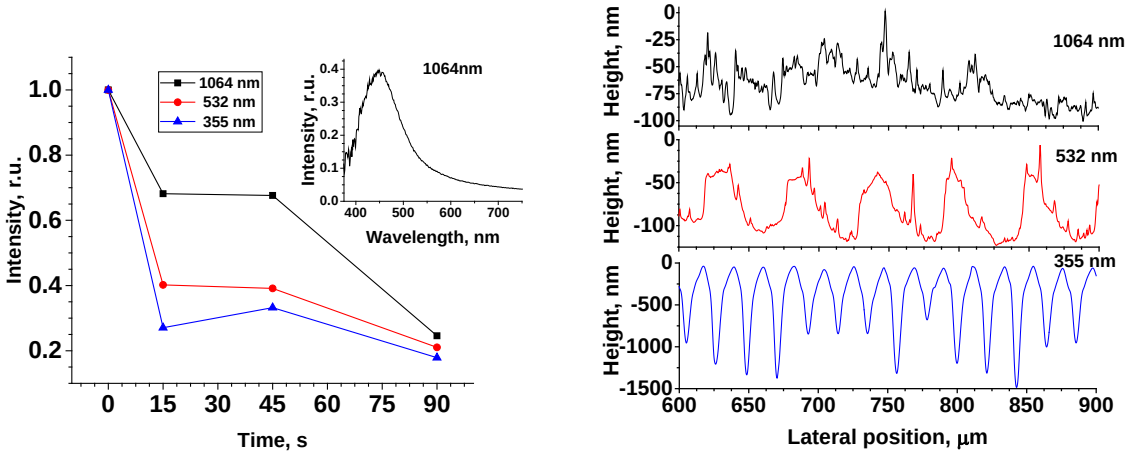

Figure 1. (a) Temporal behavior of the maxima of extinction spectra of the irradiated regions. Inset: the spectrum after 1064 nm irradiation **(b)** Surface profiles of the irradiated regions after 90 s RIE.

Presented results allow us concluding that the irradiation at all wavelength results in the formation of silver nanoparticles, which are similarly distributed within ~100 nm subsurface layer of the glass for all used wavelength. Importantly, the modification of the glass with 355 nm wavelength pulses essentially fastens RIE, which could be due to switching of non-bridging oxygen bonds to bridging ones [5].

4. Acknowledgments

The study was supported by the Ministry of Science and Higher Education of Russian Federation, project FSRM-2020-001.

References

[1] Wackerow S, Abdolvand A 2014 *Opt. Expr.* **22** (5076
[2] Tyrk M A, Gillespie W A, Seifert G, Abdolvand A 2013 *Opt. Expr.* **21** 21823
[3] Lipovskii A A, Melehin V G, Petrov M I, Svirko Yu P, Zhurikhina V V 2011 *Appl. Phys. Rev.* **109** 011101
[4] Antonov I, Bass F, Kaganovskii Yu, Rosenbluh M, Lipovskii A 2003 *J. Appl. Phys.* **93** 2343
[5] Leech P, Reeves G K 1999 *Proc. SPIE* **3680** 839

The optical properties study of the Sn-doped ZnO thin films grown on glass substrate

M G Volkova[1], V Yu Storozhenko[1], V V Petrov[2], E M Bayan[1]
[1]Department of Chemistry, Southern Federal University, Rostov-on-Don, 344090, Russia,
[2]Research and Education and Centre "Microsystem technics and multisensor monitoring systems", Southern Federal University, Taganrog, 347922, Russia

Abstract. The optical properties of synthesized zinc oxide films doped with tin in different concentrations (0-5 mol.%) were studied. X-ray diffraction revealed that the main phase of the obtained films is ZnO (wurzite). According to SEM data, the film consists of nanocrystallites, which are 10-20 nm in size. It was shown that the introduction of 0.5 mol.% tin ions leads to an increasing in the absorption of wavelengths (in the range of 300-370 nm) and a slight narrowing of the band gap.

1. Introduction

Multifunctional thin film materials based on metal oxides have unique optical, electrical, gas-sensitive properties and have great opportunities for application. One of the widely used semiconductor materials is zinc oxide (ZnO) due to its unique physical and chemical properties, cheapness and ease of production. Nanoscale ZnO films possess transparency in the visible range and good optical properties, have low resistance, and are highly sensitive to different toxic gases, such as ammonia, hydrogen sulfide, and organic compounds [1, 2]. To improve the materials properties, doping with different atoms and ions is used. For example, doping of ZnO with fluorine ions leads to decreasing of the band gap; when the concentration of modifying agents is equal to 6%, materials showed a minimum resistance and maximum carrier concentration [3]. When zinc oxide is doped with tin, the temperature dependence of resistance changes in comparison with pure ZnO [4]. The introduction of aluminum and tin ions into the ZnO structure also led to changes in the material properties: the films transparency increased from 65% to 81%, and the electrical conductivity of the samples reached 0.335 $(\Omega.cm)^{-1}$, the band gap increased to 3.3 eV [5]. In this paper, the optical properties of synthesized zinc oxide films doped with tin ions in different concentrations are studied.

2. Experiment

As precursors, $SnCl_4 \cdot 5H_2O$, $Zn(CH_3COO)_2 \cdot 2H_2O$ and organic acid were used. The molar ratios of zinc and tin were 0:100, 0,5:99,5, 1:99 and 5: 95 for materials 1, 2, 3, and 4, respectively. Synthesis was carried out through the formation stage of organic Zn^{2+} and Sn^{4+} salts, which were dissolved in an organic solvent. The solution was applied to pre-prepared glass substrates and dried at room temperature. In this way 3 layers of the precursor solution were applied. Then the materials were heat-treated at 500 ^{o}C for 1 h. The obtained samples were studied using the X-ray powder diffraction analysis (powder diffractometer Thermo ARL) in CuKα radiation, electron microscopy (SEM, EMXplus 10/12 Bruker). Optical properties were studied using optical absorption spectra obtained on the Varian Cary-100 spectrophotometer in the wavelength range of 300 – 1100 nm.

3. Results and discussion

The main phase of obtained films is the typical wurzite crystal structure for zinc oxide that was confirmed with X-ray diffraction analysis. According to SEM data, the film consists of nanocrystallites, which are 10-20 nm in size. The average thickness of three-layer films is 180-200 nm. Analysis of optical absorption spectra (Fig. 1) showed that the maximum absorption coefficient in the wavelength range up to 370 nm is observed for films obtained in the Sn:Zn ratio equal to 0.5:99.5 and the minimum for films with the Sn:Zn ratio equal to 5:95. Above 380 nm, the absorption coefficient for all synthesized materials was close to zero. The band gap (E_g) estimation of the Sn-doped ZnO films was performed based on the material's absorption edge analysis [6] and showed that for materials 1-4 it was 3.31; 3.28; 3.30 and 3.31 eV, respectively. The obtained values of E_g are close to the band gap of crystalline ZnO, equal to 3.37 eV.

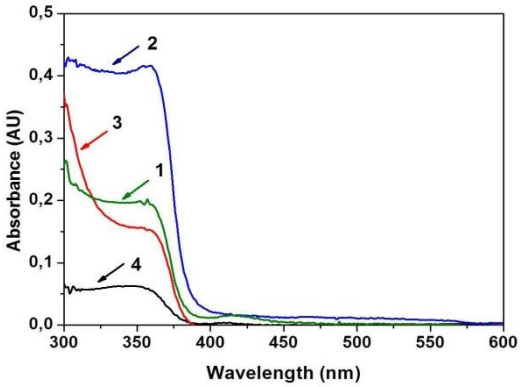

Figure 1. Optical absorption spectra of materials 1-4 (explanations are presented in the text).

The decreasing of the obtained films band gap in comparison with their single crystals is a consequence of their nanoscale structure and tin doping. On the one hand, the presence of nanocrystallites leads to a significant increasing in the material's surface area, which has a high defect. On the other hand, it leads to the "blurring" effect of the band gap border. It is also seen that the tin introduction into the ZnO structure with a concentration of 0.5 % leads to a certain narrowing of the band gap from 3.31 to 3.28 eV.

4. Conclusion

Based on the obtained results, it is possible to create transparent nanostructured films with controlled optical properties, which are of great interest for solving various problems of modern optoelectronics and photovoltaic energy.

5. Acknowledgments

This work was financially supported by the RFBR, project 20-07-00653 A. The authors are grateful to the Molecular Spectroscopy Center of Southern Federal University for the registration of spectra.

References

[1] Znaidi L 2010 *Mater. Sci. Eng. B* **174** 18
[2] Petrov V V, Abdullin Kh A, Starnikova A P, Varzarev Yu N 2019 *J. of Physics: Conf. Series*. **1410(1)** 012006
[3] Hurma T, Caglar M 2020 *J. Mater. Sci. Semicond. Process.* **110** 104949
[4] Petrov V V, Varzarev Y N, Bayan E M, Storozhenko V Yu, Rozhko A A 2019 *Proceedings of the 2019 IEEE International Conference on Electrical Engineering and Photonics* **8906834** 242
[5] Salim K, Medles M, Nakrela A, Miloua R, Bouzidi A, Desfeux R 2020 *Optik* 164504
[6] Shalimova K V 1976 *Physics of Semiconductors* (Moscow: Energia)

Near-infrared photoluminescence and micro-Raman study of spark discharge germanium nanoparticles

D Malo[1,2], A A Lizunova[1], A A Ramanenka[3], B I Masnaviev[1], V R Solovey[1], V V Ivanov[1]

[1]Phystech School of Electronics, Photonics and Molecular Physics, Moscow Institute of Physics and Technology, Dolgoprudny, 141701, Russia

[2]Biomedical Engineering Department, Faculty of Mechanical and Electrical Engineering, Damascus University, Damascus, Syria

[3]B.I. Stepanov Institute of Physics NASB, 220072 Minsk, Belarus

Abstract. We report the investigation of near-infrared (NIR) photoluminescent and structural properties of aerosol germanium nanoparticles, synthesized by spark discharge method followed by sintering in a tube furnace at different temperatures varying from 25 to 775 °C. We demonstrate a growth of mean primary particle size from 7 to 51 nm and change in crystal structure from agglomerates of germanium nanocrystals in amorphous matrix to individual pure crystal germanium nanoparticles with temperature increase. Pure germanium nanoparticles are prepared at temperatures above 600 °C and distinguished by absence of near-infrared photoluminescence. However, according to Raman spectroscopy the presence of amorphous germanium in the samples, sintering at 25 to 475 °C, leads to the luminescence intensity increase from 1100 to 1550 nm.

1. Introduction

Germanium nanoparticles (NPs) continue to be a subject of interest for achieving enhanced properties of light emitters in various quantum technologies especially for biomedical applications and optoelectronic devices due to its unique photoluminescent properties, in particular, the possibility of emission in wide range, from UV through the visible to the near-infrared (~ 1.7 mkm) [1]. The aim of our work is to study the size, structural properties and NIR luminescence of aerosol Ge NPs produced in a gas discharge.

2. Materials and Methods

Ge nanoparticles were synthesized using the aerosol spark discharge generator [2], which was supplemented by a tube furnace for NPs sintering at different temperatures directly in gas flow. Five samples were produced at various temperatures: 25, 325, 475, 625 and 775 °C. Cylindrical n-type germanium was used as electrodes for electrical erosion. Spark processing was performed in argon gas of 99,9999 purity, the pressure was maintained at 1.5 bar. The frequency of the discharges and the capacitor voltage were 370 Hz and 1,5 kV, respectively. Aerosol NPs were collected on a cellulose filter and TEM copper grids with carbon film directly in the setup chamber.

Fluorescence measurements in the IR region were performed on the Fluorolog-3 spectrofluorometer (Horiba Scientific) with laser excitation at 532 nm. Micro-Raman spectroscopy studies was carried out

with a LabRAM HR Evolution (Horiba Scientific) using the 532 nm excitation wavelength of the He-Ne laser (0.1mW). The particle size properties and crystal structure of the samples were analyzed with the aid of transmission electron microscopy (TEM) Jeol JEM 2100 (200 kV).

3. Results and Discussion

According to the analysis of TEM images, the mean size of primary nanoparticles increased with raising of sintering temperature from 6.8 ± 5.2 for 25 °C sample to 51.3 ± 31.8 nm for 775 °C, the width of the particle distribution by size and the proportion of large particles also increased. The particles sintered at temperatures from 25 to 475 °C formed agglomerates, at 775 °C individual Ge particles were observed.

Raman spectra of germanium nanoparticles synthesized at different temperatures (Figure 1a) shows that for 25, 325, 475 °C samples there were two peaks at ~ (275 – 280) cm^{-1} and 298 cm^{-1}, while for 625, 775 °C samples was detected one peak at 298 cm^{-1}. Figure 1b shows absence of near-IR luminescence for Ge NP, sintered at 625, 775 °C, while for 25, 325, 475 °C samples photoluminescence intensity increased from 1100 to 1550 nm.

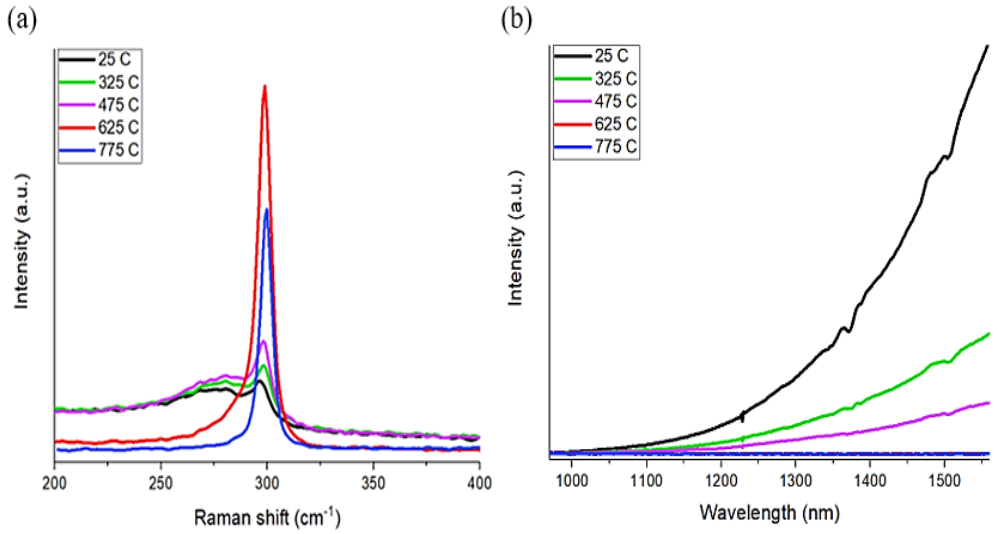

Figure 1(a, b). (a) Raman spectra; **(b)** Near-IR luminescence of Ge NPs, sintered at various temperatures.

The Raman peak at 298 cm^{-1} refers to a crystalline germanium with a cubic lattice characteristic of bulk germanium. The presence of a wide peak with a maximum of about 275 cm^{-1} is associated with the presence of amorphous germanium in samples synthesized at low temperatures from 25 to 475 °C.

By comparing the data of Raman spectroscopy and NIR luminescence, it can be assumed that luminescence occurs either in amorphous Ge or on the interface of the crystal – amorphous germanium.

4. Acknowledgments

This work was financially supported by Russian Science Foundation (project No. 19-79-00337).

References

[1] Vaughn D D, Schaak R E 2013 *Chem. Soc. Rev.* **42** 2861

[2] Ivanov V V, Efimov A A, Mylnikov D A, Lizunova A A, Bagazeev A V, Beketov I V, Shcherbinin S V 2016 *Tech. Phys. Lett.* **42** 876

Study of silicon nitride O-ring resonator for gas-sensing applications

A Elmanova[1], P An[1,2,3], V Kovalyuk[1,2,3], A Golikov[1,2,3], G Goltsman[1,2,3]
[1]Department of Physics, Moscow State Pedagogical University, 119992, Russia
[2]National Research University Higher School of Economics, Moscow 101000, Russia
[3]Zavoisky Physical-Technical Institute of the Russian Academy of Sciences, 420029, Russia

Abstract. In this work we experimentally studied the influence of different gases on silicon nitride O-ring resonator transmission. We compared the obtained results with a numerical calculations and theoretical analysis. We found a good agreement between the theoretical experimental data. Our results have a great potential for gas sensing applications where compact footprint and high efficiency are desired simultaneously.

1. Introduction

Photonic integrated circuits (PICs) are a very powerful platform for miniaturized and precision sensors. For example, PICs can be used for defining properties of different gases [1], chemical and biological materials [2] etc. For the gas sensing different integrated photonic devices and circuits can be used. In this paper we had studied silicon nitride optical ring resonator (ORR) as a gas sensing device in helium, propane and air atmosphere.

2. Theoretical and numerical study

The principle work of the ORR is close to the Fabry-Perot resonator cavity operation. On the transmission spectrum, we can determine picks, the location of which directly depends on the refractive index of the ring's waveguide material and its environment. Thus, changing the environment of the ring, we thereby change the group refractive index, which, in turn, leads to changes positions of the resonant peaks in the transmission spectrum. To describe the transmission spectrum and to calculate the optimal sizes of ORRs, we used both theoretical calculation and numerical simulation. For ORR the main parameter is free spectrum range (FSR) and peaks' positions λ_{res} can be found by well-known equations according to [3]. Another approach is to use numerical methods and compute the resonance curves using modelling in COMSOL Multiphysics**.** We used a standard ring resonator 2D model with real device parameters. In the first step, we have defined an effective refractive index by modeling the cross-section of the substrate with a half-etched silicon nitride waveguide. Then, we calculated the transmission spectrum of the chip with various ring's gas claddings. All calculated data are in good agreement with experimental results, which shows the validity of the use of the 2D model for our research.

3. Device design and fabrication

For device fabrication we used commercially available silicon substrates with SiO_2=2.6 μm and Si_3N_4=450 nm layers atop. From the one step of e-beam lithography (Crestec, CABL-9500C) followed half etched with reactive ion etching (RIE) in CHF_3 atmosphere for device finalizing. In Figure 1b one of the fabricated O-ring resonator is shown. The device consists of two focusing grating couplers (FGCs)

for input/output light, connected by a 1 μm waveguide bus, separated from the O-ring waveguide of 1.6 μm width by a gap of 1.4 μm.

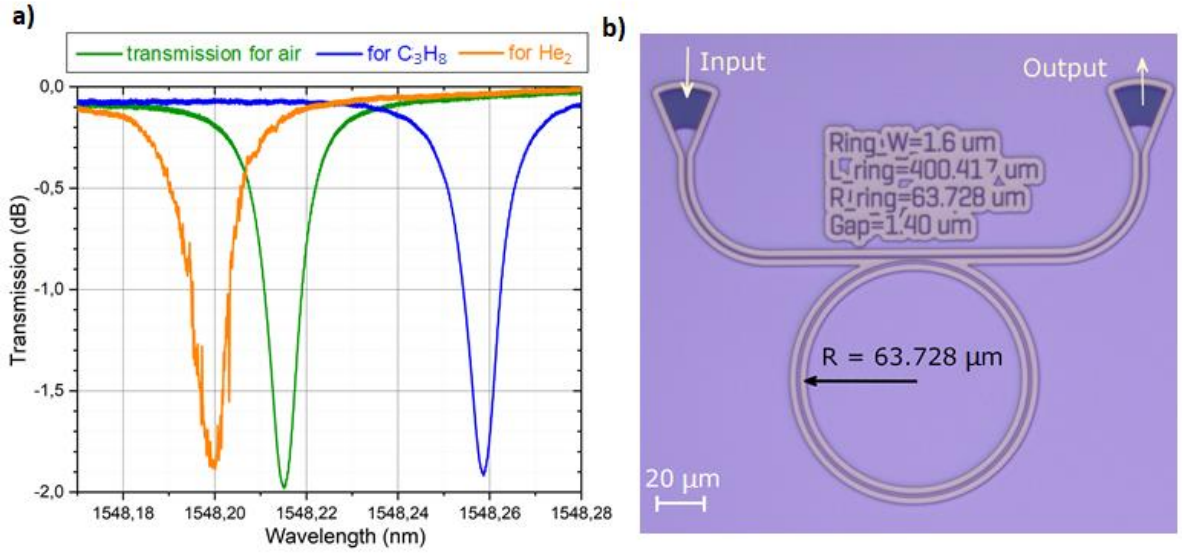

Figure 1. (a) Experimental ORR transmission spectra data for three gaseous: helium, air, and propane. It can be seen from the plot that the position of the maximum shifts with the change of the gas refractive index. **(b)** Microphotograph of the fabricated optical O-ring resonator. On the photo, the input and the output of the light are shown with the white arrows.

4. Experimental setup and results

Our experimental setup for transmittance spectra measurements consist of a tunable laser (NewFocus TLB-6600 with tune range 1510-1620 nm), a polarization controller to align the polarization, 3D sample holder with piezo motors, a fast photodetector as well as a fast analog-to-digital converter. To match the light in an optical fiber with the ORR, we used a fiber array and FGS on a chip. For measurements in various gases, we made a thin pipe for blowing gas around sample, while the sample itself was securely fixed on the table. In our work, in addition to the surrounding air (n_{Air} = 1.000292), we used two gases: helium (n_{He} = 1.000035) and propane (n_{C3H8} = 1.2898). The experimental results are shown in the Fig. 1(a). It is clearly seen that the position of the resonance peak substantially depends on the environment.

5. Conclusions

We studied the dependence of the transmission spectrum of the ring resonator depending on the gas surroundings through evanescent mode interaction. Obtained experimental results are in a good agreement with theoretical data and numerical calculation. This work is important for miniaturization of nanophotonics, biomedical devices and chemical devices detection.

6. Acknowledgments

The research was performed by support of Ministry of Education and Science of the Russian Federation (contract № 14.586.21.0063, unique identificatory RFMEFI58618X0063).

References

[1] Andreas Hänsel and Martijn J R Heck 2020 *J. Phys. Photonics* **2** 012002

[2] Rohith Chandrasekar, Zachary J. Lapin, Andrew Nichols et.al., 2019 *Opt. Eng.* **58**(2) 020901

[3] Bogaerts W, De Heyn P, Van Vaerenbergh T, et.al. 2011 *Laser Photonics Rev.* **6**(1)

Feature of Optical Soliton Sequence Propagation in Single-Mode Fiber

Andreeva E.I., Mitlener A.A., Potapov I.A.
The Bonch-Bruevich Saint-Petersburg State University of Telecommunications,
St.Petersburg, 193232, Russian Federation

Abstract. Estimates of information capacity of the optical system as product of maximum data rate in single soliton channel and long span distance are considered. The linear (fiber group velocity dispersion and optical losses) and nonlinear (self-phase modulation and Raman self-frequency shift) effects, the signal/noise ratio of pulse source are included in pulse evolution description. It was shown, that maximum optical system capacity can be achieved with NZDS-fiber.

1. Introduction

One important parameter of the fiber optic data system is the information capacity defined as the product of the bit rate B by the transmission distance z (the length of the span). Information capacity of a data transmission system directly depends on symbol pulse width - T_o and their peak power P. Increase in speed of data transmission assumes reduction of duration of symbol pulse: the bit rate $B = (Q^* T_o)^{-1}$, where Q- is on-off time ratio, that leads to broadening of a spectrum of symbol pulse that accelerates dispersive broadening of symbol pulse, on the one hand, and at the high power causes manifestation of nonlinear effects in the fiber light guide with another. Nonlinear effects of different nature have different effects on momentum evolution [1-5]. The self-phase modulation can be used to compensate for the dispersion expansion of the pulse in the region of abnormal dispersion. However, other nonlinear effects may have a negative effect on bit pulse dynamics. Thus, at the subpicosecond width of the symbol pulse, Raman self-scattering can have a significant influence on its evolution. The features of propagation of optical pulses of subpicosecond width in the fiber considering both linear (fiber dispersion and optical losses) and nonlinear (self-phase modulation, Raman self-frequency shift) effects, as well as influence of noise of the source of these pulses are considered. It is shown that it is possible to optimize the parameters of the fiber-optics communication system in order to increase its information capacity.

2. Thefeatures of propagation of optical soliton of subpicosecondwidth

The solitons can be used as the symbol pulses in bit stream in order to overcome the dispersion limitation. The initial balance between the dispersion and nonlinearity represents the fundamental optical soliton when the initial powerP_o of the solitons:$P_o=|\beta_2|/(\gamma\tau_o^2)$,where β_2 – is the fiber dispersion $d^2\beta/d\omega^2$,β – is the propagation constant, $\omega = 2\pi f$ is the frequency, γ - nonlinear Kerr coefficient, $\tau_o = T_o/1.763$. The initial soliton energy $E_o = 2P\tau_o$. For SSMF $\beta_2 = 18$ ps^2/km, and $\beta_2 = 2$ ps^2/km for NZDS fiber can be used. In a real fiber there is some small loss. When fiber loss is included, the total energy $E(z)$ in a pulse decay with the distance along the fiber and is proportional to $\exp(-2\alpha z)$, z – distance, α - fiber loss. If we assume a level loss in SSMF of 0,2 dB/km, $\alpha = 0{,}023$ km^{-1}. If the loss

length $\alpha^{-1}$is long compared to the dispersion length L_D: $L_D = \tau^2/\beta_2$, the pulse width changes as $\tau(z) = \tau_o \exp(2\alpha z)$.

The self-frequency shift of a soliton is extremely sensitive to the pulse width [4, 5]:

$\Delta\omega_R(z) = \frac{8}{15}\frac{|\beta_2|T_R z}{\tau^4}$,

T_R – is the Raman parameter, typically T_R = 3 fs for the optical fiber [3], $g(\tau_o)$ – weak function of τ_o.

This frequency shift in center of each pulse in a bit stream would not cause problem to data carrying capacity. But if the initial pulse width fluctuates as result of laser noise an error can occur at the end of fiber-optics communication system.The self-frequency shift result to the change in position of the center t_R from its original value. In practical the fluctuations in the solitons pulse width ΔT can be induced by changes in the energy ΔE from the laser as well as noise in the input pulse: $\Delta E/E = \Delta T/T$.

The change in the output pulse position Δt_R is obtained:

$$\Delta t_R = \frac{4}{15}\frac{\beta_2^2 T_R}{\tau_o^4}\frac{\Delta\tau_o}{\tau_o}\frac{g(\tau_o)}{\alpha}\left(z - \frac{1-exp(-8\alpha z)}{8\alpha}\right) \quad (1)$$

Let us determine the admissible value of Δt_R less than half the clock interval: $\Delta t_R < 2/B$, where B is the bit rate. For soliton systems, $Q = 10$ is usually taken.Then the permissible range of information transfer z can be estimated from (1), for the case when the input fluctuations $\Delta T_o/T_o$ = 0.001(signal/noise ratio of the symbol pulses source 10^3). With an increase in the initial width T_o, the self-scattering effect weakens and the permissible range z increases. However, the length of the soliton propagation regime also depends on T_o.

The information capacity defined as the product of the bit rate B by the transmission distance z for soliton system is presented in Fig. When using NZDS fibers with a symbol pulse width T_o nearly 1 ps, the maximum information capacity is achieved.

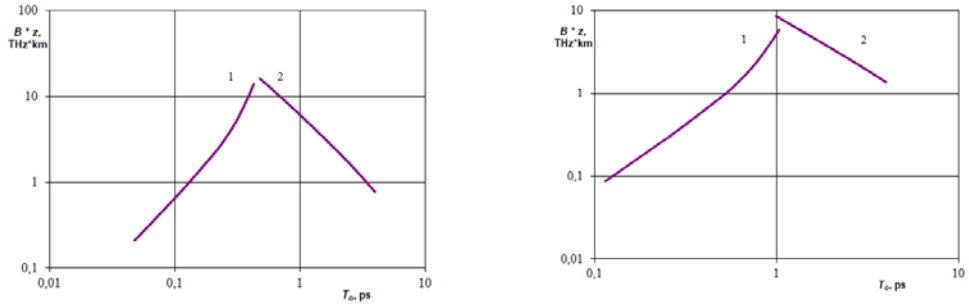

a **b**

Figure (a, b). The information capacity B*z in the fiber with biased dispersion with β_2 = 2 ps^2/km (a) and with biased dispersion with β_2 = 18 ps^2/km (b) as a function of initial pulse width T_o.

3. Conclusion

It is shown that for fiber with predetermined parameters, it is possible to determine a range of initial symbol pulse durations T_o at which it is possible to realize a maximum range z at a high bit pulse rate B such that the time jitter cased source amplitude fluctuation will be small.

References

[1] Andreeva E., Bylina M., Glagolev S., Chaimardanov P. Proceedings of Telecommunication Universities. 2018;4(1):5–12;

[2] Shcherbakov A.S., Andreeva E.I. Optical Fiber Technology. V.2, p.127-133.

[3] V B Fadeenko, V A Kuts, D A Vasiliev, V VDavydov Journal Physics: Conference Series. 2018. 1135(1). P. 012053.

[4] Kivshar Y.S. Agrawal G.P. The Institute of Optics University of Rochester. New York, USA, 2003.

[5] Wood D. J.of Lightwave Techn., **v**.8,p.1097-1106.

A Control Method For the Optimal Quantum Receiver

M S Elezov[1], M L Shcherbatenko[1], D V Sych[1,2,3] and G N Goltsman[1]
[1]Moscow State Pedagogical University, Moscow 119992, Russia
[2]QRate, Skolkovo, Moscow 143025, Russia
[3]P.N.Lebedev Physical Institute, Russian Academy of Sciences, Moscow, 119333, Russia

Abstract. We propose a method for controlling optical displacement of the optimal quantum receiver. The optimal receiver is able to discriminate between two phase-modulated states of a coherent optical signal. The optimal receiver controlling method can be used in various physical implementations of the optimal receiver.

1. Introduction

With the rapid development of fiber-optic technology and single-photon detectors, we have the possibility to create an optimal quantum receiver, which can detect weak coherent signals with an error below the standard quantum limit. We have developed a controlling method of the optimal quantum receiver for detecting coherent signals with discrimination error close to the Helstrom bound.

2. Optimal receiver control

We assume that the coherent signal has two states $|\alpha\rangle$ and $|-\alpha\rangle$, where α^2 is mean photon number of the coherent signal. In order to distinguish two signal states, it is necessary to mix the signal with a local oscillator (LO) on a 99/1 beam-splitter and then measure by a single-photon detector. We can change intensity of LO. We transform the phase-modulated signal into amplitude-modulated by mixing coherent signal with LO. The initial states of the signal is transformed to $|-\alpha+\Delta\rangle$ and $|\alpha+\Delta\rangle$. Where Δ is the optical displacement. After a beam-splitter the coherent signal interferes with the LO. We can distinguish two states with an error below the standard quantum limit by measuring the beam intensity using a single-photon detector and analyzing the data. If the displacement is $\Delta = \alpha$, then one state is completely nulling and the optimal receiver is transformed into Kennedy receiver mode [1]. However, such a coherent signal detection mode is not the most effective one.

It was shown in [2] that the optimal displacement signal can be more effective if we do not null one of the states. There is a more effective displacement of signal $\Delta = |\alpha + \beta_{opt}\rangle$. In order to find out β_{opt}, it is necessary to take into account the imperfection of the optical scheme. We have two parameters. The first parameter γ_c is constant and is characterized radiation background and dark counts of a single-photon detector. The second parameter γ_0 is integral parameter and characterizes non-ideality of optical system. In fact, intensity of interference minimum is not zero. We assumed that $\gamma_0 = k \cdot m_1$. Where k – non-ideality coefficient. Then two states of output light we can describe by system of equations:

$$\begin{cases} (2\alpha+\beta)^2 + \gamma_0 + \gamma_c = m_{max} \\ \beta^2 + \gamma_0 + \gamma_c = m_{min} \end{cases} \quad (1)$$

Where m_{max} and m_{min} – mean photon numbers for constructive and destructive interferences. We can experimentally measure non-ideality coefficient k, if $\beta_{opt} = 0$ and we knows γ_c. Nulling of β_{opt} corresponds to maximal extinction $C_{max} = \frac{m_{max}}{m_{min}}$, when two signals have the same intensity. Optimal displacement β_{opt} is determined that distinguishing error of two states of coherent signal must be minimal. For this we should use formulae (2) from [1]. Then, using system of equations (1), we get

$$C = \frac{4\alpha^2+\gamma_c}{{\beta_{opt}}^2+4k\alpha^2(\alpha+\beta_{opt})+\gamma_c} \quad (2)$$

Note, extinction C and optimal displacement β_{opt} depend on value α (see Fig. 1).

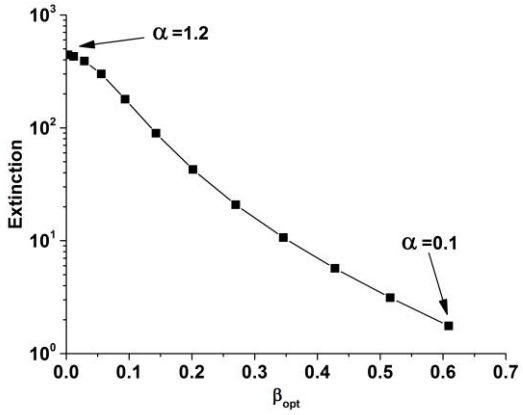

Figure 1. Extinction vs optimal displacement β_{opt} for different

3. Conclusion

We propose a method for controlling the optimal quantum receiver to distinguish between two coherent states of the measured signal. We can control optimal displacement value and measure signal with the minimal error. Further refinement of the method should be made taking into account the specific technical implementation of the receiver.

4. Acknowledgments

We acknowledge support of the Russian Science Foundation grant No.17-72-30036.

References

[1] R. Kennedy MIT Research Laboratory of Electronics Quarterly Progress Report 1973 **108**: 219-225

[2] Sych, D., Leuchs, G. *Phys. Rev. Let.* 2016 **117** (20) 200501

[3] M.L. Shcherbatenko, M.S. Elezov, D.V. Sych, G.N. Goltsman 2020 *Phys Rev A* **101** 032306

Development of focusing grating couplers for lithium niobate on insulator platform

I Elmanov[1], F Sardi[2], K Xia[2], T. Kornher[2], V Kovalyuk[1,3], A Prokhodtsov[1,4], P An[1,3], A Kuzin[1,5], G Goltsman[1,3,4] R Kolesov[2]
[1]Department of Physics, Moscow State Pedagogical University, Russia
[2]3rd Institute of Physics, University of Stuttgart, Germany
[3]Zavoisky Physical-Technical Institute of the Russian Academy of Sciences, Russia
[4]National Research University Higher School of Economics, Moscow, Russia
[5]Skolkovo Institute of Science and Technology, 121205, Russia

Abstract. In this paper we fabricated and studied focusing grating couplers for lithium niobate on insulator photonic platform. The transmittance with respect to the grating period before and after silicon dioxide covering was measured. Our results showed the influence of silicon dioxide cover on efficiency and central wavelength of grating couplers and can be used for further grating coupling efficient improvement.

1. Introduction

Lithium niobate on insulator is a promising platform for different on-chip scalable devices offering nonlinear wavelength conversion and high-speed modulation [1]. One of the challenges is efficient in- and out-coupling of light into and out of planar on-chip photonic circuits. Focusing grating couplers (FGCs) are potentially a way highly efficient extraction of light from planar optical structures [2]. Here, we present our first preliminary results on in- and out-coupling of light by means of FGCs created by reactive ion etching.

2. Device design and fabrication

For LNOI coupler development, we optimized the geometry of FGC demonstrated on SOI [3]. Single nanophotonic circuit included two FGCs connected by a 900 nm wide ridge waveguide (Fig. 1 a, b). To study FGC in a detail we created an array of devices with grating period variation in a range of 800 - 900 nm at a fixed filling factor 0.5. Such array including 15 nanophotonic schemes, was organized in three doubled rows and was made twice. For the device fabrication we used commercially available lithium niobate on insulator (LNOI) wafers (NanoLN) with 500 nm thick lithium niobate film residing on a silicon wafer with 2 μm SiO_2 spacer. The fabrication process was realized by e-beam lithography using double-layer PMMA as positive e-beam resist. The top PMMA layer (thickness 80 nm) with 950K molecular weight was put on top of more sensitive 200 K layer (thickness 400 nm). This facilitates undercut of the developed structures and promotes smooth lift-off of the hard metal mask. After the e-beam writing is completed and PMMA structures are developed with MIBK developer, 120 nm thick nichrome (50/50 Ni/Cr) hard mask was deposited by e-gun evaporation. Lift-off of the hard mask was performed in warm N-ethyl pyrrolidone. Lithium niobate structures were then produced by etching $LiNbO_3$ through the nichrome mask in an Ar/SF_6 low pressure plasma with no ICP component. After etching, the residual nichrome mask was removed in a mixture of chromium etchant and nitric acid.

3. Experimental results

For the experimental study we used tunable laser source (New Focus TLB-6600) in a range of 1510÷1620 nm, optically connected with single mode 12th channel fiber array (FA) and polarization

controller with chip placed on top of a *x*, *y*, *z*, rotation piezo stage. Transmission spectra of devices was measured by a fast photodetector and after preliminary amplification of the electrical signal were registered by NI DAQ system. Several measured transmission spectra of nanophotonic devices from the array are shown in Fig. 1c. It can be seen that with an increase in the period of the grating, the maximum intensity moves to greater wavelengths (Fig. 1 (c)).

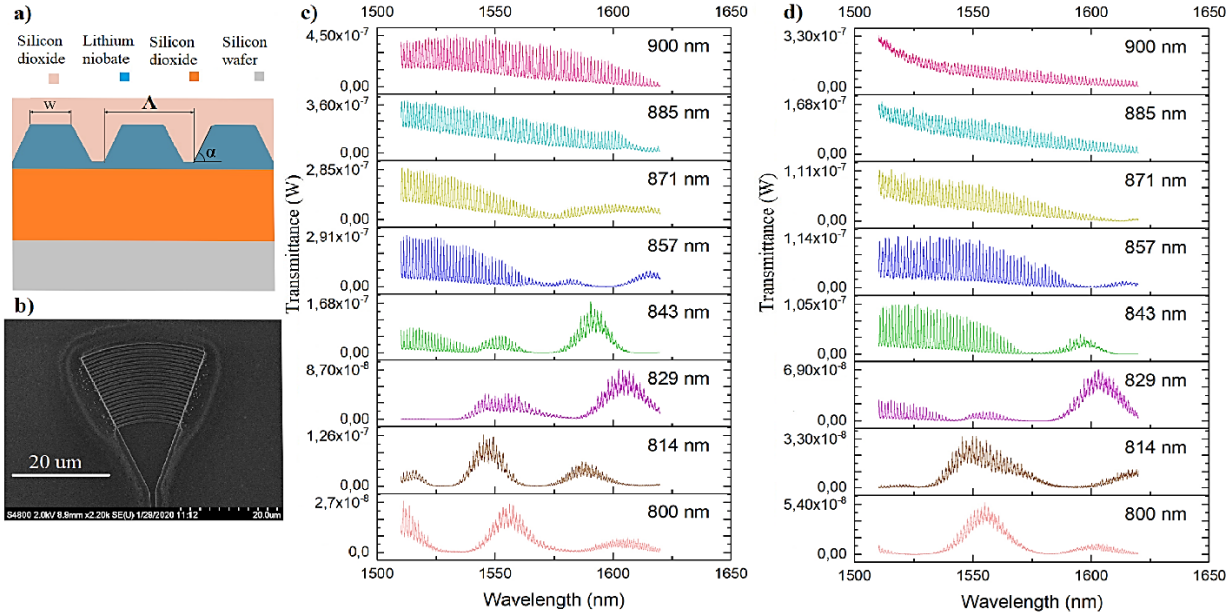

Figure 1 (a-d). (a) Schematic image of cross-section of a FGC, where Λ is the grating coupler period, w is a tooth width, filling factor ff = w/Λ, α is an angle of a tooth's side inclination **(b)** SEM image of FGC on lithium niobate on insulator. Transmission spectra for different grating periods before **(c)** and after SiO_2 sputtering **(d)**

Nevertheless, the main Gaussian transmission spectra are outside the possible range of wavelengths. The 1 μm SiO_2 coating increases the refractive index, but nonetheless, is not sufficient to move the maximum to the wavelength of 1.55 μm. (Fig. 1 (d)). Also shift of the central wavelength due to SiO_2 layer will be to the longer wavelengths, but this layer decreases total coupling efficiency. The maximum coupling efficiency for 1.55 μm wavelength was found as ≈ - 17 dB for the 900 nm grating period.

4. Conclusions

We studied FGCs efficiency depending on grating coupler period and a cap layer of SiO_2 and determined ≈ -17 dB maximum coupling efficiency for 1.55 μm wavelength. A further increase of FGC's grating period with a fixed filling factor allows shifting the Gauss like transmission maximum closer to 1.55 μm wavelength. Our results can be used for developing of high efficient coupling on LNOI, which can be used in the various quantum photonics applications, where compact design and high nonlinearity are needed simultaneously.

5. Acknowledgments

We acknowledge support of the Russian Science Foundation project 19-72-10156 (waveguide design), project 16-12-00045 (experimental study), Deutsche Forschungsgemeinschaft DFG KO4999/3-1 (nanoptotonic circuits fabrication).

References

[1] Zhang M, et.al. 2017 *Optica* **4** 1536–1537
[2] Vermeulen, D. et.al. 2010 *Opt. Express* **18** 278
[3] Van Laere F, et.al. 2007 *Optics Express* **19** 21–24

Dielectric surrounding bleaches the optical bond between a microdisk resonator and a straight optical waveguide

A V Raskhodchikov[1,3], S A Scherbak[1,2,3], A A Lipovskii[1,3], N V Kryzhanovskaya[1,2]

[1]Department of Physics and Technology of Nanostructures, Alferov University, St. Petersburg 194021, Russia

[2]International Laboratory of Quantum Optoelectronics, High School of Economy, St. Petersburg 194100, Russia

[3]Institute of Physics, Nanotechnology and Telecommunications, Peter the Great St. Petersburg Polytechnic University, St. Petersburg 195251, Russia

Abstract. We studied numerically the influence of a surrounding medium on coupling efficiency of a microdisk resonator supporting optical whispering gallery modes and a straight optical waveguide. Quality factors of the WGMs and the optical power coupled to differently wide waveguides and for different indices of the surrounding medium were calculated. It was shown that increasing index of the surrounding medium provides more efficient coupling.

1. Introduction

Semiconductor microdisk (MD) lasers, which support high-quality optical whispering gallery modes (WGMs), are of great interest as light sources for all-optical interchip communications [1]. However, such sources have to provide directional optical power output, which MD lasers generally lack. Coupling a MD laser with a bus optical waveguide (OW) can close this gap [2, 3]. However, the coupling is typically weak due to high localization of WGMs. Here we propose covering a MD with a dielectric to strengthen the coupling and increase the fraction of optical power transferred to the OW.

2. Modeling

We analyzed optical properties of a MD resonator coupled to a straight optical waveguide using a numerical simulation via finite elements method in COMSOL Multiphysics environment. An eigenfrequency solver was used to find WGMs of the MD in the near infrared region (around 1.3 μm) and the fraction of their optical power coupled to the waveguide. The MD diameter was 6 μm and its index n_{in}=3.4 (close to GaAs). The OW of the same material as the MD was considered. Q-factor of the passive optical resonator under consideration was matched to Q-factor of real lasing structures with a quantum dots active region (a few tens of thousands [4]) via setting imaginary part of the MD index k_{in}=5e-5 to introduce additional losses. We chose d=200 nm the gap between the MD and the OW, whereas the OW width, w, and a surrounding medium index, n_{out}, were varied.

Also we considered 2D geometry instead of 3D to reduce required computational power and only the TM-polarized WGMs, for the phenomena under discussion are qualitatively the same.

3. Results and discussion

We simulated several WGMs of the isolated MD in air: TM(1,44) – 1263.1 nm, TM(2,39) – 1261.3 nm, TM(3,35) – 1258.0 nm. In these notations, numbers in the brackets are radial and azimuthal orders of

the mode, respectively. Further, we watched over the behavior of these modes while varying the OW width and the surrounding medium index. The OW width barely affects the WGMs eigenfrequencies, for the coupling is weak. Whereas, increase of the outer medium index causes red-shift of the modes as we demonstrated in our previous work [4].

In Figure 1, we show the dependences of Q-factor of the mode TM(1,44) on the OW width for different n_{out}. The dips in the dependences correspond to the widths, at which the OW modes propagation constant matches the effective one of the WGM at the WGMs wavelength that is resonant (most efficient) coupling. The dips are about equidistant and correspond to subsequent TM_m modes of the OW, where m = 1, 2 … is a number of the **H**-field maxima in the transverse direction of the OW. The local minimum value in Figure 1 characterizes the magnitude of the coupling of the MD and the OW. With the rise of the outer index the minima significantly decrease, i.e. the coupling strengthens.

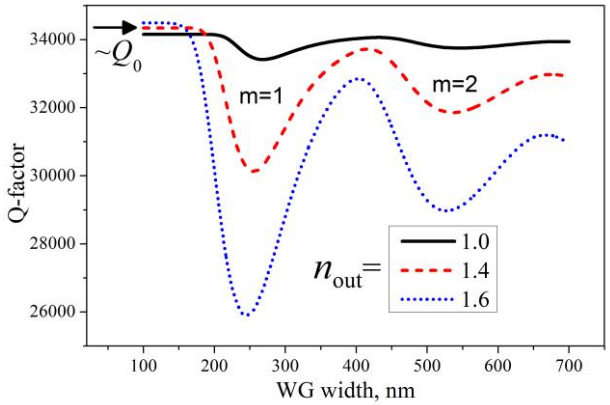

Figure 1. Q-factor of the mode TM(1,44) coupled to the straight optical waveguide vs its width

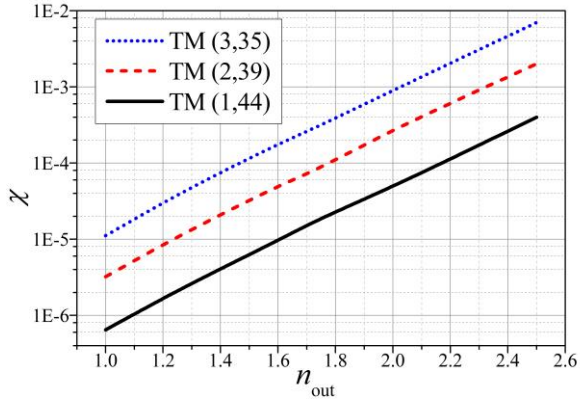

Figure 2. Relative optical power resonantly coupled to the optical waveguide vs n_{out}

Q-factor of a mode is defined by its optical losses. For the isolated MD, $Q_0=W_{in}/P_{in}$, where W_{in} is an optical power stored in the MD and P_{in} are both inner losses caused by k_{in} and radiation losses from the MD surface. For the MD loaded with the waveguide: $Q=W_{in}/(P_{in}+P_{out})$, where P_{out} is radiation losses through the waveguide. Thus, the fraction of the optical power coupled to the waveguide $\chi = P_{out}/W_{in}$ expressed through quality factors is: $\chi = 1/Q - 1/Q_0$.

The dependence of χ on the outer medium index for the considered WGMs is shown in Figure 2 (OWs width chosen to correspond to the resonant coupling). There is a significant increase in the fraction of the optical power coupled to the OW with the growth of the outer index: about 10-fold gain for n_{out}=1.5 (close to many polymers) and more than 150-fold gain for n_{out}=2.4 (close to TiO_2). Essentially, the optical power coupled to the OW does not exceed 1% of optical power stored in the MD, and that should not noticeably disturb laser generation. The exponential behavior of the dependencies in Figure 2 indicates that the coupling is driven by the exponentially decaying tail of the WGMs field, and the decay length is longer in an optically denser medium. Also noteworthy that the OW-coupling of the higher radial order modes is generally higher. However, as was shown in [4], higher radial modes also suffer with considerable decrease of their Q-factor under increase of the outer medium index.

4. Acknowledgments

This study was funded by Russian Foundation for Basic Research, project #20-02-00334

5. References

[1] Kryzhanovskaya N V, Maximov M V, Zhukov A E 2014 *Quantum Electron* **44** (3) 189
[2] Rowald D R, Love J D, 1993, *IEE Proc. J-Optoelectronics,* **140** (3) 177-188
[3] Cai D P, Lu J H, Chen C L, Lee C C, Lin C E, Yen T J 2015 *Scientific Report* **5** 100078
[4] Reduto I V, Fetisova M V, Kryzhanovskaya N V, Lipovskii A A et al, 2019 *JOSA* B **36** (8) 2285

Experimental new ultra high-speed all-optical coherent streak-camera

S N Bagayev[1], I B Mekhov[2,3], I A Chekhonin[2], M A Chekhonin[2]

[1]Institute of Laser Physics, Novosibirsk 630090, Russia
[2]St. Petersburg State University, St. Petersburg 199034, Russia
[3]University of Oxford, Oxford OX1 3PU, UK

E-mail: chekhonin@mail.ru

Abstract. We have experimentally studied for the first time a new operation principle of the all-optical coherent streak-camera (Rabi deflector). In the experiment, we observed an effect of significant dynamical angular deflection of a pulse of semiconductor laser during the resonant pumping of the D_2 line (780.24 nm) of ^{87}Rb vapour in the range of diffraction angles $\varphi = \pm 5.45^{o}$. We propose to use the Rabi deflector as an energy efficient shaper of classical and single-photon wave packets. We analyze a possibility of the Rabi deflector operation in quantum systems with feedback.

1. Introduction

A problem of the angular deflection of laser radiation is the most difficult problem of the laser radiation control [1,2]. In [2-4], we proposed a new principle of the angular deflection of radiation wave vector during the laser pulse diffraction off the atomic resonant diffraction grating with the spatial pitch, which is time dependent – the Rabi deflector. For this, the pump-field transversal profile E(t,x) should have a form of $E(t,x) = \varepsilon(t)\cdot saw(x)$ for the discrete angular deflection [2-4], or $E(t,x) = \varepsilon(t)\cdot ramp(x)$ for the continuous in time angular deflection.

2. Experimental

A cell with ^{87}Rb vapour was pumped by a pulsed tunable laser diode with the duration of 5.15 ns at the wavelength of transition D_2 (780.24 nm). Laser pulse power did not exceed 10÷40 mW. The rubidium vapour density was $N_o = 2.9\cdot 10^{11}$ cm^{-3}. For the Rabi deflector operation, we created the transverse pump-field profile $E(t,x) = \varepsilon(t)\cdot ramp(x)$ (S-type) of the size of 800 x 20 μm.

In the experiment, we analyzed the form of the diffraction pulse scattered from the cell at different diffraction angles φ. The pulse form was registered by the single-photon counting method using Single Photon Avalanche Diode MPD PD-050-CTD-FC with the time resolution of 27 ps and the multichannel time analyzer of single-photon pulses BH SPC130. The recording of the form of diffraction pulses was done using temporal beats between the pump pulse and moving diffraction maxima of the field of resonant medium radiation (cf. Figures 1, 2). The temporal beat signal was observed in the angle range of $\varphi = \pm 5.45^{o}$.

In this report, we analyze a possibility to use the Rabi deflector as an energy efficient shaper of classical and single-photon wave packets as well as its use in the perspective quantum systems with feedback loop [5].

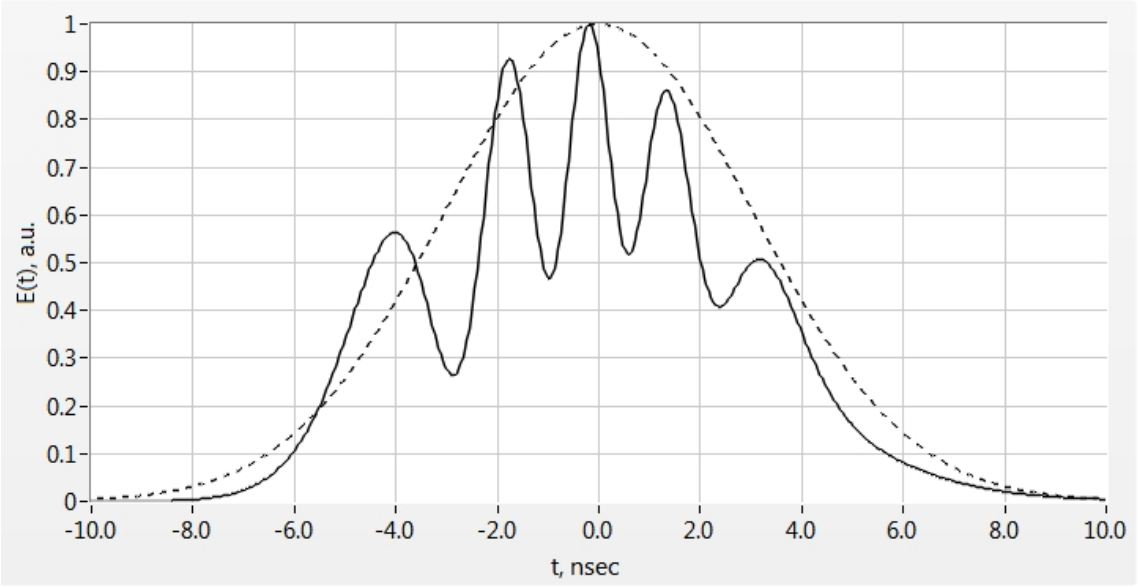

Figure 1. The result of numerical solution of the Maxwell-Bloch equations. The dashed line is the pump pulse; the solid line is the beats between pump pulse and dynamical diffraction maxima. The angle of the pulse diffraction observation is $\varphi = -0.05^{o}$.

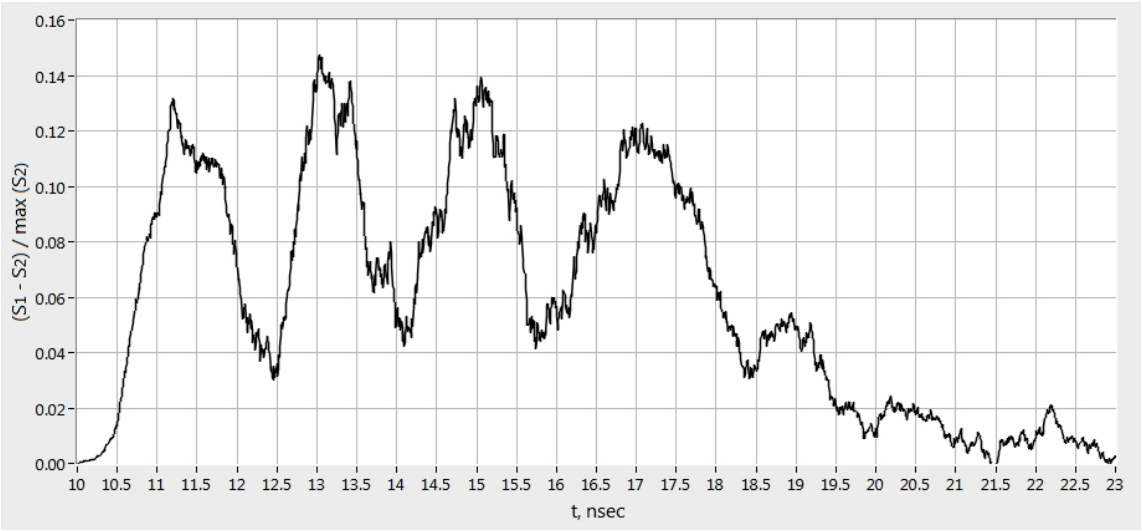

Figure 2. Temporal beats between the pump pulse and dynamical diffraction maxima in the experiment. The angle of the pulse diffraction observation is $\varphi = -0.05^{o}$.

3. Acknowledgements

This work was supported by Russian Science Foundation (project № 17-19-01097).

References

[1] Sarantos C H, Heebner J E 2010 *Opt. Lett.* **35** (9) 1389-1391

[2] Arkhipov R M, Arkhipov M V, Egorov V S, Chekhonin I A, Chekhonin M A, Bagayev S N 2015 *J. Phys.: Conf. Ser.* **643** 012029

[3] Arkhipov R M, Bagayev S N, Egorov V S, Chekhonin I A, Chekhonin M A 2009 Proc. VI Int. Conf. HOLOEXPO-2009 **(**Kiev) p 81

[4] Arkhipov R M, Arkhipov M V, Bagayev S N, Egorov V S, Chekhonin I A, Chekhonin M A 2013 *Scientific notes of the Physics Department of Moscow State University* **5** 135034

[5] Ivanov D A, Ivanova T Yu, Caballero-Benitez S F, Mekhov I B 2020 *Phys. Rev. Lett.* **124**, 010603

Optical image processing in attribution of paintings

J. Asmus[1], **V. Parfenov**[2]

[1]Department of Physics, University of California, Sand Diego, 92093-0319, USA
[2] Department of Photonics, St.Petersburg Electrotechnical University, 197376, Russia

Abstract. We present a computational technique to aid the authentication of paintings based on analyses of high-resolution digital images of the original works. This technique builds a statistical model (amplitude histogram) of the digital images of authenticated works against which copies and forgeries then are compared. It illuminates the individual brushstroke characteristic of paintings created by a master to be analyzed. We show preliminary results from our analyses for 36 self-portraits that at various times have been attributed to the Dutch painter Rembrandt van Rijn. These results demonstrate the conformity of histograms for paintings which are considered by art experts as authentic self-portraits by Rembrandt, and reveals statistical differences when compared to copies as well as paintings executed by others in the Rembrandt works.

Introduction

The attribution of great paintings is one of the most important activities in modern museum work. The attribution of an artwork is the result of authentication – a procedure for the confirmation of its authenticity. The main task in authentication is to find material evidence by which it is possible to indisputably acknowledge the experts' conclusions about the authorship and the painting's time of creation. The author's signature, the dates and monograms left by artists on the front or back of the picture, as well as accompanying inscriptions and historical information on the provenance of the work are among such proofs. Unfortunately, the influence of the environment, adverse storage conditions and the consequences of radical restoration intervene in the structure of the painting and often lead to these proofs disappearing.

Furthermore, in many paintings, the artist's signature is actually absent. In such situations, it is necessary, in order to remain objective, to use natural-scientific approaches, including various optical

and physical methods for studying the structure of the painting. However, despite the availability of a wide range of contemporary analytical research methods, they do not always prove to be effective enough to obtain the necessary information. In fact, the determination of the composition of the paint layers and the dating of a painting's support (by means of carbon dating and dendrochronological analyses), even combined with research results by art history experts, does not always allow for its attribution to the hand of a certain artist. Hence, the need to develop a new scientific method for studying paintings, which provides information that cannot be obtained with the use of traditional research methods, and which avoids subjective opinion.

In recent years, numerous computer methods based on the analysis of optical images obtained with the aid of digital photography have appeared in the field of the authentication of artworks. Most methods of computer analysis serve as a means for studying the visual characteristics of an artist's brushstrokes. Till now this information has been used to study paint layers and style. However, since in most cases the technique of applying the paint is highly individual for each artist, it can be considered as a "fingerprint". How to extract and analyse this "fingerprint"? The mathematical methods of processing a digital picture ("quantification") include the statistical method of a wavelet analysis, the support vector method, the fuzzy clustering method, etc., which are all used to analyze the brushwork technique [1] – [4]. In some cases, these methods are combined with analysis methods from other scientific fields, e.g. biometrics and medicine. In this paper, a scientific method for the comparative analysis of paintings is described, which employs intensity histograms of their digital optical images being the extraction of this "fingerprint". The possibilities provided by this method are illustrated by a case studies of self-portraits created by the Dutch painter Rembrandt van Rijn and case study of analysis of two paintings created by great Italian master Leonardo da Vinci.

Experimental results

For our analysis we used high-resolution digital images of Rembrandt`s self-portraits. In some instances some images to be analyzed were taken from available books and then scanned at maximum resolution (this was done in our first efforts to analyze paintings). However, it is important to precisely scale analyzed images to the same size and to equalize their resolution – in our case we used size of 600x800 pixels and a resolution of 300 dpi. For the comparative analysis of histograms of self-portraits we used only a central part of grayscale images of Rembrandt`s face. It is clear that the face is the main part of any portrait and any artist would have concentrated his attention mainly on it. There is a high probability that an artist painted his face by himself rather than with others of his studio.

Our analysis did show interesting features of self-portraits by Rembrandt, which complicated our analyses. The intensity distributions of his histograms is different for the young faces appearing in his early portraits and aged faces (see Fig. 1). The distribution of intensity changed many times and some later self-portraits, for instance, from the Kenwood House (c. 1665-1669) look similar to most early self-portraits. Evidently, it is connected to a shift in Rembrandt`s technique during his life.

Taking into account the above mentioned variety of histograms of self-portraits corresponding to different periods of Rembrandt`s life, we decided to focus our analysis on a study of self-portraits of his later period as their attribution is less questionable than that of his early works.

Our results suggest a plausible approach for the identification of brushstrokes of painters by means of the analyses of luminosity histograms taken from digital images of paintings. Our studies and results, described in this paper, clearly demonstrate that it is possible to determine the mathematical mean and variance of a histogram in order to attempt a rigorous comparison of different paintings. However, these values are subject to minor differences in the composition of the imaged figure (including angle of observing of face, tilt of head, etc.). It is obvious that restoration treatments also can influence the distribution of intensity in histograms. Furthermore, histogram distributions are sensitive to changes of the artist`s technique during his life. From this point of view, our approach can be considered as an excellent guide to the attribution of paintings. Also, it can be very useful for *comparative* analyses of

those paintings, where final attribution can not be achieved solely on the basis of stylistic and historical studies or technical characterization. If it is known that a particular painting was created by a certain artist, then comparing its histograms with those of images of a painting to be analyzed, allows for the determination if both of these paintings were created by the same artist. In these complicated situations the histogram approach can give additional and what is even more important – objective *quantitative* information, which is useful for making the final decision on the attribution of a painting.

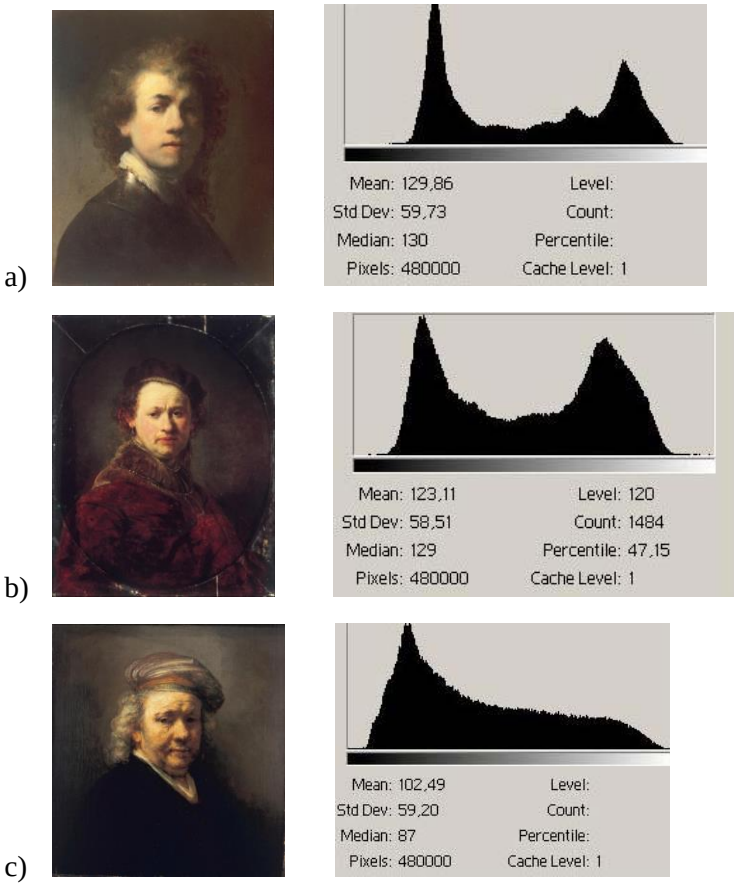

Fig.1. Self-portraits by Rembrandt of different periods of his life and their histograms: a) Nuremberg 1629 (age 23); b) Karlsruhe 1645-48 (age 39-42); c) Hague 1669 (age 63).

References

[1].B. Mandelbrot, "The fractal geometry of nature", W. H. Freeman, New York, NY, 1982.

[2]. S. Lyu, D. Rickmore, and H. Farid, "A digital technique for art authentication", Proceedings of the National Academy of Sciences. **101** (49), pp. 17006–17010, 2004.

[3]. M. Shahram, D. G. Stork, and D. Donoho, "Recovering layers of brushstrokes through statistical analysis of color and shape: An application to Van Gogh`s Self-portrait with grey fell hat", in Computer image analysis in the study of art, D. G. Stork and J. Coddington, eds., **6810**, pp. 68100D–1–8, SPIE/IS&T, Bellingham, WA, 2008.

[4]. S. Jafarpour, G. Polatkan, E. Brevdo, S. Hughes, A. Brasoveanu, and I. Daubechies, "Stylistic Analysis of Paintings Using Wavelets and Machine Learning" // European Signal Processing Conference (EUSIPCO), 2009.

Control of the on-chip silicon nitride O-ring resonator signal parameters by changing the phase state of the $Ge_2Sb_2Te_5$ thin cover

P Lazarenko[1], V Kovaluyk[2], P An[2,5], A Prokhodtsov[2,3], A Sherchenkov[1], S Kozyukhin[4], G Goltsman[2,3,5]

[1]Institute of Advanced Materials and Technologies, National Research University of Electronic Technology, Zelenograd 124498, Russia

[2]Department of Physics, Moscow State Pedagogical University, Moscow 119992, Russia

[3]National Research University Higher School of Economics, Moscow 101000, Russia

[4]Kurnakov Institute of General and Inorganic Chemistry of the RAS, Moscow 119991, Russia

[5]Zavoisky Physical-Technical Institute of the RAS, Kazan 420029, Russia

Abstract. Here we studied the change in the transmission spectrum of integrated resonators with thin film $Ge_2Sb_2Te_5$ atop. We found a change in the transmission spectrum depending on its length and phase state. The obtained results can be used to create electrically and optically switched on-chip devices and complex fully functional nanophotonic circuits based on them.

1. Introduction

The fast switching time of Ge-Sb-Te (GST) thin films between amorphous (a-GST) and crystalline (c-GST) states initiated by low energy impact as well as significant change of their optical properties and the preservation of metastable states for tens of years open wide perspectives for the application of these materials to fully optical devices [1]. In this work, we investigated the influence of the phase state and size of GST thin cover on the optical characteristics of on-chip silicon nitride O-ring resonator with different waveguide width.

2. Experimental

The rib waveguide of the resonator was formed the first stage of e-beam lithography and subsequent reactive-ion etching. We used the second stage of e-beam lithography combining with lift-off method for the formation of GST active region on the resonator ring surface (Fig. 1 a,b). The amorphous GST films with a thickness of about 20 nm were obtained by magnetron spattering target, and were capped by thin silicon oxide on their tops. Crystallization of as-deposited amorphous thin films was carried out using heating stage at the temperature of 250 °C for 30 minutes in argon. The microstructures of the a-GST and annealed GST thin films were characterized by the high-resolution transmission electron microscopy (HRTEM) with fast Fourier transform (Fig. 1 c,f).

3. Results and Discussion

The measured transmission spectra for the fabricated devices with a-GST and c-GST covers in comparison with data for the uncovered O-ring resonator are presented in Fig. 1 e,i. It is seen that the

deposition of a-GST cover on the surface of the waveguide leads to a decrease of the optical power, transmitted through the waveguide (Fig. 1, e), and increase in the optical losses. Comparison of the optical transmittance for O-ring resonators with and without GST cover allowed to identify the change in the Q-factor and the wavelength peak shift.

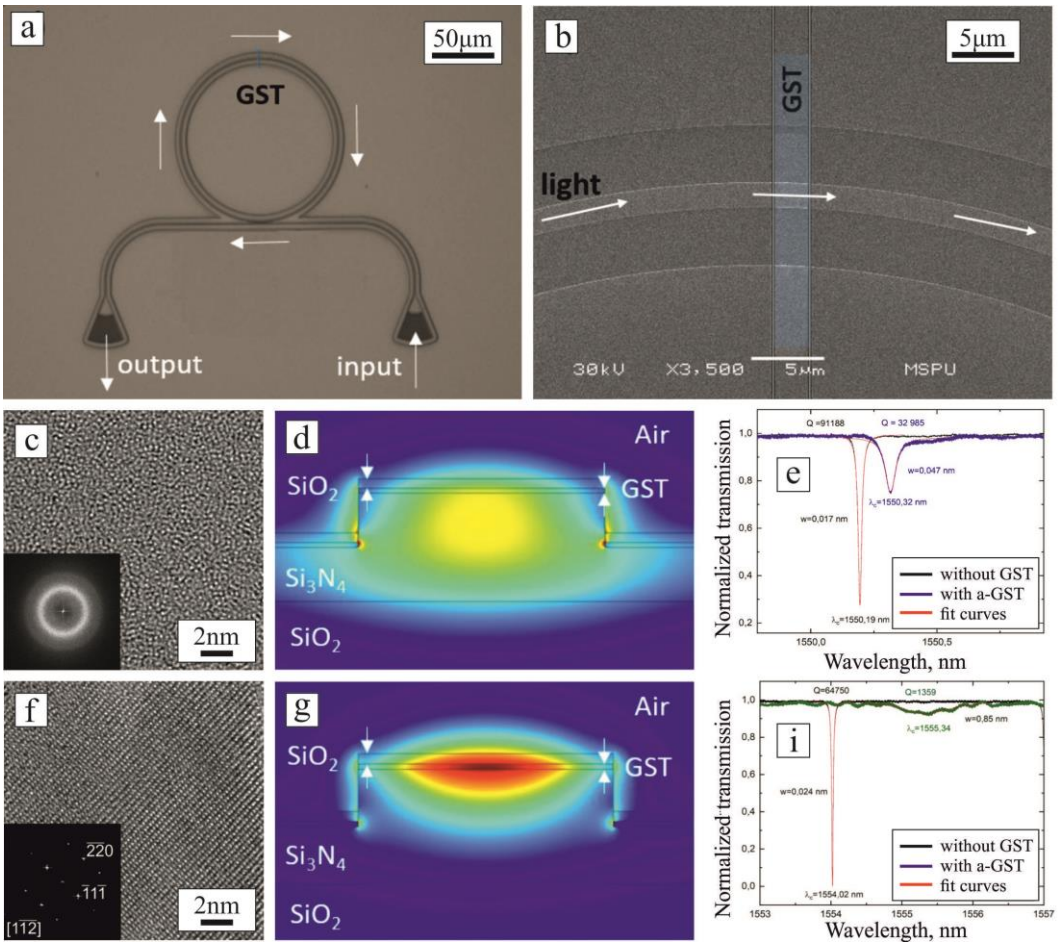

Figure 2 (a-f). (a) The optical micrograph of a fabricated O-ring resonator; **(b)** SEM image of the area with GST cover; **(c, f)** HRTEM images and Fourier transform patterns (insets); **(d, g)** 2D model cross sections of the resonators; **(e, i)** transmittance spectra for the fabricated resonators. Images (c,d,e) and (f,g,i) show the results for the a-GST and c-GST cover, respectively.

Crystallization of the cover leads to a further change in optical transmission. It was observed that crystallization of amorphous GST film lead to a decrease of the transmitted optical power (Fig. 1, i). This can be explained by the differences of the complex refractive indexes of a-GST and c-GST thin films. From the measurement data, the GST effective refractive index was also extracted depending on the ring waveguide width of the resonator for a wavelength of 1550 nm. The influence of the GST cover length and the width of the waveguide in the ring part of the microcavity on the optical mode distribution was simulated based on the ellipsometric data and confirmed the experimental results.

4. Acknowledgments
The study was supported by RFBR (project 20-07-01092).

References
[1] Wuttig M, Bhaskaran G, Taubner T 2017 *Nature Photonics* **15** 465

Compensation of radiation-induced losses in optical fibers

D S Dmitrieva[1], V M Pilipova[1], V V Davydov[2, 3], V Yu Rud[3]
[1]The Bonch-Bruevich Saint-Petersburg State University of Telecommunications, Saint Petersburg 193232, Russia
[2]Peter the Great Saint Petersburg Polytechnic University, Saint Petersburg 195251, Russia
[3]All Russian Research Institute of Phytopathology, Moscow Region 143050, Russia

Abstract. In article the necessity of developing a method of the compensation of radiation-induced losses in the fiber optic communication lines is substantiated. Reasons of appearance of radiation color centers in the optical fibers are considered. A method of increasing the rate of the relaxation processes after finishing the γ-radiation's influence on the fiber optic communication line is developed. The received results are presented.

1. Introduction

Nowadays high-speed large data exchange is impossible without using the fiber optic communication lines (FOCL). Like other communication systems, FOCL are also subjected to the negative influences because of the human activity. There is γ-radiation among them. It is the most unpleasant because it changes the optical fiber's properties. Optical signal power losses increase in the fiber. The recovery of FOCL's parameters takes a lot of time after irradiation. During this time, it is very difficult to use them for information transfer. Moreover, prolonged influence of γ-radiation and the high doses of irradiation can lead to irreversible changes in FOCL. Most of the used fiber optic diagnostic devices are not able to establish the fact of the influence of γ-radiation on the fiber. Therefore, the tasks of establishing the fact of the γ-radiation's influence on the FOCL and the development of a method of compensating losses are the actual tasks in applied Physics.

2. The new method, experimental results and discussion

The increasing of losses in the optical fiber is connected to the appearance the color centers. These is the microdefects, which appear after the radiation influence. The color centers appear as the result of the displacement and ionization effects [2]. The increasing of ionization atoms leads to the formation of the defects in the optical fiber. It discourages for information transfer. The relaxation processes don't allow to quickly eliminate these defects even after short-time exposure [2]. If the rate of the new color centers formation will be higher then the relaxation rate of the excisting color centers, the process of increasing the attenuation of the optical signal in the fiber will increase. As the result it can lead to the loss of information during the transmitting it via FOCL.

We conducted researches, which helped us to establish the following. The rate of the relaxation processes, which lead to the destruction of color centers, depends on several factors. There are the most significant of them: the optical fiber's temperature and the optical signal's power, which transmits via fiber. We was also established, that the rate of the relaxation of color centers (the value of radiation-induced losses α_s) also changes according to the type of laser radiation, continuous or pulsed. This result helped us to develop a methodology of determining the presence of the fact of the influence of γ-radiation on FOCL

The analysis of the received results after research of the value of radiation-induced losses from laser radiation's power helped us to suggest a new compensation method. It is based on a using of additional high-power laser radiation with other wavelength, It's necessary to note that there is no data exchange via FOCL during the measures to compensate the α_s values. At the Figure 1 there are the

results of a study of the rate of change in the relaxation color centers from the power of additional laser radiation. There was full data exchange via FOCL during the experiments.

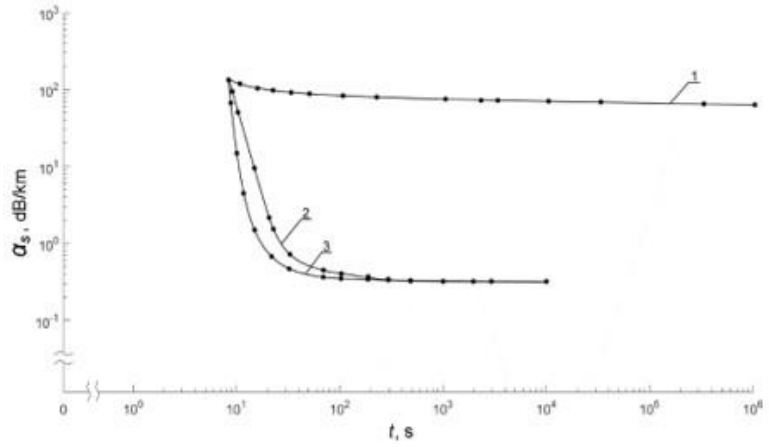

Figure 1. Dependence of the change in loss α_s with time t at a wavelength of λ =1550 nm for a single-mode fiber with a $Si0_2 – GeO_2$ core (alloyage 1.5 %) at T = 294.2 K. Charts 1, 2, and 3 correspond to different laser radiation powers in mW: 0, 20, 40.

As an experiment example we used a single-mode fiber with an irradiation dose of 100 G. The additional laser radiation with a wavelength of λ =1310 nm was inputted in the optical fiber with using the multiplexer. The received results show that the increase of additional high-power laser radiation increases the rate of the relaxation of color centers in the irradiated optical fiber. Initial properties of the optical fiber were recovered. It was done for 100 sec during using the radiation with the power of 20 mW and for 10 sec during using the radiation with the power of a 40 mW

This method significantly reduces relaxation time. The optical fibers were recovered for 10^8 sec without this method. A multiplexer is installed at the output of the optical fiber, in which signals with different λ are divided into two channels.In each channel there is a photodetector (one of them is for receiving information, other of them is for controlling irradiation power)

3. Conclusion

The received results show that the developed method is more effective for compensating the radiation-induced losses than previously used.

Using the calibration dependencies α_s from the power of laser radiation and pulse duration, it is possible to establish the fact of the γ-radiation's influence on the FOCL

It was also established that in FOCL the interferences occur, when we use a high-power level of additional laser radiation. Therefore, we will continue our studies to solve this problem.

References

[1] Tomashuk A L, Filippov A V, Kashaykin P F, Byshkova E A, Guryanov A N and Dianov E M 2019 *Journal of Lightwave Technology* **37(3)** 956-962

[2] Kashaykin P F 2018 Proceedings of SPIE - The International Society for Optical Engineering (Moscow) vol. 10681 1068110

About the origin of the second harmonic generation in poled silicate glasses

I V Reshetov[1], **V P Kaasik**[1], **A A Lipovskii**[1,2], **D K Tagantsev**[1,3]
[1]Peter the Great St. Petersburg Polytechnic University, St. Petersburg 195251, Russia
[2]St. Petersburg Academic University RAS, St. Petersburg 194021, Russia
[3]Vavilov State Optical Institute, St. Petersburg 192171, Russia

Abstract. We studied thermal relaxation of the second harmonic generation (SHG) observed in thermally poled soda-lime silicate glass. At least two relaxation processes could be distinguished. Determined activation energy of the fastest SHG relaxation process is equal to about 0.5 eV. This SHG relaxation occurs at temperatures essentially below ones, at which the thermally stimulated depolarization current (TSDC) measurements show the relaxation of the spatial charge formed in thermal poling of the glasses. This confirms that SHG in poled glasses is not mostly conditioned by the "frozen" spatial charge and electric field of this charge.

Introduction

Thermal poling (polarization) of silicate glasses is known to result in structural and compositional changes in their subsurface layer. Poled glasses also demonstrate properties of anisotropic optical media: linear electrooptic effect, second harmonic generation (SHG), etc. [1,2] which are of interest for optoelectronics. According to the prevalent point of view [3], the anisotropy originates in the static electric field created by the spatial electric charge formed in glasses in poling and "frozen" after their cooling. However, in the previous study [4], we have demonstrated that in the heating of poled glasses the complete relaxation of the SHG signal precedes the spatial charge relaxation process which takes place at essentially higher temperatures and is confirmed by the TSDC (thermally simulated depolarization current) measurements. Here we present the studies of the kinetics of the SHG relaxation.

Experimental and results

A soda-lime glass (1 mm thick microscope slides) were poled at 300 ^{O}C and 1 kV DC voltage for 40 min. The intensity of the SHG signal in poled sample was measured using Maker fringes technique [5]. The isothermal kinetics of the signal relaxation (decay) in the temperature range 150 – 190^{O}C (with 10 ^{O}C step) was recorded (see Fig.1a). The character of the kinetic curve in Fig. 1a evidences in favour of two processes taking place in the SHG relaxation; one of them is fast and another is slower. Thus, it appears that the relaxation process can be described by the sum of two exponential functions: $I(t) = I_1 exp(-t/\tau_1) + I_2 exp(-t/\tau_2)$, where I is the SHG intensity, I_1 and I_2 are the constants, t is the time, τ_1 and τ_2 are the relaxation times of the fast and second relaxation processes, respectively. From Fig. 1a it follows that the relaxation time of the slow process (τ_2) is much higher than the one of the fast process (τ_1). For rough evaluation of values τ_1 at different temperatures, we neglected the presence of the slow process for time <1000 sec and approximate relaxation kinetics in this time interval using a single exponential function. To evaluate the activation energy of the fast process, W, we plotted the Arrhenius graph: $ln(\tau)$ vs $1/T$, where T is the temperature. This graph is shown in Fig.

1b, and it was used to calculate the activation energy of the fast process: $W = k \times d(ln\tau)/d(1/T)$, where k is the Boltzmann constant. Calculated activation energy is equal to ~0.5 eV.

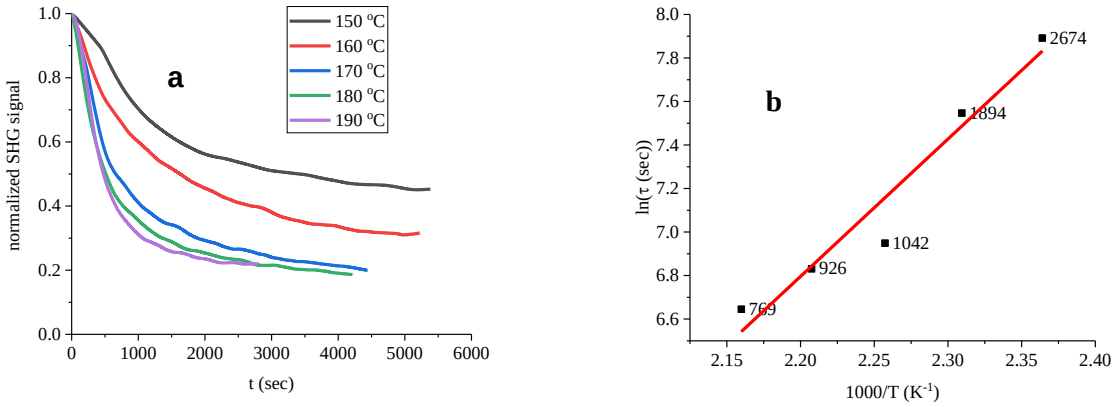

Figure 1. (a) SHG relaxation at different temperatures, (b) Temperature dependence of the relaxation time of the fast process: red line is the result of the approximation with linear function; figures at the points are the values of calculated relaxation times in sec.

Discussion

SHG relaxation curves shown in Fig. 1a correspond well to a single exponential function in the first 1000 sec time interval. Evaluated activation energy of the fast relaxation process which dominates in this time interval is equal to about 0.5 eV. It is worth noting that in accordance with TSDC study [6], the relaxation of "frozen" spatial charge (charge carriers redistribution) is negligible in the temperature range used in the present research, and the main relaxation of the spatial charge takes place above the glass transition temperature with activation energy equal to about 3 eV. In fact, in the temperatures below 200 ^{O}C, TSDC, that is, thermally simulated depolarization current, is extremely low and hardly measurable. Thus, the present research confirms that the appearance of SHG signal in poled glasses is not mostly conditioned by the spatial "frozen" charge and electric field of this charge. By now, the microscopic mechanism of the SHG relaxation process characterized by activation energy 0.5 eV is not identified.

Conclusion

Thus, performed studies allow concluding that only a negligible part of charge carriers redistributed in thermal poling of the glass and forming the spatial charge is responsible for the SHG.

Acknowledgments

The study was supported by the Ministry of Science and Higher Education of Russian Federation, project FSRM-2020-001.

References

[1] Dussauze M, Rodriguez V, Lipovskii A, Petrov A, Smith C, Richardson K, Cardinal T, Fargin E and Kamitsos E 2010 *J. Phys. Chem*. **114** 12754

[2] Redkov A, Melehin V, Raskhodchikov D, Reshetov I, Tagantsev D, Zhurikhina V and Lipovskii A 2019 *J. Non. Cryst. Solids.* **503 – 504** 279

[3] Nasu H, Suzuki Y, Ohta H, Yamamoto Y, Ito Y, Hashimoto T, Kamiya K, Narasaki A, Tanaka K, Hirao K 2000 *Japan. J. Appl. Phys.* **39** 6530

[4] Reshetov I, Kaasik V, Lipovskii A, Tagantsev D 2019 *J. Phys. Conf. Ser.* **1410** 012148

[5] Maker P, Terhune R, Nesenoff M, Savage C 1962 *Phys. Review Letters* **8** 21

[6] Lipovskii A A, Morozova A I, Tagantsev D K 2016 *J. Phys. Chem. C* **120** 23129

Enhance of the superconducting properties of the NbN/Au bilayer bridges

N O Simonov[1], **Yu P Korneeva**[1], **A A Korneev**[1,2], **G N Goltsman**[1,2]
[1]Moscow State Pedagogical University, Moscow 119991, Russia
[2]National Research University Higher School of Economics, Moscow 101000, Russia

Abstract. We experimentally demonstrate strong temperature dependence of the critical current of the superconducting 600-nm-wide and 5-μm-long bridge made of NbN/Au bilayer. The result is achieved due to the proximity effect realized between the highly disordered superconducting NbN layer and low resistive normal metal Au layer.

1. Introduction

Single photon detection by superconducting NbN strips of micron width [1] demonstrate that in a practical single-photon detector made of several-micron-wide NbN strip the critical current must be close to Ginsburg-Landau depairing current. To achieve this, the superconducting strip must be of high homogeneity with the minimum of geometric constrictions. This goal is a technological challenge, as superconductor with high normal state resistance has a spatially fluctuating superconducting energy gap and the critical current in it is usually determined by a weak point. As a result, the measured critical current is much lower than the depairing current.

A promising approach can be a usage of a bilayer consisting of highly disordered (with high normal state resistivity) superconductor (S) and a good (low resistive) normal metal (N) films. An increase of critical current was theoretically predicted and experimentally demonstrated in NbN/Ag and NbN/Al bilayers [2]. The authors explain the increase of the critical current in the SN layer compared to a single S-layer by the fact that injected supercurrent is redistributed in such a way that the largest part of the current flows via the N-film without dissipation due to proximity effect. Besides, their results demonstrate that proximity induced superconductivity in N-film is weakly sensitive to local inhomogeneities of the superconductor, therefore there are no requirements for high quality of the superconducting film.

2. Experimental results and methods

Our samples are made of NbN/Au bilayer film according to the recipe of ref. [2]: the ratio of resistivities of S-layer in normal state and N-layer and are chosen of about 50. The thickness of the S-layer d_S is equal to 1.6 of the coherence length ξ and the thickness of normal metal d_n is $3.8\xi_N$, where ξ_N is the coherence length in normal metal near the border with the S-layer. The NbN and Au layers are deposited in in-situ process by DC-magnetron sputtering. Then the wafer is cut in two pieces and the Au layer is removed from one of them by chemical etching. This piece of the wafer is used further as a reference to monitor the properties of the S-layer. For our experiment the samples are patterned as 600-nm-wide and 5-μm-long strip (bridge) as shown in the inset of Fig 1(a). The zoomed-in SEM image in the inset of Fig 1(a) shows a noticeable granularity of the Au surface. To prove the presence of the proximity effect, we measure critical temperature T_c of the bilayer film and compared it with the T_c of the reference NbN film. The blue curve in Fig 1(a) is the resistance vs temperature of the bilayer. It has two transitions: the

larger one which is 80% of the normal state resistance takes place at 6.3K and corresponds to the T_c of the bilayer, while the smaller one corresponding to 20% of the normal state resistance is observed at 9K and we attribute it to non-homogeneous quality of the bilayer: there are regions where there is no proximity effect due to bad contact between Au and NbN layers. The red curve in Fig 1(a) is for the refence NbN film and has T_c of 9.7K.

Figure 1(b) shows the dependence of the critical current on the temperature which is important for the feasibility of the bilayer for practical devices. The black curve is the depairing current calculated for the reference NbN film by the Bardeen formula [3]: $I_{dep}(T)=I_{dep}(0)*[1-(T/T_c)^2]^{3/2}$, and $I_{dep}(0)=0.74*(w*\Delta(0)^{3/2})/(e*R_s*(h*D)^{1/2})$, where w is the width of the sample, $\Delta(0)$ is the superconducting energy gap at zero temperature, e is electron charge, R_s is sheet resistance (575 Ω), D is diffusion coefficient which we take 0.34 cm^2/s. The critical current of the reference NbN film (red curve) follows the theoretical $I_{dep}(T)$, while $I_c(T)$ for bilayer at $T/T_c=0.2$ is 3 times higher than the I_{dep} for single NbN layer.

We hope that this research gives us an opportunity to use the bilayer system for improving the characteristics of the future superconducting single-photon detectors.

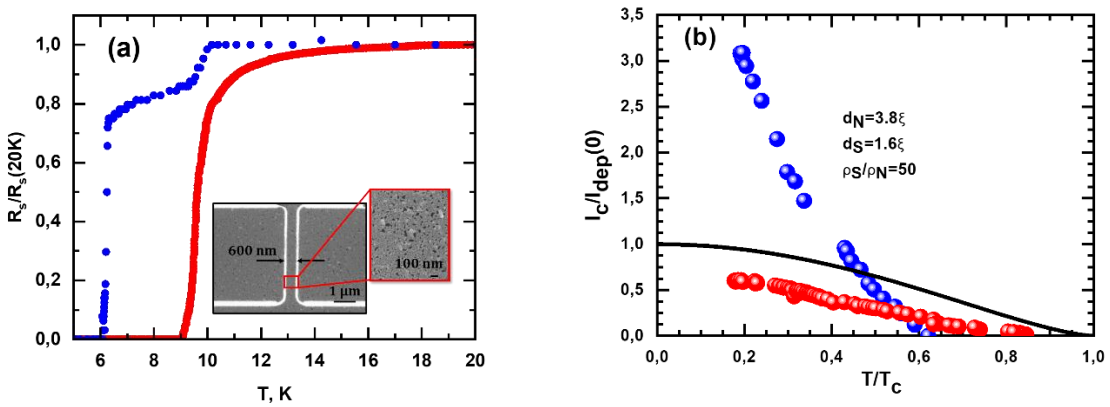

Figure 1. (a) Temperature dependence of the sheet resistance R_s normalized to the sheet resistance at 20K temperature $R_s(20K)$ for NbN/Au bilayer (blue) and reference single NbN layer (red). The inset is the SEM image of the sample which is NbN/Au 600-nm-wide and 5-μm-long bridge and the zoomed-in surface of the Au layer. **(b)** Temperature dependence of the critical current I_c normalized to the depairing current at 0 K temperature $I_{dep}(0)$ for the NbN/Au bridge (blue), reference NbN film (red) and theoretical dependence $I_{dep}(T)$ (black).

This work is supported by the Russian Science Foundation (RSF) Grant No. 17-72-30036.

References

[1] Korneeva Yu *et al* 2018 *Phys. Rev. Applied* 9(6) 064037
[2] D Yu Vodolazov *et al* 2018 *Supercond. Sci. Technol 31*, 115004
[3] J. Bardeen 1962 *Rev. Mod. Phys.* 34, 667

Calculation of a binary diffractive optical element to increase the imaging system depth of field in the task of classifying images by a neural network

A P Dzyuba[1], **S N Khonina**[1,2], **A V Nikonorov**[1,2], **P G Serafimovich**[2]
[1]Samara National Research University, Moskovskoe Shosse 34A, Samara, Russia
[2]IPSI RAS – Branch of the FSRC "Crystallography and Photonics" RAS, Molodogvardeyskaya st. 151, Samara, Russia

Abstract. Using an example of a real-world data set, it is shown that the accuracy of the image classifier based on a convolutional neural network does not deteriorate when using only one color channel. The binary diffractive optical element was calculated, which allows to increase the imaging system depth of field by several times. This is achieved by using the different color channels for various defocus values. A comparison of the MTF curves of the original and apodized imaging systems for a given minimum acceptable value of image contrast is presented.

1. Introduction

Image classification refers to one of the tasks in the implementation of computer vision. For example, an image classification algorithm may be developed to determine if the image of the number on the container in the warehouse corresponds to the number of the container that the robot should move. Although such a task is trivial for humans, reliable classification of images is still a problem in computer vision applications. The task is even more complicated if the analyzed image is distorted, in particular defocused.

Optical systems are known to be sensitive to defocusing and chromatic aberration. An increase in the depth of field of the optical system makes it possible to weaken this sensitivity and its negative consequences in blurring defocused images. However, a simple increase in the depth of field (DOF) by reducing the pupil or numerical aperture of the system leads to deterioration in resolution. One way to increase DOF without degrading resolution is to "encode" the wavefront, which is actually a phase apodization of the pupil of the lens [1-3]. As a rule, apodization is accompanied not only by positive effects (an increase in DOF and a decrease in the size of the focal spot), but also by a significant change in the structure of the point scattering function (PSF) and the growth of side lobes.

In the task of classifying images, specific requirements are imposed on the imaging system. In particular, in this paper it is shown that for a relatively reliable classification of the image, it is sufficient to have a focused image in only one color channel. This observation is based on the study of only one data set. However, it logically follows from the very specifics of the task, in which the structure of the object is important, not its color.

2. Results

To classify the images we use a VGG-like convolutional neural network (CNN). The CNN architecture contains seven convolutional layers and two fully connected layers. As training data for

CNN, the Street View House Numbers (SVHN) dataset is selected. SVHN is a real-world image dataset that contains about 70000 digits for training and 25000 digits for testing. CNN was consistently trained in three conditions: (1) on color images (3 color channels), (2) on images that contained two color channels, and (3) on images that consisted of one color channel. For all cases, the classification accuracy on the test data was about 93%. Thus, it was concluded that one color channel is sufficient to classify the images of the SVHN dataset. Given the variety of lighting conditions, color palettes, and image position angles in SVHN, this conclusion can probably be generalized to other similar data sets, where the structure of the object is important for classification, not its color. For the last CNN layer, the *softmax* activation function was used, which calculates the probability of correct image classification. This, firstly, made it possible to demonstrate a decrease in CNN "confidence" in the correct classification for defocused images. Figure 2 (a) show an example of test image of defocused image of either "1" or "3" and bar graph of classification probabilities. The probability bar graph to the right of the image reflects this uncertainty. Secondly, the calculated probabilities for each color channel allow you to choose the most reliable channel for classification.

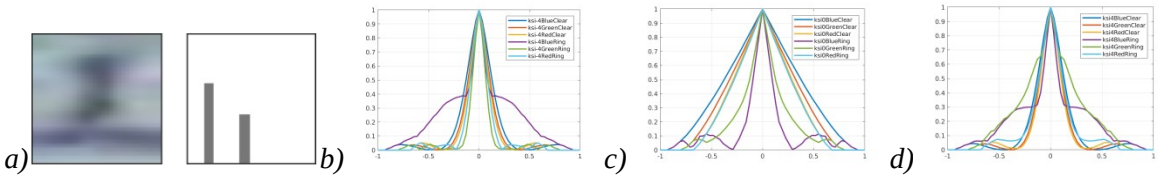

Figure 2. (a) an example of test image and bar graph, (b), (c), (d) MTF plots for defocused images.

Binary diffractive optical elements introduce significant chromatic aberration. As a rule, the compensation of these aberrations requires additional efforts in optimizing the optical element. In this work, chromatic aberration was used to optimize PSF separately for each color channel in order to increase DOF. For this, the phase apodization of the aperture using a radially symmetric (ring) binary phase element is used. When optimizing this element, the value of the maximum resolvable frequency is set (in fractions of the cutoff frequency, 0.5 was set) and the value of the minimum allowable contrast at this frequency (20% was set). The optimized parameters are the height of the phase ring and its inner radius (the normalized outer radius is assumed to be 1). Figures 2 (b), (c), (d) show MTF plots for the source and apodized imaging systems. These graphs are calculated for various defocus values. We assume that the imaging system (aperture 1.8 mm) is focused at a distance of 1.2 m from the lens. Figures 2 (b), (c), (d) show MTF at distances of 1.2, 0.65, 0.44 m, respectively. Comparison of MTF plots for the initial and apodized imaging systems allows us to conclude that in the apodized system the focus depth is increased by about an order of magnitude.

3. Conclusions

The binary optical element for phase apodization of the pupil function of the optical system is calculated. This optical element provides an increase in the depth of focus of the optical system through at least one color channel for a certain value on the optical axis. The calculated optical element can be used in machine vision problems for image classification. Using the appropriate training data set, the obtained results can be generalized, for example, to the task of classification examination of ships and offshore structures.

4. Acknowledgements

The work was funded by RFBR, projects number 19-29-01235 мк, 18-07-01390 а.

References

[1] Bagheri S, Javidi B 2008 *Opt. Lett.* **33** 757
[2] Reddy A N K, Khonina S N 2018 *Appl. Phys. B* **124** 229
[3] Elmalem S, Giryes R, Marom E 2018 *Opt. Express* **26** 15316

Optical Spectroscopy of a Resonant Bragg Structure with 100 InGaN Quantum Wells

A A Ivanov[1,2], **V V Chaldyshev**[1,2]
[1] Peter the Great St. Petersburg Polytechnic University, St. Petersburg 195251, Russia
[2] Ioffe Institute, St. Petersburg 194021, Russia

Abstract. The optical reflectance and transmittance spectra of a periodic InGaN semiconductor heterostructure with 100 quantum wells are studied at room temperature. Numerical modeling with a single set of parameters gave a quantitatively accurate fit of the experimental reflection and transmission spectra in a wide wavelength range. The radiative decay parameter is determined to be 0.25 meV.

1. Introduction

An optical medium with periodic perturbations on the dielectric susceptibility shows an enhanced light-matter interaction when the periodicity-related Bragg resonance meets the resonant frequency of the perturbations. Such a medium can be realized via a sequence of quantum wells (QWs) with poles in the dielectric susceptibility provided by excitation of the quasi-two-dimensional excitons. The collective behaviour of the excitonic system in response to the electromagnetic field gives rise to a superradiant optical mode that transforms into the photonic band gap when number of periods becomes large. Such resonant Bragg structures (RBS) are quite attractive for all-optical and electro-optical applications since the excitonic states are sensitive to external and internal electric fields.

Unfortunately, most of semiconductor materials and nanostructures exhibit exciton resonance only at cryogenic temperatures due to a small exciton binding energy. When room-temperature operations are required, wide-band-gap III-N compounds seem to be materials of choice. In fact, the binding energy of excitons in GaN is ~ 20 meV, which is comparable with thermal fluctuation energy at room temperature. This fact allowed to observe double exciton-Bragg resonance at room temperature in an RBS composed of 60 InGaN/GaN QWs [1].

In this paper we studied optical properties of an RBS composed on 100 periods of InGaN/GaN QWs.

2. Sample, experiment and analysis

Structure was grown by the metal-organic vapor-phase epitaxy (MOVPE). After the growth of the buffer layer, the major part of the structure was grown with 100 InGaN 2.4 nm thick QWs separated by GaN barriers. Optical reflectance and transmittance spectra were studied at room temperature for different polarization of the incident light. Computer-based simulation (fitting) of the spectra was performed using the method of transfer matrices. The matrices of transfer through the QW layers were formed on the basis of formulas for exciton-related reflectance and transmittance derived by Ivchenko [2].

3. Results and discussion

Fig. 1 shows the reflectivity spectrum in a vicinity of the main peak corresponding to fulfilment of the Bragg condition near resonant frequency of QW excitons. The Bragg peak has a specific fine structure and appears on the background of the Fabry–Perot oscillations. The Fabry–Perot oscillations are pronounced at the long-wavelength side but diminish at the opposite side when approaching the GaN fundamental absorption edge at 365 nm.

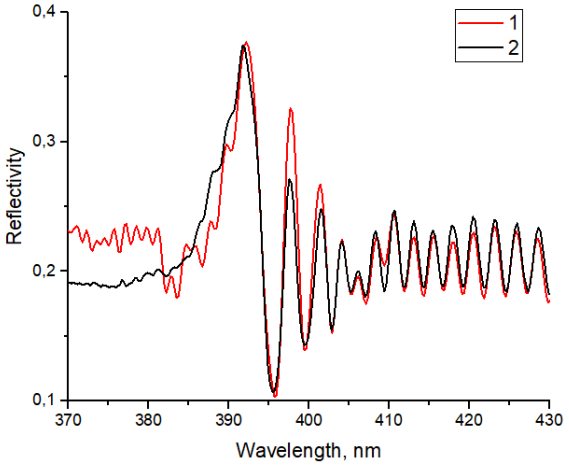

Fig. 1. Reflectance spectra of the structure under study. Curve 2 is the experimental spectrum, curve 1 is the calculated spectrum. The angle of incidence of light is 20°, S polarization, room temperature.

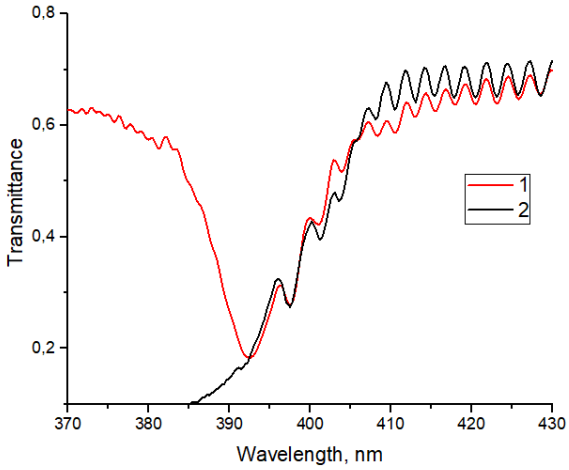

Fig. 2. Transmittance spectra of the structure under study. Curve 2 is the experimental spectrum, curve 1 is the calculated spectrum. The angle of incidence of light is 20°, S polarization, room temperature.

Fig. 2 shows experimental and calculated optical transmission spectra. The Fabry–Perot oscillations, which attenuate in the short-wavelength region, can also be seen in the above spectra. The fine structure is also observed at the wavelength of Bragg resonance.

The results of the calculations are shown in Fig. 1 and 2 along with the corresponding experimental curves. The best-fit parameters of the calculations are as follows: resonant energy of the QW excitons is 3.15 eV, their radiative decay parameter is 0.25 meV and the nonradiative decay parameter is 40 meV. Our calculations successfully describe the fine structure of the Bragg peak originated from the deviation of the exact periodicity of the structure.

4. Conclusion

Our experimental study revealed noticeable enhancement of the light reflection from the InGaN RBS with 100 periods. Numerical simulations showed a reasonably good agreement with the experimental reflectivity and transmission spectra. It allowed us to determine the parameters of the QW excitons. It is apparent that the excitons in the InGaN RBS are well suitable for room temperature operations.

References

[1] V. V. Chaldyshev, A. S. Bolshakov, E. E. Zavarin, A. V. Sakharov, W. V. Lundin, A. F. Tsatsulnikov, M. A. Yagovkina, Taek Kim, Youngsoo Park. Appl. Phys. Lett. 99, 251103 (2011).
[2] E. L. Ivchenko, Sov. Phys. Solid State 33, 1344 (1991).

Optical densitometry method for liver function assessment using indocyanine green

I Kolokolnikov, I Lavrenyuk, E Savchenko, E Nepomnyashchaya
Institute of Physics, Nanotechnology and Telecommunications,
Peter the Great St. Petersburg Polytechnic University,
Saint Petersburg 195251, Russia

Abstract. Indocyanine green is a tricarbocyanine dye, that is stable in human blood plasma and can be completely eliminated by liver in several days. Due to its properties it can be used to assess the metabolic liver function. We present optical densitometry device and theory for taking measurements of concentration of indocyanine green in patient's blood in vivo.

1. Introduction

Dynamic assessment of liver function can be critically important for patients before and after liver surgery. There is a number of methods to diagnose and predict course of liver condition. Analysis of blood samples for special contents incudes blood sampling from a patient which is not always available option, and also it takes a lot of time to get results. Ultrasound scan, MRI and computer tomography scan can show liver form, structure and appearance, but they are not capable to measure liver function. [1, 2]

There is a method based on measurement of disappearance rate of a dye injected to patient intravenously. Indocyanine green is popular solution by reason of it can be easily detected in patient's body by optical methods, because it has notable peak of absorption spectrum in near infrared section. Bounded with plasma indocyanine green has absorption peak on 805 nm [2, 3].

Measurement of plasma disappearance rate of indocyanine green with light sensor is approved method for assessment of liver function [2-4], but existing commercial realization – LiMON device (Pulsion, Germany) – does not give complete data set of measurement process and also is quite expensive. Our sensor and processing system design is aimed to be cheaper and to give the full access to the data collected.

2.Theory of solution concentration measurement

Optical densitometry method is based on the Beer–Lambert–Bouguer law which describes intensity of light transmitted through the solution.

$$I(z) = I_0 \exp(-Xcz) \quad (1)$$

where I_0 – reference light intensity, z – light path length through solution, $I(z)$ – intensity of light traveled distance z, c – solute concentration, X – coefficient describing light absorption by one particle depending on wavelengths.

To calculate the concentration of solution first we have to determine I_0 value which is equal to intensity of transmitted light when solute concentration c is zero. Also we need to determine coefficient X, taking into account diode emission spectrum, dye absorption spectrum and photodiode spectral sensitivity. Alternatively X can be calculated in serial experiments with known concentration.

$$c = -\frac{\ln(\frac{I(z)}{I_0})}{Xz} \quad (2)$$

3. Experimental setup

To test optical densitometry method before applying it to measure the concentration of indocyanine green in patient's blood, we use the following scheme (see Fig. 1). Light from the emitting diode (peak wavelength 808 nm) passes through cuvette with the studied solution and finger (to calibrate setup for finger-clip sensor design) and is received by photo detector. The microcontroller is applied to operate light-emitting diode, to control and collect data from photodetector (I^2C protocol) and to transmit data by USB interface.

Measurements proceed by the following method. A number of solutions of different concentrations are prepared. Then we take measures of transmitted light intensity for every concentration.

As a result, we have series of measurements, which can be used to calculate coefficient *X* for our setup, or to calculate concentration of solution, if we take *X* as known.

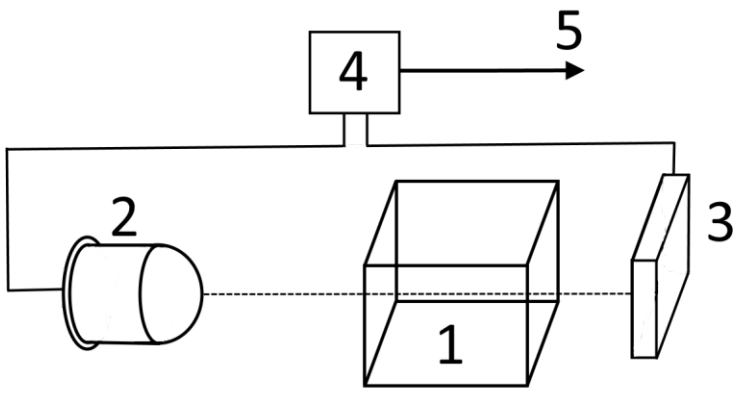

Figure 1. The experimental setup: 1 — cuvette; 2 — emitting diode; 3 — photodetector; 4 — microcontroller; 5 — USB interface.

4. Results and conclusions

In this work optical densitometry device and theory for taking measurements of concentration of indocyanine green are presented. We demonstrated the basic principles of light absorption in solution. The theory we suggested allow concentration measurements by referent method. Experimental results and comparisons to theoretical calculations will be demonstrated in full paper.

5. Acknowledgements

This research work was supported by Peter the Great St. Petersburg Polytechnic University in the framework of the Program "5-100-2020".

References

[1] Hemming A et al. 1992 *The American Journal of Surgery* vol 163, p 515
[2] Tsubono T et al. 1996 *Hepatology* **24(5)** p 1165
[3] Sakka S 2017 *Journal of Clinical Monitoring and Computing* **32**, p 787
[4] Malbrain et al. 2012 *Annals of Intensive Care* **2**, S19

The investigation of the influence of optical pumping on optical properties of thin film bismuth in terahertz frequency range

E A Litvinov[1], **D Zykov**[1], **N S Kablukova**[2], **M K Khodzitsky**[1]
[1]"Terahertz Biomedicine Lab", ITMO University, Saint Petersburg 199034, Russia
[2]Department of General and Applied Physics, Herzen University, Saint Petersburg 191186, Russia

Abstract. The research is aimed to investigate the influence of optical pumping on optical properties of thin film bismuth in terahertz frequency range. Experimental results were obtain using terahertz time-domain spectroscopy technique and showed strong tunability for optical pumping of different values of power. Due to its properties thin bismuth film becomes a promising alternative platform for realizing tunable hyperbolic medium.

1. Introduction

Nowadays active research work is developing in the field of electromagnetic metamaterials. They have far more advantages in comparison with 'ordinary' materials, because metamaterials are composite structures in its nature with specific geometrical configuration which allows to design brand new materials not existed in nature and often possessed exotic properties. The opportunity of setting up the geometrical parameters gives us a space for creativity and afford create composite media with desired properties. Still, there are a lot of restrictions on fabrication and properties of the 'ordinary' materials which make up the composit [1].

In this work bismuth has a hyperbolicity of optical parameters in terahertz and far-infrared frequency range what makes it a perfect addition to the set of 'ordinary' materials of use. The tunability of optical parameters of the bismuth with external force will have such useful applications in terahertz photonics such as sensor development, imaging and development of telecommunication systems.

2. Results

The crystalline structure of the Bi film is an altered structure of the massive Bi. The thermal spraying method is used with the spraying mode: spraying temperature 70 ◦C and annealing at 180 ◦C for 30 minutes to create bismuth films. Mica (17 μm thick) and polyimide (42 μm thick) are used as a substrates. Such a regime allows to obtain thin bismuth films on dielectric with the same crystallographic orientations of the trigonal axis. The triangles directed in opposite directions are separated by crystallite boundaries. From the point of view of transport phenomena, such an inversion almost does not introduce restrictions. The main scattering factor in the films is the thickness (classic size effect)30. The thin-film crystal is a deformed quasimonocrystal (0.7 GPa as estimated) for charge carriers [2]. Thin film thicknesses were checked using the Linnik interferometer.

The measurements were performed using terahertz time-domain spectroscopy technique [3]. The processing of measurements has done using 4th order coiflet-based denoising technique and rectangular signal windowing, which allowed to obtain noise-free spectra in the 0.25-1.0 THz range. Simple windowing was performed to exclude noise in low-frequency part of spectra.

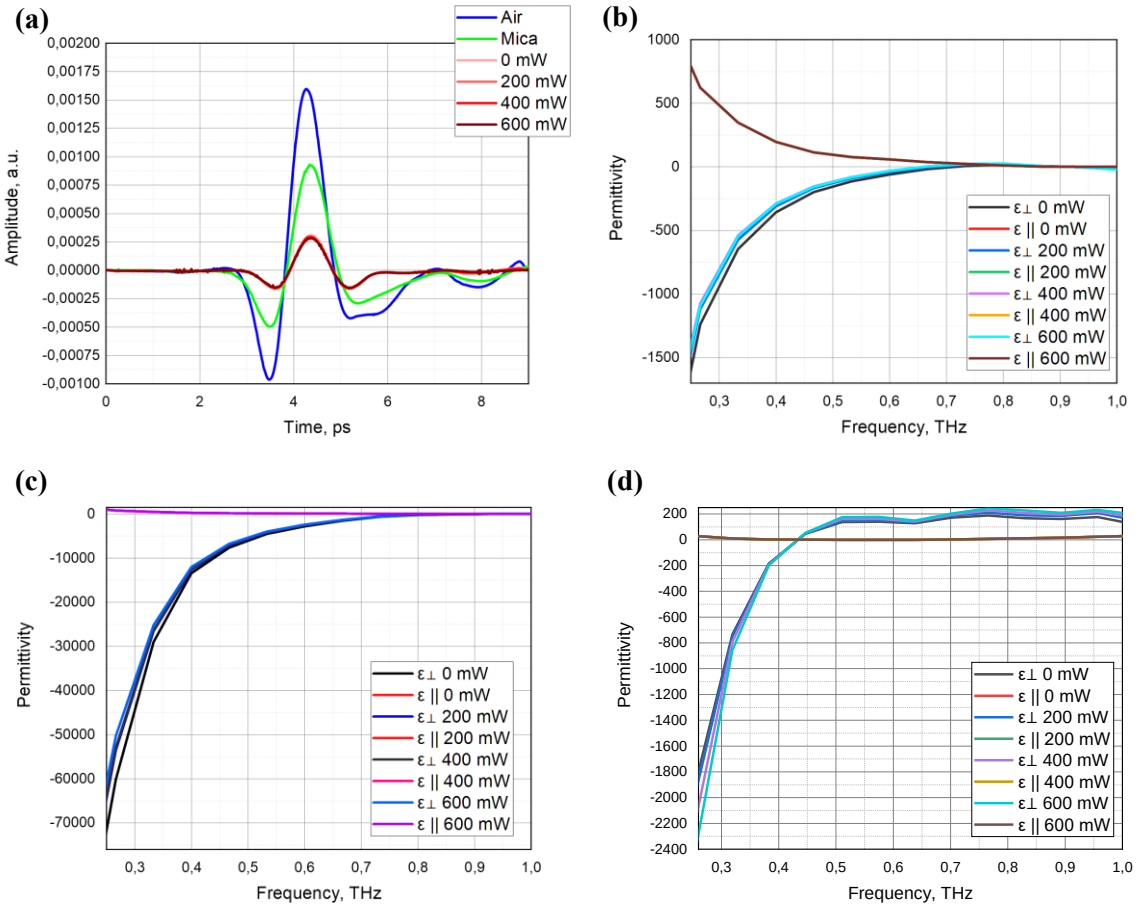

Figure 1(a-d). (a) Waveforms of terahertz pulses obtained using THz-TDS; **(b)** components of the real part of the permittivity of thin film bismuth with thickness 40 nm; **(c)** 120 nm; **(d)** 160 nm.

3. Conclusions

In conclusion, it has been demonstrated that a structure composed of bismuth and dielectric layer can show hyperbolic behavior in the THz frequency range, where tuning can be achieved by changing the power of optical pumping. The work indicates that the bismith-based structures are a promising alternative platform for realizing tunable hyperbolic medium.

References

[1] N. Engheta и R. W. Ziolkowski, *Metamaterials: Physics and Engineering Explorations*. John Wiley & Sons, 2006.

[2] V. M. Grabov, E. V. Demidov, V. A. Komarov, Optimization of the conditions for vacuum thermal deposition of bismuth films with control of their imperfection by atomic force microscopy, *Phys. Solid State*, 52 (6), pp. 1298–1302, 2010.

[3] V. G. Bespalov *и др.*, «Methods of generating superbroadband terahertz pulses with femtosecond lasers», *J. Opt. Technol.*, 75 (10), p. 636, 2008.

Effective absorption coefficient of a graphene atop of silicon nitride nanophotonic circuit

S Komrakova[1,2,4], V Kovalyuk[1,3], P An[1,3], A Golikov[1,3,4], M Rybin[3,5], E Obraztsova[3,5], G Goltsman[1,2,3]

[1]Department of Physics, Moscow State Pedagogical University, 119992, Russia
[2]National Research University Higher School of Economics, Moscow 101000, Russia
[3]Zavoisky Physical-Technical Institute of the Russian Academy of Sciences, 420029, Russia
[4]Moscow Institute of Physics and Technology (State University), 141700, Russia
[5]Prokhorov General Physics Institute of the Russian Academy of Sciences. 119991, Moscow, 38 Vavilov st.

Abstract. In this paper, we demonstrate the results of a study of the optical absorption properties of graphene integrated on silicon nitride O- ring resonator circuit. We fabricated an array of O-ring resonators with a different graphene coverage area on it. By measuring the transmission spectra of micro resonators with and without graphene, we calculated the absorption coefficient of the graphene-waveguide integrated circuit.

1. Introduction

The combination of the unique electronic and optical properties of graphene makes it an ideal candidate for use in nanophotonic optoelectronic devices [1]. Due to graphene properties: electroabsorption and electrorefraction, it can be used in modulators and switches, photo-thermoelectric devices [2]. Also, graphene can be easily integrated into various passive photonic platforms, such as Si, silicon nitride (SiN), and silicon dioxide [2].

In this article, we integrated graphene on O-ring resonators and investigated its absorption properties on its length.

2. Device design and fabrication

For experimental verification of the absorption properties of graphene devices, we have designed an array of O-ring resonators, shown in Fig. 1 (a-b). For array of 144 devices in horizontal direction the width of waveguide is varied form 1,7 μm to 3.08 μm. In vertical direction the gap is varied form 686 nm to 2.52 μm.

For the device fabrication, we used commercial available 450 μm thickness silicon wafers with 2.6 μm thermally oxidized layer and low pressure chemical vapor deposited (LPCVD) 450 nm layer Si_3N_4 on a top. Our photonic devices, depicted in Fig 1(a-b), were fabricated by e-beam lithography (Crestec, CABL-9500C) using positive resist ZEP 520A as a sensitive layer. After development, resist was used as a protective mask in the reactive ion etching in CHF_3 atmosphere to remove Si_3N_4 inside resist window. Then the resist was removed using acetone as a remover.

Graphene was synthesized by cold-wall chemical vapor deposition method on copper foil from gas mixture of methane, hydrogen and argon with pressure 100 mbar and at temperature 850 °C. The synthesized on copper foil graphene was transferred onto device by standard “wet” transfer using PMMA as support layer and etching copper foil in ammonium persulfate solution. To form rectangular areas of graphene with a variable dimensions, optical lithography was used with AZ1505 resist. The width of the areas varies from 10 to 70 μm in increments of 10 μm. Afterwards unprotected graphene is removed by O_2 plasma etching.

3. Experimental setup and results

To obtain the absorption coefficient, we measured the transmission spectra of O-ring resonators before and after graphene deposition on the following scheme. The light from the tunable laser source (NewFocus TLB -6600 with tune range 1510-1620 nm) passed through the polarization controller and fiber array to to be collected by focusing grating coupler (FGC) on the chip [3]. To digitize data a fast photodetector, as well as a fast analog-to-digital converter, was used.

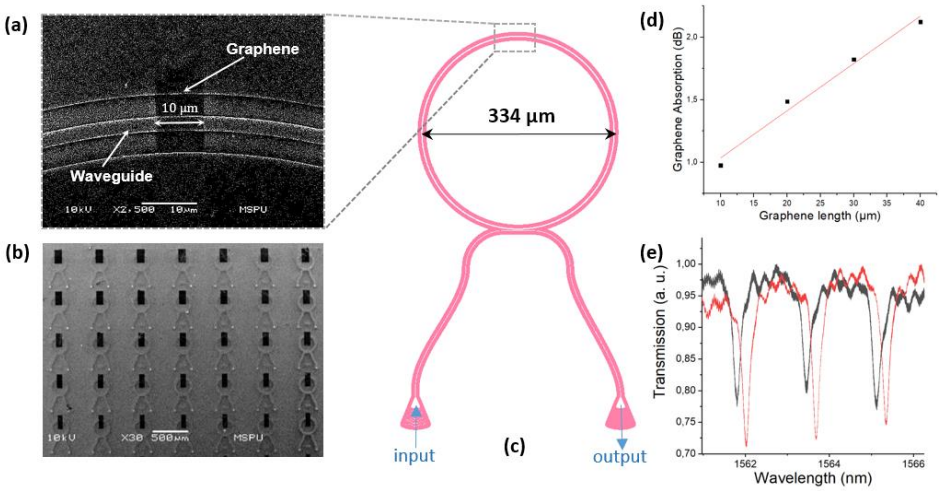

Figure 1 (a-d). **(a)** Enlarged SEM image of the resonator waveguide with graphene on it, graphene is the black area. **(b)** SEM image of array of O-rings with graphene atop. **(c)** The draw of the O-ring resonator. The pink areas correspond to the positive resist buffer. **(d)** Graphene absorption on different lengths. The red line is a linear fit, showing graphene absorption rate. **(e)** Part of the normalized O-ring transmission spectra with 10 µm graphene width (black line) and without it (red line).

On the transmission spectra, firstly we determined the maxima due FGCs. On the second step, we chose resonance picks and fitted them by Lorentz function, which helps us to determinate resonance wavelength and full width at half maximum with high precision. Thus, we have obtained Q-factors of rings before and after graphene deposition.

The dependence of the effective absorption coefficient of graphene α_{eff} [dB/µm] can be found by the following expression:

$$\alpha_{eff} = 10\log_{10} e^{\frac{4\pi^2 R n_g}{\lambda_0 l}\left(\frac{1}{Q_a}-\frac{1}{Q_b}\right)}, \quad (1)$$

where R is ring radius (R = 117 µm), n_g is group refractive index, λ_0 is the central wavelength of the resonance peak, Q_a and Q_b are Q-factors without and with graphene, respectively, α_{eff} is the effective absorption coefficient of the structure graphene-waveguide and l is graphene length.

Thus, we determined the graphene absorption on its length (Fig 1(d)). The linear fit and extrapolation of this data allow us to find absorption coefficient per unit length of grapheme was found as α_{eff} = 0.037±0.003 dB/µm. In comparison with other articles, where α_{eff} = 0.067±0.004 dB/µm [4] and 1.26 dB/µm [5] we have a lower coefficient value, we associate this with a wider waveguide compared to other works, leading to lesser interaction of graphene and evanescent mode.

4. Conclusion

Thus, we fabricated nanophotonic devices based on graphene and characterized its optical absorption. We found α_{eff} = 0.037±0.003 dB/µm. In future work, we are going to produce fully integrated circuits with graphene including sources, modulators and photodetectors.

5. Acknowledgments

We acknowledge support of the Russian Science Foundation project 19-72-10156 (waveguide fabrication), as well as project 16-12-00045 (experimental study).

References

[1] Wang, J., Cheng, Z., & Li, X. *2018 Advances in Condensed Matter Physics*

[2] Giambra, M. A., Sorianello, V., Miseikis, V., Marconi *et al.* 2019 *Optics Express*, 15 20145

[3] Van Laere F, Claes T, Schrauwen J, Scheerlinck S *et al.* 2007 *Optics Express* 19 21–24

[4] Gruhler N, Benz C, Jang H, Ahn J-H *et al.* 2013 *Optics Express* 25 31678-31689

[5] Demongodin P, Dirani El H, Lhuillier J, Crochemore R *et al.* 2019 *APL Photonics* 7

Luminescence spectra in square resonators with a dense spectrum of photon modes interacting with exciton resonance.

A V Belonovskii[1,2], **K M Morozov**[1,2] **and M A Kaliteevski**[1, 2, 3]
[1]St-Petersburg Academic University, St. Petersburg 194021, Russia
[2]ITMO University, St. Petersburg 197101, Russia
[3]Ioffe Institute, St. Petersburg 194021, Russia

Abstract. In this work, we research structures whose characteristic sizes correspond to several wavelengths of exciton radiation in the material, and the frequency interval between the eigenmodes is comparable or smaller the value of Rabi splitting between the exciton and photon modes. The distribution of the eigenmodes of the square-shaped cavities by frequencies and Q factors is presented. The formal structure of the emission spectrum was simulated for square-shaped cavities in the case of the implementation of the strong and weak coupling regimes between exciton and photon modes.

Recently, new nanostructures grown by selective area metal-organic vapor phase epitaxy were presented in [1, 2]. Several peaks were observed in the low-temperature cathodoluminescence spectrum of these nanostructures. Such behavior can be associated with the interaction of the exciton and photon modes in these structures. These structures are characterized by large sizes (of the order of 10 wavelengths of exciton radiation in the material) and a dense spectrum of eigenmodes. In this paper, we study these structures.

For these structures, we consider the full system state, which is described by the density matrix ρ, and its evolution is determined by the equation $\partial_t \rho = \mathcal{L}\rho$ with the Lindblad terms in the Liouvillian $\mathcal{L}$, accounting for damping [3]:

$$\mathcal{L}\rho = i[\rho, H] + \frac{\gamma_0}{2}(2x\rho x^+ - x^+ bx - \rho x^+ x) + \sum_k \frac{\gamma_k}{2}(2a_k \rho a_k^+ - a_k^+ a_k \rho - \rho a_k^+ a_k) \qquad (1)$$

where $H = w_0 x^+ x + \sum_k w_k a_k^+ a_k + \sum_k g_k (a_k^+ b + a_k b^+)$, w_0 is the exciton frequency, w_k are the frequencies of cavity modes, g_k are the constants, describing the exciton-photon interactions, and $\hat{x}, \hat{c}_k$ ($\hat{x}^+, \hat{c}_k^+$) are the operators of annihilation (creation) of exciton and photons, respectively. γ_0 and γ_k are rates of damping of the emitter and the cavity respectively.

Then, the first-order correlation functions necessary for modeling the formal structure of the spectra are calculated. Finally, a spectrum is modeled for square microresonators in the case of strong and weak coupling [3]:

$$\mathrm{S(w)} = \langle a^+(w) a(w) \rangle \qquad (2)$$

This analysis will make it possible in the future to predict under what conditions it is possible to realize the strong and weak coupling between light and matter in the presence of a large number of eigenmodes of the system interacting with exciton resonance.

[1] Pozina G, Hemmingsson C, Belonovskii A V, Levitskii I V, Mitrofanov M I, Girshova E I, Ivanov K A, Rodin S N, Morozov K M, Evtikhiev V P and Kaliteevski M A 2019 *physica status solidi (b)* 00894
[2] Belonovskii A V, Pozina G, Levitskii I V, Morozov K M, Mitrofanov M I, Girshova E I, Ivanov K A, Rodin S N, Evtikhiev V P and Kaliteevski M A 2020 *Semiconductors* **54** 127
[3] Laussy F P, Valle E, Tejedor C 2009 *Phys Rev B* **79** 235325

The research of temperature instability influence of optic communication line on the phase difference a deep-sea direction finder.

S M Smirnova[1], A S Lukiyanov[2], A S Podstrigaev[2, 3], V V Davydov[1, 4], V Yu Rud[4]
[1]Higher School of applied physics and space technologies, Peter the Great Saint Petersburg Polytechnic University, Saint Petersburg 195251, Russia
[2]Scientific-Research Institute Vector OJSC, St. Petersburg, 197342, Russia
[3]Saint Petersburg Electrotechnical University "LETI", St. Petersburg, 197376, Russia
[4]All-Russian Research Institute of Phytopathology, Moscow Region 143050, Russia

Abstract. This article discusses the effect of temperature changes in the information transmission channel in fiber-optic communication lines. The results of an experimental study are shown for various cases of the effect of temperature changes on direction finder elements.

1. Introduction

At this point of time there is a great number of methods determining the location (coordinates) of various objects. These methods can be divided into three types (by the principle of the station): active, passive and combined. The combined methods are mainly used in space systems for determining the coordinates of an object on Earth or in the solar system. The active methods are mostly used in radar stations (RLS) of various locations. Passive methods are used to detect ground-based or submarine-based radio sources. To determine the sources of radio emission on air objects this method is auxiliary to RLS. The most accurate among the passive methods of direction finding are the amplitude and amplitude-phase. For ensure high accuracy in phase direction finding method need to create the large base between receiving antennas (hundreds of meters). In addition, the equipment for receiving and processing information should also be located at a considerable distance from the antennas.

For high accuracy in determining the coordinates of the desired object, it is best to use fiber-optic communication lines (FOCL). Using the FOCLs is a solution the problem of large signal losses during the transmission of information that appear when using microwave cables [1-3]. The main negative factor for the use of VOLS is the temperature. In the transmitted optical signal the change of temperature leads to a phase shift (foray) $\delta\varphi$ [4]. This leads to a change in temperature of the fiber, which causes an additional phase shift $\delta\varphi$ in optic fiber. In case of large value of $\delta\varphi$, the difficulties arise when using time-phase and amplitude-phase method of direction finding for object coordinates determination. Therefore, for each design of radio direction finder it is necessary to investigate the effect of temperature on phase shifts during transmission of the microwave signal in the optical line.

2. Experimental research of temperature difference influence on the phase difference in the optical channel and results discussion.

The features of the equipment operation in the direction deep-sea finding station in the experimental setup for the research developed by us have taken into account. These features are related to the facts, that depending on the deep-sea radio direction finder design and the conditions of its location in a

number of radio direction finder units, it is not possible to provide a thermal insulation, including optical fiber.

With the use of the experimental setup, we studied the effect of temperature on the phase difference of the two optical channels. In addition, the experimental setup allows us to investigate the intrinsic noise dependence of the entire optoelectronic tract from temperature and the dependence of the transmission coefficient of FOCL on the frequency of the microwave signal for different temperatures. In figure 2 as an example is presented the dependence of microwave signal phase advance δφ in optic channels from temperature change only for FOCL or for all equipment of optoelectronic tract.

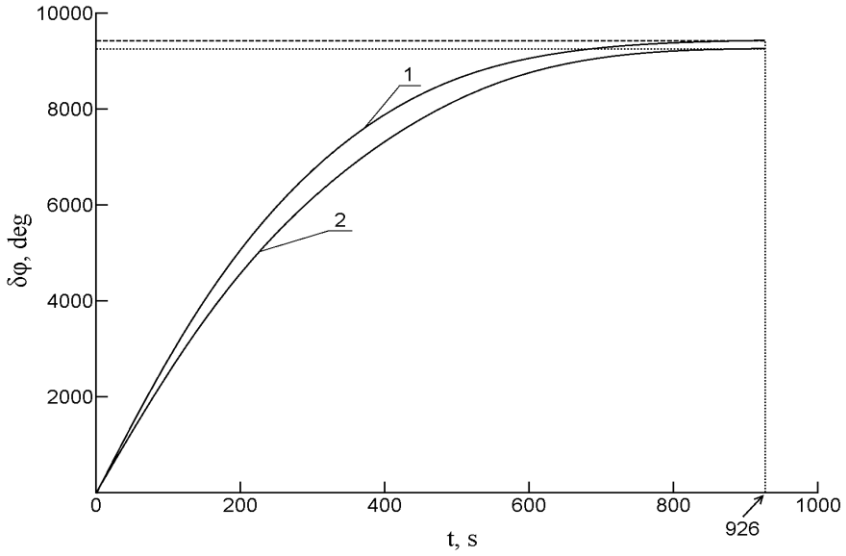

Figure 1. Dependence of phase incursion on time. Graph 1 and 2 correspond to the following temperature changes from 284 K to 294 K: 1 - the temperature of only the fiber optic link changes, 2 - the temperature of the entire equipment changes.

Analysis of the results shows that the foray δφ for each of the channels does not significantly differ from each other, if the FOCL is placed side by side in a single retractable probe. The temperature difference in different FOCL must not exceed 0.2 K in the finder in a few hours.

3. Conclusion

The obtained research results show that long-term significant temperature changes at a frequency of 18 GHz (wide band diaper) do not create a phase difference of more than 12 degrees between channels [4]. With decreasing frequency the phase difference is reduced accordingly. The resulting phase difference is acceptable for rough direction finding system that performs instant radio review space.

References

[1] Friman, R K 2012 *Fiber-optic communication systems* (NJ. Wiley-Inter science)

[2] Karim A and Devenport J 2008 *J. Lightwave Technol.* **26** 2718-2724

[3] Urick V J, Diehl J F, Draa M N, McKinney J D and Williams K J 2012 Proc. SPIE 8259, RF and Millimeter-Wave Photonics II p. 825904

[4] Podstrigaev A S, Davydov R V, Rud' V Yu and Davydov V V 2018 *Lecture Notes in Computer Science (including subseries Lecture Notes in Artificial Intelligence and Lecture Notes in Bioinformatics)* **11118 LNCS** 624-630

Laser action in Ag-catalyzed ZnO grown on *r*-sapphire

A P Tarasov[1,2], **C M Briskina**[1], **V M Markushev**[1], L **A Zadorozhnaya**[3], **I S Volchkov**[3]
[1]Kotel'nikov Institute of Radioengineering and Electronics of RAS, Moscow 125009, Russia
[2] Moscow Regional Research and Clinical Institute named after M.F. Vladimirsky, Moscow 129110, Russia
[3]FRSC "Crystallography and Photonics" RAS, Moscow 119333, Russia

Abstract. Edge emission of ZnO grown on *r*-sapphire using catalysis with Ag under- and interlayer was studied. The synthesized structures showed lasing of different nature depending significantly on ZnO morphology. Random lasing was observed from ZnO nanowalls grown on Ag-coated substrates. In the case when ZnO was regrown on top of ZnO with Ag coating, lasing is attributed to the optical modes of individual crystals.

1. Introduction

Silver thin films and nanoparticles (NP) are known to significantly influence the spontaneous and stimulated emission properties of ZnO via surface plasmon resonance in the ZnO near band edge region [1,2]. However, this influence is determined by various factors, such as shape and size of NPs, ZnO-metal distance, excitation fluence, not mention that such coatings deteriorate in the air ambience [2-4]. This forces one to perform additional control during fabrication, which complicates it and increases its cost.

On the other hand, the effect of Ag on the ZnO optical properties may be indirect, in particular, by changing morphology of ZnO during its growth. This, avoiding above-mentioned difficulties, may result in significant changes in ZnO emission characteristics. In the present work, we show this on the example of ZnO structures grown on *r*-sapphire.

2. Experimental

ZnO was grown from gaseous phase. Three types of samples were fabricated and compared. The samples of the 1st type (T1) are ZnO on bare substrates. The 2nd type ones (T2) were grown on substrates coated with 8 nm thick Ag film (ZnO/Ag). The part of T1 samples were coated by 8 nm Ag with further ZnO regrowth. These ZnO/Ag/ZnO structures are of the 3rd type (T3). Excitation of ZnO emission was performed by the 3rd harmonics of pulsed Nd:YAG laser.

3. Results and discussion

Fig.1 shows SEM-images of the samples. The first thing we noticed is T2 morphology in form of vertically aligned nanowalls that was significantly different from those of T1 and T3. Further, morphologies of T1 and T3 were similar only at first glance. Both structures consist of disordered with respect to the substrate crystals of different shapes and sizes. However, many crystals of T1 are very thin and resembles ZnO nanosheets, while crystals of T3 are mostly rather large with some of them having hexagonal shape.

The morphology change reflected significantly on emission properties of the samples. In this respect, the main difference of T2 and T3 from T1 is the demonstration of laser action. Moreover, lasing behaviors differ in T2 and T3. Under slight shift of the excitation spot on the sample, laser modes change in T2 and preserve their positions in T3 under one pulse excitation. While the spectral positions and intensity ratios of the laser peaks were constant in T3, they vary somewhat in T2 from shot to shot at the constant excitation level. This results in smoothing of the T3 lasing profile under signal averaging over several excitation pulses, while it retains its shape in the case of T3. According to spectral behavior, we attribute laser action in T2 to random lasing, while in the case of T3 lasing is excited at the eigenmodes of individual crystals. Fig. 2 shows averaged lasing spectra of T2 and T3.

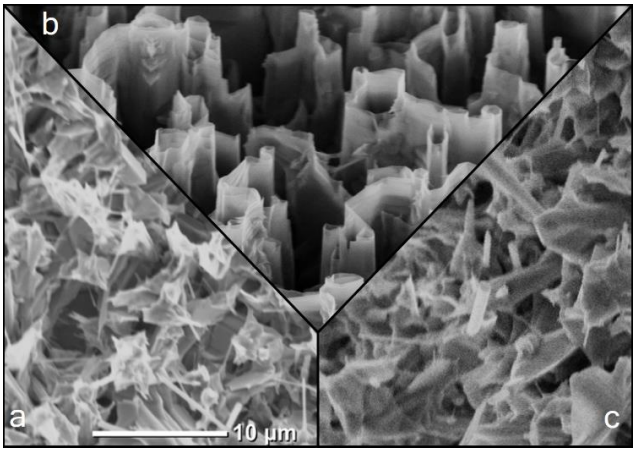

Figure 1. SEM-images of T1 (a), T2 (b), T3 (c).

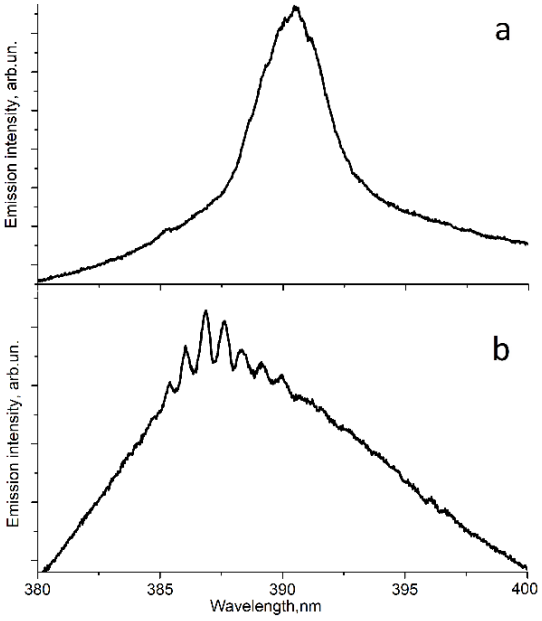

Figure 2. Lasing spectra of T2 (a) and T3 (b).

Well-developed morphology of T2 allowed achievement of rather low random lasing thresholds of 2 – 4 mJ/cm^2. This allows us to appraise the possible benefits of such structures for developing intense near-UV light sources based on them. In the case of T3, we suggest that lasing is from stand-alone well-faceted crystals. We assume that lasing in this case is of Fabry-Perot type since shape and behavior of lasing spectra as well as the range of lasing thresholds were similar with those observed by us in [5] for Fabry-Perot lasing.

4. Conclusions

To sum up, we showed that Ag being used as a catalyst for growth of ZnO can significantly change its morphology and emission properties. In the case of ZnO/Ag growth, ZnO nanowalls were formed, which exhibited random lasing. Lasing from individual crystals was observed in the case of ZnO/Ag/ZnO structures.

References

[1] Abiyasa A P, Yu S F, Lau S P, Leong E S, Yang H Y 2007 *Appl. Phys. Lett.* **90** 231106
[2] Cheng P, Li D, Yuan Z, Chen P, Yang D 2008 *Appl. Phys. Lett.* **92** 041119
[3] Rumyantsev S, Tarasov A, Briskina C, Ryzhkov M, Markushev V, Lotin A 2016 *J. Nanophoton.* **10** 016001
[4] Lawrie B J, Haglund R F, Mu R 2009 *Opt. Exp.* **17** 2565
[5] Tarasov A P, Briskina Ch M, Markushev V M, Zadorozhnaya L A, Lavrikov A S, Kanevskii V M 2019 *JETP Lett.* **110** 739

Double-Resonance Plasmonic Excitation for Sensing Application

S V Tomilin, A V Karavaynikov, O A Tomilina, V N Berzhansky
Physics and Technology Institute, V.I. Vernadsky Crimean Federal University, Crimea, Simferopol, 295007, Russian Federation

Abstract. In paper the results of modeling, synthesis and research of a two-resonance scheme for surface plasmon-polaritons (SPP) excitation are presents, and the modelling analysis results of the possibilities for using it as a sensitive element of a plasmonic sensor. It's demonstrated the possibility for excitation of SPP resonances using the Kretschmann and Otto schemes on one device, and the structural parameters of such device are optimized. It's considered the possibilities for using the proposed double-resonance scheme as an individual SPP-sensor and as a sensitive element of a plasmonic biosensor.

1. Introduction

The operation principle of sensors on surface plasmon polariton resonances (SPPR) is based on the physical effect of changing the resonant frequency of surface plasmon polariton waves depending on the dielectric constant of the environment which adjacent to a sensitive metal (plasmon) layer [1]. There are two classical schemes of prismatic excitation of surface plasmon-polariton waves: the Kretschmann scheme and the Otto scheme. The structure that allows combining Kretschmann and Otto schemes in one device has been developed by the authors of this article. A feature of this structure is that between the prism and the plasmonic metal film an additional (buffer) layer of a transparent dielectric is presents and it has a refractive index less than that of the prism, but bigger than that of the environment. So, at small angles of the light beam incidence, the effect of total internal reflection (TIR) occurs at the interface of the dielectric layer and the environment, and a plasmon-polariton wave is excited on the external surface of the plasmonic film according to the Kretschmann scheme. At large angles of the light beam incidence, the TIR effect is observed at the interface between the prism and the dielectric layer, and a plasmon-polariton wave is excited on the internal surface of the plasmonic film according to the Otto scheme. For the described structure, two resonances (according to Kretschmann and Otto) will be observed on the angular reflectometry curve. In this case, the condition of resonance by Kretschmann and the appropriate resonant angle will significantly depend on the dielectric properties of the environment. This makes it possible to realize a sensor system for detecting changes in the properties of this environment. Otto resonance, on vice versa, depends mainly on the properties of the dielectric buffer layer and will changed weakly. Such resonant peak can be used as a standard peak when compared with a change in the position of the Kretschmann peak, which will improve the accuracy and stability of the double-resonance scheme in the sensory application compared to a single-resonance scheme.

2. Experimental technique and results

The developed double-resonance scheme is realized on the basis of a structure including a rectangular prism from a single crystal of gadolinium gallium garnet $Gd_3Ga_5O_{12}$ (GGG_{prism}) with a high refractive index $n = 1.960$ for $\lambda = 632.8$ nm, on which a dielectric buffer layer with a refractive index less than that of the prism and more than that of the environment (quartz SiO_2, $n = 1.456$ for $\lambda = 632.8$ nm) is deposited. An Au plasmonic metal film with a purity of no worse than 99.95% is deposited over the buffer layer (Fig. 1a).

The numerical modeling of the structure of the double-resonance SPPR sensor, and also the optimization of its structural parameters and operating regimes were carried out using the WinSpall software. The structural parameters were optimized in the model by varying the thicknesses of the buffer and plasmonic layers, and the conditions for the excitation of both types of resonances were analyzed when changing the parameters of the external environment and the external sensitive ligand layer (biosensor version of model).

The model optimization of the parameters showed that for the proposed scheme $GGG_{prism}/SiO_2/Au$, the optimal thickness of the SiO_2 buffer layer is 200 – 220 nm, and the Au plasmonic layer thickness is 45 – 50 nm.

Modeling the operating conditions of the double-resonance scheme as a plasmonic sensor showed that a change in the real part of the environment dielectric constant ε_{env} by 0.05 leads to a shift in the Kretschmann resonance peak by 2 deg, while the Otto peak practically does not shift and it can be used as a standard in the scheme of comparing the position of both peaks. Modeling the operation of a plasmonic sensor with an external sensitive layer (ligand) $GGG_{prism}/SiO_2/Au/Lg$ showed that the using of a ligand layer above 200 nm is redundant, and the change in the real part of the dielectric constant of the layer ε_{Lg} leads to a change in the position of the resonance peaks similarly compared to a change of ε_{env}.

For verification the conditions of the plasmon-polariton resonances excitation, a double-resonance structure GGG_{prism}/SiO_2(grad h)/Au(50) was synthesized with a gold layer thickness of 50 nm and a gradient of the thickness of buffer layer h_{SiO2}. The thickness of the h_{SiO2} buffer layer varied from 0 to 600 nm; and the investigation was carried out at various points of the gradient. The SiO_2 layer was deposited by ion-reactive sputtering in vacuum, the Au plasmonic film was obtained by thermal evaporation in vacuum [2].

On Fig. 1b the resonance curve which obtained on the range with 220 nm thickness of buffer layer is presented.

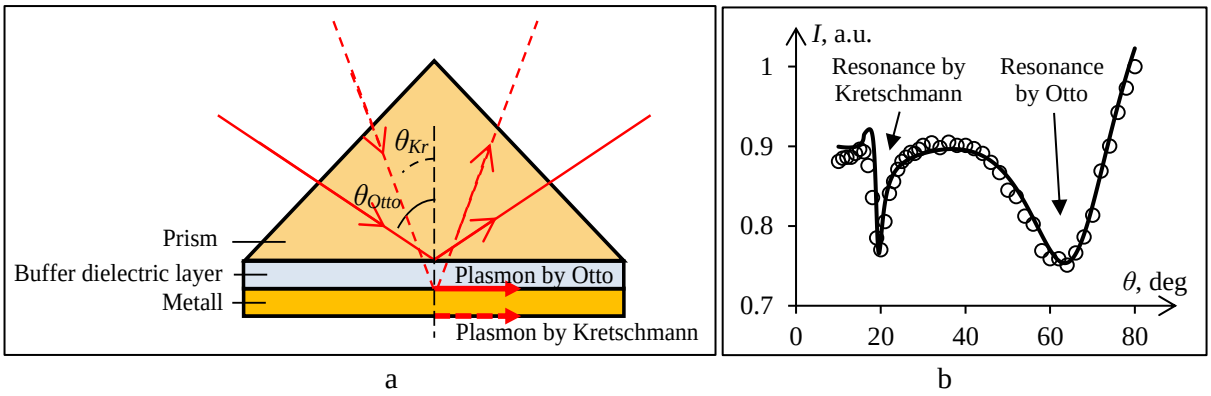

Figure 1. Double-resonance scheme for SPPR excitation: a – structure of double-resonance scheme, b – resonance curve (circles – experimental data, line – modelling curve).

At a buffer layer thickness h_{SiO2} = 220 nm a clear peak of plasmon-polariton resonance by Otto scheme is observed at an incidence angle 64 deg of the exciting beam. The resonant angle of the peak by Kretschmann is 19.5 deg. The results which presented in Fig. 1b clearly demonstrate good agreement between the experimental data and modelling calculations.

3. Conclusion

So, the possibility of creating a double-resonance scheme for SPPR excitation, in which the Kretschmann and Otto excitation schemes are realized on the same device, was demonstrated theoretically and experimentally in this work. A modelling optimization of the parameters of a double-resonance scheme was carried out, and modelling calculations were carried out on the use of the scheme as a sensitive element of a plasmonic sensor and a biosensor.

4. Acknowledgments

This work was financially supported by the State Council of Crimean Republic in the framework of the grant for young scientists of the Crimea (resolution № п66-2/20 from 04.02.2020) and by the Russian Ministry of Science and High Education, Megagrant project N 075-15-2019-1934.

5. References

[1] Mejia-Salazar J.R., Camacho S.A., Constantino C.J.L., Oliveira O.N. An. Acad. Bras. Cienc. 2018, **90**, 779.

[2] Tomilin S V, Yanovsky A S. Journal of Nano- and Electronic Physics. 2013, **5, 3,** 03014.

The Investigation of Spectral Shift of Localized Plasmonic Resonance

O A Tomilina, V N Berzhansky, S V Tomilin
Physics and Technology Institute, V.I. Vernadsky Crimean Federal University, Crimea, Simferopol, 295007, Russian Federation

Abstract. In paper the investigation results of dielectric environment influences on spectral shift of localized plasmonic resonance in a system of self-assembled metallic nanoparticles was introduced. It was shown, that the value of spectral shift of localized plasmonic resonance has a linear proportion towards the changes of environment refractive index. For investigated plasmonic system of self-assembled Au nanoparticles the coefficient of proportionality was determined.

1. Introduction

Discrete conducting nanoobjects and nanostructured materials are very perspective materials for creating sensory plasmonic structures [1, 2]. The interaction of the electromagnetic field with metallic nanoobjects is determined by the properties of their electronic subsystem, which is limited by spatial restrictions. In conducting nanoparticles with a band nature of the energy spectrum, the conduction electrons are plasma with a certain resonant frequency of plasma oscillations (plasmons) [3]. The absorption of quanta of electromagnetic radiation for resonant excitation of plasmons can be observed on transmission spectra in the form of "dips" at the resonant frequency. In this case, the dielectric environment of the conducting nanoobject has a significant effect on its properties, in particular, on the processes of transfer and relaxation of energy excitations, and as a consequence, on a change in the conditions of localized plasmon resonance (LPR) [4]. Therefore, on the basis of various types plasmonic systems the sensors are actively developed and studied to detect changes in the properties of dielectric media, including the medical and biological application. Based on the foregoing, the great fundamental and practical importance have investigations of the influence of the dielectric environment on the shift of the LPR resonance frequency in metallic nanoparticles.

2. Experimental technique and results

In the present work, as the investigated plasmonic system are used self-assembled gold nanoparticles (Au (NP)) which formed on the surface of the dielectric substrate by thermal activated granulation of the original ultrathin gold film. This design is the simplest and cheapest for realization, and the placing of plasmonic particles on a carrier substrate makes it easy and convenient to change their dielectric environment without destroying the integrity of the system, and also allows the use of similar plasmonic systems in more complex composites and structures.

In the experimental part of the work, a plasmon system was synthesized in the form of self-assembled gold nanoparticles $Au_{(NP)}$ on a substrate of single-crystal gadolinium-gallium garnet $Ga_3Gd_5O_{12}$ (GGG). Nanoparticles $Au_{(NP)}$ have been obtained by thermal activated granulation of a continuous gold film with thickness of 3 nm (annealing in air at 950 ° C during 10 min). The initial Au/GGG film has been synthesized by method of thermal evaporation in vacuum (residual pressure no more than $4 \cdot 10^{-4}$ Pa) on a substrate at temperature of 150°C.

For investigation, the plasmonic system was placed in a cell which was filled with a transparent dielectric medium. Isotropic materials with different dielectric constant ε_{env} were used as a dielectric medium such as: air, distilled water, an aqueous NaCl solution (with a mass percentage of 4.17%, 7.14%, 11.11%) and glycerin (in increasing order). In addition, a nanocomposite sample was prepared

in which a system of self-assembled Au nanoparticles was coated by a Bi: YIG (bismuth-substituted ferrite garnet) with thickness of 100 nm.

The results of investigation the influence of the dielectric environment on the optical transmission of the plasmonic system $Au_{(NP)}$/GGG are presented on Fig. 1. For convenience of observing the spectral shift of plasmonic resonance, the figure shows the spectral dependences of the first derivative on the transmittance $dT/d\lambda$, where the intersection of the curve with the abscissa axle corresponds to the resonant wavelength of the LPR [5].

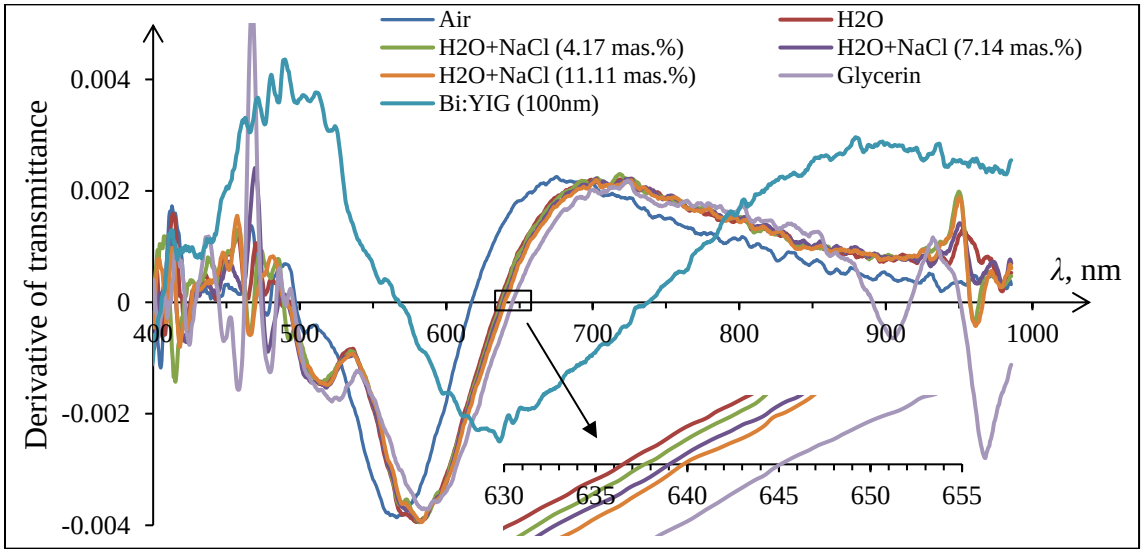

Figure 1. Spectral dependence of derivative of the transmittance $dT/d\lambda$.

It can be seen that an increase of the environment dielectric constant ε_{env} leads to a “red" shift of plasmonic resonance. The analysis showed that the dependence of the spectral shift of the LPR on the refractive index of the environment is close to linear ($\lambda_{LPR} = 63.64 \cdot n_{env} + 552.68$). Those. for the studied plasmonic system $Au_{(NP)}$/GGG, the proportionality coefficient of the λ_{LPR} shift with respect to the change in n_{env} is 63.64 nm, i.e. a change in the refractive index by 0.016 leads to a spectral shift of the LPR by 1 nm.

3. Conclusions

Thus, it was shown in the work that an increase in the dielectric constant of the environment leads to a red spectral shift of the localized plasmonic resonance in the system of self-assembled Au nanoparticles. The dependence of the shift of the LPR resonant wavelength on the refractive index of the environment is linear, which allows the creation of plasmonic sensors based on plasmon self-assembled nanoparticles.

4. Acknowledgments

This work was financially supported by the State Council of Crimean Republic in the framework of the grant for young scientists of the Crimea (resolution № п66-2/20 from 04.02.2020) and by the Russian Ministry of Science and High Education, Megagrant project N 075-15-2019-1934.

5. References

[1] Ch. Zhuang, Y. Xu, N. Xu, J. Wen, H. Chen, Sh. Deng. Sensors, 2018, **18**, 3458.
[2] M.I. Stockman. Applied Optics, 2015, **348**, **6232**, 287.
[3] T. Chung, S.-Y. Lee, E.Y. Song, H. Chun, B. Lee. Sensors, 2011, **11**, 10907.
[4] K.L. Kelly, E. Coronado, L.L. Zhao, G.C. Schatz. J. Phys. Chem. B. 2003, **107**, 668.
[5] K. Kolwas, A. Derkachova. Opto-Electr. Rev. 2010, **18**, **4**, 421.

Optically tunable terahertz polarization-selective planar metamaterial based on multi-layered graphene

M Masyukov, A Vozianova, A Grebenchukov, K Gubaidullina, A Zaitsev, M Khodzitsky
Terahertz Biomedicine Laboratory, ITMO University, St. Petersburg 199034, Russia
E-mail:msmasyukov@itmo.ru

Abstract. In this paper we firstly propose the planar metamaterial, or metasurface, based on multi-layered graphene. The influence of optical pumping on polarization selectivity of the metasurface was studied. It was shown that polarization state of the transmitted wave may be changed by optical pumping of multi-layered graphene. A change in ellipticity angle of 20 degrees is shown at the frequency 0.76 THz. The present work paves the way for the realization of terahertz components capable of active polarization manipulation.

Introduction

The polarization state is an important characteristic of light, accordingly, converting and manipulating the polarization of light are crucial for many potential photonics applications. The weakness of polarization manipulation provided by natural materials can be overcomed by chiral metamaterials. Although chirality has been known for a long time, recently chiral structures are the subject of study both for applied and fundamental electrodynamics. Chirality is a property of asymmetry when an object is distinguishable from its mirror image by any rotations. Chiral metamaterials have a huge potential to achieve the necessary polarization effects, hence they provide the basis for ultracompact polarization components. The integration of materials with tunable properties, such as graphene, allows the creation of universal devices for polarization states control in terahertz frequency range based on metamaterials. Since graphene monolayer weakly interacts with pumping infrared radiation, we decided to use the multi-layered graphene [2] in order to get rid of this drawback and to increase the efficiency of THz wave polarization control.
In this work, we firstly propose MLG-based chiral planar metamaterial with tunable transmission and polarization properties under the impact of optical pumping.

1. The structure under the investigation

The sketch of the unit cell of the studied metasurface is shown in Figure 1 [3]. The metasurface consists of an array of geometrically identical multi-layered graphene (MLG) chiral rosettes and gold ones, mirrored relatively to each other and placed on the top and bottom sides of the TPX (ε=2.1) substrate with thickness of 80 μm, respectively. The inner diameter of the rosette petal D is 120 μm, while its width is w=38 μm, the turnaround angle is $\alpha = 265°$.

2. Results

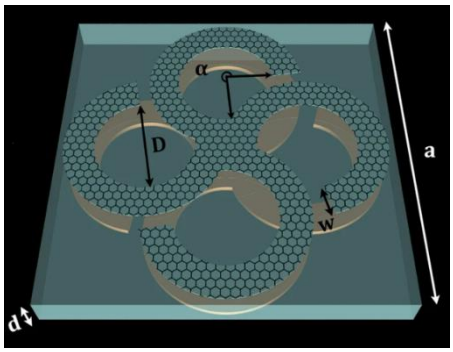

Figure 1. The unit cell of the metasurface.

The numerical simulations were performed in CST Microwave Studio, which is based on FEM method. Multi-layered graphene was simulated using experimental data obtained in THz-TDS measurements with optical pumping of continuous wave 980 nm laser. Five different values of optical pumping power were applied.

Using numerically obtained transmission coefficients for left-handed (T_{--}) and right-handed (T_{++}) circularly polarized waves, one can calculate the ellipticity angle η of the radiation, transmitted through the metasurface, as follows (Figure 2):

$$\eta = \frac{1}{2} arcsin\left(\frac{|T++|^2 - |T--|^2}{|T++|^2 + |T--|^2}\right), \quad (1)$$

The value of +45° of ellipticity angle corresponds to right-handed circularly polarized wave, −45° is equal to left-handed circularly polarized wave, and 0° reports about linearly polarized wave.

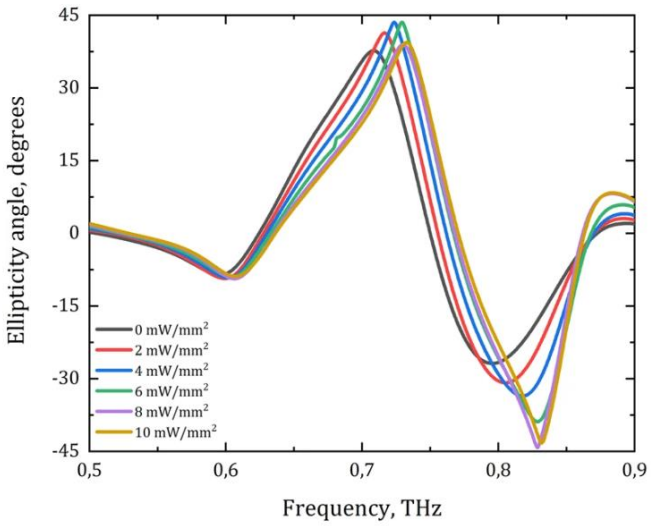

Figure 2. The ellipticity angle spectra depending on the optical pumping power.

It should be noticed that frequencies of maximal and minimal values are shifted at the value of $\Delta\nu = 300$ GHz by the increasing OP. The OP-based tunability shows a great value of ellipticity angle tunability, achieving $\Delta\eta = 20°$ at the frequency of $\nu = 0.76$ THz.

3. Conclusions

In this paper, we have proposed the polarization-selective tunable chiral metasurface. After the propagation through the metasurface, in general linearly-polarized incident terahertz wave is transformed into elliptically-polarized one, or almost to circularly-polarized wave at certain frequencies. A change in ellipticity angle of 20 degrees is shown at the frequency 0.76 THz.

References

[1] Yan F, et al. 2013 *Journal of infrared, millimeter, and terahertz waves*, **34**(9), 489-499.
[2] Grebenchukov A, et al. 2020 *Optics Communications* 459, 124982.
[3] Masyukov M, et al. 2020 *Scientific Reports* **10** 3157

Towards an efficient GST-based nonvolatile optical memory

D S Korolev[1,2], R T Minnulin[1,3], M E Makarov[1], A A Sapegin[1,3], K V Sidorenko[2], A A Nikolskaya[2], A N Mikhaylov[2], Y I Chigirinsky[2] and M Yu Barabanenkov[1,4]

[1]Molecular Electronics Research Institute, 12/1, 1st Zapadnyi Proezd, Moscow, Zelenograd, 124460, Russia
[2]Lobachevsky University, 23/3 Gagarin prospect, Nizhny Novgorod, 603950, Russia
[3]Moscow Institute of Physics and Technology, Dolgoprudny, 141701, Russia
[4]Institute of Microelectronics Technology RAS, Chernogolovka, 142432, Russia

Abstract. The results of modeling the reflection and transmission spectra of a diffraction grating from a Ge-Sb-Te (GST) compound lying on an "silicon-on-insulator" (SOI) single-mode waveguide structure are presented. The optical parameters for modeling the spectra were obtained from experimental measurements of GST films deposited by the magnetron sputtering. The optimal parameters of the diffraction grating are determined, which make it possible to reduce the energy budget for switching the GST phase due to the excitation of guided mode in the diffraction grating.

1. Introduction

The development of technology for creating traditional devices of modern silicon electronics is currently faced with limitations associated with the problems of scaling devices to sizes of the order of a few nanometers [1]. It can be replaced by a dynamically developing field of silicon nanophotonics, which allows to increase the speed of integrated circuits due to a significant increase in the signal transmission speed. One of the important tasks required to implement fully photonic integrated circuits is the creation of non-volatile optical memory elements. The implementation of such memory became possible due to the development of phase change materials (PCM), which have the ability to quickly reversibly switch between amorphous and crystalline states with significantly different electrical and optical characteristics [2]. A well-established material for optical applications is the Ge-Sb-Te (GST) compound, which is used as an active material in phase-change memory (PCM) and optical disks. However, the combination of such materials with silicon-based waveguides for the implementation of fully optical memory for use in radio photonics devices has been clearly studied insufficiently. In this work, we present the results on the formation of GST layers by magnetron sputtering with a variation in the deposition parameters, as well as the calculation of the transmission and reflection spectra of a GST diffraction grating on an SOI waveguide.

2. Experimental and simulation details

The experimental samples were 10-100 nm-thick films of the $Ge_2Sb_2Te_5$ compound deposited by RF magnetron sputtering at room and elevated temperature on silicon, quartz, and sapphire substrates. The optical characteristics of the samples were studied using optical transmission and spectroscopic ellipsometry, the morphology of the films was studied by atomic force microscopy, and the structure of the samples was studied by electron diffraction.

The transmission and reflection spectra were simulated based on the method of the Riccati equation using the original program code.

3. Results and discussion

Creating an element of non-volatile optical memory requires both testing the technology for their synthesis and a theoretical description of the processes occurring in them. Various possible implementations of an optical memory element include the deposition of a GST film on the surface of a silicon waveguide, followed by the creation of the desired relief using lithographic methods. In particular, the creation of diffraction gratings from GST of various dimensions, which allows to increase the absorption of electromagnetic field energy and to provide less power consumption of the memory cell, is an original approach. To simulate the reflection and transmission spectra from a GST diffraction grating, it is necessary to know the optical characteristics of the deposited films.

Let us consider the features of GST films obtained by magnetron deposition. GST films were deposited on the surface of silicon, quartz and sapphire. The deposition of films at room temperature leads to the formation of films with an amorphous structure. Heating the deposited film leads to its crystallization. However, a change in the conditions for the synthesis of films can lead to a change in the initial structural state. In particular, the deposition of a GST film at elevated temperatures (~ 400-500 °C) leads to the appearance of a polycrystalline structure of the samples.

The data obtained in the study of the optical characteristics of the deposited films can be used in theoretical modeling of the propagation of light in GST-based diffraction gratings. Based on these data, the reflection and transmission spectra were calculated for GST diffraction gratings on a SOI waveguide. The spectra obtained, as well as the spatial distribution patterns of the electromagnetic field, make it possible to determine the grating parameters at which the guided mode is excited in the lattice itself, which leads to an increase in the absorption of electromagnetic field energy and a decrease in cell energy consumption.

4. Acknowledgments

This study was supported by the Russian Foundation for Basic Research, project 19-29-03040.

References

[1] Krasnikov G Ya, Zaitcev N A, *Nano and Microsystem Technique*, **1** (102), 2–5 (2009) (*in Russian*)
[2] Krasnikov G Ya, Zaitcev N A, Krasnikov A G, *Nano and Microsystem Technique*, **4** (177), 60–64 (2015) (*in Russian*)

Optimal fiber optic scheme for sub-SQL quantum receiver realization

M. Shcherbatenko[1], **M. Elezov**[1], **D. Sych**[1,2,3], **G. N. Goltsman**[1,4]
[1]Moscow State Pedagogical University, Moscow, Russia
[2]P. N. Lebedev Physical Institute, Russian Academy of Sciences, Moscow, Russia
[3]QRate LLC, Moscow 121353, Russia
[4]National Research University Higher School of Economics, Moscow, Russia

Abstract. One of the main parts of the quantum receiver is the optical scheme. We developed and tested several optical circuits based on different types of interferometers. On the basis of the obtained data, it can be concluded that the most suitable is the scheme based on the Mach-Zehnder interferometer.

1. Introduction

Increasing the precision of optical measurements is an actual task of modern science. Although, the limit of the precision of such measurements (Helstrom bound) [1] was determined back in the 60-s of the last century, in practice, it has not been possible to approach it so far. Traditional coherent optical receivers based on homodyne detection operate at the shot-noise limit, which leaves a clear gap in the error rate well above the Helstrom bound. To date, several strategies have been developed to improve the accuracy of signal measurement above the standard quantum limit (SQL) or shot noise limit. One of the first, a strategy was proposed using optical bias to completely nulling one of the states [2]. If the case of binary phase-shift keying (BPSK) is considered, the discrimination strategy is to null one of the states by adding an optical displacement of equal amplitude and different in phase by π. To realize the extreme accuracy of measurements in practice, it is necessary to have a high-efficiency single-photon detector integrated with a high-performance interference optical scheme. In this article, we consider optical schemes that are potentially suitable for implementing a quantum receiver. All these schemes are based on optical fibers and fiber components, since the fiber implementation is closest to application in practical devices. Realization realistic measurement strategies to attain the Helstrom bound is of utmost importance for high-precision applications, long-distance free-space and optical fiber communication, gravitational wave detection, and optical sensing in biology and medicine, to name a few.

2. Experimental setup and results

The efficiency of the optical scheme was evaluated according to two important characteristics. The first is high interference extinction. For this, high mode matching must be ensured. Second, high temporary stability, i.e. the receiver must maintain high performance for the longest time. There are certain specifics in working with fiber optic interferometers. It is the temperature expansion of the fiber, which results in phase instability and polarization distortions due to fiber deformation and refractive index change. Also, parasitic effects associated with vibration and acoustic exposure. To solve these problems, it is necessary to select the optimal interference scheme with a minimum set of fiber components. In this paper, we have considered three different interferometric schemes (Fig. 1).

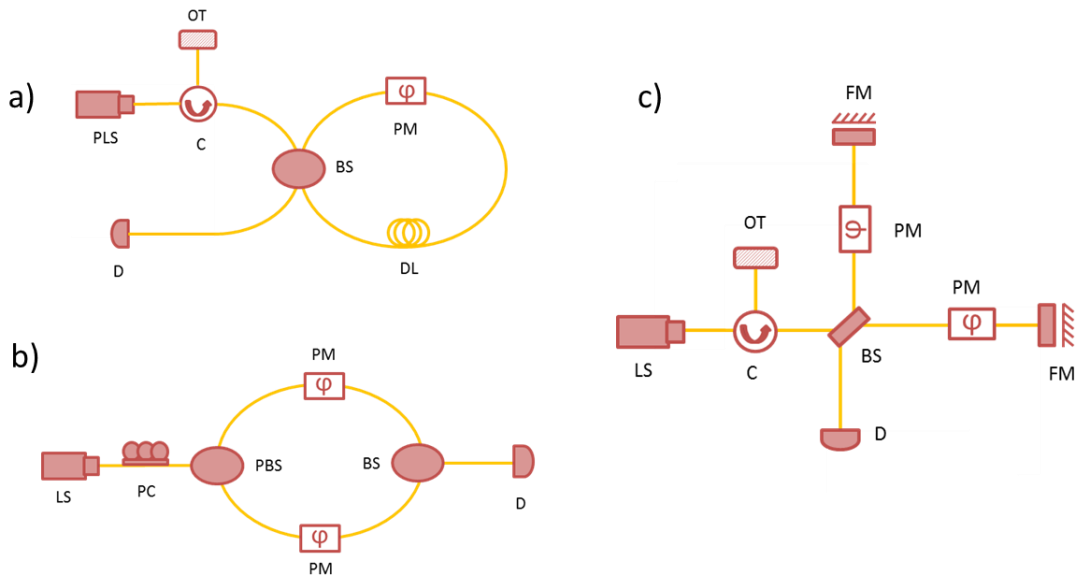

Figure 1 (a, b, c). (a) Sagnac-based scheme; **(b)** Mach-Zehnder-based scheme, **(c)** Michelson-based scheme. PLS – pulse laser source, LS – laser source, D – detector, BS – beam splitter, PBS – polarization beam splitter, PC – Polarization controller, PM – phase modulator, DL – delay line, C – circulator, FM – Faraday mirror, OT – optical terminator

Scheme based on the Sagnac interferometer (Fig. 1a). Due to the fact that the signal and the local oscillator pass through the same optical path, phase and polarization stability is achieved. For this scheme, we obtained a low extinction value (about 13 dB). This is due to the short coherence time of the pulsed source. The use of such a circuit is limited, since it only works in pulsed mode.
Scheme based on the Mach-Zehnder interferometer (Fig. 1b). This scheme looks most promising. It can operate both in pulsed and continuous mode. In continuous mode, we were able to obtain an interference extinction about 30 dB. However, when working with this scheme, the greatest number of problems occurs. The scheme requires the use of polarization maintaining optical fiber components, which increases the cost of the system. To achieve acceptable temporal stability (few minutes), it is necessary to thermally and acoustically stabilize the circuit.
Scheme based on the Michelson interferometer (Fig. 1c). The scheme, like the previous one, works both in pulsed and continuous mode. Using Faraday mirrors in each of the arms of the interferometer allows you to get rid of polarization distortions, which makes it possible to use conventional single-mode fiber. To achieve acceptable temporal stability, it is necessary to thermally and acoustically stabilize the circuit. This allowed achieving phase stability in time in a few minutes. In continuous mode, we were able to obtain an interference extinction about 23 dB.

3. Conclusion

Having tested several optical schemes, we came to the conclusion that the most suitable for the implementation of a quantum receiver is a scheme based on the Mach-Zehnder interferometer. The scheme has the greatest extinction (about 30 dB) and allows us to obtain acceptable temporal stability.

4. Acknowledgments

We acknowledge support of the Russian Science Foundation grant No.17-72-30036.

References

[1] C. W. Helstrom, Inf. Control 10, 254 (1967).
[2] R. Kennedy, MIT Res. Lab. Electron. Quart. Prog. Rep. 108, 219 (1973).

A research of the photoresponse of graphene produced by chemical vapor deposition

A V Babichev[1], **A A Vasiliev**[1], **K Yu Shubina**[1], **A A Blokhin**[2], **E I Moiseev**[1,3], **S A Kadinskaya**[1], **N V Kryzhanovskaya**[1,3], **S A Blokhin**[2], **S I Troshkov**[2], **I S Mukhin**[1]

[1]Saint Petersburg National Research Academic University of the Russian Academy of Sciences, St. Petersburg 194021, Russia
[2]Ioffe Institute, Saint Petersburg 194021, Russia
[3]National Research University Higher School of Economics, Saint Petersburg 190008, Russia

Abstract. In this work, the conditions were optimized for the fabrication of a dielectric microresonator in the spectral range of 850 nm. A low surface roughness of a distributed Bragg reflector and a high reflection coefficient were demonstrated. The conditions for the transfer and fabrication of mesas based on graphene produced by chemical vapor deposition were optimized. The reflection spectra and the value of graphene photocurrent at local optical pumping were measured.

1. Introduction

In comparison with photodetectors based on A3B5 compounds [1], lately there has been considerable interest in new types of photodetectors including those based on graphene. Due to its short interaction length, graphene only absorbs 2.3% of light. To the present time, several approaches have been presented for improving the absorption of graphene, the main of which are the use of plasmonic nanostructures, the use of nanoparticles, the integration of graphene in a waveguide configuration, the fabrication of doped graphene nanoscale discs, the generation of graphene-dielectric superlattices, the integration with photosensitive materials (quantum dots), and the fabrication of a resonant photodetector. Graphene produced by chemical vapor deposition demonstrates high structural quality and can be grown on a big area [2].

In the report, the results will be presented of the fabrication and research of the optical characteristics of photodetector structures that are based on graphene produced by chemical vapor deposition (CVD).

2. Experiment details

Fig. 1 shows a schematic image of a dielectric microresonator with a spectral range of 850 nm that consists of a dielectric DBR based on 10 pairs of quarter-wave layers of SiO_2-Ta_2O_5 and a $\lambda/2$ thick optical resonator. The microresonator structure was fabricated by reactive magnetron sputtering [3]. The substrate applied was Si (100) in order to improve the adhesion of the dielectric layers to the substrate during deposition at low temperatures. After the formation of alignment marks, monolayer CVD graphene was transferred through the liquid [4]. It should be noted that the graphene layer is located in an antinode of the electromagnetic field of the standing wave of the dielectric microresonator.

(a) (b)

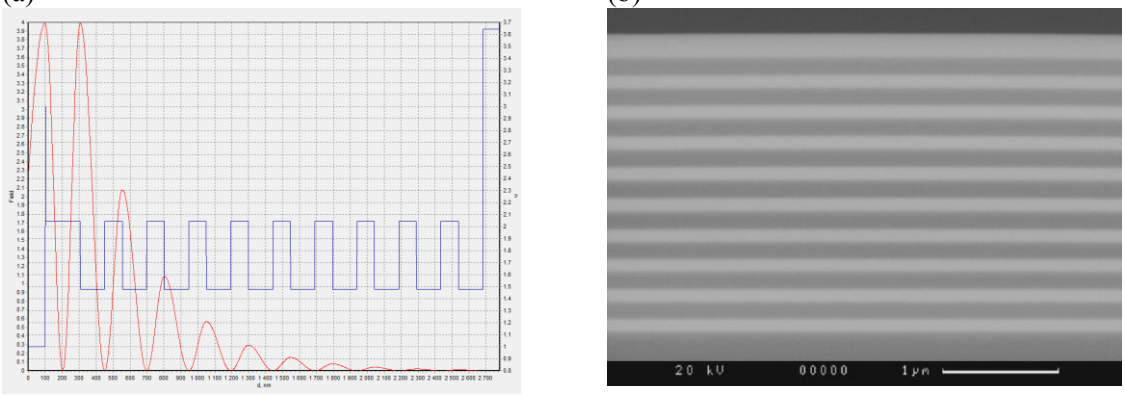

Figure 1(a, b). (a) The red curve is the distribution of the square of the field intensity in the microresonator; the blue curve is the change of the refraction index in the microresonator layers; **(b)** A SEM image of the microresonator.

The fabrication of mesa from graphene was performed by etching in oxygen plasma. The contact metallization formed by lift-off were layers of Ti and Au with a thickness of 10 and 20 nm. For an analysis of the SiO_2-Ta_2O_5 dielectric microresonator surface, atomic force microscopy (AFM) examinations were performed on a Veeco Dimension 3100 microscope in contact mode. For an evaluation of graphene conductivity, an Agilent B1500 analyzer of semiconductor device parameters was used in combination with a Zuss PM6 probe station. The photocurrent was measured with an SR 830 synchronous detector with modulation of radiation from a laser diode (Thorlabs L850P010, λ=850 nm). The pump current of the laser itself was controlled with the control unit of Thorlabs LTC56B/M.

3. Results

The current voltage characteristics of graphene on the surface of a dielectric microcavity demonstrate a linear dependence in a ±6 voltage range. The average value of graphene resistance R measured by the two-probe method was (10.4 ± 3.0) kOhm. The analysis of images of the SiO_2-Ta_2O_5 dielectric microcavity in a (110) cross-sectional geometry by scanning electron microscope (SEM) (see Fig. 1 (b) shows a high planarity of the interfaces and a thickness uniformity of the layers. Due to a large contrast of SiO_2-Ta_2O_5 refraction coefficient combined with a low surface roughness and a high planarity of the interfaces, one can expect the implementation of the reflectivity of the lower SiO_2-Ta_2O_5 DBR by more than 99% in a broad range of wavelengths. The report will present the results of measurements of reflection spectra and microreflections of the microcavity with graphene as well as the results of photocurrent measurement.

4. Acknowledgments

The authors would like to acknowledge the support of the Russian Science Foundation (Project No. 18-72-00157).

References

[1] Yu Q, Wang Y, Xie L, Nadri S, Sun K, Zang J, Li Q, Weikle R M, and Beling, A 2018 Proc. CLEO: Science and Innovations 2018 (San Jose) (OSA Technical Digest, Optical Society of America) p SM2I-1.
[2] Kobayashi, T, et al., 2013 *Appl. Phys. Lett.*, **102** 023112
[3] Blokhin, S A, et al., 2016 *Tech. Phys. Lett.*, **42** 1049–1053
[4] Mancini, L, et al., 2019 *Nanotechnology*, **30**, 214005

Nuclear magnetic spectrometer of differential type for determining the longitudinal relaxation time in turbulent fluid flows

N S Myazin[1], **V V Davydov**[1, 2], **V Yu Rud'**[2]
[1]Peter the Great St. Petersburg Polytechnic University, St. Petersburg 195251, Russia
[2]All-Russian Research Institute of Phytopathology, Moscow Region 143050, Russia

Abstract. The article substantiates the necessity of measuring the longitudinal relaxation time T_1 of the flowing liquid to control its state. For such measurements, a new method for measuring T_1 in a flowing fluid is proposed. This method allows to measure relaxation time in a wide range of a flow rate (more than two orders of magnitude).

The development of fast and reliable methods for monitoring the state of the flowing liquid in a wide range of changes in its flow q is one of the urgent tasks of technical physics [1]. It is necessary to control the state of the flowing liquid both during experiments and during automation of industrial production of various liquid media, biological solutions, etc.

Since the monitoring devices of the flowing liquid must operate effectively when the value of q changes in at least two orders of magnitude, a few problems arise. The main one is related to the limitations of the previously developed methods for measuring T_1 relaxation time of a liquid. This is because during the experiments or control of technological process it is difficult to perform measurements of T_1 on optimum value of flow q_{opt} when the flow rate q changes within two orders or more [2].

One of the recently proposed methods [3] requires including an additional coefficient in the ratio for the determining q_{opt} to exclude "binding" of the T_1 measurement to the value of q_{opt}. This is because the coefficient is obtained from the Bloch's equations. Unfortunately, this method showed low accuracy. Results of the experiments have shown that the value of the coefficient depends on changes in liquid flow q. However, the authors of the paper propose to consider it constant in a certain range of flow rate values. It contradicts both the theory of NMR and the experimental data. This contradiction becomes especially noticeable at large values of q. Moreover, it is not always possible to run a "reference" fluid on already installed equipment, as it may differ in physical and chemical properties from the fluid usually used in the equipment. It can lead to failure of the equipment and expensive repair. Therefore, it is almost impossible to use this method in industry.

Thus, the development of the method for determining the longitudinal relaxation time of the flowing liquid by the nuclear magnetic spectrometer is extremely relevant. Such measurement must be performed with an error of less than 1%, even in cases where the liquid flow rate varies by more than two orders of magnitude.

One of the possible solutions to this problem has been proposed in our work. To implement the new method, we have considered the evolution of the magnetization vector along all its paths from the polarizer magnet to the registration coil. As a result of the research it was found that under certain conditions the magnetization of the liquid changes only because of relaxation processes. These conditions are mean the fulfilling conditions of the of adiabatic theorem on the whole length of the magnetized liquid flow from the polarizer to the registration coil.

If two sections of the pipeline with different volumes are used, the magnetization M_1 of the liquid will change, and so does the amplitude of the recorded NMR signals. In this case, it was found that the ratio of amplitudes of the recorded signals was proportional to the ratio of magnetization change factors:

$$\frac{U_1}{U_2} = \frac{e^{-\frac{V_{c1}}{qT_1}}}{e^{-\frac{V_{c2}}{qT_1}}}$$

where T_1 is the time of longitudinal relaxation of the liquid.

After some mathematical conversions, this ratio takes the following form:

$$T_1 = \frac{V_{c2} - V_{c1}}{q \cdot ln\frac{U_1}{U_2}}$$

In the meantime, figure 1 shows the example of the recorded signals.

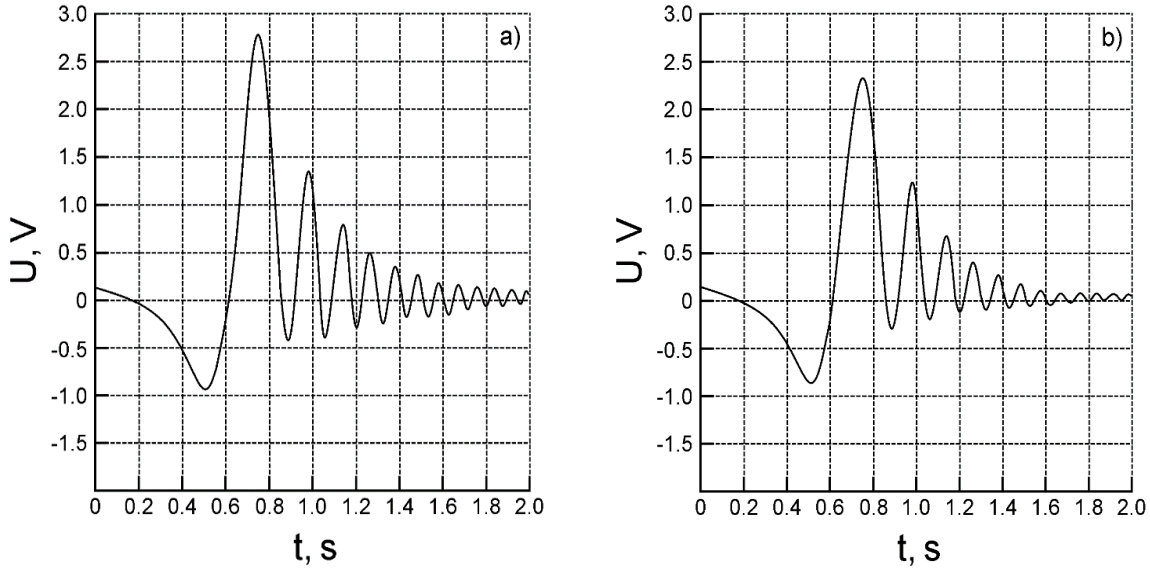

Figure 1. NMR signals from tap water for different volumes of pipeline connection section. Graph **a)** correspond to V_{C1} = 146 ml and graph **b)** correspond to V_{C2} = 204 ml.

The obtained results of T_1 measurements for different flowing liquid coincided within the limits of the measurement error with the measured values of relaxation times on the stationary NMR relaxometer Minispec mq 20M. This confirms the reliability of the measurement method proposed by us using the design of the differential type NMR spectrometer.

References

[1] Myazin N S, Logunov S E, Davydov V V, Rud' V Yu, Grebenikova N M, Yushkova V V 2017 *Journal of Physics: Conference Series* **929(1)** 012064

[2] Zhernovoi A I, Latyshev G D 1964 *Nuclear Magnetic Resonance in a Flowing Liquid* (Moscow: Atomizdat) p 216 (in Russian).

[3] Fatkhutdinova L I, Mamonkina A N, Ermak S V, Semenov V V 2018 *Journal of Physics: Conference Series* **1124(5)** 051043.

Inverse opal photonic crystals for sensing the composition of liquid mixtures

M S Ashurov[1], S A Ikrami[2], S O Klimonsky[1,3]
[1]Faculty of Materials Science, Lomonosov Moscow State University, Moscow, 119991 Russia
[2]Nikitin Institute of Chemistry, Dushanbe, 734063 Tajikistan
[3]Department of Chemistry, Lomonosov Moscow State University, Moscow, 119991 Russia

Abstract. The possibility of using inverse opal films from ethoxylate trimethylolpropane triacrylate (ETPTA) photoresist as sensors for determining the concentration of alcohols in water has been studied. The spectral position of the transmittance dip corresponding to the first photonic stop band is used as the analytical signal. Impregnation of an inverse photonic crystal with water-ethanol and water-ethylene glycol mixtures results in a red shift of the transmittance minimum. Refractive index sensitivity is about $\Delta\lambda/\Delta n$ = 414 nm/RIU.

1. Introduction

Photonic crystals (PhCs) have attracted much attention because of possessing tunable photonic band gaps, which could induce tunable color. The structural color is given from the periodic structure of photonic crystals and is characteristic of a particular material [1]. The position of the photonic stop band can be considered as a convenient analytical signal for detecting the composition of water-alcohol mixtures [2]. In this work we investigated the possibility of using inverse PC from ETPTA as sensors of the composition of water-alcohol mixtures and determined the sensitivity of the analytical signal to the studied liquids.

2. Experimental

Inverse photonic crystal films were prepared by template method using photopolymerization of photocurable resin ETPTA [3]. Opal PhC films composed of close packed SiO_2 colloidal microspheres were used as templates. SiO_2 colloidal microspheres of 250 nm in diameter were synthesized by the method presented in [4]. After the removal of SiO_2 colloids free-standing ETPTA inverse opal PhCs were obtained. Fig. 1a shows the typical SEM image of the surface of the resultant ETPTA inverse opal film. Lambda 35 (Perkin Elmer) spectrophotometer was used to study the possibility of using the obtained inverse films as chemical sensors of the composition of liquids by recording their transmission spectra in the normal direction after impregnation with different liquids: water, ethanol, isopropanol, ethylene glycol, and their mixtures with water. The transmittance spectra were recorded in spectral range of 350–750 nm with the monochromator slit width of 0.5 nm and a registration step of 0.2 nm. The position of the transmittance dips was determined using cubic approximation. Taking into account all random errors, the accuracy of determining the minima was approximated about ±0.5 nm.

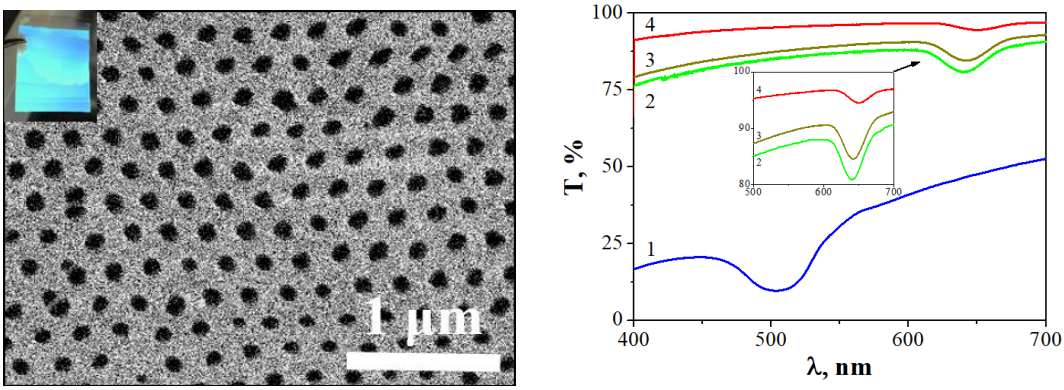

Fig. 1 (a-b). (a) Scanning electron microscopy image of surface of ETPTA inverse opal PhC. Inset: inverse opal film's photograph; **(b)** Transmission spectra for the ETPTA inverse PhC sample in dry state (1) and immersed in various liquids: 2-ethanol, 3-isopropanol, 4- ethylene glycol. Inset: minima of curves 2-4 in the enlarged scale.

3. Results

Fig. 1a shows a high degree of ordering of the inverse PhC films. In the inset of fig.1a a photograph of ETPTA inverse PhC with a characteristic structural color is shown. The minimum on the transmittance curve of the dry sample was about 509 nm. Inverse photonic crystals based on ETPTA photoresist films demonstrate clear stop band shift with the impregnation by different liquids. Fig. 1b shows examples of transmittance spectra of the ETPTA inverse PhC sample infiltrated by ethanol, isopropanol and ethylene glycol (curves 2-4). The red shift in transmittance spectra was observed when refractive index of the studied liquids increased. The observed red shift of the stop band with an increase in n is associated both with an increase in the effective refractive index of inverse PhC (n_{eff}) and with an increase in the interplane distance due to the swelling of the ETPTA photoresist. In accordance with transmittance spectra the dip locates at 609 nm for water (n = 1.333) and at 650 nm for ethylene glycol (n = 1.432). Based on these data, we can calculate the refractive index sensitivity of our samples as $\Delta\lambda/\Delta n$ = 414 nm/RIU.

4. Acknowledgments

The work was supported by the Russian Foundation for Basic Research (Grant Number 19-33-90266).

References

[1] Aguirre C.I, Reguera E, Stein A, 2010 *Adv. Funct. Mater.* **20** 2565
[2] Ashurov M, Gorelik V, Napolskii K, Klimonsky S 2019 *Photonic Sensors* (https://doi.org/10.1007/s13320-019-0569-2)
[3] Ashurov M.S, Bakhia T, Saidzhonov B.M, Klimonsky S.O 2020 *J. Phys.: Conf. Ser.*, in press
[4] Klimonsky S.O, Bakhia T, Knotko A.V, Lukashin A.V 2014 *Dokl. Chem*. **457** 115

Development and research of a linearly changing narrow bandpass optical filter for hyperspectral equipment

S A Fomchenkov[1,2]
[1]IPSI RAS - branch of the FSRC «Crystallography and Photonics» RAS, Samara 443001, Russia
[2]Samara National Research University, Samara 443086, Russia

Abstract. This paper reports on the development and investigation of a linearly changing narrow bandpass optical filter (LCOF) fabrication process. We researched and optimized parameters of manufacturing process steps, such as vacuum sputtering, thickness controlling, phase diffractive optical element writing, plasma chemical etching and etc. Most important moment and parameters of producing influence on the final result shown in this paper. As a result of work, experimental sample of multilayer optical filter for narrow spectral selection obtained.

1. Introduction

In recent years, the development of diffractive optical elements (DOE) have attracted the researchers due to the prospects of their use in optical signal and image processing systems, including in computational optics. The optical characteristics of multilayer DOE depend on many factors such as their structure, materials used and their refractive indices, the order and ratio of layer thicknesses and micro-relief. Optical filter is one of the most common and wildly used elements in optical sets. The filter's wavelength can be moved in filter's wavelength range. Micro-cavity filters are used as steady filters [1], adjustable filters [2] and chemical detectors [3,4]. Dielectric optical filters with Fabry – Perot structures are used in telecommunication, lasers and spectrometers in order to control and measure the exact wavelength range of visible and non-visible spectrum. In a spectrometer, the optical filter is used to detect the wavelengths that are very close together.

2. Experimental part

In this work for high refractive index layer was chosen TiO2, for low index refractive layer was chosen SiO2. Refractive index of TiO2 for wavelength 532 nm is 2,45 and of SiO2 is 1,47. Optical filter can be fabricated in a resist layer by just one lithography process. The profile of resist structure is subsequently transferred into defective layer of optical filter by plasma etching. Complete optical filter fabrication involves deposition of a lower dielectric mirror using a stack of dielectrics on the substrate, tapered layer formation and deposition of the top dielectric mirror [5]. The main idea of this filter is providing of defective layer by direct laser writing and plasma chemical etching. Typically so kind of structures produced with help of slanted deposition. It means sputtering with not normal angle between sputtering source of material and substrate. With help of direct laser writing by UV laser on circular laser writing station we can provide 256 different levels or steps inside resist volume. It gives us possibility for transfer of this structure to transparent dielectric layer by plasma chemical etching. For manufacturing process were used common equipment: magnetron sputtering system

CarolineD12A (ESTO-Vacuum, Inc.), circular laser writing system “CLWS-200S” and plasma chemical etching, providing by setup Caroline PE-15 (ESTO-Vacuum, Inc.). We used a technological process with main steps like vacuum sputtering, lithography and chemical etching. In details, manufacturing process consists of the following steps, shown on figure 1.

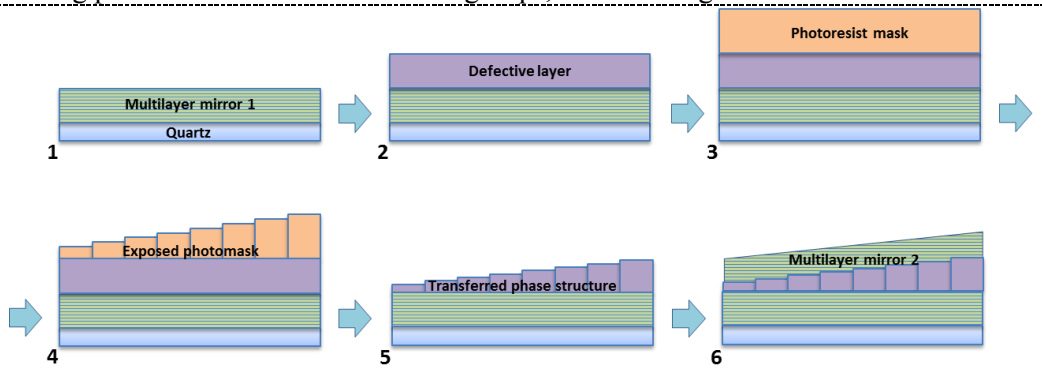

Figure 3. Linearly changing narrow bandpass optical filter fabrication process.

The main advantage of this filter over linear variable filters is that it can be made on a small surface area. This advantage allows the use of a similar filter in optical circuits, where space and mass are important, for example for portable hyperspectrometers [6].

3. Conclusion

Technological process of the multi steps optical filter manufacturing on a fused quartz substrate, which includes available common producing steps demonstrated. Produced filter has high quality and allows using it as optical filters for narrow selection in different devices. Thus, we find and demonstrate solution included in technological process of filter producing on a fused quartz substrate. It could be used in optical setups and hyperspectral equipment.

4. Acknowledgments

The work was financially supported by RFBR grants # 18-58-14001, 18-07-01380, 18-07-01122 in part of design and experimental investigation of multilayer diffractive optical elements and by Russian Federation Presidential grant for support of the leading scientific schools (NSh-6307.2018.8) in part of manufacturing of diffractive optical elements.

References

[1] Bria D. 2002 J. Appl. Phys 91 2569.
[2] Kazanskiy NL, Khonina SN, Butt MA. 2020 Physica E: Low-Dimensional Systems and Nanostructures 117 113798.
[3]Butt MA, Khonina SN, Kazanskiy NL. 2018 Journal of Modern Optics 65 1135.
[4]Butt MA, Khonina SN, Kazanskiy NL. 2020 IEEE Sensors Journal 20 1355.
[5]Fomchenkov SA, Porfirev AP 2018 Proc. of SPIE 10691 106911Z.
[6]Blank VA, Skidanov RV 2018 J. Phys. Conf. Ser. 1096 012003.

Realizing topological corner states in two-dimensional Su-Schrieffer-Heeger model with next-nearest neighbor couplings

N A Olekhno[1], P A Ivanova[1], D V Zhirihin[1], V I Kachin[1], P S Seregin[1], and M A Gorlach[1*]

[1]ITMO University, 197101 Saint Petersburg, Russia

E-mail: *m.gorlach@metalab.ifmo.ru

Abstract. In the present work, we consider a two-dimensional Su-Schrieffer-Heeger model with alternating positive tunneling couplings between the neighbor sites. We show that introducing next-nearest neighbor couplings results in the emergence of topological corner states for some values of the corresponding tunneling coupling. Our work resolves the contradiction that arose when such corner states absent in the original two-dimensional Su-Schrieffer-Heeger model were observed experimentally in its photonic realization based on the array of cylindrical microwave resonators.

1. Introduction

Photonic topological states are actively studied currently due to their robustness against geometrical imperfections of the structure which opens great avenues for realizing highly efficient nanophotonic devices [1]. Recently, higher-order topological states in the form of zero-dimensional excitations localized at the corners of a two-dimensional system attracted considerable attention, and have been realized in photonic systems [2].

Su-Schrieffer-Heeger model which is the one-dimensional array of sites with alternating tunneling couplings of magnitude J and $K > J$ between the nearest neighbors serves as a paradigmatic one-dimensional topological model featuring zero-energy topological edge states [3]. However, its direct generalization to the two-dimensional case with positive tunneling couplings $J > 0$, $K > 0$ does not give rise to the localized corner states [4]. On the other hand, Ref. [5] has recently reported the observation of zero-dimensional corner states in the electromagnetic realization of a two-dimensional Su-Schrieffer-Heeger model in the form of a two-dimensional array of cylindrical microwave resonators.

2. Results

To resolve this contradiction, we consider an extended two-dimensional Su-Schrieffer-Heeger model with additional positive tunneling couplings M between the closest pairs of next-nearest neighbors, Figure 1(a). Such tunneling couplings, as well as tunneling couplings between even more distant neighbors, should inevitably arise in photonic systems with long-range electromagnetic interactions. In this work, we show that depending on the relation between next-nearest neighbor coupling M and conventional couplings J and K, topological corner states

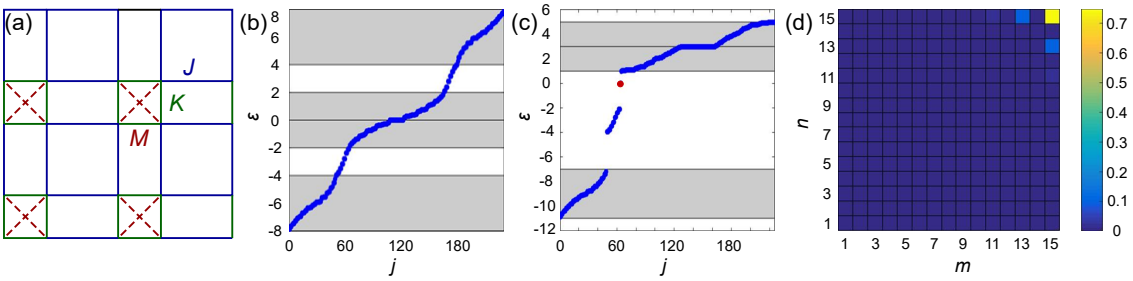

Figure 1. (a): Geometry of the considered tight-binding model. (b): Spectrum of the eigenvalues ε_j for the model of size 15×15 sites with tunneling amplitudes $J = 1$, $K = 3$, $M = 0$. (c): The same as (b), but for $J = 1$, $K = 3$, $M = 3$. A band gap opening and the appearance of the spectrally isolated state inside the band gap are observed. (d): Eigenmode corresponding to the isolated energy level for $M = 3$ from panel (c).

can arise, Figure 1(b-d). We further extend this theoretical observation by implementing the considered tight-binding problem with the aid of resonant topolectrical circuits [6, 7].

Acknowledgments

This work was supported by the Russian Science Foundation (grant No. 16-19-10538). NAO and MAG acknowledge partial support by the Foundation for the Advancement of Theoretical Physics and Mathematics "BASIS".

References

[1] Ozawa T et al 2019 *Rev. Mod. Phys.* **91** 015006
[2] Li M et al 2020 *Nat. Photon.* **14**, 89-94
[3] Su W P, Schrieffer J R, and Heeger A J 1979 *Phys. Rev. Lett.* **42** 1698
[4] Mittal S et al 2019 *Nat. Photon.* **13** 692-696
[5] Xie B-Y et al 2019 *Phys. Rev. Lett.* **122** 233903
[6] Imhof S et al (2018) *Nat. Phys.* **14** 925-929
[7] Olekhno N A et al (2020) *Nat. Commun.* **11** 1436

Twinning superlattices in doped GaAs nanowires

A S Sokolovskii[1], **D P Wilson**[1,2], **N I Goktas**[2], **R R LaPierre**[2], **V G Dubrovskii**[1,3]

[1]ITMO University, Kronverkskiy prospekt 49, Saint Petersburg 197101, Russia

[2]Department of Engineering Physics, McMaster University, Hamilton L8S4L7, ON, Canada

[3]St. Petersburg State University, Universitetskaya Emb. 13B, St. Petersburg 199034, Russia

Abstract. A model is presented for the formation of twinning superlattices in Te-doped and Be-doped self-catalyzed vapor-liquid-solid GaAs nanowires. The period of twinning superlattices and its dependence on the distance from droplet are quantified versus the doping level for both types of doping.

1. Introduction

Nanowires (NWs) of III-V semiconductor compounds are interesting from the fundamental viewpoint as well as for applications in nanoscale photonics [1-3]. NWs enable a much more efficient relaxation of elastic stress on their strain-free sidewalls compared to nanoislands, and hence can be grown without dislocations on lattice-mismatched Si substrates. Twining superlattices (TSLs) has been observed, for example, in undoped Si NWs [4] and Zn-doped InP NWs [5]. In this work, we try to understand the unified mechanism governing the formation of TSLs, observed experimentally in Te- and Be-doped self-catalyzed VLS GaAs NWs. We want to quantify the TSL period versus the doping level and its dependence on the distance from droplet in inverse-tapered NWs.

2. Results

We were able to explain the formation of TSLs in Te and Be-doped VLS GaAs NWs entirely on surface energetic grounds. The model geometry is shown in Figure 1 (a) [1,2]. We speculate that accumulation of dopants on the NW sidewalls decreases the surface energies of (111)A and (111)B side facets with respect to vertical facets, which makes the formation of TSLs energetically preferred [Figure 1 (b)]. This surface energy change is reflected in the experimentally observed decrease of the Ga droplet angle. The period of TSLs increases for higher doping levels and is proportional to the NW radius. This explains why the period gradually increases in the inverse-tapered NWs grown under Ga-rich conditions [Figure 1 (c)].

We use an extension of the model of Refs. [4] and [6] in 2D case, yielding the TSL period in the form

$$\lambda = AR\frac{(\beta_0-\beta_*)}{2tan^2\theta sin^2\beta_*(2+cos\beta_*)}, \quad (1)$$

where R is the NW radius in a given position from the droplet, $\beta_*$is the measured contact angle of the droplet (which depends on the doping type and level), $\theta = 19.5°$, $\beta_0 \cong 133°$, and A is a constant. This expression provides the escellent fit to all the data, as demonstrated in Figures 1 (d) and (e).

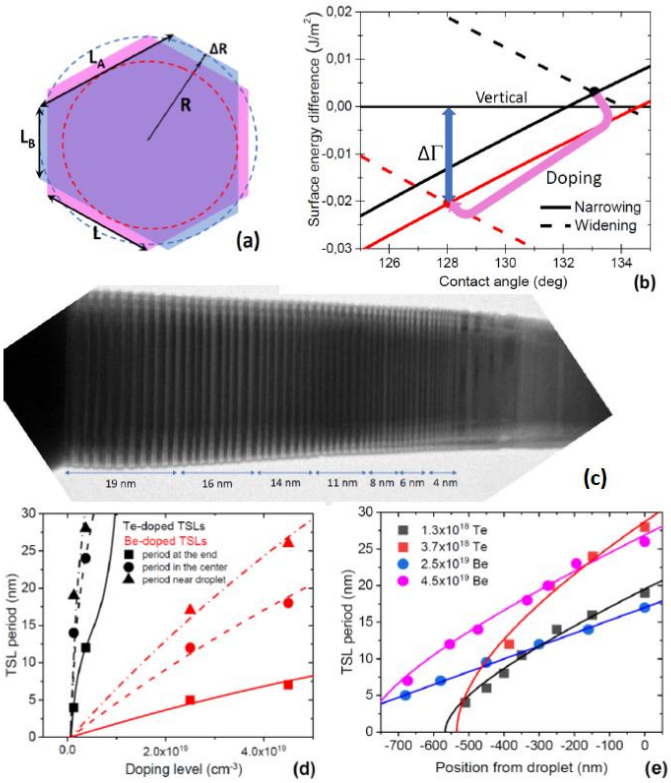

Figure 1. (a) Geometry of a TSL NW, whose (111)A and (111)B facets periodically change their lengths L_A and L_B. (b) Surface energies of (111)A and (111)B GaAs facets relative to the (110) facet. Without doping, these surface energies cross above zero, corresponding to vertical growth at a stable contact angle of around 133°. In the presence of doping, the surface energies of (111)A and (111)B facets decrease. At a certain doping level, the surface energy of TSL NW becomes smaller than that of vertical NW, with the corresponding decrease of the droplet contact angle β_*. (c) Inverse-tapered Te-doped GaAs NW, showing the increase of TSL period toward the droplet. (d) Measured TSL periods near the droplet versus the doping levels (symbols), fitted by the model (lines). (e) Measured TSL periods versus the distance from the droplet (symbols), fitted by the model (lines).

References

[1] Cirlin G E, Bouravleuv A D, Soshnikov I P, Samsonenko Yu B, Dubrovskii V G, Arakcheeva E M, Tanklevskaya E M, Werner P 2010 *Nanoscale Res. Lett.* **5** 360

[2] Matteini F, Dubrovskii V G, Rüffer D, Tütüncüoğlu G, Fontana Y, Morral A F I 2015 *Nanotechnology* **26** 105603

[3] Dubrovskii V G, Grecenkov J 2015 *Cryst. Growth Des.* **15** 340

[4] Ross F M, Tersoff J, Reuter M C 2005 Phys. Rev. Lett. **95** 146104

[5] Algra R E, Verheijen M A, Borgström M T, Feiner LF, Immink G, van Enckevort W J P, Vlieg E, Bakkers E P 2008 *Nature Lett* **456** 369

[6] Dubrovskii V G 2017 *Cryst. Growth Des.* **17** 2544

Peculiarities of the electronic and magnetic characteristics in Co_2YSi (Y = Ti, V, Cr, Mn, Fe, Co, Ni) Heusler alloys close to the half-metallic ferromagnets and spin gapless semiconductors

P S Korenistov[1], Yu A Perevozchikova[1], A A Semyannikova[1], P B Terentyev[1,2], E B Marchenkova[1], E I Patrakov[1], A N Domozhirova[1], V V Marchenkov[1,2]

[1]M.N. Mikheev Institute of Metal Physics, Ural Branch of RAS, Kovalevskaya Str., 18, Ekaterinburg 620108, Russia

[2]Ural Federal University, Mira Str., 19, Ekaterinburg 620002, Russia

Abstract. The Hall Effect, residual resistance, and magnetization of Heusler alloys Co_2YSi (Y = Ti, V, Cr, Mn, Fe, Co, Ni) were measured at T = 4.2 K and in magnetic fields of up to 100 kOe. It was shown that there are a clear correlation between the residual resistance ρ_0, saturation magnetization M_s, normal coefficient R_0 and anomalous Hall Effects depending on the number of valence electrons, which may be due to the appearance of the states of the half-metallic ferromagnet and/or spin gapless semiconductor.

1. Introduction

There are the intermetallic compounds with a general formula X_2YZ (X and Y are 3d-metals, Z is s-, p-elements of the Periodic Table), which are called the Heusler alloys. These compounds have plenty of useful functional properties, such as the shape memory effect, magnetocaloric effect, giant magnetoresistance etc. [1].

Particular attention is paid to the half-metallic ferromagnets (HMF) and spin gapless semiconductors (SGS), since the close to 100% spin polarization of charge carriers can be realized in HMF and SGS. Therefore, such materials are promising ones for practical applications in spintronics.

The high spin polarization of charge carriers was observed in Co_2FeSi [2]. At varying the Y and/or Z components in the Co_2YAl and Co_2FeZ alloy systems (Y = Ti, V, Cr, Mn, Fe, Co, Ni; Z = Al, Si, Ga, Ge, In, Sn, Sb) the significant changes occur in the electronic band structure near the Fermi level [3]. Therefore, the task of this report is to study the magnetic properties, electroresistivity and Hall Effect in Co_2YSi (Y = Ti, V, Cr, Mn, Fe, Co, Ni) alloys at varying the Y component.

The alloys were obtained by the method of arc melting followed by annealing. The Co_2VSi, Co_2CrSi, Co_2FeSi, and Co_3Si ingots were annealed at $T_{an.} = 1100^0$ C for 3 days, and the Co_2TiSi, Co_2MnSi, and Co_2NiSi alloys were annealed at $T_{an.} = 800^0$ C for 9 days. The field dependences of the magnetization M(H) and Hall resistance ρ_H (H) were measured at T = 4.2 K in magnetic fields of up to 100 kOe. The samples have the form of plates with dimensions of ~ (0.5 x 1.5 x 4.5) mm.

The coefficients of the normal and anomalous Hall Effect, residual resistance, and saturation magnetization were obtained. It was found that the dependences of measured characteristics on the number z of valence electrons have a clear correlation. Thus, the coefficient of the anomalous Hall Effect

R_S and the residual resistance ρ_0 increase near z = 28, while there is a minimum for the normal Hall coefficient R_0 and magnetization Ms at this point.
In addition, a power-law dependence of the coefficient of the anomalous Hall Effect on the residual resistance with an exponent k = 3.1 was observed, which does not correspond to the existing theoretical concepts, but correlates with the experimental data obtained on similar Heusler alloy systems. The results can be used at the development and creation of new materials for spintronics.

2. Acknowledgments
This work was carried out as part of the state task of the Russian Ministry of Education and Science (themes “Spin”, No. AAAA-A18-118020290104-2 and “Magnet”, No AAAA-A18-118020290129-5) with partial support from the Russian Foundation for Basic Research (projects Nos. 18-32-00686 and 18-02-00739) and the Government of the Russian Federation (Act No. 211, contract No. 02.A03.21.0006).

References
[1] Tanja Graf, Claudia Felser, Stuart S.P. Parkin, Progress in Solid State Chemistry 39, 1 (2011) DOI: 10.1016/j.progsolidstchem.2011.02.001
[2] D. Bombor, C.G.F. Blum, O. Volkonskiy, S. Rodan, S. Wurmehl, C. Hess, B. Buchner, Physics Review Letter **110,** 066601 (2013) DOI: 10.1007/s10948-017-4206-2
[3] V.V. Marchenkov, Yu.A. Perevozchikova, N.I. Kourov, V.Yu. Irkhin, M. Eisterer, T. Gao. JMMM 459, (2018) P. 211.DOI: 10.1016/j.jmmm.2017.11.019

Accumulation dynamics of protoporphyrin IX induced by 5-aminolevulenic acid in A549, HeLa and 3T3 cell lines

D A Gorbenko[1,2] , A V Belashov[1], T N Belyaeva[3], I K Livinov[3], E S Kornilova[3,4], I V Semenova[1], O S Vasyutinskii[1]
[1]ITMO University, St. Petersburg, 197101, Russia
[2]Ioffe Institute, St. Petersburg, 194021, Russia
[3]Institute of Cytology of RAS, St. Petersburg, 194064, Russia
[4]Peter the Great St. Petersburg Polytechnic University, St. Petersburg, 195251, Russia

E-mail: daryarogova7@gmail.com

Abstract. By applying the confocal fluorescence microscopy, we investigated the dynamics of the synthesis and accumulation of protoporphyrin IX induced by 5-aminolevulinic acid (5-ALA) in three cell lines: malignant - human epithelial carcinoma HeLa and human lung adenocarcinoma A549 - and fibroblast-like immortalized mouse embryonic 3T3 cells. The accumulation of protoporphyrin IX in cell cultures was evaluated based on the analysis of its fluorescence intensity. The dynamics of changes in fluorescence intensity was studied depending upon the duration of cells incubation with 5-ALA and its concentration.

1. Introduction

Photodynamic therapy (PDT) is widely used in modern oncology for the treatment of a wide range of malignant neoplasms. The basis for its successful application is the generation of reactive oxygen species using photosensitizers (PSs) - substances of synthetic and natural origin. The accumulation of PSs in malignant tumor cells and their generation of reactive oxygen species under the influence of laser radiation triggers cell death. PSs is also actively applied for diagnostic purposes to determine the location of a tumor, trophic ulcers and some other pathologies, as well as to evaluate their size and study morphology [1]. By now, various types of PSs have been developed and used in clinical practice: chlorins, porphyrins, phthalocyanines, and 5-aminolevulinic acid (5-ALA). As known, 5-ALA is a precursor of endogenously formed protoporphyrin IX (PpIX), which, in turn, is an important precursor of myoglobin, cytochrome, and heme [2]. The PpIX was demonstrated to exhibit photosensitizer properties and synthesized in the mitochondria of cells [3]; therefore, detailed information on its accumulation in tumor cells of various localizations is of high importance for applications in PDT and diagnostics.

2. Experimental section

In experiments we studied the dynamics of 5-ALA-induced accumulation of PpIX in cells of the three established cell lines: HeLa, A549 and 3T3. Samples were cultured in Petri dishes in DMEM containing 10% fetal bovine serum and 1% penicillin/streptomycin in the atmosphere of 5% CO2,

50% humidity at 37°C. Prior to experiments, 5-ALA was added to the culture medium and cells were further incubated in this solution.

In the first set of experiments, HeLa, A549 and 3T3 cells were incubated for 1, 2, 3, and 4 hours at four concentrations of 5-ALA in the culture medium: 0, 50, 100 and 200 μg/mL. Afterwards, cells were washed with PBS and ivestigated using the Olympus FV3000 confocal fluorescence microscope. PpIX fluorescence was excited at 405 nm and detected in the wavelength range of 610-650 nm. 3D distibutions of PpIX fluorescence were recorded in several fields of view in each sample. The analysis of total fluorescence intensity in cells was performed using the ImageJ software. The total fluorescence intensity was analysed as funcion of incubation time and 5-ALA concentration. It was shown that the maximal accumulation of PpIX occurs in all the three cell lines after 3-hour incubation in 5-ALA containing solution at the concentration of 100 μg/mL. Further increase of 5-ALA concentration from 100 to 200 μg/mL did not cause any increase in PpIX fluorescence.

In the second set of experiments, HeLa, A549 and 3T3 cells were incubated for 3 hours at 5-ALA concentrations in the culture medium varied with a smaller pitch: 0, 50, 75, 100, 125, 150 and 175 μg/mL. The data obtained demonstrated that 5-ALA concentrations higher than 100 μg/mL did not provide any rise in PpIX accumulation. The experimental dependencies of total PpIX fluorescence intensity in cells as function of 5-ALA concentration are shown in Fig. 1.

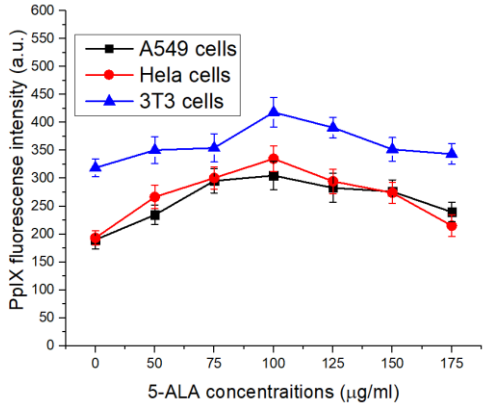

Figure 1. PpIX fluorescence intensity in the studied cell lines as a function of 5-ALA concentration.

3. Conclusion

From the data obtained, the relative increase in the signal of integrated fluorescence PpIX in the cells of the studied lines was determined. The maximum increase in PpIX fluorescence signal in immortalized cells obtained from tumor tissues (HeLa and A549), in comparison with control samples without 5-ALA in the culture medium, is on average 63.2%. In immortalized cells of normal fibroblasts (3T3 line), this increase is only 30%. It should be noted that the fluorescence signal in 3T3 cells in control samples is 1.7 times higher on average than in HeLa and A549 cells, which indicates a more efficient synthesis of endogenously formed PpIX in immortalized 3T3 cells.

References

[1] H. Abrahamse, M.R. Hamblin., Biochem J., 473(**4**), 2016, 347–364
[2] M. Wachowska, A. Muchowicz, M. Firczuk, M. Gabrysiak, M. Winiarska, M. Wańczyk, K. Bojarczuk, J. Golab, Molecules, 2011,**16**, 4140-4164
[3] Mahmoudi K, Garvey K.L., Bouras A., Cramer G., Stepp H, Jesu Raj J.G., Bozec D., Busch T.M., Hadjipanayis C.G., J Neurooncol. 2019, 141(**3**), 595-607

Electronic transport features of $MoTe_2$ caused by quenching

V V Marchenkov[1,2], A N Domozhirova[1], S V Naumov[1], S M Podgornykh[1], V V Chistyakov[1], P S Korenistov[1], J C A Huang[3]
[1]M.N. Mikheev Institute of Metal Physics, UB RAS, 620108 Ekaterinburg, Russia
[2]Ural Federal University, 620002 Ekaterinburg, Russia
[3]National Cheng Kung University, 70101 Tainan, Taiwan

Abstract. The electro- and magnetoresistivity of $MoTe_2$ single crystals before and after quenching were measured at temperatures from 1.8 to 300 K and in magnetic fields of up to 9T. It was demonstrated the quenching can lead to strong changes in values of the electro- and magneresistivity studied as well as in their temperature and field dependences. The peculiarities of these electronic transport characteristics changes were studied in details.

1. Introduction

Transition metal dichalcogenides (TMDs) are currently believed to be very promising materials for optoelectronics, nanoelectronics and spintronics. TMDs are a large group of compounds with the chemical formula MX_2, where M is a transition metal and X is a chalcogen. These materials have very diverse properties within the TMD-group, in participant, WTe_2 and $MoTe_2$ in Td-phase are known to exhibit the properties of II-type topological Weyl semimetals (TWSs). TWSs are characterized by the presence of massless Weyl fermions in their bulk and Fermi arcs on the surface. Such massless quasiparticles can be controlled faster than the conventional carriers that is promising for creating ultrafast electronic devices. At the same time, the crystal structure of $MoTe_2$ and its electronic characteristics, in particular, the electrical resistivity, are known to strongly depend on the heat treatment. Thus, in “commonly” synthesized $MoTe_2$ compound, it exhibits the semiconductor characteristics: high values of the electrical resistivity and a "semiconductor" type of its temperature dependence $\rho(T)$, i.e. ρ decreases with T. Quenching leads to the fact that the value of the electrical resistivity decreases significantly, and $\rho(T)$ becomes the “metallic” one, increasing with temperature [1, 2]. In addition, investigating the effect of magnetic field on the electronic properties of these materials is of interest since a number of such papers is scarce. Therefore, the aim of this work is to study in details the features of the electro- and magnetoresistivity in $MoTe_2$ before and after quenching.

2. Materials and Methods

$MoTe_2$ single crystals were grown by the chemical vapor transport method using Br_2 as a transport agent. The growth procedure was carried out according to the method described in [3]. X-ray diffraction analysis revealed that $MoTe_2$ before quenching crystallizes in a hexagonal structure with the lattice parameters a = 3.540(7) Å and c = 13.983(5) Å. The chemical composition of the samples was confirmed by X-ray microanalysis using a FEI Inspect F scanning electron microscope equipped with an EDAX attachment. The temperature and field dependences of the resistivity $\rho(T)$ were measured by the standard four-contact method in the temperature range from 1.8 to 300 K in magnetic fields of up to 9T. The measurements were carried out using the PPMS-9 system (Quantum Design) in

Collaborative Access Center "Testing Center of Nanotechnology and Advanced Materials" of IMP, UB of RAS.

3. Results and Discussions

Figure 1 shows the temperature dependences of the electroresistivity *ρ(T)* of $MoTe_2$ before (a) and after (b) quenching in the temperature range from 1.8 to 300 K. The dependence *ρ(T)* before quenching (figure 1a) demonstrates a "semiconductor" behaviour with a very large resistivity value at low temperatures of more than 10^5 Ohm·cm, while the resistivity is less than 1 Ohm·cm in the temperature range 50–300 K. As can be seen from figure 1b, quenching leads to a drastic change in the behaviour and value of the electrical resistivity. The temperature dependence *ρ(T)* of $MoTe_2$ after quenching shows a "metallic" type with a resistivity value of ~ (1.1-6.8) mOhm·cm.

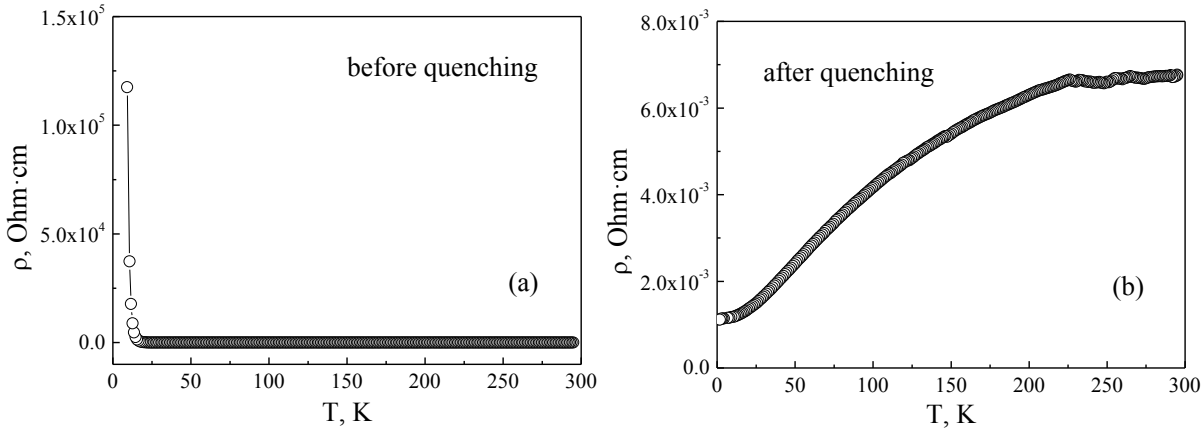

Figure 1. The temperature dependences of the electroresistivity of $MoTe_2$ before (a) and after (b) quenching.

At low temperatures, the field dependence of the magnetoresistivity (MR) of non-quenched $MoTe_2$ is close to quadratic one and is about 7% at T = 12 K in a field of B = 9T. Quenching leads to increasing the MR up to 15% (T = 12 K, B = 9T), and along with a quadratic field contribution, a linear term also appears. With increasing temperature, the MR decreases and becomes less than 1% at T = 150 K, and its field dependence becomes close to a linear behavior for both samples.

4. Conclusions

It was shown that quenching the $MoTe_2$ single crystals leads to the dramatic changes in the electro- and magnetoresistivity. In this case, the resistivity value decreases up to 8 orders of magnitude (!) at low temperatures and a type of its temperature dependence changes from “semiconductor” to “metallic” one. The magnetoresistivity, which is positive for both samples, is also modified, although these changes are not so huge as in a case of the electrorestivity.

5. Acknowledgments

The research was carried out within the state assignment of the Ministry of Education and Science of the Russian Federation (theme “Spin”, No. AAAA-A18-118020290104-2), supported in part by RFBR (Project No. 17-52-52008) and the Government of Russian Federation (Decree No. 211, Contract No. 02.A03.21.0006).

References

[1] Lv Y-Y et al. 2017 *Sci. Rep.* **7** 44587
[2] Keum D H et al. 2015 *Nat. Phys.* **11** 482
[3] Marchenkov V V et al. 2020 Accepted for publication in *Journal of Physics: Conference Series*

Anomalous Hall and Nernst-Ettingshausen effects in diluted magnetic semiconductors

Y Kuznetsov[1], M Dorokhin[1], A. Kudrin, V Lesnikov[1]
[1]Physical Technical Research Institute of Lobachevsky State University of Nizhny Novgorod, Nizhny Novgorod, 603950 Russia

Abstract. The paper presents a study of the magnetic field dependences of the Hall and Nernst-Ettingshausen effects in diluted magnetic semiconductors (III, Mn)V and (III, Fe)V based on InFeSb, GaFeSb, InMnAs formed on a GaAs substrate by pulsed laser deposition in vacuum. In addition to the presence of the anomalous Hall-effect, the occurrence of the anomalous Nernst-Ettingshausen-effect in the studied systems is shown. The difference in the characteristic form of the magnetic field dependences of the effects in systems with Mn and Fe is demonstrated, which is presumably related to the different nature of the appearance of magnetism in the film.

1. Introduction

One of the main directions of development of alternative electronics is spintronics. For the implementation of electronic devices, the principle of which is based on the use of the spin of charge carriers, diluted magnetic semiconductors (DMS) with a Curie temperature close to room temperature are required. The main technique for studying the magnetic properties of the magnetic field near the Curie point today is the long-developed and well-studied anomalous Hall effect (AHE) [1]. However, this technique has a number of limitations that reduce the possibilities for studying, for example, the transport and magnetic properties of high-resistance structures, or do not allow determining their parameters with the necessary accuracy. An additional research method, and in certain cases an alternative method, are effects based on a combination of thermoelectric and thermomagnetic phenomena (Nernst-Ettingshausen effects). These methods, in combination with the Hall effect, can reliably determine the nature of carrier scattering, and, as a result, more accurately calculate the transport parameters of structures.

In addition, in ferromagnetic structures, along with the “ordinary” NE effect, the anomalous NE effect can also be recorded (by analogy with the anomalous AHE). The parameters of the anomalous NE effect, in particular, its sign, provide information on the nature of carrier scattering in ferromagnetic materials above and below the Curie point and, in some cases, on the mechanisms of ferromagnetic ordering.

2. Experimental

The NE effect, by analogy with the Hall effect, is described by the expression

$$U_{NE} = Q_0 B\Delta T + Q_M M(B)\Delta T, \qquad U_H = R_0 BI + R_M M(B) I, \tag{1}$$

where Q_0, R_0 are the ordinary constants of the NE effect and Hall effect, respectively, B is the induction of an external magnetic field, M (B) is the magnetic field dependence of the magnetization

of the structure, I is the current passed through the structure, ΔT is the temperature gradient, Q_M, R_M are the anomalous constants of the NE effect and Hall effect respectively.
In recent years, layers of ferromagnetic semiconductors (Ga, Fe) Sb [1] and (In, Fe) Sb [2] with a Curie temperature have been obtained above room. A study of Fe-doped III-V semiconductor layers indicates that ferromagnetism is not connected in them directly with exchange interaction through carriers charge (carrier-mediated ferromagnetism), as in the widely studied system (III, Mn) V, but is associated with some kind of superexchange interactions between Fe atoms [2-5]. The fundamental difference between the occurrence of magnetism in the systems (III, Mn) V and (III, Fe) V is reflected in the characteristic form of the magnetic field dependence of the Nernst-Ettingshausen voltage, which is the basis of the study in this paper.

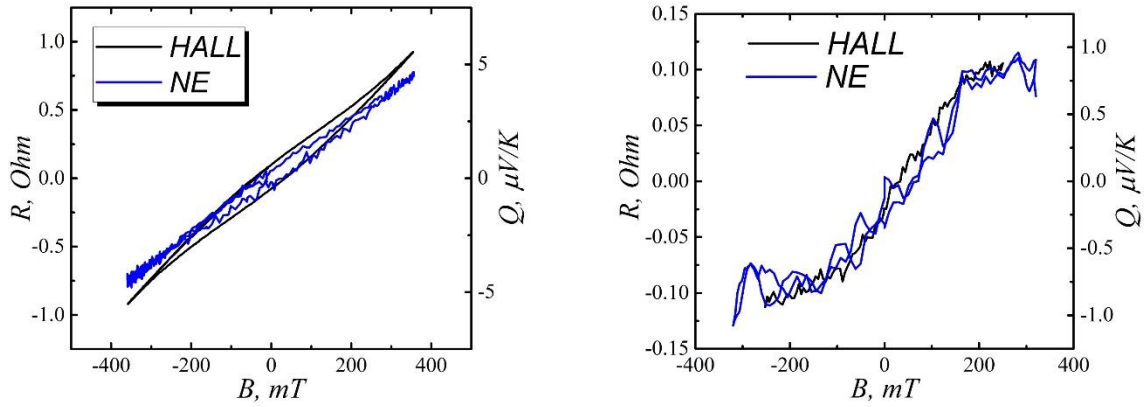

Figure 1. The magnetic field dependence of the Hall and Nernst-Ettingshausen effects in the GaMnAs structure at 150 K: a - structure with Mn clusters, b - structure without Mn clusters.

For example, Figure 1 shows the magnetic field dependences of the Hall effect and the Nernst-Ettingshausen effect in the GaMnAs structure at a temperature of 150 K containing the Mn (a) cluster and without the Mn (b) cluster. On the obtained dependences, nonlinearity is clearly observed. The presence of clusters of magnetic atoms was diagnosed by transmission electron spectroscopy.

In conclusion

The paper presents the results of studies of the magnetic field dependences of the Hall and NE voltages in a wide temperature range (10-400) K in the InFeSb, GaFeSb, GaMnAs, InMnAs. The structures for the study were obtained on substrates of gallium arsenide and sapphire by pulsed laser deposition in vacuum. An analysis is made of the presence or absence of an anomalous effect depending on the type of structure and the degree of ferromagnetic ordering.

Acknowledgments

This work was supported by the Russian Science Foundation (grant No. 17-79-20173). Obtaining InFeSb and GaFeSb layers with the support of the Russian Science Foundation project (grant No. 18-79-10088).

References

[1]. Nagaosa N. Rev. Mod. Phys. – V. 82, n.2. – P.1539-1592 (2010).
[2]. S. Goel et. al., Phys. Rev. B 3, 084417 (2019).
[3]. A.V. Kudrin et. al., J. Appl. Phys. 122, 183901 (2017).
[4]. N.T. Tu et. al., Appl. Phys. Exp. 11, 063005 (2018).
[5]. A.V. Kudrin et. al., J. Mag. Mag. Mat. 485, 236–243 (2019).

Study of (A3,Fe)B5/GaAs heterostructures as elements of a spin light-emitting diode

M Ved, M Dorokhin, V Lesnikov, A Zdoroveyshchev, Yu Danilov, P Demina and A Kudrin
Research Institute for Physics and Technology of Lobachevsky State University of Nizhny Novgorod, Nizhny Novgorod, 603950, Russia

Abstract. The circular polarization of the electroluminescence of InGaAs/GaAs spin light-emitting diodes with injectors based on A_3B_5 semiconductors doped with Fe atoms, namely (Ga,Fe)Sb, (In,Fe)Sb, and (Ga,Fe)As, was studied. The role of the formation of a (A3,Fe)B5/GaAs heterobound in electron transport and spin injection is discussed.

1. Introduction

Diluted magnetic semiconductors (DMS) are non-magnetic semiconductor materials doped with magnetic impurities (3d transition metals), and therefore combine magnetic and semiconductor properties [1]. Such materials are considered promising as elements of spintronics devices because they have a high degree of spin polarization of charge carriers and a relatively simple technology of incorporation into structures based on semiconductors [2]. DMS (A3,Fe)B5 are considered to be the most promising, since the Curie temperature in such materials exceeds 300K [3]. The main objectives of this work were the introduction of (Ga,Fe)Sb, (In,Fe)Sb and (Ga,Fe)As layers as functional elements of a spin light emitting diode (SLED), as well as measuring the circular polarization of the formed devices.

2. Experimental technique

The samples were grown in several stages. At the first stage, semiconductor heterostructures with quantum well InGaAs/GaAs were grown by MOCVD method on p-GaAs (for SLED with (In,Fe)Sb and (Ga,Fe)As injectors) and n-GaAs (for SLED with the injector (Ga,Fe)Sb) substrates. At the second stage, the layers of diluted magnetic semiconductors (A3,Fe)B5 were formed on the surface of semiconductor structures by pulsed laser deposition. At the last stage Au contacts were deposited, mesa structures were made and a basic ohmic contact was formed.

For studies of electroluminescence, forward bias was applied to the samples. When structures are introduced into a magnetic field, the EL becomes partially circularly polarized. The degree of circular polarization of EL is calculated by the formula

$$P_{EL} = (I_1 - I_2)/(I_1 + I_2) \times 100\% ,$$

where I_1, I_2 are the relative EL intensities measured for light polarized along the left and right circles respectively. The degree of circular polarization was measured at a temperature range of 10 – 300 K.

3. Results and discussion

The magnetic field dependences of the circular polarization degree are presented in Fig. 1.

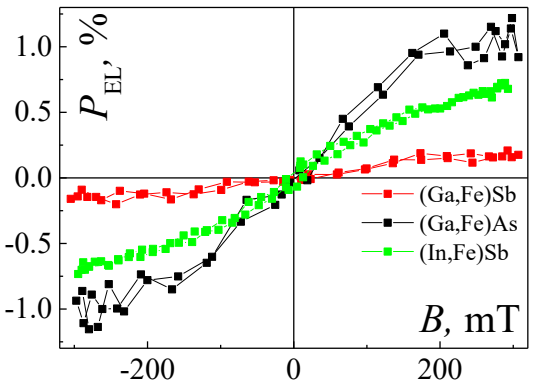

Figure 1. Magnetic field dependences of P_{EL}, measurement temperature - 10K.

The maximum value of the degree of circular polarization was found at 10 K for a SLED with an (Ga,Fe)As injector and amounted to 1% in the saturation region of DMS magnetization. For SLED with (In,Fe)Sb, the maximum polarization value was 0.7%, and for (Ga,Fe)Sb 0.2%. It should be noted that when studying the magnetic field dependences of the degree of circular polarization for control structures without a ferromagnetic injector (A3,Fe)B5, P_{EL} did not exceed the level of measurement error. This indicates that the circular polarization of electroluminescence is associated with the spin injection of carriers from a dilute magnetic semiconductor.

The degree of circular polarization is determined by the efficiency of spin injection, as well as spin relaxation during scattering of charge carriers. In the SLED with the (Ga,Fe)Sb injector, injection of spin-polarized holes is realized, while for the structures with (In,Fe)Sb and (Ga,Fe)As, electron injection is realized. This explains the relatively low value of the degree of circular polarization for SLED with (Ga,Fe)Sb, since the spin diffusion length for holes is shorter than for electrons.

With an increase of the measurement temperature, the EL intensity and P_{EL} decrease monotonically. For spin LEDs with (Ga,Fe)As injectors at temperatures above 200 K, the EL intensity becomes comparable with the noise level, which does not allow reliable measurements of circular polarization. For the structure with the (Ga,Fe)Sb injector, it was not possible to measure P_{EL} at temperatures above 50 K due to the initially low degree of polarization. Only in an SLED with an (In,Fe)Sb injector it was possible to achieve circular polarization in the temperature range of 10-300K.

Table 1. Comparative table of test samples.

Ferromagnetic injector material	P_{EL} measurement temperature range	Maximum P_{EL}
(In,Fe)Sb	10-300 K	0,7%
(Ga,Fe)Sb	50K	0,2%
(Ga,Fe)As	10-200 K	1%

Thus, spin light-emitting diodes with injectors in the form of diluted magnetic semiconductors (A3, Fe) B5 are formed and investigated in the work.

4. Acknowledgments

Authors would like to acknowledge Dr. B.N. Zvonkov for the fabrication of investigated samples. This work was supported by the Russian Science Foundation project # 18-79-10088 (structure's fabrication and polarization measurements) and the Grant of the President of Russian Federation, project # MD-1708.2019.2 (GaAs-based spin light-emitting diode structure development).

References

1. M. Holub, P. Bhattacharya // J. Phys. D: Appl. Phys., **40**, P.R179–R203 (2007).
2. I. Zutic, *et. al*. // Rev. Mod. Phys., **76**., P. 323 (2004).
3. A. V. Kudrin, *et al.* // Journal of Appl. Phys., **122**, P. 183901 (2017).

Quantum detector tomography of superconducting single photon detector based on MoSi film

M I Polyakova[1], **A A Korneev**[2,3], **A V Semenov**[2,3]
[1] National Research University Higher School of Economics, Moscow 101000 Russia
[2] Moscow State Pedagogical University, Moscow 119991
[3] Moscow Institute of Physics and Technology, Moscow region, Dolgoprudny, 141700, Russia

Abstract. In this work, we present results of quantum detector tomography of superconducting single photon detector (SSPD) based on MoSi film.

1. Introduction

The first observation of single- and double-photon modes of operation of a superconducting single-photon detector was demonstrated in [1]. When a photon hits a strip of superconductor a special area appears, called a hot spot. For estimation of hot spot dimensions in literature, a diffusion coefficient in normal state is used, which could lead to some inaccuracies. Direct method of hot spot sizes measurement, was introduced by Renema *et al.* [2]. They used nanowires with width from 100nm to 400 nm. But nonuniform distribution of the current and absence of saturation of detection efficiency (DE) makes the interpretation difficult. After that Elezov *et al.* [3] used a nanowire with length of 500 nm, but the impact of double-photon counts was comparably small. Afterwards, in our work [4] a samples on waveguides with different width from 80 to 280nm, were fabricated. Number of absorbed photons is known exactly (due to 100% internal DE and 100% absorption). But a total length of 80-280 nm, was yet too long. Previously we reported a usage of our protocol to specially fabricated samples of NbN [5]. A correlation length for hot spots was obtained and was equal to 70nm. In this work we applied our method to the samples of MoSi films, and compared with fabricated previously NbN films.

2. Experimental results

Fig.1 shows plots of the interaction length of two hot spots versus the critical current (I_c) normalized to the deparing current (I_{dep}). The goal is to extract hot spot interaction length, measuring quadratic contribution to the photo-count probability vs. mean number of photons in the laser pulse. Detectors made from MoSi film show saturation at a lower I / I_{dep} value than detectors made from NbN. It can be seen that MoSi spots are more efficient than NbN hot spots. The experimental data obtained in this work are consistent with the model presented by Vodolazov et al [6]

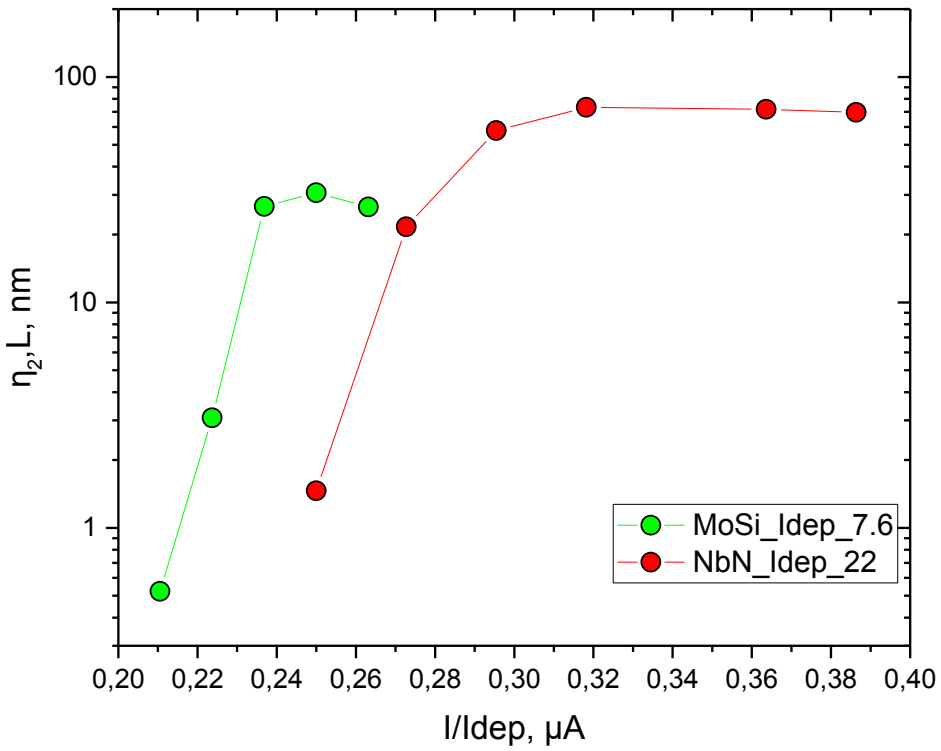

Figure 1. The interaction length of two hot spots versus the critical current (Ic) normalized to the deparing current (Idep). Red dots is NbN green dots is MoSi

3. Acknowledgments
The work was supported by RSF grant # 17-72-30036.

References

[1] G. Goltsman *et al*, "Picosecond superconducting single-photon optical detector." (2001).
[2] Renema *et al*., Applied Physics Letters, 110(23), 233103 (2017))
[3] Elezov *et al*., Journal of Optical Technology, 80(7), 435-438 (2013)
[4] Polyakova M. *et al.* Protocol of Measuring Hot-Spot Correlation Length for SNSPDs with Near-Unity Detection Efficiency IEEE Trans. Appl. Supercond. 29, 8–12 (2019)
[5] Polyakova M. *et al.*, Extracting hot-spot correlation length from SNSPD tomography data Journal of Physics: Conference Series, 1410 (2019) 012166
[6] D.Vodolazov, Theory of single photon detection by 'dirty' current-carrying superconducting strip based on the kinetic equation approach Phys. Rev. Applied 7, 034014 (2017)

Size effect in the kinetic properties in "sized" films of Bi_2Se_3 topological insulator

V V Chistyakov[1], **A N Domozhirova**[1], **J C A Huang**[2], **V V Marchenkov**[1,3]
[1]M.N. Mikheev Institute of Metal Physics UB RAS, Ekaterinburg 620137, Russia
[2]National Cheng Kung University, Tainan 70101, Taiwan
[3]Ural Federal University, Ekaterinburg 620002, Russia

Abstract. The Hall resistivity and magnetoresistivity of thin films of a topological insulator of Bi_2Se_3 with a thickness of 10 nm to 75 nm in the temperature range from 4.2 to 80 K was measured. A size effect in the kinetic properties of Bi_2Se_3 films was observed, i.e. linear dependence of the Hall coefficient and magnetoconductivity of the film on its reciprocal thickness. It is suggested that a similar effect can be observed in other TIs and systems with an inhomogeneous current distribution over the cross section of the sample.

1. Introduction

In recent years new quantum materials with a topologically nontrivial band structure resulting from strong spin-orbit interaction have been predicted theoretically and discovered experimentally. First of all, these are topological insulators (TI). In these compounds there is an energy gap in the bulk of the material, characteristic of an insulator, and protected gapless conducting states on its surface. The rigid coupling between the directions of the pulse and the electron spin leads to the appearance of spin polarization of charge carriers and the possibility of spin-polarized current flowing near the surface of the TI with virtually no losses [1].

2. Experimental

Thin films of Bi_2Se_3 were grown by the molecular beam epitaxy method on Al_2O_3 substrates with thickness from 10 to 75 nm. The Hall resistivity ρ_{xy} and magnetoresistivity ρ_{xx} were measured by the conventional 4-points method at dc-current in the temperature range from 4.2 to 80 K and in magnetic fields of up to 10 T. The results are presented in units of conductivities $\sigma_0 \approx 1/\rho_0$, $\sigma_{xx} \approx 1/\rho_{xx}$ and Hall coefficient R_H.

3. Results

Since TIs of conductivity in its volume and near the surface differ significantly, TI can be represented as a system of two parallel-connected conductors: a “metal” surface and a “semiconductor” bulk (see [2, 3] and references therein). As was shown in [2, 3], the conductivity σ of such a system can be represented as:

$$\sigma \approx \sigma_{surf.} \cdot \frac{\delta}{d} + \sigma_{bulk} \qquad (1)$$

Where $\sigma_{surf.}$ is a surface conductivity of the surface layer with a thickness of δ, σ_{bulk} is a bulk conductivity. Thus, the dependence of conductivity σ on the inverse film thickness d^{-1} should be

observed, i.e. $\sigma = f(d^{-1})$. The purpose of this work is to search for and study the size effect in the kinetic properties of the topological insulator Bi_2Se_3.

As a result of the experiments performed, a size effect was discovered, i.e. the dependence of the kinetic coefficients (magnetoconductivity, Hall coefficient) on the inverse film thickness. In fig. 1a shows the dependence of the magnetoconductivity in the magnetic field of 10 T at T = 4.2 K on the inverse thickness of the samples of TI Bi_2Se_3. In fig. 1b shows a similar dependence for Hall coefficient.

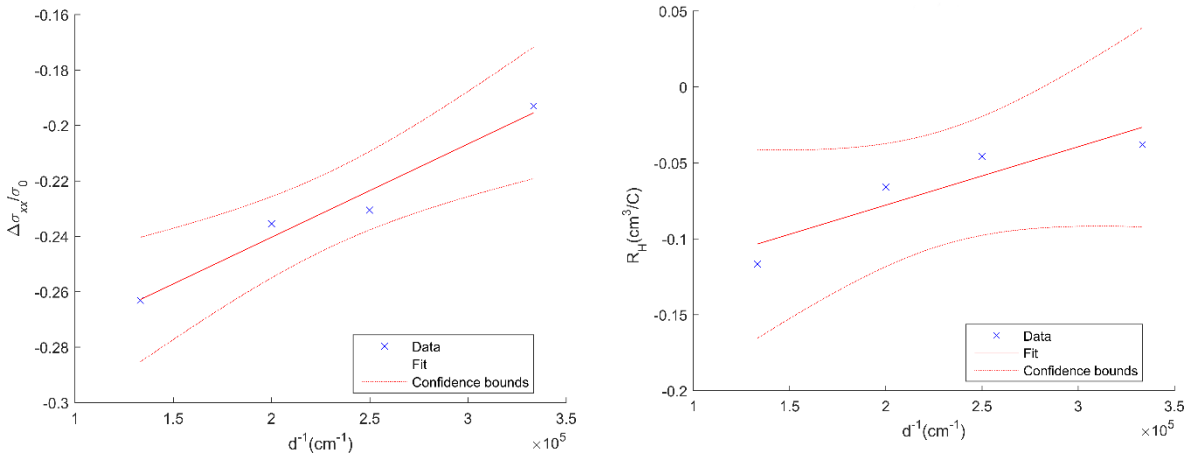

Figure 1(a, b). Size effect for magnetoconductivity **(a)** and Hall coefficient **(b)** in TI Bi_2Se_3 in the magnetic field of 10 T at T = 4.2 K.

4. Conclusions

The results of this work allow to experimentally "separate" the bulk and surface contributions. It was found that the value of the surface contribution by almost an order of magnitude exceeds the value of the bulk. The obtained results can be used for "separation" and evaluation of the values of surface and bulk contributions in kinetic coefficients also in other TIs and systems with non-uniform distribution of direct current over the cross section of the sample.

5. Acknowledgments

This work was partly supported by the state assignment of FASO of Russia (theme "Spin" No. AAAA-A18-118020290104-2) and by the RFBR (project No. 17-52-52008).

References

[1] Zhang H, Liu C X, Qi X L, Dai X, Fang Z, Zhang S C 2009 *Nat. Phys.* **5** 438

[2] Marchenkov V V, Chistyakov V V, Huang J C A, Perevozchikova Y A, Domozhirova A N, Eisterer M 2018 *EPJ Web of Conferences* **185** 01002

[3] Chistyakov V V, Domozhirova A N, Huang J C A, Marchenkov V V 2019 *Journal of Physics: Conference Series* **1389** 12051

Simulation of induction chemical-thermal treatment of titanium disks in a massive refractory container

A Voyko[1], **A Fomin**[1]
[1]Yuri Gagarin State Technical University of Saratov, Saratov 410054, Russia

Abstract. The results of numerical simulation of chemical-thermal treatment, namely, heating of a massive metal container with a working medium and a small-sized titanium disk sample, are presented. To study the heating kinetics of this system, the effect of the parameters of chemical-thermal treatment, in particular the inductor current from 3.4 to 8.0 kA at a frequency of 90 kHz, was determined.

1. Introduction

Titanium and its alloys are widely used in industry for the production of critical items in aircraft and machine building, medicine, and the chemical industry. However, titanium alloys have low values of hardness and coefficient of friction and this structural material is characterized by a tendency to contact setting and tear. These problems can be solved by the use of surface modification. One of the effective methods is chemical-thermal treatment (CTT), *e.g.* carburization [1,2]. The developed process of carburization is used to increase the hardness and wear resistance of small-sized titanium products (disks, cylinders, bushings and fasteners). This process is usually performed in a sealed container, inside which the working medium is poured and a modified sample is placed. When heating the "container – working medium – sample" system the temperature on the outer surface of the technological chamber (container) differs from the internal temperature [3,4]. The presence of the modifying medium also reduces the allowable temperature of treatment, which is determined by the Ti–C state diagram.

Thus, the aim of this work is to determine the temperature field in the working area of the container with the given CTT parameters due to the use of numerical simulation by the finite element method.

2. Methodology

The CTT process, namely carburization, was conducted in a sealed container of refractory metal *1* with a carbon-containing medium *2* in the form of graphite powder and a titanium sample *3* inside. The loading container was located in an inductor *5*, which was cooled by water *6*. There was a quartz tube *4* between the container and the inductor, which served as thermal and electrical insulation.

The current of inductor I during simulation varied from 3.4 to 8.0 kA at a fixed frequency f of 90 kHz. The current values from 3.4 to 5.5 kA were the main ones and corresponded to the modes for quasi-stationary exposure at the given carburization temperatures. The highest current value I = 8.0 kA was used during carburization to ensure the accelerated heating of the system to the required temperature of exposure.

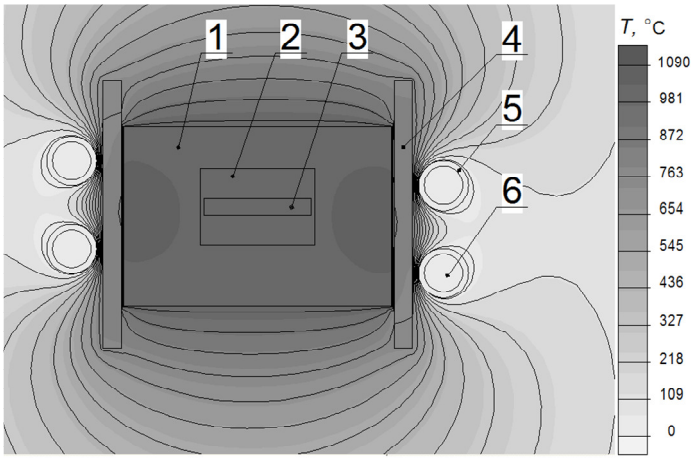

Figure 1. A plot showing the temperature distribution of the temperature fields in the "container – working medium – sample" system: *1* – a container, *2* – working medium, *3* – a disk-shaped titanium sample, *4* – a quartz tube, *5* – an inductor, *6* – water

3. Results

The results of heating and distribution of the temperature fields during heating of the model of the considered system at the current strength I = 3.4–5.5 kA showed that the temperature range from 1100 to 1400 ºC was reached in the working area of the container. This temperature range was sufficient for the carburization to occur [2,5]. At the current of 8.0 kA, rapid heating of the active part of the system to a temperature exceeding the melting point of titanium was ensured. The selected design contributed to the formation of a uniform thermal field inside the massive container.

4. Conclusions

Thus, the theoretical results of the heating kinetics of the "container – working medium – sample" system showed that the application of the considered values of the inductor current in the range 3.4–5.5 kA ensured the necessary conditions for the CTT process in a carbon containing medium (graphite). The use of an increased inductor current of 8.0 kA made it possible to accelerate the heating of the active part of the system elements and, thereby, to increase the productivity of the carburization process.

Acknowledgments

The research was supported by the Russian Science Foundation (project No. 18-79-10040).

References

[1] Cheng K, Pagan N, Bijukumar D, Mathew M T and McNallan M 2018 *Thin Solid Films* **665** 148
[2] Fomina M, Voyko A, Egorov I, Shchelkunov A, Zakharevich A, Skaptsov A and Shumilin A 2018 *Proc. SPIE* **11065** 110661G
[3] Voyko A and Fomina M 2019 *J. Phys. Conf. Ser*. **1410** 012193
[4] Voyko A, Fomina M. Shumilin A, Rodionov I, Kalganova S, Artyukhov I, Fomin A 2018 *J. Phys. Conf. Ser* **1124** 071021
[5] Fomin A, 2019 *Ceram. Int.* **7** 8258

Near-electrode polarization and determination of the mobility of intrinsic charge carriers in PVDF films

M E Borisova[1] **A M Kamalov**[2] **B M D N S Jayasinghe**[1]
[1]Higher school of High Voltage Energy, Peter the Great St. Petersburg Polytechnic University, Saint Petersburg 195251, Russia
[2]Mechanics of polymers and composite materials Laboratory, Institute of Macromolecular Compounds RAS, Saint Petersburg 199004, Russia

Abstract. The process of near-electrode polarization in a polyvinylidene fluoride (PVDF) film was studied using reverse currents $I_{rev}(t)$. It was proved that the maxima on the $I_{rev}(t)$ curves are characteristic of near-electrode polarization. The dependences of the reversal currents on time were analyzed based on various representations. The mobilities of the intrinsic charge carriers in the film and the magnitude of the charge transferred through the dielectric layer from electrode to electrode were calculated. The conductivity of PVDF was studied and analyzed in the temperature range 90°C-130°C.

1. Introduction

If blocking layer appears between the dielectric and the electrode, then under the influence of a constant electric field the own charge carriers move to the electrodes. A bulk hetero charge is formed in the near-electrode region. This phenomenon is called near-electrode polarization. In this case, the electric field strength in the near-electrode layer increases sharply, and a charge of the opposite sign is induced on the electrode. This phenomenon is important to consider in electrical insulation, as well as in determining the dielectric constant in the low frequency region.

In the present work, it is shown that using reverse currents determines the presence of near-electrode polarization. From the maxima at reverse currents, one can determine the mobility of free charge carriers

2. Methods

2.1. Measuring charge and discharge currents

The electrical conductivity was studied in isothermal conditions (90-130)°C. The currents were measured using a picoammeter A2-1 with a two-electrode system. The sensitivity of the picoammeter A2-1 is 10^{-15}A. The measurement error of current is 1%. The films were coated with aluminum foil. The diameter of the electrodes was 16 mm. The charging currents were measured on constant voltage ±100V, electrical field strength was ~$5*10^5$V/m. The time of current measurement was 10 minutes.

2.2. Reverse Current Measurement

When measuring reverse currents $I_{rev}(t)$ on the electrodes between which the film is located, a constant voltage U is first applied, later change polarity to another (-100V). On the $I_{rev}(t)$ curve, one or more maxima can be observed.

3. Results and Discussion

The dependences of charging current on time are presented in Fig. 1. As can be seen from the Fig. 1 the electric current decreases over time. On a stationary basis, the charging current is calculated for the specific volume of conductivity of the PVDF film, which is shown in Fig. 2.

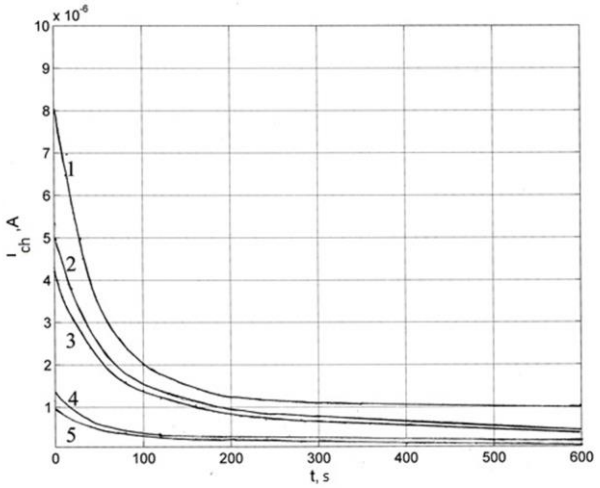

Figure 1. The dependences of charging current on time: 1-130^{0}C, 2-120^{0}C, 3-110^{0}C, 4-100^{0}C

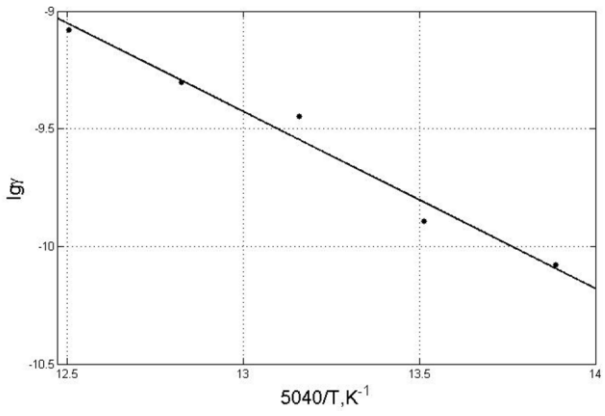

Figure 2. The dependence of electrical conductivity on return temperature.

3.3. Study of reverse currents

In Fig. 3. it can be seen that the higher the temperature, the narrower the maximum, the shorter the time tm and the greater the magnitude of the current by Irev (t). The appearance of a current maximum at Irev (t) indicates near-electrode polarization. The calculation of the mobility of their own charge carriers was carried out according to several models [1].

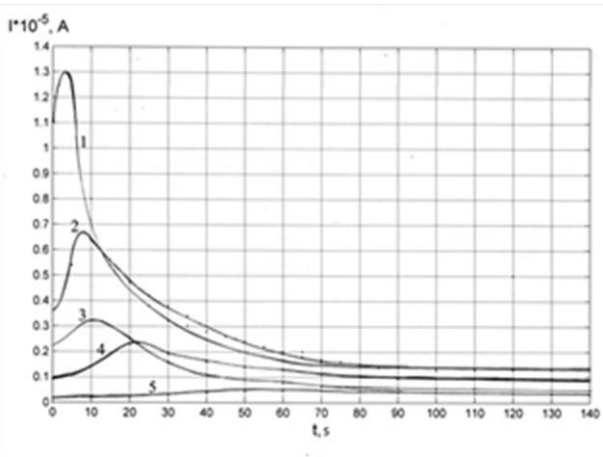

Figure 3. Dependence of reversal currents on time Irev(t) for various temperatures: 1-130^{0}C, 2-120^{0}C, 3-110^{0}C, 4-100^{0}C, 5-90^{0}C.

Conclusions

Transient processes of electric transport and polarization in a PVDF film are investigated. On the Irev(t) curves, systematic reproductions of current maxima were found, which confirms the presence of near-electrode polarization in the PVDF film. Dependences Irev(t) were studied in the temperature range at field strength. Using the maxima on the curves Irev(t) calculated the mobilities of the proper charge carriers in the dielectric $\mu = \left(10^{-12} \div 10^{-13}\right) m^2 / V \cdot s$.

The temperature dependence of mobility is described by an exponential law, and the activation energies are (0.5-0.8) eV.

References

[1] Borisova M. E. Modeling of processes of near-electrode polarization in polymer films // INTERNATIONAL JOURNAL OF MATHEMATICAL MODELS AND METHODS IN APPLIED SCIENCES Vol. 9, 2015

Research of low noise pHEMT transistors in equipment for microwave radiometry using numerical simulation

V G Tikhomirov[1], A G Gudkov[2], S V Agasieva[2,3], M K Popov[1], S V Chizhikov[2]

[1]Saint-Petersburg State Electrotechnical University "LETI", St. Petersburg197376, Russia
[2]Bauman Moscow State Technical University, Moscow 105005, Russia
[3]Peoples' Friendship University of Russia, Moscow 117198, Russia

Abstract. The numerical impact modeling of some external effects on devices based on AlGAs/InGaAs/GaAs heterostructures (pHEMT) was carried out. The mathematical model was created that allowed to predict the behavior of the drain current depending on condition changes on the heterostructure in the barrier region and to start the process of directed construction optimization of the devices based on AlGaAs/InGaAs/GaAs pHEMT with the aim of improving their noise characteristic.

1. Introduction

Amplifiers based on MMIC that are the part of microwave radiometry equipment have special requirements for noise characteristics. It should be noted that it includes not only the desire to minimize the noise of active MIC amplifying elements, in our case, heterostructured pHEMT, but also the stability of noise characteristics with the thermodynamic balance of the system "biological body - the radiometer input circuits" even in conditions of special antenna noise.

Optimization of such transistors production cycle is still a complicated and expensive procedure [1-3]. This paper presents the results of numerical simulation and calculation of the low noise features pHEMT for increasing efficiency when they are operating as a part of amplifiers for microwave radiometry equipment.

2. Simulation results

According by previous studies [4], the most important influence on the characteristics of heterostructured field-effect transistors is provided by the parameters of the gate region (thickness, composition and doping profile of individual layers, geometric dimensions and profile of the gate groove, topological dimensions and spatial location of the gate electrode). The choice of optimal parameters of the gate area was very important, for example, to obtain optimal noise characteristics at a given length of the gate electrode, providing the required level of the breakdown voltage, enhance the stability of device characteristics to possible fluctuations of technological process parameters.

Additional calculations of the distribution dependence of local noise sources in the volume of the structure from the concentration of charges at the dielectric-semiconductor interface were performed for the most accurate prediction of the behavior of noise parameters. The developed software package was successfully applied in the work for this purpose [4].

According calculation results that are shown in Fig.1 the value of the introduced charge q=1e12 [cm-2] corresponds to the location of 1e12 electron charges on the cm-2 of dielectric-semiconductor boundary surface.

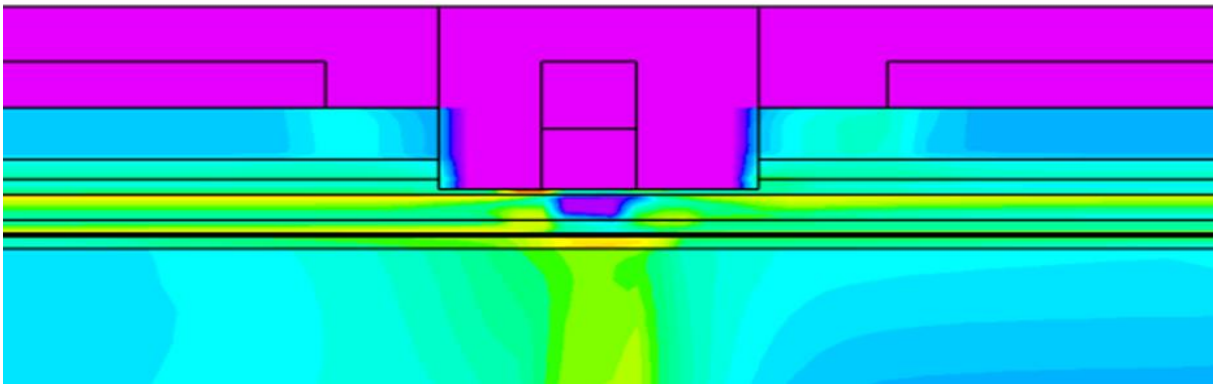

Figure 1. The image of the screen for a calculating of the local noise sources through the transistor in the state of normal depletion of the sub-gate region.

3. Conclusion

Performed calculations of the distribution of local noise sources in the volume of the heterostructure from the concentration of charges at the dielectric-semiconductor interface show strong interconnection. The existence of an optimal charge at the heterostructure boundary for achievement of minimal noises in the device without taking into account self-heating were predicted by numerical modeling [5-7]. It is quite correct taking into account the modes of small displacements on the electrodes in the MMIC equipment for microwave radiometry.

The research is carried out to the research project No. 19-19-00349 on the theme: “A method and a multichannel multifrequency microwave radiothermography on the basis of monolithic integrated circuits for finding the 3D distribution and dynamics of brightness temperature in the depths of the human body” (Russian Science Foundation).

References

[1] Uren M J et al. Buffer design in GaN-on-Si power devices,J. Phys. D: Appl. Phys. 51 (2018) 163001

[2] Stutzmann M, Steinhoff G, Eickhoff M, Ambacher O, Nobel CE, Schalwig J, et al, Diamond Rel Mater 2002; 11:886.

[3] Duffy S J et al. Strain-reduction induced rise in channel temperature at ohmic contacts of GaN HEMTs, IEEE Access, vol. 6, pp. 42721–42728, 2018.

[4] Agasieva S., Gudkov A., Tikhomirov V.G., Chizhikov S. et al Dependence analysis of the GaN HEMT parameters for space application on the thickness AlGaN barrier layer by numerical simulation, 2nd International Conference on Opto-Electronic Information Processing, pp. 79-82, 2017.

[5] Tikhomirov V.G., Gudkov A.G., Agasieva S.V., Dynaiev D. D., Popov M.K., Chizhikov S.V. Increasing efficiency of GaN HEMT transistors in equipment for radiometry using numerical simulation, Journal of Physics Conference Series,2019. 1410:012191.

[6] Tikhomirov V, Zemlyakov V, Volkov V, ParnesYa, Vyuginov V, Lundin W, Sakharov A, Zavarin E, Tsatsulnikov A, Cherkashin N, Mizerov M, and Ustinov V, Semiconductors, 2016, Vol. 50, N. 2, pp. 244–248.

[7] Benbakhti B, Soltani A, Kalna K, Rousseau M, and DeJaeger J. Effects of self-heating on performance degradation in AlGaN/GaN-based devices, IEEE Trans. Electron Devices, vol. 56, no. 10, pp. 2178–2185, Oct. 2009.

QUANTUM SIZE EFFECT AND CRITICAL TEMPERATURE OF THIN ALUMINUM FILMS

E Sedov[1]
[1]Moscow Institute of Electronic and Mathematics, Higher School of Economics, Moscow, 101000, Russia

Abstract. With the size decreasing of conductors, near a certain critical size, new effects are observed that are invisible in massive bodies. They are called quantum size effects (QSE), and one of these effects is the shift of the critical temperature Tc in superconductors.

1. Introduction

At the moment, it is known that in superconductors such as lead, niobium and mercury, the value of Tc decreases, while in indium, tin and aluminium, this value, on the contrary, increases [1]. However, it is still not clear what effect is responsible for such a change in Tc and why in some materials the temperature increases, while in others it decreases. In the mid-60s of the last century, two main factors responsible for this change were identified: the electron – phonon interaction and disordering effects caused by the fact that the structures are not ideal in their structure [2]. The topic would seem to be closed, but nonetheless, the quality of nanostructures is growing every year, and the effect is preserved. In the early 2000s, there was an assumption that the presence of plays a significant role in this problem. We are trying to prove or disprove this statement in our work.

2. Experiment

Thin films of aluminium were investigated in our work, since Tc in aluminium is reasonably well predicted, and most importantly, the Tc value in it increases, which opens some prospects for practical application. Aluminium has already been studied before, but nevertheless, in many works the data are very fragmented and do not tolerate any criticism when compared with theory. The problem is primarily associated with the manufacture of samples: it is quite difficult to produce technologically equivalent samples even in one batch. For a complete study of various effects, aluminium films were fabricated on gallium arsenide and sapphire substrates by two methods: electron sputtering and molecular beam epitaxy. The thickness range is between 5 nm and 100 nm for sprayed films and between 5 and 60 nm for epitaxial films. This is due to the fact that in epitaxial films the increase in Tc is less pronounced and becomes noticeable at thicknesses of the order of 60 nm, while in ordinary films the difference is already visible at 100 nm. Aluminium films were measured in a cryostat by direct pumping of helium-4 and in a sorption cryostat with pumping of helium-3. The measurements were carried out at a direct current of 0.1 μA - 1 μA, using the four-point method, with an error in determining the temperature of ~ 1 mK.

3. Results

In the frame of the BCS model, the critical temperature of the superconducting transition exponentially depends on the density of electronic states at the Fermi level N (EF) and the electron-phonon coupling constant V:

$$T_c \sim exp(-N(E_F)V)^{-1}$$

In [3], it was shown that due to the QSE in thin superconducting films, both parameters N (E_F) and V nonmonotonically change with the sample thickness. Such an effect is explained by the theory of shape resonance [4]. Based on the high quality of the films, it is assumed that the influence exerted by various defects and inhomogeneities of the films on the shift in the value of Tc is minimal, and thus is not the dominant factor. Surface effects also introduce minimal disturbance due to the fact that the film sizes are quite large.

The measurements showed an increase in the critical temperature in all samples: up to 2 K in evaporated films and up to 1.6 K in epitaxial films [5], however, epitaxial films on gallium arsenide at small thicknesses are island growths, so they could not be measured below a certain thickness. Nevertheless, epitaxial films on a sapphire substrate have a continuous structure along the entire length of the film and have the same thickness over its entire length. Their study also showed an increase in Tc, however, much less than in conventional sprayed films.

References

[1] A. M. Toxen 1961 Phys. Rev. 123 2
[2] V. L. Ginzburg 1964 Journ. Experimental Theoret. Phys. (U.S.S.R.) 47 2318
[3] A. A. Shanenko, M. D. Croitoru, F. M. Peeters 2008 Phys. Rev. B 8 054505
[4] J. M. Blatt and C. J. Thomson 1963 Phys. Rev. Lett. 10 8
[5] K. Yu. Arutyunov Et al. 2019 Physics of the Solid State 61 9

Resonant activation of resistive switching in $ZrO_2(Y)$ and $ZrO_2(Y)/Ta_2O_5$ based memristors

V N Baranova, D O Filatov, D A Antonov, I N Antonov, O N Gorshkov
Lobachevsky University of Nizhnii Novgorod, Nizhnii Novgorod 603950, Russia

Abstract. We report on a comparative study of resistive switching in the memristors based on $ZrO_2(Y)$ films and on $ZrO_2(Y)/Ta_2O_5$ stacks by triangle pulses with high-frequency sinusoidal signal. The dependencies of the current difference in the low resistance state and in the high resistance one on the sinusoidal signal frequency for the memristors based on $ZrO_2(Y)$ and on the $ZrO_2(Y)/Ta_2O_5$ stack manifested one and two maxima, respectively attributed to the resonant activation of the oxygen ion migration by the alternating electric field in $ZrO_2(Y)$ and Ta_2O_5.

1. Introduction

Recently, resistive switching (RS) attracted much attention due to potential applications in non-volatile memory, the neuromorphic computing, etc. [1]. RS consists in a bistable (multistable) switching of the resistance of a dielectric film between two conductive electrodes under a voltage applied. The RS mechanism in oxides consists in forming and rapture of conductive filaments (composed of oxygen vacancies, V_Os) in an electric field between the electrodes. The electronic devices based on the RS are called *memristors*.

At present, application of memristors is limited by instability of the RS parameters, which is an intrinsic property of RS originating from its stochastic nature. Recently, a novel approach to solving this problem based on noise-enhanced stability effect in multistable stochastic systems was proposed [2]. Earlier, we found the high-frequency (HF) sinusoidal signal added to the switching pulses to improve the RS stability in $ZrO_2(Y)$-based memristors [3]. The effect was attributed to the resonant activation of the O^{2-} ion motion (drift/diffusion) via the V_Os in the alternating electric field, which promotes the rapture and restoring of the filaments. Resonant activation of the transitions between metastable states is another phenomenon manifesting a beneficiary role of noise [4].

In the present work, we studied the effect of the HF signal frequency on the RS in memristors based on $ZrO_2(Y)$ and on $ZrO_2(Y)/Ta_2O_5$ stacks. The Ta_2O_5 sublayers were found to improve the RS stability because of self-forming of Ta-rich nanoinclusions in the Ta_2O_5 layers, which play the role of the electric field concentrators promoting the filament growth [5]. The goal of the present study was to confirm resonant activation of the O^{2-} ion motion to be the origin of the RS improvement.

2. Materials and Methods

The dielectric films were deposited by HF magnetron sputtering. The thickness of the $ZrO_2(Y)$ (≈12 % mol. Y) films was ≈40 nm, the one of the Ta_2O_5 sublayers was ≈10 nm. The cross-point memristors of 20 × 20 μm^2 in size were fabricated by optical lithography.

The RS was studied using a protocol shown in in Figure 1(a). The HF sinusoidal signal pulses with amplitude A = 0.2 V, duration T_m = 0.1s, and frequency f = 0.1 – 25 kHz were added to the tops of the triangle switching pulses with the amplitudes V_{SET} = 3.5 to 4.5 V and V_{RESET} = −3.5 to −2.5 V and the durations T_{SET}, T_{RESET} = 1 s. Here V_{SET} and V_{RESET} are the switching voltages from the high resistance state (HRS) to the low resistance one (LRS) and back, respectively. The values of the current through the memristor in the LRS and HRS I_{ON} and I_{OFF}, respectively were recorded at the read voltage V_{READ} = 2 V and averaged over N_{READ} = 20 samplings. The measured values of I_{ON} and I_{OFF} were averaged over 30 write/erase switching cycles.

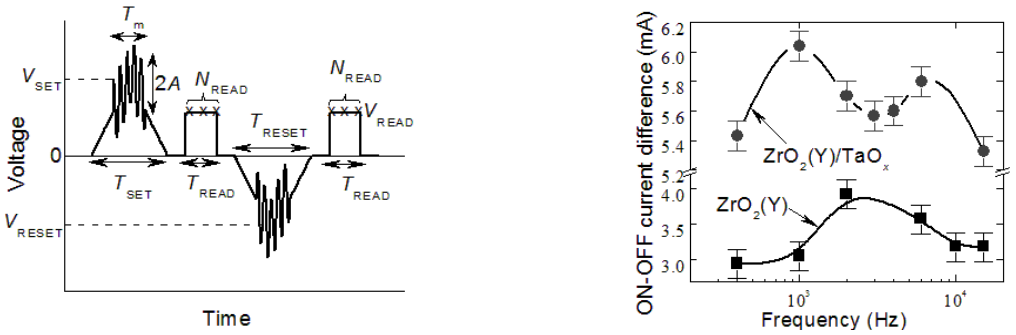

Figure 1(a, b). (a) Switching protocol; **(b)** Frequency dependencies of the difference $I_{ON} - I_{OFF}$.

3. Results and Discussion

The dependence of the difference $I_{ON} - I_{OFF}$ for the $ZrO_2(Y)$-based memristor of f shown in Figure 1(c) manifested a maximum at $f \approx 2.5$ kHz corresponding to the frequency of the O^{2-} ion jumps to the adjacent V_O^s in $ZrO_2(Y)$ at 300 K (0.4 – 8 kHz [6]). This observation confirmed the resonant activation of the O^{2-} ion motion to be the origin of the improvement of the RS performance. The dependence of $I_{ON} - I_{OFF}$ on f for the memristor based on the $ZrO_2(Y)/Ta_2O_5$ stack manifested two maxima. The higher frequency one at $f \approx 6.5$ kHz can be attributed to the resonant activation of the O^{2-} ion motion in the $ZrO_2(Y)$ layer whereas the lower frequency maximum at $f \approx 1$ kHz can be ascribed to the resonant activation in the Ta_2O_5 sublayer. One can estimate the activation energy for the thermoactivated jumps of the O^{2-} ions onto the adjacent V_Os in the Ta_2O_5 sublayer E_a from the maximum frequency f_i according to the formula

$$f_i \sim f_0 exp\left(-\frac{E_a}{kT}\right), \quad (1)$$

where $f_0 \sim 10^{13}$ Hz is the phonon frequency, k is Boltzmann constant, and T is the temperature. For $f_i = 1$ kHz one obtains $E_a \approx 0.6$ eV at 300 K. This value is ≈2 times smaller than the activation energy of oxygen diffusion in Ta_2O_5 (≈1.2 eV at $T > 700$ K [7]). On the other hand, it is ≈3 times greater than the one extracted from the electrical parameters of the Ta_2O_5 based memristors (≈0.2 eV [8]). This discrepancy can be attributed to formation of the non-stoichiometric Ta-rich nanoinclusions in the Ta_2O_5 sublayer [5].

4. Conclusion

The results of present study confirm the resonant activation of the O^{2-} ion motion in the alternating electric field to be the origin of the beneficiary impact of adding the HF sinusoidal signal to the switching pulses on the RS performance in the memristor based on the $ZrO_2(Y)$ films and the $ZrO_2(Y)/Ta_2O_5$ stacks. These results manifest the fundamental properties of memristor as a stochastic multistable system and indicate the prospects for development of innovative switching protocols to improve the RS stability.

Acknowledgments

The present study was supported by Russian Foundation for Basic Research (18-42-520059).

References

[1] Ielmini D and Waser R 2016 *Resistive Switching: From Fundamentals of Nanoionic Redox Processes to Memristive Device Applications* (Saarbruken: Wiley-VCH)

[2] Patterson G A, Fierens P I, Grosz D F 2013 *Appl. Phys. Lett*. **103** 74102

[3] Filatov D O, Antonov D A, Antonov I N, Belov A I, Baranova V N, Shenina M E, Gorshkov O N 2020 *Phys. Solid State* **62** 556

[4] Horsthemke W, Lefever R 1984 *Noise-Induced Transitions: Theory and Applications in Physics, Chemistry, and Biology* (Stuttgart: Springer)

[5] Mikhaylov A, Belov A, Korolev D, Antonov I, Kotomina V, Kotina A, Gryaznov E, Sharapov A, Koryazhkina M, Kryukov R, Zubkov S, Sushkov A, Pavlov D, Tikhov S, Morozov O, Tetelbaum D 2019 *Adv. Mater. Technol*. 1900607

[6] Yakimov A V, Filatov D O, Gorshkov O N, Antonov D A, Liskin D A, Antonov I N, Belyakov A V, Klyuev A V, Carollo A, Spagnolo B 2019 *Appl. Phys. Lett*. **114** 253506

[7] Gries U N, Schraknepper H, Skaja K, Gunkel F, Hoffmann-Eifert S, Waser R, De Souza R A 2018 *Phys. Chem. Chem. Phys*. **20** 992

[8] Hur J-H 2019 *Sci. Rep*. **9** 17019

An artificial neural network as a predictor of electrical characteristics of nanoelectronic device channel based on a low-dimensional heterostructure

NA Vetrova[1], KP Pchelintsev[1], VD Shashurin[1]
[1]Bauman Moscow State Technical University, Moscow105005, Russia

Abstract. In this paper a computational algorithm for calculating current density of low-dimensional semiconductor heterostructures based on an artificial neural network is proposed. The neural network training is performed using the quantum-mechanical model of Green's Functions.

Introduction

The rapid development of modern electronics has allowed the use of low-dimensional semiconductor heterostructures to increase the operating frequency range of devices called "ultrafast" [1,2]. However, such a small channel size of nanoelectronic devices leads to difficulties in ensuring their reliability due to the critical influence of degradation processes not only during their operation, but even during their manufacture. Modern technology computer-aided design (TCAD) systems in most cases are based on the use of semi-classical current transfer models [3], which makes them impossible to implement in the latest structures with quantum restriction and does not allow degradation in such structures at the design stage. In practice, developers are forced to use "blind" selection methods or intuitive methods "from production experience" to select the design parameters of ultrafast devices that provide the required performance characteristics. For the above reasons, an actual problem is the development of a TCAD software package for devices based on low-dimensional semiconductor structures with a quantum constraint, which allows evaluating the operating properties and reliability parameters of a nanoelectronic device at the design stage [4].

Simulation model

When developing TCAD tools for electronic devices, the efficient use of computing resources is very important. For example, in order to estimate the reliability of a device, it is necessary to perform at least 10^3 iterations of the calculation of operating characteristics. Correspondingly, the overall efficiency of the software package directly depends on the efficiency of the most frequently performed operating characteristics prediction module. The authors proposed to use an artificial neutral network, trained by quantum-mechanical model [5], as a predictor of operational characteristics in the technology computer-aided design system of modern microelectronic devices based on low-dimensional semiconductor heterostructures with quantum limitation.

Nowadays artificial neural networks are widely used in various fields of technology for approximation of complex functional associations [6]. It is known that any continuous function of many variables can be approximated by a neural network with a given accuracy. For simulation of current density the authors used forward propagation neural network (multilayer perseptron). The sigmoid function was chosen as a function of neuron activation. Training was carried out using the reverse propagation

method, and the Bayesian regularization was used as the minimization algorithm. The training set was obtained using a quantum-mechanical model based on Green's functions. Figure 1 (a) shows a 3D-graph, describing the dependence of current density on well width. As part of the verification, the results obtained by developed model and model based on Landauer-Buttiker formalism were compared. The final error in predicting current density using a model with an artificial neural network as a predictor does not exceed 3% (Fig. 1 (b)).

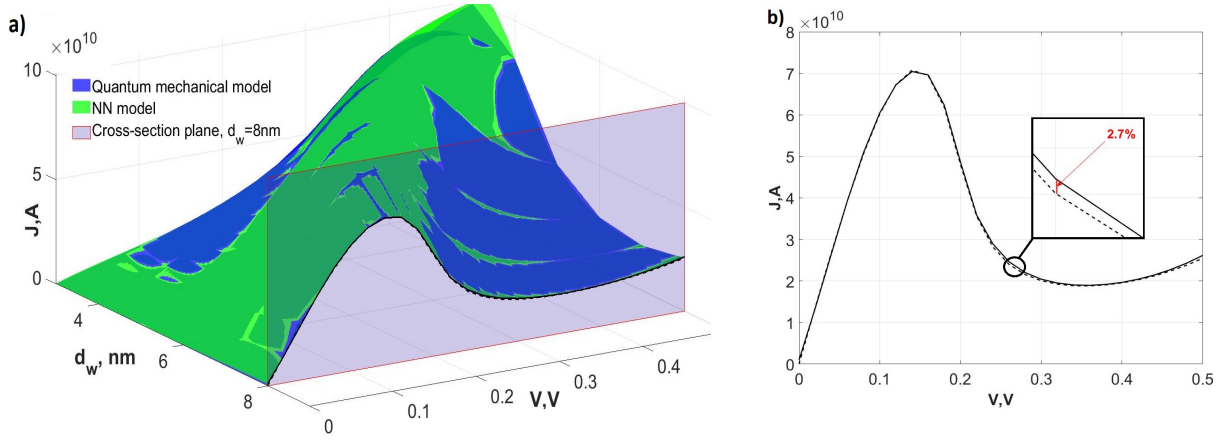

Figure 1 (a, b). (a) 3D graph describing the dependence of current density on well width;**(b)** The cross-section of a three-dimensional graph of the current density by the plane (well width is 8 nm)

Conclusion

The authors developed an effective computational algorithm for modeling the current-voltage characteristic of ultrafast devices based on low-dimensional semiconductor heterostructures. An artificial neural network trained on the basis of a quantum-mechanical model, based on the formalism of Green's functions, was used as a predictor. According to the benchmark tests of algorithms for predicting the current-voltage characteristics, an algorithm based on a trained artificial neural network demonstrated an increase in computational efficiency by more than two orders of magnitude in comparison with other quantum-mechanical models or models based on conditional analytical methods. As part of the validation of the developed computational algorithm, the difference between the model and the experimental beginning section of the CVC of resonant tunnel diode was estimated, and obtained error does not exceed 5%. Wide possibilities for modification by taking into account additional parameters and further complication of the model used for the formation of the training set, and also high efficiency of the proposed approach allow to conclude that it is reasonable to use artificial neural networks as an optimal in terms of efficiency predictor during the development of a software for technology computer-aided design of ultrafast devices based on low-dimensional heterostructures.

References

[1] M. Bozzi, L. Pierantoni, S.Bellucci, Radioengineering, VOL. 24, NO. 3
[2] Nadar S, Zaknoune M, Wallart X, Coinon C, Emilien P, Ducournau G, Gamand F and Thirault M 2017 IEEE Trans. On Terah. Sc. And Techn.6 780
[3] A. Ciprut, A. Chelly, Karsenty A., Active and Passive Electronic Components, 2015, 1–9.
[4] O. Morales, F. Periago, J.A. Vallejo, Mathematical Problems in Engineering 2018
[5] NA Vetrova, KP Pchelintsev, VD Shashurin, SA Meshkov, AA Koziy Journal of Physics: Conference Series 1410, 2019
[6] J. Schmidhuber Neural Networks 61 (2015) 85–117

Test element for high voltage SiC Schottky diodes quality control

S V Sedykh[1], S B Rybalka[1], E A Kulchenkov[1], A A Demidov[1], A Yu Drakin[1], N A Bryukhno[2], I V Kuftov[2]
[1]Bryansk State Technical University, Bryansk, 50 let Oktyabrya 7, 241035, Russia
[2]AO «GRUPPA KREMNY EL», Bryansk, Krasnoarmeyskaya 103, 241037, Russia

Abstract. In this study was constructed test element for quality control of SiC Schottky type high voltage diodes. It is shown that proposed test element give possibility for determination of parameters for testing diode before Schottky contact formation and therefore can be decrease production costs in production of SiC Schottky type high voltage diodes.

1. Introduction

The Schottky type diodes on the base of silicon carbide (SiC) have several advantages over traditional diodes because of high values of breakdown voltage and now are key components of power electronics [1]. In our previous studies it is established that SiC Schottky diodes produced by company the AO «GRUPPA KREMNY EL» (Bryansk, Russia) demonstrate good characteristics by *dV/dt* parameter [2]. However, one of some problems is determination of quality of produced diodes during their manufacturing procedure. Early was proposed test element for quality control of the manufacture of GaAs Schottky diodes, consisting of a Schottky diode formed on an epitaxial structure of one type of conductivity [3], but the main disadvantage of this test element is increased leakage currents of the Schottky diode because of higher field strength at the boundary of the metallization edge of the Schottky contact and the semiconductor. Therefore, structure 4H-SiC diode proposed in paper [4] is more preferable. Therefore the main goal of this study is to construct test element for quality control of SiC Schottky type diodes based on proposed in paper [4] Schottky structure diode.

2. Materials and methods

The proposed test element (see Fig. 1) has the following structure: on the silicon carbide substrate of n^+-type conductivity from 4H-SiC (1), an n^--type epitaxial layer with 13 μm thick (2) with an impurity concentration of 5×10^{15} cm^{-3} is formed. Further, for increasing of breakdown voltage was carried out implantation with boron ions (doses of 3×10^{15} cm^{-2} and 6×10^{15} cm^{-2}) with energies of 150 keV and 350 keV, respectively (depth of ≈0.67 μm), then p-type planar working junction 3 and a p-type dividing ring were formed (4) by annealing at a temperature of 1580 °C. Then, a silicon oxide layer SiO_2 (5) is formed two contact windows 6 were etched in oxide layer SiO_2.

3. Results and discussion

If voltage is applied between the planar working junction (3) and the dividing ring (4) (see Fig. 1) we can determine the pinch-off potential of ring after the formation of the dividing rings before the step

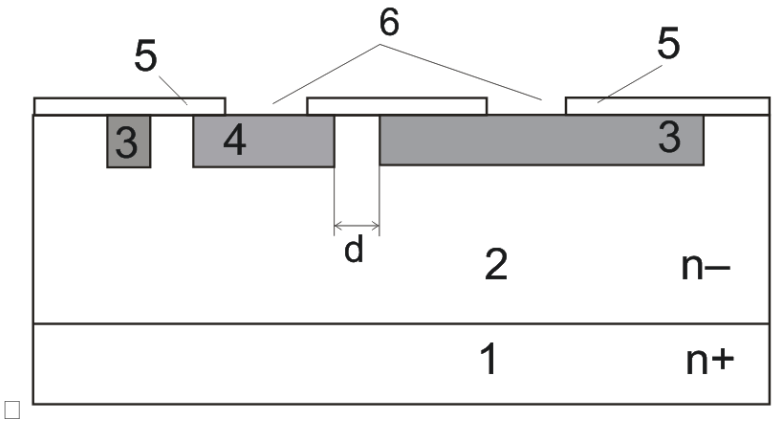

Figure 1. The structure of the test element: 1 – n^+-type substrate; 2 – n^--type epitaxial layer; 3 – p-type planar working junction (collector); 4 – p-type dividing ring (emitter); 5 – layer of SiO_2 silicon oxide; 6 – contact windows; d – is the gap between the emitter and the collector.

when Schottky contact is formed. Then, based on the obtained value of the ring potential, we can draw conclusions about the correct choice of the gap and the annealing mode, which increases the efficiency of control. As a rule, if pinch-off voltage $U_{p.o.}$ is high (>150 V) there is possibility redistribute of boron by mean of impulse annealing, but in case if $U_{p.o.}$ is small (<70 V) it lead to rejection of testing diode before Schottky contact formation that can be decrease production costs. Some test results of diode with various gap between emitter and collector are shown in Table 1. As follows from obtained data the optimal gap is 2.5 μm when breakdown voltage (~1550 V) is more then in case of 1.0 μm (~1150 V).

Table 1. The measurement results of the two test elements and Schottky diodes with different gaps d, fabricated on the same epitaxial structures and technological conditions.

No.	*d* (μm), gap between emitter and collector	Number of rings in testing diode	$U_{p.o.}$ (V), pinch-off voltage of emitter–collector for test cell	*U* (V), breakdown voltage (25°C)	*U* (V), breakdown voltage (60°C)	*dV/dt* (V/ns), speed of reverse voltage increase before failure
1	2.5	5	130	1550	1540	200
2	1.0	5	50	1150	1140	200

4. Conclusions.

Finally, the proposed test element allows to choose optimal parameters for SiC Schottky type high voltage diodes before Schottky contact formation operation and spare production costs.

Acknowledgements

This work was carried out with financial support of the Russian Ministry of Science and High Education (project No. 075-11-2019-035) at the Bryansk State Technical University.

References

[1] Baliga B J 2019 *Wide Bandgap Semiconductor Power Devices: Materials, Physics, Design, and Applications* (Cambridge: Woodhead Publishing–Elsevier)

[2] Sedykh S V, Rybalka S B, Drakin A Yu, Demidov A A, Kulchenkov E A 2019 *J. Phys.: Conf. Ser*. **1410** 012195

[3] Timofeev G O, Dragut' M V, Luk'yantsev O A 2013 *Bulletin Novgorod State University* **75**(1) 39

[4] Ivanov P A, Grekhov I V, Il'inskaya N D, Samsonova T P, Potapov A S 2009 *Semiconductors* **43**(4) 505

Planar Schottky Diode with a Γ-shaped Anode Suspended Bridge

A Shurakov[1], D Mikhailov[1,4], I Belikov[1], N Kaurova[1], T Zilberley[2], A Prikhodko[1,4], B Voronov[1], I Vasil'evskii[3], G Goltsman[1,4]
[1]Moscow State Pedagogical University, Moscow 119435, Russia
[2]Moscow Institute of Physics and Technology, Dolgoprudny, Moscow Region 141701, Russia
[3]National Research Nuclear University MEPhI, Moscow 115409, Russia
[4]National Research University Higher School of Economics, Moscow 101000, Russia

Abstract. In this paper we report on the fabrication of a planar Schottky diode utilizing a Γ-shaped anode suspended bridge. The bridge maintains transition between the top and bottom level planes of a 1.4 μm thick GaAs mesa. To implement the profile of a suspended bridge and inward tilt of a mesa wall adjacent to it, we make use of a selective etching of gallium arsenide. The layout proposed enables fabrication of a diode with mesa thickness of an arbitrary value to mitigate AC losses in the diode layered structure at terahertz frequencies of interest. At frequencies above 1 THz, it is also beneficial to use the layout proposed for the implementation of InGaAs Schottky diodes grown on InP substrate.

1. Introduction

Nowadays, GaAs is in vast demand in the monolithic microwave integrated circuit receiver technology including development of power amplifiers, frequency multipliers, coherent and direct detectors for both scientific and civilian purposes [1, 2]. GaAs planar Schottky diodes can successfully act as key elements for the development of sources and detectors of electromagnetic radiation. Shift towards terahertz frequencies of observations inspired by the increase of output power provided by modern solid-state sources leads to the need to create new efficient designs and technologies for implementing Schottky diodes based frequency conversion devices. For these purposes, we develop geometry and fabrication technology of a GaAs planar Schottky diode utilizing Γ-shaped anode suspended bridge. We also suggest that it is beneficial to use the layout proposed for the implementation of InGaAs Schottky diodes grown on InP substrate.

2. Implementation of diodes under study

The layered structure of a planar Schottky diode utilizing a Γ-shaped anode suspended bridge is provided in Fig. 1. Referring to Fig. 1(a), the following designations are employed: 1 – SI-GaAs, 2 – $Al_xGa_{1-x}As$, 3 – n_+-GaAs, 4 – n-GaAs, 5 – SiO_2, 6 – ohmic contact, 7 – cathode outer contact, 8 – Γ-shaped anode suspended bridge. The handle wafer (1) is presented by a 350 μm thick SI-GaAs layer. Presence of a 50 nm thick $Al_{0.8}Ga_{0.2}As$ etch-stopper (2) enables formation of an n-GaAs/n_+-GaAs mesa (1400 nm) (3, 4) without lowering of the handle wafer surface plane with respect to the mesa bottom level. Schottky contact is produced with the aid of Ti/Pt/Au (50/20/20 nm) metallization system deposited on the mesa surface through a 1 μm wide circular opening in 250 nm thick SiO_2 layer (5). Ohmic contact to n_+-GaAs (6) is implemented on the mesa top surface through an opening in n-GaAs

layer and makes use of Ni/Ge/Au/Ni/Au (5/20/35/15/80 nm) metallization system. Cathode outer contact (7) and Γ-shaped anode suspended bridge (8) are presented by Ti/Au (5/450 nm) bilayer, which thickness should exceed total thickness of n-GaAs, SiO_2 layers and can be significantly less than the mesa thickness. Vertical profile of the suspended bridge is determined by the mesa geometry, and the tilt angle (α) equals ~135˚ if the SiO_2 layer symmetry plane is oriented along the wafer primary flat direction. The bridge width cannot exceed thickness of the mesa. The spacing between the Schottky contact and the bridge bend may vary from one thickness of the mesa to several tens of it. In case of 2 μm spacing, EM modelling [3] suggests the diode total parasitic capacitance of ~3 fF.

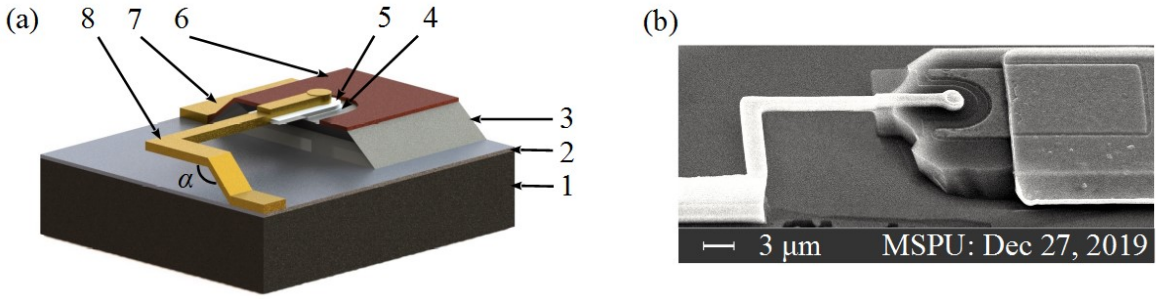

Figure 1(a, b). (a) 3d model of a diode; **(b)** SEM image of a diode.

The fabrication process described hereinabove was used to produce diodes with ideality factor of less than 1.2 and series resistance as low as 4 Ohm (Fig. 1(b)). In contrast to the air bridge diode technology relying on melting of special photoresist [1], the layout proposed enables fabrication of a diode with mesa thickness of an arbitrary value. The latter is beneficial for mitigation of AC losses in the diode layered structure [4] at terahertz frequencies of interest. At frequencies above 1 THz, it is also efficient to use the layout proposed for the implementation of InGaAs Schottky diodes grown on InP substrate. In addition to lowering of the Schottky barrier height attractive in case of a multipixel direct detector, the use of indium phosphide as a handle wafer can enable to avoid the need for membrane implementation of the diode device. The latter option is due to the recently discovered strong frequency dependence of the optical density of indium phosphide in the subterahertz and terahertz ranges [5].

3. Acknowledgments

The research has been carried out with the support of the Russian Science Foundation, project No. 17-72-30036.

References

[1] I. Mehdi et al. 2017 *Proc. IEEE* 105(6) 990-1007
[2] T. Tokumitsu et al. 2014 *SEI TECHNICAL REVIEW* 79 57-65
[3] A. Shurakov et al. 2018 *Microelectron. Eng.* 195 26-31
[4] A.Y. Tang et al. 2011 *IEEE Trans. Electron Devices* 58(10) 3260-3269
[5] X. Xu et al. 2015 *Proc. of SPIE* 9625 96250B-1

Choosing the electrode material for the fast electrochemical actuator

P S Shlepakov[1], I V Uvarov[1], V V Naumov[1], V B Svetovoy[2,3]
[1]Valiev Institute of Physics and Technology RAS, Yaroslavl Branch,
Universitetskaya 21, 150007 Yaroslavl, Russia
[2]A.N. Frumkin Institute of Physical Chemistry and Electrochemistry RAS,
Leninsky pr. 31, 199071 Moscow, Russia
[3]University of Twente, PO 217, 7500 AE Enschede, The Netherlands

Abstract. Electrochemical actuators are promising candidates for implementation in various microfluidic systems, but they suffer from a long response time due to slow gas recombination. Using a series of short voltage pulses of alternating polarity (AP) instead of one single-polarity (SP) pulse increases the operation frequency of the actuator by several orders of magnitude. However, high current density of the AP process results in fast degradation of electrodes. Besides, each electrodes works as anode and cathode. Durable material for these conditions has to be found. In this work, the electrodes made of six different materials are tested in the AP electrolysis. Current flowing through the cell, threshold voltage for the explosive operation and wear of the electrodes are analyzed and compared.

1. Introduction

Microfluidic systems such as labs-on-a-chip and drug delivery devices are widely used in biology, chemistry and medicine [1]. These systems require a compact, energy-efficient and microtechnology-compatible actuator to pump the fluid through the channels. Electrochemical actuators meet these criteria. A main part of the device is a working chamber with two metallic electrodes inside. The chamber is closed by a flexible membrane and filled with an aqueous electrolyte solution. Voltage applied to the electrodes induces electrochemical decomposition of water. Hydrogen and oxygen bubbles generated in the chamber push the membrane up. Using a series of microsecond AP voltage pulses instead of a SP pulse reduces the response time of the actuator by several orders of magnitude [2]. However, lifetime of the electrodes in the AP process is strongly limited. Firstly, the material is destroyed due to a high current density of >10 A/cm^2. Secondly, in contrast with conventional SP electrolysis, each electrode alternately plays a role of a cathode and anode. The durability can be increased by proper selection of the electrode material. In this work, we test several metals and choose one that ensures the highest values of the current flowing through the cell and the longest lifetime.

2. Materials and methods

Planar electrodes of a circular shape are fabricated of several metals (Ta, Cu, Ti, Pt, Au and Ni) on an oxidized silicon wafer. A photograph of the electrodes is presented in Fig. 1a. The metals are deposited by magnetron sputtering. The sample is placed in a Petri dish filled with the electrolyte, which is a molar solution of Na_2SO_4 in distilled water. A layer of SU-8 protects the signal lines from the electrolyte. Square voltage pulses of a positive and negative polarity are applied to the circle electrode while the ring is grounded. The frequency of the pulses is 500 kHz. The samples are tested in

two regimes. In the first one, the pulses of a fixed amplitude are applied continuously during 30 min. The amplitude is not large enough to produce explosions of the microbubbles. We record the current flowing through the cell and calculate its average absolute value I_{av}. In the second regime, a series of pulses is applied to the sample every 2 s. The amplitude is adjusted to the threshold level U_{th}, at which the concentration of nanobubbles in the electrolyte reaches a critical value. They merge into a microbubble that explodes. The experiment lasts until the electrodes are destroyed or U_{th} reaches 17 V.

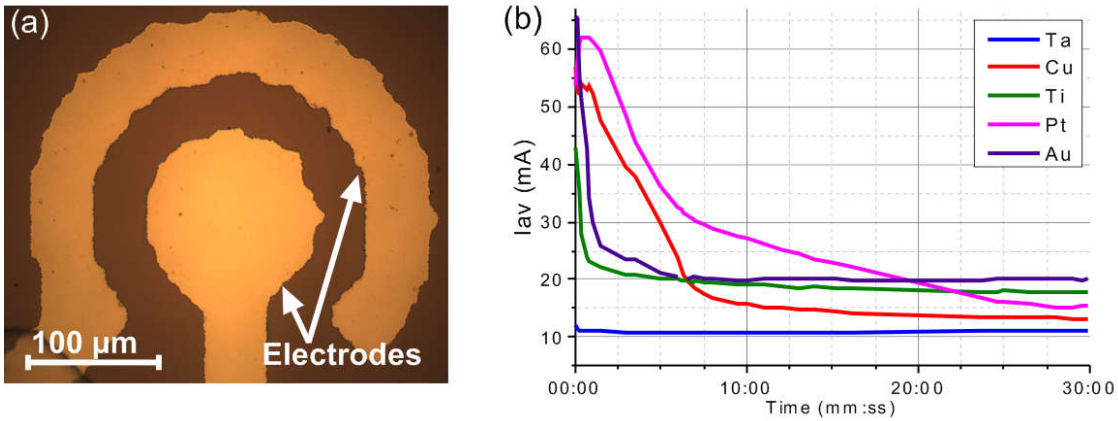

Figure 1 (a,b). (a) Top view of the electrodes; **(b)** Time dependence of I_{av} in the continuous test.

3. Results and discussion

In the continuous regime, I_{av} decreases and then reaches a constant value (Fig. 1b). This is observed for all the metals under test. At the beginning of the process, Cu, Pt and Au electrodes demonstrate the highest average current of 55-65 mA. For Ti structures, I_{av} starts with 43 mA. Ta electrodes show the lowest values of I_{av} (below 12 mA). Ni electrodes are destroyed in 5 s of the process. Pt and Cu structures demonstrate the lowest decrease rate of I_{av}, while for Ti and Au the current drops faster. At the end of the test, Ti and Au structures provide the highest current. Ti, Cu, Ta structures are oxidized, while Au, Pt and Ni electrodes are destroyed. The amount of generated gas is proportional to I_{av}. Therefore, Ti, Au, Pt and Cu electrodes are suitable for the continuous operation. These metals are tested in the explosive regime.

Cu and Au samples have the lowest initial value of $U_{th} = 9.5$ V. Pt and Ti electrodes start to generate explosions from 11 V. At the end of the test, only Ti structures are not destroyed. The threshold voltage reaches 17 V. Cu and Pt electrodes are destroyed in 3 min, while Au layer withstands 10 min.

Among the tested metals, titanium is the most suitable for the actuator based on the AP electrolysis. It is prone to oxidation, but the oxide keeps electrical conductivity and protects the electrodes from mechanical damage of explosions. Gold electrodes demonstrate slightly higher current in the continuous regime, but are quickly destroyed during explosive operation.

4. Acknowledgments

This work is supported by the Russian Science Foundation, Grant No. 18-79-10038.

References

[1] Whitesides G M 2006. *Nature*, **442** 7101

[2] Uvarov I V, Lokhanin M V, Postnikov A V, Melenev A E, Svetovoy V B 2018 *Sensor Actuat. B: Chem.* **260** 12

Efficiency of a Microwave Reflectometry for Readout of a THz Multipixel Schottky Diode Direct Detector

A Shurakov[1], **A Prikhodko**[1,2], **D Mikhailov**[1,2], **I Belikov**[1], **N Kaurova**[1], **B Voronov**[1], **G Goltsman**[1,2]
[1]Moscow State Pedagogical University, Moscow 119435, Russia
[2]National Research University Higher School of Economics, Moscow 101000, Russia

Abstract. In this paper we report on the results of investigation of efficiency of a microwave reflectometry for readout of a terahertz multipixel Schottky diode direct detector. Decent capabilities of the microwave reflectometry readout were earlier justified by us for a hot electron bolometric direct detector. In case of a planar Schottky diode, we observed increase of an optical noise equivalent power by a factor of 2 compared to that measured within a conventional readout scheme. For implementation of a multipixel camera, a microwave reflectometer is to be used to readout each row of the camera, and the row switching is to be maintained by a CMOS analog multiplexer. The diodes within a row have to be equipped with filters to distribute the probing microwave signal properly. Simultaneous use of analog multiplexing and microwave reflectometry enables reduction of the camera response time by a factor of its number of columns.

1. Introduction

Nowadays, gallium arsenide is in vast demand in the monolithic microwave integrated circuit receiver technology including development of power amplifiers, frequency multipliers, coherent and direct detectors for both scientific and civilian purposes [1, 2]. Planar Schottky diodes based on gallium arsenide wafers can successfully act as key elements for the development of sources and detectors of electromagnetic radiation. In this paper we report on the results of investigation of efficiency of a microwave reflectometry for readout of a terahertz multipixel Schottky diode direct detector. Decent capabilities of the microwave reflectometry readout were earlier justified by us for a hot electron bolometric direct detector [3]. In case of a planar Schottky diode, we observed increase of an optical noise equivalent power by a factor of 2 compared to that measured within a conventional readout scheme. For implementation of a multipixel camera, a microwave reflectometer is to be used to readout each row of the camera, and the row switching is to be maintained by a CMOS analog multiplexer. The diodes within a row have to be equipped with filters to distribute the probing microwave signal properly. The frequency of a probing signal incident to the diode on the upper side is only limited by the output line HF losses. Thus, the requirement for a Q-factor of the filters is relaxed for a 32×32 pixels camera interesting from a practical point of view. Simultaneous use of analog multiplexing and microwave reflectometry enables reduction of the camera response time by a factor of 32 which is beneficial for implementation of a real-time imaging system.

2. Experimental setup and results

Referring to Figure 1, a microwave reflectometer is employed to readout response of a terahertz planar Schottky diode to incident AM radiation produced by a 150 GHz CW source. The source modulation

frequency is equal to 4 MHz. A weak probing signal is injected into the diode through a directional coupler at 4 GHz, and the probing signal power is chosen to cause an increase of the diode bias current of 5 %. For the experiments, we used off-the-shelf diodes produced within a fabrication route similar to that previously employed by us in [4]. The diodes possessed ideality factor of 1.4, series resistance of 20 Ohm, and total parasitic capacitance of ~4 fF. The diodes were operated at bias voltage of ~0.6 V corresponding to bias current of 210 μA. We measured an optical noise equivalent power of 320 and 160 $pW/Hz^{0.5}$ at 150 GHz with the aid of a microwave reflectometer and within a conventional readout scheme, respectively. During the measurements, the 150 GHz CW source power was set to ~1 μW to insure linear response of the diodes within both readout schemes. Given that the lately enhanced MSPU fabrication technology enables fabrication of the diodes with better crucial parameters and yield of ~97 %, our findings encourage further implementation of a terahertz Schottky diode camera comprising readout scheme making use of both the microwave reflectometry and CMOS analog multiplexing [5].

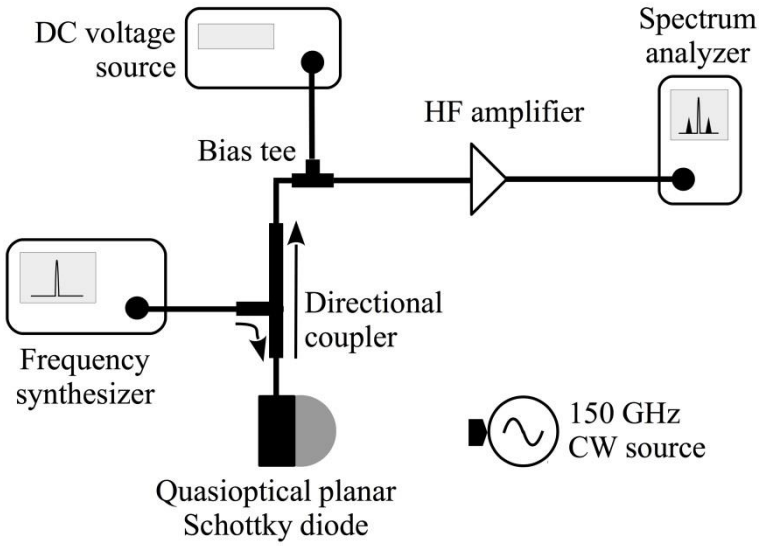

Figure 1. Experimental setup.

3. Acknowledgments

The research has been carried out with the support of the Russian Science Foundation, project No. 17-72-30036.

References

[1] Mehdi I, Siles J V, Lee C, Schlecht E 2017 *Proceedings of the IEEE* **105(6)** 990-1007
[2] Tokumitsu T, Kubota M, Sakai K, Kawai T 2014 *SEI Technical Review* **79** 57-65
[3] Shurakov A, Tong C Y E, Grimes P, Blundell R, Golt'sman G 2015 *IEEE Transactions on Terahertz Science and Technology* **5(1)** 81-84
[4] Shurakov A, Mikhalev P, Mikhailov D, Mityashkin V, Tretyakov I, Kardakova A, Belikov I, Kaurova N, Voronov B, Vasil'evskii I, Gol'tsman G 2018 *Microelectronic Engineering* **195** 26-31
[5] Han R, Zhang Y, Kim Y, Kim D Y, Shichijo H, Afshari E 2013 *IEEE Journal of Solid-State Circuits* **48(10)** 2296-2308

An improved design of a seesaw-type MEMS switch for increased contact force

N V Marukhin, I V Uvarov
Valiev Institute of Physics and Technology of Russian Academy of Sciences,
Yaroslavl Branch, Universitetskaya 21, 150007 Yaroslavl, Russia

Abstract. Microelectromechanical systems (MEMS) switches have a wide range of possible applications due to their promising working characteristics, but commercial success of these devices is limited by low reliability. In contrast with macroscopic electromechanical relays, MEMS switches typically develop a small contact force, which results in unstable and high contact resistance. In this paper we propose the design that ensures several times higher contact force in comparison with previously used structures. Enhancement of the force is achieved without increasing the footprint and operating voltage of the switch.

1. Introduction

MEMS switches with resistive contact combine advantages of electromechanical and solid state relays. They provide superior radio frequency characteristics, small size, low power consumption and high integration capability [1]. An important parameter of the switch is the contact resistance that strongly depends on the contact force. In contrast with macroscopic counterparts, MEMS switches develop rather weak forces ~10 μN. This results in a high and unstable contact resistance due to a small contact spot and inability to break thin contamination films [2]. For reliable operation, the contact force has to be increased. Here we describe the optimized design, which provides several times higher force in comparison with previously demonstrated switch. The force is increased without enlargement the size and actuation voltage of the device. Analytical calculations and finite element simulation of the modified switch are performed.

2. Design of the switch

The basic seesaw-type switch is shown in Fig. 1a. The movable electrode is an aluminium beam attached to the anchors by torsion hinges. Platinum gate and drain electrodes are placed under the each arm of the beam. Platinum contact bumps are located on the bottom side of the beam. The switch demonstrates an average contact resistance R_c = 380 Ω with a scatter from 30 to 2000 Ω. Such a high and unstable value are due to low contact force F_c of about 10 μN at the driving voltage V_g = 30 V [2]. A straightforward way to increase F_c is to increase the electrostatic force between the beam and the driving electrode. It can be done by increasing the lateral size of the switch and the actuation voltage, or reducing the gap between the beam and the electrode. However, these approaches make a switch bulky and deteriorate its performance. Another way is to optimize the design in order to enlarge the overlap area of the beam and the driving electrodes without increasing an overall footprint of the switch. The optimized design is shown in Fig. 1b. Firstly, the area of the signal electrode is reduced in comparison with the basic design. It allows lengthening the driving electrode. Secondly, the width of the beam and the driving electrodes is increased. Thirdly, the part of the driving electrode located close to the hinges is removed since it negligibly contributes to the contact force.

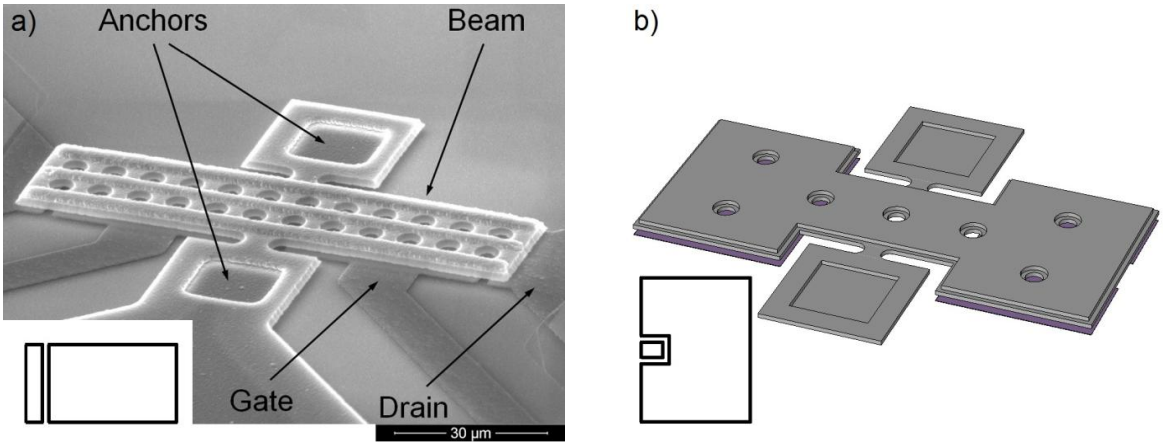

Figure 1(a, b) A seesaw-type MEMS switch: **(a)** SEM image of the basic device; **(b)** A model of the modified switch. The insets schematically show configuration of driving and signal electrodes.

3. Results and discussion

The analytical calculation gives $F_c = 13$ μN at $V_g = 60$ V for the basic design. The modified switch develops $F_c = 46$ μN, which is 3.5 times higher than the force of the basic structure. Since the contact resistance is proportional to $F_c^{-0.5}$, the increment in the force should reduce R_c by 1.5 times. The contact force is also simulated by the finite element method. The simulation provides higher F_c than the analytical approach. The difference is less than 5% for the actuation voltage below 60 V. However, it increases up to 30%, when V_g reaches 100 V. The reason of such a high difference is the bending of the beam towards the driving electrode, which is not taken into account in the analytical calculation. Nevertheless, the analytical approach is applicable below 60 V. It is worth noting that at $V_g = 100$ V the modified switch provides the contact force as high as 120 μN, which is an order of magnitude higher than the force developed by the basic device. It is expected that the optimized switch will have significantly lower and more stable contact resistance.

4. Acknowledgments

This work is supported by Program No. 0066-2019-0002 of the Ministry of Science and Higher Education of Russia for Valiev Institute of Physics and Technology of RAS and performed using the equipment of Facilities Sharing Centre “Diagnostics of Micro- and Nanostructures”.

References

[1] Rebeiz GM 2003 RF MEMS: Theory, Design, and Technology (Hoboken, New Jersey: John Wiley & Sons)
[2] Uvarov I V, Kupriyanov A N 2019 Microsyst. Technol. **25** 3243

Bipolar resistive switching in memristors based on Ge/Si(001) epitaxial layer

O Gorshkov[1], D Filatov[1], S Koveshnikov[2], M Shenina[1], O Soltanovich[2], V Shengurov[1], S Denisov[1], V Chalkov[1], I Antonov[1], D Pavlov[1], V Vorontsov[1], A Kruglov[1], E Yakimov[2]

[1] Lobachevskii State University of Nizhnii Novgorod, 603950 Nizhnii Novgorod, Russia
[2] Institute of Microelectronics Technology RAS, Chernogolovka, 142432, Russia

Abstract. Ag/Ge/Si stacks with threading dislocations in Ge layer demonstrating the I-V curves typical for the bipolar resistive switching are investigated. Cross-sectional transmission electron microscopy and electron beam induced current measurement results confirmed the resistive switching mechanism to be the formation of conductive filaments across the entire Ge layer via the electric-field driven transport of Ag^+ ions along the threading dislocations.

In recent years, the physical and chemical processes underlying the resistive switching effect (RS) in thin dielectric films have been studied intensively. The RS is a reversible change in the resistance of a thin dielectric layer enclosed between two conducting electrodes under the voltage applied to the electrodes. The electronic devices based on the RS effect are called memristors. The RS in such devices is realized via a filamentary mechanism [1]. In so-called conducting bridge (CB) memristors, the filaments consist of metal atoms injected into the dielectric layer from the electrodes. At present, main disadvantage of the memristiors is a large scatter of their parameters due to uncontrolled filament dynamics [3]. Recently, a new type of CB memristor based on a relaxed $Si_{0.9}Ge_{0.1}$/Si(001) epitaxial layer was proposed [4]. The authors intended to limit the lateral spreading of the Ag filament by its spatial confinement in the threading dislocations in the SiGe layer. As a result, a high stability of the RS parameters, a small variation of memristor parameters from device to device, and a sufficiently long information storing time were achieved. However, despite the promising preliminary results [4], the details of RS mechanisms in memristors based on dislocations in SiGe remain unexplored [5].

The present work was devoted to studying memristors based on Ge/Si(001) heterostructures grown by hotwire chemical vapor deposition (HW CVD) at low temperature (325 C). The HW CVD method admits controlling the threading dislocation density in the epitaxial structure by varying the growth conditions. The active single crystal Ge layers were ~190-nm-thick, the dislocation density was $\sim 3 \cdot 10^7 cm^{-2}$. Prior to magnetron deposition of the upper 40-nm thick Ag electrodes, the Ge layers were chemically etched to form the pits decorating the dislocations. These pits stimulated the electrodiffusion of Ag^+ ions via dislocations into the Ge layer due to the concentration of electric field. The structure of the Ag/Ge/Si stacks was examined with Jeol JEM 2100/F transmission electron microscope (TEM) with energy-dispersion spectrometer (EDS). The electrical properties were

investigated by electron beam induced current (EBIC). The *I–V* curves were measured with Keithley 2450 meter.

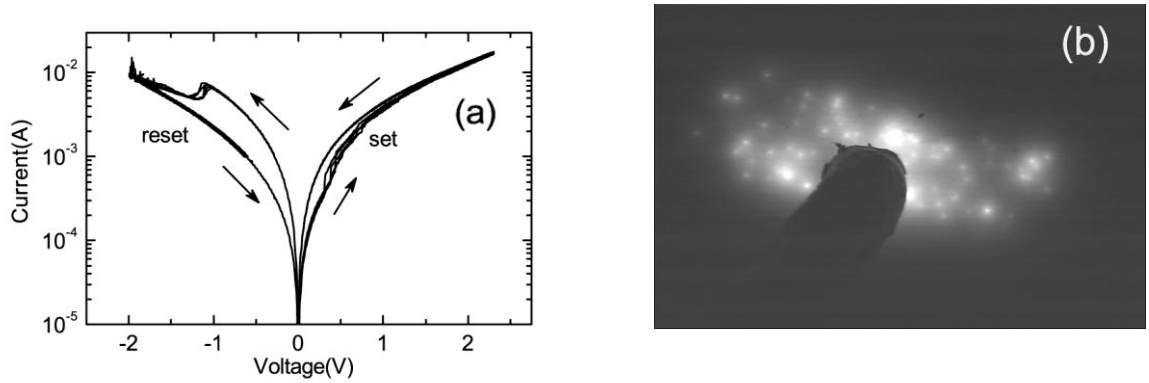

Figure 1(a, b). Typical bipolar *I–V* curves **(a)** and EBIC image (accelerating voltage 18 kV) **(b)** of Ag/Ge/Si stack.

The bipolar RS was observed in the range of voltage sweep from –2.5 to 2.5 V (Fig.1a). TEM and EDS data measured on studied stacks after several cyclic RS shows the presence of Ag with concentration ~3 % at. in the threading dislocations (Fig.2). In contrast, no Ag was observed in the Ge layer prior to forming. The white spots observed in the EBIC image (Fig.1b) can be attributed to individual dislocations in the Ge layer filled with Ag.

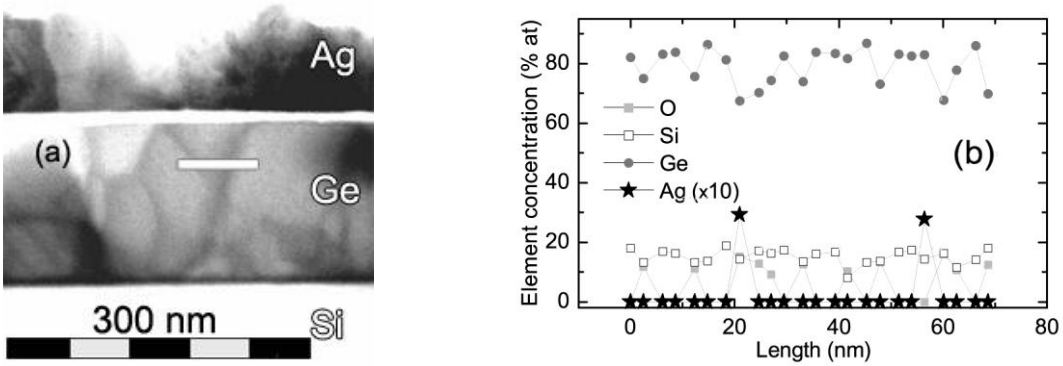

Figure 2(a, b). TEM image **(a)** and EDS profiles **(b)** of Ag/Ge/Si stack after several RS cycles. White bar in Ge layer show the places of EDS profiling. Accuracy of EDS profiling ~1% at.

Thus, the obtained results confirm the mechanism of bipolar RS in the studied stacks to be the electrophoretical metallization of Ge along dislocations.
The present study was supported by RF BR (19-29-03026).

References

[1] Ielmini D, Waser 2016 *Resistive Switching: From Fundamentals of Nanoionic Redox Processes to Memristive Device Applications*. (Wiley-VCH)
[2] Riess I 2017 *J. Electroceram.* **39** 61
[3] Goswami S et al. 2017 *Nat. Mater.* **16** 1216
[4] Choi S et. al. 2018 *Nat. Mat.* **17** 335.
[5] Strukov D B 2018 *Nat. Mater.* **17** 293

Features of signal transmission through a fiber-optic system for an interference compensation module for an active phased array antenna

A.V. Moroz[1, 2], V.V. Davydov[1, 3], R.V. Davydov[1], K. Yu. Malanin[2], V. Yu. Rud'[3]

[1]Peter the Great Saint Petersburg Polytechnic University, Saint Petersburg, 195251, Russia
[2] NTC JSC "Zaslon", Saint Petersburg 196084, Russia
[3] All Russian Research Institute of Phytopathology, Moscow Region 143050, Russia

Abstract: The article describes the operation of the X-band radar under the influence of active and passive interference. The rationale for using the interference compensation module in a radar station with a small-sized active phased array antenna is presented. A fiber-optic system has been developed for transmitting a signal from a compensation module. The results of experimental studies of the transmission system are presented. The advantages of using a fiber-optic system in a radar station in comparison with a coaxial cable are shown.

1. Introduction

Currently, there is a constant increase in the number of different stations and active objects, as a result of which the number of emitted and reflected signals increases. This leads to an increase in the congestion of the frequency ranges in which radar stations operate, and various kinds of interference are also created. The greatest influence is exerted by the active interference transmitted at the radar operating frequency. Such interference creates a noise background in which it is impossible to track the useful signal [1, 2]. Therefore, the challenge of combating such interference is paramount.

To eliminate the influence of active interference on the operation of a radar with an active phased antenna array (APAA) operating in the X band (8-12 GHz), we developed a jamming compensation module. But the operation of the module is interfered with interference to which the connecting elements of coaxial cables and other parts of transmission systems are exposed. A malfunction in the operation of the interference compensator is caused by the transmission of the information signal from the antennas through areas with increased electromagnetic load. In our work, one of the solutions to this problem is presented – the use of a fiber-optic transmission system (FOTS) [2, 3].

2. Features of the transmission of microwave signals and a laboratory model of a fiber-optic transmission system

The most difficult task is the thermal stabilization of the laser transmitting module under various difficult conditions. The use of feedback loops for this has been experimentally proven. Also, when using four horn antennas in the compensation module, it is rational to use one laser source and an optical divider. Given these features, we have developed new designs of transmitting and receiving modules for FOTS (figure 1).

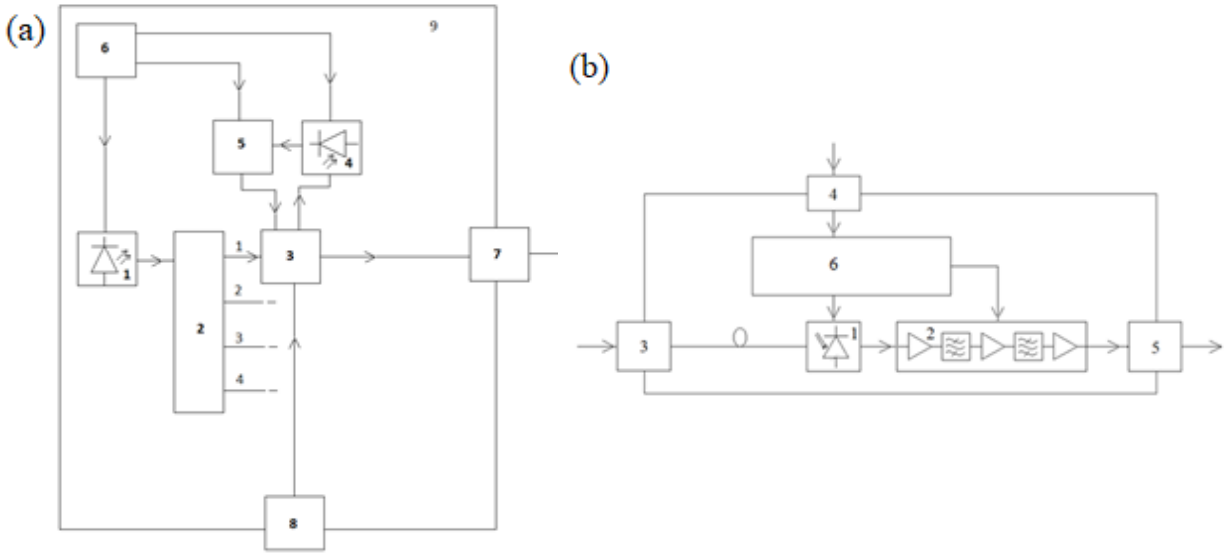

Figure 1. Block diagram of (a) - transmitting module, where 1 is a laser; 2 - optical divider; 3 - electro-optical Mach-Zehnder modulator; 4 - photodiode providing feedback; 5 is a power supply voltage control circuit; 6 - multifunctional power supply; 7 - optical connector; 8 - microwave connector; 9 - shielded case; (b) a receiving module, where 1 is a p-i-n diode based on InGaAs / InP; 2 - power amplifiers and bandpass filters; 3 - input optical connector; 4 - power connector; 5 - output microwave connector; 6 - bias voltage stabilization board.

The results showed that the frequency response unevenness (4-5 dBm) and tangential sensitivity (78 dBm) when using FOTS allow transmitting the microwave signal from the horn antenna to processing devices located in a shielded case with protection systems. And the dynamic range of stable operation (112 dBm) was no worse than that of a coaxial cable. The advantages of fiber in flexibility and compactness are obvious.

3. Conclusion

The experimental data indicate that the use of the FOTS developed by us as part of the interference compensation module allows increasing the radar protection efficiency. The main restriction on the use of the types of compensation antennas that we developed in the airborne APAA with FOTS is the availability of the necessary installation space.

References

[1] Lenets V A, TarasenkovM Yu, Davydov V V, Rodugina N S, Moroz A V 2018 *Journal of Physics: Conference Series* **1038(1)** 012037

[2] Filatov D L, Galichina A A, Vysoczky M G, Yalunina T R, Davydov V V, Rud' V Yu 2017 *Journal of Physics: Conference Series* **917(8)** 082005.

[3] Davydov,V V, Sharova N V, Fedorova E V, Vologdin V A, Karseev A Yu 2015 *Lecture Notes in Computer Science (including subseries Lecture Notes in Artificial Intelligence and Lecture Notes in Bioinformatics)* **9247** 712-721

dV/dt testing of high voltage 4H-SiC Schottky diodes with different types of melal-polymeric packages

D A Knyginin, S B Rybalka, E A Kulchenkov, A A Demidov, N A Zhemoedov, A Yu Drakin
Bryansk State Technical University, Bryansk, 50 let Oktyabrya 7, 241035, Russia

Abstract. The *dV*/*dt* values for 4H-SiC Schottky type diodes with different type packages have been determined experimentally. It is determined that obtained *dV*/*dt* values for 4H-SiC Schottky type diodes in small-sized metal-polymeric packages (SOT, QFN) are varying in interval of 670÷990 V/ns.

Introduction

At present the SiC-based high-voltage Schottky type diodes are based on absolutely new generation of power semiconductors, posses the maximal values of breakdown voltage and minimal leakage currents [1]. Earlier, in our previous studies were investigated 4H-SiC Schottky type diodes in respect of their stability to rate of reverse voltage rise *dV/dt* [2]. In particular, it was established that in 4H-SiC Schottky diodes packaged in standard large-sized package of TO (Transistor Outline) type demonstrate the value of $dV/dt \approx 150 \div 200$ V/ns [2]. It is known that the diode package is one of the main elements that determines the characteristics of the diode [3]. Moreover, at present power electronic industry comes down to use of small-sized type of metal-polymeric package such as SOT (Small Outline Transistor), QFN (Quad Flat No-leads) and others [1,3]. However, effect of packaging type on *dV/dt* characteristics of 4H-SiC Schottky diodes to present are almost not studied, therefore the goal of this work is to study *dV/dt* characteristics for Schottky diodes in different types of packages.

2. Materials and methods

The used experimental measuring test makes it possible to test on *dV/dt* characteristics of a SiC Schottky type diodes which was described in detail earlier [2]. The main parameters of tester of *dV/dt* value in interval from 100 V/ns up to 1000 V/ns at amplitude of pulse of reverse voltage applied through a testing diode $V_A = 0.05 \div 0.9$ kV. Analyses of oscillograms has been carried out with used Tektronix MDO3102 oscillograph (bandwidth 1 GHz, refresh rate 5×10^9 s^{-1}).

3. Results and discussion

To prevent experimental errors, the equipment was initially calibrated with a control signal from the equipment by applied amplitude of pulse of reverse voltage (maximal amplitude of 0.7 kV) without diode which is shown in Fig. 1 (curve *1*). Then, were tested the following 4H-SiC type Schottky diodes: diode C3D06060F (CREE/Wolfspeed, US) in large-sized TO package type (TO-220-F2); diode 5DS402A (AO «GRUPPA KREMNY EL», Bryansk, Russia) in small-sized SOT package type (SOT-89); diode C3D1P7060Q (CREE/Wolfspeed, US) in small-sized QFN package type (PowerQFN). All obtained *dV/dt* test results for diodes are shown in Table 1.

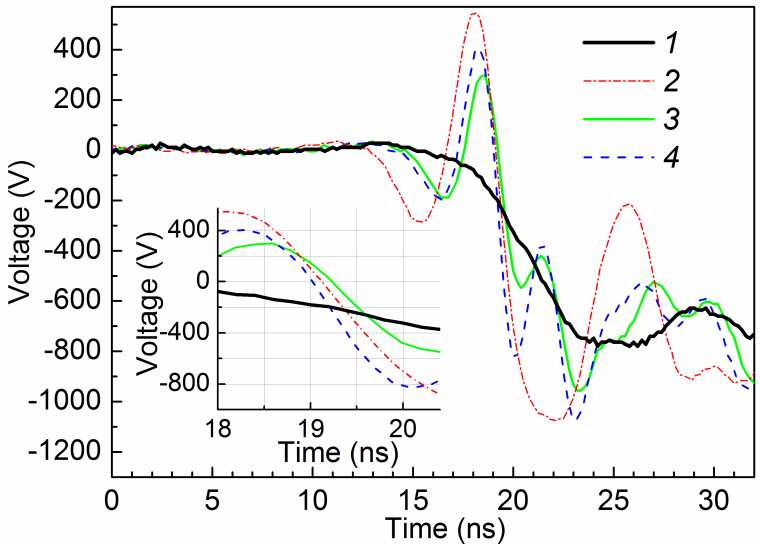

Figure 1. The reverse voltage waveform for diodes (pulse amplitude of 0.7 kV): *1* – without diode, *2* – C3D06060F (Cree), *3* – 5DS402A9 («GRUPPA KREMNY EL»), *4* – C3D1P7060Q (Cree).

The obtained *dV/dt* value for diode C3D06060F (curve *2* in Fig. 1) in large-sized TO package is equal of 880 V/ns. The testing results for diode 5DS402A (curve *3* in Fig. 1) in small-sized SOT package type is equal of 670 V/ns and for C3D1P7060Q (curve *4*) in small-sized QFN package is 990 V/ns.

Table 1. *dV/dt* results for testing of 4H-SiC Schottky diodes with different packages type.

No.	Package type	Diode's type	Package dimensions (mm)	*dV/dt* (V/ns)
1	TO-220-F2	C3D06060F	10.3×16.07	880
2	SOT-89	5DS402A	4.6×2.6	670
3	QFN 3.3	C3D1P7060Q	3.3×3.3	990

4. Conclusions.

The obtained results indicated that the package's size miniaturization not lead to *dV/dt* characteristics degradation and *dV/dt* values for small-sized metal-polymeric packages type (SOT, QFN) not only are comparable with large-sized TO package type, but in case of QFN package type the *dV/dt* results are greater than in case of the large-sized TO package.

Acknowledgements
This work was carried out with financial support of the Russian Ministry of Science and High Education (project No. 075-11-2019-035) at the Bryansk State Technical University.

References

[1] Baliga B J 2019 *Wide Bandgap Semiconductor Power Devices: Materials, Physics, Design, and Applications* (Cambridge: Woodhead Publishing–Elsevier)
[2] Sedykh S V, Rybalka S B, Drakin A Yu, Demidov A A, Kulchenkov E A 2019 *J. Phys.: Conf. Ser.* **1410** 012195
[3] Lu D, Wong C P 2017 *Materials for advanced packaging* (Cham: Springer International Publishing)

Application of developed MIC LNA in microwave radiometry equipment

S V Chizhikov[1], **Yu V Solov'ev**[1,2], **A G Gudkov**[1]

[1] Bauman Moscow State Technical University, Moscow 105005, Russia
[2] JSC «Svetlana-Electronpribor», St. Petersburg 194156, Russia

Abstract. The analysis of the developed crystals of MIC LNA of Russian production is carried out. The possibility of their application as an active element base in the development of microwave radiometry equipment was confirmed.

1. Introduction

The method of microwave radiothermometry (RTM-method) allows you to obtain information about the internal temperature of the patient's tissues based on measuring the intensity of the physical body's own electromagnetic radiation in the microwave range (the power of the noise signal at the antenna output). This method can be used for early diagnosis of cancer in various fields of medicine (mammology, urology, gynecology, neuropathology, etc.) [1-3].

Microwave radiometers can be based on different principles of structural schemes. Most of the radiometers is based on the scheme presented on Fig. 1, or its modifications. The noise signal power is measured in microwave receivers-radio thermometers, which must have a high sensitivity necessary for receiving and processing extremely weak noise signals and high accuracy of measuring the object's temperature. At the same time, the design of the radiothermometer must be miniature and allow several temperature measurements to be performed simultaneously. To date, medical radiometers operate in the frequency range of 1-3 GHz with a depth of penetration into soft tissues of 16-30 mm. One of the possible ways to ensure compliance with these requirements is the use of a modern semiconductor microwave component base for various purposes in a monolithic integrated design [1, 3-5].

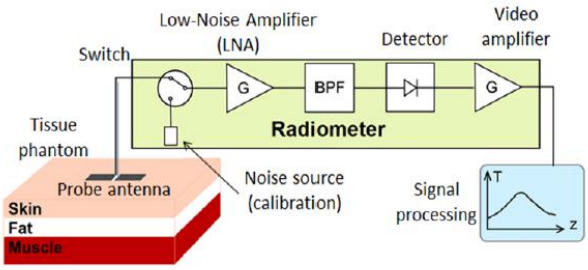

Figure 1. Circuit design of a medical radiothermometer. [5]

The key element of the medical radiothermometer design that provides high-quality reception of the microwave signal is a low-noise amplifier (LNA). The main criterion for selecting the MIC LNA from a sufficiently large product range is to coordinate with the MIC switch and ensure high gain and low noise levels [1].

2. Main part

In the manufacture of monolithic LNA, it is advisable to use transistor heterostructures based on GaAs, which have the lowest noise coefficient. Today among Russian enterprises, JSC "Svetlana-electronpribor" has experience in developing and manufacturing MIC LNA in the frequency range of 1-3 GHz based on GaAs. LNA crystals were manufactured using two types of transistor heterostructures-MESFET and pHEMT based on GaAs by the "explosive" lithography technology. To ensure optimal performance in the frequency range of 1-3 GHz, transistors in LNA crystals were manufactured using a technology with a design norm for the gate length of 0.5 microns. Such topological dimensions were provided by the use of electronic lithography in the manufacturing process of the installation. Ohmic contacts were formed using AuGe-Ni-Au metallization, and inter-element isolation was performed by ion implantation. Ti/Au metallization was used as the Schottky barrier. The protection of active (transistors) and passive (capacitance, resistance, inductance) elements of the LNA crystal topology was carried out using plasma-chemical deposition of dielectric films based on silicon nitride. From the point of view of signal amplification, it is more preferable to use pHEMT heterostructures for creating LNA – high values of the concentration of the main charge carriers in the channel and mobility allow to significantly increase the gain, which is an important condition for receiving weak signals. However, with common approaches to manufacturing transistors in LNA (MESFET and pHEMT heterostructures), a critical operation for transistors based on pHEMT heterostructures is liquid selective etching. JSC "Svetlana-electronpribor" has carried out a number of works, the result of which is the developed technology of liquid etching of epitaxial heterostructures using various selective etchants based on hydrogen peroxide, an aqueous solution of ammonia, sulfuric acid and various citrate compounds. The developed technology allows to provide a high percentage of the output of suitable saturation currents. Experimental samples of MIC LNA crystals had gain values in the range of 18-20 dB, which is a fairly good result in terms of amplifying weak signals. In Fig.2 a fragment of a MIC LNA crystal made on GaAs pHEMT is presented. The developed MIC LNA crystals are planned to be used in the future as an active element base in the development of the multi-channel radiometer.

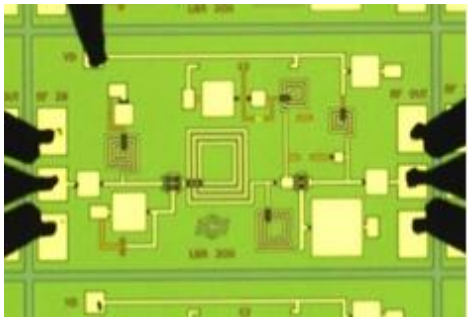

Figure 2. A fragment of the topology of a MIC LNA crystal developed on the basis of pHEMT GaAs heterostructures for operation in the frequency range of 1-3 GHz.

3. Conclusion

The analysis of the developed MIC LNA crystals of Russian production showed the possibility of their application as an active element base in the development of a multi-channel medical radiothermometer.

The use of MIC LNA based on semiconductor heterostructures of A3B5 group materials allows to provide the required performance characteristics of the radiometer in terms of receiving, amplifying and processing the microwave signal, significantly increase the functionality and implement a design with a significant reduction in the mass and size characteristics of the developed medical device.

The research is carried out to the research project No. 19-19-00349 on the theme: "A method and a multichannel multifrequency microwave radiothermography on the basis of monolithic integrated circuits for finding the 3D distribution and dynamics of brightness temperature in the depths of the human body" (Russian Science fondation).

References

[1] Gudkov A. The prospects of creating of microwave radiothermography based on monolithic integrated circuits, *ITM Web of Conferences* **30**, 13001 (2019)

[2] Sedankin M. K., Gudkov A. G., Leushin V. Yu., Vesnin S. G., Sidorov I. A., Chupina D. N., Agasieva S. V., Skuratov V. A., Chizhikov S. V. Microwave Radiometry of the Pelvic Organs. *Biomedical Engineering*. Vol. 53. Issue 4. 2019 Pp. 288-292.

[3] Vesnin S., Sedankin M., Ovchinnikov, Leushin V., Skuratov V., Nelin I., Konovalova A. Research of a microwave radiometer for monitoring of internal temperature of biological tissues, *Eastern-European Journal of Enterprise Technologies*, 4/5 (100), 2019.

[4] Gudkov A.G. Complex technological optimization of parameters of microwave devices based on heterostructures, *Nanotechnology: development and applications*. V. 11. № 2. 2019. P. 5-25.

[5] Parisa Momenroodaki, Zoya Popovic, Robert Scheeler A 1.4-GHz Radiometer for Internal Body Temperature Measurements, *Proceedings of the 45th European Microwave Conference*, pp.694-697

Analysis of the radio-frequency micromechanical switch

I E Lysenko[1], **A V Tkachenko**[1,2], **O A Ezhova**[1], **S I Shafrostova**[1]
[1]Southern Federal University, Taganrog 347922, Russia
[2] «RF Microsystems», Llc., Taganrog, 347939, Russia

Abstract. This article is devoted to optimization and calculation of the main electromagnetic parameters of the developed design of an integrated radio-frequency microelectromechanical switch with a capacitive switching principle in a configuration with a coplanar waveguide using numerical modeling methods in the ANSYS software package, as well as developed parametrizable geometric and finite element models. The proposed radio-frequency microelectromechanical switch is capable of operating in the frequency range from 18 to 26 GHz, usually called the K-band, which is used mainly for radar, as well as for satellite radio communications.

1. Introduction

Radio-frequency (RF) microelectromechanical systems (MEMS) are a rapidly developing and growing segment of modern communication technologies, both ground – based and space-based. RF MEMS segment was formed from the huge MEMS market today, which includes such miniaturized devices and devices as accelerometers, gyroscopes, microphones, mobile micromirrors, microfluidic devices, temperature and pressure sensors, etc., which are used, for example, in cars (for opening airbags) or in mobile communication devices (gyroscopes for rotating the display). This class of switches represents the potential for designing low-power, high-performance microwave circuits with high linearity, operating at frequencies up to 100 GHz with a reflection loss in the on-state of about -0.5 dB and isolation in the on-state of more than -20 dB, for example, for phase rotators of phased array antennas [1] or reconfigurable resistance control circuits [2].

RF MEMS switches can be classified as resistive and capacitive. Resistive switches are preferred for low-frequency applications, while capacitive switches are preferred for high-frequency applications. In capacitive switches, the insulation loss mainly depends on the dielectric material used between the electrodes, usually using silicon nitride, silicon dioxide and aluminum nitride. The structure of the RF MEMS switch can have a suspension type in the form of a membrane or cantilever. The use of a membrane structure with elastic suspension elements made in the form of a meander is a compromise solution that allows you to get a low actuation voltage and high switching speed.

This article presents the design of a capacitive RF MEMS switch characterized by a small value of the actuation voltage and high switching speed, as well as low reflection losses and high isolation in the K frequency range. In addition, this RF MEMS switch design allows to switch high-power RF signals, which is important for a number of different applications, such as transmitters in terrestrial or satellite radio stations.

2. Design and simulation

In this work the researched design of the capacitive RF MEMS switch is shown in Figure 1. The developed capacitive RF MEMS switch contains a gallium arsenide substrate, the coplanar waveguide,

the membrane suspended from the anchor areas using elastic suspension elements, the pull-down electrode and dielectric layers. Dielectric layers 1 are designed for electrical isolation of the constant actuation voltage offset from the RF signal on the CPW transmission line.

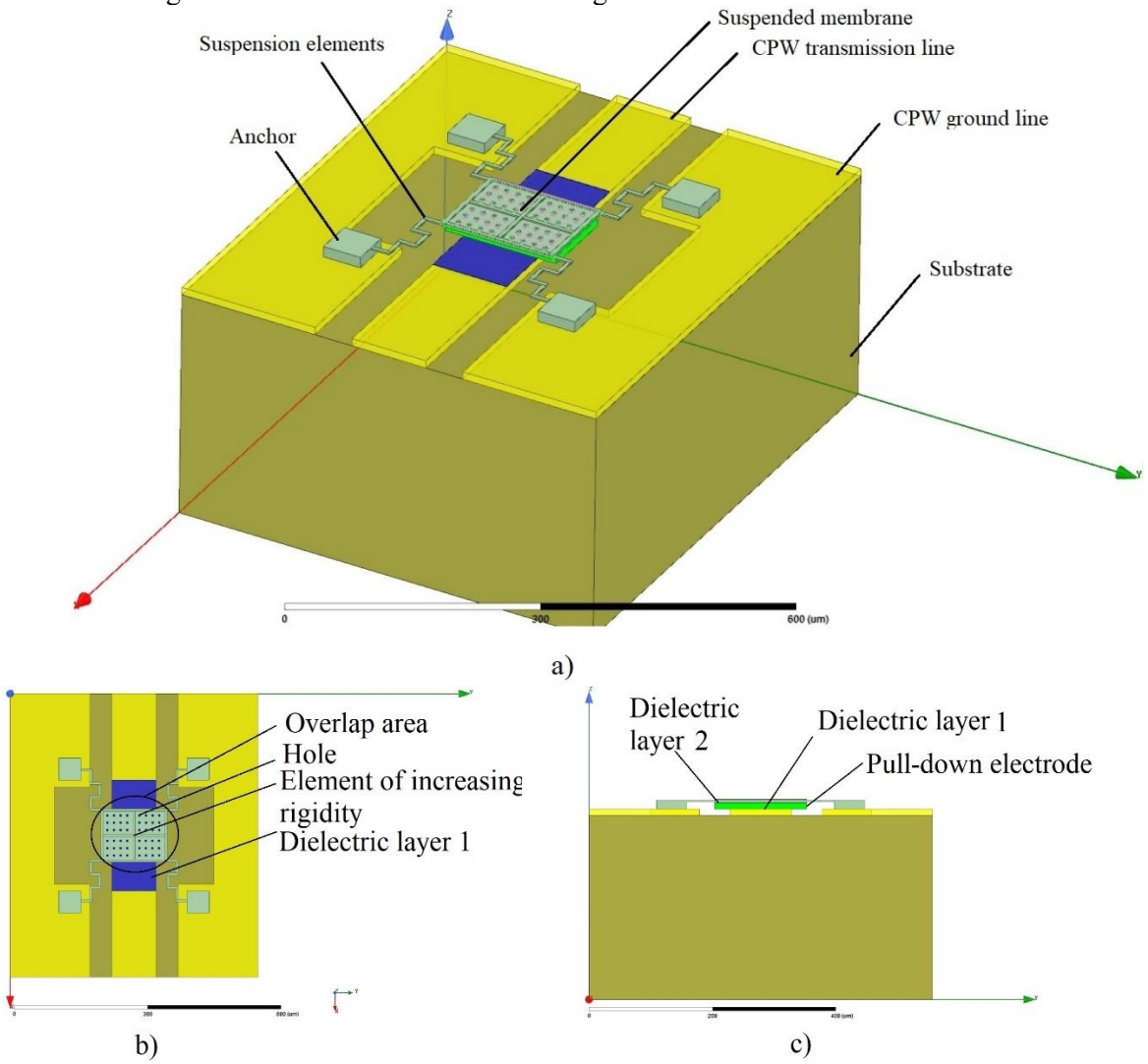

Figure 1. (a) 3D model of a capacitive RF MEMS switch; **(b)** Design topology of a capacitive RF MEMS switch; **(c)** Cross section of the design of the capacitive RF MEMS switch.

The results of modeling electromagnetic parameters are shown in Figure 2 and Figure 3. From the data provided, it follows that the value of reflection losses in the initial position of the suspended membrane is -8 dB at a frequency of 18 GHz and -7.18 dB at a frequency of 26 GHz, which indicates a good agreement of the RF transmission line on the input and output. In this case, the value of the reflection loss in the down position is within -0.2 dB for this frequency range. The level of insertion loss in the initial position of the suspended membrane is -0.9 dB this frequency range, and the value of isolation in this frequency range is in the range from -36 dB to -48 dB.

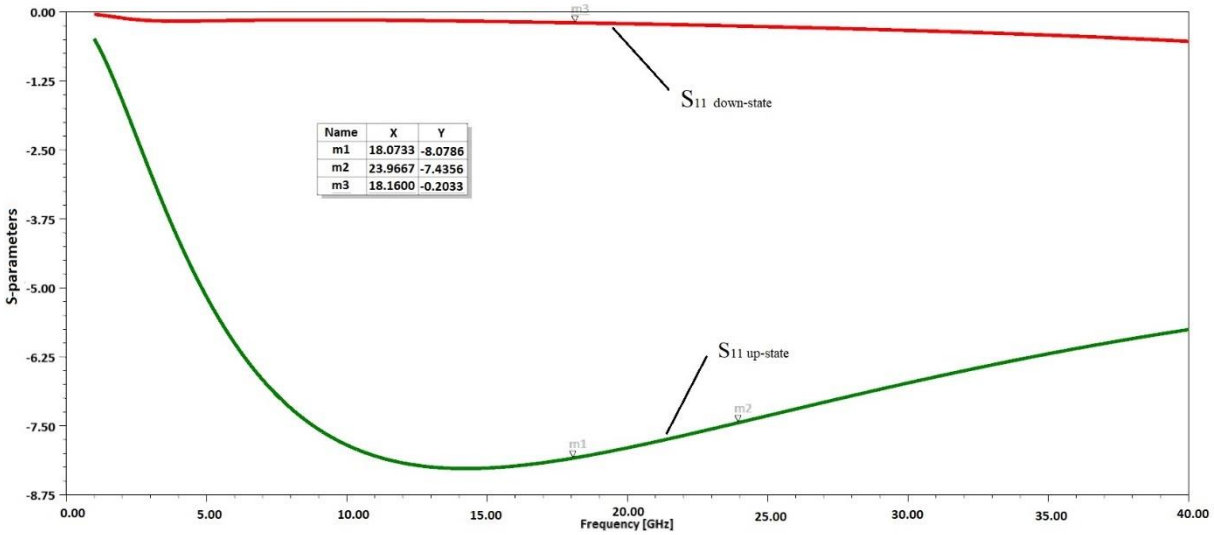

Figure 2. Modeling of electromagnetic (S) parameters of RF MEMS switch.

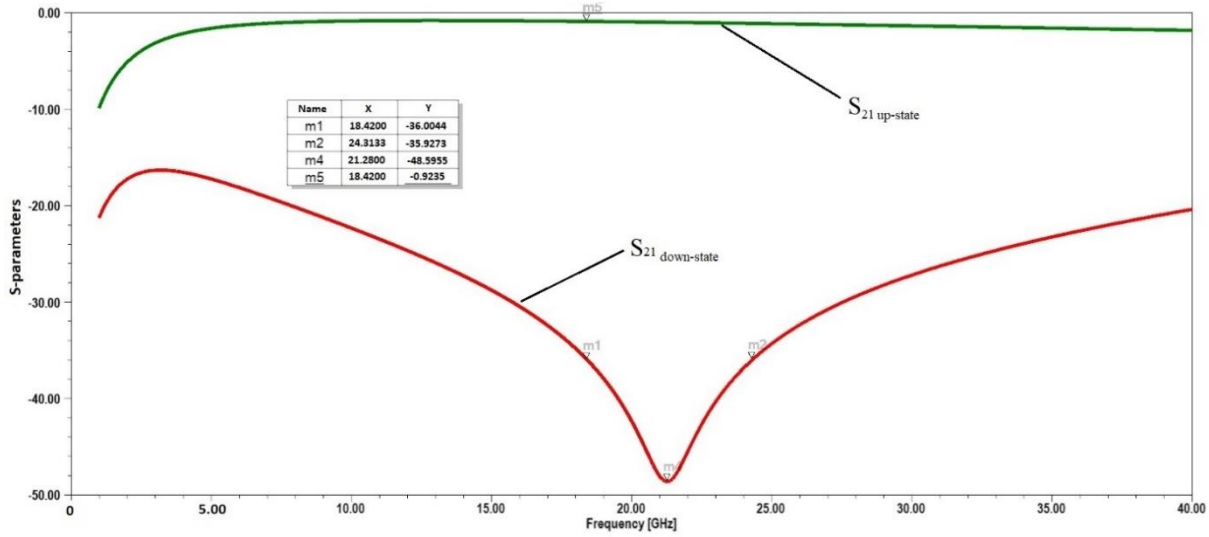

Figure 3. Modeling of electromagnetic (S) parameters of RF MEMS switch.

3. Conclusion

As a result of modeling and optimization of electromagnetic parameters using numerical methods, a design of a capacitive RF MEMS switch was obtained that is suitable for use in the K-band of frequencies with a small value of the actuation voltage, high switching speed, and provides a high power of the switched RF signal. For this frequency range, the isolation value in the closed switch position is in the range from -36 dB to -48 dB; the reflection loss is in the range of -0.2 dB. This approach in the design of RF MEMS switches allows to improve the integration of these types of switches in RF devices.

4. Acknowledgments

The work was supported by the Foundation for Assistance to Small Innovative Enterprises (FASIE) under the program "Start-1" (Contract No.3412GS1/55632) to conduct research and development work on the topic: «Development and testing of experimental samples of a single-pole RF MEMS switch».

References

[1]. Qi H., Lixin X., Lin C., Bo F., Dong L. Monolithic integrated MEMS phased array antenna scanning in two dimensions. IEICE Electronics Express – June 2017– 14(12). – p. 1 – 12.
[2]. Vaha-Haikkila T. RF MEMS impedance tuners for 6–24 GHz applications. International Journal of RF and Microwave Computer-Aided Engineering. – 2007. – 17(3). – p. 265 – 278.

Rotator for electromagnetic emission based on conformal mapping

V Pesnyakov[1], **A Vozianova**[1], **M. Khodzitsky**[1]
[1] Terahertz Biomedicine Laboratory, Department of Photonics, ITMO University, St. Petersburg 197101, Russia

Abstract. With the help of conformal mapping it is proposed a device, which brings illusion effect. Emission from current sheet source placed centered on X-axis would be almost fully rotated at an angle of 90 degrees. As a result, observer would detect that current sheet source is placed on Y-axis.

For centuries materials have led the progress of humanity: from stone to copper and glass. In the 21st century, it can be created materials with artificial predefined properties. With the help of these materials can be achieved "magical" effects. For instance, different kinds of illusions including invisibility.
One convenient mathematical tool to calculate the refractive index of material with interesting properties is transformation optics and conformal mapping. For example, in paper [1] was proposed a simple method of illusion optics based on conformal mappings. Authors made an object look like another with a significantly different shape. Another illusion was achieved in the article [2]. The resulting emission of two point sources placed symmetry to the center of the axis will be the same as from a single point source placed in the center. Another kind of illusion was achieved in paper [3]. By our colleagues using the cylindrical polar angle-dependent coordinate transformation was achieved a creation the mirage of a point source radiation at any predetermined angular direction. In the paper [4] authors also shown an illusion with sources: proposed lenses can make one active source appear omnidirectionally as two in-phase sources. In this paper, we have shown an illusion of a rotated source using similar conformal mapping as in [4] but with a more feasible range of the refractive index.

In the theory of conformal mappings, there are two complex planes (or spaces): physical $z = x + iy$ (P1) and virtual $w = u + iv$ (P2). To calculate a profile corresponding to any conformal mapping $w(z)$, it should be taken a derivative [5]

$$n = \left|\frac{dw}{dz}\right| n' \tag{1}$$

where n' is the refractive index in virtual space which is taken as 1 if the virtual space is empty.
In this paper we use a conformal mapping

$$w(z) = k\left((z^2 - 1)^{1/2} + Arch\, z\right) \tag{2}$$

where $k = h/\pi$ – is arbitrary constant. Hence a refractive index profile is taken as:

$$n = \left|\frac{z}{(z^2-1)^{1/2}} + \frac{1}{(z^2-1)^{1/2}}\right| \tag{3}$$

where we used $k = 1$ and $n' = 1$.
As it can be seen in fig. 1(a) refractive index profile is equal to 1 in the origin. Material with such refractive index is easier to fabricate than the one in [4].

To simulate a proposed effect current sheet source (from z = - 1 to 1) was placed in the medium with the calculated refractive index. It can be noticed that the emission from the source is rotated and propagate at an angle of 90 degrees. Thus, the observer would see a rotated at this angle source. It should be also noticed from the radiation pattern diagram that the beam is more collimated than from the same source placed in the air.

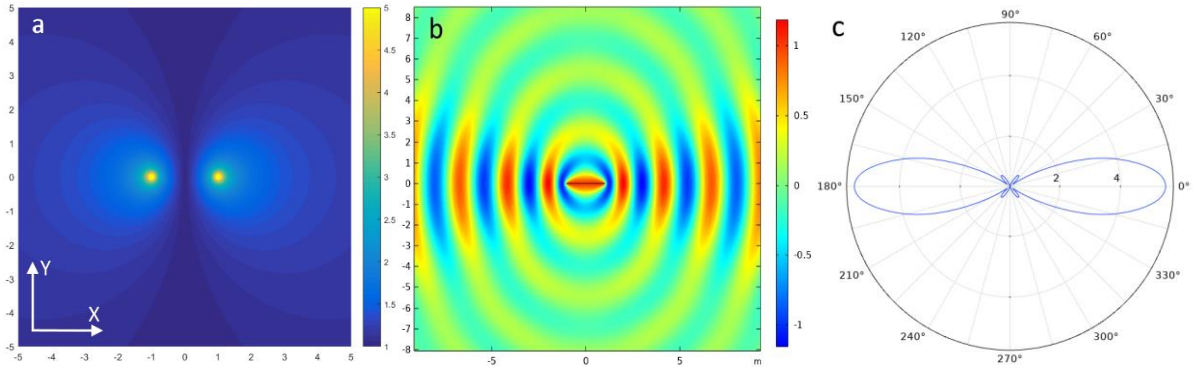

Figure 1(a,b,c). **(a)** Refractive index profile; **(b)** Full wave simulation; **(c)** Radiation pattern diagram

In conclusion, we have proposed a device to rotate emission from the specifically placed source. The refractive index of this device is calculated according to (3). As a result, the source would be perceived as rotated one by a detector or the observer. This effect was described previously [4] but with another conformal mapping. The advantage of our device is in the refractive index profile which does not become less than 1. This feature makes our device more feasible. Also, it should be noted that this effect can be realized not only for electromagnetic emission but also for any kind of waves (sound, plasmons) [6].

References

[1] Xiong Z. et al. Broadband illusion optical devices based on conformal mappings 2017 *Frontiers of Physics* 124202
[2] Xu L. et al. Conformal Singularities and Topological Defects from Inverse Transformation Optics 2019 *Physical Review Applied* 034072
[3]Vozianova A. et al. Emission illusion at an angle 2019 *Journal of Nanophotonics* 026013.
[4] Chen H. et al. Playing the tricks of numbers of light sources 2013 *New Journal of Physics* 093034
[5] Leonhardt U. Optical conformal mapping 2006 *Science* 1777-1780
[6] McCall M. et al. Roadmap on transformation optics 2018 *Journal of Optics* 063001

Analysis of the micromechanical three-axis accelerometer

I E Lysenko[1], O A Ezhova[1], A VTkachenko[1], D V Naumenko[1]
[1]Department of Electronic Apparatuses Design, Southern Federal University, Taganrog347922, Russia
[2]Department ofElectronics & Communication Engineering,National Institute of Technology, Silchar788010, India

Abstract. Micromechanical linear acceleration sensors are widely used in modern inertial orientation and navigation systems of technical equipment used in industry. The paper presents the developed design of a MEMS linear acceleration sensor with three sensitivity axes, modal and static analysis is performed, design parameters are found that ensure equality of natural frequencies along the sensitivity axes, and experimental samples are created and studied.

1. Introduction

The development of modern electronics is associated with the development of devices with low weight, dimensions, low cost, energy consumption and high enough reliability. Micromechanical accelerometers are widely used in modern technical means for various purposes: from specialized products of aerospace technology to household appliances, such as cell phones and gaming platforms of a new generation.Therefore, an urgent task today is to improve the mass and size characteristics of Microsystems, providing the possibility of registering linear acceleration of a mobile object along three axes of sensitivity [1-2].

2. Design and simulation

The developed design of a linear acceleration sensor with three sensitivity axes is shown in figure 1. This linear acceleration sensor is able to register acceleration along three axes of sensitivity using a single sensor element (CHE).

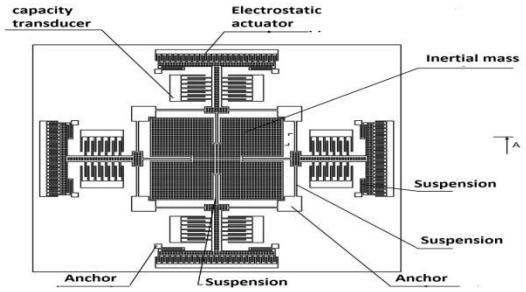

Figure 1. Design of the developed linear acceleration sensor

The principle of operation of the device is based on measuring the displacement of the inertial mass relative to the position at rest and converting this data into an electrical signal.

For behavioral research of dynamic characteristics based on the presented mathematical model (1), a VHDL-AMS description of the developed sensor was developed.

3. Experimental samples

Based on the studies of the developed single-mass design, projects of linear acceleration sensors were created, which are a developed design with different parameters of elements. When creating projects, the same natural frequencies were obtained for the three axes of sensitivity of the linear acceleration sensor, which ensures the same response of the sensor to external influences on the sensitivity axes and the same limit conditions for each axis, under which the sensor operation mode is violated.
During the research, static and modal analysis of the developed projects was carried out.
As part of this work, an experimental sample of a micromechanical sensor was created. As a result of calculating the design of an experimental sample of a micromechanical sensor, the values of the thickness of the structural layer, the parameters of the structural elements, and the capacitive displacement transducers were determined. Figure 2 shows a SEM image of the topology of an experimental sample of a multi-axis micromechanical accelerometer.

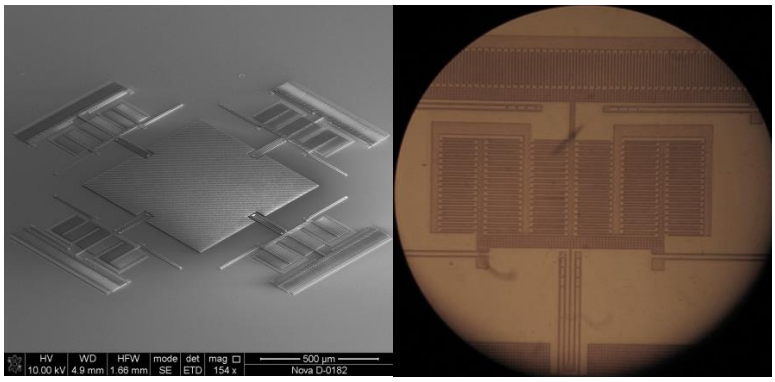

Figure 2. SEM image of the topology of an experimental sample of a micromechanical accelerometer

4. Conclusion

As a result the parameters of the micromechanical accelerometer are confirmed. The parametres were planed at the design stage: quantity of axes of sensitivity – 3; the range of the measured accelerations – ±10 g; level of suppression of cross interference – at least 50 dB; sensitivity of the capacity micromechanical transformer – at least 0,5 fF/g, sensitivity of the signal processing devices over 800 kHz/fF. Novelty of the received results consists in a solution of the problem of increase of the functional capabilities of micromechanical accelerometers by using of the principle of the functional integration. This approach provides increase of the functional capabilities of sensors and allows to register the linear accelerations on three axis of sensitivity.

5. Acknowledgments

This work was supported by RFBR research project No. 19-37-90136 “Development of the fundamental foundations for the construction of high-aspect torsion suspensions for inertial MEMS sensors”.

References

[1] Raspopov V Ja 2007*Micromechanical devices*(Tula: Tul'skijgosudarstvennyjuniversitet)
[2] Ramadoss R 2013*Solid State Technology***10**10

Simulation of the action of a three-dimensional nonlinear spiral phase plate in the near diffraction zone

PA Khorin[1], **AV Ustinov**[2]

[1]Samara National Research University, 34, Moskovskoye Shosse, Samara, Russia, 443086
[2]IPSI RAS - branch of the FSRC «Crystallography and Photonics» RAS, 151 Molodogvardejskaya street, Samara, Russia, 443001

Abstract. The report investigates the action of a spiral phase plate in the near-field diffraction zone, taking into account the three-dimensional structure of the optical element. Simulation of the diffraction of a Gaussian beam with linear polarization is performed on the basis of the finite difference in the time domain method. Numerical comparison of the action of linear and nonlinear phase plates showed a difference in their action at distancing from the optical element.

1. Introduction

A spiral phase plate [1] is an optical element with a complex transmission function $\exp(im\varphi)$, where φ is the polar angle, and m is the topological charge of the formed vortex beam. There are two main options for implementing traditional SPP: 1) a "refractive" plate with a monotonous increase in phase from 0 to $2\pi m$, 2) a "diffractive" or sector plate divided into m sectors with a change in phase from 0 to 2π in each of the sectors. The first variant is called "refractive", since the height of the optical element increases with the growth of the topological charge m.

The use of "diffractive" sector SPP does not require the formation of a high relief, but their production requires a greater transverse resolution [2]. It is known that the beams formed by diffractive SPP strongly transform when the wavelength of the illuminating radiation changes, "falling apart" into m beams with a single topological charge [3, 4]. Previously, an unconventional SPP with a phase distribution with a nonlinear dependence, described as $\exp(im\varphi^n)$, was presented . The vortex beams formed in this case have a spiral shape with an intensity and phase gradient. The unique structure of such vortex beams causes the energy flow directed in spirals, which can be used in the field of laser surface structuring [5]. In this case, it is important to know the distribution of the field that is formed in the near diffraction zone.

The report investigates the effect of a "refractive" spiral phase plate in the near diffraction zone, taking into account the three-dimensional structure of the optical element. Simulation of the diffraction of a Gaussian beam with linear polarization is performed on the basis of the finite difference in the time domain method.

2. Results and discussion

The finite difference in the time domain (FDTD) method was used to model the action of an optical element taking into account the three-dimensional structure.

Consider a nonlinear SPP of the following type: $\tau(x,y)=\exp[i\psi(x,y)]$, $\psi(x,y)=\alpha(\tan^{-1}(y/x))^q$, where α is a real number, and q is a positive integer.
We calculate the action of a three-dimensional optical element (Fig.1) with a phase defined by the function $\psi(x,y)$.

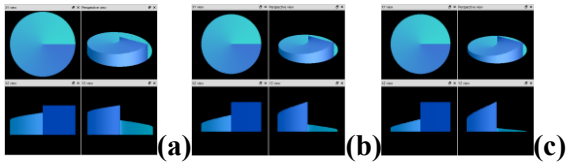
(a) (b) (c)

Figure 1. Model of SPP with parameters: α=1, n=1.5, h=3 μm, R= μm, q=1 (a) q=2 (b) q=3 (c)

To simulate the action of a spiral phase plate, it is necessary to direct a light beam at the optical element and calculate the intensity distribution formed in a certain area (Table 1).

Table 1. Modeling of SPP action. Parameters of Gaussian beam: λ=1.5 μm, σ=3 μm. Parameters of SPP: α=1, n=1.5, h=3 μm, R = 5 μm. Parameters of environment: $x,y\in$ [-5, 5] μm, $z\in$ [0,20] μm, n_c=1

q	1		2		3	
z	Longitudinal section YZ	Transverse section XY	Longitudinal section YZ	Transverse section XY	Longitudinal section YZ	Transverse section XY
20	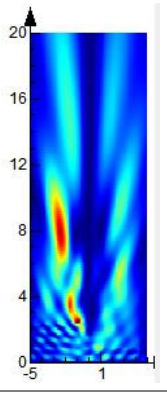	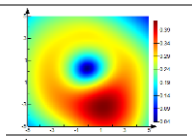	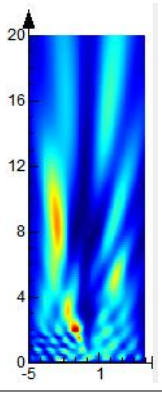	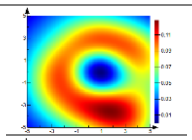	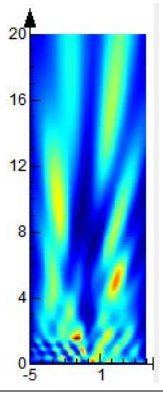	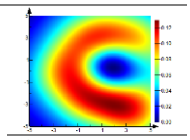
10		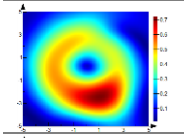		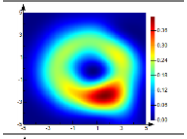		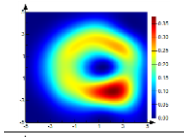
3		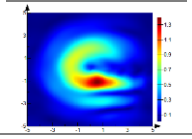		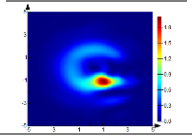		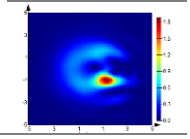

It can be seen that at a very small distance, the intensity distribution is similar to a ring with a gap. When moving away from the element, a qualitative difference appears: with a linear plate, the cross-section shape approaches the ring, and with a non-linear one, it remains an arc.

Conclusion

This report shows the action of a spiral phase plate in the near-field diffraction zone, taking into account the three-dimensional structure of the optical element. Based on the results obtained, the action of linear and nonlinear phase plates is compared.

3. Acknowledgments

This work was partially supported by the Russian Foundation for Basic Research (grant No. 20-37-70025, 18-37-00056) and by the Ministry of Science and Higher Education of the Russian Federation (agreement No. 007-GZ/Ch3363/26).

References

[1] Higgins T V 1992 *Laser Focus World* **28** 18-20
[2] Massari M, Ruffato G, Gintoli M, Ricci F, Romanato F 2015 *Appl. Opt.* **54** 4077-4083
[3] Degtyarev S A, Porfirev A P, Khonina S N, Karpeev S V 2016 *J. of Physics: CS* **735** 01202
[4] Khonina S N, Porfirev A P, Ustinov A V 2015 *J. Opt.* **17** 125607
[5] Omatsu T, Miyamoto K, Toyoda K, Morita R, Arita Y 2019 *Adv. Opt. Mater* **7(14)** 1801672

Investigation of current generation in a vertically aligned carbon nanotube under the strain gradient

A V Guryanov, M V Il'ina, O I Il'in, O I Osotova and O A Ageev
Southern Federal University, Institute of Nanotechnologies, Electronics and Electronic Equipment Engineering, Taganrog, 347922, Russian Federation

Abstract. The results of theoretical and experimental studies of the current generation process in an aligned carbon nanotube during its deformation are presented. It is theoretically established that there is a strain gradient equal to 8 in the vertically aligned nanotube under the influence of the external field strength of 10^9 V/m. The strain gradient results in a current generation of up to 12 nA. It is shown that the simulation results correlate with experimental data. The obtained results can be used to develop the nanopiezotronics devices based on vertically aligned carbon nanotubes.

1. Introduction

The new physical effects are observed in the materials on going from bulk to nanoscale. So, in the carbon nanostructures a polarization occurs in the action of the deforming strain [1]. As results a electric current generates due to the manifestation of the piezo - and flexoelectric properties [1, 2]. This fact can be used for the creation the fundamentally new devices of nanopiezotronics [3, 4]. This research direction is just beginning to actively develop and needs research on physical effects that can be the basis for creating the new devices.

The aim is theoretical and experimental studies of the current generation process due to strain gradient in a vertically aligned carbon nanotube (VA CNT).

2. Theoretical studies

The theoretical calculation of the current generated under the action of the VA CNT strain gradient was based on the process of polarization of materials under the action of piezo-and flexoelectric effects:

$$j = \frac{\varepsilon_{\parallel}}{\varepsilon_{\parallel} - 1}\left(b\frac{\partial \Delta L(L,t)}{\partial t}\frac{1}{L} + b_{fl}\frac{\partial^2 \Delta L(x,t)}{\partial x \partial t}\frac{1}{L}\right) \quad (1)$$

when j – generates current, $\varepsilon_{\parallel}$ – longitudinal dielectric constant of VA CNT, b – piezoelectric coefficient of VA CNT, b_{fl} – flexoelectric coefficient of VA CNT, L – length of VA CNT.

Simulation of the VA CNT deformation process under the action of an external electric field was carried out taking into account the previously obtained results [5]. The strain gradient of VA CNT (a diameter of 90 nm, a length of 2 μm and a Young's modulus of 1 TPa) arising from the application of a voltage pulse from 0 to 10 V and a tunnel gap of 1 nm is shown in Figure 1(a). The solution of the equation (1) is shown in Figure 1(b) for the strain gradient at $\varepsilon_{||} = 8$, $b = 0.107\,\mathrm{C \cdot m^{-1}}$, $b_{fl} = 10^{-10}\,\mathrm{C \cdot m^{-2}}$.

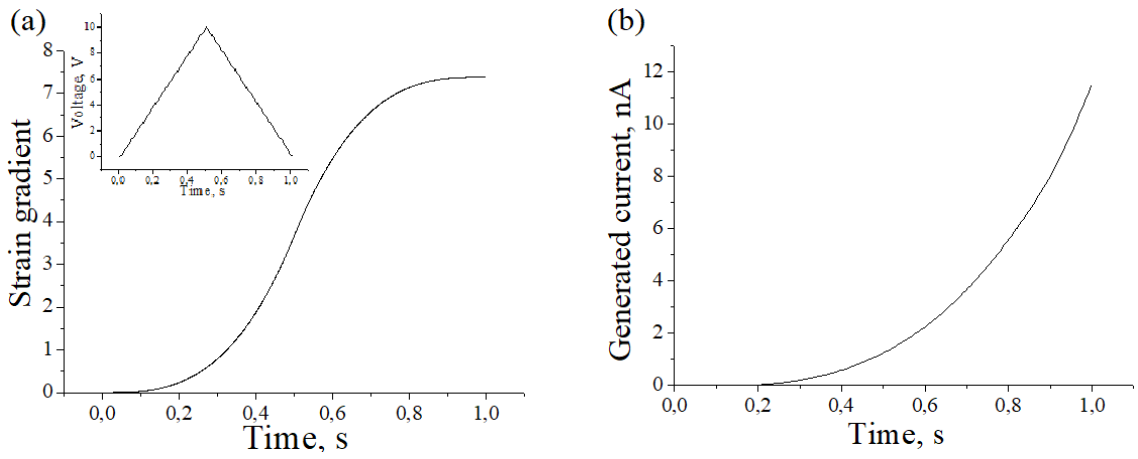

Figure 1 (a, b). (a) Theoretical time dependence of the VA CNT strain gradient on the external electric field. The insert presents the applied voltage pulse; **(b)** Theoretical time dependence of the current on the VA CNT strain gradient.

Thus, it is theoretically established that the current exponentially increases from 0 to 12 nA with an increase in the deformation gradient of the carbon nanotube from 0 to 8.

3. Experimental studies

Experimental studies of current generation in the VA CNT with a diameter of 92 nm, a length of 2.2 μm and a Young's modulus of 1.4 TPa were carried out by atomic force microscopy (AFM) on the basis of the previously developed technique [2]. It was found that the current flows in the system "lower electrode/VA CNT/ AFM probe" up to 20 nA when a force is applied to the AFM probe up to 415 nN. The obtained values correlated well with the theoretical studies.

4. Conclusion

Thus, the current generation in a vertically aligned carbon nanotube during its deformation was studied. It is theoretically established that a current arises up to 12 nA at the VA CNT stain equal to 8. The results are confirmed by experimental studies, which confirm the adequacy of the proposed model. The obtained results can be used to develop the nanopiezotronics devices based on vertically aligned carbon nanotubes. The results were obtained using the equipment of the Research and Education Center and Center of Common Using "Nanotechnologies" of Southern Federal University.

5. Acknowledgments

The reported study was funded by RFBR according to the research projects No. 20-37-70034.

References

[1] Kundalwal S.I., Meguid S.A. and Weng G.J. 2017. *Carbon* **117**, 462–472

[2] Il'ina M.V., Il'in O.I., Blinov Y.F., Konshin A.A., Konoplev B.G., Ageev O.A. 2018 *J. Materials* **11** 638

[3] Wen X., Wu W., Pan C. et al. 2014 *J. Nano Energy*

[4] Il'ina M.V, Il'in O.I., Blinov Yu.F., Smirnov V.A., Kolomiytsev A.S., Fedotov A.A., Konoplev B.G. and Ageev O.A.. 2017 *Carbon* **123**, 514–524

[5] Il'ina M.V, Il'in O.I., Blinov Yu.F., Smirnov V.A. and Ageev O.A., 2018 *Technical Physics* **63** (11), 1672–1677

Study of the ion current through the liquid meniscus between the glass nanopipette and the free surface of the electrolyte using SPM

M V Zhukov, S Yu Lukashenko, I D Sapozhnikov, A O Golubok

Laboratory of scanning probe microscopy and spectroscopy, Institute for Analytical Instrumentation RAS, St. Petersburg 198095, Russia

E-mail: cloudjyk@yandex.ru

Abstract. The ion conductivity of liquid meniscus-like nanocontact between electrolyte inside glass nanopipette and free electrolyte surface has been studied. For stabilization of the liquid meniscus arising in the gap between the nanopipette and the free electrolyte surface the feedback loop of scanning probe microscope has been used. Current to voltage characteristics of local contacts in dependence of the concentration of ions in electrolyte and the immersion depth of the pipette into the liquid surface have been measured. Both linear and nonlinear I(V) dependencies of liquid nanocontacts were observed. In addition, periodic current oscillations were observed, depending on the parameters of the feedback loop.

1. Introduction

Much attention is currently being paid to research of the fluid dynamics in nanocapillaries and the ionic conductivity of nanochannels. Thus, in [1], a direct and inverse effect of the diode characteristic of the ion current was shown depending on the charge of the walls of a solid-state nanocapillary. The idea of a nanoscale liquid diode was proposed by Daiguji and his colleagues as accumulation of charges in a narrow channel [2]. In [3] describes the fabrication of an artificial solid-state asymmetric pore ~40 nm in the form of an hourglass, which allows describing behavior in many asymmetric biological ion channels. However, for a more detailed study of ion transport in nanochannels, it is necessary to control the geometric parameters and interaction properties of capillaries and meniscus over time.

Thus, the purpose of this study is to create an adaptive nanochannel in the form of a liquid nanobridge between macro reservoirs with liquid electrolyte, using a scanning probe microscope with a probe in the form of a pointed borsilicate glass capillary.

2. Experimental setup

To achieve a stable fine adjustable liquid contact between an electrolyte (NaCl solution) flooded in pointed capillary nanopipette (NP) and the free surface of an electrolyte the scanning probe microscope (SPM) has been used. Borosilicate glass capillary was used for NP fabrication on a PMP-107 puller (MDI, USA) by thermal melting and bursting. A nanopipette filled with electrolyte with Ag/Cl electrode acted as an SPM tip and an electrolyte in Petry dish with Ag/Cl electrode acted as a sample. To achieve a meniscus-like stable liquid contact between a nanopipette filled with an electrolyte and free liquid surface of an electrolyte in Petry dish a common SPM algorithm of approaching tip to the sample was used.

In figure 1 Petri dish (1) filled with a NaCl solution and an Ag/Cl electrode (2) placed on a piezoscanner (3) with Z displacement about ~ 20 microns. The bias voltage Ub is applied to the Ag/Cl electrode (6). The stepper motor (4) provides coarse movement along the Z coordinate of the holder with NP filled with a NaCl solution (5) with an Ag/Cl electrode (6). Active anti vibration table was used to reduce mechanical oscillation (7). The ion current on the AgCl electrodes (2, 6) is converted to an electrical current. The feedback loop keeps the constant value of the ion current moving the Petri dish (1) filled with a NaCl solution with an Ag/Cl electrode along Z direction, stabilizing the liquid nanobridge between the two liquid reservoirs.

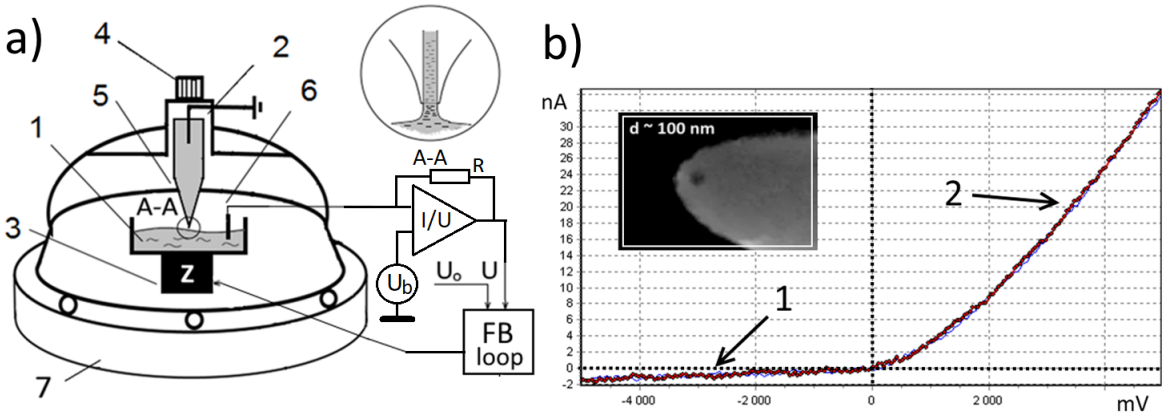

Figure 1. Scheme of the experimental setup (a): 1 – Petri dish with NaCl electrolyte, 2 – Ag/Cl electrode in the NP, 3 –piezoscanner, 4 – stepper motor, 5 - pointed capillary NP, 6 - Ag/Cl electrode, 7 – active vibration protection system, U_b – bios voltage applied to the nanocontact , U_0 – set point voltage signal. The diode current-voltage characteristic (CVC) (b) at first contact between the NP and the liquid, where 1 - the reverse (locking) diode line, 2 - the straight diode line. On the insert is the SEM image of the NP.

3. Results and Discussions

We studied the features of the diode characteristics of nanopipettes at different interaction parameters and buffer concentration (0,1%, 0,9%, 10% of NaCl) at the first moment of meniscus formation (fine contact - FC). The Debye radius, the buffer drying time, the effective length of the NP, the period of meniscus constriction and the diode rectification coefficient at different values of buffer concentrations were evaluated. Inverse CVC and current oscillations at FC mode were detected.

In the FC mode the tracking system captures some average current, while there are oscillations in the current. It is assumed that the current oscillations characterize mechanical vibrations of the thin meniscus, which can be described by the Rayleigh-Plateau instability. When changing the FB gain, a shift in oscillation frequency was detected. This can be associated with intermittent contact of the meniscus with the NP or fluctuations of the meniscus in FC mode. Reducing the current (meniscus stretching) led to a decrease in the oscillation frequency, whereas an increase of voltage led to an increase of the amplitude of oscillations.

In addition, the influence of surfactants at diode characteristics of NP was studied. Thus, anionic surfactant retains the diode characteristic at FC mode, while the sugar nonionic surfactant and glycerol in concentrations up to 50% of the buffer volume gives a linear CVC characteristic. The rectification coefficient of the diode CVC increases when the concentration of anionic surfactant increases.

Work carried out with the support of the state assignment №075-00780-19-02 (theme № 0074-2019-0007) of the Ministry of education and science of the Russian Federation.

References

[1] Ivan Vlassiouk and Zuzanna S. Siwy 2007 *Nano Lett.* **7**(3) 552-556.
[2] H. Daiguji, Y. Oka and K. Shirono 2005 *Nano Lett.* **5** 2274–2280
[3] Huacheng Zhang, Xu Hou, Jue Hou, Lu Zeng, Ye Tian, Lin Li, and Lei Jiang 2015 *Adv. Funct. Mater.* **25** 1102–1110.

New processing algorithm in quantum frequency standard on Hg-199 ions

N A Lukashev[1], V Yu Rud'[2]
1- The Bonch-Bruevich Saint-Petersburg State University of Telecommunications, Saint Petersburg 195251, Russia
2 - Department of Ecology, Russian Research Institute for Phytopathology, 143050, Moscow Region, Odintsovo district, B.Vyazyomy, Russia

Abstract. In the paper the new processing algorithm for low mass-dimensional microwave frequency standards is developed. The newly constructed design for the driver system is presented. The comparisons of experimental Allan deviation data for the previously designed prototype are performed

1. Introduction

The frequency standards are presently an integral element: for any high precision systems for object location determination, global time scales, signal transmission and processing, metrological systems [2]. These devices are widely applied for solving various tasks (for instance, ecological monitoring) on Earth and in outer space [4,5]. Frequency standard application in mobile flying vehicles faces a set of issues. They are mostly connected with mass-dimensional restrictions and power consumption for the device. Besides, frequency standards especially the ones for location determining on land or in the outer space, must possess high precision characteristics. [3]. The best solution for such cases is quantum frequency standards (QFS). These devices allow to generate or maintain a highly stable frequency.

The modernization process of standards' construction while lowering their mass-dimensional properties mostly leads to searching for new technical ideas leading to sufficient decreasing of mass and size for one of the main functional blocks as well as for developing new algorithms for automatic control and desired signal registration systems, signal that is used for determining the resonant frequency [1]. As it's often occurring, there is not enough time and resources for holding a global fundemential research and developing brand new low mass-dimensional QFS models, that is why the majority of researches regarding QFS improvement are in fact a logical continuation of previously successfully implemented developments and methods in currently functioning devices.

2. Developing a new algorithm

In the current paper we present an algorithm for handling optical signal that is based on the handled research and calculations. The pattern for photon count and PEM (Photomultiplier tube) voltage output was taken into account while processing the received signal in microcontroller MCS-51. After final processing and calculations in the controller the operation signal is formed, the one used for driving power circuits which supply electrodes of the magnetic trap (core element in the device) through a coil system.

The photon counter determines time interval τ that could be varied in a certain range depending on deployment conditions: from 1 to 10 seconds, the number of registered photons by PEM: from 10^4 to $5 \cdot 10^5$. The driving system produces processing commands judging by the number of photons emitted with the help of the newly developed algorithm in order to drive the frequency of the main quartz generator and also the power circuits. Voltage output from these circuits passes transformer coils and corrects the magnetic field in the trap in order to ensure stable and precise maintenance of the device.

The construction block scheme is presented on the fig. 1.

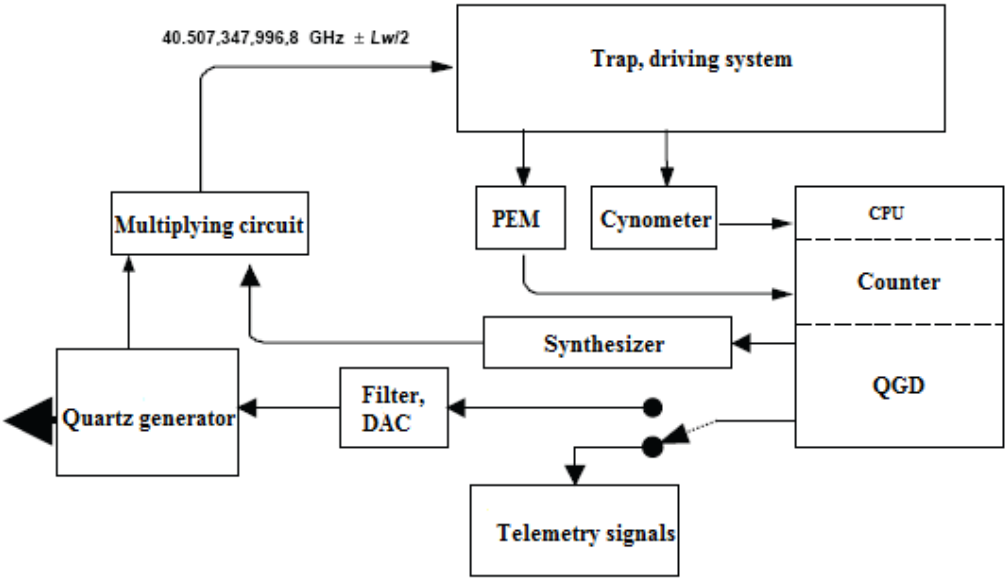

Figure 1. Block scheme of the developed control system

The whole correction cycle is represented as a feedback loop where the magnetic trap provides the controller with information regarding its resonance shift. The programmable part consists of CPU, counter and quartz generator driver (QGD), quartz generator itself receives the error signal information and shifts the produced frequency to resonance. The whole work is performed inside the counter and CPU-related parts, thus taking the most crucial tasks, digital and analog circuitry are also separated making it easier for developers to maintain the device as well as further reducing its size.

3. The results of the experimental research

The held research has shown that spectrums of the driving voltages in the new magnetic trap construction have no sufficient perturbations which may affect the stability of operation. The experiments show the slight short-term stability improvement by Allan deviation. On the fig. 2 the measurement results are presented.

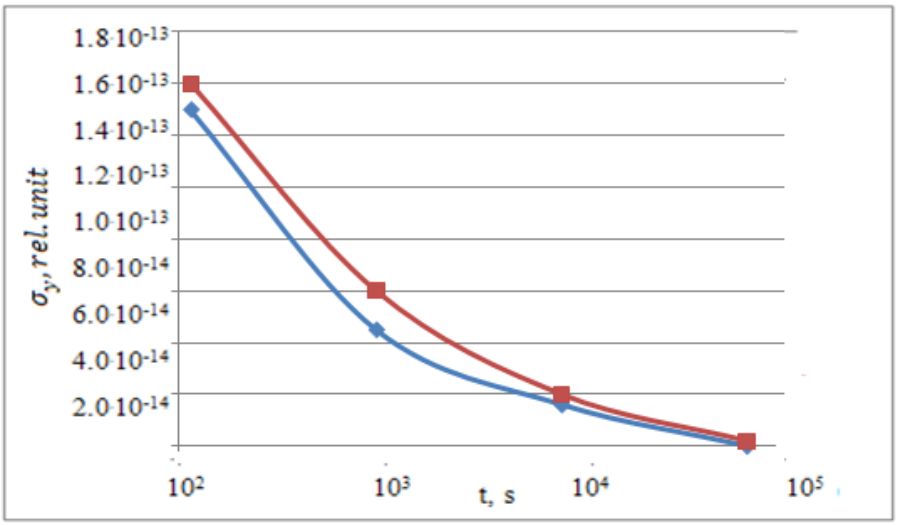

Figure 1. Allan deviation compared to the prototype

The gained data has shown a stable work of the core physical block and low level of perturbations (negative 70 dB and less).

4. Conclusion

The experimental data provides the results that it was possible to ensure the magnetic trap stable maintenance while improving short term stability characteristics by 5% and long-term stability by 3% in comparison with previously designed Hg+ 199 prototype for navigational devices and communication systems in mobile flying vehicles.

References

[1] Riechle F 2004 Frequency Standards. Basics and Applications (Wiley-VCH, New Jersy)

[2] Petrov A A, Vologdin V A, Davydov V V and Zalyotov D V 2015 *Journal of Physics: Conference Series* **643(1)** 012087

[3] Amelis Detti, Marco De Pas, Lucia Duca, Elia Perego, Carlo Sias, «A compact radiofrequency drive based on interdependent resonant circuits for precise control of ion traps», Physics.Atom-ph, 2018

[4] Balaev R I, Malimon A N, Fedorova D M, Kurchanov A F and Troyan V I 2017 *Measurement Techniques* **60** 806 – 812

[5] Kolmogorov O V, Shchipunov A N, Prokhorov D V, Donchenko S S, Buev S G, Malimon A N, Balaev R I and Fedorova D M 2017 *Measurement Techniques* **60** 901 – 905

Method of improving the rubidium – 87 quantum frequency standard's metrological characteristics

A P Valov[1], **V Yu Rud**[2]
[1] The Bonch-Bruevich Saint - Petersburg State University of Telecommunications (Russia, St. Petersburg, 193232, 22 Bolshevikov)
[2]All Russian Research Institute of Phytopathology (Russia, Moscow Region, 143050, B.Vyazyomy, Institute str., ownership 5)

Abstract. The need of using quantum frequency standard in satellite navigation systems is considered. The experimental results of improving the metrological characteristics of the standard using median filtering are presented.

1. Introduction

Requirements for navigational systems which are installed on non-stationary objects are increasing and related to the need to determine the coordinates of an object with an accuracy of less than 1.5 m for solving various problems [1-4]. The use of quantum frequency standards (QFS) as reference generators in these objects is the only possible solution that allows these requirements to be met, because they are sources of highly stable, high-precision, spectrally pure signals [1, 4].
The use of rubidium – 87 frequency standards is the most appropriate solution, because they have small dimensions in comparison with caesium – 133 QFSs, although they don't have such high metrological characteristics as caesium QFSs do. An improvement in their accuracy characteristics is required to ensure the solution of these problems. Experience with these QFSs has shown that the most optimal solution is the modernization of devices in operation [3, 4].

2. Principle of operation of the rubidium frequency standard

The operation of the rubidium – 87 QFS is based on the principle of tuning the less stable frequency of the voltage-controlled crystal oscillator (VCXO) to the highly stable frequency of the quantum transition of rubidium – 87 atoms. A microwave excitation signal is generated in the frequency multiplier block. The interaction of the microwave field with rubidium – 87 atoms causes their transitions to the corresponding unpopulated level. It is possible to determine the frequency of the microwave field at which the transition probability is maximal by measuring the population of this level after interacting with the microwave field. The signal-to-noise ratio (S / N) of the recorded resonant signal from the emitted photons at the photodetector in this case will be maximum. The received signal is used to generate a highly stable frequency which equal to 6834.7 MHz [1 - 4].
This frequency is corrected for effects that lead to frequency shifts of the central resonance. The main contribution to the frequency shift of the central resonance is made by the parameters of the microwave excitation signal. Therefore, the process of generating a microwave signal, which is fed into the interaction zone of rubidium-87 atoms with the field along the waveguide path, needs to be given increased attention when upgrading the design of the QFS.

3. Experimental studies

Studies have shown that the accuracy of tuning to the resonant frequency f0 in the QFS will depend on the step of the microwave excitation signal frequency tuning Δf_{MW}. With this in mind, we proposed a new method for generating frequency adjustment codes for a microwave excitation signal in a frequency converter, which can significantly reduce the Δf_{MW} value compared to previously used QFS designs.

The principle of operation of the new technique is based on the use of median filtering of the QFS's error signal (ES). Median filtering sorts and filters the digitized error signal values sent to the QFS control unit. After calculating the ES difference, the control unit generates codes for adjusting the frequency of the VCXO. This makes it possible to fine-tune the frequency of the microwave excitation signal to the central resonance frequency f_0 (maximum S / N ratio in the photodetector). These changes are clearly visible on the phase noise spectral power density S_φ of the error signal shown in Fig. 1.

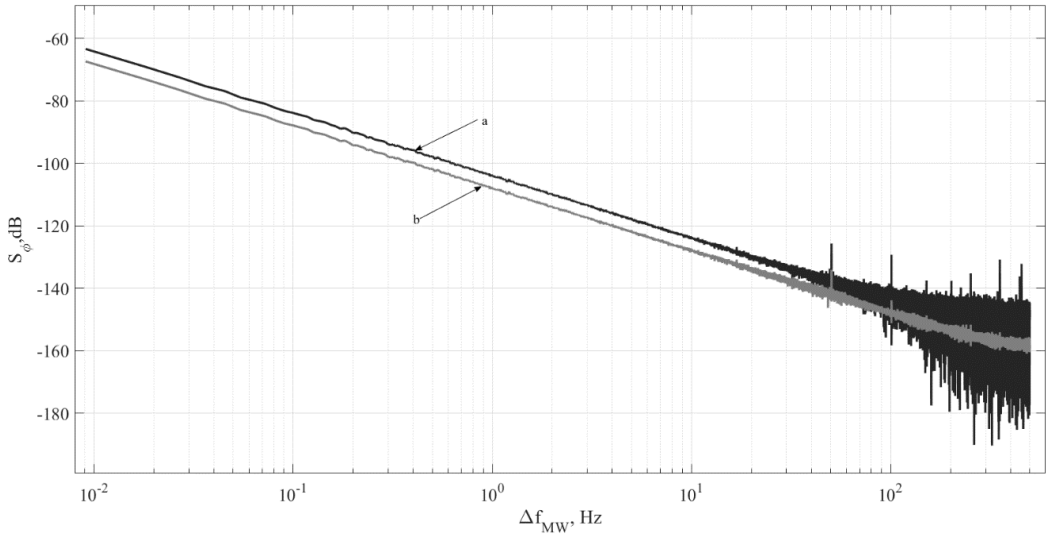

Fig. 1(a,b). The phase noise spectral power density of error signal: a - the previous version of the software; b - the new version

4. Conclusion

The studies showed the universality of the proposed method for using the improvement of metrological characteristics, in particular, it can be used for QFS on caesium atoms - 133, because the principle of operation of the standard on caesium atoms is also based on the principle of tuning the frequency of the crystal oscillator according to the frequency of the caesium atomic transition - 133. It was also found that the use of a new method for adjusting the frequency codes of the microwave excitation signal improved the Allan dispersion of the output signal of the QFS by more than 5% compared with previously used designs. This allows to solve the problem of determining the coordinates of the object with an accuracy of less than 1.5 m.

References

[1] V.M. Polyakov, E.A. Viktorov, A.V. Kovalev, and O.A. Orlov, "A RF frequency standart design based on a beat note between longitudinal modes of a frequency locked CW-laser," Proceeding-International Conference Laser Optics, LO 2014, Saint Petersburg,.6886216, pp. 123, July 2014.

[2] A.V. Kovalev, V.M. Polyakov, and A.A. Mak, "Progress in opticalspace-based clocks: Status, perspectives and applications," Proceeding- International Conference Laser Optics, LO 2016, Saint Petersburg, 6886216, pp. 201, July 2016.

[3] N.A. Lukashev, A.A. Petrov, V.V. Davydov, N.M. Grebenikova, and A.P. Valov, "Improving performance of quantum frequency standard with laser pumping," Proceeding-International Conference Laser Optics, LO 2018, Saint Petersburg, 8435889, pp. 271, July 2018.

Modeling of dispersive grain-boundary transport in polycrystalline electrodes

E.V. Morozova[1], R.T. Sibatov[1,2]
[1]Ulyanovsk State University, Ulyanovsk, 432017, Russia
[2]Institute of Nanotechnology of Microelectronics of the Russian Academy of Sciences (INME RAS), Moscow, 115487 Russia

Abstract.
The effect of anomalous grain-boundary diffusion on the measurements of drift mobility in polycrystalline semiconductors is studied within the fractional differential model of dispersive transport. Inhomogeneous distributions of the electric field and the density of localized states are also considered. Analytical solutions are obtained by the method of separation of variables applied to the fractional Fokker-Planck equation and validated by the Monte Carlo simulation of hopping transport on inhomogeneous distributions of localized states. Obtained results can be useful in the interpretation of the time-of-flight measurements of charge carrier transport in perovskite solar cells.

An important method for studying electron transfer in low-conductivity semiconductors is the time-of-flight (ToF) experiment, which has recently been used to study the features of charge transport in perovskite solar cells [1] and organic bulk heterojunction cells [2]. In the ToF method, the photocurrent response is studied after the injection of nonequilibrium charge carriers by a short laser pulse from the side of the transparent electrode. Typically, a strong electric field ($> 10^5$ V / cm) close to the dielectric breakdown conditions is applied to the sample in order to eliminate the effects of space charge and reduce the contribution of carrier diffusion to the observed response. The correct interpretation of the ToF measurements in inhomogeneous structures remains relevant, since not only the density of states determines the kinetics of the photocurrent, but also the morphology of the percolation regions, the presence of defective layers, inhomogeneity of the electric field, recombination, etc. For charge carriers in disordered semiconductors, dispersive transport is usually observed, which is characterized by subdiffusive behavior, power law decay of transient current and nonlinear dependence of the time of flight on the sample width [3].

Using the ToF method, the author of Ref. [1] measured the drift mobilities of electrons and holes in the perovskite methylammonium lead iodide. It was determined that the dispersive transport mode is typical for both photoinjected charge carriers. It is indicated, that the optimal thickness of the perovskite layer can be determined by calculation and dispersive transport must be taken into account in these calculations.

In the present work, we study the effect of diffusion along grain boundaries, the inhomogeneity of the distribution of the electric field and the density of localized states along the width of the sample in the framework of the fractional differential model of dispersive transport [3,4]. The model of anomalous grain-boundary diffusion leads to the generalized Fokker-Planck equation with a truncated fractional derivative [5]. The transient current curves demonstrate a transition from the dispersive transport mode to the normal drift-diffusion with the sample thickness increase. The presence of traps at grain boundaries leads to a distributed dispersion parameter and, as a consequence, competition between subdiffusion modes.

In the case of an inhomogeneous distribution of the electric field over the sample thickness, the assumption of homogeneity leads to underestimated values of drift mobility [1]. The transition current curves show maxima near the time of flight. A similar effect occurs in the case of an increased concentration of localized states at the surface of the sample (near the electrodes).

Analytical solutions are found by solving the initial-boundary value problem for the fractional Fokker-Planck equation by the method of separation of variables, using the representation of a subordinated random process. The solutions are in agreement with the results of Monte Carlo simulation of hopping transport on inhomogeneous distributions of localized states.

The study is supported by the Russian Science Foundation (project 19-71-10063).

References

1. Maynard, B. (2018). Dispersive Transport and Drift Mobilities in Methylammonium Lead Iodide Perovskites. PhD thesis.
2. Morfa, A. J., Nardes, A. M., Shaheen, S. E., Kopidakis, N., & Van De Lagemaat, J. (2011). Time-of-Flight Studies of Electron-Collection Kinetics in Polymer: Fullerene Bulk-Heterojunction Solar Cells. *Advanced Functional Materials*, *21*(13), 2580-2586.
3. Sibatov, R. T., & Uchaikin, V. V. (2009). Fractional differential approach to dispersive transport in semiconductors. *Physics-Uspekhi*, *52*(10), 1019.
4. Metzler, R., Barkai, E., & Klafter, J. (1999). Anomalous diffusion and relaxation close to thermal equilibrium: A fractional Fokker-Planck equation approach. *Physical review letters*, *82*(18), 3563.
5. Sibatov, R. T. (2019). Anomalous Grain Boundary Diffusion: Fractional Calculus Approach. *Advances in Mathematical Physics*, *2019*.

Simulation of one-dimensional van der Waals heterojunction formed by a carbon nanotube embedded into MoS_2 nanotube

D.A. Timkaeva[1], R.T. Sibatov[1,2]
[1]Ulyanovsk State University, Ulyanovsk, 432017, Russia
[2]Institute of Nanotechnology of Microelectronics of the Russian Academy of Sciences (INME RAS), Moscow, 115487 Russia

Abstract.
The concept of van der Waals (vdW) heterostructures provides a wide range of possibilities of combining two-dimensional (2D) layered materials for heterogeneous integration at atomic level without the constraint of lattice matching. The resulting structures exhibit unique physical properties and are promising for nanoelectronic and photonic applications. Recently, the concept of vdW heterostructures has been extended to 1D materials, and coaxial heteronanotubes have been synthesized. In the present work, we simulate a one-dimensional vdW heterojunction based on a carbon nanotube (semiconducting or metallic) embedded into a uniaxial MoS_2 nanotube. Using first-principles methods, electron difference density and transmission spectra are calculated for two vdW junctions at room temperature. This junction can serve as a nanodiode with controlled width of a space charge region.

Vertical heterostructures based on 2D materials can be combined from one atom thick layers. Due to strong covalent bonds inside layers and weak vdW interation between them, there is no the atomic interdiffusion. As a consequence, vdW heterostructures have atomically regulated interfaces, and the constraint of lattice matching is removed. The recent paper [1] reported on the extension of the vdW heterostructures concept to 1D materials. Coaxial single-crystal layers of hexagonal boron nitride (BN) and molybdenum disulfide (MoS2) crystals were grown on single-walled carbon nanotubes (SWCNTs).

In this report, we present the simulation results of a 1D vdW heterojunction formed by SWCNT embedded into a uniaxial molybdenite (MoS_2) nanotube. Metal dichalcogenide (MX_2) nanotubes are one-dimensional quantum systems with a wide bandgap. Unlike nanoribbons, they do not have rough edges with dangling bonds and are characterized by higher thermodynamic stability. MX_2 nanotubes in combination with carbon nanotubes are promising for applications in nanoelectronics and photonics [2]. In contrast to [2], where Schottky diodes MX_2 – CNTs with a contact at the edges of nanotubes are studied, we consider a 1D vdW heterojunction formed by the SWCNT inserted inside MoS_2 nanotube. The simulation in [3] indicates an inhomogeneous distribution of the space charge region (SCR) in the Schottky junction with a tendency to charge transfer from metal and chalcogen atoms to carbon atoms. Figure 1 shows a simulated nanodiode based on a 1D vdW heterostructure MoS_2-CNT. Using the density functional theory (DFT) based method implemented in the QuantumATK package, electron difference density, electrostatic difference potential and projected local density of states are calculated. From electron difference density, one can see that SCR is located near the SWCNT surface over the length of vdW junction. This confirms the tendency mentioned above.

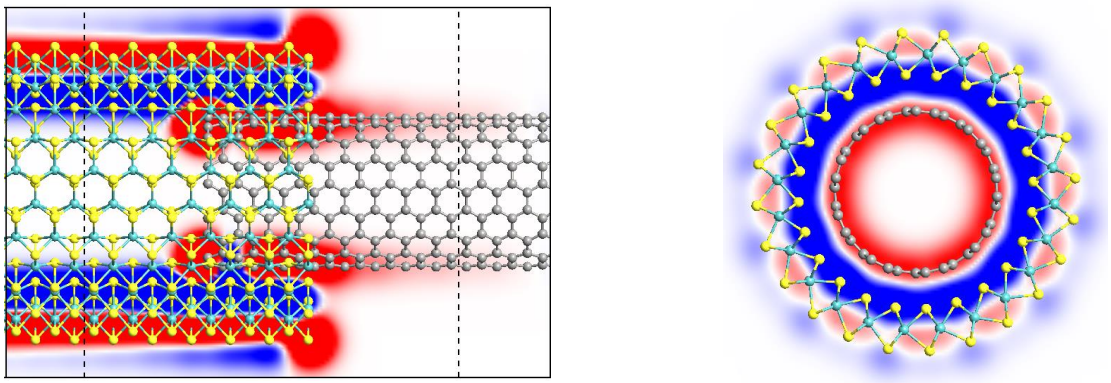

Figure 1. 1D vdW heterojunction MoS_2 - CNT(9,9) and calculated electron difference density.

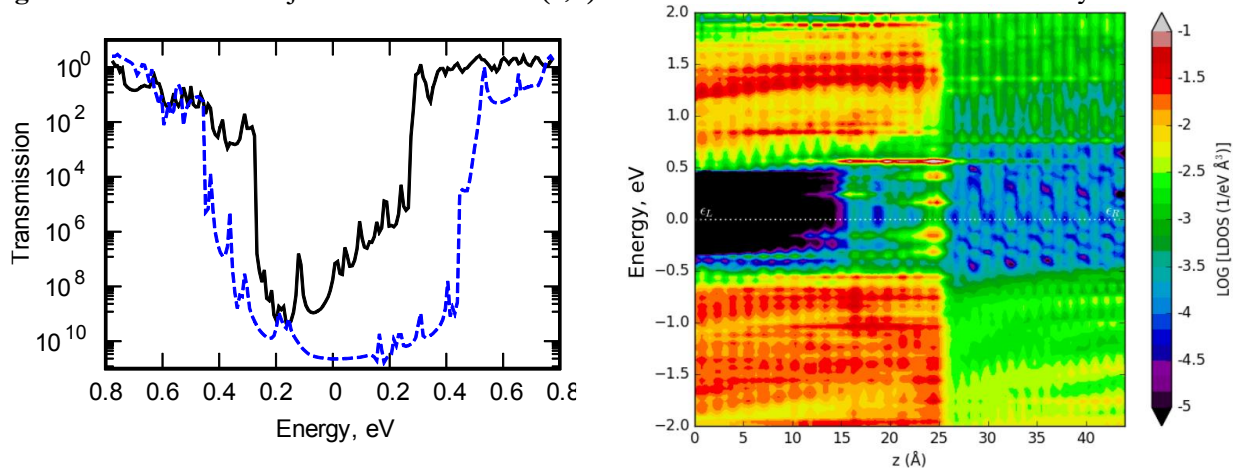

Figure 2. Transmission spectrum of 1D vdW heterojunctions MoS_2 with CNT(9,9) (blue dashed line) and CNT(17,0) (black solid line) and projected local density of states for junction MoS_2-CNT(9,9) .

The transmission spectra and IV curves were calculated using the method of nonequilibrium Green functions (NEGF) implemented in the QuantumATK package. The current is calculated via

$$I = \frac{e}{h}\int T(E)[f_L(E,T_L) - f_R(E,T_R)]dE \quad (1)$$

where f_L and f_R are Fermi-Dirac distributions of electrons in the left and right electrodes at corresponding temperatures, $T(E)$ – transmission spectrum calculated by DFT and NEGF. In Figure 2, the transmission spectra for MoS_2 contacts with semiconducting SWCNT (17,0) and metallic SWCNT (9,9). The MoS_2-SWCNT(17,0) junction demonstrates a higher rectification index than the considered Schottky diode, for which the projected local density of states is shown in Figure 2 (right panel). In SCR, there is enhanced concentration of states with energies in the bandgap of the MoS_2 nanotube. The size of SCR and, therefore, its capacity can be easily varied by selecting the diameter and chirality of nanotubes, as well as changing the length of the heterojunction attachment.

This work is supported by the Ministry of Science and Higher Education of the Russian Federation (state program 0830-2020-0009).

References

[1] Xiang, R., Inoue, T., Zheng, Y., Kumamoto, et al. (2020). Science 367 (6477), 537.
[2] Sengupta, A. (2017). Applied Physics A 123(4), 227.

Numerical calculation of GaN NW / Si Schottky diode operation

K Yu Shugurov[1], A M Mozharov[1], V V Fedorov[1], A D Bolshakov[1], G A Sapunov[1] and I S Mukhin[1,2]

[1] Alferov University (former St. Petersburg Academic university), 8/3 Khlopina st., St. Petersburg 194021, Russian Federation

[2] ITMO University, 49 Kronverksky pr., St. Petersburg 197101, Russian Federation

E-mail: shugurov17@mail.ru

Abstract. Numerical model of GaN nanowire /Si Schottky diode was performed. Volt-ampere, capacitance-voltage and relaxation characteristics of the structure were calculated. It is shown that such diodes based on GaN NWs demonstrate high operation rate.

1. Introduction

A large number of modern technical solutions are implemented with the use of high-speed electronics. First of all it concerns mobile, wireless, satellite communications, local data transmission systems (Wi-Fi, Bluetooth, WiGig, WirelessHD), telecommunications, radar systems, medical diagnostic and therapeutic equipment, aircraft onboard weapon guidance and navigation systems, security inspection systems. Current trends are dictating necessity to reduce the size of electronic components, to increase their output power, speed, operating temperatures, resistance to radiation (spacecrafts). To achieve this, it is necessary to develop semiconductor devices based on materials capable to work in adverse conditions, integration of new materials with the silicon platform is more economically favorable than using expensive growth substrates (for example, Ge, GaAs , SiC, sapphire).

During last years there is an increase in investigations concerned with devices based on NWs, for example [1-3].

This work is dedicated to the numerical calculation of the high-speed Schottky diode based on gallium nitride (GaN) nanowire (NW) on silicon substrate.

2. Modeling

In this work Comsol Multiphysics package was used to simulate the operating mode of the Schottky diode based on GaN NWs. This model includes tunnel effects at metal/semiconductor interface as well as surface states density. Different metals forming Schottky barrier were considered. NW and substrate doping levels, NW diameter and length were varied during simulation to obtain optimum parameters of structure operation. Current-voltage (I-V), capacitance-voltage (C-V) were obtained. RC-constants of modeled structure were calculated to estimate the cut-off frequency of the device.

3. Summary

In the course of this work, numerical simulation of the operating mode of the Schottky diode based on GaN NW was carried out, its configuration was numerically optimized and the original design of the structure was formed for further experimental studies.

References

[1] Sabui G, Zubialevich V Z, White M, Pampili P, Parbrook P J, McLaren M et al. 2017 *IEEE Transactions on Electron Devices* **64(5)** 2283-90

[2] Reddeppa M, Park B G, Lee S T, Hai N H, Kim M D and Oh J E 2017 *Current Applied Physics* **17(2)** 192-6

[3] Sanjay S and Baskar K 2018 *Applied Surface Science* **456** 526-31

Nonradiative recombination channel of dark excitons in colloidal CdSe nanoplatelets

A A Golovatenko[1]
[1]Laboratory of spin and optical phenomena in semiconductors, Ioffe Institute, Saint Petersburg 194021, Russia

Abstract. Nonradiative recombination channel of spin-forbidden dark excitons in colloidal 4 ML thick CdSe nanoplatelets synthesized in argon and ambient atmosphere is revealed by theoretical analysis of time-resolved photoluminescence. The nonradiative recombination lifetime τ_{nr} = 12 ns is found to be independent on nanoplatelets synthesis atmosphere. It is shown that presence of nonradiative recombination channel affects spin polarization of dark excitons and results in temporal dependence of circular polarization degree of photoluminescence in external magnetic field.

1. Introduction

Recombination dynamics of excitons in ensembles of colloidal semiconductor quantum dots usually demonstrates multiexponential behavior. The reason is dispersion of exciton lifetimes within an ensemble as well as trapping and de-trapping processes of photoexcited electrons and holes. These factors make it difficult to directly evaluate such an important parameter as the intrinsic lifetime of excitons [1]. The present work demonstrates that in the case of ensembles of colloidal quasi two-dimensional bare-core 4 ML thick CdSe nanoplatelets synthesized in argon or ambient atmosphere low-temperature recombination dynamics of excitons in zero magnetic field is fully described by three characteristic lifetimes τ_1=100 ps, τ_2=11 ns, τ_3=114 ns [2] having a specific physical meaning.

Analysis of magnetic field and temperature dependences of these lifetimes shows that lifetime τ_1 is independent both from temperature and magnetic field, allowing to ascribe it to radiative recombination lifetime of bright (spin-allowed) excitons. The lifetimes τ_2 and τ_3 demonstrate temperature dependence of activation type, typical for thermal population of bright excitons from the dark (spin-forbidden) excitons bath (Fig.1a,b, upper panels). Magnetic field dependences of lifetimes τ_2 and τ_3 is proportional to B^{-2} indicating mixing of bright and dark exciton states in transverse magnetic field (Fig.1a,b bottom panels). It worth noting that for both temperature and magnetic field dependences of lifetimes τ_2 and τ_3 the relation $1/\tau_2(B,T) = 1/\tau_3(B,T) + 1/\tau_{nr}$ holds, where τ_{nr} = 12 ns. Additionally, in applied magnetic field increase of time-integrated photoluminescence (PL) intensity from decay component with lifetime τ_2 proportional to B^2 was observed. It results in two-fold increase of total time-integrated PL intensity in magnetic field 15 Tesla. As increase of total PL intensity is a direct evidence of enhanced PL quantum yield, one can ascribe lifetime τ_2 to dark excitons in nanoplatelets with nonradiative recombination channel. In turn, lifetime τ_3 corresponds to dark exciton lifetime in nanoplatelets without nonradiative recombination channel, i.e. intrinsic radiative recombination lifetime of dark excitons. The origin of nonradiative recombination channel according to [3] can be associated with surface trap states.

Additionally, analysis of magnetic field-induced degree of circular polarization (DCP) of time-resolved PL was performed. It was found that presence of nonradiative recombination channel besides

the dark exciton lifetime affects the DCP of the dark excitons. In the case of nanoplatelets synthesized in the argon atmosphere DCP of dark excitons with lifetimes τ_2, τ_3 is negative while differ in absolute value. In the case of nanoplatelets synthesized in the ambient atmosphere DCP of dark excitons with lifetimes τ_2, τ_3 is positive in low magnetic fields. However, in magnetic fields higher than 7 Tesla DCP of dark excitons with lifetime τ_3 becomes negative. The latter fact results in change of the total DCP sign with time.

To conclude, regardless of synthesis atmosphere a fraction of bare-core CdSe nanoplatelets in ensemble contains a nonradiative recombination channel, which manifests itself both in recombination dynamics and degree of circular polarization of excitons.

2. Figures

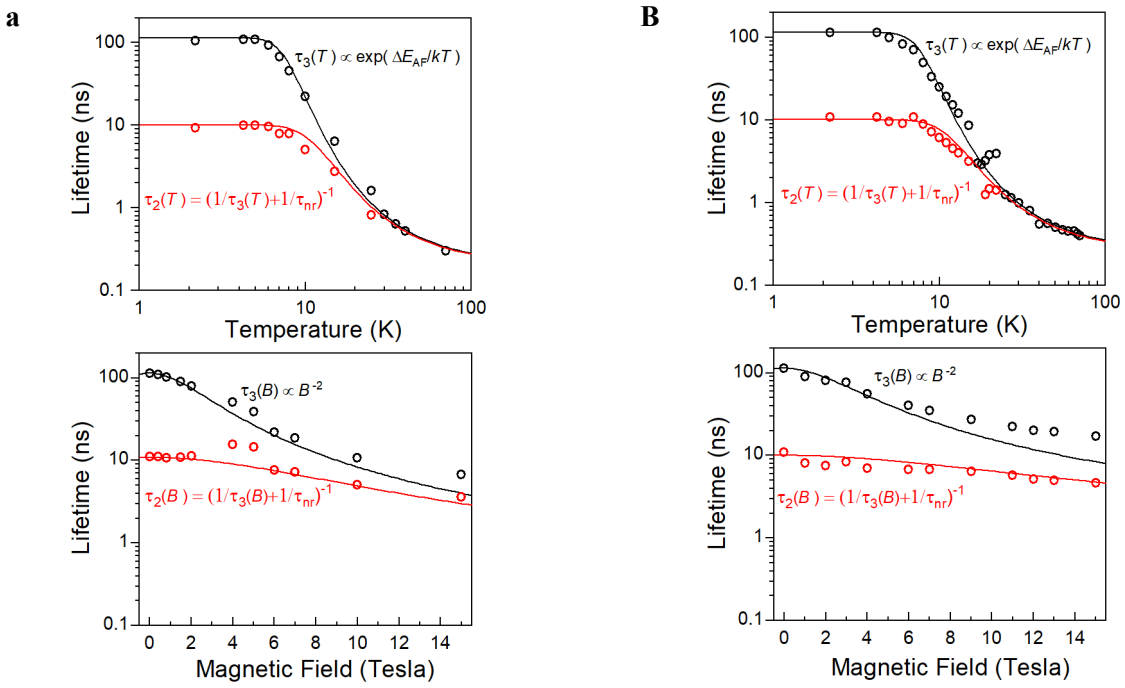

Figure 1(a, b). Temperature and magnetic field dependences of lifetimes τ_2 and τ_3 in **(a)** argon-synthesized CdSe nanoplatelets; **(b)** ambient-synthesized CdSe nanoplatelets. Open circles show lifetimes τ_2 and τ_3 obtained from three-exponential fitting of PL decay. Curves show results of theoretical modeling.

3. Acknowledgments

I wish to acknowledge A.V. Rodina, E.V. Shornikova and D.R. Yakovlev for fruitful discussions, and Presidium RAS Program No. 5: «Photonic technologies in probing inhomogeneous media and biological objects» for financial support.

References

[1] Jones M, Lo S S, Scholes G D 2009 *J. Phys. Chem.* C **113** 186322

[2] Shornikova E V, Golovatenko A A, Yakovlev D R, Rodina A V, Biadala L, Qiang G, Kuntzmann A, Nasilowski M, Dubertret B, Polovitsyn A, Moreels I, Bayer M 2020 *Nat. Nanotechnol.*

[3] Kunneman L T, Schins J M, Pedetti S, Heuclin H, Grozema F C, Houtepen A J, Dubertret B, Siebbeles L D A 2014 *Nano Lett*. **14** 7039

The spin-filtering properties in two coupled Rashba quantum rings

M O Smolkina[1], **I Ju Popov**[1], **I V Blinova**[1]
[1]Faculty of Control Systems and Robotics, ITMO University, St. Petersburg, 197101, Russia

Abstract. The spin-dependent electron transport in two coupled quantum rings with Rashba spin-orbit interaction and magnetic flux was studied by using quantum waveguide theory.We show the dependance of spin-polarization on system parameters such as the Rashba coupling constant, the radius of the rings, the angles between the leads and the attachment point of the rings. The spin-polarization can be controlled and changed from -1 to +1 by using a magnetic flux. Also it was shown that this model is a limiting case of double Rashba quantum ring when the length of the middle lead between rings vanishes.

1. Introduction

In recent years improvement in technology has led to a growing interest in spin-dependent transport in mesoscopic systems[1]. Manipulating spin degrees of freedom is an important fundamental subject. The most useful instrument to control the electron spin is the Rashba spin-orbit interaction (RSOI)[2]. The strength of RSOI can be easily controlled by an external electric field or a gate voltage. Low-dimensional quantum nanostructures such as quantum rings also have attracted an interest in nowadays and play an important role in microelectronic[3]. Some of the theoretical researchers posed quantum rings as a multipurpose and flexible spintronic device. Naeimi et al. explored spinfiltering properties of transmitted electrons through a quantum ring[4], double quantum ring[5] and triangular network[6] in the presence of RSOI and magnetic flux.

In this paper we have studied the spin-dependent electron transport, particularly spin-filtering and spin-polarization, in two coupled quantum nanorings connected to two external leads in the presence of RSOI and magnetic flux using quantum waveguide theory.

2. Theoretical model

We consider two one-dimensional coupled quantum rings. The leads are considered as the incoming and outgoing leads, respectively. The strength of Rashba SOI in the left (right) ring is denoted by $\alpha_L(\alpha_R)$. There are tunable magnetic fluxes through the center of each ring such that there is no magnetic field on them. The thickness of the ring is small enough, so we can consider only the lowest level of electron subband with a good approximation.

The electron wave functions in the incoming and outgoing leads are as follows:

$$\psi_I(x_I)=\begin{pmatrix} f_\uparrow \\ f_\downarrow \end{pmatrix} e^{ikx_I} + \begin{pmatrix} r_{L\uparrow\uparrow}+r_{L\downarrow\uparrow} \\ r_{L\uparrow\downarrow}+r_{L\downarrow\downarrow} \end{pmatrix} e^{-ikx_I},\ \psi_{II}(x_{II})=\begin{pmatrix} t_{L\uparrow\uparrow}+t_{L\downarrow\uparrow} \\ t_{L\uparrow\downarrow}+t_{L\downarrow\downarrow} \end{pmatrix} e^{-ikx_{II}},$$

for upper and lower arms of two similar rings:

$$\psi_{Lup}(\varphi)=\sum_{\mu=1,2}\sum_{j=1,2}a_{Lj}^{\mu}e^{K_{Lj}^{\mu}\varphi}\mathrm{X}_{L}^{(\mu)}(\varphi),\ \psi_{Llow}(\varphi)=\sum_{\mu=1,2}\sum_{j=1,2}b_{Lj}^{\mu}e^{K_{Lj}^{\mu}\varphi}\mathrm{X}_{L}^{(\mu)}(\varphi),$$

$$\psi_{Rup}(\varphi)=\sum_{\mu=1,2}\sum_{j=1,2}a_{Rj}^{\mu}e^{K_{Lj}^{\mu}\varphi}\mathrm{X}_{R}^{(\mu)}(\varphi),\ \psi_{Rlow}(\varphi)=\sum_{\mu=1,2}\sum_{j=1,2}b_{Rj}^{\mu}e^{K_{Lj}^{\mu}\varphi}\mathrm{X}_{R}^{(\mu)}(\varphi),$$

where L and R denote the left and right rings respectively, $f_{\sigma}(\sigma=\uparrow,\downarrow)$ is the amplitude of injected electron with spin σ, $t_{L\sigma\sigma'}(t_{R\sigma\sigma'})$ is the transmittion amplitude of electron with incoming spin σ and outgoing spin σ' , and similarly $r_{L\sigma\sigma'}(r_{R\sigma\sigma'})$ is the reflection amplitude of electron.

Next using Griffith's boundary conditions and employing the Gaussian elimination method, we can obtain all the unknown coefficients $a_{Lj}^{\mu},b_{Lj}^{\mu},a_{Rj}^{\mu},b_{Rj}^{\mu},t_{R\sigma\sigma'}r_{L\sigma\sigma'}$ for the left and right rings. Finally, the transmission coefficient for the outgoing lead can be determined by $T_{\sigma\sigma'}=\left|t_{\sigma\sigma'}\right|^{2}$.

3. Numerical results

In this section we perform a numerical study of the spin-dependent electron transport in two coupled quantum rings with Rashba spin-orbit interaction. The effects of different system parameters such as the Rashba coupling constant, the radius of the rings, the angles between the leads and the attachment point of the rings, on spin-polarization were also obtained. We have found an appropriate value of Rashba SOI constant when the system of two coupled quantum rings can work as a perfect electron spin-inverter. This property can be used in spintronic as a magnetic spin-switching. Perfect spin-inversion can be obtained when the angles between rings and corresponding leads are π , radiuses of the rings are 1 and Rashba constants in left and right rings are equal 1. Also the system of two coupled rings can be used as a controllable spin-polarization device, by using magnetic flux. Also it was shown that a model of two coupled rings is a limiting case of double Rashba quantum ring when the length of the middle lead between rings vanishes.

4. Acknowledgements

The reported study was funded by RFBR, project number 19-31-90164 and partially financially supported by the Government of the Russian Federation (grant 08-08), by grant 16-11-10330 of Russian Science Foundation.

References

[1] D. Awschalom, D. Loss, and N. Samarth 2002 Semiconductor Spintronics and Quantum Computation (Springer-Verlag, Berlin).
[2] E. I. Rashba 1960 Sov. Phys. Solid State **2** 1109.
[3] L. Eslami, E. Faizabadi, S. Ahmadi 2016 Quantum nano ring composed of quantum dots as a source of pure persistent spin or charge current Phys. Lett. A 380 (45) 3854–3860.
[4] A. Naeimi, M. Esmaeilzadeh 2013 A wide range of energy spin-filtering in a Rashba quantum ring using S-matrix method *Appl. Phys.* **113** (4), 044316–044322.
[5] A. Naeimi , L. Eslami, M. Esmaeilzadeh, M.R. Abolhassani 2013 Spin transport properties in a double quantum ring with Rashba spin-orbit interaction *Appl. Phys.* **113** 014303.
[6] E. Dehghan, D.S. Khoshnoud, A. Naeimi 2018 Logical spin-filtering in a triangular network of quantum nanorings with a Rashba spin-orbit interaction *Physica B Condensed Matter* **529** 21-26.

Deposition of a titanium coating on a steel base by contact welding and study of the resulting layered system structure

I Egorov[1], **A Fomin**[1]
[1]Yuri Gagarin State Technical University of Saratov, Saratov 410054, Russia

Abstract. The paper describes a method for the deposition of a titanium coating on a base of steel grade Cr12MoW for further modification of the layered system. The resistance welding parameters required for the formation of the "steel – titanium" structure with an increased hardness of 300–800 HV were established.

1. Introduction

To increase the service life of metal parts operating under the conditions of increased wear (in friction pairs) or in harsh environment, the working parts are coated with protective films or coatings by various methods [1-3]. In almost all cases, after the coating deposited on the surface of the product, there is a problem in achieving a strong connection of dissimilar metals. This occurs when applying a titanium layer (coating) on a steel base in the form of a foil or a thin sheet. Therefore, the use of resistance welding for the formation of an integral connection between steel grade Cr12MoW and commercially pure titanium is studied in this work.

2. Methodology

The experimental samples were made in the form of disks of Cr12MoW steel with a diameter of 14 mm and a thickness of 3.5 mm. The coating was obtained from a 0.2 mm thick sheet of a titanium alloy of the TA2 grade (VT1-00 analogue). After preparing the surfaces to be welded (machining and cleaning), resistance welding was performed with a variable value of the consumed voltage U and pulse duration t. As a result, a layered "Cr12MoW steel + Ti coating" structure was obtained, the total height of which was 3.65–3.75 mm.

The microstructure and quality of the welded joint of the resulting system were analyzed using optical microscopy. The prepared microsection samples of the composite structure were studied in the active spot of resistance welding. To analyze the stress state, the microhardness was measured by the Vickers method (HV) at a load of 50–100 gf.

3. Results

At the voltage U = 160 V and pulse duration t = 250 ms, a high-quality and strong joint could not be formed. The microscopy results showed that titanium *1* had no permanent deformation. No significant thermal effect on the steel base was observed as well *2* (**Fig. 1*a***). Analysis of the microstructure of the sample obtained at U = 160 V and the welding pulse duration t = 1000 ms proved that there occurred the formation of intermetallic compounds *3* (**Fig. 1*c***). Their presence usually causes a decrease in bond strength and increased fragility.

An increase in voltage to 175 V at t = 250 ms led to a significant deformation of the titanium layer *5* and a decrease in thickness by half (**Fig. 1*d***). With the given treatment parameters, pores *4* were also formed in the fusion region.

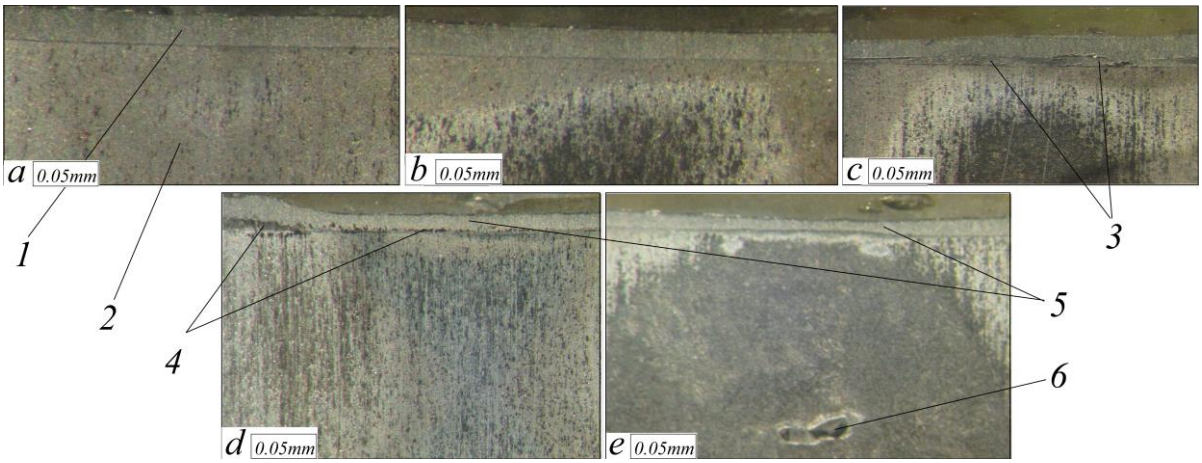

Figure 1. Cross section of a welded joint and its layered structure consisting of a base and a coating: ***a*** – U = 160 V, t = 250 ms; ***b*** – U = 160 V, t = 500 ms; ***c*** – U = 160 V, t = 1000 ms; ***d*** – U = 175 V, t = 250 ms; ***e*** – U = 175 V, t = 500 ms.

An increase in the pulse duration t = 500 ms at a voltage of 175 V led to excessive heat exposure and the formation of voids *6* in the central part of the steel base (**Fig. 1*e***). The use of the reduced voltage U = 160 V at t = 500 ms led to the formation of a uniform joint. A low degree of deformation in titanium under the compression of the electrodes was practically not observed with a moderate thermal effect of the current pulse (**Fig. 1*b***). The indicated pulse duration was sufficient for the formation of a strong and uniform joint (without defects in the form of pores) and the formation of intermetallic compounds in the joint region.

4. Conclusion

Thus, when welding dissimilar materials, in particular steel and titanium, energy-efficient contact welding modes were determined in order to form a strong joint of the layered "Cr12MoW steel + Ti-coating" system. The resulting structure can be further thermally modified to increase the wear resistance of the working surface, *e.g.* of a metalworking tool [4].

5. Acknowledgments

The research was supported by the grant of the President of the Russian Federation MD-157.2019.8. Part of the work related to optical microscopy of the welded joint was conducted within the scholarship of the President of the Russian Federation (SP-571.2019.1).

References

[1] Koshuro V A, Nechaev G G, Lyasnikova A V 2014 *Tech. Phys.* **59** 1570
[2] Fomin A A, Fomina M A, Koshuro V A, Rodionov I V, Voiko A V, Zakharevich A M, Aman A, Oseev A, Hirsch S and Majcherek S 2016 *Tech. Phys. Lett.* **42** 932
[3] Chu Q, Bai R, Zhang M, Li J, Lei Zh, Hu N, Bell JM and Yan Ch, 2017 *Mater. Charact.* **132** 330
[4] Fomin A, Egorov I, Shchelkunov A, Fomina M, Koshuro V and Rodionov I 2018 *Compos. Struct.* **206** 467

Study of the relationship of induction heating parameters and mechanical properties of commercial purity titanium

A Shchelkunov[1], **M Fomina**[1]
[1] Yuri Gagarin State Technical University of Saratov, Saratov 410054, Russia

Abstract. In this work, the relationship between the parameters of voltage, inductor current, duration, temperature of induction heat treatment and the hardness of commercial purity titanium was studied. As a result, the temperature ranges were established at a fixed voltage and current of the inductor. At certain technological conditions, with various durations of heat treatment, the hardness of the titanium surface was determined.

1. Introduction

Titanium and its alloys have become widespread in the aerospace and engineering industries due to a combination of mechanical and chemical properties. Low specific weight, high corrosion resistance and biocompatibility ensured their widespread use in medicine [1]. However, titanium can not satisfactorily withstand friction under high loads. Wear resistance mostly depends on the crystal structure, surface treatment quality, friction coefficient and hardness [2]. To increase the wear resistance, titanium and its alloys, as well as zirconium and tantalum, undergo structural and chemical surface modification [3-6].

There are several methods used to obtain a surface layer with the required mechanical properties, one of which is chemical-thermal treatment. When titanium is heated in the air, the oxide film growth and the saturation of the surface layer with oxygen are observed. This effect contributes to the improvement of mechanical properties, *e.g.* hardness and wear resistance [4].

The purpose of this work is to study the influence of induction heating parameters (voltage, inductor current) and the duration of exposure in the air atmosphere on the treatment temperature and the obtained hardness values.

2. Methodology

For the experiment, titanium (commercially pure titanium VT1-00) samples of a disk shape with a diameter of 13.9–14.1 mm and a thickness of 1.95–2.00 mm were prepared. The sample preparation included finishing turning, grinding (Ra 0.32) and cleaning in ethanol. This was followed by a high-temperature induction treatment of the surface, which provided for the exposure time t at a given temperature ≈1, 60, 120 and 300 s, respectively. The process of induction heat treatment (IHT) comprised several stages, in particular intensive heating, exposure and cooling (without forced blowing). ITT was performed in a laboratory setup, the main parameters of which were voltage U = 70–90 V, inductor current I = 2.5–3.5 kA and exposure temperature T = 900–1250 °C. The operating current was measured using "UNI-T UT205" current clamps. Temperature measurements were conducted by the methods of thermal imaging analysis and colorimetry. The main dimensions were checked using a caliper combined with a visual inspection of the resulting workpiece in order to identify the macro-size defects. Mechanical tests were performed using a "PMT-3" microhardness tester according to the Vickers method with an indenter load of ≈0.98 N (100 gf).

3. Results

The maximum temperature in the course of IHT reached 1250±50 °C. The control of geometric dimensions showed that all samples retained their shape after heating and can be further used for hardness testing. With increasing voltage, the samples were characterized by a significant change in thickness and subsequent delamination of the scale.

At a voltage of 70 V, with an increase in the exposure duration, the consumed current fell from 2.4–2.5 to 2.2–2.3 kA. For t = 1 s and t = 60 s, the temperature interval corresponded to T = 900–950 °C, and as t grew to 120–300 s, the temperature reached 1000–1050 °C. The hardness at the voltage of 70 V and t = 1 s was 3.3 GPa, at the same time inclusions with high hardness of about 9.3 GPa were noted. In the remaining samples, with a duration t = 60–300 s, the hardness increased to 11.7–15.1 GPa, respectively.

At a voltage of 80 V, the inductor current stabilized at 2.9–3.1 kA. The temperature of the sample with an exposure duration t = 1 s reached 1000–1050 °C, whereas for the rest it was 1050–1100 °C. The hardness of the samples varied in the range 12.5–15.5 GPa. IHT of titanium at U = 90 V showed that the inductor current gradually decreased from 3.5 to 3.1 kA with increasing duration. The temperature range during the exposure was in the range of 1200–1250 °C, while the hardness decreased slightly and amounted to H = 10.8–14.5 GPa.

4. Conclusions

Thus, the influence of ITT parameters (voltage, inductor current and exposure duration) on the process temperature in the range of 900–1250 °C and the resulting hardness values on the titanium surface in the range of 10.8–15.5 GPa was shown. This value significantly expands the scope of application of commercially pure titanium, in particular in the form of a wear-resistant element (insert) for instrumental products or cutting elements of intraosseous designs of titanium implants [4] operating in difficultly loaded conditions and harsh environments.

Acknowledgments

Scientific research was carried out with financial support from the Grant of the President of the Russian Federation (MD-157.2019.8).

References

[1] Aniolek K, Kupka M, Barylski A, Dercz G, 2015 *Appl. Surf. Sci.* **357** 1419
[2] Fomin A, 2020 *Int. J. Refract. Met. H.* **88** 105201
[3] Guleryuz H, Cimenoglu H, 2004 *Surf. Coat. Technol.* **192** 164
[4] Fomin A, 2019 *Ceram. Int.* **45** 8258
[5] Fomin A, 2019 *Compos. Struct.* **220** 318
[6] Fomina M, Koshuro V, Shumilin A, Voyko A, Zakharevich A, Skaptsov A, Steinhauer A, Fomin A, 2020 *Compos. Struct.* **234** 111688

Gd_2O_3:Nd^{3+}/ Er^{3+}/ Tm^{3+} nanoparticles. Luminescent properties and foaming synthesis method

D V Mamonova[1], I E Kolesnikov[1], M D Mikhailov[2,3], A A Manshina[1]
[1] Institute of Chemistry, Saint-Petersburg State University, Saint Petersburg 199034, Russia
[2]S.I. Vavilov State Optical Institute, Saint Petersburg 192171, Russia
[3]Peter the Great St. Petersburg Polytechnic University, Saint Petersburg 195251, Russia

Abstract. Tm^{3+}, Er^{3+} and Nd^{3+}-doped Gd_2O_3 nanoparticles were synthesized by combined Pechini-foaming. The structural and luminescence properties of nanocrystalline powders were studied using XRD, SEM, SLS and photoluminescence spectroscopy. The samples demonstrate weak agglomeration of nanoparticles and well-formed crystalline phase simultaneously. Changes of crystal unit cell parameters and sizes of coherent scattering regions for samples doped with one rare earth ion and co-doped with three ions are calculated. A comparative analysis of the luminescent properties of these samples has also been carried out.

It is necessary to visualize the processes occurring both in the body and in an individual cell for fundamental research and diagnostics in the field of medicine, molecular and cellular biology. Luminescent labels are studied for application in the field of immunoassay, high-speed imaging and medical diagnostics [1]. The requirements for multiplex biological analysis without complex equipment and processing have led to the development of unique fluorescent nanolabels.

Metal oxides are the most promising compounds for rare earth ions (REI) doping due to their chemical inertness and the stability of the physical and chemical properties over a wide temperature range [2, 3]. Nanoparticles of gadolinium oxide (Gd_2O_3) have been investigated as a novel contrast agent for Magnetic Resonance Imaging (MRI) [4, 5]. Gadolinium oxide doped with rare earth ions will have two functional properties: a luminescent label and the contrast agent for MRI.

Previously, the authors developed the combined Pechini-foaming method [6] where foam-forming component is added to the precursors. Synthesis is based on the standard Pechini technique. During the synthesis the foam fills the gel's structural network and prevents the agglomeration of the oxide particles. The method results in the formation of the uniformly doped weakly agglomerated oxide particles with well-organized crystalline structure. The structure ensures the high luminescence yield, while the small size of the particles affords to prepare stable colloid solutions and suspensions. We developed the temperature treatment parameters of the synthesis, which lead to the best structural and morphological properties of the powders.

It is known that each rare earth ion embedded into specific crystalline matrix is characterized by the unique set of luminescent parameters, namely spectral line positions and emission intensity ratio. A system containing three rare earth ions will be characterized by a set of luminescence bands characteristic of each REI.

As part of this work, gadolinium oxide nanoparticles were synthesized by combined Pechini-foaming method. The structural properties and morphology have been studied. Diffraction analysis confirms the presence of a single phase. Changes of crystal unit cell parameters during the doping of different REI into the oxide matrix were shown. SEM and SLS results confirmed the presence of weakly agglomerated particles below 100 nm. The luminescence spectrum contained non-overlapping emission lines originated from each rare earth ion (for example, Nd - 1065 nm, Er - 554 nm and Tm - 476 nm).

Acknowledgments
Authors are grateful to “Interdisciplinary Resource Centre for Nanotechnology”, Resource Center "Innovative technologies of composite nanomaterials”, “Research Centre for X-ray Diffraction Studies” and “Centre for Optical and Laser Materials Research” of Saint-Petersburg State University Research Park. The authors are grateful to "Russian president grant" No. MK-1306.2020.3

References

[1] Lee H. et al. Colour-barcoded magnetic microparticles for multiplexed bioassays //Nature materials. – 2010. – T. 9. – №. 9. – C. 745
[2] Sankar S. et al. Room temperature synthesis of high temperature stable lanthanum phosphate–yttria nano composite //Materials Research Bulletin. – 2012. – T. 47. – №. 7. – C. 1835-1837
[3] Huang P., Chen D., Wang Y. Host-sensitized multicolor tunable luminescence of lanthanide ion doped one-dimensional YVO_4 nano-crystals //Journal of Alloys and Compounds. – 2011. – T. 509. – №. 7. – C. 3375-3381
[4] Klasson A. et al. Positive MRI contrast enhancement in THP-1 cells with Gd_2O_3 nanoparticles //Contrast Media & Molecular Imaging. – 2008. – T. 3. – №. 3. – C. 106-111
[5] Hedlund A. et al. Detection of Gd_2O_3 Nanoparticles in Hematopoietic Cells for MRI Contrast Enhancement. – 2011
[6] Kolesnikov I. E. et al. Photoluminescence properties of Eu^{3+} ions in yttrium oxide nanoparticles: defect vs. normal sites //RSC advances. – 2016. – T. 6. – №. 80. – C. 76533-76541

Design and simulation high aspect ratio torsion suspension of MEMS z-axis accelerometer

I E Lysenko[1], **D V Naumenko**[1], **O A Ezhova**[1]
[1] Department of Electronic Apparatuses Design, Southern Federal University, Taganrog 347922, Russia

Abstract. This paper presents new design torsion suspension of MEMS z-axis accelerometer. These prototypes Z-axis accelerometer are based on pantograph lever structure is out-of-plane devices. The results of finite element analysis of the structure are presented.

Introduction

An increase in the thickness of the instrument layer of inertial sensors manufactured on SOI structures using the technology of deep reactive-ion etching (DRIE) allows you to create designs with an instrument thickness of more than 100μm and an aspect ratio of up to 1:50 [1]. Such designs can increase the inertial mass without increasing the area of the sensitive element, so that you can reduce noise, increase sensitivity and reduce the cost of the MEMS sensors. Torsion suspensions are widely used in MEMS out-of-plane devices as like micromirrors, accelerometers, energy harvesters, switches.

Design of the MEMS acceleration sensor

The MEMS z-axis accelerometer sensitive element is shown in Figure 1a. This sensor designed to measure the acceleration of the perpendicular plane of the substrate and contains the inertial mass (1), four suspensions of a sensitive element (2), capacity transducer (3), contact pads (4,5). The size of the inertial mass is 500x500x100 microns and sensor size is 900 x 900 microns.

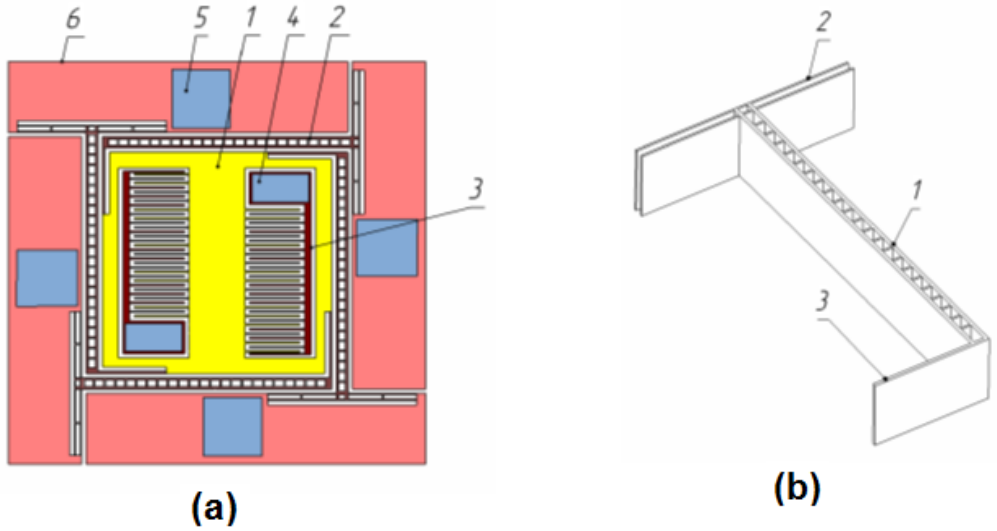

Figure 1. Figure 1(a, b). (a) Topology of MEMS accelerometer; (b) Suspension beam.

The MEMS suspension of the accelerometer is shown in Figure 1b and consists of a lightweight rigid beam 1 and a pair of vertical torsion beams 2 and 3. Torsion beam 2 consists of two parallel connected

torsion elements, which allows isolation of torsion strain from bending strain due to the spacing of the primary torsion elements[2,3]

Simulation of micromechanical accelerometer

The result of the finite element modal analysis is shown in Figure 2. The first mode of vibrations with a natural frequency of 7582 Hz corresponds to a deformation perpendicular to the plane. The second and third modes of oscillation occur in the plane of the silicon wafer at frequencies of 10459 Hz and 10465 Hz.

The amplitude of displacements was obtained as a result of static finite element analysis and is proportional to the magnitude of the effective acceleration. At 1 g acceleration: 4.5 nm along the Z axis, and 2.2 nm along the X, Y axis. At 10 g acceleration: 46 nm along the Z axis, and 23 nm along the X, Y axis.

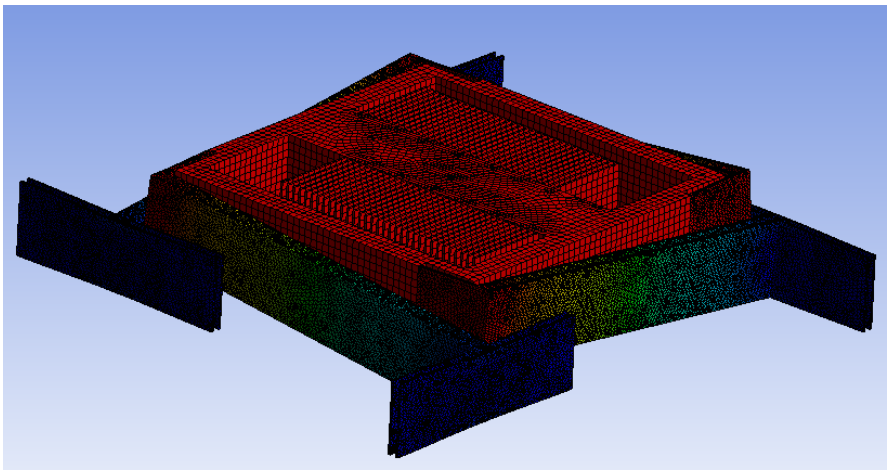

Figure 2. General frequency mode

Conclusion

The design of an integrated micromechanical accelerometer is proposed. Optimization of structural suspensions can have equal frequencies along three axes and can serve as the basis for a three-axis MEMS accelerometer.

Acknowledgments

This work was supported by RFBR research project No. 19-37-90136 “Development of the fundamental foundations for the construction of high-aspect torsion suspensions for inertial MEMS sensors”.

References

[1] Chai, J.; Zhang, K.; Xue, Y.; Liu, W.; Chen, T.; Lu, Y.; Zhao, G. Review of MEMS Based Fourier Transform Spectrometers. Micromachines 2020, 11, 214.

[2] Alessandro Caspani, Claudia Comi, Alberto Corigliano, Giacomo Langfelder, Valentina Zega, and Sarah Zerbini. "A Differential Resonant Micro Accelerometer for Out-of-plane Measurements" Procedia Engineering, vol. 87, 2014. doi:10.1016/j.proeng.2014.**11**.569

[3] 5. Miao, T.; Xiao, D.; Li, Q.; Hou, Z.; Wu, X. A 4 mm2 Double Differential Torsional MEMS Accelerometer Based on a Double-Beam Configuration. Sensors 2017, **17**, 2264.

Modeling of the protective coatings formation mechanism by micro-arc oxidation method

P E Golubkov, E A Pecherskaya, O A Melnikov, T O Zinchenko, G V Kozlov, A E Shepeleva[1]
[1]Department of Information and measuring equipment and metrology, Penza State University, Penza 440026, Russia

Abstract. An electrophysical model of the micro-arc oxidation process, which allows, on the basis of the equivalent electric circuit and fundamental laws of physics and chemistry, to describe the formation mechanism of protective coatings by the micro-arc oxidation method taking into account the large number of physical effects inherent in this process is proposed. The proposed model can be used to increase the controllability of micro-arc oxidation technology.

1. Introduction

At present, the micro-arc oxidation (MAO) technology is actively developing: oxide films that protect against wear and corrosion, antibacterial coatings for titanium implants and even radiation sensitive layers have been obtained [1, 2].The main interest of scientists at present is directed to the modification of MAO coatings with nanoparticles in order to further increase their functional properties and expand the scope [3] – [5]. However, the main problem of the MAO process - the complexity of the technological parameters selection, the solution of which is of great importance for industrial production is not taken into account [6].

For effective control the MAO process, knowledge of the physical phenomena occurring during the coating formation, which makes it possible to purposefully act on them in order to obtain oxide layers with desired properties, is necessary. There are a large number of works aimed at studying the mechanism of the MAO coatings formation, but there is still no comprehensive mathematical description that takes into account all the physical effects inherent in the MAO process, in particular, the microdischarges burning [7].

The electrophysical model proposed in this work allows us to mathematically describe the formation of MAO coatings to determine the oxide layer properties (thickness, porosity, corundum content) during the MAO processing, on the base of equivalent electrical circuit of the metal-oxide-electrolyte system and known physicochemical regularities.

2. Development of an electrophysical model of the MAO process

The metal-oxide-electrolyte system can be represented in the form of an equivalent electrical circuit (Fig. 1), the parameters of which depend on the stage of the MAO process. In this case, the experimentally measured voltage drop across the oxide layer depends on the thickness and capacity of the coating, as well as on porosity. Porosity is determined from geometric relationships according to the Keller model (at the anodizing stage).

At the stages of microdischarges (spark, micro-arc, arc), dielectric breakdowns of the formed coating occur, and the thickness of the coating can be calculated according to known empirical formulas. The

minimum current of a single microdischarge is determined based on the calculated parameters of the equivalent circuit and the porosity of the coating. The length of the discharge gap at the beginning of the sparking stage is determined from the condition of electrolyte boiling in the pore during dielectric breakdown. The content of crystalline alumina modifications in the coating depends on the temperature of the walls and bottom of the pore during microdischarge and obeys the Kolmogorov-Johnson-Mehl-Avrami equation.

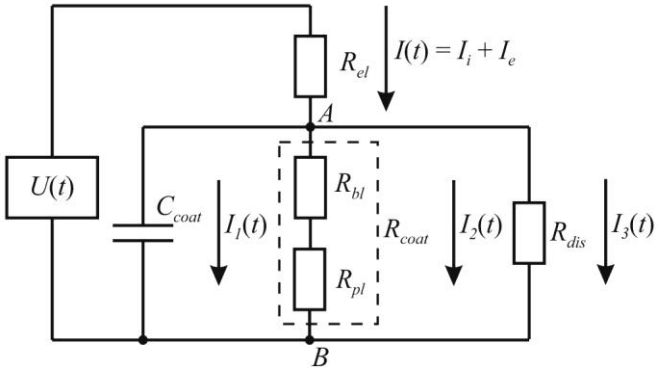

Figure 1. Equivalent circuit of the MAO process: $U(t)$ – source of alternating voltage; $I(t)$ – technological current, including electronic I_e and ionic I_i currents; R_{el} – electrolyte resistance; R_{coat}, R_{bl}, R_{pl} – resistances of the coating, barrier and porous layers respectively; C_{coat} – coating capacity; R_{dis} is the microdischarges resistance.

3. Conclusion

The proposed model has some limitations associated with insufficient knowledge of the MAO coatings formation mechanism at the spark and micro-arc stages. Nevertheless, this model can be used to develop more general mathematical models, as well as to create an intelligent automated system for the controlled synthesis of oxide coatings in order to increase the controllability of the MAO process [8].

References

[1] Santos J S, Rodrigues A, Simon A P, Ferreira C H, Santos V A Q, Sikora M S, Cruz N C, Mambrini G P, Trivinho-Strixino F 2019 *Adv. Eng. Mater.* **21** 1900119

[2] Zolotarjovs A, Smits K, Laganovska K, Bite I, Grigorjeva L, Auzins K, Millers D, Skuja L 2019 *Rad. Meas.* **124** 29-34

[3] Mashtalyar D V, Sinebryukhov S L, Imshinetskiy I M, Gnedenkov A S, Nadaraia K V, Ustinov A Yu, V. Gnedenkov S V 2020 *Appl. Surf. Sci.* **503** 144062

[4] Zhang Y, Chen F, Zhang Y, Du C 2020 *Tribology International* **146** 106135

[5] Rudnev V S, Kharitonskii P V, Kosterov A, Sergienko E S, Shevchenko E V, Lukiyanchuk I V, Adigamova M V, Morozova V P, Tkachenko I A 2020 *J. of Al. and Com.* **816** 152579

[6] Golubkov P E, Pecherskaya E A, Shepeleva Y V, Martynov A V, Zinchenko T O, Artamonov D V 2018 *IOP Conf. Series: J. of Phys.: Conf. Series* **1124** 081014

[7] O'Hara M, Troughton S C, Francis R, Clyne T W 2020 *Surf. & Coat. Technol.* **385** 125354

[8] Golubkov P., Pecherskaya E., Karpanin O., Safronov M., Shepeleva J. and Bibarsova A. 2019 Proc. 24th Conf. of Open Innovation Association, FRUCT (Moscow) vol 1 p 96-103

Scenarios of excitation energy relaxation in a system of Landau levels in quantum well structures

Yu.A. Mityagin[1,2], **M.P. Telenkov**[1,3], **Sh.Amiri**[1,3], **K.K. Nagaraja**[4], **P.S. Klemmer**[1,3]

[1]P.N. Lebedev Physical Institute of Russian Academy of Sciences, Moscow 119991, Russia

[2]National Research Nuclear University «MEPhI», Moscow 115409, Russia

[3]National University of Science and Technology «MISiS», Moscow 119049, Russia

[4]Manipal Institute of Technology, Manipal Academy of Higher Education, Manipal 576104, India

Abstract. The kinetics of intrasubband energy relaxation of electrons in quantum wells in a quantizing magnetic field is studied when electrons are excited to the Landau level lying below the optical phonon energy. Quite different relaxation scenarios of the interlevel kinetics were revealed and discussed. The type of observed scenario is determined by the interplay of electron-electron scattering and electron-phonon interaction as well as by the initial electron concentration in the system.

Introduction

The work is devoted to studying the kinetics of intrasubband energy relaxation of electrons in quantum wells (QWs) in a quantizing magnetic field. In this system the electron-electron (e-e) scattering becomes the main scattering mechanism, resulting in a specific two-stage scenario [1,2] of the energy relaxation – the fast thermalization of the electron subsystem due to e-e scattering, resulting in a formation of a quasi-Boltzmann distribution of electrons over Landau levels (LLs) and subsequent the much slower relaxation of energy due to the emission of optical phonons by electrons from the upper LLs, while the electron distribution continues to remain Boltzmann-type with slowly decreasing temperature of electron subsystem.

Here we report a quite different scenario of the energy relaxation in the LL system of QWs, observed in the situation with low initial population of the ground LL ($N_{n=0}(t=0)$). In this case a considerable part of the excitation energy is relaxed long before the Boltzmann-like distribution is established. It was shown that the intensity of the e-e scattering when one of the interacting electrons is situated at the ground (0-th) LL and other on the excited one is an important factor determining the type of the relaxation scenario.

Method and results

In the present work the energy relaxation kinetics in an n-type GaAs/$Al_{0.3}$ $Ga_{0.7}$As QW of 25 nm width in a quantizing magnetic field applied perpendicularly to the layers of the structure at the lattice temperature T_L=4.2K was studied. A nonequilibrium electron population is created by selective electrons injection to one of the upper LLs in the lowest subband, say the LL n=3, i.e. at the initial instant, only the levels n=0 and n=3 are populated. The temporal evolution of the level populations is

calculated from rate equations expressing the balance between the number of electrons coming to and leaving the LL owing to the e-e scattering and optical phonon emission [1, 2].
The e-e scattering probabilities are calculated according to [2] taking into account the band nonparabolicity [3].
The energy relaxation rate is characterized by the energy relaxation time (t_{relax}) determined as that of e^{-1} energy decay. Thermalization time (t_{therm}); the time of the Boltzmann-like distribution formation; is determined as a time moment when the deviation of the lower (n=0,1,2,3) LL populations from the Boltzmann ones does not exceed 1%.
The dependencies of the both t_{therm} and t_{relax} are shown in figure 1(a). As can be seen in this figure, t_{therm} and t_{relax} depend significantly on the initial population of the ground LL ($N_{n=0}(t=0)$). For high $N_{n=0}(t=0)$, the t_{relax} is much longer than t_{therm}. This situation is similar to the two-stage relaxation mechanism described in our earlier work [2]. The t_{therm} increases with lowering $N_{n=0}(t=0)$, and exceeds the t_{relax} at sufficiently low values of $N_{n=0}(t=0)$, i.e. $N_{n=0}(t=0) << N_{n=3}(t=0)$. It means that the relaxation scenario in this case differs considerably from the two-stage one – a considerable energy loss due to the optical phonon emission is already occurring in the thermalization process, and the most part of the excitation energy is relaxed before the Boltzmann-like distribution formation.
The relationship between energy relaxation and thermalization rates was revealed by their magnetic field dependences (figure 1(b)). The general rule is that an increase in the rate of energy relaxation is accompanied by a corresponding deceleration of thermalization and vice versa.

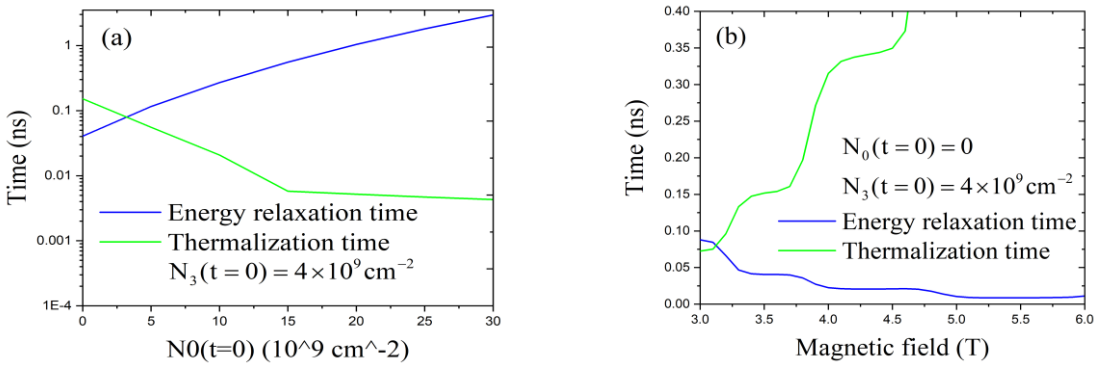

Figure 1(a, b). Dependences of t_{relax} and t_{therm} **(a)** on the initial population of the ground LL $N_{n=0}(t=0)$ (B= 3.5 T); **(b)** on the magnetic field strength.

Acknowledgments

The work was carried out with financial support from the Russian Basic Research Foundation (project No.18-02-00874-a).

References

[1] M. P. Telenkov, Yu. A. Mityagin, V. V. Agafonov, and K. K. Nagaraja 2015 JETP Letters **102** 678
[2] M.P. Telenkov, Yu.A. Mityagin, T.N.V. Doan, K.K. Nagaraja 2018 Physica E, **104** 11
[3]U. Ekenberg 1998 Phys. Rev. B **40** 7716

A theory of flexural modes in graphene

I O Raikov[1], D A Conyuh[2], A N Ipatov[1], D A Parshin[1]
[1] The Alferov Academic University RAS, Saint Petersburg 194021, Russia
[2] The Ioffe Institute RAS, Saint Petersburg 194021, Russia
E-mail: ioraikov@gmail.com

Abstract. We present an analytical theory of flexural modes in graphene. In this theory, the dynamical matrix of flexural modes is a square of the dynamical matrix of phonons, and the dispersion law of flexural modes is a quadratic one. Using a scalar model in which the atomic displacements are scalar values, we obtain analytical expressions for the dispersion law and the vibrational density of states of flexural modes in graphene. Using numerical methods, we then investigate the effect of disorder on the transfer of such modes at different frequencies.

1. Introduction

One of the most important topics in condensed matter nanophysics today is the study of such unusual material as crystalline graphene. Crystalline graphene is a 2-d material, a monoatomic hexagonal lattice of carbon where each atom is connected by sp^2 valence forces with its three nearest neighbors. The graphene, due to its unique Brilluine zone construction, possesses exceptional mechanic, physical, and optical properties [1, 2] which are now used in many applications. In particular, it has a record-high value of thermal conductivity, which is very important for heat dispersion in nanostructural devices. As it is well known, the heat transfer in dielectrics and semiconductors is due to the vibrations of the crystalline lattice. Usually they are phonons which propagate through the crystal with constant velocity – velocity of sound v, and they have a linear dispersion law $\omega = vk$. Phonons give a linear contribution to the vibrational density of states $g(\omega) \propto \omega$. The phonon modes in graphene are polarized in the plane of the graphene sheet. But besides phonon modes, graphene has another type of vibrational modes – flexural modes, which have a quadratic dispersion law $\omega = bk^2$. Their polarization is perpendicular to the graphene plane. At small k it gives to the vibrational density of states $g(\omega) \propto \text{const}$. Due to the symmetry, the flexural modes are not mixed with phonon modes at all [3]. Their contribution to the heat transfer is necessary to take into account. They also interact with electrons and holes in graphene and their contribution is very important for electronic properties.

2. Model

In the present paper, we build up an analytical theory of flexural modes in graphene. We derive the dispersion law and the vibrational density of states of flexural modes. The result is shown in fig.1. The dispersion law is given by the formula

$$\omega^2(\boldsymbol{k}) = \Omega^2\left(3 \pm \sqrt{3 + f(\boldsymbol{k})}\right)^2,$$

where the $f(\boldsymbol{k})$ function is

$$f(\boldsymbol{k}) = 2\cos\left(2a_y k_y\right) + 4\cos(a_x k_x)\cos(a_y k_y).$$

Here $a_x = 3a/2$, $a_y = \sqrt{3}a/2$, where a is a nearest neighbor distance.

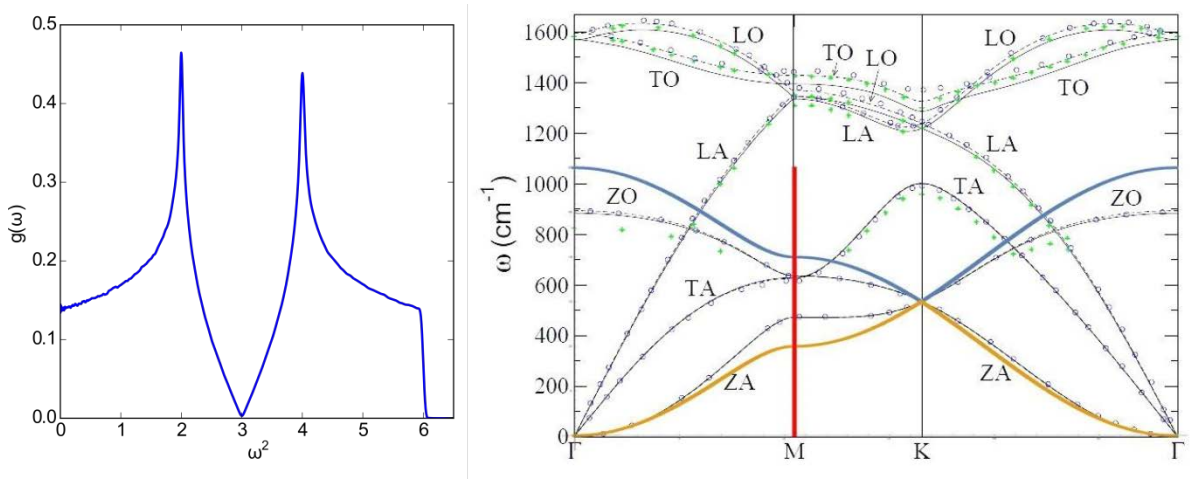

Figure 1. Left: The density of states of flexural modes. The analytical expression through elliptical integrals is given in [4]. Right: The dispersion law of phonon modes in graphene from [5]. The blue and yellow solid lines are our predictions for the dispersion law of ZO and ZA phonons respectively, for the crystalline dynamic matrix M_0^2.

To derive these equations we have used a scalar model, which for graphene is an exact model. In this model, the atomic displacements are not vectors, but scalar values. As a result, each atom in graphene has a single degree of freedom, but the number of bonds for each atom is equal to 3/2. Therefore, according to the Maxwell criterion [6], such scalar model is a stable one. In order to investigate the effect of force constant disorder on flexural modes, numerical methods are used. We construct the dynamical matrix as $M = \mu M_0^2 + AA^T$, where M_0 is the crystalline matrix, $\mu\epsilon[0;+\infty)$ is a parameter specifying the level of order, and A is a random force constant matrix built on the graphene lattice.

3. Summary

Using this approach, we find the dynamical matrix of phonon modes M_0 in the plane. We are utilizing the model of three springs in the first coordination sphere. In the macroscopic limit, the atomic motion is described by the wave equation. It means that from the mathematical point of view, the dynamical matrix is a discrete Laplacian on the graphene plane. The flexural modes have a different dispersion law and a different dynamical matrix. In the macroscopic limit, they are described by elasticity theory, where instead of the Laplacian we have the Laplacian squared [7]. Therefore, the dynamical matrix of flexural modes is the dynamical matrix of phonons M_0 squared, and the dispersion law of flexural modes is a quadratic one. Afterwards, we show that when force constant disorder is introduced into the lattice, at low frequencies the flexural modes are destroyed and become phonons, and the dispersion law is linear instead.

References

[1] Geim A K, Novoselov K S 2007 *Nature Mater* **6** 183
[2] Castro Neto A H, Guinea F, Peres N M R, Novoselov K S, and Geim A K 2009 *Rev. Mod. Phys.* **81** 109
[3] Falkovsky L A 2012 *JETP* **142** 560
[4] Hobson J P, Nierenberg W A 1953 *Phys. Rev.* **89** 662
[5] Wirtz L, Rubio A 2004 *Sol. State Comm.* **131** 141
[6] Maxwell J C 1865 *Phil. Mag.* **27** 294
[7] Landau L D, Lifshits E M Theory of elasticity 1987 (Moscow, Science, **7**)

Sensors of pre-explosive concentrations of hydrogen based on thin films of tin dioxide

S V Kim[1], **N K Maximova**[2]

[1]Department of Semiconductor Electronics, Tomsk State University, Tomsk 634050, Russia
[2] Laboratory Semiconductor Devices, V. D. Kuznetsov Siberian Physical-Technical Institute at Tomsk State University, Tomsk 634050, Russia

Abstract. The results of a study of the electrical and gas-sensitive characteristics of H_2 sensors based on thin nanocrystalline SnO_2 films with dispersed Pt, Pd layers deposited on the surface and Sb, Pt additives in bulk are presented. It was shown that these samples are capable of detecting high hydrogen concentrations (up to 2.5 vol.%) while the sensors do not reach saturation and the characteristics are weakly dependent on changes in the level of environmental humidity. Multiple annealing of the samples at T = 600 ° C was also carried out to increase the value of the response of the sample and subsequent stabilization of the parameters.

Introduction

The need to study the parameters of gas sensors based on thin SnO_2 films is due to the need to develop devices for detecting pre-explosive hydrogen concentrations of 0.1-2.5 vol. % These sensors can be used in hydrogen energy, for monitoring the concentration of hydrogen in the premises of a nuclear power plant, for monitoring H_2 leaks in the batteries of submarines and train cars, in the chemical industry, in rocket fuel, etc. In an earlier work [1], a study was carried out where it was shown that sensors based on thin SnO_2 films with Pt/Pd catalysts deposited on the surface and an additive in the volume of Sb have a high sensitivity to hydrogen. However, the concentration dependence reaches saturation at high concentrations of hydrogen (more than 0.5 vol.%). The aim of this work was to create sensors of high concentrations of H_2 based on thin films of tin dioxide. To detect high hydrogen concentrations, sensors based on thin SnO_2 films with Pt/Pd catalysts deposited on the surface and Sb and Pt bulk additives were developed (Pt/Pd/SnO_2:Sb, Pt).

Experimental results

The concentration dependences of the response (G_H/G_0) of four sensors were measured at a temperature of 400°C in the range of hydrogen concentrations from 0.1 vol. % up to 2.5 vol. % (Fig.1)

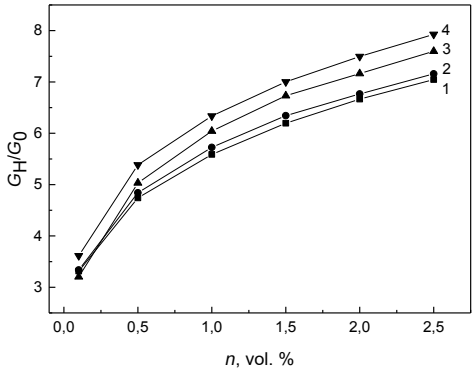

Figure 1. Concentration dependences of the response to H_2 of four sensors measured at T = 400°C

It can be seen that with a slight difference in the characteristics of sensors from different series, their main feature is the absence of saturation of the concentration dependence: with increasing gas concentration, the response increases up to 2.5 vol. % hydrogen. This means that the introduction of Pt additive into the bulk of SnO_2 thin films makes it possible to use these sensors to detect pre-explosive H_2 concentrations.

The effect of additional annealing at T = 600°C for 15 min on the characteristics of the sensors, as well as on their stability, was investigated. The sensors were annealed in a measuring chamber with the specified temperature and duration set. The concentration dependences were measured several days after annealing. Then the experiment was repeated 5-7 times (Fig.2)

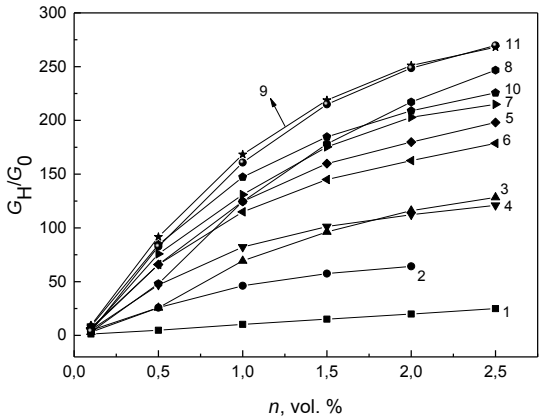

Figure 2. Concentration dependences of the response measured for a freshly prepared sensor (curve 1), then the measurements were carried out after each annealing (curves 2 - 7). Curves 8-11 obtained during the test.

From the data presented in Fig.2, it can be seen that after additional heat treatments, the resistance of all films decreased. This is due to the fact that after annealing of the samples, an increase in the size of crystallites and, possibly, the structure of supported catalysts occurs. Apparently, partial annealing of adsorption centers takes place. As a result, the SCR width decreases, which leads to a decrease in the effect of overlapping conduction channels.

One of the main reasons for the instability of the parameters of gas sensors based on metal oxide semiconductors is the influence of the humidity level of the environment. It was previously shown that with increasing humidity levels, the resistance of the sensors decreases.

Therefore, a study was carried out of the characteristics of the studied sensors of high hydrogen concentrations based on thin Pt /Pd/SnO_2: Sb, Pt films that underwent additional thermal annealing, depending on the humidity level. The concentration dependence of the sensor response at various humidity levels from 9 to 72% is shown in Figure 3. For the sample, it can be seen that there is a slight variation in the response values for different humidity levels. Apparently, the studied sensors are characterized by low sensitivity to humidity.

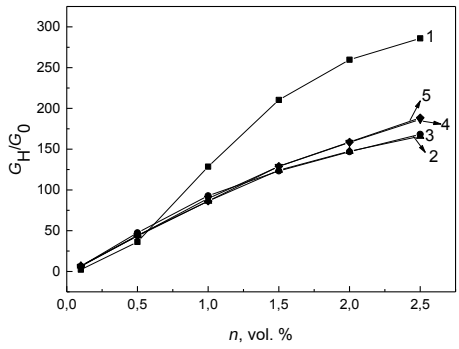

Figure 3. Concentration dependence of the sensor response at various humidity levels RH, %: 1-9, 2-15, 3-30, 4-50, 5-66

References

[1] Maksimova N K, Sevastyanov E Yu, Sergeychenko N V et al. 2016 *Semiconductor thin films gas sensors* (Tomsk: Scientific and technical literature publishing house) p 164

Solid-state phase transition of tetracosan $C_{24}H_{50}$

S A Gureva[1,2], A K Borisov[1,2], V A Marikhin[1], V M Egorov[1]
[1]Strength Physics Lab, Ioffe Institute RAS, St. Petersburg 194021, Russia
[2]Peter the Great St. Petersburg Polytechnic University, St. Petersburg, 195251, Russia

Abstract. The heterogeneous structural phase transition in the even n-alkane tetracosan $C_{24}H_{50}$ was studied by IR spectroscopy and DSC. It was found that the initial nanonuclei of the hexagonal phase are formed in the lamellas cores and their volume was calculated.

1. Introduction

The purpose of this work was a fundamental study of temperature phase transitions (PTs) in normal alkanes with even chain lengths using tetracosane $C_{24}H_{50}$ as an example.

The objects of research are long-chain molecular crystals (LCMCs) of n-alkanes, consisting of numerous nanolamels layered on each other (thick~3 nm for tetracosan). Lamellar cores are extended trans sequences of methylene CH_2 groups, the stacking of which corresponds to the triclinic symmetry of the unit sub-cells for tetracosan. The van der Waals interaction of neighboring lamellas is carried out by the contact of terminal methyl CH_3 groups.

2. Experiments and results

IR Fourier spectroscopic analysis reveals subtle shifts in the molecular vibration spectra that occur when the symmetry of sub-cells in the crystalline cores of elementary lamellas changes during a first-order solid-state phase transition (PT-1) [1].

In our previous works [2, 3], the development kinetics of structural PT-1 in monodisperse tetracosan samples was studied by FTIR spectroscopy. The absorption spectra of monodisperse samples of tetracosane $C_{24}H_{50}$ were recorded on IFS-88 FTIR spectrometer (Bruker, Germany). The temperature dependences of the frequencies and intensities of rocking ($\nu \sim 720$ cm^{-1}) and bending ($\nu \sim 1470$ cm^{-1}) vibrational modes of extended methylene CH_2 trans sequences in the lamellas cores were investigated. It was shown that in the cores PT-1 develops to a heterogeneous mechanism in a temperature range $\Delta T = 45.5 - 47.6^{\circ}C$ in accordance with the diffuse phase transitions theory. It was found that the transition is due to a change in the crystallographic sub-cells symmetry with the transformation of the initial into hexagonal.

To detect changes in the surface lamellas layers, the spectral region $\upsilon = 2800 - 3000$ cm^{-1} was studied, including stretching vibrations of C–H bonds in terminal methyl CH_3 groups (we use the notation: r^+ - symmetric; r_a^-, r_b^- - antisymmetric, in-plane and out of-plane components, respectively). In addition, stretching vibrations in the CH_2 groups are located in the studied spectral region.

It was found that the C–H stretching vibrations undergo a frequency shift $\sim 1 - 2$ cm^{-1} in the PT-1 region. The temperature study of the methylene CH_2 stretching vibrations in the lamellas cores confirms the results obtained in previous works. While the rearrangement of the crystal structure manifests at higher temperatures ($46.2^{\circ}C$) in changes of vibrations in the terminal groups. Temperature dependences of the positions of absorption band maximums were constructed for symmetric and antisymmetric stretching vibrations of C–H bonds in CH_3 groups of tetracosane on Figure 1.

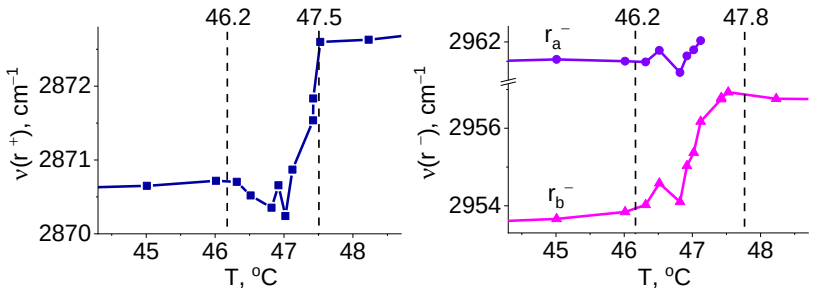

Figure 1. Temperature variations of the symmetric **(left)** and antisymmetric **(right)** stretching vibrational frequency of C–H bonds in CH_3.

It can be concluded that for even n-alkane $C_{24}H_{50}$ the initial nuclei of a new phase arise in the lamellas cores and then gradually spread to the entire volume. We explain this effect by the fact that it is energetically beneficial to verticalize of initially tilted molecules in triclinic sub-cells before a complete transition to the hexagonal phase. The terminal groups maintain the structure integrity up to 47°C, when all the molecules become vertical.

Also, the temperature dependence of heat capacity was obtained for tetracosan samples by differential scanning calorimetry (DSC). The scanning speed and the sample mass were varied (V = 0.1, 0.2, 0.5, 1, 2, 5 K/min, m = 0.25, 2.7 mg) to obtain methodically undistorted phase transition temperatures by extrapolation to zero speed [1] and minimize the effect of thermal delay and thermal resistance.

Figure 2 shows the experimental thermogram of the tetracosan sample, corresponding to the solid-phase transition. It can be seen that the transition covers the interval ΔT = 47.0 – 48.2°C, that is consistent with IR data on the complete transition to the hexagonal phase.

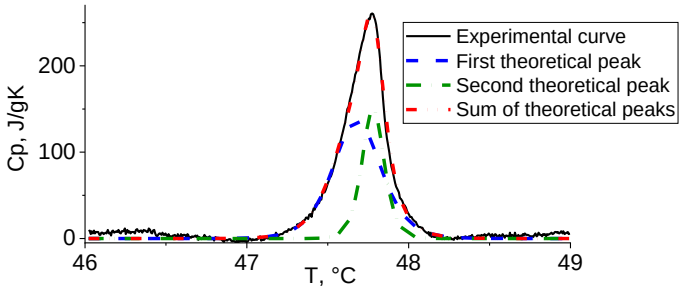

Figure 2. DSC PT-1 curve for tetracosan with m = 0,25 mg, V = 1 K/min.

The first-order solid-phase transition has a Λ-shaped peak on the DSC curve, for the analysis of which the self-consistent field theory is applied. The asymmetric heat capacity peak was divided into two symmetric Λ-shape peaks, that the total enthalpy was equal to the enthalpy of the experimentally obtained peak (Figure 2). For each of the peaks, the new-phase nuclei volumes were calculated according to the diffuse phase transitions theory [4] $\omega_1 = 329$ nm^3, $\omega_2 = 1722$ nm^3. Such nanonuclei volumes capture ~ 600 and 3000 molecules, respectively. Thus, it is seen that the transformation region covers a very large domain.

References

[1] Egorov V M, Marikhin V A 2017 *Physics of the solid state* **59** 2044
[2] Marikhin V A, Gur'eva S A, Myasnikova L P, Volchek B Z, Medvedeva D A 2019 *Physics of the solid state* **61** 1785
[3] Gureva S A, Marikhin V A, Myasnikova L P, Volchek B Z, Medvedeva D A 2019 *J. Phys.: Conf. Ser.* **1400** 055040
[4] Malygin G A 2001 *Physics-Uspekhi* **171** 187

XRD study of long-term structural evolution in the product of SHS reaction in Ni/Al multilayer foil

V S Osipov[1], S A Udovenko[1], P G Gabdullin[1], O E Kvashenkina[1], A V Arkhipov[1], V Ye Babyuk[1] and R G Burkovsky[1]
[1]Peter the Great St. Petersburg Polytechnic University

Abstract. We present results of XRD investigation of the product of self-propagating high-temperature synthesis (SHS) reaction in Ni/Al reactive multilayer foil (RMF) produced by vacuum magnetron sputtering. Evolution of XRD spectra for the reacted foils on the time scale of hours and days was detected. This effect, previously observed only for SHS reaction in powder mixtures, may be significant for RMF-based soldering technologies.

1. Introduction

One of the applications of the phenomenon of exothermic self-propagating high-temperature synthesis (SHS) is associated with bonding materials by soldering. Ni/Al reactive multilayer foils (RMFs) represent the controllable thermal power source most commonly used for this purpose [1-3]. Obviously, the quality of the produced soldered junction can be affected by the microstructure and the phase composition of the SHS reaction products. The reaction is known to be a complex multi-stage phenomenon involving solid-state diffusion, grain boundary diffusion, melting of some (or all) of the components, dissolution, precipitation, product's grain coarsening, which hampers its comprehensive theoretic description [3]. It is also known that the reaction may be followed by slow recrystallization process driven by solid-state diffusion at room temperature accompanied by redistribution of mechanical stresses. These slow processes potentially capable of having either positive or negative effects on the joining strength were the object of the reported study.

2. Experimental

The studies were made with an RMF comprising numerous alternating Ni and Al layers, each ~30 nm thick. Full thickness of the foil amounted to 60 μm. A sample of such foil was installed in XRD spectrometer and the corresponding spectrum was measured. Then, the foil was ignited by electric spark and the reaction product structure was analyzed at three more different time moments: immediately after the combustion, 24 hours and 168 hours after reaction, to reveal possible long-term evolution of the sample's phase composition.

The XRD spectra were recorded using SuperNova (Oxford Diffraction) single crystal diffractometer. Measurements where performed using Cu X-Ray source with the sample being 5 by 2 mm fragment of foil, rotated along the axis parallel to the foil. The powder diffractograms were produced by integrating the scattering signal over the sample rotation angle in the range ±30°, and then - over the polar angle within the CCD image.

3. Results and discussion

The XRD spectra of the sample before its combustion and at three moments of time after it are shown in Figure 1.

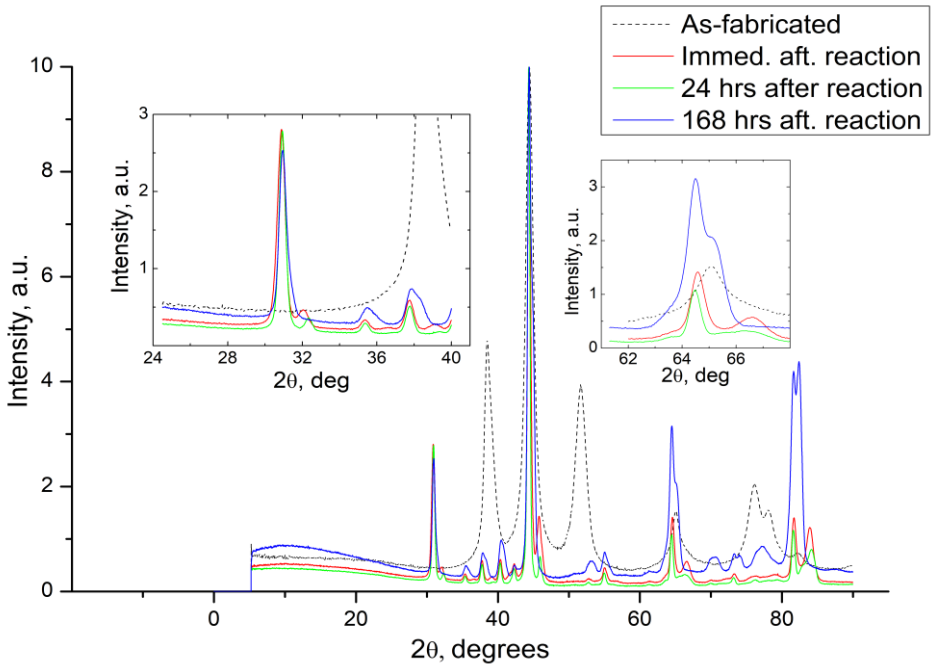

Figure 1. XRD spectra of the Ni/Al RMF before reaction and at three different times after.

As expected, the intensive Al and Ni peaks seen in the spectrum of as-fabricated foil vanish after the reaction, and characteristic NiAl product peaks around 31°, 65° and 82° appear. It can also be clearly seen that these peaks appear to be split immediately after the reaction and tend to merge as the time passes. We attribute such changes to the manifestation of the recrystallization process. During the dissolution–precipitation stage, precipitation is realized from either Al-rich or Ni-rich melt depending on the specific nucleus. The equiatomic Ni–Al 1:1 melt cannot exist in the considered conditions as the stoichiometric NiAl solid phase is known to be the most refractory of all binary Ni/Al compositions and does not melt at temperatures at which the precipitation starts. So, immediately after the reaction the product contains slightly non-stoichiometric NiAl crystallites, some of them having excessive Al and some having excessive Ni content – which results in the observed XRD peaks' splitting. With time passing, slow room-temperature diffusion leads to gradual recrystallization of the reaction product, consumption of the inter-grain amorphous phase and eventual formation of the final stoichiometric NiAl. Previously, such processes were reported for SHS reactions in powder mixtures [5], but not for Ni/Al RMFs.

References

[1] Rogachev A S, Vadchenko S G, Nepapushev A A, Rogachev S A, Scheck Yu B and Mukasyan A S 2018 *Adv. Eng. Mater.***20** 8 1701044
[2] Adams D P 2015 *Thin Solid Films* **576** 98
[3] Kvashenkina O E, Gabdullin P G and Arkhipov A V 2018 Proc. Int. Conf. on Electrical Engineering and Photonics (St. Petersburg, Russia) # 8564437 (Piscataway, NJ, USA/IEEE)
[4] Baras F, Turlo V, Politano O, Vadchenko S G, Rogachev A S and Mukasyan A S 2018 *Adv. Eng. Mater.***20** 8 1800091
[5] Kovalev D Yu, Ponomarev V I 2019 *Int. J. Self Propag. High Temp. Synth* **28** 2 114

Investigation of the influence of the geometric parameters of AFM cantilever balks on the resonant frequency of their vibrations

I V Panchenko[1], **N A Shandyba**[1], **A S Kolomiytsev**[1], **O A Ageev**[1]
[1]Southern Federal University, Taganrog 347924, Russia

Abstract. The paper presents the results of theoretical and experimental studies of the influence of the geometric parameters of AFM cantilever balks on the resonant frequency of their vibrations. It is shown that the use of local ion-beam etching by a focused ion beam makes it possible to modify the geometric parameters of probe balks with high accuracy, which in turn makes it possible to change the resonant frequency of cantilever oscillations. The dependences of the resonant frequency of oscillations on the geometric parameters of the balks are analyzed. It has been established that a decrease in the balk length from 110 mkm to 80 mkm leads to an approximately twofold increase in the resonant frequency of cantilever oscillations from 320 kHz to 620 kHz. The obtained graphs of the dependences of the resonant frequency on the length of the probe balk are presented.

1. Introduction

Micromechanical structures based on cantilever balks are widely used in the creation of dynamic sensors, such as displacement sensors or interaction sensors in atomic force microscopy [1]. In this case, one of the key parameters of microbalk structures is the value of the resonant frequency of their vibrations. In atomic force microscopy, force interaction sensors - cantilevers are made according to standard technological processes and have fixed balk sizes, which means certain values of resonant frequencies. However, for a number of tasks, it is necessary to adjust the resonant frequency of the cantilevers to achieve maximum sensitivity of the sensors.

Therefore, to improve the quality of research of materials and structures, to increase the accuracy of detection of parameters, it is necessary to be able to adjust the resonant frequency of oscillations in a given range. The resonant frequency of oscillations of the cantilever balk is influenced by the geometric parameters and the material from which the balk is made. To fine-tune the resonant frequency of oscillations by changing the geometric shape of the AFM probe balk, we used the method of local ion-beam etching by focused ion beam (FIB).

The FIB method allows in high vacuum conditions to perform technological operations of local ion beam etching and ionically stimulated deposition of materials from the gas phase without the need for resistors, masks and chemical etchants. A wide range of materials deposited by this method allows the use of FIB in the formation of nanoscale structures, in particular, probes for nanodiagnostics. The aim of this work is to establish the dependence of the resonant frequency of oscillations of the AFM probe balk on its geometric parameters.

2. Experimental

At the initial stage of the work, mathematical modeling of the vibration parameters of the silicon probe balk was carried out depending on its geometric parameters using the finite element method. In the

course of theoretical studies, it was found that with a decrease in the length of the balk, the resonant frequency increases almost linearly, and when the values of the length of the balks of 60 mkm are reached, the dependence becomes exponential.
In the course of experimental studies, ion-beam modification of three NSG11 probe sensors with 2 balks was carried out, with lengths of 123 mkm and 93 mkm, respectively. Our studies have shown that the balks have a different thickness from 2.5-3 mkm. The balk length was reduced using the Nova NanoLab 600 scanning electron microscope (FEI Company) equipped with a FIB system [2]. In the course of the study by ion-beam etching, a part of the balk, on which the tip of the sensor was located, was cut off and the resonance frequency was studied using a Solver P47 PRO probe microscope (Figure 1).

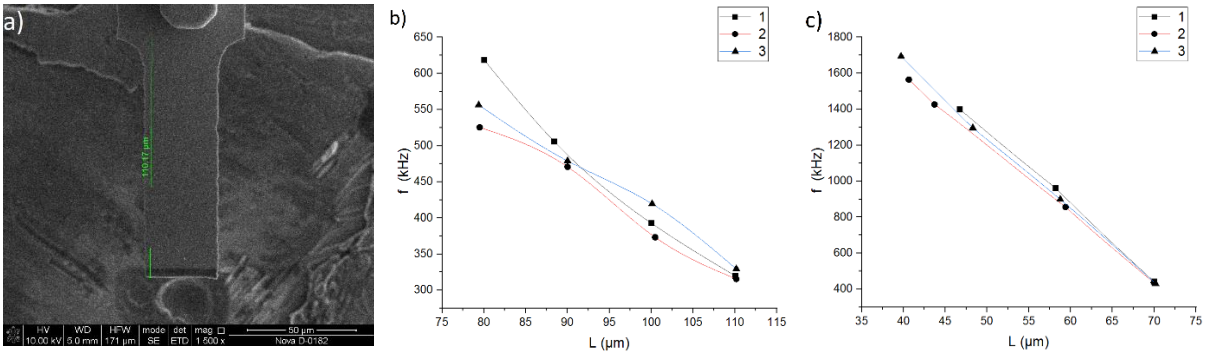

Figure 1(a, b, c). (a) Cantilever prepared for research (without probe); Resonance frequency for **(b)** 123 mkm and **(c)** 93 mkm cantilevers.

Further, the balks were shortened sequentially with a step of 10 mkm; after each step, the values of the resonant frequency of oscillations were controlled. The dependences of the resonance frequency on length for the 93 mkm and 123 mkm balks of three probe sensors were investigated. The data was systematized and displayed on figure 1 (b, c).
Thus, for various cantilever balks, dependencies are obtained that make it possible to predict the value of the resonant frequency for a given balk length. Due to the difference in thicknesses of 123 mkm and 93 mkm balks, the dependences show slightly different values, however, the trends generally coincide for all 3 experimental samples. Differences in resonant frequencies for one balk length, for example, for a balk length of 100 mkm (graph b), are associated with availability a large number of resonant frequencies for longer cantilevers, the value of which are automatically determined by the program.

3. Conclusions

Thus, in the work we obtained graphs of experimental dependences of the resonant frequency of cantilever oscillations on the balk length, which correspond to the results of mathematical modeling. The results can be used in predicting the dynamic parameters of micromechanical systems, in particular, when creating gas and biological sensors based on micromechanical structures. The method of focused ion beams makes it possible to fine-tune the resonant frequency of oscillation of cantilever balks by changing their geometric parameters.

4. Acknowledgments

This work was supported by the Russian Science Foundation Grant No. 18-79-00175.

References

[1] Lang, Hans & Hegner, Martin & Gerber, Christoph. (2005). Materials Today. 8. 30-36.
[2] Nanotechnology in Microelectronics / Ed. O.A. Ageev B.G. Konoplev. - M.: Nauka, 2019 .-- 511 p. - ISBN 978-5-02-040201-0.

Research of the mechanical parameters of silicon membranes for acoustic sensors

S V Malokhatko[1], E Yu Gusev[1], E A Rassolov[2], A M Khannanov[3], O A Ageev[1,4]

[1]Department of Nanotechnologies and Microsystems, Southern Federal University, Taganrog 347922, Russia

[2]Optoelectronics Department, Institute of Automation and Control Processes Far Eastern Branch of the Russian Academy of Sciences (IACP FEB RAS), Vladivostok 690041, Russia

[3]Department of ship energy and automation, School of Engineering Far Eastern Federal University, Vladivostok 690091, Russia

[4]Research and Education Center "Nanotechnologies", Southern Federal University, Taganrog 347922, Russia

Abstract. This paper presents the modeling results of silicon membranes for acoustic sensors with resonant frequency from 2 kHz to 60 kHz and pressures from 0.1 to 14 Pa. An analysis of the constructive and mechanical parameters of monocrystalline silicon membranes is performed. The range of membrane edge length (6–20 mm) at a fixed thickness of 50 μm determined. The etching process of a silicon wafer by anisotropic **wet** etching was studied. A process flow for manufacturing silicon membranes is proposed. The results of experimental studies of amplitude-frequency characteristic of membranes are obtained.

Introduction

Micromechanical acoustic sensors have emerged as an alternative to standard ones due to such advantages as increased bandwidth, flexible geometry, matching of impedances between the transducer and the environment [1]. The scope of the acoustic sensor is defined by such parameters as the amplitude-frequency response and the minimum detectable acoustic pressure. In [2], a fiber-optic hydrophone was proposed, which sensitive element is a fiber sensor. In the frequency range from 2 kHz to 60 kHz, the sensitivity of the adaptive acoustic hydrophone was in the range of 0.1 to 14 Pa. The choice of material, shape and size of the membrane allows to adapt the sensors to different applications [3,4]. Thus, an issue is to optimize the geometric and mechanical parameters of the membranes in such a way that the resulting design satisfies the above ranges pressure and resonant frequency values. The purpose of the work is to study the structural and mechanical parameters of silicon membranes for sonar sensors.

Experimental details and results

In this paper, we study the use of a primary membrane-type acoustic pressure receiver. Based on technological capabilities, a silicon membrane with a square shape and a thickness of 50 μm was selected. When modeling by the finite element method, the length of the edge (a) varied within 6–20 mm. The values of the geometric parameters of the membrane are selected taking into account the values of pressure (0.1-14 Pa), resonant frequency (2-60 kHz) and the dynamic range of the interferometer, which allows measuring the deflection of the membrane from 2-130 nm. Based on the implemented model in

Comsol Multiphysics, the values of the first 6 resonant frequencies (fn) were obtained depending on the length of the membrane edge (Fig. 1), which are shown in Table 1.

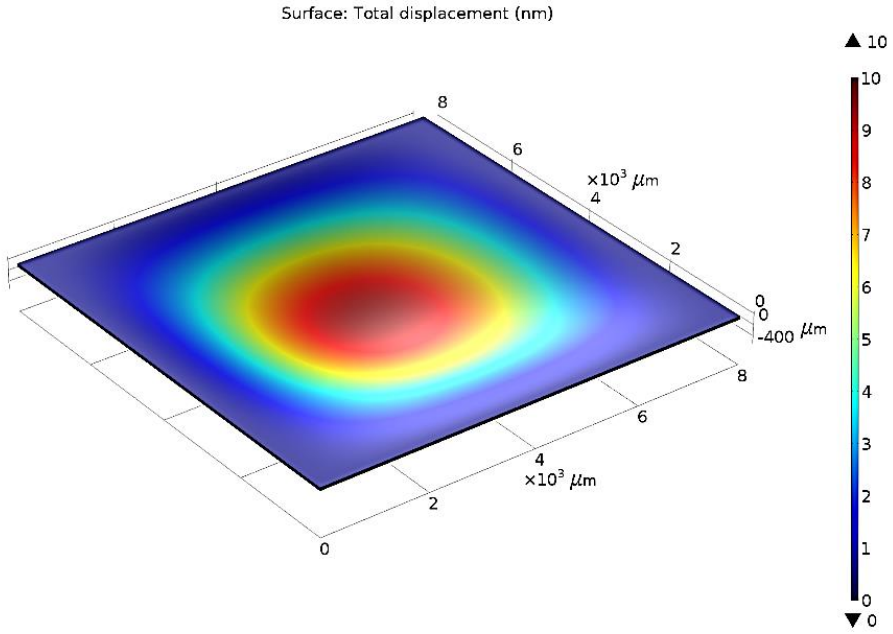

Figure 1. Three-dimensional model of the membrane under load

Table 1. The values of the first 6 resonant frequencies of the silicon membrane.

a, mm	f_1, Hz	f_2, Hz	f_3, Hz	f_4, Hz	f_5, Hz	f_6, Hz
6	20478	41573	41755	61546	74826	75185
10	7376.7	15048	15049	22195	26990	27118
15	3280	6692.6	6692.7	9875	12005	12063
20	1845.8	3768.6	3768.9	5562.8	6761.5	6795.1

Based on the obtained results, mock-ups of silicon membranes of square shape with a thickness of 50 µm with edge lengths from 6 to 20 mm were made. The etching parameters of a Si wafer were studied by anisotropic wet etching. The amplitude-frequency characteristic of membranes were experimentally obtained. The results can be used to optimize the designs and fabrication processes of acoustic sensors based on silicon membranes.

Acknowledgments
The research is supported by the Russian Science Foundation (project #19-12-00323). The results were obtained using the equipment of Research and Education Centre "Nanotechnologies" of Southern Federal University.

References
[1] Ergun S, Yaralioglu G, Khuri-Yakub T 2003 *J. Aerosp. Eng*. **16** 76.
[2] Romashko R V, Bezruk M N, Ermolaev S A, Zavestovzkaya I N, Kulchin Yu N 2015 *Bulletin of the Lebedev Physics Institute* **42** 201.
[3] Qiu Y, Gigliotti J, Wallace M , Griggio F, Demore C ,Cochran S, Trolier-McKinstry S 2015 *Sensors* **15** 8020.
[4] Ageev O A, Konoplev B G 2019 *Nanotechnology in microelectronics* (Moscow: Nauka) 511.

Polymer-salt synthesis of $Gd_2O_3:Nd^{3+}$ nanophosphors

N K Kuzmenko[1], S K Evstropiev[1,2], V A Aseev[1], D P Danilovich[2], N V Nikonorov[1], A I Ignatiev[1], A S Matrosova[1,3], V V Demidov[3], A V Emerson[2], I M Sevastyanova[1]

[1]ITMO University, St. Petersburg 197101, Russia
[2]Saint-Petersburg State Institute of Technology, St. Petersburg 190013, Russia
[3]R&P Association Vavilov State Optical Institute, St. Petersburg 192171, Russia

Abstract. The paper describes $Gd_2O_3:Nd^{3+}$ nanophosphors synthesis by the liquid polymer-salt method. The properties of powder samples fabricated in different temperature conditions were studied by luminescence spectroscopy and X-ray diffraction (XRD). It was found that prepared nanophosphors demonstrate high photoluminescence in the near IR spectral range.

1. Introduction

Gadolinium oxide (Gd_2O_3) is a well-known inorganic compound which is widely used for nano-sized phosphors fabrication [1]. Gd_2O_3 doped with rare earth ions is considered as a promising material for optical thermometry applications [2]. The effectiveness of Nd^{3+}-containing oxide nanoparticles for photoluminescence nanothermometry was demonstrated [3]. These nanoparticles exhibit luminescence bands in the near IR spectral range and have an ability to operate in the optical windows of biological tissues. The combination of high magnetic properties of Gd_2O_3 and luminescent properties of Nd^{3+} ions can enable obtaining a photoluminescence nanothermometer controlled by the magnetic field.
This paper discusses synthesis of $Gd_2O_3:Nd^{3+}$ nanophosphors by the technologically flexible liquid polymer-salt method [4] as well as structural and luminescent properties of the powder samples fabricated in different temperature conditions.

2. Materials and Methods

Aqueous solutions of $Gd(NO_3)_3$ and $NdCl_3$ were used as the precursors for $Gd_2O_3:Nd^{3+}$ nanophosphors synthesis. These solutions along with a solution of high-molecular polyvinylpyrrolidone were mixed at the room temperature while being vigorously stirred. After drying the powders for 24 hours, they were thermally treated in the electrical furnace at the temperatures of 550, 900 and 1000 °C for 2 hours. The content of Nd^{3+} ions in the fabricated powder samples varied from 0.1 to 2.0 at.%.
Structural properties of the synthesized materials were determined by a high-resolution diffractometer Rigaku Ultima IV. Luminescent properties were measured by the technique described earlier [5].

3. Results and Discussions

The XRD patterns of the powder samples, presented in Figure 1, show that the main part of Gd_2O_3 nanocrystals has a cubic structure. However, crystals calcined at the temperatures of 550 and 900 °C are characterized by a few small peaks at $\theta = 27 \div 33°$ assigned to a monoclinic structure. At the same time, the powder thermally treated at the temperature of 1000 °C exhibits peaks characteristic only to cubic Gd_2O_3 crystals. Calculations based on the peaks positions in the XRD patterns point the absence of crystal lattice strains.

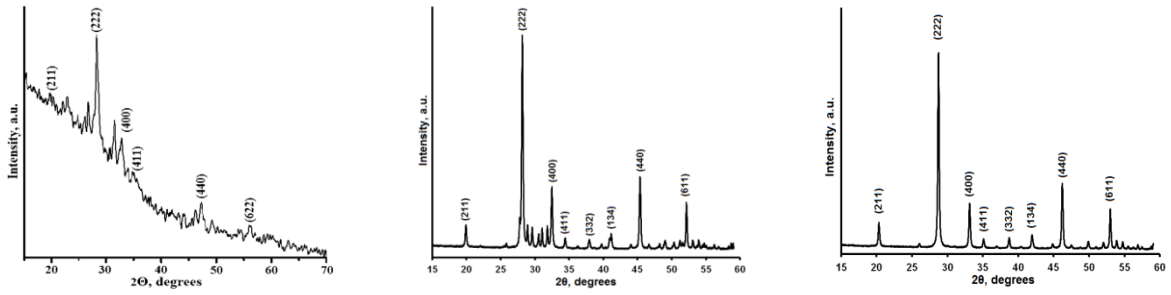

a) b) c)

Figure 1. XRD patterns of the powder samples thermally treated at the temperatures of 550 °C (a), 900 °C (b) and 1000 °C (c) for 2 hours.

The presence of monoclinic crystals in the powder samples calcined at the temperatures of 550 and 900 °C can be related to high heat generation during the combustion of initial mixtures and strong local heating at the first stages of Gd_2O_3 nanocrystals formation.

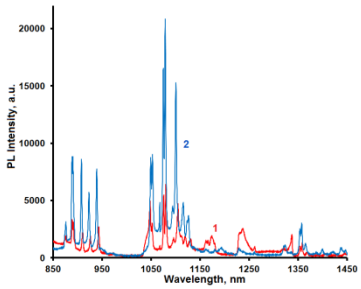

Figure 2. Photoluminescence spectra of the powder samples thermally treated at the temperatures of 550 °C (curve 1) and 1000 °C (curve 2) for 2 hours (neodymium content is 0.4 at.%).

As can be seen from Figure 2, there are three photoluminescence bands with peaks at the wavelengths of 900, 1064 and 1340 nm which correspond to electron transitions $^4F_{3/2}$-$^4I_{9/2}$, $^4F_{3/2}$-$^4I_{11/2}$ and $^4F_{3/2}$-$^4I_{13/2}$ respectively. The main emission peak is located at the wavelength of 1064 nm.

4. Conclusions

The aspects of Gd_2O_3:Nd^{3+} nanophosphors synthesis by the liquid polymer-salt method have been studied. It has been found that polyvinylpyrrolidone, on the one hand, stabilizes the process of nanocrystals formation prohibiting their growth and aggregation and, on the other hand, plays the role of a fuel during its combustion increasing the temperature of reaction mixture and affecting the crystal structure and luminescent properties of Gd_2O_3:Nd^{3+} nanophosphors.

5. Acknowledgments

This research is supported by the Russian Science Foundation (Project No. 19-19-00596).

References

[1] Xu L, Yu Y, Li X, Somesfalean G, Zhang Y, Gao H, Zhang Z 2008 Opt. Mater. **30(8)** 1284
[2] Singh S K, Kumar K, Rai S B 2009 Sens. Act. A **1491(1)** 16
[3] Kolesnikov I E, Kalinichev A A, Kurochkin M A, Mamonova D V, Kolesnikov E Yu, Kurochkin A V, Lahderanta E, Mikhailov M D 2018 J. Luminescence **204** 506
[4] Evstropiev S K, Gatchin Yu A, Evstropyev K S, Romanova E B 2016 Opt. Eng. **55(4)** 047108
[5] Evstropiev S K, Aseev V A, Demidov V V, Kuzmenko N K, Matrosova A S, Khokhlov A V, Komarov A V, Dukelskii K V, Nikonorov N V, Oreshkina K V 2019 Quantum. Electron. **49(12)** 1145

Formation and growth of carbon nanostructures in flame

O V Vasilyeva[1], S I Ksenofontov[2], A N Lepaev[3]

[1]Chuvash State University named after I.N. Ulyanov, Cheboksary 428015, Russia
[2]Chuvash State Pedagogical University named after I.Y. Yakovlev, Cheboksary 428000, Russia
[3]Cheboksary Institute (branch) of the Moscow Polytechnic University, Cheboksary 428000, Russia

Abstract. Carbon nanostructures in the form of tubes are formed in a heterophase mode of combustion of a metal with fluoroplastic. These tubes are filled with condensed particles of combustion products and change the optical properties of the flame.

The flame of the pyrotechnic composition, which contains metallic fuel, is characterized by high temperature. A high temperature zone is located at the base of the flame. As rule, the metal in this zone burns in vapor mode. However, the metal burns in flame in heterophase mode too. The metal reaction rate in the heterophase mode is much lower than in the vapor-phase mode and depends on the surface contact of the fuel and the oxidizing agent.
The flame of a model pyrotechnic composition based on aluminum-magnesium alloy and fluoroplastic F-3 was studied. The photopyrometric measurement methods developed by the author make it possible to measure the flame temperature. The maximum temperature is at the base of the flame. It is 2440 K. The flame temperature decreases to 1715 K at a height of 300 mm above the combustion surface. At this temperature, possible condensed combustion products (fluorides, chlorides and carbides of magnesium and aluminum) are either in a liquid state or a sublimation process is under way. Fluorides and aluminum chlorides (AlF_3 and $AlCl_3$) are sublimated. Magnesium and aluminum fluorides (MgF_2 and AlF) and magnesium chloride ($MgCl_2$) can be in the molten state. Carbon in a flame can be represented in a various state: a) particles of fine soot, b) soot in the composition of complex dispersed particles.

a) b)

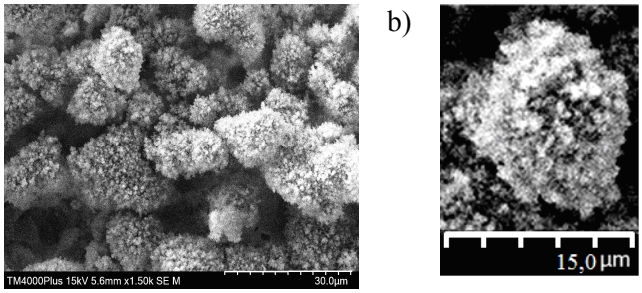

Figure 1 (a, b). Micrograph of the sample area. Magnification (a) 1500x, (b) 6000x

The dispersed particles of the combustion products were sampled onto glass plates by passing the sampler through the flame. Samples were studied by microscopy. Two types of particles can be distinguished among the condensed combustion products. One of the types of particles is coral-shaped

formations, consisting of a set of particles with a size of 0.2 ÷ 0.4 microns. They accumulate directly at the reacting particle (Fig. 1a, b). Metal fluorides and chlorides are part of the chemical composition of a particle. Another type of particle is a filamentous structure that originates from the surface of the reacting particle. A detailed study of these particles on a scanning electron microscope showed that the filaments are a complex structure (Fig. 2a, b). The outer part of the particle consists of a carbon net in the form of a tube. The dimensions of the tube are several tens of microns across and coincide with the external dimensions of the reacting particle. The presented electronic images differ in magnification factor.

The tube is a net of carbon nanotubes. The transportation of metal products of combustion with fluoroplastic takes place inside a hollow tube in the form of a two-phase flow. The gas component of the flow freely passes through the carbon net of the tube. Dispersed particles of submicron size cannot penetrate through the net and linger on the inner surface of the tube. The size distribution function of the deposited particles is such that most particles have a diameter of ~ 0.15 μm.

a) b)

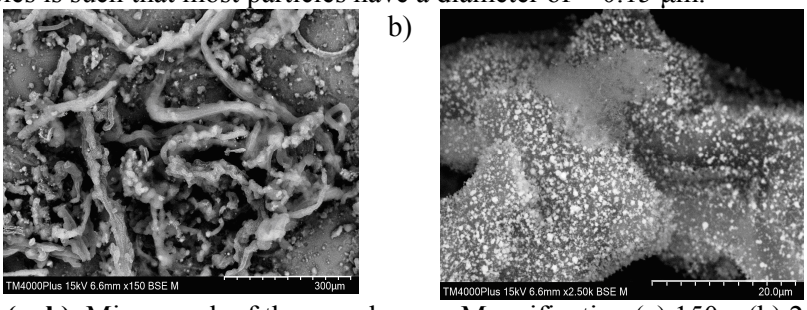

Figure 2 (a, b). Micrograph of the sample area. Magnification (a) 150x, (b) 2500x

The X-ray spectral method, implemented on a scanning electron microscope, allows element-by-element identification of the composition of these particles. Indeed, the elemental composition of the particles and the maps of the arrangement of elements within the tube make it possible to isolate magnesium, aluminum, fluorine, and carbon in them (Fig. 3).

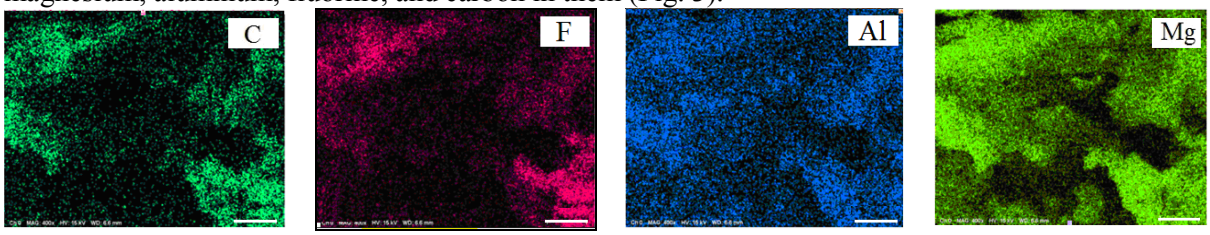

Figure 3. Distribution map of chemical elements. The length of the frame 100 microns.

The formation of nanocarbon particles in a high-temperature flame of a different component composition was studied in [1, 2].

Carbon formations in the form of a tube measuring several tens of microns across and up to several millimeters in length were first discovered in combustion products. The length of the carbon tube is determined by the hydrodynamic resistance during the movement of a two-phase flow. Larger particles of combustion products deform the carbon net of the tube. In this case, the transverse dimensions of the tube increase. The formation of parallel tubes or their branching is possible with increasing hydrodynamic resistance. It is confirmed by the above images.

The reactive combustion products are energy carriers, and the outer surface of tubes with embedded dispersed particles is a radiator of electromagnetic energy in the near infrared range of the spectrum.

References

[1] Vasilyeva O V, Ksenofontov S I, Kokshina A V 2019 J. Phys Conf. Series **1410** 012232

[2] Ksenofontov S I, Vasilyeva O V 2018 Proc. All-Russian Scientific Conf. on Nanostructured Materials and Converters for Solar Energy (Cheboksary: Chuvash State University) p 86

Modification of glass durability in reactive ion etching with thermal poling and ion exchange

D V Raskhodchikov[1], E S Babich[1,2], V.P. Kaasik[2], I V Reshetov[2], A A Lipovskii[1,2]

[1]Department of Physics and Technology of Nanostructures, Alferov University, St. Petersburg 194021, Russia

[2]Institute of Physics, Nanotechnology and Telecommunications, Peter the Great St. Petersburg Polytechnic University, St. Petersburg 195251, Russia

Abstract. The influence of thermal poling and ion exchange on the rate of reactive ion etching of a soda-lime silicate glass in CF_4-Ar plasma was studied. It is shown that the replacement of Na^+ by Ag^+ ions increases the durability of the glass etching while thermal poling of the glass increases the etching rate. The fastest etching was registered for the glasses poled using deposited metal film anodic electrode and using corona discharge in N_2 atmosphere. Corona poling of the glass in atmospheric air instead of nitrogen essentially decreased the rate.

1. Introduction

Reactive ion etching (RIE) of glasses is a technique allowing precise fabrication of profiled structures for microfluidics, diffractive optical and integrated optical structures. The formation of the latter is often based on using ion exchange processing of the glasses in the melts of salts containing ions with higher polarizability than ones presenting in the composition of these glasses. Silver-to-sodium ion exchange is conventionally used. It has recently been demonstrated that the modification of silicate glasses with thermal poling allows using of poled glass regions to mask RIE [1]. The conditions of the thermal poling, e.g. poling in open or closed anode configuration, essentially influence that modification [2]. In this paper, we compare results of the RIE of virgin, silver ion-exchanged and differently poled soda-lime glass.

2. Experiments and results

In the experiments, we used soda-lime glass slides which composition is presented in Table 1.

Table 1. Composition of Menzel glass in molar % of oxides.

SiO2	Al_2O_3	Na_2O	K_2O	MgO	CaO	others
72.2	1.2	14.3	1.2	4.3	6.4	0.33

The samples were ion-exchanged in the melt of $Ag_{0.05}Na_{0.95}NO_3$ for 20 minutes at the temperature of 325 °C (sample #2). In thermal poling experiments, we poled the virgin glass slides using 60 nm thick gold film deposited on the slide with 5 nm chromium sublayer (closed anode configuration), poling voltage V and temperature T being 500 V and 300 °C, respectively - sample #3; pressed carbon electrode (V=300, T=300 °C) - sample #4; pressed silicon electrode (V=500, T=300 °C) - sample #5; corona poling in air (V= 4kV, T=20 °C, duration of 50 minutes) - sample #6; corona poling in dry

nitrogen (V= 4 kV, T=300 °C, duration of 2 h) - sample #7. These ion-exchanged and poled glass samples were subjected to RIE with the use of 10Ar - 20CF_4 gas composition. The RIE rate of pure soda-lime glass was also measured – sample #1. The RIE of the samples was performed in PLASSYS MU400 station, RIE pressure was 6.0 mTorr. The plasma was generated with a radio frequency powered magnetic field combined by two methods: using inductively coupled plasma (ICP 400W) and capacitively coupled plasma (CCP 150W).

To define the rate of the RIE for differently prepared samples parts of the samples were covered with masks presenting thin glass slips with the same composition as the glass samples used. The etching process was interrupted several times to measure the step between the etched and protected parts of the samples with a tip profilometer. The results of the measurements are shown in Figure 1.

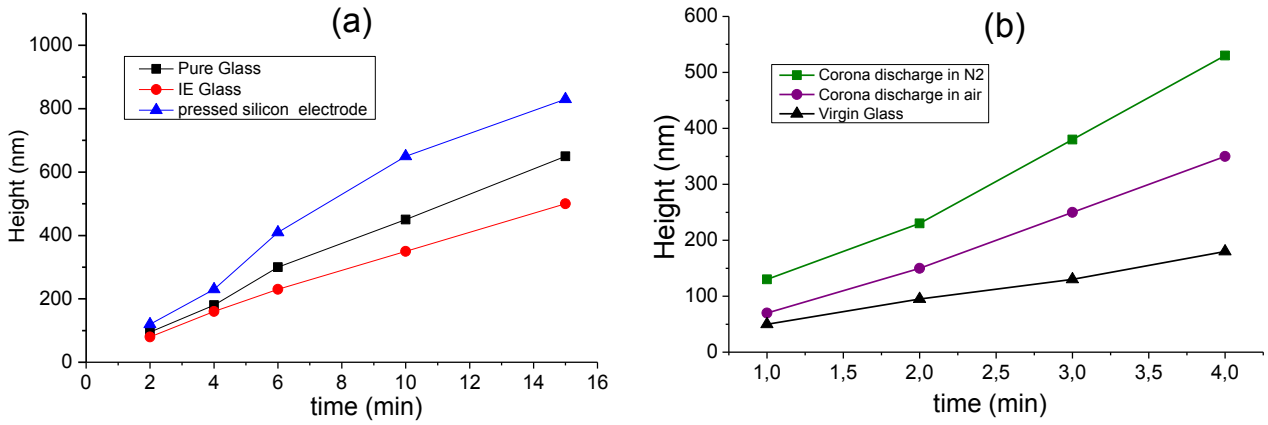

Figure 1(a)(b). Time dependences of the etching depth of the ion exchanged and differently poled glasses

Obtained data allowed us calculating the rates of RIE of the samples, which are presented in Table 2.

Table 2. RIE rates of differently processed samples.

Sample #	1	2	3	4	5	6	7
RIE rate, nm/min	50	40	120	55	60	70	130

3. Discussion

These rates show that the replacement of smaller Na^+ with bigger Ag^+ ions slows the RIE. That influence of the ion size looks similar to the effect of mechanical stresses, induced by replacing ions on chemical etching of glasses [3]. In air corona poling, we, contrary, introduce smaller H^+ ions into the glass instead of Na^+. Opposite sign of arising stresses in this case fastens the RIE of this sample. Also, on can notice the effect of corona poling atmosphere - replacement of air by nitrogen fastens the etching, and also the similarity in the effect of the both types of the pressed anodic electrodes.

4. Acknowledgments

The study was supported by the Ministry of Science and Higher Education of Russian Federation, project FSRM-2020-001.

5. References

[1] Reduto I, Kamenskii A, Zhurikhina V, Svirko Yu, Lipovskii A 2019 *Opt. Mater. Express* **9** 3059
[2] Dussauze M, Rodriguez V, Lipovskii A, Petrov M, Smith C, Richardson K, Cardinal T, Fargin E, Kamitsos E I 2010 *J. Phys. Chem.* C **114** 12754
[3] Talimian A, Sglavo V M 2017 *J. Non-Cryst. Solids* **456** 12

Features of the formation and properties of Al-CuO_x multilayer energetic materials for micro- and nanojoining

K I Sobolev[1], **A V Sysa**[2], **S Yu Pereverzeva**[1,2], **L I sorokina**[1], **E A Lebedev**[1,2]
[1]Institute of Advanced Materials and Technologies, National Research University of Electronic Technology, Moscow, Zelenograd, Russia
[2]Scientific-Manufacturing Complex "Technological Centre", Moscow, Zelenograd, Russia

Abstract. Development of methods for groups of components joining, including heat-sensitive devices, using local heat sources is one of the promising universal approaches to solving the problem of the reliable joint of various surfaces formation. The results of studying the features of the formation and properties of Al-CuO_x multilayer energetic materials formed by magnetron sputtering are presented in this work. The results obtained allowed \to determine the optimal composition and geometric parameters of multilayer structures from the point of view of the maximum thermal effect, wave combustion front propagation velocity and the size effect.

1. Introduction

Currently, progress in micro- and nanoelectronics is associated not only with a decrease in the topological dimensions of logic elements, but also with an increase in the level of integration. The development of technologies and methods for 3D-assemblies, systems on a chip (system-on-crystal), micro- and nanoelectromechanical systems formation will allow the transition to advanced technologies and systems. Development of joining methods for groups of heat-sensitive components using local heat sources is one of the promising universal approaches for this problem solving and formation of a reliable joint of various surfaces. Due to the growing role of low-temperature bonding processes for three-dimensional integration and packaging of microelectronic and microelectromechanical components, traditional bonding processes, such as direct thermocompression, anodic and eutectic bonding or splicing using an intermediate layer of glass become ineffective. And that is why a new approach using multilayer energetic materials acting as a local heat source is the most promising [1-4]. In this paper, we consider the features of the formation process, present the results of a study of the thermal properties and size effect in Al-CuO_x multilayer energetic materials formed by magnetron sputtering.

2. Experimental details

Al-CuO_x multilayer energetic materials were formed by the method of alternating magnetron sputtering of aluminum and copper oxide targets. The thermal properties of the formed materials were studied by differential scanning calorimetry and thermogravimetric analysis using TA Instruments SDR Q600. The thicknesses of individual layers and the total thickness of the multilayer structure, as well as the composition, were determined using a JEOL JSM-6010 scanning electron microscope with an attachment of energy dispersive X-ray spectroscopy. The propagation characteristic and velocity of the wave combustion front were determined using high-speed video recording.

3. Results

This paper presents the results of the features of a CuO_x target magnetron sputtering study. The material was sputtered in a mixture of argon and oxygen gases with different partial pressures of the components. The dependences of the ratio of Cu to oxygen in the formed films of copper oxide and their deposition rate on the partial pressure of oxygen in the process were obtained. It was found that with an increase in the oxygen content in the gas mixture, its content in the deposited films also increased, but a linear decrease in the sputtering rate of the material was observed. The results obtained made it possible to determine the optimal technological conditions for the formation of CuO_x layers.
To study the thermal and size effects, a set of experimental samples of Al-CuO_x multilayer structures with different ratios of component layer thicknesses (to determine the effect of the composition of the material on its thermal characteristics) with different values of the total thickness and thickness of the bilayer (the total thickness of one layer of aluminum and copper oxide) was formed. The study results of the formed materials by DSC and TGA methods allowed to determine the optimal composition of the energetic material from the point of view of the overall thermal effect. Using high-speed video recording, the size effect on the propagation velocity of the wave combustion front in the formed multilayer energetic materials was characterized. Figure 1 shows the storyboard of the combustion process of an experimental sample of a multilayer Al-CuO_x structure formed on the surface of a silicon substrate.

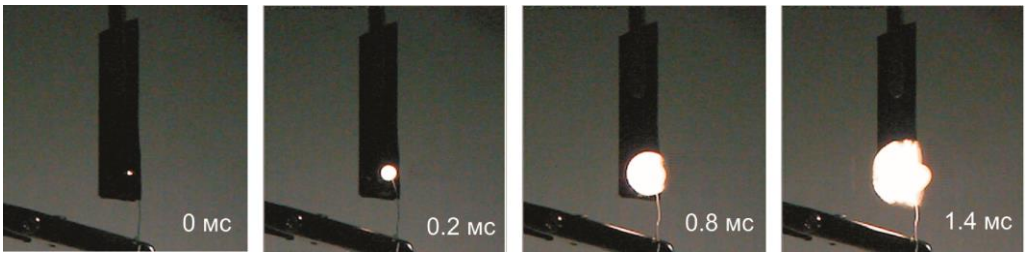

Figure 1. Storyboard of wave front propagation after initiation in multilayer energetic material Al-CuO_x.

4. Acknowledgments
This work was supported by the Russian Federation President's grant (МК-1262.2019.8).

References
[1] Wang X, Li M, Zhu W 2020 J. of Alloys and Comp. **817** 153210
[2] Zhu W, Wang X, Liu C, Zhou Z, Wu F 2019 Mater. & Design **174** 107781
[3] Maj Ł, Morgiel J, Mars K, Cios G, Tarasek A, Godlewska E 2019 Mater. Charact. **154** 31–39
[4] Sorokina L I, Lebedev E A, Trifonov A Y, Gromov D G 2019 Heliyon **5** (2) e01267

Morphology and redispersibility of silver nanoparticles prepared by chemical reduction

Lukhmyrina, M. S. Shestakov, A.V. Shvidchenko, B. A. Matveev
Ioffe Institute, Saint Petersburg 194021, Russia

Abstract. In the present work we fabricated colloidal Ag nanoparticles (NPs). NPs were synthesized by the chemical reduction method of Ag_2SO_4 using NaBH4 in presence different surfactants. Morphological properties of synthesized colloidal Ag-NPs were studied by ultraviolet-visible (UV-vis) spectroscopy and dynamic light scattering (DLS). Average NP size varied in the range from 3 to 16 nm. Redispersibility of dried NPs with various stabilizers was also investigated.

1. Introduction

Metal nanoparticles (NPs) demonstrate unique physicochemical properties arising from nanoscale dimension and high surface to volume ratio [1]. This opens path for a wide range of promising NPs applications in the diverse fields of photonics, nanoelectronics, sensing, imaging, information storage and medicine [1, 2]. In particular, contact conductive layers formation in microelectronic devices by using sintered NPs is of great interest due to high conductivity and thermal stability [3]. Low NP melting temperature T_m is crucial in this case. It was shown that due to increased surface-to-volume ratio, the lower the NP size, the lower is T_m [4, 5].

The exciting application potential of NPs has resulted in a plenty of experimental recipes for their synthesis either in water or in nonpolar organic solvents. The common methods are laser ablation, electron irradiation, biological synthetic and chemical reduction by $NaBH_4$, polyol, tannic acid etc. Among them, chemical methods are the most expedient and cost-effective [6]. In most cases, Ag NPs were stabilized by surfactants, polymeric stabilizers, or amphiphilic block copolymers [7]. Despite such a huge variety of synthesis techniques, most of them are experienced problems with stability and aggregation of NPs, control of morphology, size and size distribution.

In this work, we study the influence of surfactants on the morphological properties of the Ag NPs and the impact of polymeric stabilizers on NP redispersibility.

2. Experimental Details

As a silver precursor we used Ag_2SO_4. $NaBH_4$ was used as a reducing agent for the reduction of silver ions to Ag atoms. As surfactants of Ag NPs were used sodium dodecyl sulfate (SDS) and sodium bis(2-ethylhexyl)-sulfosuccinate (AOT), and as stabilizers were used cycloxecane, glycerol and fish oil. In each case Ag NPs were synthesized by slow addition solution of $NaBH_4$ to Ag_2SO_4 solution in presence of different surfactants. All reactions were carried out at room temperature and maintained for 24 hours.

The optical absorption spectra of the NPs colloid in the UV and visible ranges were recorded using a UNICO SpectroQuest UV-2800 spectrophotometer (quartz cuvette; optical path length – 10 mm). The particle size distribution of Ag NPs was obtained at a Zetasizer Nano ZS (Malvern Instruments, UK) by DLS technique.

3. Results and discussion

Colloids diluted with distilled water until concentration 5 mg per liter were characterized via UV-vis spectroscopy and DLS (see figure 1). NPs average size in the colloid with AOT surfactant (1 in Fig.1) turned out to be 15 nm, particle aggregation also was obtained. In the next colloid surfactant SDS was added to the solution of $NaBH_4$. In this case (2 in Fig.1) average size of Ag NPs was found to be 5 nm. In another colloid SDS was added to the solution of Ag_2SO_4, which led to reduction average particle size (3 in Fig.1) to 3 nm.

After that four colloids were synthesized by the third recipe with various stabilizers. Ag NPs were dried and their redispersibility was studied.

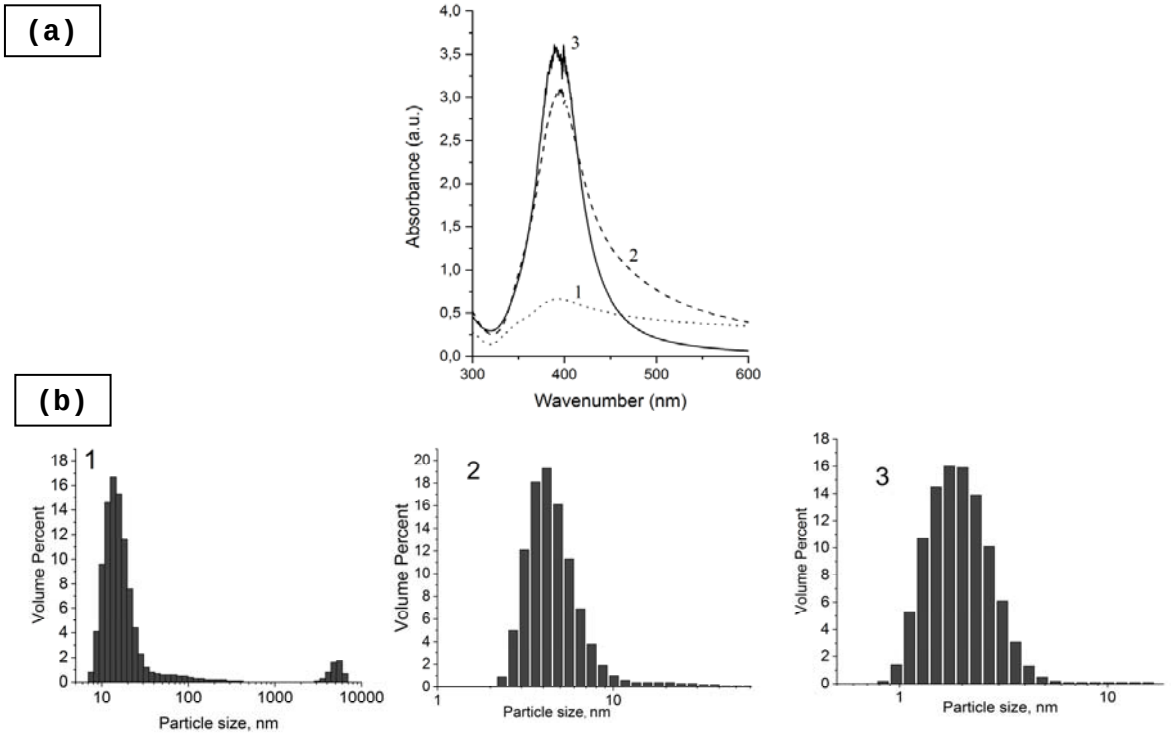

Figure 1(a, b). (a) The UV-vis absorption spectra of the Ag NPs colloids synthesized in presence of the different surfactants. Dot line: AOT was added to the solution of Ag_2SO_4; dash line: SDS was added to the solution of $NaBH_4$; solid line: SDS was added to the solution of Ag_2SO_4. **(b)** Size distribution of nanoparticles obtained using DLS; the numbers correspond to specified earlier

References

[1] S. K. Das and E. Marcili 2011 *Nanotechnology and Nanomaterials* **11** 253
[2] Ahmad, T. 2014 *Journal of Nanotechnology* ***2014***
[3] Tan Y., Li X., Chen X., Yang Z., and Lu G. Q. 2019 *Soldering & Surface Mount Technology*
[4] Darroudi M., Ahmad M. B., Zamiri R., Zak A. K., Abdullah A. H., and Ibrahim N. A. 2011 *International journal of nanomedicine* ***6*** 677
[5] P. Buffat and J.-P. Borel 1976 *Phys. Rev. A* **13** 2287
[6] S. Iravani, H. Korbekandi, S. V. Mirmohammadi, and B. Zolfaghari 2014 *Research in pharmaceutical sciences 9*(**6**) 385
[7] Kim N. H., Kim J. Y., Ihn K. J. 2007 *Journal of nanoscience and nanotechnology* **7(11)** 3805.

Development and research of a technology for producing a low-dimensional porous platinum-based catalyst by thermal evaporation in vacuum on an ion-exchange polymer membrane of a hydrogen generator electrolytic cell

A V Fimin[1], **S A Nesterov**[1], **S A Gurin**[2], **S A Shelokhaev**[1], **E A Pecherskaya**[1]
[1]Polytechnic Institute, Penza State University, Penza 440026, Russia
[2]CJSC Medtekhnika, Penza 440018, Russia

Abstract. The use of hydrogen structures as a universal energy carrier led to its application in various fields of industry. Currently used production methodologies make it possible to produce systems with high reliability and a long service life. However, at the moment, the creation of such structures is limited by the lack of natural origin materials necessary for the production of such structures, which leads to the search for alternative and most universal manufacturing methods against the background of increasing needs.

1. Introduction

Particular interest in the hydrogen energy development is based on the wide possibilities of energy storage, highly efficient production of chemical compounds based on pure hydrogen, the ecological situation improvement , as well as limited reserves of organic resources [1]. Under such conditions, multifunctional electrolytic cells of a hydrogen generator are capable of fulfilling the assigned tasks in electric energy storage systems, microelectronics and recovery [2]. In this paper, we consider a phased technology for the manufacture of such assemblies using completely different from the traditional methods of structure growth, as well as an analysis of the created structures that are not inferior in their characteristics to existing analogues.

2. Modeling

One of the most important aspects of platinum deposition technology on an ion-exchange polymer membrane using the thermal vacuum method is surface preparation, which cleans the membrane surface from various organic and inorganic contaminants, as well as surface modification to increase the adhesive and adsorption activity of the surface relative to the coating [3], [4].
To minimize the thermal effects of the evaporation process, a special volume holder of ion-exchange membranes was developed and manufactured with the aim of more heat removal from the substrates. Additionally, to avoid overheating, the deposition was carried out on a rotating tooling in order to remove the membrane from the zone of constant deposition. As a heating element, a tungsten evaporator, consisting of several wires stacked in a row with copper tips was used.
As a weighed sample, approximately 500 mg of 99.9% pure platinum, which was placed on an evaporator preliminarily annealed by a spraying method without a sample, was used. The equipment rotation began when the pressure in the chamber reached the values (3-5) 10^{-6} mm Hg and a gradual increase in current to values of 430-450 A. The shutter was opened after the sample was melted. To prevent platinum spraying, the evaporator current was reduced by 10-15 A. The deposition duration was about 5-7 minutes.
Because of the remnants of platinum material on the evaporator, leading to current shunting, the second side was sprayed in the same way, except for a peak current value of 500 A. The duration of spraying on the second side was 8-10 minutes.

After spraying, ion-exchange membranes were given for visual inspection, control of surface resistance and electrical insulation. The surface resistance of the active catalyst layer (ACL) on the membrane ranged from 20 to 50 MOmh. Insulation resistance showed more than 100 GOmh.
Figure 1 shows the Images of the two sides of the ion-exchange membranes with ACL performed on an optical microscope at fifty times increase. In the obtained structures, the “cellular” structure of the ion-exchange membrane with platinum islands without the presence of thermal damage is clearly traced.

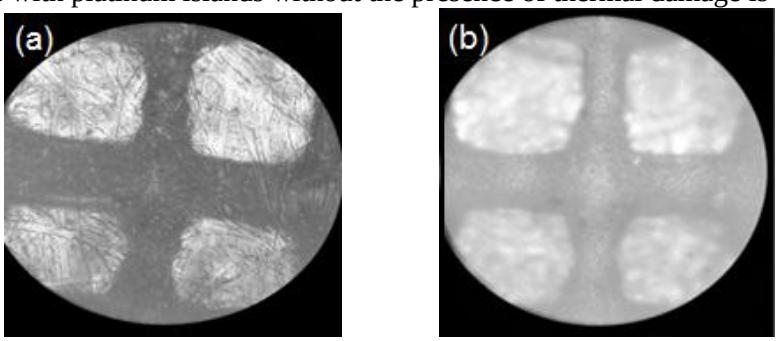

Figure 1(a, b). **(a)** image of the front side of the membrane; **(b)** image of the back side of the membrane.

An increase in the ion-exchange membrane with a nanostructured ACL layer obtained by thermal evaporation in vacuum, using SEM indicates a clearly traceable porous ("island") structure of the catalytic coating, which is the activation centers for subsequent electrochemical deposition at the three-phase boundary.
The total accumulated spectrum using X-ray energy dispersive SEM analysis is shown in Figure 2.

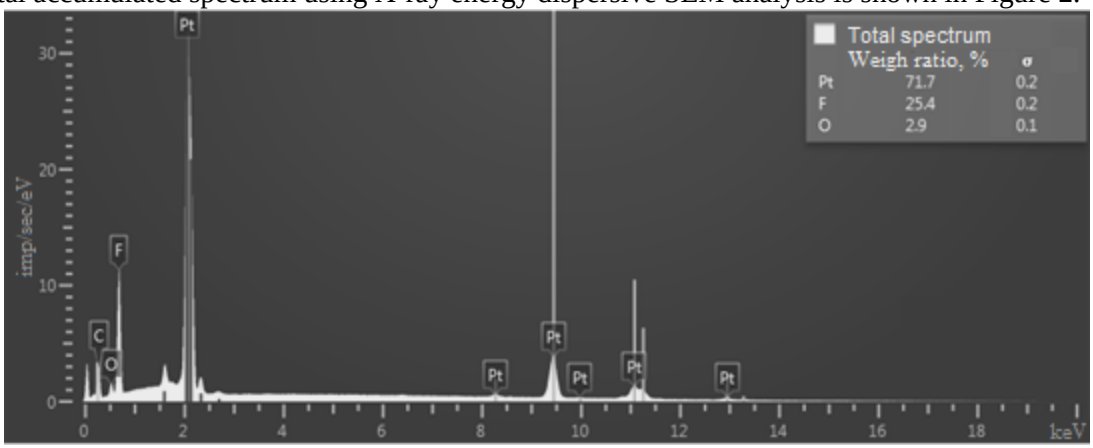

Figure 2. X-ray energy dispersive analysis of the ion-exchange membrane with ACL obtained by thermal evaporation in vacuum.

3. Conclusion

According to the obtained total spectrum of X-ray energy dispersive analysis, shown in Figure 2, pronounced peaks of platinum of the active catalyst layer, as well as fluorine ion exchange membrane with a minimum amount of impurities are visible. Therefore, we can conclude that the catalytic nanostructured coating did not completely cover the membrane structure and fully preserved the characteristics and functions performed by it. In this case, the simulation results confirm the technical feasibility of manufacturing prototypes of such structures.

References

[1] Pecherskaya E A, Zinchenko T O, Golubkov P E, Pechersky A V, Fimin A V, Nikolaev K O 2018 *Moscow Workshop on Electronic and Networking Technologies (MWENT)* 1 - 4
[2] Tsukada K, Takeichi S, Sakai K, Kiwa T 2014 *Japanese Journal of Applied Physics* **53** (7)
[3] Gurin S A, Pecherskaya E A, Fimin A B, Nikolaev K O, Artamonov D V, Shepeleva Y V 2019 *Journal of Physics: Conference Series* **1410** 012021
[4] Oigawa H, Ikezawa S, Ueda 2016 *TIEEJ Transactions on Sensors and Micromachines* **136**(12) 511

Analysis of a nanometer catalyst layer using various methods of spraying an active catalytic coating of an ion-exchange polymer membrane embedded in an electrolytic hydrogen cell

S A Gurin[1], **E A Pecherskaya**[2], **S A Nesterov**[2], **D A Shelakhaev**[2], **A V Fimin**[2]
[1]CJSC Medtekhnika, Penza 440018, Russia
[2] Polytechnic Institute, Penza State University, Penza 440026, Russia

Abstract. Today, the industrial production of hydrogen by traditional methods (high-temperature conversion of hydrocarbons, steam-water conversion of natural gas) against the background of a reduction in natural resources does not allow achieving the necessary purity of the produced gas and imposes serious economic and environmental restrictions. As a result, the solution of the task of developing technologies providing the improvement, high specific and operational characteristics of new methods for producing hydrogen is extremely urgent.

1. Introduction

Progress in various fields of energy, chemical, electronic, medical, pharmaceutical and other areas of industry has led to the widespread use of hydrogen in systems where it serves as an energy carrier [1]. Particular interest in the development of hydrogen energy is based on the wide possibilities of energy storage, highly efficient production of chemical compounds based on pure hydrogen, the ecological situation improvement , as well as limited reserves of organic resources [2]. This paper presents an analysis of existing technologies for obtaining such structures and identifies their operational shortcomings, as well as provides a cost-effective and technologically optimal method for their production.

2. Modeling

The main functional characteristics of the membranes according to the stated requirements require comprehensive modernization not only in their production process, but also during testing directly in flow reactors. However, despite all the numerous requirements for membranes, the intensity of degradation processes in them is often determined by the quality of the active catalyst layers (ACL) coating [3].
1. One of the first methods for the ACL formation was the use of a phosphoric acid electrolyte with an impregnation procedure that expanded the region of the three-phase boundary of already sintered active electrode layers, which did not fully ensure the structure uniformity and did not allow efficient use of the platinum introduced into the active layers.
2. The use of Nafion film as a binder of thin-film technology, as well as an upgraded method using a colloidal design, increased the platinum use efficiency. However, the “clogging" of the membrane pores due to the large thickness of the deposited layer, the heterogeneity of the coating, which does not allow activation of the entire membrane area, the complexity of the process preparation and the purity of the reagents involved in the process, did not allow the full use of this technology.
3. The ACL production is possible by vacuum deposition, as well as the deposition of organometallic precursors from solutions in supercritical media, followed by the precursor conversion to metal (MOCVD) and the direct current magnetron sputtering method of ultrapure platinum targets in an inert argon working gas. Such application methods provide a high degree of homogeneity, as a result, platinum loading is significantly reduces without loss of productivity, improving the adhesion of the active catalyst layer to the polymer electrolyte and the purity of the process [1, 4].

4. One of the most promising methods for ACL producing is electrochemical (galvanic) metal deposition. In subsequent work of OIE the catalyst efficiency also remains high, which reduces the loading of platinum; however, the structures fabricated by this method had an unsatisfactory adhesion degree to the surface, which is a critical factor when applied to movable flexible substrates [5].
The palladium-based ACL structures did not meet the required characteristics, the “cell” structure of the ion-exchange membrane was absent and completely “overgrown” and when they were built into the electrolytic hydrogen cell were inoperative. The accumulated spectrum shown in Fig. 1, obtained by X-ray energy dispersive SEM analysis, also did not show the presence of ion-exchange membrane materials, in which only palladium and technological materials are observed.

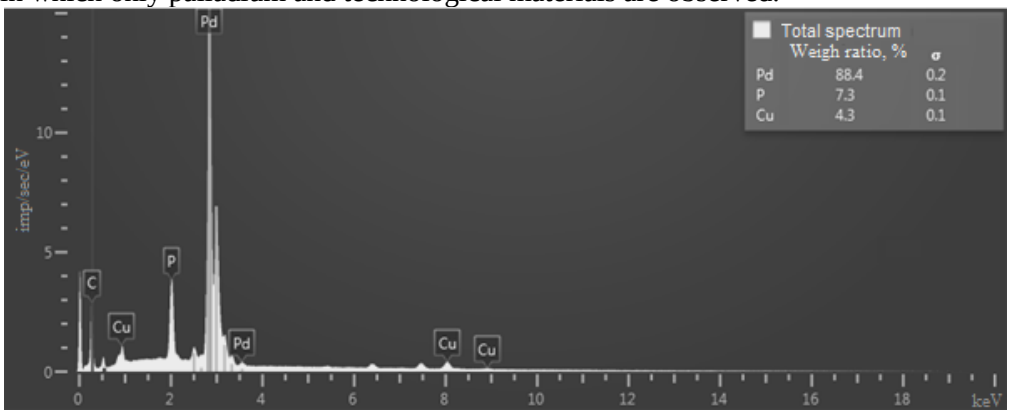

Figure 1. X-ray energy dispersive analysis of an ion-exchange membrane with ACL based on palladium.

5. Works on obtaining a high-quality structure using a nanostructured coating only due to thermal vacuum evaporation also did not lead to positive results. To the changed properties on the membrane due to thermal damage, clogging of the pores by the catalyst material was detected, which led to an ionic conductivity violation through the membrane. Sprayed by this technology with pronounced thermal damage, the ion-exchange polymer membrane is shown in Figure 2.

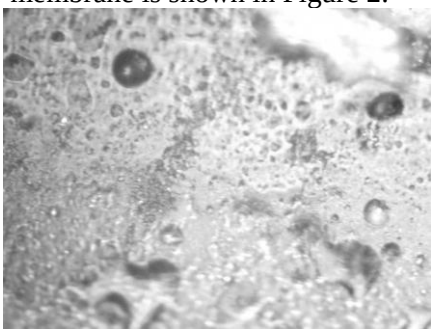

Figure 2. Image of an ion-exchange polymer membrane with ACL.

3. Conclusion

As a result of the analysis, the most technologically advanced and economically feasible method for producing an active catalytic coating of an ion-exchange polymer membrane embedded in a hydrogen electrolytic cell in hydrogenation flow reactors, consisting in a combined method of thermal evaporation in vacuum, creating a nanostructured activation surface with high adhesion for subsequent electrochemical deposition is presented.

References

[1] Gac W, Borowiecki T, Kowalik P 2017 *Nanotechnology in catalysis* 401-420
[2] Meille V2006 *Applied Catalysis A-general* **315**, 1-17
[3] Tsukada K, Takeichi S, Sakai K, Kiwa T 2014 *Japanese Journal of Applied Physics* **53**(7)
[4] Hochepied, F 2017 *Nanotechnology in catalysis* 1-20
[5] Gurin S A, Pecherskaya E A, Fimin A B, Nikolaev K O, Artamonov D V, Shepeleva Y V 2019 *Journal of Physics: Conference Series* **1410**

Fabrication of $NbN/Si_3N_4/SiO_2$ membrane structures for study of heat conductance at low temperatures

N.A. Titova, E.M. Baeva, A.I. Kardakova, G.N. Goltsman[1]
Laboratory of quantum detectors, Moscow State Pedagogical University, Moscow 119435, Russia
National Research University Higher School of Economics, Moscow 101000, Russia

Abstract. Being in the regime of a strong electron-phonon coupling at cryogenic temperatures, thin NbN films are good candidates for study phonon contribution to thermal transport at low temperatures. In the regime of strong electron-phonon coupling and a negligible leakage of phonons to substrate, one can assume that the phononic and electronic baths are in local equilibrium. In such case, the phononic contribution to the heat conduction can be non-negligible or even dominate. Here, we report on the fabrication of $NbN/Si_3N_4/SiO_2$ membranes for investigation of the phonon contribution to thermal transport at low temperatures.

1. Introduction

Thermal transport in nanoscale structures plays a key role in various electronic devices operating at cryogenic temperatures [1]. In case of superconducting quantum sensors, based on ultrathin metals films, the thermal properties are related with the film parameters, which govern the processes of energy conversion and the nonequilibrium kinetics of charge carriers. These parameters determine the efficiency and response speed in the detectors [2-6].

The interesting and important objects for studying thermal transport at low temperatures are ultrathin superconducting films characterized by the strong electron-phonon coupling, such as NbN films [7]. In this limit, considering also a negligible leakage of phonons to substrate, one can actually assume that the phononic and electronic baths are in local equilibrium. In such case, the phononic contribution to the heat conduction can be non-negligible or even dominate. Here, we report on the fabrication of $NbN/Si_3N_4/SiO_2$ membrane structures to study the role of the phononic heat conductance in thermal transport.

2. Fabrication methods

To fabricate suspended samples, a 5-nm thick NbN film was deposited onto a GaAs substrate with thermally grown layers of silicon dioxide (SiO_2 with a thickness of 500 nm) and silicon nitride (Si_3N_4 with a thickness of 200 nm). The total thickness of the membrane is 700 nm.

The fabrication procedure includes the following steps: (1) the deposition of NbN film, (2) the formation of the golden pads, (3) the fabrication of the etching mask, and (4) the suspension of $NbN/Si_3N_4/SiO_2$ membrane. Below, we describe these steps in more details.

The NbN film was deposited by DC magnetron sputtering on a multilayer substrate ($Si_3N_4/SiO_2/GaAs$) at temperature 250 C in the mixture of Ar and N_2 gases. The preliminary pressure background in the chamber was $1.2 \cdot 10^{-7}$ Torr, the deposition rate is about 0.7 A/s. The thickness of the deposited NbN film was about 5.6 nm, and the square resistance (Rs) was in the range of 576-580 Ohm/sq. The Ti-Au metal pads were fabricated with the lift-off process using laser lithography and thermal evaporation. The thicknesses of Ti and Au metal layers were 5 nm and 200 nm, correspondingly. The next step, the fabrication of the etching mask, was also performed with the laser lithography using two layers of Az1512 as the mask. The last step was the formation of suspended bridges with etching of NbN and partially Si3N4 in plasma chemistry, then the etching of Si3N4 and SiO2 layers in a solution of hydrofluoric acid and the final etching of GaAs in the solution of hydrogen peroxide, ammonia, and water. The patterned samples are presented in Figure 1.

As the next step in this study, we are going to investigate the thermal transport in these structures using the noise thermometry [8]. To verify our assumption of an efficient of phonon heat conductance to the contacts, we are planning to examine samples of different lengths.

3. Figures

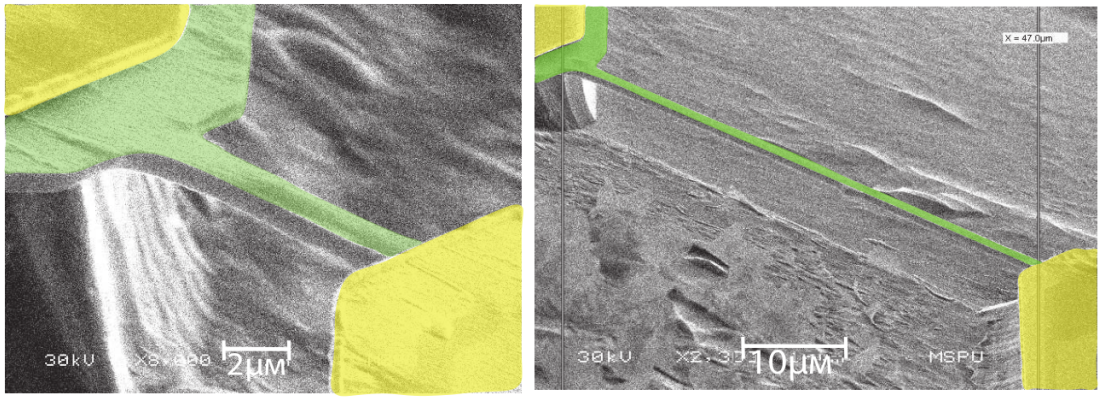

Figure 1. A false-color image of suspended NbN bridges on SiO_2/Si_3N_4 membrane obtained with a scanning electron microscope. The 5-nm thick NbN bridge is shown with green color, the golden pads are shown with yellow. Left and right figures demonstrate the samples of different length.

4. Acknowledgments

Authors wishing to acknowledge the RSF project 19-32-80037 for sample fabrication. The authors also thank V. Khrapai for useful discussion of this work.

References

[1] Giazotto F, Heikkila T, Luukanen A., Savin A.M, Pekola J.P 2006 *Rev. of Modern Phys*ics **78** 217

[2] Wei J, Olaya D, Karasik B, Pereverzev S, Sergeev A, and Gershenson M 2008 *Nature Nanotech.* **3** 496

[3] Leduc H.G, Bumble B, Day P.K, Eom B.H, Gao J, Golwala S, Mazin B.A, McHugh S, Merrill A, Moore D.C, Noroozian O, Turner A.D, Zmuidzinas J 2010 *Appl. Phys. Lett.* **97** 102509

[4] Marsili F, Stevens M.J, Kozorezov A, Verma V.B, Lambert C, Stern J.A, Horansky R.D, Dyer S, Duff S, Pappas D.P, Lita A.E, Shaw M.D, Mirin R.P, and Nam S.W 2016 *Phys. Rev. B* **93** 094518

[5] Sidorova M, Semenov A, Korneev A, Chulkova G, Korneeva Yu, Mikhailov M, Devizenko A, Kozorezov A, Goltsman G 2018 *Phys. Rev. B* **97** 184512

[6] Vodolazov D. Yu 2017 *Phys. Rev. Applied* **7**, 034014

[7] Baeva E.M, Sidorova M.V, Korneev A.A, Smirnov K.V, Divochy A.V, Morozov P.V, Zolotov P.I, Vakhtomin Yu.B, Semenov A.V, Klapwijk T.M, Khrapai V.S, Goltsman G.N 2018 *Phys. Rev. Applied* **10**, 064063

[8] Roukes M. L., Freeman M. R, Germain R. S, Richardson R. C, and Ketchen M. B, 1985 *Phys. Rev. Lett.* **55** 422

Improving the mechanical resistance of the glass surface for optoelectronic devices by electron beam processing

S P Avdeev, E Yu Gusev, D A Ryabova
Southern Federal University, Institute of Nanotechnology, Electronics and Equipment Engineering, Taganrog 347922, Russia
savdeev@sfedu.ru

Abstract. The paper considers the issues of hardening the surface of phosphate glasses for optoelectronic devices. The effect of electron-beam processing on the physical-mechanical properties of the glass surface is investigated. It was found that the processing of phosphate glass "SZS23" increases the surface microhardness by 24% owing to removing the damaged layer and changing the elemental composition of the glass surface.

1. Introduction

In this paper, colored optical glass "SZS23" is considered, one of its promising application is the optical system for spectral filtering of orientation objects radiation in static devices [1]. It is known that the optical sensitivity of the device is directly related to the state of the surface of zinc-phosphate glass, since the glass material is considered soft [1,2]. Electron beam modification of the surface of optical glass can increase the hardness of the glass surface, so in general, the device acquires resistance to aggressive atmosphere.

2. Experimental details

Mechanically ground and polished glass of the metaphosphate group – "SZS23" type were cut into samples of 11×6×3 mm. Before processing, the samples were degreased in a soap solution and distilled water for 15-20 minutes, than were dried by centrifugation.

Electron beam processing was carried out in the high vacuum system described in [3]. Electron gun was used to form a low-energy electron beam with a current density of 50-100 mA/cm^2. Processed samples were slowly cooled (less than 1°C/min) and kept in vacuum (10^{-3} Pa) until room temperature.

Physical-mechanical properties (hardness, elasticity, recovery coefficient and ultimate load) of initial and processed glass surfaces were studied by nanoindentation using a nanosclerometric probe module with a trihedral Berkovich diamond indenter.

3. Results

The surface hardness of the processed glass samples are presented in table 1.

Table 1. Hardness (H) and elasticity (E) values of the electron beam processed surface of zinc-phosphate ("SZS-23") glass samples.

#	1	2	3	4	5	6	7	8	9	10
H, GPa	7.4	7.4	7.2	7.3	7.4	7.0	7.1	7.1	7.6	7.1
E, GPa	80.5	96	98	92.3	96.8	83.1	82.9	88.0	99.9	111.3

It is known from the authors' works [4,5] that double aluminophosphate glass, which is close in composition to aluminum metaphosphate, has the highest values of elastic modulus and hardness of 5.7 GPa, and zinc-aluminophosphate glass has the maximum value of structural strength. This assumption is explained by the fact that, in zinc-aluminophosphate glass, along with chain structures, three-dimensional sewn structures can also exist due to the incorporation of zinc ions into the anion network in tetrahedral coordination.

It was experimentally found that owing to electron beam processing, the microhardness of the glass surface increases by 24%. Based on the obtained results, it can be assumed that aluminum metaphosphate or three-dimensional sewn structures appear on the surface, e.g. zinc-potassium polyphosphate $KZn_4(PO_4)_3$, which will contribute to the strengthening of the surface layer [1,5].

4. Conclusion

Electron beam processing is accompanied by a modification of the surface of the optical details in the form of removing the damaged layer and changing the phase composition of the surface layer. Structural transformations in the surface layer contributed to a change in its mechanical properties. In addition to changing the surface morphology in the modified layer, an increase in its tribomechanical characteristics was observed.

Acknowledgment

This work was financially supported by Southern Federal University. The equipment of the Research and Education Center "Nanotechnologies" of Southern Federal University was used for the study.

References

[1] Pukh V P, Baikova L G, Kireenko M F et al. 2005 *Phys. Solid State* 47 876-881

[2] Grabco D Z, Shikimaka O A, Elisa M et al. 2012 *Surf. Engin. Appl. Electrochem.* 48 365-374

[3] Ageev O A, Konoplev B G 2019 *Nanotechnology in microelectronics* (Moscow: Nauka) 511

[4] Avdeev S P, Gusev E Yu 2019 *Proc. of SPIE* 11022 11022-69

[5] Avdeev S P, Mileshko L P, Garanga S N 2019 *Journal of Surface Investigation: X-ray, Synchrotron and Neutron Techniques* 2019 13(3) 456-457

The influence of the piezoelectric response of carbon nanotubes on their memristive properties

M V Il'ina[1], A V Guryanov[1], O I Osotova[1], O I Il'in[1], N N Rudyk[1] and O A Ageev[2]
[1]Southern Federal University, Institute of Nanotechnologies, Electronics and Electronic Equipment Engineering, Taganrog, 347922, Russia
[2]Southern Federal University, REC "Nanotechnologies", 347922, Taganrog, Russia

Abstract. The results of experimental studies of the piezoelectric response of aligned carbon nanotubes (CNT) with different geometric parameters are presented. It is shown that the magnitude of the piezoelectric response increases with decreasing diameter and length of the CNT. It is established that CNT memristive properties improve with an increase of piezoelectric response. The results can be used in the development and creation of energy-efficient storage devices and nanogenerators.

1. Introduction

The anomaly manifestation of the piezoelectric properties of multi-wall carbon nanotubes (CNT) opens up wide prospects for creating energy-efficient memory devices and nanogenerators based on them [1-5]. However, the laws of manifestation of the piezoelectric properties of CNT have not yet been established, which requires further research in this direction. The aim of this work is to study the influence of the piezoelectric response of carbon nanotubes on their memristive properties.

2. Experimental studies

The experimental samples were arrays of aligned carbon nanotubes grown by plasma-chemical vapor deposition using NANOFAB NTC-9 (NT-MDT, Russia). The parameters of the nanotubes were determined using a Nova Nanolab 600 scanning electron microscope (SEM). The average heights of CNTs ranged from 8.6 to 24.1 μm. The average diameters of CNT ranged from 44 to 63 nm. The SEM images are shown in Figure 1.

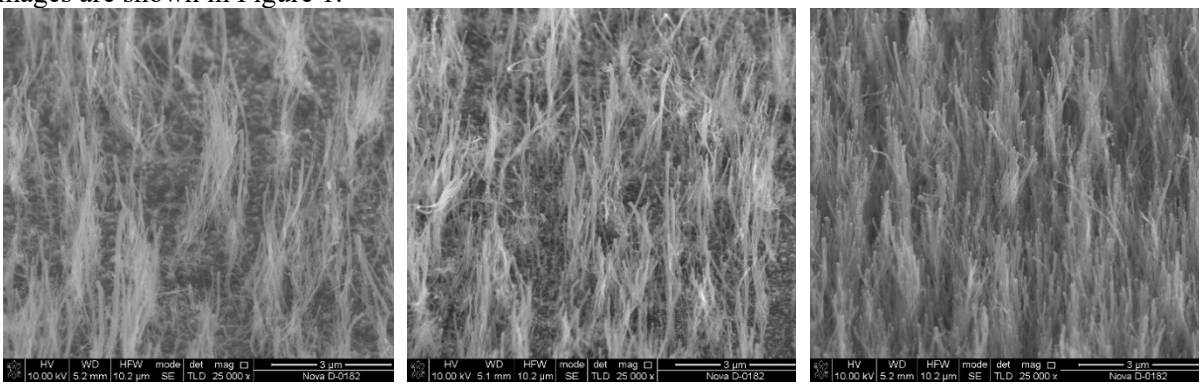

Figure 1. SEM images of experimental samples of CNT arrays.

The experimental studies of the piezoelectric and memristive properties were carried out by atomic force microscopy (AFM) using Ntegra probe nanolaboratory (NT-MDT, Russia). The magnitude of the piezoelectric response of CNT was determined based on a previously developed technique using the AFM force spectroscopy method [2]. The memristive properties of CNT were evaluated by the ratio of the resistance of CNT in high- and low-resistance states (R_{HR}/R_{LR}) obtained from current-voltage characteristics (CVC). A HA_NC/Pt cantilever with a force constant of 12 N/m was used as an AFM probe. The obtained dependences of the resistance ratio R_{HR}/R_{LR} on the value of the piezoelectric response of carbon nanotubes are presented in Figure 2.

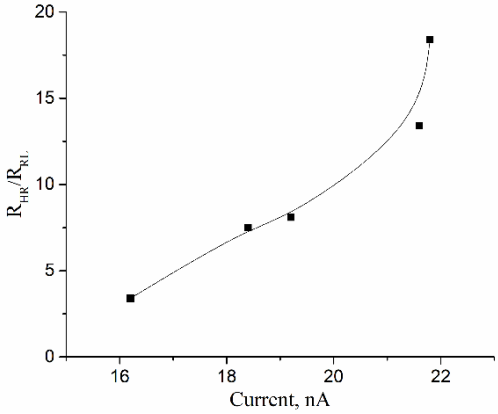

Figure 2. Dependence of the high- and low-resistance states ratio of CNT on the piezoelectric response value.

4. Results

Analysis of the results showed that all experimental samples showed a piezoelectric response of 16 to 22 nA with an applied external force of 3.6 μN. In this case, the piezoelectric response of CNT decreased with increasing height and diameter of nanotubes. Studies of the memristive properties of experimental samples showed that the resistance ratio R_{HR}/R_{LR} increased from 3 to 18 with an increase in the piezoelectric response of CNT from 16 to 22 nA, respectively. This dependence is associated with an increase the CNT internal field determined by the magnitude of the piezoelectric properties. As a result, an increase the resistance of CNT in a high-resistance state is observed. This leads to an increase in the area of the hysteresis loop of the CVC of the CNT and an increase in the R_{HR} / R_{LR} value.

Thus, it is shown that CNT memristive properties improve with increasing piezoelectric response value. This dependence is fully consistent with the previously proposed memristive switching mechanism of a strained CNT [4]. The obtained results can be used to develop the nanopiezotronics devices based on vertically aligned carbon nanotubes. The results were obtained using the equipment of the Research and Education Center and Center of Common Using “Nanotechnologies" of Southern Federal University.

5. Acknowledgments

The reported study was funded by RFBR according to the research projects No. 20-37-70034.

[1] Hu Y. and Wang Z.L. 2014 *Nano Energy* **14**, 3–14
[2] Il’ina M.V, Il'in O.I., Blinov Yu.F., Konshin. A.A., Konoplev B.G. and Ageev O.A. 2018 *Materials* **11**, 638
[3] Il’ina M.V, Konshin. A.A., Solomin E.G. 2018 *IOP Conf. Series: Journal of Physics: Conf. Series* **1124**, 071010
[4] Il’ina M.V, Il'in O.I., Blinov Yu.F., Smirnov V.A., Kolomiytsev A.S., Fedotov A.A., Konoplev B.G. and Ageev O.A.. 2017 *Carbon* **123**, 514–524
[5] Avdeev S.P., Avilov V.I. Ageev V.O. et al. Nanotechnology in microelectronics. Eds. O.A. Ageev, B.G. Konoplev. M.: Nauka, 2019. 511 p.

Characteristics of an all-solid-state lithium-ion battery prototype

I S Fedorov, L A Mazaletskiy, A A Mironenko, V V Naumov, A S Rudy, J S Tortseva

Department of Nanotechnologies in Electronics, Yaroslavl State University, Sovetskaya Street 14, Yaroslavl 150003, Russia
E-mail: rudy@uniyar.ac.ru

Abstract. The results of the study of the charge-discharge characteristics and impedance of a solid-state lithium-ion battery of the electrochemical system LiV_2O_5-LiPON-(Si-O-Al) are presented. It is shown that the features of the charge-discharge curevs are associated with a change in the Fermi level of electrode materials due to a change in the lithium concentration. The results of impedance spectroscopy in the ranges of high, medium and low frequencies are presented and equivalent circuits are proposed.

The prototypes of an all-solid-state lithium-ion batteries (SSLIB), composed of the following functional layers: anode (Si-O-Al) - 1 μm; solid electrolyte (LiPON) - 1 μm; cathode (LiV_2O_5) 0.6 μm; current collector (Cu) 0.8 μm, were manufactured by vacuum magnetron deposition [1-3]. To encapsulate the entire structure, S1813SP15 photoresist was used. SSLIB prototypes were tested in galvanostatic regime using an Elins P 20x8 multi-channel potentiostat. The tests consisted of several series of charge-discharge cycles. In each series of cycles, the value of the potential window remained constant, and increased from series to series with a step of 0.5 V. Thus, in the range from 3 to 5 V, five series of tests were performed, 25 cycles each. An example of charge-discharge curves is shown in Fig. 1.

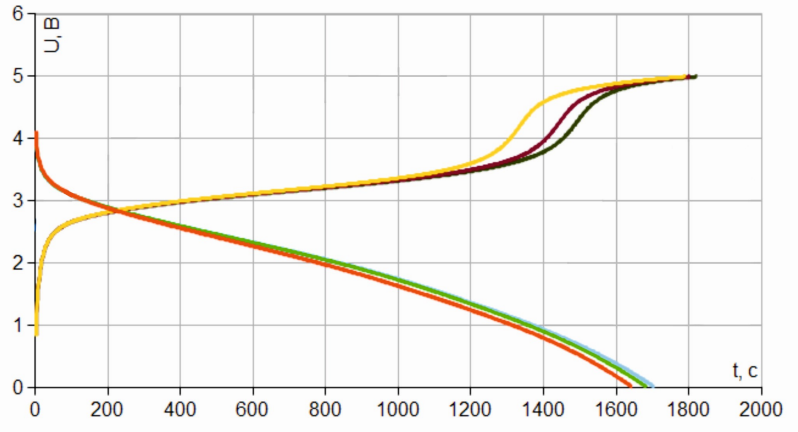

Figure 1 – The SSLIBs' charge-discharge curves - cycles number 115 – 118. The steps on the charge curves are associated with a change in the Fermi level and the formation of a Schottky barrier at the interface Si-O-Al/current collector during lithiation of the anode

Basing on the above data, it was concluded that the maximum discharge capacity of the prototypes corresponds to a voltage window of 0-5 V and a discharge-charge current of 100 μA. The specific capacity, calculated from the discharge curves, amounts to 5.56 mA·h/cm^2 and 6.54 μA·h/mm^3. Here, when calculating the volumic specific capacity, the thickness of the titanium foil was assumed to be 5 μm (half of the actual thickness), because in industrial version of battery layers are deposited on both sides of the foil.

Figure 2 shows the Nyquist diagrams for the region of high (1 - 500 kHz) and low (10 mHz - 1 Hz) frequencies. In red is shown a direct (i.e. increasing in frequency) branch of an impedance hodograph, while the reverse one (a decrease in frequency) is shown in blue. High frequencies are characterized by a low-resistance arc (R - up to 200 Ohms, C - tens of microfarads, degree of ideality > 0.9), which describes the RC section of the circuit, with an indent from the origin by 3-5 Ohms, which is usually attributed to the resistance of current collectors.

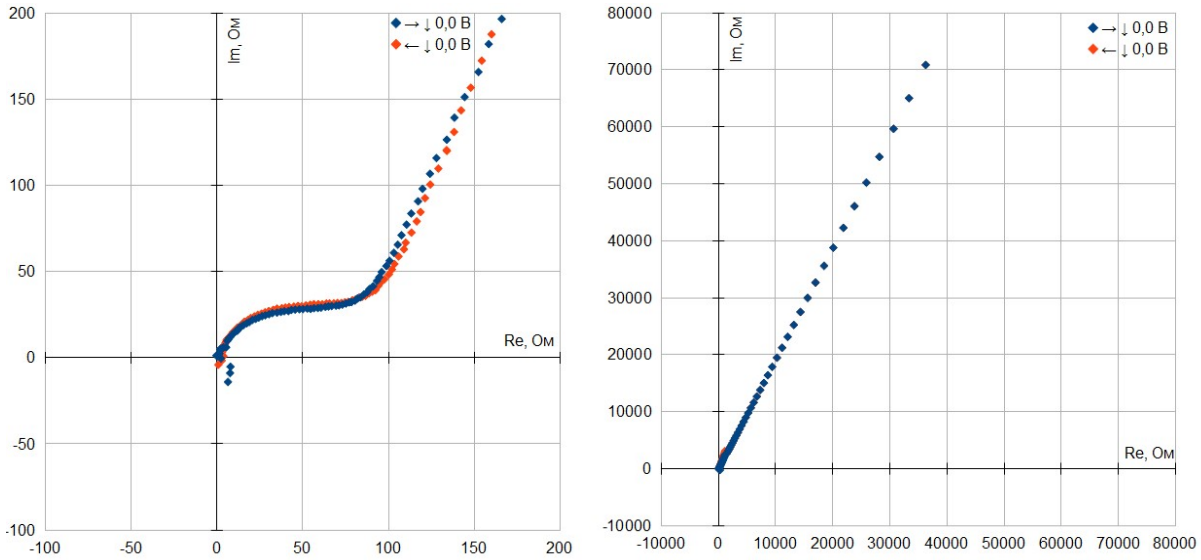

Figure 2 – Nyquist diagrams of SSLIB's impedance in the range of low (left graph) and high (right graph) frequencies

At low frequencies, the impedance hodograph is almost a straight line well approximated by the constant phase element $\hat{Z}_{CPE} = A(j\omega)^{-\alpha}$ at $\alpha = 0.7$, what corresponds to the intermediate state of the impedance between the capacity and the Warburg element.

Acknowledgments

The measurements were carried out on the equipment of Facilities Sharing Centre “Diagnostics of Micro- and Nanostructures”.

Funding

The study was financially supported by the Ministry of Science and Higher Education of the Russian Federation, subsidy agreement no. 05.604.21.0230, unique project identifier RFMEFI60419X0230.

References

[1] Kulova T L *et al.* 2016 *Int. J. Electrochem. Sci.* **11** 1370 –1381.
[2] Vasil’ev S V *et al.* 2016 *Russian Microelectronics* **45** 335–344.
[3] Rudy A S *et al. Technical Physics Letters* 2020 **46** 217–221.

The effect of low-energy ion bombardment on residual stress in thin metal films due to the generation of surface defects and their migration to the grain boundary

A S Babushkin
Laboratory of micro- and nanosystem technology, Valiev Institute of Physics and Technology of Russian Academy of Sciences, Yaroslavl Branch, Yaroslavl, 150007, Russia

Abstract. A kinetic model that describes the evolution of residual stress in thin polycrystalline films during bombardment by ions with energies below the sputtering threshold is presented. The mechanisms responsible for the change in stress are the generation of point defects on the surface and their redistribution over the film thickness along grain boundaries. The presented model was used to explain the previously obtained experimental data on the change in stress of thin Cr films after ion-plasma treatment with ion energy below the sputtering threshold (ε_i = 15-30 eV).

The ability to influence on mechanical stress in thin metal films is an actual task that has many applications in MEMS and other areas related to coatings. In our previous works [1, 2] it was shown that ion-plasma treatment (IPT) with ion energy below the sputtering threshold can have a significant effect on residual stress in Cr films. Depending on the ion energy IPT can both reduce average stress σ_0 and stress gradient σ_1 and increase them (Fig.1) that allows to use IPT as a non-destructive tool for stress regulation. However, this requires an understanding of the mechanisms that occur during IPT and ability to predict their behavior depending on treatment conditions and initial stress state of the films.

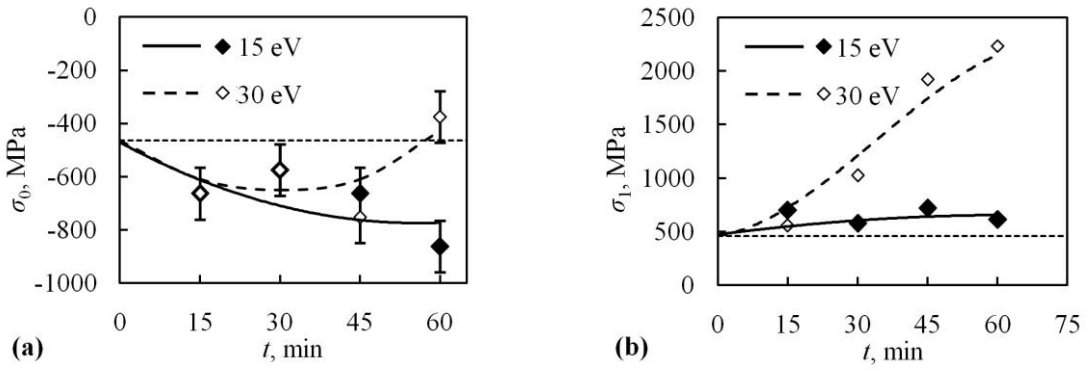

Figure 1(a, b). Dependences $\sigma_0(t)$ **(a)** and $\sigma_1(t)$ **(b)** obtained by x-ray diffractometry and by measuring the bending of the cantilevers respectively at ε_i = 15 eV and 30 eV. The straight dotted line is the original film. Curved lines are theoretical.

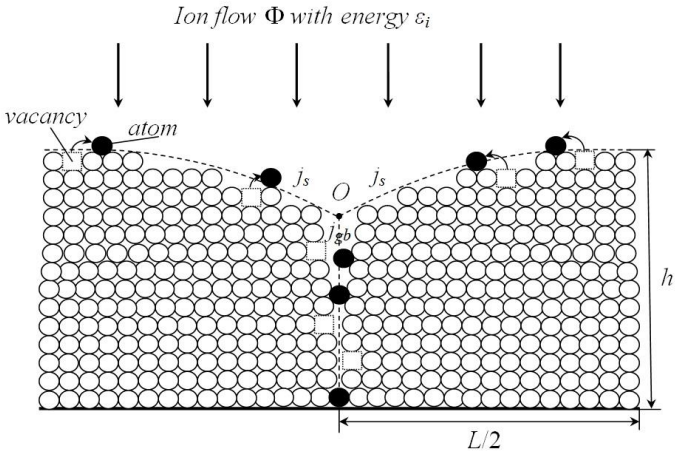

Figure 2. The scheme of the junction of the grains surfaces and the grain boundary.

Ion bombardment during IPT leads to the formation of a pair of point defects (surface atoms and vacancies) on the surface of grains (Fig. 2). Then due to surface diffusion they move to the junction of two grains (point *O*) and penetrate into the grain boundary (GB) where due to grain-boundary diffusion and drift due to the stress gradient they are distributed over the film thickness. The flows of defects along the surface and GB, respectively:

$$j_{a,v}^{s} = -D_{a,v}^{s} \frac{\partial C_{a,v}^{s}}{\partial x}, \tag{1}$$

$$j_{a,v}^{gb} = -D_{a,v}^{gb} \frac{\partial C_{a,v}^{gb}}{\partial x} + \frac{D_{a,v}^{gb} \Omega C_{a,v}^{gb}}{kT} \frac{\partial \sigma}{\partial x}, \tag{2}$$

where $D_{a,v}$– diffusion coefficients. The distribution of stress in the film during IPT is related with the concentrations of defects C_a^{gb} and C_v^{gb} penetrating in GB:

$$\sigma(x,t) = \sigma_0^{in} + \sigma_1^{in}\left(1 - \frac{x}{h/2}\right) - \frac{1}{2}\frac{E}{1-\nu}\frac{\Omega}{L}\left(C_a^{gb}(x,t) - C_v^{gb}(x,t)\right), \tag{3}$$

where σ_0^{in} – initial average stress in the film, σ_1^{in} – initial stress gradient. To obtain $\sigma(x,t)$ we must solve the kinetic equations for atoms and vacancies on the surface and in GB:

$$\frac{\partial C}{\partial t} = K - \frac{\partial j}{\partial x} - 4\pi\lambda(D + D')CC' - k_s^2 DC, \tag{4}$$

where K – generation coefficient, λ – recombination length, k_s – sink strength, an apostrophe above the letter indicates the opposite defect. Thus we have obtained a system of four differential and one algebraic equations. The solution of this system was carried out by the finite difference method. As a result the system of partial differential equations was replaced by a system of nonlinear algebraic equations, which was solved numerically by the Newton method. $D_{a,v}$ and k_s were adjustable parameters. The calculation results of $\sigma_0(t)$ and $\sigma_1(t)$ are shown in Fig. 1 in the form of curves.

Reported study was carried out under State Programs №0066-2019-0002 of the Ministry of Science and Higher Education of Russia.

References

[1] Babushkin A, Uvarov I, Amirov I 2018 *Technical Physics* **63** 1800
[2] Babushkin A, Selyukov R, Amirov I 2019 *Proceedings of the SPIE* **11022** 1102223

Modelling of single-photon absorption of a superconducting strip of micron width

M Dryazgov[1, 2], **A Semenov**[2], **N Manova**[2], **A Korneev**[1, 2]
[1]Higher School of Economics - National Research University, 101000, Russia
[2]Department of Physics, Moscow State Pedagogical University, 119992, Russia

Abstract. The present paper describes a modelling of normal domain evolution in superconducting strip of micron width using solving differential equations describing the temperature and current changes. The solving results are compared with experimental data. This comparison demonstrates the high accuracy of the model. In future, it is possible to employ this model for improvement of single photon detector based on micron-scale superconducting strips.

1. Introduction

At present Superconducting Single Photon Detectors (SSPDs) [1, 2] are used in quantum cryptography [3], optical communication systems in far space [4] and many other fields. The principle of their work is based on a local violation of superconductivity due to photon absorption [5-6].

The issue of SSPDs improvement is currently an active area of research. One of the possible improvements of single-photon detectors is the transition from the use of nanometer superconducting strips to micrometer ones [7-8]. This allows to increase the area of the detector and reduce the deadtime (the time, required to return to the superconducting state). However, the use of superconducting strips of micron width is possible only when using a shunt resistance parallel to the resistance of the coaxial line. This limitation is caused by a decrease in the detector resistance in the normal state and kinetic inductivity due to its large width.

The problem described, limits the application area of detectors. It is needed to know the value of the shunt resistance, which provides the maximum efficiency of the SSPD. The purpose of this work is modelling of normal domain evolution, temperature and current changes in superconducting strip of micron width, which will allow to determine the shunt resistance.

2. Mathematical model

The solution of the described task is based on solution of basic differential equations, which describe the processes occurring in a superconducting strip after absorption of a single photon [9]:

$$\frac{\partial cT}{\partial t} = J^2\rho + k\frac{\partial^2 T}{\partial x^2} - \frac{\alpha}{d}(T - T_{sub}), \quad (1)$$

$$L\frac{dI}{dt} = IR_n - (I_b - I)Z, \quad (2)$$

here equation 1 describes the temperature change (here c is the specific heat, J is the current density, ρ is the resistivity, k is the thermal conductivity of the superconductor, α is the thermal conductivity between the superconductor and the substrate, d is the thickness of the superconductor layer, T_{sub} is the temperature of the substrate). Equation 2 describes the change in the current flowing through the

superconducting strip (here L is the kinetic inductance, R_n is the resistance of the normal section of the superconductor, I_b is the source current, Z is the impedance of the shunt and the coaxial line, which is connected in parallel). The initial conditions are: the current in the superconductor is close to critical, one normal domain with a size of 15 nm is heated to a critical temperature by a falling photon, the remaining domains have a temperature equal to the temperature of the substrate.
These differential equations were numerically solved with the help of explicit difference scheme. The numerical solution is implemented by a python program.

3. Comparison of experimental and modelled data

Using the solutions obtained, it is possible to determine the magnitude of the shunt resistance necessary for the correct operation of a single-photon detector. Processes were simulated in 5 samples, after which they were compared with experimental data (Table 1).

Table 1. Comparison of experimental and modelled data

Size, μm	$I_c(2K)$, μA	R_{shunt}, Ω	Result	R_{crit}, Ω
2,9x30	517.6	7.4	Big	5.03
1.96x20	326.8	7.1	Small	7.16
1.14x10	134	8.5	Small	15.07
2.22x20	268	7.4	Small	8.29
3.14x30	315	7.2	Small	8.56

The value of the shunt resistance, selected during the experiment are in the column "R_{shunt}". The column "Result" describes the evaluation of the experimental shunt: "Big" means that shunt in the experiment was higher than optimal and lower resistance is required, "Small" - the experimental shunt is too small, and a shunt of higher resistance is required. The column "R_{crit}" contains the ideal values of the shunt resistance obtained from the simulation with an accuracy of $\varepsilon = 0.001$.
The simulation gives a result, which have fairly good quantitative agreement with the experimental data.

4. Conclusion

The evolution of the normal domain in a superconducting single-photon detector with a strip of micron width was modelled. The results obtained were compared with experimental data. The baseline result of the present research demonstrate high degree of compliance between modelling and experimental data. This study let to deepen understanding of superconductivity and instigate new research work on SSPDs based on micron scale superconducting strips

5. Acknowledgments

This work was supported by the Russian Science Foundation (RSF) Grant No. 17-72-30036.

References

[1] Natarajan Chandra, Tanner M, Hadfield R 2012 *Supercond. Sci. Technol.* **25**, 063001
[2] Gol'tsman G, *et al* 2001 App. Phys. Lett. **79**, 705
[3] Yamamoto, Yoshihisa *et al* 2019 Quantum Sci. Technol. **4**, 020502
[4] Hemmati H 2005 *Deep Space Optical Communications* (California Institute of Technology)
[5] Engel A, Renema J, Il'in K, Semenov A 2015 *Supercond. Sci. Technol.* **28**, 114003
[6] Zotova A, Vodolazov D 2014 *Supercond. Sci. Technol.* **27**, 125001
[7] Korneeva Yu *et al* 2018 *Phys. Rev. Applied* **9,** 064037
[8] Korneeva Yu *et al* 2020 *Phys. Rev. Applied* **13**, 024011
[9] Yang J *et al* 2007 *IEEE Transactions on Applied Superconductivity* **17**, 581

Substrate-dependent degradation of thin TMDC layers in ambient conditions

B R Borodin[1, 3]**, F A Benimetskiy**[2] **and P A Alekseev**[1]
[1]Ioffe Institute, Saint-Petersburg, 194021, Russia
[2]ITMO University, Saint-Petersburg, 197101, Russia

E-mail: [3]brborodin@gmail.com

Abstract. In this work, substrate-dependent degradation of thin layers of TMDC is demonstrated. The energy barrier heights of the $MoSe_2$/Au and $MoSe_2$/Ni heterojunctions were studied using Kelvin probe microscopy. The effect of the barrier height on the photodegradation process is shown. The results show that the Ni-covered substrate promotes the photodegradation process. While the Au-covered substrate depresses it.

1. Introduction

Currently, more and more van der Waals (vdW) layered materials and their properties are being discovered. Such great interest is caused by the presence of fascinating properties. Atomically thin transition metal dichalcogenide (TMDC) films demonstrate exciting properties such as anomalous high light absorption[1], strong photoluminescence[2], photocatalytic water splitting[1], and many others. Additionally, it is possible to create electronic and optoelectronic devices based on van-der-Waals heterostructures made of thin TMDC layers. To create such devices, thin TMDC layers are obtained by exfoliation and transferred onto a substrate[3]. The significant problem for TMDC-based devices is that TMDC materials may degrade under ambient conditions. In addition, the substrate can promote or limit the photodegradation process[4]. Our work was aimed to investigate the dependence of degradation thin TMDC layers on a substrate which they were transferred on. We transferred thin layers of $MoSe_2$ obtained by exfoliation on Si substrates coated with gold and nickel. To examine the process of degradation, we used scanning probe microscopy (SPM).

2. Samples and methods

The first sample consists of thin $MoSe_2$ layers obtained by exfoliation and transferred on a Si substrate coated with 50 nm of gold. The second sample consists of thin $MoSe_2$ layers exfoliated from the same bulk crystal on a Si substrate coated with 50 nm of nickel.

The experiment was carried out on a Ntegra Aura (NT-MDT) SPM using a Si NT-MDT probe with a tip diameter of 20 nm. The experiment was as follows. After exfoliating and transferring of TMDC layers, the topography of samples was investigated by SPM. Then the samples were left in a plastic box at room conditions ($T \approx 20$-23 °C, RH ≈ 50%, daylight) for several months. After that, the topography of the samples was again investigated.

It is well known that photocatalytic processes depend on the height of heterojunction[4]. So, work functions and heights of heterojunctions were determined using Kelvin Probe Force Microscopy (KPFM). A detailed description of this determination process is presented in our previous work[5].

3. Results and discussions

Figure 1 shows the results of the topography investigation.

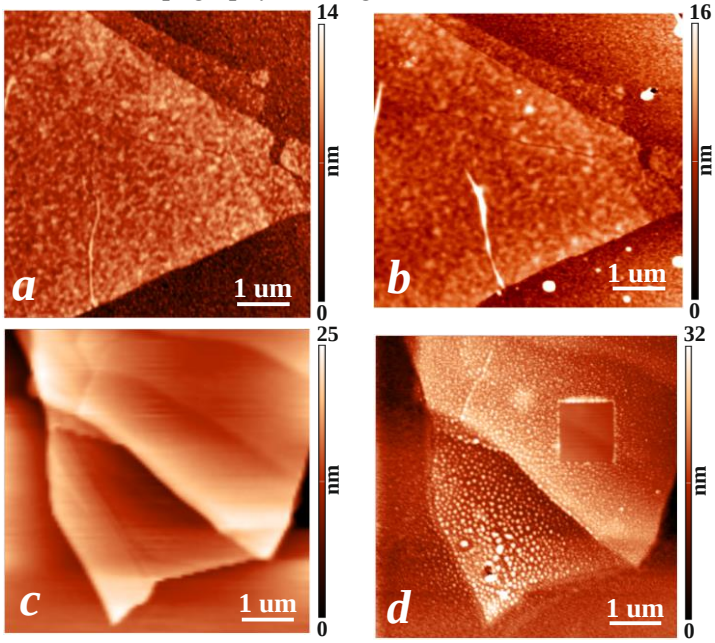

Figure 1(a, b, c, d). (a, c) $MoSe_2$ flakes on Au and Ni, respectively, immediately after transferring; **(b)** $MoSe_2$ flakes on Au and Ni, respectively, after several months.

As can be seen in Figure 1, the topography of the MoSe2 flake on the gold-covered substrate has not changed (Figure 1 a, b). Whereas the topography of the MoSe2 flake on the nickel-covered substrate has significantly changed as time passed (Figure 1 c, d). As can be seen from Figure 1d, the flake and the area around are coated with oxide. This can be explained as follows. The work function of a few-layer MoSe2 flake is about 4.4 eV. While the working functions of the substrates coated with gold and nickel are about 4.37 and 4.12 eV, respectively. It means that the barrier ~0.3 eV high is formed at the $MoSe_2$/Ni heterojunction. This results in the effective separation of photogenerated charge carriers and promotes the photooxidation. While at the $MoSe_2$/Au heterojunction, there is no barrier, and the above-mentioned process is depressed.

4. Conclusions

In this work, we demonstrated substrate-dependent degradation of thin TMDC layers. The heights of $MoSe_2$/Au and $MoSe_2$/Ni heterojunctions were studied using Kelvin probe microscopy. It was shown that the presence of a high energy barrier at the heterointerface results in effective charge carrier separation and promotes the photodegradation process. The results of this work show the importance of choosing a substrate for the stability of devices based on thin $MoSe_2$ layers.

References

[1] Bernardi M, Palummo M and Grossman J C 2013 *Nano letters* **13** 3664–3670
[2] Tonndorf P, Schmidt R, Böttger P, Zhang X, Börner J, Liebig A, Albrecht M, Kloc C, Gordan O, Zahn D R and others 2013 *Optics express* **21** 4908–4916
[3] Lee J Y, Shin J-H, Lee G-H and Lee C-H 2016 *Nanomaterials* **6** 193
[4] Borodin B, Benimetskiy F, Dunaevskiy M, Sharov V, Smirnov A, Davydov V Y, Lähderanta E, Lebedev S, Lebedev A and Alekseev P 2019 *Semiconductor Science and Technology* **34** 125007
[5] Borodin B, Benimetskiy F, Nyapshaev I and Alekseev P 2019 *Journal of Physics: Conference Series* vol 1400 (IOP Publishing) p 055012

Investigation of spontaneous activity of two hierarchically connected neural networks in vitro

Y I Pigareva[1] , A A Gladkov[1], V N Kolpakov[1], O V Grinchuk[2], A S Bukatin[3], I V Mukhina[1,4], V B Kazantsev[1], A S Pimashkin[1]

[1] Neuroengineering Laboratory, Translational technologies Center, Lobachevsky State University of Nizhny Novgorod, Nizhny Novgorod 603950, Russia

[2] The Moscow Institute of Physics and Technology, Moscow 141701, Russia

[3] Nanotechnology Research and Education Centre of the RAS, Saint-Petersburg Academic University, Saint-Petersburg 194021, Russia

[4] Central Research Laboratory, Cell Technology Department, Privolzhsky Research Medical University, Nizhny Novgorod 603005, Russia

Abstract. The combination of microfluidics and multichannel registration methods allows to construct neural networks with a defined topology and to investigate their functional properties. We present an in vitro model of two hierarchically connected neural networks and demonstrate that spontaneous activity is propagate between networks taking into account the hierarchical structure of connections.

1. Introduction

Spontaneous synchronization between separate neural networks is one of the distinguishing features of brain activity, which is important for many functions of a healthy brain (cognitive functions, memory, sleep) and pathology (epileptiform activity) [1]. Neural networks after cultivation for several days in vitro (DIV) spontaneously generate activity in the form of periodic and synchronized network discharges or bursts [2, 3]. To study the synchronization of the activity of connected neural networks in vitro, methods for structuring network geometry are used. The microfluidic method is most suitable for constructing directionally connected networks. It allows cultivating neurons in chambers connected by microchannels with asymmetric shape that provides polarization of the connections between neural networks [4]. Here we present the model of two directly connected neural networks in vitro and investigate synchronization of bursting activity between them.

2. Materials and methods

Microfluidic chips were fabricated from PDMS (Sylgard 184, Dow Corning) by “soft lithography” method and were manually mounted onto the surface of a planar microelectrode array (MEA). Chip structure consists of two chambers for neuronal cells cultivation and 16 microchannels for neuritis growth. Asymmetric design of microchannels facilitate axonal growth from “Source” chamber to “Target” chamber and reduce growth in opposite direction.

Hippocampal neuronal cells were dissociated from embryonic mice (E18) and plated on microfluidic chips at a density of approximately 8,000 cells/mm2.

Electrophysiology activity was recorded from 59 (1 reference) TiN electrodes of the MEA system (Multichannel Systems, Germany) at a sample rate of 20 kHz on 10, 15, 20, 25 days in vitro. We used

the threshold detection method for spike and burst detection as described in our previous studies [4]. To determine the direction of spikes propagation in microchannels, the distribution of delay times between spike pairs of adjacent electrodes was constructed. Peaks of histograms with high precision in delay time is consistent with spikes propagated along axons.

3. Results and Conclusions

In this study we investigated the synchronization of spontaneous bursting activity of two neuronal networks connected by asymmetric microchannels. Axons grew through microchannels from "Source" chamber to "Target" chamber within 5 days after plating cells. Microchannels consists of 3 segments, two segments has narrow triangular shape (200 μm length, 40 μm width) and one has large triangular shape (200 μm length, 150 μm width), the width of the bottlenecks between segments was 7 μm.

The spontaneous bursting activity appears in neural networks in 7-10 days in vitro. We obtained that some of bursts propagated from one network and evoked burst in second network with delay less than the initiating burst duration. We estimated probability of burst propagating from "Source" to "Target" chamber (forward direction) and from "Target" to "Source" chamber (backward direction) as the ratio of the number of propagated bursts to the total number of bursts in initiating network. We found that the probability of burst propagation in the forward direction was several times higher than the propagation in the opposite direction. Thus, the developed structure of microchannels provides a hierarchical architecture of connections between networks. Statistically significant changes in the probability of the propagation both in the forward and the opposite direction were observed between 15 and 20 DIV and may be associated with the maturation of synaptic contacts between neural networks. Also, the direction of spikes propagation in the microchannels was predominantly from the "Source" to "Target" chamber and this tendency maintained with the development of neural networks. The results suggest that spontaneous bursting activity of directly connected neural networks is synchronized taking into account the hierarchical structure of connections.

References

[1] Buzsáki G, Watson BO 2012 *Dialogues Clin Neurosci.***14** 345–367
[2] Chiappalone M, Koudelka-hep M 2007 *Int J Neural Syst***.17** 87–103
[3] Wagenaar D , Pine J, Potter SM 2006 *BMC Neurosci*.**7** 11
[4] Gladkov A, Pigareva Y, Kutyina D, Kolpakov V, Bukatin A, Mukhina I, Kazantsev V, Pimashkin A 2017 *Scientific Reports* **7(1)** 15625

Application of the Atomic Layer Etching technique to remove broken layers after plasma-etched GaAs surface treatment

V S Klimin[1,2], **A A Rezvan**[1]
[1]Department of Nanotechnology and Microsystems,Southern Federal University, Taganrog 347922, Russia
[2]Research and Education Center "Nanotechnologies", Southern Federal University, Taganrog 347922, Russia

Abstract. The work considers the application of the atomic-layer etching technique to remove layers with defects after surface treatment using focused ion beam methods and plasma chemical etching for the subsequent growth of quantum dots by molecular beam epitaxy. The work shows that this technique allows you to remove the surface layers in which the defects are contained.

1. Introduction

The task of controlled synthesis of semiconductor self-organizing nanostructures - quantum dots, filamentous nanocrystals, metallic nanodroplets - is extremely important, first of all, to create effective sources of single and entangled photons - the basis of quantum cryptography systems, as well as functional elements based on filamentary nanocrystals, single quantum dots and / or their complexes with a given topology, on the basis of which cellular automata, memory elements, integrated photonics and functional blocks quantum computing systems [1-3].

At the same time, drip epitaxy, based on separate deposition of components of groups III and V, allows not only to significantly expand the range of structures formed (quantum dots, rings, disks and complex, hybrid structures based on them), but also to realize independent control of the density and size of quantum dots, as well as to use for their creation virtually any A3B5 system, which is inaccessible to techniques based on the Stranski – Krastanov mechanism.

The use of structured GaAs and Si substrates and the features of droplet epitaxial techniques will effectively localize epitaxial growth at given points on the surface, thereby ensuring precise positioning and control of the parameters of synthesized nanostructures — metal nanoscale droplets (catalytic centers) and quantum dots based on them (in the case of GaAs).

The structuring of the substrates was carried out by a combination of methods of focused ion beams and plasma-chemical etching. However, after obtaining substrates with nanoscale relief, a broken layer was formed on the surface in the depressions caused by plasma and penetration of Ga ions after exposure to focused beams. To remove damaged layers, the best method is layer-by-layer etching of the GaAs surface [4].

2. Method

In the course of the experimental work, standard GaAs plates were used. Structures for the subsequent growth of quantum dots by molecular beam epitaxial were formed on the surface of the wafers by the method of focused ion beams and plasma chemical etching in chlorine plasma. To remove defects introduced during previous treatments, the atomic layer etching technique was used. This technique

consists in removing one atomic layer from the surface of the formed structures. At the first stage, the active gas is launched into the reactor, at the second stage, inductively coupled plasma is switched on for the reaction of gas molecules deposited on the surface, then the surface reacted layer is removed and the cycle repeats.

3. Results and Discussion

To determine the penetration depth of gallium ions, a simulation was carried out and it was revealed that after treatment in chlorine plasma, 12 atomic disturbed layers remain, which were later removed using the atomic layer etching method. When using the “soft” etching mode, the angle of inclination of the nanoscale structures changed and the growth of quantum dots did not occur.

At the end of the experimental studies, samples were obtained with nanoscale surface profiling, a combination of methods of focused ion beams, plasma chemical etching, atomic layer etching, in which GsAs quantum dots were obtained by dropping epitaxial.

Acknowledgments

This work was supported by the Grant of the President of the Russian Federation No. MK-3512.2019.8 The results were obtained using the equipment of the Research and Education Center "Nanotechnologies" of Southern Federal University.

References

[1] N. Chekurov, K. Grigoras, A. Peltonen, S. Franssila, I. Tittonen, Nanotechnology. 20 (2009) 5
[2] T.Nishinaga and X. Q.Shen, Appl. Surf. Sci. 82-83 (1994) 141
[3] A. Tseng, J. Micromech. Microeng. 14 (2004) 15
[4] V.S.Klimin, A.A. Rezvan, O.A.Ageev, J. Phys.: Conf. Ser. 1124 (2018) 022035

Method for analyzing the electrophysical properties of semiconductor quantum dots

A I Mikhailov, V F Kabanov, M V Gavrikov
Department of Nano and Biomedical Technologies, Saratov State University, Saratov 410012, Russia

Abstract. In this paper, the method of analysis of normalized differential tunneling current-voltage characteristics was substantiated and used to study some important parameters of semiconductor quantum dots. This method allowed us to analyze the position of the first three energy levels of the electron in quantum dots with acceptable accuracy. In addition, this method made it possible to estimate the size of investigated objects.

1. Introduction

Quantum dots (QDs) are one of the most interesting objects for investigations in purpose of application in optoelectronics and nanoelectronics due to the presence of a number of characteristic features. Therefore, the choice of methods for studying them is also important. The main research methods, such as transmission electron microscopy (TEM), analysis of optical characteristics, etc., allow us to estimate the size, shape and composition of objects, however, they do not allow to evaluate the energy spectrum of QD, which can be a source of useful information about their optical and electronic properties. Therefore, the purpose of this paper was the substantiation and application of a method of analysis of normalized differential tunneling current-voltage characteristics, which allows to obtain this type of information about the objects, by using the semiconductor quantum dots of materials from groups A^2B^6 (CdSe) and A^3B^5 (InSb).

2. Research methods

In this paper we investigated monolayers of quantum dots that were formed on the surface of an aqueous subphase, using the Langmuir-Blodgett technology, and transferred onto solid substrates with a conducting layer of indium tin oxide (ITO). The obtained samples were investigated by scanning tunneling microscopy (STM) using a SOLVER Nano scanning probe microscope.

3. Results and discussions

Model representations of the process of electron tunneling through discrete levels of a quantum-dimensional object into a microscope probe in the structure that characteristic for STM measurements were considered in [1]. The discrete energy spectrum of the conduction electrons of a quantum-dimensional object determines the peaks in the normalized differential CVC (Fig. 1 on the left). These peaks are typical for electron tunneling from 1, 2, and 3 energy levels of quantum dots into a metal probe of a microscope, and this allows us to determine the position of these levels (with an error in measuring the position of the peaks less than 2kT, which at T = 300K approximately corresponds to 0.05 eV). Further, as shown in Fig. 1, the voltage values that corresponds to peaks are put in accordance with the energy values on the dependences of the position of the QD first three energy levels, that was calculated with the “cubic” QD model (Fig. 1 on the right). Thus, the size range of

investigated QDs was determined. By further comparison of the obtained sizes values with the results of test measurements by TEM and analysis of optical characteristics we can confirm the accuracy of our method. In this paper, we estimated the sizes of InSb quantum dots, which, as shown in Fig. 1, were in the range of 11–13 nm, and also CdSe quantum dots: 4–5 nm. The results showed quantitative and qualitative agreement with the test ones with an error less than 10%, which allows us to talk about efficiency of this method.

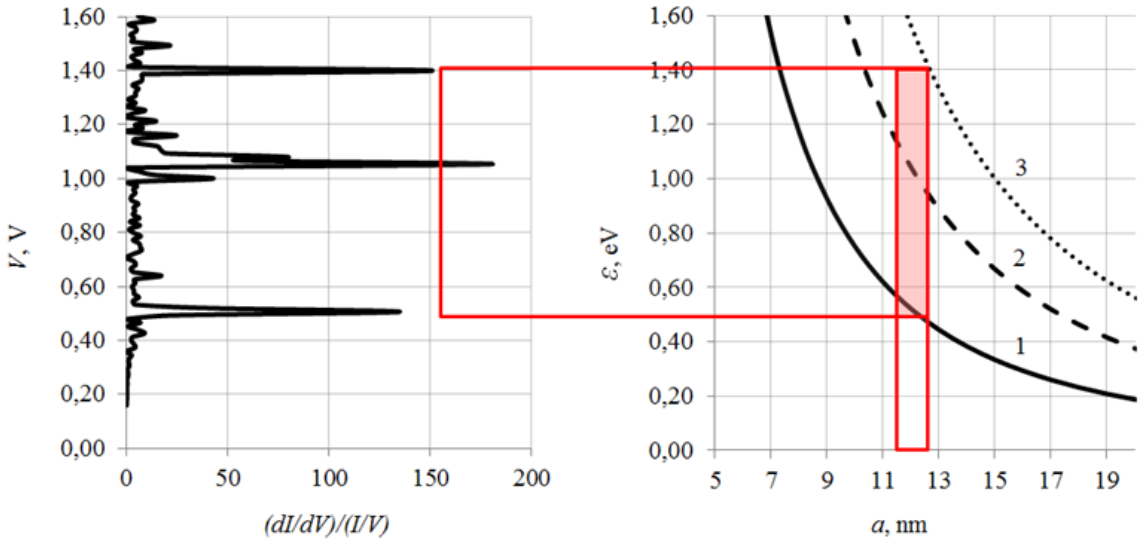

Figure 1. Typical differential tunneling CVC of InSb QDs in accordance with the calculated levels of the energy spectrum.

4. Acknowledgments
This work was supported by grant from the Russian Foundation for Basic Research №19-07-00087.

References
[1] Mikhailov A I, Kabanov V F, Zhukov N D, Glukhovskoy E G 2017 Nanosystems: Physics, Chemistry, Mathematics **8** (5) 596–599

Diffusion dynamics in ensembles of robots with variable friction

A D Rozenblit[1,2], V A Porvatov[3,4], D A Petrova[3,4], I S Khakhalin[5], K P Kotlyar[6], G Yu Gritsenko[7], A A Evreiskaya[8], M F Lebedeva[6], E I Kretov[9], D S Filonov[4], A Souslov[10], and N A Olekhno[1*]

[1]ITMO University, 197101 Saint Petersburg, Russia
[2]Peter the Great St. Petersburg Polytechnic University, 195251 Saint Petersburg, Russia
[3]National University of Science and Technology "MISIS", 119991 Moscow, Russia
[4]Moscow Institute of Physics and Technology, 141701 Moscow, Russia
[5]Baltic State Technical University 190005, Saint Petersburg, Russia
[6]Alferov University, 194021 Saint Petersburg, Russia
[7]Lomonosov Moscow State University, 119991 Moscow, Russia
[8]Novosibirsk State University, 630090 Novosibirsk, Russia
[9]Max Delbrück Center for Molecular Medicine in the Helmholtz Association, 13125 Berlin, Germany
[10]University of Bath, Bath, UK

E-mail: *olekhnon@gmail.com

Abstract. In the present work, we experimentally study the diffusive dynamics in a swarm of randomly moving robots. Each robot is a bristle-bot moving because it vibrates on top of a rigid surface and is powered by its battery. We consider the dependence of the system dynamics on the density of robots as well as the friction between individual robots. The results show that changing the friction slightly affects the diffusive dynamics but leads to a significant change in the jamming transition point corresponding to the formation of dense clusters.

1. Introduction

Active matter describes the dynamics of systems composed of particles that can extract the energy from their sources and convert this energy into individual and collective motion. Examples of such systems include biological ones such as bacterial colonies [1], flocks of birds or fish [2] as well as engineered systems, including ensembles of self-propelled micro-particles [3] or macroscopic robots [4, 5, 6]. The latter platform is especially attractive for experimental studies due to its low cost and excellent design flexibility to engineer properties of individual particles. However, the dependence of robotic ensemble dynamics on friction between robots have not yet been explored.

2. Experimental setup

In the present work, we consider the ensemble of 35 self-propelled bristle-bots vibrating at frequencies between 50 and 100 Hz, Figure 1(a). The vibration causes bristle-bots having soft deformable legs to move due to the asymmetry of its shape and mass distribution. Each robot is 32 mm in diameter and consists of the body made of ABS plastic via FDM printing technology,

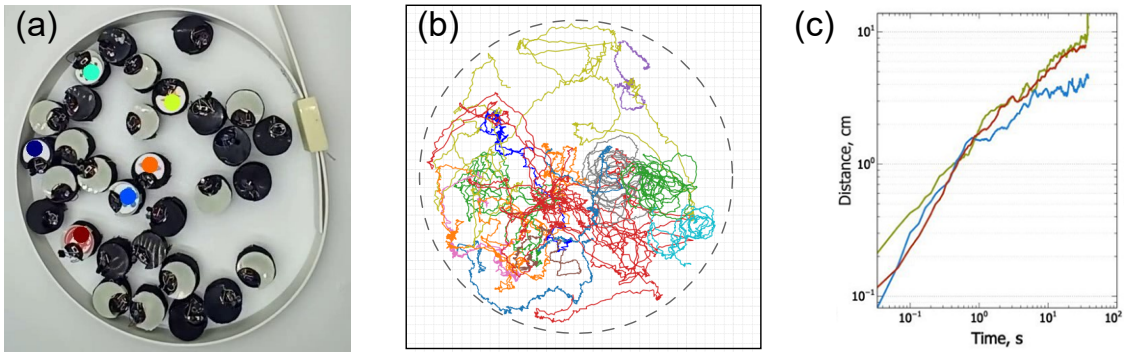

Figure 1. (a) Experimental setup. (b) Extracted trajectories of robots moving inside a boundary with the diameter 33.5 cm and at intermediate friction. Different colors correspond to different robots. (c) Root mean square displacement of robots as a function of time for different values of friction between robots: low (green), intermediate (blue), and high (red). Each curve is averaged over three realizations of the system and five different robots in each realization.

QX-6A-1 motor, a 3V battery, and a control circuit. The circuit allows turning the robots on and off by changing the ambient lighting and includes two KT315B1 transistors, Vishay BPW34 PIN photodiode and KLS7-SS03-12D02 slide switch. The robots are placed inside a plastic boundary of a diameter that we control to be between 33.5 and 40 cm to tune the density of robots. To change the friction between robots, individual bristle-bots are covered with different materials ranging from sandpaper to paper tape to a plastic tape. The motion of the system is captured with a camera and then analyzed with the aid of the DeepLabCut neural network.

3. Results

We studied the diffusion dynamics as a function of the robot density and friction coefficient between individual robots. To do so, we extract individual trajectories of robots for different diameters of the boundary and different materials covering robots, Figure 1(b). Then, we consider a root mean square displacement of robots as a function of time, averaged over different trajectories in the single realization as well as over different initial configurations of the ensemble, Figure 1(c). The results show that the jamming transition threshold corresponding to a formation of the stable cluster of bristle-bots depends on the friction between robots, whereas power-low behavior in the diffusion regime conserves.

Acknowledgments

NAO acknowledges partial support by the Foundation for the Advancement of Theoretical Physics and Mathematics “BASIS”.

References

[1] Mathijssen A J T M, Guzmán-Lastra F, Kaiser A, and Löwen H 2018 *Phys. Rev. Lett.* **121**, 248101
[2] Filella A, Nadal F, Sire C, Kanso E, and Eloy C 2018 *Phys. Rev. Lett.* **120**, 198101
[3] Bricard A, Caussin J-B, Desreumaux N, Dauchot O, and Bartolo D 2013 *Nature* **503** 95-98
[4] Giomi L, Hawley-Weld N, and Mahadevan L 2012 *Proc. R. Soc. A* **469** 20120637
[5] Slavkov I et al 2018 *Sci. Robot.* **3**, eaau9178
[6] Deblais A, Barois T, Guerin T, Delville P H, Vaudaine R 2018 *Phys. Rev. Lett.* **120**, 188002

Microscopic simulation of e-beam induced PMMA chain scissions with temperature effect.

F A Sidorov[1], **A E Rogozhin**[1]
[1]Valiev Institute of Physics and Technology of RAS, Moscow 117218, Russia

Abstract. This study presents novel microscopic algorithm of e-beam induced poly- methyl methacrylate (PMMA) chain scissions. It considers PMMA chain scissions as a result of changes in PMMA bond structure. Scission mechanisms are determined by simulation of exposed PMMA molecular weight distribution and comparison of simulated radiation scission yield with experimental values. At room temperature, PMMA chain scissions are supposed to originate from e-beam interaction with valence electrons of PMMA C-C backbone atoms. The radiation scission yield increase at higher temperatures could be explained by increase of probability of PMMA chain scission by ester side group detachment.

1. Introduction

Basic approach for the simulation of positive resist chain scissions bases on radiation scission yield (G_s), which represents mean number of chain scission per 100 eV energy deposition. G_s values obtained for electron irradiation of poly- methyl methacrylate (PMMA) by viscosity measurements were provided by different researchers, and conventional value for room temperature is 1.9±0.3 [1]. Moreover, $\log(G_s)$ seem to vary linearly on $1/T$ over the range 0-180 °C with activation energy of approximately 1 kcal/mole [2]. Recent models of e-beam induced PMMA degradation take into account changes in PMMA bond structure, instead of energy deposition [3,4]. They consider PMMA chain scissions as a result of inelastic e-beam interaction events with C–C backbone atoms. The most detailed approach, proposed by Aktary et al. [4], provides interpolated probability of PMMA chain scission, which was estimated by number of electrons, involved in electron-electron interaction at high and low energies of incident electron. However, there seems to be no explanation of G_s temperature dependence. In this study PMMA weigh distribution in e-beam lithography exposures is simulated to model the experiment of G_s determination from the exposed PMMA viscosity, related to PMMA number average weight. The temperature effect on G_s is taken into account by variation of scission mechanism with temperature growth.

2. Simulation of e-beam scattering in PMMA/Si structure

Direct Monte-Carlo algorithm, with discrete energy loss model, based on Dapor [5] and Valentin [6] approaches was used to simulate e-beam scattering in PMMA/Si structure. PMMA chains are modeled using ideal chain model based on random walk simulation with 0.28 pitch and 109º between successive monomers [7]. The processes of e-beam interaction with PMMA valence electrons were divided into 9 groups, related different bond types in MMA monomer [8]. Gryzinski formula [9] was used to estimate the contribution of each bond to total inverse mean free path of e-beam interaction with PMMA valence electrons (Fig. 1). In this approach, bond dissociation energy (BDE) was treated as binding energy, which is required parameter of Gryzinski differential cross-section. BDE was also used to determine the secondary electron energy from energy loss of primary electron.

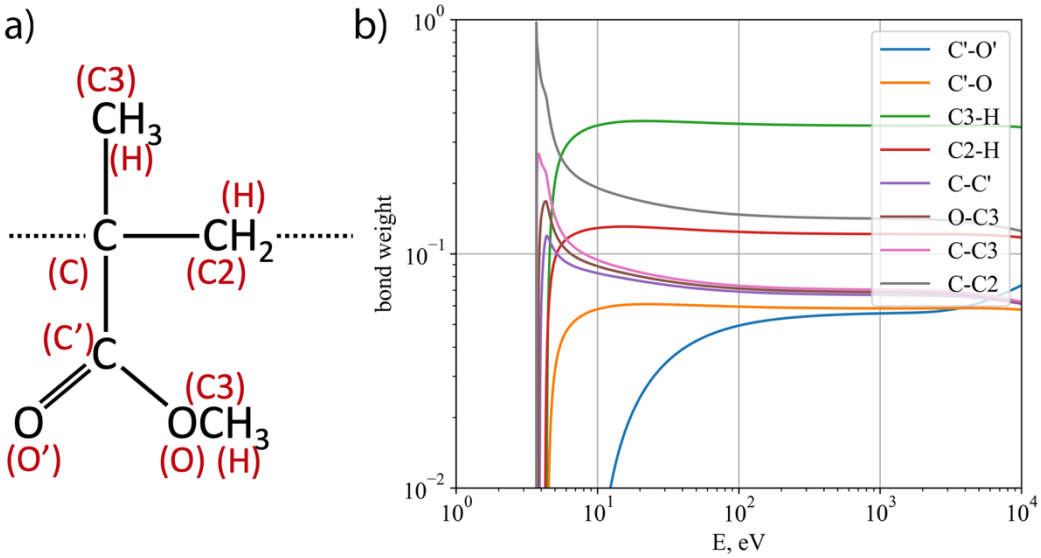

Figure 1. (a) Atomic structure of poly- methyl methacrylate monomer (MMA) with atom description (red text in brackets); (b) bond weight in total inverse inelastic mean free path for e-beam interaction with MMA valence electrons, calculated using Gryzinski formula.

3. Simulation of PMMA chain scission rate at different temperatures

Assuming that e-beam interaction with valence electrons of C–C backbone atoms results in PMMA chain scission, one could obtain G_s value of 1.84, which is in agreement with existing models of e-beam induced PMMA degradation. For the simulation of temperature effect on PMMA chain scission rate other possible PMMA chain scission mechanisms were analyzed [10]. It was determined that G_s increase with temperature raise up to 180 °C could be explained by almost linear (with T) increase of probability of PMMA chain scission by ester group detachment, which gives required G_s increase up to 3.1.

4. Acknowledgments

This study was supported by the Program no. 0066-2019-0004 of the Ministry of Science and Higher Education of Russia for Valiev Institute of Physics and Technology of RAS.

References

[1] Chapiro A 1962 *Radiation Chemistry of Polymeric Systems* (New York: Wiley)
[2] Charlesby A, Thomas D K 1962 *Proc. R. Soc. Lond. A* **269** 104
[3] Han G, Khan M, Fang Y, Cerrina F 2002 *J. Vac. Sci. Technol. B* **20** 2666
[4] Aktary M, Stepanova M, Dew S K 2006 *J. Vac. Sci. Technol. B* **24** 768
[5] Dapor M, Ciappa M, 2010 *J. Micro/Nanolithography, MEMS, MOEMS* **9** 023001
[6] Valentin A, Raine M, Sauvestre J *et al*. 2012 *Nucl. Inst. Methods Phys. Res. B* **288** 66
[7] Han G, Khan M, Fang Y, Cerrina F 2003 *J. Vac. Sci. Technol. B* **21** 3166
[8] Stoliarov S I, Westmoreland P R, Nyden M R, Forney G P 2003 *Polymer* **44** 883
[9] Gryzinski M 1965 *Phys. Rev.* **138** A336
[10] Bermudez V M 2002 *J. Vac. Sci. Technol. B* **17** 2512

Electrical characterization of nitride silicon layers SiN:x enriched in silicon at different stoichiometries - photovoltaic application

L Boudjemila[1,2], B Mahmoudi[1], Kh Khenfer[1], V V Krasnoschekov[2], V Yu Rud'[3], V V Davydov[2, 4], O S Scherbakova[5]

[1]Department of Mechanical Engineering, University of science and technology Houari Boumedien Bab Ezzouar 16111, Algiers, Algeria

[2] Peter the Great St. Petersburg Polytechnic University, St. Petersburg 195251, Russia

[3]A.F. Ioffe Physicotechnical Institute, St. Petersburg, Russia

[4]All-Russian Research Institute of Phytopathology, Moscow Region 143050, Russia

[5]PJSC"Rostelecom", St. Petersburg, Russia

Abstract. The main objective of researches in the field of photovoltaic is to increase the efficiency. This work aims a new concept which is the integration of nanoparticles in the anti-reflection layerSi3N4 (silicon nitride), in order to improve the performance of solar cells. This concept is based on the up conversion, where the nanoparticles are characterized by the ability to function as a converter of infrared rays having high energies in the receptivity in the visible. The concept of conversion leads to a better exploitation of the solar spectrum, by widening the useful range of the spectrum. Firstly, we realized SiNx layers at different compositions and proved that variation by calculating the silicon excess and the gap energy. But the focus is on the analysis of photocurrent measurements for the vertical and lateral configuration to show the role of nanparticules. And we finalize with measurement of currents at the test bench I-V to find the ideal stoichiometry for nanoparticles.

1. Introduction

Solar energy is one of the inexhaustible sources of energy for the Earth, therefore, researcher focus particularly in the conversion of solar energy to electric by using photovoltaics. Silicon is currently the most used material in photovoltaic systems. The semiconductor technology has been developed rapidly with the growth of microelectronics in recent decades. 90 % silicon is the main material of microelectronics [1]. Photovoltaic's third generation is the combination between the first generation (silicon cells), which were developed mainly from silicon, these cells have only one PN junction, and the second generation (thin films), which is based on a thin layer deposited on a substrate.

In recent years, the reduction in the size of Silicon to nanostructure has open new functionalities that have made it possible to envisage several applications based on silicon nanocrystals (nc-Si). Composite thin films of a dielectric matrix containing silicon nanoparticles can find various applications in optoelectronics: third-generation photocells, Bragg mirrors, semiconductor lasers, etc. [2]. At this point, wide changes in physical properties occur, mainly in energy characteristics; electronic levels, modes of atomic vibrations and their interactions with photons. This promises a lot of results and progress. One of the goals set is to use these nanosturturs as converters of high-energy photons into red photons that are better absorbed by the main cell. The main attention will be paid to the analysis of the properties of absorption and charge transfer of nanostructured layers in order to verify their photoelectric efficiency and assess the feasibility of manufacturing multi-junction elements based on these nanomaterials.

2. Methods of experimental characterizations

To measure the chemical composition of silicon nitride (anti reflection layer), analyzes were carried out by Mass spectrometry of secondary ions (SIMS). The SIMS technique allows obtaining the concentrations of each of the components in the atomic percentage of samples, which also allows to find out the total composition of these samples depending on the depth. The evolution of stoichiometry, which depend of the gas precursor ratio R = NH3 / SiH4, will be determined after the bombardment of the samples by an ion beam (primary ions) with energies from 0.1 KeV to 50 KeV.

Interest will be focused only on the SiNx anti-reflective layer of the samples. It consists of two essential elements, silicon Si and nitride N. According to these results, it is possible to develop alloys of silicon nitride which contains an excess of silicon compared to the standard stoichiometry $Si3N_4$. It is an essential prerequisite for obtaining the precipitation and crystallization of silicon Nanocrystals in a matrix of silicon nitride.

According to the obtained graphs, the more samples are rich in silicon, the more we notice a shift in the reflection spectrum to the near infrared, diagrams in Figure 1, this suggests that the effective refractive index increases with the rate of Silicon within the SiNx layer [3], we also notice that the fringes are not regularly spaced.

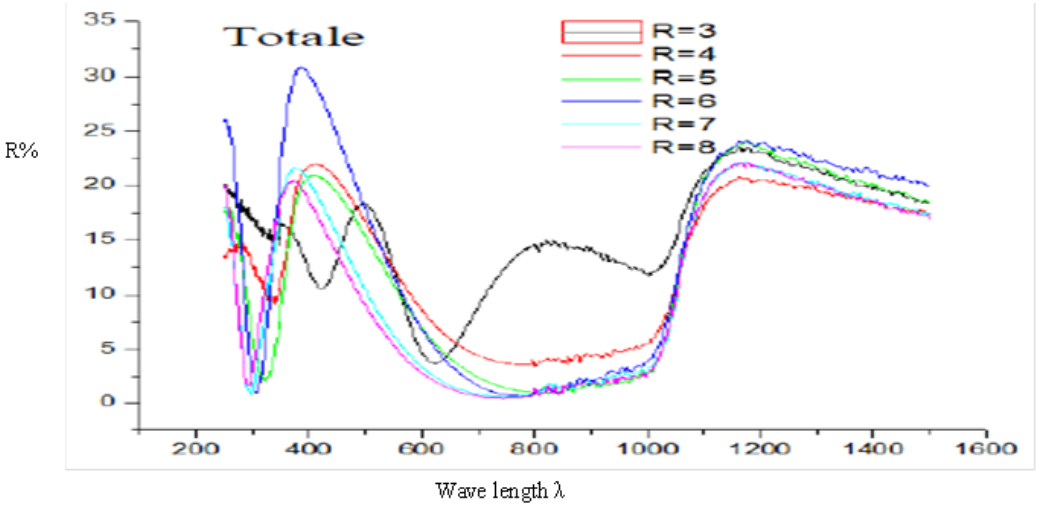

Figure 1. Reflection spectrum of silicon nitride composite layers at 7 different silicon concentrations**.**

3. Conclusion

Research on silicon nanocrystals for photovoltaic applications is barely in its infancy. Numerous research and development efforts will be necessary to ensure sufficient engineering of nanostructures so that they become a technological and industrial reality. The results obtained by this work are promising. The principle consists in obtaining silicon nanoparticles (Si-np) in a Si_3N_4 matrix. The variation of the ratio of gases R = NH_3 / SiH_4 to allows in turn to vary the concentration of silicon therefore the size of the nanoparticles due to the photo-current technique we determined the absorption levels in nc-Si using two different configurations (vertical and lateral). Thus, we have proved that a lateral transport configuration has better sensitivity than a vertical configuration and that it provides more information on the different absorption thresholds due to a very considerable reduction in the contribution of the substrate.

References

[1] Kesamanly F P, Rud' V Yu, Rud' Yu V 1999 *Semiconductors* **5** 483
[2] Canham L T 1990 Appl. Phys. Lett. **57** 1046-8
[3] Green M A 2001 *Prog. Photovolt: Res. Appl.* **9** 123-135

Defect properties of multilayer GaP/Si nanoheterostructures grown by plasma deposition

A I Baranov[1], I A Morozov[1], A V Uvarov[1], Kudyashov D. A.[1], A S Gudovskikh[1,2]
[1]St Petersburg Academic University of RAS, 194021 St Petersburg, Russia.
[2]St Petersburg Electrotechnical University "LETI", 197376 St Petersburg, Russia.

Abstract. Electrophysical properties of GaP/Si multilayer structures grown on n-GaP wafers by PE-ALD with step of argon plasma activation are studied. Firstly, capacitance-voltage measurement confirmed possibility to profile the charge carrier density in silicon quantum wells in GaP/Si multilayer structures. Further, different defect levels were detected by deep-level transient spectroscopy. In result, hole trap with Ea=0.18 eV are formed in depth of 20-30 nm from the wafer surface after PE-ALD process due to argon treatment, but no responses observed deeper in GaP wafer. Then, three types of defects were detected in GaP/Si multilayer structures: (i) complex of SiGa+Pi, (ii) extended ones associated with levels in bandgap of GaP layers grown by PE-ALD, and (iii) responses at temperature higher 300 K related to defect with higher activation energy.

1. Introduction

Nowadays, there is the challenge to grow III-V compounds on silicon wafers since it will allow to fabricate optoelectronic device, for example, multi-junction solar cells on cheap wafers. However, modern technological methods like molecular-beam and vapour phase epitaxy have not been obtained sufficient quality of such compounds and efficiency of fabricated solar cells. Also, an applied technology should be possible to be transferred in industry for fabrication of solar cells for terrestrial applications but each epitaxial method is not very suitable due to expensive and complicated equipment and strict requirements for source of atoms. Method of plasma deposition (like PECVD) is much more suitable for industry than modern epitaxial ones, and, recently, layers of GaP were deposited by adopted approach of atomic-layer deposition (PE-ALD) on Si wafer [1]. Furthermore, multilayer GaP/Si nanoheterostructures with Si quantum wells were obtained by PE-ALD for active layers in top subcells of MJ SC [2]. However, it was shown that an additional step of argon plasma treatment in PE-ALD process allows to improve homogeneity and decrease roughness of GaP layers. Therefore, here, the technology will be developed for growth of multilayer GaP/Si structures on GaP wafers by using of additional step of argon treatment in PE-ALD process. Capacitance-voltage characteristics and deep-level transient spectroscopy will be applied for characterization of structures.

2. Experiments and methods

Four different samples were grown at 380 °C on n-GaP ($n=5\times10^{17}$ cm^{-3}) wafers using an Oxford PlasmaLab System 100 PECVD (13.56 MHz) setup. Multilayer samples consist of 3-7 quantum wells of silicon grown by PECVD mode between barriers of GaP grown by PE-ALD mode. Thickness of GaP and Si layers were varied as 3-5 nm and 0.5-3 nm respectively. Schottky barriers to superlattices

GaP/Si were formed by vacuum evaporation of gold in BOC Edwards Auto500 setup, and ohmic contact was formed from the bottom side of GaP wafer. Capacitance-voltage measurements were performed using a precision E4980A Keysight (former Agilent) LCR-meter. Measurements of capacitance DLTS were performed using an automated installation based on a Boonton-7200B capacitance bridge in the temperature range of 80-360 K.

3. Results

Firstly, capacitance-voltage measurement confirmed possibility to profile the charge carrier density in silicon quantum well in GaP/Si multilayer structure with 7 QWs of silicon with thickness of 3 nm. Further, different defect levels were detected by deep-level transient spectroscopy. In result, hole trap with Ea=0.18 eV are formed in depth of 20-30 nm from the wafer surface after PE-ALD process and associated with gallium vacancies rising due to argon treatment, but no responses observed deeper in GaP wafer. Then, three types of defects were detected in GaP/Si multilayer structures: (i) complex of Si_{Ga}+P_i, (ii) extended ones associated with levels in bandgap of GaP layers grown by PE-ALD, and (iii) responses at temperature higher 300 K related to defect with higher activation energy. More detailed information for different GaP/Si multilayer structures will be presented in conference.

4. Acknowledgments

This work was supported by grant from the President of Russian Federation No СП–1207.2019.1.

References

[1] Gudovskikh A S, Morozov I A, Uvarov A V, Kudryashov D A, Nikitina E V, Bukatin A S, Nevedomskiy V N and Kleider J 2018 Low temperature plasma enhanced deposition of GaP films on Si substrate *J. Vac. Sci. Technol. A Vacuum, Surfaces, Film.* **36** 021302

[2] Gudovskikh A S et al. 2019 Materials Today: Proceedings **19** 47

MBE growth and properties of N-based and III-V NWs on SiC/Si(111) hybrid substrate

R R Reznik[1-4], K P Kotlyar[1], I V Shtrom[1,2,4], S A Kukushkin[5], A V Osipov[5], E V Nikitina[1], V G Talalaev[6] and G E Cirlin[1-3]

[1]Alferov University, Khlopina 8/3, 194021, St-Petersburg, Russia
[2]ITMO University, Kronverkskiy pr. 49, 197101, St. Petersburg, Russia.
[3]Institute for Analytical Instrumentation RAS, Rizhsky 26, 190103, St-Petersburg, Russia
[4]St Petersburg University, Universitetskaya Emb. 13B, 199034, St.Petersburg, Russia
[5]Institute of Problems of Mechanical Engineering Russian Academy of Science, Bolshoj 6, 199178, St. Petersburg, Russia
[6]Martin-Luther-University Halle-Wittenberg, ZIK SiLi-nano, 06120 Halle, Germany
E-mail: moment92@mail.ru

Abstract. The possibility of N-based and III-V nanowires growth by molecular-beam epitaxy on a silicon substrate with nanoscale buffer layer of silicon carbide has been demonstrated. Morphological, structural and optical properties of the resulting systems have been studied and compared with properties of identical nanostructures on silicon substrate.

1. Introduction

The wide-gap nanoheterostructures based on GaN are of great interest for creating electronic and optoelectronic devices. Works in growing GaN on silicon have been very promising recently. However, the lattice misfit of such materials is 17%, which leads to the formation of defects of different nature.

In this work, in order to reduce the number of misfit dislocations a nanometer (about 50 nm) buffer layer of SiC was used for MBE GaN nanowires (NWs) growth. Since the difference in the lattice parameters is only 3%, so growth on such surface can radically reduce the density of structural defects in GaN.

Growth experiments are carried out using Riber Compact12 MBE setup. After the growth, the samples are studied by applying the scanning electron microscopy (SEM) and low-temperature photoluminescence (PL) techniques. Comparison of photoluminescence spectra of grown GaN on hybrid and the most successful GaN NWs structures on silicon shows that the intensity of radiation from grown on SiC buffer layer GaN NWs is more than two times higher than the intensity from the best GaN structures on silicon. This fact leads to the conclusion that grown structures have fewer defects compared with GaN NWs on silicon substrate. This is caused by a smaller lattice constant mismatch between GaN and SiC compared with GaN and Si.

Besides we have discovered a novel mechanism that allows Si to be incorporated into GaN NWs beyond the solubility limit. It is based on the use of vicinal SiC/Si hybrid substrates. The NWs

grown on step bunches of vicinal become heavily Si doped. This is verified by the observation of high carrier concentrations in PL and high Si concentrations by SIMS. Moreover, Raman spectroscopy in concert with quantum chemical modelling indicates the formation of Ga(Si)N solid solution. The microscopic mechanism responsible for heavy doping and even alloying beyond the solubility is diffusion driven by the mechano-chemical effect, which allows extremely efficient injection of Si atoms at the step bunces of vicinal SiC/Si substrates.

Moreover, a possibility of GaAs, AlGaAs and InAs nanowires growth on a silicon substrate with a nanoscale buffer layer of silicon carbide has been demonstrated for the first time. The diameter of these NWs is smaller than diameter of similar NWs which were grown on a silicon substrate, because of significant lattice mismatch. In particular, InAs NWs diameter was less than 10 nm. In addition, based on photoluminescence measurements, it was found that, in case of AlGaAs NWs growth on such substrates, complex structure forms.

Finally, in this work we present the results of a set of experimental studies on the synthesis by molecular beam epitaxy and the study of the morphological and optical properties of InGaN nanostructures of branched morphology (resembling nanoflowers, NF) directly on the surface of the silicon substrate.

Formation of luminescent nanoclusters by etching silver nanoparticles with biomolecules

Kubenko V.G. [1], **Chuyko Ya.V.**[1], **Reveguk Z.V.** [1], **Kapitionova M.A.** [1], **Kononov A.I.** [1]

[1]Department of Molecular Biophysics and Polymer Physics, Saint-Petersburg State University, 199034 St. Petersburg, Russia

Abstract. A new approach to the preparation of silver clusters on biomolecule matrices was tested. Silver nanoparticles were synthesized and then etched by different proteins, cytosine rich DNA sequences and peptides. Dark and luminescent silver nanoclusters were detected and described.

Introduction

Noble metal nanoclusters have attracted more and more attention over the past decade. Luminescent metal nanoclusters can serve as sensors for various analytes, and can be used in biomaging applications [1]. Metal nanoclusters are simple to synthesize and possess high brightness and photostabilty in comparison with dyes and quantum dots. Biomolecules are very convenient templates for cluster growth. Luminescent nanoclusters based on biomolecules are well compatible with living systems. Biopolymer matrices also protect metal clusters from an aggressive environment [2]. The mechanism of the cluster growth on polymer templates have been unclear. The typical synthesis includes the reduction of silver ions bound to the matrix by sodium borohydride. We have tested another approach, namely etching of silver nanoparticles (NPs) in the presence of DNA and protein matrices [3].

Experiment

Spherical silver NPs were synthesized on an ice bath by reducing silver ions with sodium borohydride [4]. Then, nanoparticle and biomolecule (cytosine rich oligonucleotides, glutathione (GSH), bovine serum albumin (BSA), lysozyme, insulin) solutions were mixed in equal volumes and stored at 37 °C. Next, measurements of the absorption and luminescence spectra were made. Changes in the absorption spectrum of nanoparticles were noticed in 24 hrs.

Results and discussions

GSH, BSA and lysozyme are able to completely dissolve silver NPs. Silver luminescent clusters with excitation / emission maxima at 390/460 nm were detected on BSA. The presence of insulin had

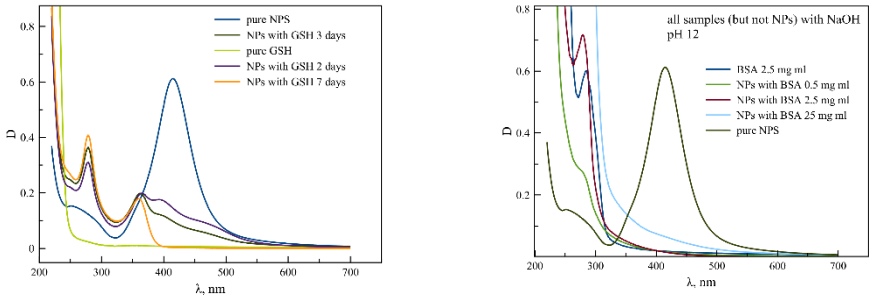

a weak effect on the nanoparticles. Lysozyme dissolved NPs, however, no luminescent clusters were observed. In GSH solution, “dark” clusters are formed. They have two excitation bands at 280 nm and 360 nm and the emission maximum at 620 nm.

Figure 1. Abosrbance spectra of silver NPs with GSH (left)and BSA (right).

For all used DNA sequences, a decrease and a small blue shift of the plasmon absorption maximum were observed. Therefore, cytosine-rich oligonucleotides are capable of etching silver NPs, however, they are not able to completely dissolve the nanoparticles. Some DNA sequences showed the presence of a luminescent fraction of the clusters. After adding the reducing agent to the oligonucleotide solution, filtered to remove excess nanoparticles and silver ions, luminescent silver nanoclusters typical for these sequences were synthesized.

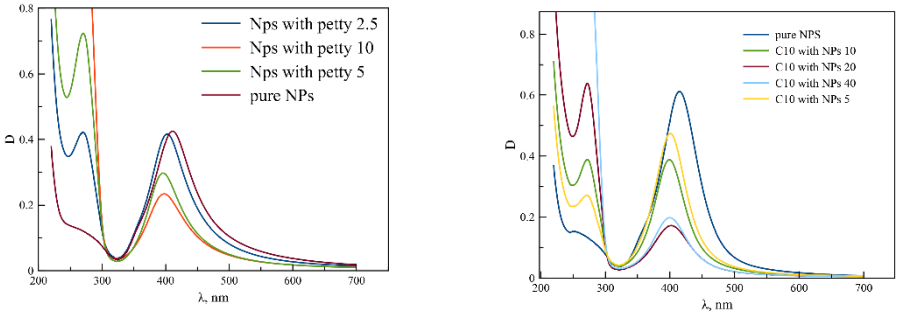

Figure 2. Abosrbance spectra of silver NPs with cytosine rich DNA sequences.

Acknowledgments

This work was carried out using equipment of the Centre for Optical and Laser Materials Research and the Centre for Diagnostics of Functional Materials for Medicine, Pharmacology and Nanoelectronics at Saint Petersburg State University.

References

[1] Volkov I., et al., Nucleic Acids Research, Vol. 46, No. 7 3543–3551 (2018).
[2] Obliosca J. M., Biosensors, 3, 185−200 (2013).
[3] Shengqiang Hu, Jianxiu Wang and Juewen Liu, JPC C, 123, 12015−12022 (2019).
[4] Larmour I.A. et al, J. of Raman Spectroscopy, 43(2):202-206 (2012).